

INTERNATIONAL JOURNAL
OPTICA ACTA

European Journal
of Optics

Journal Européen
d'Optique

Europäische Zeitschrift
für Optik

VOLUME 8

Printed and Published by

TAYLOR & FRANCIS LTD

RED LION COURT, FLEET STREET, LONDON, E.C.4

CONTENTS OF VOLUME 8

NUMBER 1—JANUARY 1961

	Page
Effect of retinal image motion on visual acuity. OLOF BRYNGDAHL ..	1
A 'sky lens' for an auroral spectrograph. N. J. RUMSEY	17
The saturation of spectral colours viewed in a small field. K. J. MCCREE	21
An estimation of Smith-Purcell effect as the light source in the infra-red region. K. ISHIGURO and T. TAKO	25
Beugungsexperimente zur Vielstrahlinterferometrie. G. SIMONSOHN ..	33
Vielstrahlinterferenz als Hohlleiterproblem. G. SIMONSOHN	49
Multiple diffraction by an aperture in a hard screen. SAMUEL N. KARP and JOSEPH B. KELLER	61
Interferometric methods for the photographic production of large gratings. J. M. BURCH and D. A. PALMER	73
Some factors in brightness discrimination with constraint of retinal image movement. M. B. CLOWES	81
Diffraction of partially coherent light by a plane aperture. GEORGE B. PARRENT, Jr. and THOMAS J. SKINNER	93
Addendum	103
Notice of Colloquium on Optical Materials, July 1961	104

NUMBER 2—APRIL 1961

The transmission and degree of polarization of quarter-wave stacks at non-normal incidence. PHILIP BAUMEISTER	105
Visual recovery following local adaptation of the peripheral retina (Troxler's Effect). F. J. J. CLARKE	121
The reflectivity of glass and aluminium gratings at grazing incidence below 1000 Å. R. S. CRISP	137

	Page
Measurement of the horizontal extent of Panum's Area by a method of constant stimuli. D. A. PALMER	151
Restitution des images aberrantes par le filtrage des fréquences spatiales. III. Restitution de l'image prise avec un filtre à deux foyers. JUMPEI TSUJIUCHI	161
Errata	168
The optical performance of windows with axial temperature gradients. J. V. RAMSAY	169

CORRESPONDENCE

Approximate synthesis of a prescribed diffraction pattern by means of different aperture distributions. LUIGI CAPRIOLI, ANNA MARIA SCHEGGI and GIULIANO TORALDO DI FRANCIA	175
Reviews	181

NUMBER 3—JULY 1961

On some degenerate cases of thin film interference. PAUL G. KARD and ZDENĚK KNITTL	185
Colorimetric daylight illuminant with high ultra-violet content. B. HISDAL	199
Definitionshelligkeit und Kontrastübertragung. F. I. HAVLIČEK ..	213
Optical alignment devices based on a two-mirror system. J. DYSON ..	217
Focal tolerances and best focal setting for model photographic images with primary spherical aberration. E. H. LINFOOT	233
Thin-lens aberration theory. C. G. WYNNE	255
Interpretation des aspects particuliers des images obtenues dans une expérience de détramage. MME M. MARQUET et J. TSUJIUCHI ..	267
Reviews	279
Errata	279

NUMBER 4—OCTOBER 1961

	Page
Scattering of evanescent waves by cylindrical structures. LAURA RONCHI, VERA RUSSO, GIULIANO TORALDO DI FRANCIA and CORRADO ZACCAGNINI	281
On the reversibility of light beams in conducting media. IVAN ŠANTAVÝ	301
A simple after image method demonstrating the involuntary multi- directional eye movements during fixation. F. J. VERHEIJEN ..	309
The sensitivity performance of the eye, in the presence of various limiting mechanisms of different origin. M. v. MENTS	313
The refractive index of materials from 0.2μ to 5μ . J. W. GATES, K. J. HABELL and A. JACKSON	323
The colour change of monochromatic light with retinal angle of incidence. J. M. ENOCH and W. S. STILES	329
International Commission for Optics. Nomenclature for Fourier transforms of spread functions	359

Effect of retinal image motion on visual acuity

by OLOF BRYNGDAHL

Institute of Optical Research, Royal Institute of Technology,
Stockholm 70, Sweden

(Received 9 May 1960)

An attempt to correlate visual acuity measurements with eye movements has been made. The Linear Filter theory (applicable only as far as small retinal illumination increments are concerned) has been applied to the system, eye/lens/retina. A description of the transmission of spatial information over a single-channel system has been performed. This requires translation of intensity functions into one-dimensional time-functions by the scanning motion of the eye. An image sharpening mechanism of the eye can be related to an overall sine wave response characteristic which decreases at very low line numbers. In this way, the visual acuity of single-line targets can be explained.

1. INTRODUCTION

The present paper contains an examination of some of the mechanisms occurring in the human eye (characteristics of the eye) in an attempt to account for the overwhelming superiority of visual acuity over that which might be expected from the gross optical construction of the eye. Many attempts have been performed in order to relate visual functions and registrations of eye movements. Visual acuity measurements—(a) using grid targets and liminal brightness increment experiments, and (b) using a single fine wire where consideration must be given to both thickness and contrast, i.e. a combination of the measurements in the first case—are often performed. Physiologists have long been confused concerning the comparison of the results obtained using the different methods.

It has been confirmed that the eye presents different visual acuities for different test objects [1], [2], [3]. Using the results provided by the new, refined methods for studying eye movements and by the modern mathematical treatment of optical processes and information channels, it is possible to get a rough explanation of the different effects occurring in measurements on visual acuity. It also opens a way for a better understanding of the functions of the human eye and the different problems in vision.

The desire for objectivity cannot be fully satisfied in this field of research. Only the part of the vision cascade from the object to the retina can be examined in an objective way because an investigation of the other parts is dependent on a yes or no answer by the subject. A subjective result is therefore also obtained when studying the full cascade from the object to what one really comprehends (i.e. object→brain).

With the recent developments of eye-movement recording techniques, a way has been opened for an examination of the information channel existing between eye and brain. Questions in this field can be treated by either information theory or linear filter theory. In the following, the linear filter theory will be employed.

Measurements of the CT- (contrast transfer, sine-wave response) curve of the visual system have recently been made [4, 5, 6]. A transfer characteristic (overall sine-wave response) which decreases at very low line numbers (see figure 1) has been found. This curve can be related to many functions of the visual system.

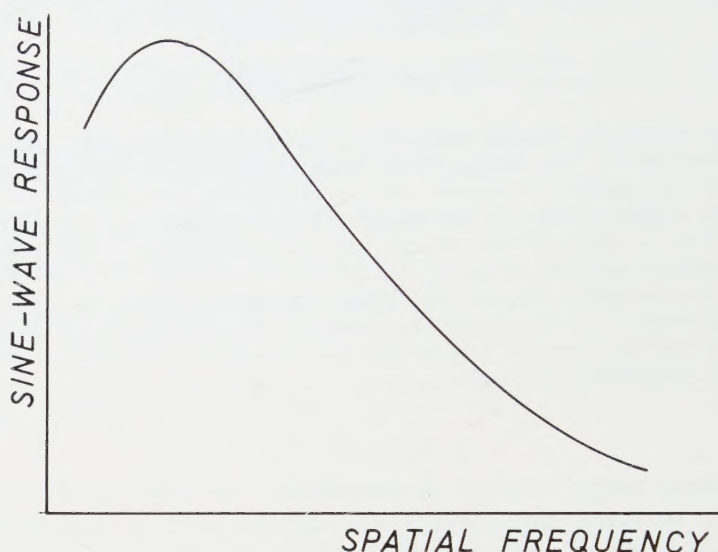


Figure 1. Response of visual system to sine-wave patterns.

2. MOVEMENTS OF THE HUMAN EYE

In recent years, eye movements have been studied with very sensitive and exact methods [7, 8, 9, 10]. It has been found that the eye performs movements all the time, without which one would lose the possibility of perception (maintenance of vision), i.e. the movements of the eye play a very important part in the vision process.

Work on eye movements has shown that, when a subject fixes his vision on an object as steadily as possible, the following eye movements are present [8, 11]:

(a) a tremor of amplitude of the order of 15 sec arc and frequency ranging from 30 to 80 c.p.s. with a maximum at 50 c.p.s.;

(b) a series of flicks of up to 20 min arc occurring at irregular intervals ranging from 0.03 to 5.0 sec;

(c) slow drifts of up to 5 min arc in the intervals between the flicks.

Because of the importance of the eye movements in the visual process, several attempts have been made to assess their importance by studying the effect on visual acuity when the eye views an object which moves so that its image on the retina does not move across the retinal receptors [11, 12]. This is described as a stabilized retinal image ('stopped image') and, in this way, it is possible to cut out the eye movements, i.e. a signal constant in time is supplied to the retinal elements. The recent development of the 'stabilized image' technique presents the possibility of performing experiments in which retinal image motion is a controlled variable. A stabilized image may be obtained by reflecting the light from a stimulus projector on to a surface in front of the observer by means of a mirror attached to a contact lens worn in the viewing eye. The angular

movement of the reflected image on the screen is twice that of the eye. However, the screen is viewed not directly but over an optical path twice the length of the path projector-mirror-screen. This arrangement results in an apparent halving of the image motion on the screen; thus the net effect is that the retinal image moves through exactly the same angular distance as the eye. Although the line of vision shifts with the eye movements occurring during fixation, the projected stimulus moves with it and thus remains in the same retinal position.

3. DYNAMIC NATURE OF THE SYSTEM FOVEA-BRIGHTNESS PERCEPTION

In recent research [13, 14] dynamic investigation has been applied to the visual system by means of sinusoidally time-modulated illumination. The system works logarithmically for large variations at low frequencies—an extension of Fechner's law for the dynamic case—while for limited variations *the system appears to work linearly*. It is shown quite generally, using Talbot's law, that at the critical frequency the system must work linearly. However, at single phenomena, such as a sudden variation in luminance or a single light-impulse, the system does not work linearly.

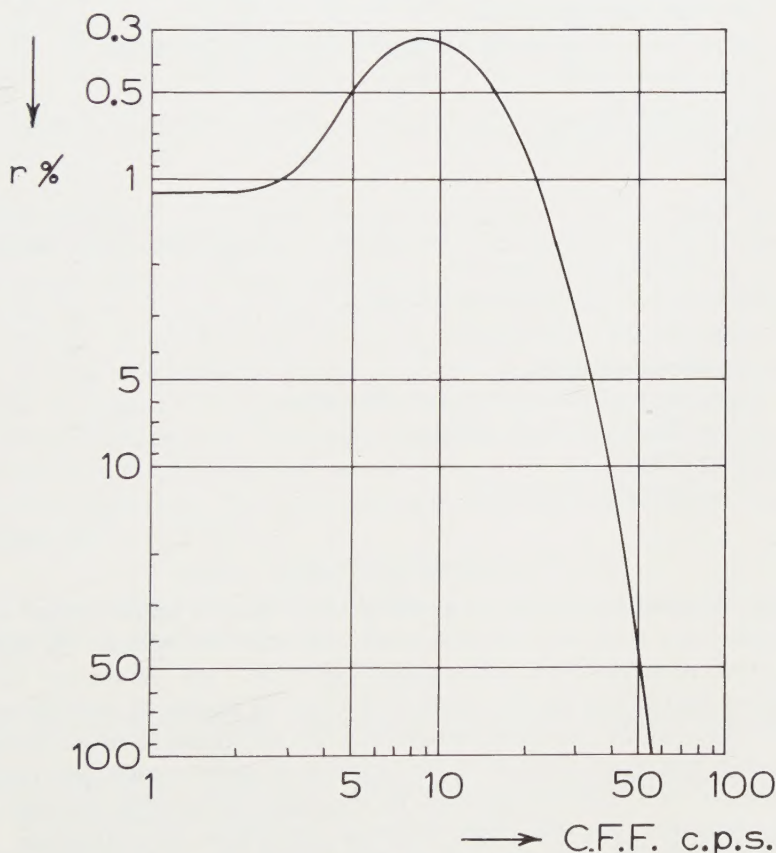


Figure 2. Attenuation characteristic for white light (375 trolands retinal illumination = 12 foot-lamberts field luminance) and a sinusoidal variation in the luminance of the system fovea-brightness perception, according to ref. [13]. The modulation depth of the luminance of the test field r in per centage is plotted *versus* C.F.F. (critical flicker frequency) in c.p.s.

The frequency response of the visual organ for cone seeing (attenuation characteristic) shows a filter action for intermittent light. The response function has a maximum at about 10 c.p.s. (see figure 2)†.

This opens a way to determine the constants of the visual transfer system (cf. figure 3) and to explain a correlation between eye movements and CT-curves.

4. EYE MOVEMENTS—A TRANSFER SYSTEM OF SPATIAL FREQUENCIES

4.1. List of symbols

A	Electrical signal arising from photoelectric process.
\hat{A}	Amplitude of electrical signal.
\hat{B}	Amplitude of tremor oscillation.
d	Iris diameter.
E	Retinal illumination.
E_s	Sinusoidal component of total receptor illuminance.
\hat{E}	Amplitude of sinusoidal component of total receptor illuminance.
f	Time frequency; $f(x, y)$ a function of x and y .
I	Field luminance.
\bar{I}	Average field luminance.
\hat{I}	Amplitude of sinusoidal component of field luminance.
m, n	Summation indices.
N	Line-number.
r	Modulation depth.
S	Area.
t	Time.
T	Line-transmittance of a receptor, i.e. transmittance of the line-image falling on to a receptor.
v	Velocity of linear eye movement.
$w = 2\pi N$	Angular spatial frequency.
x	Spatial coordinate.
x_r	Spatial coordinate referred to the retina.
δ	Cone diameter; δ -function.
ϑ	Phase angle.
$\omega = 2\pi f$	Angular time frequency.

4.2. Eye movements—a transfer system

The eye lens and pupil may be grouped together as a single optical system, which images the visual scene on to a mosaic of retinal receptors. In the fovea centralis, these receptors have a diameter (δ) $\approx 2 \times 10^{-4}$ cm (20 sec arc) [15, 16]. The image is scanned across the receptor surface by means of eye movements.

The accuracy in the reproduction of detail by an optical transfer system can be specified in the space domain by its response of point-image, line-image, or edge transition, or it can be specified in the spatial frequency domain by its Fourier transforms: the sine-wave response and phase-characteristics. Here we will regard the sine-wave spectrum as the basic characteristic determining the quality of the vision process, because any form of luminance variation can be expressed by Fourier series of sine-wave components with particular amplitude

† See note on page 15.

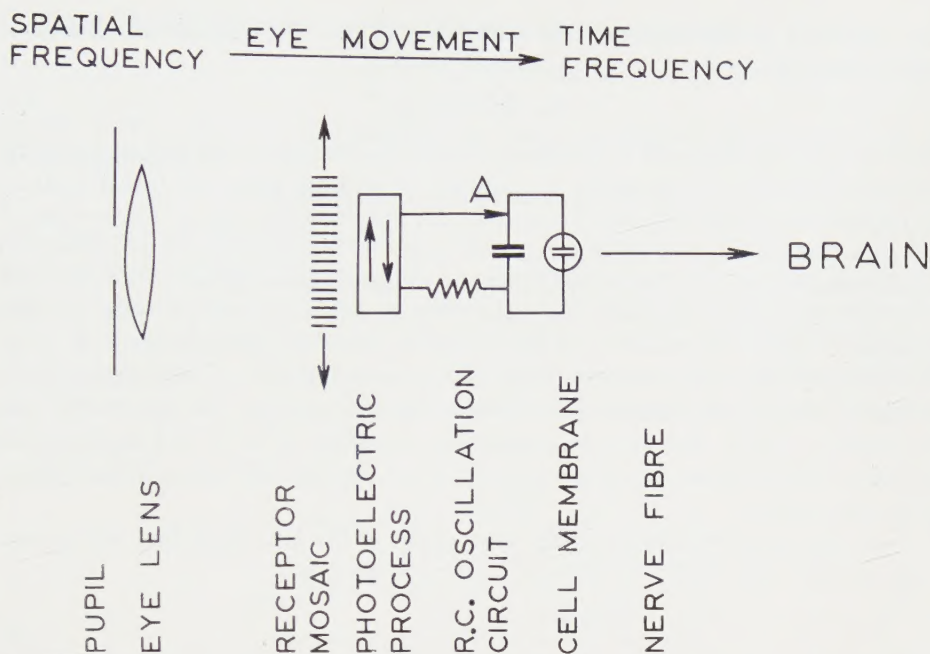


Figure 3. Simplified diagram of analogue representing the visual system.

and phase relations. To avoid waveform distortion the sine-wave response is determined with small signals for which all transfer characteristics are linear.

The transmission of visual information over a single-channel cone-nerve fibre system (cf. figure 3) requires translation of two-dimensional luminance functions $I=f(x,y)$ into one-dimensional electric signals $A=f(t)$, which is accomplished by the process of scanning. Because of the complexity of two-dimensional functions, we choose here the luminance distribution of an optical line pattern, which can be expressed by a one-dimensional periodic function (Fourier series) containing an average term and one or a series of harmonic sine-wave terms termed a line spectrum. The luminance of a one-dimensional sine-wave pattern is expressed by

$$I(x) = \bar{I} + \hat{I} \cos wx \quad (1)$$

where \bar{I} is the spatial average of $I(x)$ and \hat{I} is the amplitude of the sinusoidal luminance having the spatial angular frequency

$$w = 2\pi N; \quad (2)$$

N is the line-number (spatial frequency) defined as number of lines in a unit length.

We consider here a single cone (receptor)—the resultant illumination falling upon it is modulated in time by the eye movements.

The illuminance of the retinal image depends upon the luminance of the external light source and the area of the entrance pupil of the eye. Pupil size itself, however, depends upon the flux density of the light falling on the eye [17]. Here, we can replace the liquid-immersed optical system of the eye by an automatically focused lens having a focal length in air of 17 mm [16] and an

iris controlled by the average field luminance [17]. The retinal illuminance E in trolands is given by

$$E = 2.69d^2I(x_r) \quad (3)$$

where d is the iris diameter in millimetres and I is the luminance in foot-lamberts corresponding to x_r (position on the retina). The total light flux transferred by the receptor is obtained by convolution, i.e. by scanning the retinal illumination E with the transmittance T of the receptor area. T (termed line-transmittance) is the transmittance of a line-image falling on to the receptor surface. We presume here that the cone transmittance probably is non-uniform but has circular symmetry. It is important to keep in mind that the transmittance is two-dimensional, while the corresponding line-transmittance is a one-dimensional function, having eliminated one variable by integration permitted by the line-object. Thus, the line-transmittance function T is a one-dimensional equivalent which depends on the orientation of the receptor coordinate relative to the line-object.

With this notation the sinusoidal component of the total light flux taking part in the primary photoelectric process in the receptor is

$$\mathbf{E}_s = \frac{\text{const } d^2 \hat{I}}{S} \int_{\delta} T(x - x_r) \cos wx \, dx. \quad (4)$$

This function (instantaneous receptor input signal) represents a pure sine wave

$$\mathbf{E}_s = \hat{\mathbf{E}} \cos wx_r \quad (5)$$

and S is equal to the area of the receptor

$$S = \int_{\delta} T(x) \, dx = \pi \delta^2 / 4, \quad (6)$$

$$\hat{\mathbf{E}} = \frac{\text{const } d^2 \hat{I}}{S} \int_{\delta} T(x) \cos wx \, dx, \quad (7)$$

which shows that the amplitude $\hat{\mathbf{E}}(w)$ for each spatial frequency is obtained by multiplying the amplitude of the retinal sinusoidal illumination by a factor which is proportional to the contrast transmittance factor of the receptor area for the spatial frequency w and to the iris area depending on the field average luminance. This is true for an aperture with circular symmetry like the cone in question here.

From equations (5) and (7) we get the sinusoidal component of the receptor input signal

$$\mathbf{E}_s = \hat{\mathbf{E}} \cos \{w\hat{B} \sin(\omega t + \vartheta)\} \quad (8)$$

where $\hat{B} \sin(\omega t + \vartheta)$ gives the time displacement of a given point on the retina due to eye movements if these, for the sake of simplicity, are looked upon as harmonic oscillations with an angular time frequency ω . This certainly applies to the tremor with good approximation. ϑ is the phase between x_r and ωt . \hat{B} is here the amplitude (x -component) of the tremor oscillation.

This waveform, equation (8), is oscillatory with a Fourier spectrum [18]:

$$\cos \{w\hat{B} \sin(\omega t + \vartheta)\} = J_0(w\hat{B}) + 2 \sum_{n=1}^{\infty} J_{2n}(w\hat{B}) \cos 2n(\omega t + \vartheta). \quad (9)$$

The fundamental has therefore a frequency of about 100 c.p.s., or between 60 and 160 c.p.s.

From an object presenting the following spatial frequencies

$$\sum_m \hat{I}_m(w_m, x) \cos w_m x \quad (10)$$

on the retina receptor and considering only one tremor movement $\hat{B} \sin \omega t$, an a.c. potential

$$A_m = \hat{A}_m(\delta, w_m, x, d) \cos(w_m \hat{B} \sin \omega t) \quad (11)$$

will then act on the nerve bundle. (\hat{A} is proportional to the luminance \hat{E} , if we regard the transfer function of the photoelectric process in the receptor as a linear complex ratio.) In the receptor signal A_m , the amplitude \hat{A}_m is somewhat reduced and a phase difference is introduced due to the limited rate of the photoelectric reactions in the receptors. This effect does not have to be considered for frequencies well below 500 c.p.s. which is the upper limit for the frequency spectrum in a nerve fibre [19].

If $w_m B \ll 1$, we then get

$$A_m = \hat{A}_m \left(1 - \frac{w_m^2 \hat{B}^2}{2} \sin^2 \omega t \right), \quad (12)$$

or

$$A_m = \hat{A}_m \left(1 - \frac{w_m^2 \hat{B}^2}{4} - \frac{w_m^2 \hat{B}^2}{4} \cos 2\omega t \right).$$

The fact that the *main* signal-transmitting system of the eye, consisting of 'on', 'off', and 'on-off' fibres, does not transmit d.c. signals [20] (indicated by blocking capacitor and leaky resistance in the main signal lead in figure 3) gives the following expression for the electrical responses to spatial frequencies of the object by a single receptor unit in the eye:

$$A_m = \hat{A}_m \frac{w_m^2 \hat{B}^2}{4} \cos 2\omega t. \quad (13)$$

The frequency of the signal is twice that of the tremor oscillation and the amplitude is a function of \hat{A}_m , w_m and \hat{B} . Moreover it is clear that it is easier for high spatial frequencies to pass through.

On the other hand, let us look somewhat closer at a linear scanning action such as drift or flick given by

$$x = vt$$

with the sinusoidal term of the receptor signal

$$\hat{A} \cos wvt.$$

We now have the receptor signal (tremor + linear motions)

$$A = \int_0^\infty \hat{A}(w) \cos \{w(vt + \hat{B} \sin \omega t)\} dw. \quad (14)$$

The cosine term can be expanded in the following form [18]:

$$\begin{aligned} \cos \{.. \} &= \cos wvt \cos (w\hat{B} \sin \omega t) - \sin wvt \sin (w\hat{B} \sin \omega t) \\ &= J_0(w\hat{B}) \cos wvt + \sum_{n=1}^{\infty} J_{2n}(w\hat{B}) \cos (wv + 2n\omega)t \\ &\quad + \sum_{n=1}^{\infty} J_{2n}(w\hat{B}) \cos (wv - 2n\omega)t + \sum_{n=0}^{\infty} J_{2n+1}(w\hat{B}) \cos \{wv + (2n+1)\omega\}t \\ &\quad - \sum_{n=0}^{\infty} J_{2n+1}(w\hat{B}) \cos \{wv - (2n+1)\omega\}t. \end{aligned} \quad (15)$$

By comparing (9) and (15), we conclude that the linear scanning action introduces a new component in the receptor signal. For $wv \ll \omega$, we get from (14) and (15):

$$A = \int_0^\infty \hat{A}(w) \{J_0(w\hat{B}) \cos wvt + 2 \sum_{n=1}^\infty J_{2n}(w\hat{B}) \cos 2nwt\} dw. \quad (16)$$

The second term of (16) has already been treated in (12) and (13). Considering only the first term we have

$$A = \int_0^\infty \hat{A}(w) J_0(w\hat{B}) \cos wvt dw. \quad (17)$$

If \hat{A} is independent of w (frequency spectrum of a δ -function object) we then have

$$A_\delta = \hat{A} \int_0^\infty J_0(w\hat{B}) \cos wvt dw. \quad (18)$$

This integral is the well-known Fourier cosine transformation of the Bessel function $J_0(w\hat{B})$:

$$\int_0^\infty J_0(w\hat{B}) \cos wvt dw = \begin{cases} (\hat{B}^2 - v^2 t^2)^{-1/2} & \text{if } 0 < vt < \hat{B}, \\ \infty & vt = \hat{B}, \\ 0 & vt > \hat{B}. \end{cases} \quad (19)$$

To obtain the signal A in the general case we have (either to integrate (18) over an infinite set of δ -functions or) to solve (17) using the convolution theorem:

$$A = \int_0^\infty \hat{A}(w) J_0(w\hat{B}) \cos wvt dw, \\ A = \frac{1}{2} \int_{vt-\hat{B}}^{vt} F(x) H(vt-x) dx = \frac{1}{2} \int_0^{\hat{B}} F(vt-x) H(x) dx \quad (20)$$

(the integral is performed between 0 and \hat{B} —outside this interval the integrand vanishes according to equation (19)) where

$$F(x) = \sqrt{\left(\frac{2}{\pi}\right)} \int_0^\infty \hat{A}(w) \cos wx dw, \quad (21)$$

and

$$H(x) = \sqrt{\left(\frac{2}{\pi}\right)} \int_0^\infty J_0(w\hat{B}) \cos wx dw = \sqrt{\left(\frac{2}{\pi}\right)} (\hat{B}^2 - x^2)^{-1/2}. \quad (22)$$

Note on the mathematical transformation:

Without loss of generality, we suppose $\hat{A}(w)$ in equation (17) to be an even function in order to make possible a general mathematical treatment:

$$\alpha(w) = \hat{A}(w), \quad \alpha(-w) = \hat{A}(w).$$

$J_0(w\hat{B})$ is also an even function.

We have now the convolution integral

$$\begin{aligned} \mathcal{A} &= \int_{-\infty}^{+\infty} \alpha(w) J_0(w\hat{B}) \exp(iwvt) dw = \int_0^\infty \hat{A}(w) J_0(w\hat{B}) \exp(iwvt) dw \\ &\quad + \int_0^\infty \hat{A}(w) J_0(w\hat{B}) \exp(-iwvt) dw \\ &\quad \underbrace{\int_{-\infty}^0 \alpha(w) J_0(w\hat{B}) \exp(iwvt) dw}_{\text{---}} \\ &\quad - \underbrace{\int_0^\infty \alpha(w) J_0(w\hat{B}) \exp(iwvt) dw}_{\text{---}} \end{aligned}$$

Replacing w by $-w$, we obtain :

$$\mathcal{A} = \int_0^{\infty} \hat{A}(w) J_0(w\hat{B}) 2 \cos wvt \, dw = 2A = \int_{-\infty}^{+\infty} \alpha(w) J_0(w\hat{B}) \exp(iwvt) \, dw,$$

$$2A = \int_{-\infty}^{+\infty} \alpha(w) J_0(w\hat{B}) \exp(iwvt) \, dw = \int_{-\infty}^{+\infty} F(x) \cdot H(vt - x) \, dx,$$

$$F(x) = \frac{1}{\sqrt{(2\pi)}} \int_{-\infty}^{+\infty} \alpha(w) \exp(iwx) \, dw = \frac{2}{\sqrt{(2\pi)}} \int_0^{\infty} \hat{A}(w) \cos wx \, dw,$$

$$H(\phi) = \frac{1}{\sqrt{(2\pi)}} \int_{-\infty}^{+\infty} J_0(w\hat{B}) \exp(iw\phi) \, dw = \frac{2}{\sqrt{(2\pi)}} \int_0^{\infty} J_0(w\hat{B}) \cos w\phi \, dw,$$

for the case where the object is symmetrical ($F(x) = F(-x)$).

We therefore have the following expression for the signal :

$$A = \frac{1}{2} \int_{-\infty}^{+\infty} F(x) H(vt - x) \, dx.$$

4.3. *Physiological conditions of the information channel retina→brain*

The fundamental nature and the inherent properties of the receptors and the design of the accessory structures on which the receptors are deployed determine how the patterns of neural activity they generate will represent the external information. The end result of receptor excitation is the generation of nervous influences in its attached nerve fibre [21]. As yet not much is known about the nature of the excitatory process following the initial photoelectrical reaction in visual receptors until one comes near the end of the receptor process where the actual production of nerve impulses in the axon of the excited neuron in the receptor unit occur. Changes occur in the electrical polarization of the cell membrane of the neuron which are associated with the trains of impulses initiated by this cell when the receptor unit is illuminated. When the retina is illuminated, the cell membrane becomes somewhat depolarized, and simultaneously there is a speeding up of the discharge of impulses in its axon. Such depolarization is referred to as a 'generator potential' [23], in the belief that the nerve impulses are generated by local electric currents flowing as a result of the difference in potential between the axon and the depolarized cell body. The discharge of trains of impulses by depolarized neurons is a familiar process in neurophysiology. For the photo-receptor, the question how the initial photoelectrical reaction produces the depolarization almost nothing is known.

4.4. *Connections between the model of the eye and anatomical data*

Figure 4 contains a schematic representation of the signal A arising from the photoelectrical process in the receptor acting on the nerve fibre with time. The photo-receptors use an amplitude, heavily time-influenced code which translates signals from one energy modality into another. This transducer operates on a pulse-code modulation characteristic much like that which would be anticipated for a leaky resistance-condenser coupling decay characteristic. In figure 4 is shown the dependence of the frequency of eye movements on the characteristics of the signals referred to the side before the filter. It seems as though we may find in this curve an explanation for the upper boundary (about 50 bits/sec) for the human information channel.

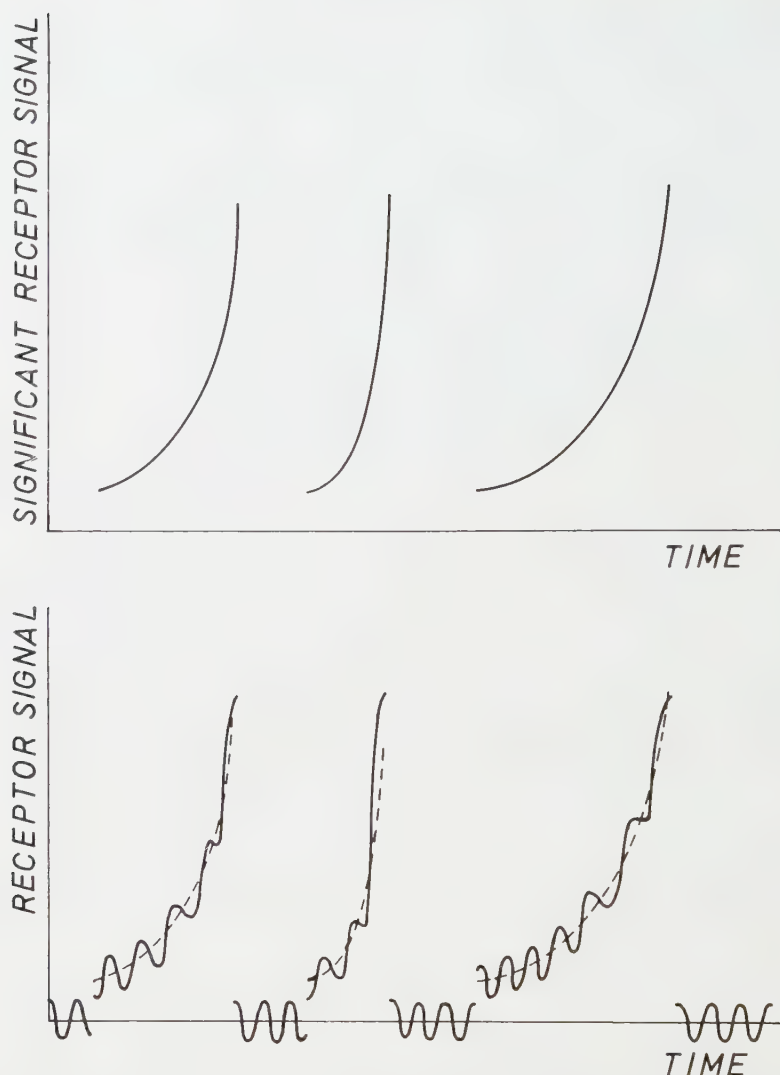


Figure 4. Receptor signal *versus* time. Graphical representation of equation (16) when A is independent of ω .

In the receptor, the light energy produces an electric potential (A) which acts on a nerve cell membrane—this membrane corresponds to the RC oscillation circuit in figure 3. The charging of the condenser continues until the voltage corresponding to the threshold value of the membrane is reached. The membrane is then discharged (or 'depolarized') and a nerve impulse is propagated. The membrane then recharges (or 'repolarizes') and the whole process is repeated periodically—hence the frequency of the series of propagating nerve impulses observed on the optic nerve fibre is proportional to the total amount of light energy absorbed by the retina receptor [23].

The agreement between the above mentioned spectrum equation (8) and that of a frequency modulated electrical signal is noteworthy.

It is known from electrophysiological studies that most of the retinal signals to the brain are generated at the onset or removal of illumination, i.e. by the

on/off system [24]. It is also known that an upper limit to the frequency spectrum in a nerve fibre is set by the inertia of the impulse-propagating system (≈ 500 c.p.s. [19]).

Hence the visual pathway will act as a band-pass filter upon signals initiated in the photo-receptors. These signals, as has been pointed out, are oscillatory with respect to time due to eye movements and will thus escape the attenuation imposed upon the steady signals. In the absence or partial loss of eye movements, the ability of the main signal to transfer information will be partially absent, thus resulting in a partial or total loss of vision (Stabilization phenomena).

4.5. *Relations between eye movements and different regions in spatial frequency domain*

The signal (A) time-frequency is a characteristic of the transfer system (information channel) related to the velocity and frequency of eye movements. However, a connection exists between the signal frequency and the transmitted spatial frequency (c.f. equations (14) and (2))— $2\pi Nv = 2\pi f$, where N is the spatial frequency, v is the velocity of linear eye movements such as drift and flick and f is the time-frequency. In this way limited spatial frequency ranges can be correlated to different kinds of eye movements (figure 5).

A consideration of the receptor signal indicates that tremor will carry the main signal in the frequency band, 100–500 c.p.s., for spatial frequencies of about $(1 \text{ min arc})^{-1}$ or less. Drift will transduce spatial frequencies $\approx (5 \text{ sec arc})^{-1}$ into oscillations of about 12 c.p.s. in the receptor channel. Flicks with a velocity $\approx 500 \text{ min arc/sec}$ cut-off spatial frequencies higher than $(1 \text{ min arc})^{-1}$.

5. VISUAL ACUITY—AN HYPOTHESIS

We may now view the function of eye movements with respect to a very important threshold measurement—namely Visual Acuity.

It is one of the features of the 'Linear Filter theory', applied here, that it has indicated the fundamental connection between Visual Acuity and Contrast Discrimination.

Experimentally, it is possible to distinguish between two orders of Visual Acuity:

- (a) for repetitive test objects $\approx 1 \text{ min arc}$ separation [1];
- (b) for single test objects $\approx 1 \text{ sec arc}$ width [2, 3].

At a normal illumination of about 10 foot-lamberts, the resolution limit for the eye lens (assumed perfect) will be $\approx 3 \times 10^{-3} \text{ mm}$. The equivalent focal length of an average adult eye (distance between second nodal point and image) with accommodation relaxed is very nearly 17 mm. Hence the resolution limit of the eye corresponds to an angle of $3 \times 10^{-3}/17 \text{ rads} = 0.00018 \text{ rads} = 40 \text{ sec arc}$ [16].

When account is taken of probable aberrations [25], this figure (based on the Rayleigh criterion) agrees with the first category of visual acuity.

With grid targets, Ratliff [26] demonstrated that visual acuity is inversely related to the magnitude of the high-frequency tremor under normal viewing conditions. On the other hand, with single-line targets, Krauskopf [27] found that oscillations at frequencies below 10 c.p.s. may be constructive if they are of sufficient amplitude (1 min arc peak-to-peak) and that high frequency motion appears to have a detrimental effect.

The response function of a lens falls off rapidly with spatial frequency. Moreover the aperture response of the photo-receptors further alters the signal and it seems difficult to account for the lower order of visual acuity unless we introduce some super-linearity at the very high spatial frequencies involved (i.e. an image-sharpening mechanism). The existence of such a mechanism seems likely in view of the following experimental data.

Most visual acuity experiments are made with high contrast step functions or sharp-edged test objects. They are observed as a gradual change in intensity and a process of contour enhancement like a second-difference correction occurs [28]. A finite gradient of illumination presented in a visual scene gives the observer a feeling of characteristic light and dark bands located at points of discontinuity—i.e. Mach bands [29].

A similar effect is known from observations of photographic emulsions (Eberhard or adjacency effect [30, 31]) and is described by a CT- (contrast transfer) curve which rises above 100 per cent for a certain range of spatial frequencies. This effect arises in part from the grain size of the emulsion and the complex chemical process subsequently undergone (development effects).

The most probable site for such an abnormal response function would be in the band-pass filter of the retina and would result from the existence of resonance effects. Such resonance effects have long been recognized in vision—(Talbot effect) [32]—and they arise mostly from the storage time in the receptors (Schade) [19]. Memory and experience contribute much to the interpretation of levels and the loss of amplitude response at low line numbers by incomplete restoration which must be taken into consideration to obtain the dynamic operating response of the eye to complex wave forms as interpreted by the brain. Other effects which contribute to the amplitude response at low spatial frequencies are the diffusion of the photo-pigments and the integration effect which is carried out by the bipolar- and ganglion cells which, at high illumination levels, gather and relay signals from a few receptors and, at low levels, integrate signals from thousands of receptors for transmission over a single nerve fibre [21]. This is known as inhibitory interaction [33] (when more than two interacting receptors are illuminated simultaneously, each is subject to the combined inhibitory influences from all the others—if the influences on a given unit are measured by the reduction they produce in its frequency of nerve impulse discharge, then the combined effect of all the other units is simply given by the sum of the influences exerted by each) [24]. This inhibitory interaction is caused by the fact that the patterns of optical nerve fibre activity yield a distorted representation of the patterns of the incident illumination. This distortion serves a useful function since it is clear that inhibitory interactions must enhance contrast: brightly illuminated elements in the receptor mosaic inhibit the dimly lighted ones more than the latter inhibit the former [34]. The postulate of such an image-sharpening mechanism is further strengthened by the reported disappearance of the Mach bands in the absence of eye movements [29].

A correlation between the time-frequency response of the retina/cortex system (§ 3 and figure 2) and the contrast transfer curve of the eye can be performed by comparing the eye movements with their transferred spatial frequencies (see figure 6). The eye movements present during normal fixation

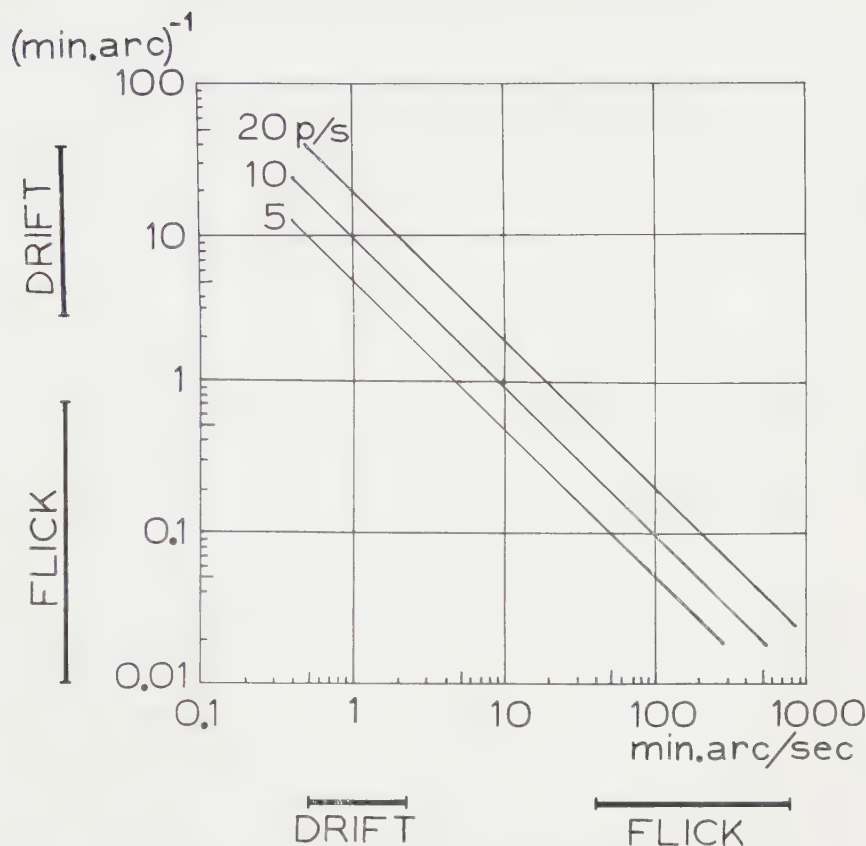


Figure 5. Correspondence between the velocity of linear eye movements and their transferred spatial frequencies for three different (5, 10 and 20 c.p.s.) signal frequencies. The ranges for drifts ($v \approx 1$ min arc/sec [12]) and flicks ($v = 40$ –800 min arc/sec [12]) have been indicated.

are a mixture of drift, flick and tremor motions. Figure 6 suggests that the flicks are capable of supporting normal vision, which is in accordance with experimental results reported by Ditchburn *et al.* [12]. The curves in figures 5 and 6 are in accordance with Krauskopf [27] and Ditchburn *et al.* [12], who demonstrated that the amplitude of the high-frequency motion (\hat{B}) had to exceed 1 min arc in order to have a demonstrable effect on the contrast threshold (corresponding to the left end of the tremor region in figure 6).

The critical resonance frequency is known to be ≈ 10 c.p.s. [13, 14] (the eye movements try to make this signal as large as possible) and it will be observed that, as in the frequency spectrum, this frequency is transduced by the *drift* for 1 sec arc targets. Thus we may account for the second category of visual acuity on the assumption of the resonance effect outlined above. *It should be noted that this mechanism will operate in all cases and thus improve all categories of visual acuity.*

The fact that the visual acuity is a function of the orientation of the target is also surprising. It has been found that the visual acuity is better when the test object is horizontal or vertical than when it is oriented obliquely [35, 36]. This is very likely related to the eye movements. Eye movements have been

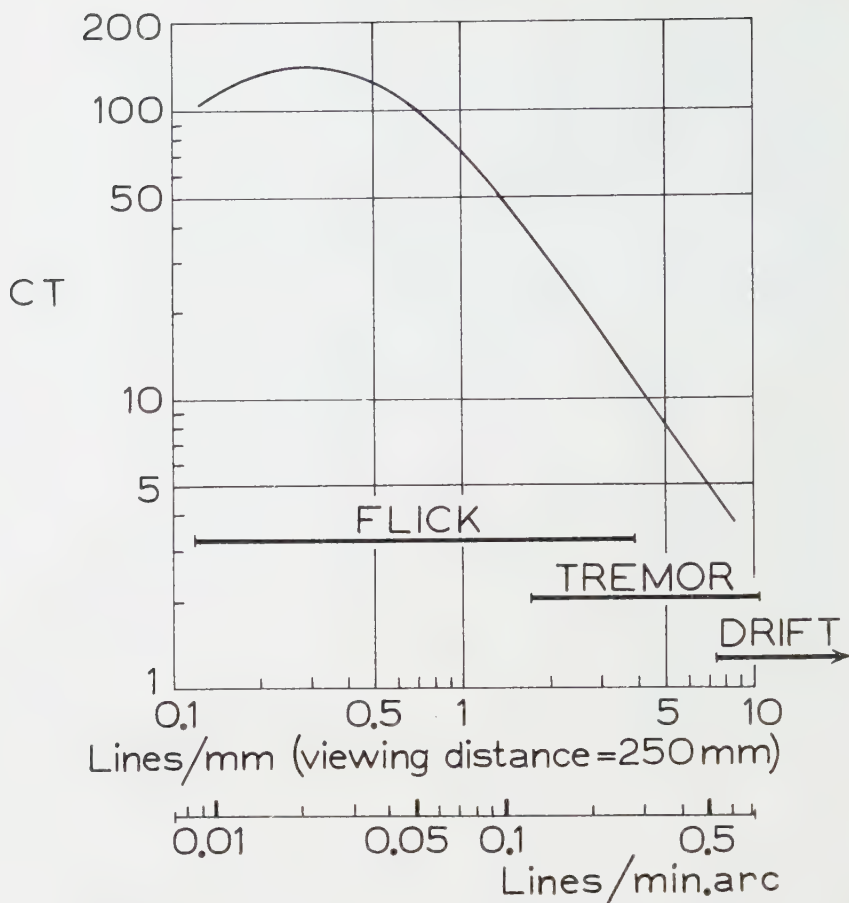


Figure 6. Response function of the eye taken from ref. [5] and correspondence between eye movement and spatial frequencies. As the average intensity is decreased, the gain of response function is reduced in the high spatial frequency region, but the maximum value remains almost unchanged. The modulation depth of the luminance of the test field (test field luminance = 200 lx = 18.6 foot-lamberts) is plotted along the vertical axis.

registered (free search) while the attention of the subject was fixed on a point light source moving with a sine motion 45° to the horizontal line. A remarkable difference was found between horizontal and vertical eye movements. The horizontal movements agreed well with the sine form while the vertical ones, on the other hand, were in poor agreement [37].

6. EXPERIMENTAL VERIFICATION

Since the existence of the resonance effect is already known, the most important further experimental verification of this hypothesis would be with respect to the compensated (stabilized) viewing conditions. The recent development of the 'stopped image' technique presents the possibility of performing experiments in which retinal image motion is a controlled variable [12, 27, 38]. It is possible to study the effect of various types of movement by stopping the image and then introducing controlled movement in the optical system.

We should then expect that the fast movements (flick+tremor) would be operative in the regeneration of targets for which the angular frequency $< 1(\text{min arc})^{-1}$ and that the slow movements (drift) would restore targets for which the angular frequency $\approx 1(\text{sec arc})^{-1}$.

An interesting point revealed by Fender is the dependence of focusing upon tremor, thus suggesting a feedback mechanism designed to maximize the tremor-transduced signals [37].

7. SUMMARY

1. Linear Field theory is applied to the system eye-lens/retina for small variations in illumination in order to obtain the relations between visual acuity and contrast discrimination. The sine-wave spectrum is regarded as the basic characteristic determining the quality of the visual process.

2. A model of the eye in which eye movements preserve visual acuity and contrast discrimination is built up. Physiological conditions and explanation of the model are given.

3. Translation of illumination variations into one-dimensional electric signals by means of eye movements are performed mathematically.

4. An image-sharpening mechanism of the eye related to physiological resonance effects, sine-wave and critical flicker frequency measurements is discussed which improves all categories of visual acuity.

5. Recently performed measurements of controlled movements of the retinal image show good agreement with this model, e.g. the predominant importance of flick movement supporting normal vision can be well understood.

6. Connections between different eye-movements and the transferred spatial frequencies are made clear. According to this model the fast eye movement (flick) is operative in the regeneration of targets of high spatial frequency $< 1(\text{min arc})^{-1}$ and the slow movement (drift) restores targets with frequency $\approx 1(\text{sec arc})^{-1}$.

Note to page 4, added in proof.

In figure 2 deLange used a 2° test field with a 60° light surround of the same luminance as the time average of his flickering field. Other spatial patterns which cause a different retinal adaptation change the region of low frequency sensitivity. The most significant result of experiments recently performed [39] is that the steep rise of sensitivity to be expected at low frequencies is restored by the use of an 'edgeless' field; a slightly flatter response curve is obtained with a dark surround. The light-surround response (figure 2) is ten times greater than the response of the 'edgeless' field in the frequency band from 2 to 5 c.p.s. The visual frequency response curves show a remarkable 'overshoot'.

Nous avons effectué un essai en vue de relier les mesures d'acuité visuelle aux mouvements de l'oeil. La théorie du filtre linéaire (applicable seulement lorsqu'il s'agit de faibles augmentations de l'éclairement rétinien) a été appliquée au système oeil-lentille-rétine. Nous avons décrit un mode de transmission de l'information spatiale sur un système à un seul canal. Ceci nécessite la conversion des fonctions d'intensité en fonctions de temps à une dimension, par l'intermédiaire du mouvement de balayage de l'oeil. Un mécanisme renforceur de l'acuité de l'oeil peut être relié à une réponse caractéristique sinusoïdale qui décroît aux très faibles fréquences spatiales. On peut expliquer ainsi l'acuité visuelle pour des mires à un seul trait.

Diese Arbeit stellt den Versuch dar, das Auflösungsvermögen des Auges in ein Funktionsverhältnis zu den Eigenbewegungen des Auges zu bringen. Die lineare Filtertheorie (nur in Bezug auf geringe Intensitätsdifferenzen) ist für das System Augenlinse/Rezeptoren der Netzhaut zur Anwendung zu kommen. Es wird eine Beschreibung der normalen unwillkürlichen Bewegungen des Auges gegeben, die die Ortsfrequenz des Objektes in Verbindung zu einer eindimensionalen Zeitfunktion bringt. Eine Kontrastübertragungsfunktion, die bei niedrigen Linienzahlen sinkt, ist als ein dem Auge eigenen Mechanismus anzusehen; er gibt dem Auge die Fähigkeit, das Bild in seinem Eindruck zu verschärfen. In dieser Weise kann das Auflösungsvermögen des Auges in Bezug auf eine Einzellinie als Objekt erklärt werden.

REFERENCES

- [1] DUKE-ELDER, W. S., 1934, *Text-book of ophthalmology*, **1**, XXIX (St. Louis, Mo.: The C.V. Mosby Co.).
- [2] SHLAER, S., 1937, *J. gen. Physiol.*, **21**, 165.
- [3] HECHT, S., ROSS, S., and MUELLER, C. G., 1947, *J. opt. Soc. Amer.*, **37**, 500.
- [4] SCHADE, O. H., 1958, *R. C. A. Rev.*, **19**, 495.
- [5] OQUE, S., 1959, *J. appl. Phys., Japan*, **28**, 531.
- [6] MENZEL, E., 1959, *Naturwissenschaften*, **46**, 316.
- [7] RIGGS, L. A., ARMINGTON, J. C., and RATLIFF, F., 1954, *J. opt. Soc. Amer.*, **44**, 315.
- [8] DITCHBURN, R. W., 1955, *Opt. Acta.*, **1**, 171.
- [9] CORNSWEET, T. N., 1956, *J. opt. Soc. Amer.*, **46**, 987.
- [10] RIGGS, L. A., 1958, *Ann. Rev. Psychol.*, **9**, 19.
- [11] DITCHBURN, R. W., and FENDER, D. H., 1955, *Opt. Acta*, **2**, 128.
- [12] DITCHBURN, R. W., FENDER, D. H., and MAYNE, S., 1959, *J. Physiol.*, **145**, 98.
- [13] DELANGE DZN, H., 1958, *J. opt. Soc. Amer.*, **48**, 777.
- [14] DELANGE DZN, H., 1957, *Attenuation characteristics and phase-shift characteristics of the human fovea→cortex systems in relation to flicker-fusion phenomena*, Thesis, Technical University, Delft.
- [15] POLYAK, S., 1941, *The Retina* (Chicago: University of Chicago Press).
- [16] O'BRIEN, B., 1951, *J. opt. Soc. Amer.*, **41**, 882.
- [17] DEGROTT, S. G., and GEBHARD, J. W., 1952, *J. opt. Soc. Amer.*, **42**, 492.
- [18] WATSON, G. N., 1952, *A Treatise on the Theory of Bessel Functions* (Cambridge: University Press), p. 22.
- [19] SCHADE, O. H., 1956, *J. opt. Soc. Amer.*, **46**, 721.
- [20] RIGGS, L. A., RATLIFF, F., CORNSWEET, J. C., and CORNSWEET, T. N., 1953, *J. opt. Soc. Amer.*, **43**, 495.
- [21] HARTLINE, H. K., 1959, *Rev. mod. Phys.*, **31**, 515.
- [22] GRANIT, R., 1947, *Sensory Mechanisms of the Retina* (London: Oxford University Press).
- [23] KAMIYA, S., 1958, *Bull. math. Biophys.*, **20**, 343.
- [24] HARTLINE, H. K., and RATLIFF, F., 1958, *J. gen. Physiol.*, **41**, 1049.
- [25] IVANOFF, A., 1956, *Opt. Acta*, **3**, 47.
- [26] RATLIFF, F., 1952, *J. exp. Psychol.*, **43**, 163.
- [27] KRAUSKOPF, J., 1957, *J. opt. Soc. Amer.*, **47**, 740.
- [28] O'BRIEN, V., 1958, *J. opt. Soc. Amer.*, **48**, 112.
- [29] RONCHI, L., and DI FRANCIA, G. T., 1957, *J. opt. Soc. Amer.*, **47**, 639.
- [30] EBERHARD, G., 1912, *Phys. Z.*, **13**, 288.
- [31] MEES, C. E. K., 1942, *The Theory of the Photographic Process* (New York), p. 1033.
- [32] TALBOT, S. A., 1951, *J. opt. Soc. Amer.*, **41**, 895.
- [33] GRANIT, R., 1955, *Receptors and Sensory Perception* (New Haven: Yale University Press).
- [34] FRY, G. A., 1948, *Amer. J. Optom.*, **25**, 162.
- [35] OGILVIE, J. C., and TAYLOR, M. M., 1958, *J. opt. Soc. Amer.*, **48**, 628.
- [36] OGILVIE, J. C., and TAYLOR, M. M., 1959, *J. opt. Soc. Amer.*, **49**, 898.
- [37] FENDER, D. H., 1958, private communication.
- [38] RIGGS, L. A., and TULUNAY, S. U., 1959, *J. opt. Soc. Amer.*, **49**, 741.
- [39] KELLY, D. H., 1959, *J. opt. Soc. Amer.*, **49**, 730.

A 'sky lens' for an auroral spectrograph

by N. J. RUMSEY

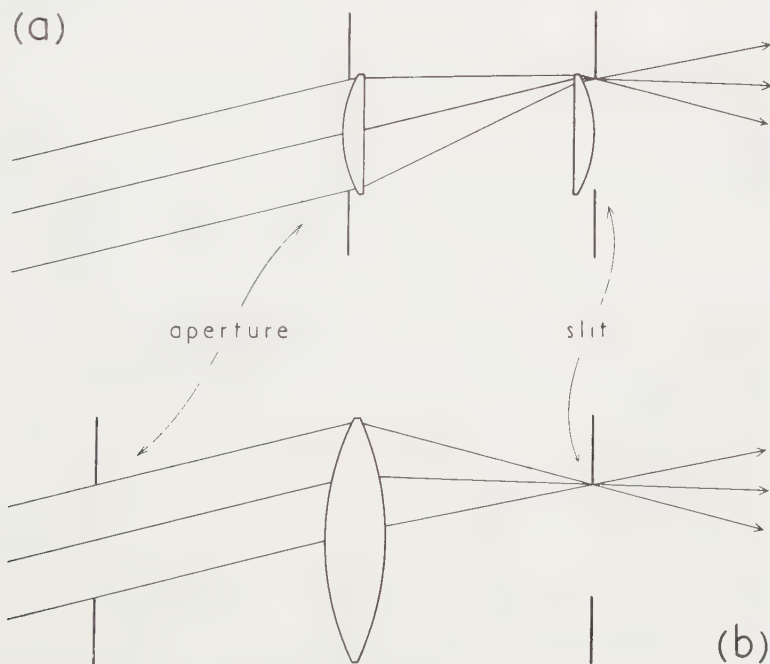
Dominion Physical Laboratory, Lower Hutt, New Zealand

(Received 13 July 1960)

A 'sky lens' images a strip of sky on the entrance slit of a spectrograph. Then the intensity distribution of each spectral emission from the strip of sky is mapped along the corresponding spectral line. In order to reduce light losses to a minimum a single lens component may be used for this purpose (in place of the usual two components), but one surface should be aspherized. If this surface is made an hyperboloid the lens performs very well over a 20° field.

The spectrographs of the Dominion Physical Laboratory's Auroral Station at Invercargill, New Zealand, are each fitted with a 'sky lens' which images a strip of sky on the entrance slit of the spectrograph. In this way the intensity distribution of each spectral emission along this strip of sky is mapped along the length of the corresponding spectral line. For one of these lenses special steps have been taken to reduce light losses to the minimum possible, because exposures are sufficiently lengthy for the photographic emulsion to show considerable reciprocity failure so that light loss in the optical system must be offset by a disproportionate increase in exposure time.

If the strip of sky subtends, say, 20° the lens system shown in the figure (a) is commonly used. Here the first component images the sky on the entrance slit,



(a) Conventional lens system; (b) single component system.

while the second images the first onto the collimator of the spectrograph. The lens components are normally made from fused quartz or from optical glass selected for excellent transparency, so that light loss by absorption is negligible. The significant loss is by reflection at the lens surfaces. This loss can be reduced by blooming; but any simple and mechanically robust reflection-reducing layers are not very efficient optically on substrates with the low refractive index characteristic of very transparent materials, nor over a wide range of wavelengths on any substrate. Thus the number of surfaces should be reduced to the minimum possible, which suggests the arrangement of the figure (b).

This consists of a single lens with an aperture stop placed in front at a distance a little greater than its focal length. The lens images the sky on the entrance slit, and it also images the aperture stop on the collimator. (A real aperture stop is not absolutely essential but is very desirable for reducing stray light inside the spectrograph.) Oblique pencils pass eccentrically through the lens and they meet it while they still have their full initial cross-section. The lens must therefore have a greater diameter and thickness than either of the components of (a). The increased thickness does not introduce objectionable absorption since a very transparent material is used; but the eccentric passage of the oblique pencils introduces serious aberration if the surfaces remain spherical. This is partly a result of the unusually large distance of the aperture stop from the lens, and partly of the fairly large relative aperture required to match that of the collimator, $f/6.2$ in our case.

One surface of the lens must therefore be aspherized if its full advantages are to be realized. The Burch 'see-saw diagram' method [1-3], followed by a slight adjustment of the eccentricity of the aspheric surface, was used to design a lens free from coma and with an effectively flat tangential field. The spherical aberration remains slightly undercorrected. The lens is roughly equiconvex, but with its first surface an hyperboloid. Its specification, for unit focal length, is as follows:

The first surface is a convex hyperboloid whose profile satisfies the equation

$$y^2 = 1.905x + 2.39x^2$$

(referred to the pole of the surface as origin and with the x -axis along the optic axis). The second surface is a convex sphere (concave to the incident light) of radius 1.094. The central thickness is 0.125, and the refractive index 1.52.

A refractive index of 1.52 was chosen because there are a number of optical glasses of excellent transparency among the borosilicate crowns, hard crowns and phosphate crowns whose indexes reach this value at various wavelengths between the near ultra-violet and the near infra-red. One can therefore always find a transparent glass whose mean index over any range of wavelengths of interest is very close to 1.52.

The most serious residual aberration of the lens is its uncorrected longitudinal chromatic aberration. This is not, however, very objectionable. In our case, for a wavelength range of 3800 to 9000 A.U., this defect acting alone would limit the angular resolution along the imaged strip of sky at the extreme wavelengths to about the same value as would result at all wavelengths from the limited resolving power of the photographic emulsion acting alone. Because diffraction also affects the resolution, the smallest angle resolved at the extreme wavelengths can not be as much as twice that at the perfectly focused wavelength. If, as is usual, a smaller range of wavelengths is being examined, the effect of the longitudinal chromatic aberration is correspondingly reduced.

The residual undercorrected spherical aberration in the axial pencil is within the Rayleigh Limit for lenses of focal lengths up to 4.5 in., and in the meridian section of the $7\frac{1}{2}^\circ$ oblique pencil up to 2.7 in. Coma and tangential field curvature are very well corrected over a 20° total field. (For larger fields the hyperboloid surface should be replaced by one of higher degree which departs even more sharply from a sphere near the edge.) There is a little transverse chromatic aberration and distortion, which change the height scale on different spectral lines and along individual spectral lines respectively; but these merely modify similar scale changes which already arise within the spectrograph.

Our lens of 2.33 in. focal length and 1.47 in. diameter required the removal of glass to a maximum depth of 0.0023 in. in changing the first surface from a sphere (touching the desired surface at the pole and crossing it at the edge) to an hyperboloid. This was ground away by hand. Our first hyperboloid was not perfect, but as the resulting aberrations were only small amounts of field curvature and 'hour-glass aberration'† the lens has been put into use and performs well.

ACKNOWLEDGMENTS

The author is indebted to Mr. R. Aspden for the ray tracing carried out during the design and checking of this lens, to Mr. R. J. Barnes for making the lens, and to Mr. B. P. Sandford for investigating several methods of determining the profile of the aspheric surface while it is still being ground to the correct shape.

Une 'lentille céleste' forme l'image d'une bande du ciel sur la fente d'entrée d'un spectrographe. La distribution d'intensité de chaque émission spectrale de la bande du ciel est reproduite le long de la raie spectrale correspondante. Afin de réduire le plus possible les pertes de lumière, on peut utiliser une seule lentille (au lieu des deux utilisées habituellement), mais une des surfaces doit être asphérique. Si cette surface a la forme d'un hyperboloïde, la lentille se comporte de façon très satisfaisante sur un champ de 20° .

Eine 'Sky-lens' bildet einen Streifen des Himmels auf den Eintrittsspalt eines Spektrographen ab. Dann wird die Intensitätsverteilung für jede spektrale Ausstrahlung des Himmelsstreifens längs der entsprechenden Spektrallinie aufgezeichnet. Um die Lichtverluste möglichst klein zu halten, kann eine Einzellinse dafür anstelle der üblichen aus zwei Komponenten zusammengesetzten Linse verwendet werden, aber wenigstens eine Oberfläche sollte asphärisch sein. Bei einer hyperbolischen Form dieser Fläche zeichnet die Linse ein Feld von mehr als 20° recht gut aus.

REFERENCES

- [1] BURCH, C. R., 1942, *Mon. Not. R. astr. Soc.*, **102**, 159.
- [2] BURCH, C. R., 1956, *Observatory*, **76**, 173.
- [3] LINFOOT, E. H., 1955, *Recent Advances in Optics* (Oxford: Clarendon Press), Ch. IV.
- [4] STEWARD, G. C., 1928, *The Symmetrical Optical System* (Cambridge: University Press).

† 'Hour-glass aberration' causes the image of a point of light to become a symmetrical figure-of-eight shaped patch. In the language of Steward [4] this would *not* be called a form of coma.

The saturation of spectral colours viewed in a small field

by K. J. McCREE†

Technical Optics Section, Imperial College, London

(Received 29 June 1960)

Saturation was derived from the quantity of spectral light which had to be added to white to produce a perceptible change of colour. When the field size was reduced from 80' to 15', at a retinal luminance of 50 trolands, the saturation fell to zero in the yellow, and was much reduced in the blue-violet. The effect of using different reference-whites was also investigated; with a white of lower colour temperature, the minimum of saturation occurred at a longer wavelength.

1. INTRODUCTION

Spectral colours, although the most saturated which can be obtained, are not all equally 'saturated' in the subjective sense. Yellow, for instance, is much less saturated than red. Quantitative measurements of the saturation of spectral colours have been made several times, with fields of normal size, and by normal and colour-defective observers [1], but no measurements have been reported for a small field. Small-field observations are of some interest in view of the doubts which have recently been expressed about the existence of tritanopic effects in small fields [2]. The measurements reported here were made with a 15' divided field; a control set was made with an 80' ('normal') field. All the observations were made by the author.

2. METHOD

One of the standard methods of measuring saturation is to add the spectral light to white light until there is a just perceptible change of colour. The more saturated the spectral light, the smaller the amount which has to be added. In these measurements, the spectral colour was added until there was a definite colour change, and the control was then turned back until the mixture only just seemed to match the original white. This technique was the same as that adopted in other measurements recently made by the author [3, 4].

The measurements were made on the Wright colorimeter [5]. White light was provided primarily by a tungsten lamp operating at the colour temperature of C.I.E. Source A, 2854°K. (Two Chance OB9 glass filters were used to raise the colour temperature to that of Source B or Source C as required.) This light was reflected from the vanes of a white sector disc, while spectral light from the colorimeter passed through the apertures. At high speeds of rotation, the white and spectral lights appeared to mix. This mixture was compared with a constant pure white light reflected into the lower half of the field of view. The luminances of the spectral and white lights could be varied independently and, when that of the spectral light was increased, to produce a perceptible change of colour, that of the white light was decreased so that the net luminance always matched that of the lower half of the field. This luminance was 50 trolands. The observer was dark adapted for at least five minutes before the experiment began.

† Now at the Dominion Physical Laboratory, Lower Hutt, New Zealand.

After the saturation measurement had been made, the lower half was blacked out, and the speed of the disc was reduced until a 'flicker match' of the luminance of the spectral colour and the white could be made. From the result of this match, the relative amounts of spectral colour and white used in the saturation measurements could be expressed in luminance units. If F_λ was the luminance of the spectral colour, and F_w that of the white, then the 'saturation' was plotted as $\log_{10}(F_\lambda + F_w)/F_\lambda$, which is the log of the reciprocal of the colorimetric purity of the mixture.

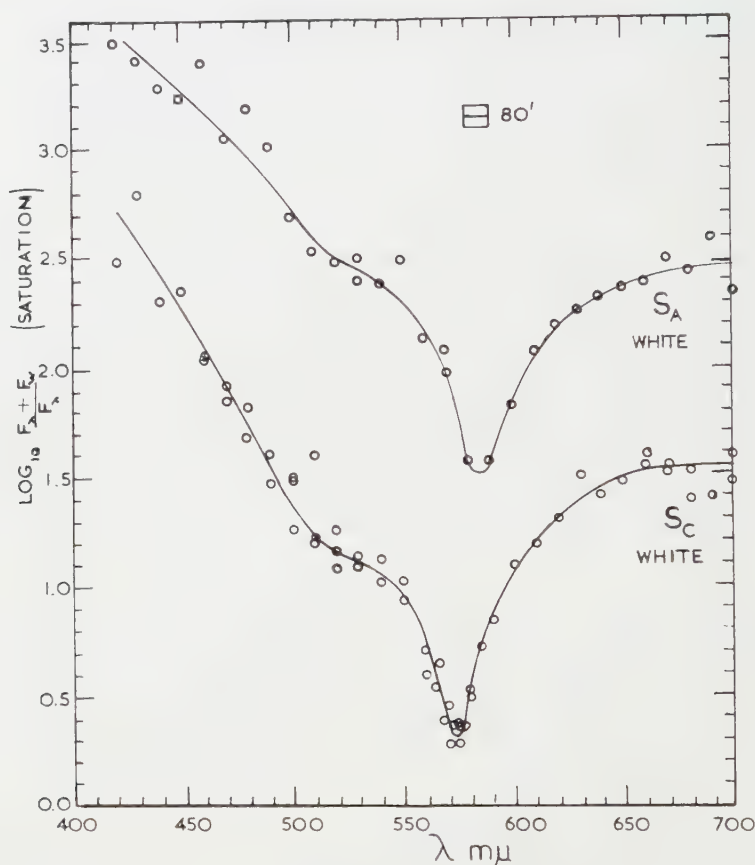


Figure 1. The relative saturation of the spectral colours. The curves measured with the two whites have been arbitrarily separated.

In all the observations, care was taken to avoid fixating on the field, since it had been shown [3] that colour discrimination could be strongly affected by fixation. A few saturation measurements which were taken with steady fixation showed that the spectral colour could generally be increased without limit and still apparently match white. The only exception was in the red part of the spectrum, beyond $610 \text{ m}\mu$, where the spectral colour could be detected if it was sufficiently strong. The proportion required was some ten times that required when fixation was avoided. The gaze was allowed to wander, within the natural limits imposed by the ability to resolve the two halves of the divided field.

3. RESULTS

The saturation measurements made with an 80' field (figure 1) are quite similar to those found by other investigators. There is a sharp minimum of saturation in the yellow. The exact position of this minimum has varied slightly from one investigation to another. As figure 1 shows, this could easily have been due to the use of different whites as reference colours; with the yellower white (S_A), the least saturated colours were the more reddish yellows. (Subjectively, the Source C reference looked quite colourless, while Source A looked slightly, yellow.) The other difference between the two curves is that the Source A curve is slightly shallower throughout.

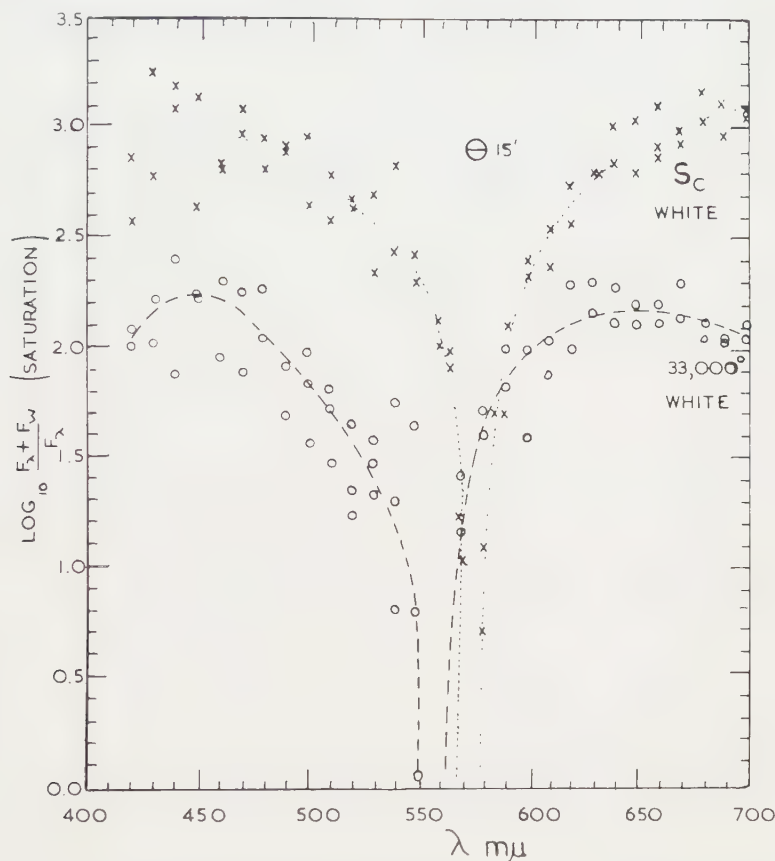


Figure 2. Relative saturation for small-field conditions. The two curves have been arbitrarily separated.

For the small-field measurements (figure 2) the two whites were Source C and a source of colour temperature about 33 000°K, obtained by using the Source B and Source C blue filters together. The colour temperature had to be raised in this way in order to produce a really colourless white.

The feature of the small-field curves is that the minimum in the yellow now falls to 'zero', or, in other words, there is a wavelength which completely matches white. This wavelength is 575 or 560 $m\mu$ respectively, for the lower and higher

colour temperatures. Wright also found a 'white point', when measuring small-field colour mixture functions [6]. It was at $578\text{ m}\mu$, for a 4800°K white. He indicated that there was probably a second white point in the 'violet' at $410\text{ m}\mu$. Our saturation curves show no more than a tendency to fall at the violet end. Blues and violets are certainly relatively much less saturated than in the $80'$ measurements, but if there is a 'white point' in the violet it must be well below the end of the curve ($420\text{ m}\mu$).

La saturation a été déduite de la quantité de lumière spectrale qui devait être ajoutée au blanc pour produire un changement de couleur perceptible. Lorsque la dimension du champ était réduite de $80'$ à $15'$, pour une luminance rétinienne de 50 trolands, la saturation tombait à zéro dans le jaune et était fortement réduite dans le bleu-violet. L'influence de l'utilisation de divers blancs de référence a été étudiée aussi; avec un blanc de température de couleur plus basse, le minimum de saturation avait lieu pour une longueur d'onde plus grande.

Fügt man zu weißem Licht eine solch kleine Menge einer Spektralfarbe hinzu, daß die Farbänderung grade erkannt werden kann, so bedeutet dies eine gewisse Stufe der Sättigung. Wenn nun die Feldgröße von $80'$ auf $15'$ Bogenminuten gerabgesetzt wird, dabei aber die Beleuchtungsstärke auf der Netzhaut 50 trolands bleibt, dann geht die Sättigung im Gelben auf 0 zurück und wird im Blau-violett stark herabgesetzt. Es wurde auch der Einfluß untersucht, den die Verwendung verschiedener Arten von Bezugsweiß nach sich zieht; bei einem Weiß niedrigerer Farbtemperatur verschiebt sich das Minimum der Sättigung zu längeren Wellenlängen hin.

REFERENCES

- [1] JAMESON, D., and HURVICH, L. M., 1955, *J. opt. Soc. Amer.*, **45**, 546.
- [2] BEDFORD, R. E., and WYSZECKI, G. W., 1958, *J. opt. Soc. Amer.*, **48**, 129.
- [3] MCCREE, K. J., 1960, *Opt. Acta*, **7**, 281.
- [4] MCCREE, K. J., 1960, *Opt. Acta*, **7**, 317.
- [5] WRIGHT, W. D., 1946, *Researches on Normal and Defective Colour Vision* (London: Henry Kimpton), Ch. 13.
- [6] WILLMER, E. N., and WRIGHT, W. D., 1945, *Nature, Lond.*, **156**, 119.

An estimation of Smith-Purcell effect as the light source in the infra-red region

by K. ISHIGURO and T. TAKO
University of Tokyo, Japan†

(Received 20 August 1959 and in revised form 22 January 1960)

When an electron beam streams along the surface of a metallic diffraction grating, the Smith-Purcell effect occurs. The radiation of electro-magnetic waves is expected and the wavelength of the emitted wave is estimated by the formula which was originally given by Smith and Purcell from the consideration of Huygens' principle. In the present paper, an alternative derivation of the formula is presented under the assumption that the radiation is dipole radiation from the running dipole due to the electron and its image charge. The intensity of the radiation and the effect of the shape of the groove of the grating on the radiation are also calculated. The results of a preliminary experiment are briefly compared with the calculation.

1. INTRODUCTION

When an electron beam passes close to the surface of a metallic diffraction grating, emission of electro-magnetic radiation is expected [1-3]. Smith and Purcell [1] explained this effect as the radiation of an oscillating dipole consisting of the moving electron and its image charge in the metal. They derived a formula for the wavelength of radiation

$$\lambda = d(\beta^{-1} - \cos \theta) \quad (1)$$

where d is the grating constant, $\beta = v/c$, v is the velocity of the electron, and θ is the angle between the direction of the electron beam and the radiation (figure 1).



Figure 1.

In the present paper, it is intended to show that an alternative derivation of (1), which takes into account the Doppler effect on the dipole radiation, enables the formula for the intensity of radiation to be derived in a simple way.

2. SURVEY OF THE PHASE RELATION

The emission of a dipole at the instant when it crosses the points A and B will be observed as in-phase emission, if the distance between A and B is d and the relation

$$\frac{d}{v} - \frac{d \cos \theta}{c/n} = \frac{m}{\nu}, \quad m = 0, 1, 2, \dots \quad (2)$$

is satisfied, where n is the refractive index of the medium and $\nu = c/n\lambda$ is the frequency of the emitted light. It is clear that the case $m = 0$, that is $n\beta \cos \theta = 1$, is the Čerenkov radiation and the case $m = 1$ is the Smith-Purcell effect.

† Present address: Central Inspection Institute of Weights and Measures, Tokyo, Japan.

3. DOPPLER EFFECT

Let us distinguish coordinates relative to the electron by primes. Then the frequency relation between both systems is given by the usual Doppler effect equation,

$$\omega' = \frac{\omega(1 - n\beta \cos \theta)}{\sqrt{1 - \beta^2}} \quad (3)$$

and the grating constants in both systems are connected by the Lorentz contraction and it is

$$d' = d\sqrt{1 - \beta^2}. \quad (4)$$

The angular frequency of the emitted wave in the primed system must be apparently

$$\omega' = \frac{2\pi v}{d'}. \quad (5)$$

Putting (5) into (3), we have

$$\omega = \frac{1}{1 - n\beta \cos \theta} \frac{2\pi v}{d} \quad (6)$$

or considering

$$\lambda = \frac{2\pi c}{\omega n},$$

$$\lambda = \frac{d}{n} (\beta^{-1} - n \cos \theta)$$

is derived. This is identical with (1) which was derived from Huygens' principle considerations [4].

4. INTENSITY OF THE EMITTED RADIATIONS

In the prime system, the energy, emitted into the unit area of θ' direction per unit time is given by the usual formula for the dipole radiation

$$I_s' = \frac{\mu_0 \sqrt{(\epsilon_0 \mu_0)} n' \omega'^4}{32\pi^2 r'^2} P_0^2 \cos^2 \theta' \quad (\text{MKSA units}) \quad (7)$$

where P_0 is the strength of the dipole moment and

$$\begin{aligned} r'^2 &= x'^2 + y'^2 \\ &= \frac{r^2 - \beta^2 y^2}{1 - \beta^2} + \frac{\beta^2 (ct)^2 - 2\beta x(ct)}{1 - \beta^2} \\ &= \frac{r^2 - \beta^2 y^2}{1 - \beta^2}, \quad (ct \approx 0). \end{aligned} \quad (8)$$

To the order of approximation, which takes into consideration only the lowest power of β , $I_s = I_s'$. Substituting from (8) and (6) and simplifying the resultant expression, we obtain:

$$I_s = \frac{\pi^2 n \mu_0 c^3}{2r^2} P_0^2 \cos^2 \theta \frac{\beta^4}{d^4}. \quad (9)$$

The intensity per steradian is given by

$$I = I_s r^2.$$

When the electron rest mass is m , and the accelerating potential is V , the kinetic energy of a slow electron is

$$\frac{m \cdot c^2}{2} \beta^2 = eV \quad (10)$$

and eliminating β in (10) we have

$$I = 2\pi^2 n\mu_0 c^3 \frac{P_0^2 \cos^2 \theta}{d^4} \left(\frac{eV}{mc^2} \right)^2. \quad (11)$$

This is the intensity per electron as a function of the accelerating voltage.

Since the number of electrons on the grating surface, N , is

$$N = \sqrt{\left(\frac{m}{2e^3 V} \right)} \cdot J \cdot L$$

where L is the length of the grating along the electron path and J is the electric current, the total intensity I_{total} is given by

$$I_{\text{total}} = NI.$$

Putting the effective distance between the electron and its image charge equal to l , P_0 is replaced by el . If constants and units are chosen thus:

$$\begin{aligned} l \text{ and } d & \text{ in microns,} \\ V & \text{ in kilo volts,} \\ L & \text{ in cm,} \\ J & \text{ in mA,} \end{aligned}$$

and

$$\begin{aligned} c &= 3 \times 10^8, \\ \mu_0 &= 4\pi \times 10^{-7}, \\ m &= 0.91 \times 10^{-30}, \\ e &= 1.60 \times 10^{-19}, \end{aligned}$$

we obtain the useful formula to estimate the emitted light intensity

$$I_{\text{total}} = 2.2 \times 10^{-4} \cdot \frac{nl^2}{d^4} \cdot L \cos^2 \theta \cdot V^{3/2} \cdot J \frac{\text{watt}}{\text{steradian}}. \quad (12)$$

5. THE FREQUENCY PURITY OF THE EMITTED RADIATION

5.1. Angular dependence

Differentiating (6) by θ , we have

$$d\omega/\omega = \frac{n\beta \sin \theta}{1 - n\beta \cos \theta} \cdot d\theta.$$

Since the rest mass energy of electron is 5.10×10^5 electron volts and the kinetic energy of the electron in the region of our interest is a few kilo electron volts, we have $\beta \div 1, 10$ from (10) and if $d\theta$ is chosen to be 10 degrees, it is estimated that

$$\frac{d\omega}{\omega} \approx 10^{-2}.$$

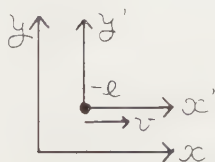


Figure 2.

This is the practical limit of the purity of the frequency of our radiation.

5.2. *Electron velocity dependence*

Differentiating (6) by β , we have

$$\frac{d\omega}{\omega} = \frac{1}{1 - n\beta \cos \theta} \cdot \frac{d\beta}{\beta}, \quad (13)$$

Therefore, the width of the line emitted is proportional to the fluctuation of the electron velocity.

6. THE STRENGTH OF THE DIPOLE MOMENTS

When the distance of the electron from the surface along the normal is s , the distance of the image charge from the surface s_+ is given by

$$s_+ = s$$

in the case of the infinitely extended plane surface and

$$s_+ = Rs/(R \pm s)$$

in the case of a sphere of radius R . The double sign allows for the possibility of the electron being either inside or outside the sphere. Even in these last cases, when $s \ll R$, we can take $s_+ \approx s$. The boundary useful for our case is the sinusoidal one and the exact solution of it is not simple. However, when s is sufficiently small compared with the radius of the curvature of the surface, the approximation $s_+ = s$ will still be valid. Then, if the shape of the surface is given by

$$y = a - a \cos \left\{ \frac{2\pi}{d} (x + \xi) \right\}$$

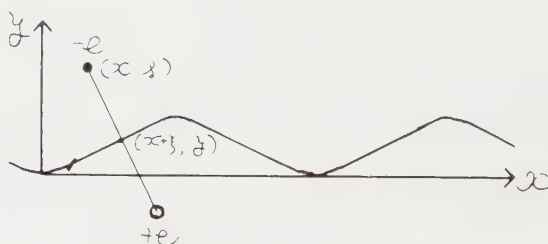


Figure 3.

as shown in figure 3, the coordinate of the intersection of the normal to the surface from the electron and the surface must be $(x + \xi, y)$, (x, s) being the coordinate of the electron. ξ is the difference between the x coordinates of electron and the intersection, and is given by

$$\xi = (s - a) \frac{2\pi a}{d} \sin \left\{ \frac{2\pi}{d} (x + \xi) \right\} + \frac{\pi a^2}{d} \sin \left\{ 2 \frac{2\pi}{d} (x + \xi) \right\}. \quad (14)$$

Therefore, the perpendicular and parallel components of the dipole moment to the direction of the electron beam are given respectively by

$$\begin{aligned} P' &= 2e(s - y) - 2e(s - a) \\ &= 2ea \cos \left\{ \frac{2\pi}{d} (x + \xi) \right\} \end{aligned}$$

and

$$\begin{aligned} P'' &= 2e\xi \\ &= 2e \left[(s - a) \frac{2\pi a}{d} \sin \left\{ \frac{2\pi}{d} (x + \xi) \right\} + \frac{\pi a^2}{d} \sin \left\{ 2 \frac{2\pi}{d} (x + \xi) \right\} \right]. \end{aligned} \quad (15)$$

When $a \ll d$, we can put

$$P' \approx 2ea \cos\left(\frac{2\pi}{d}x\right),$$

$$P'' \approx 0,$$

and l in (12) must be considered as equal to $2a$. When the shape of the grating $y=f(x)$ is not sinusoidal, it must be decomposed into the Fourier components as was remarked by van Heel [2]. If the fundamental space frequency of $f(x)$ is $1/d$, it must be

$$f(x) = a_0 + a_1 \cos\left(\frac{2\pi}{d}x\right) + b_1 \sin\left(\frac{2\pi}{d}x\right) \\ + a_2 \cos\left(2\frac{2\pi}{d}x\right) + b_2 \sin\left(2\frac{2\pi}{d}x\right) + \dots,$$

and in the emission, the component with the frequencies ω , 2ω , $3\omega \dots$ will be involved.

From (7) the intensity is proportional to ω^4 and unless coefficients of higher terms a_n , b_n decrease rapidly with the higher powers of $(1/n)$, the higher harmonics will be very strong.

In this view, among the simple shapes given by

$$f(x) = \begin{cases} 0 & 0 \leq x \leq d/2, \\ 2a & d/2 \leq x \leq d, \end{cases}$$

$$f(x) = 2ax/d \quad -d/2 \leq x \leq d/2,$$

$$f(x) = 8ax^2/d^2 \quad -d/2 \leq x \leq d/2,$$

$$f(x) = 4(a/d)|x| \quad -d/2 \leq x \leq d/2,$$

$$f(x) = 2a \cos[(2\pi/d)\lambda x] \quad -d/2 \leq x \leq d/2, (\lambda \text{ is not integer}),$$

the last three will be more favourable than the former two, since the last three have the coefficients proportional to $(1/n)^2$ and the former two are proportional to $(1/n)$.

7. PRELIMINARY EXAMINATION TO DETECT THE RADIATION

From (6) and (10) the wavelength of the emitted wave can be calculated as a function of the accelerating potential V as is shown in figure 4. For example, when V is fixed at 5 kilo volts and the grating constant d is 1 micron, λ must be 6μ , but if d is increased to 10μ , λ will also increase to 60μ . Our apparatus consists of the electron gun E, a vacuum chamber of diameter 30 cm and height 15 cm with an ordinary optical grating, anode target T, reflecting mirror C and the thermopile D to detect the radiation as shown in figure 7. A typical example of the measures is shown in figure 5. When the effect of the temperature rise of the apparatus is subtracted from the experimental value, it is seen that the output of the thermopile increases linearly with the increase of the electron current under the condition of constant V and increases in proportion to $V^{3/2}$ when the current is kept constant, as expected from (12) (figure 6). The expected emission of our experiment I_{total} was *ca.* 500 μ watt and the experimentally confirmed emission was *ca.* 50 μ watt.

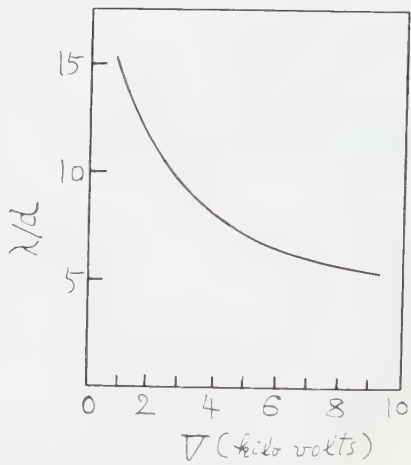


Figure 4.

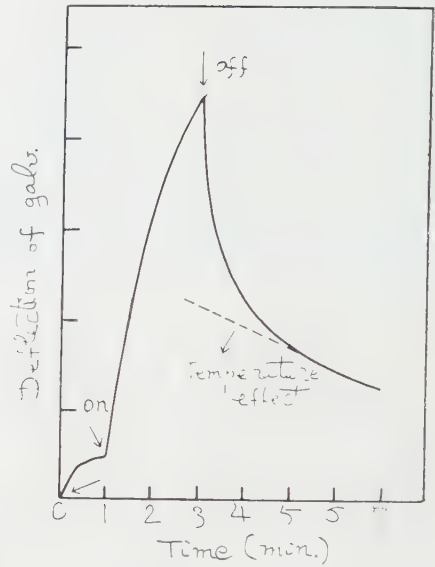
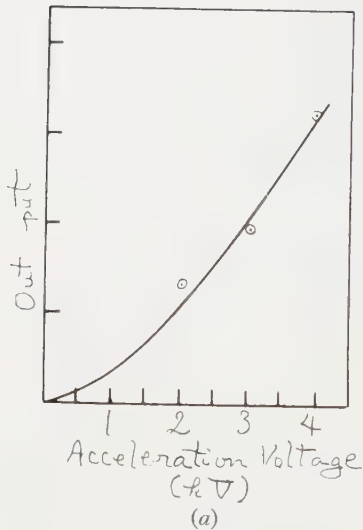
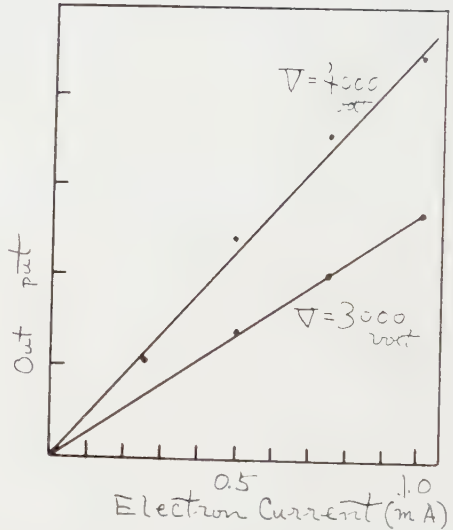


Figure 5.



(a)



(b)

Figure 6.

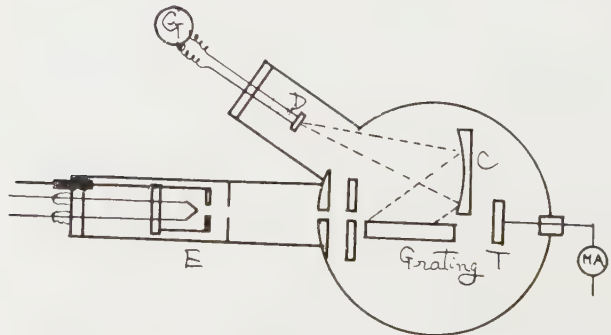


Figure 7.

L'effet Smith-Purcell a lieu lorsqu'un faisceau d'électrons s'écoule le long de la surface d'un réseau de diffraction métallique. On s'attend à un rayonnement d'ondes électromagnétiques et la longueur d'onde de l'onde émise est estimée à l'aide de la formule qui a été donnée d'abord par Smith et Purcell à partir du principe d'Huygens. Dans le présent article, on présente une autre démonstration de la même formule en supposant que le rayonnement est celui d'un dipôle en mouvement dû à l'électron et à sa charge image. On calcule aussi l'intensité du rayonnement, ainsi que l'effet de la forme du sillon du réseau sur le rayonnement. On compare les résultats d'une expérience préliminaire avec le calcul.

Wenn ein Elektronenstrahl längs der Oberfläche eines metallischen Beugungsgitters verläuft, so tritt der Smith-Purcell-Effekt auf. Die Strahlung der elektromagnetischen Welle wird beobachtet, und die Länge der ausgesandten Welle läßt sich nach der Formel ermitteln, die ursprünglich von Smith und Purcell aus dem Huygens'schen Prinzip hergeleitet worden ist. In der vorliegenden Arbeit wird eine andere Ableitung der Formel unter der Annahme gegeben, daß die Strahlung eine Dipolstrahlung ist von dem mit dem Elektron verbundenen laufenden Dipol und seinem Ladungsbild. Die Intensität der Strahlung und der Einfluß der Furchenform des Gitters auf die Strahlung lassen sich ebenfalls berechnen. Die Ergebnisse eines Vorversuches werden überschlägig mit der Rechnung verglichen.

REFERENCES

- [1] SMITH, J. J., and PURCELL, E. M., 1953, *Phys. Rev.*, **92**, 1069.
- [2] KASTLER, A., 1955, *Nuovo Cim.*, Suppl., **2**, 761.
- [3] TOSHIHARU TAKO, and KOZO ISHIGURO, 1957, *Ohyoh Buturi*, **26**, 129.
- [4] MOTZ, H., 1951, *J. appl. Phys.*, **22**, 527.

Beugungsexperimente zur Vielstrahlinterferometrie†

von GERHARD SIMONSOHN

I. Physikalisches Institut der Freien Universität, Berlin

(Received 29 August 1960)

In einem fast undurchlässigen Silberbelag auf ebener Glasunterlage verläuft eine Furche der Breite 3 bis $30\ \mu$; darüber steht planparallel in Abständen zwischen 8 und $50\ \mu$ ein teildurchlässig bedampfter Glasspiegel. Der Furchengrund ist im ersten Teil der Untersuchungen unbedampft, im zweiten Teil teildurchlässig bedampft. Dieses Objekt wird im Durchlicht nach der Methode der Streifen gleicher Farbordnung untersucht. Es wird Strahlung nachgewiesen, die das Objekt unter endlichen Winkeln θ gegen die Richtung der beleuchtenden Welle (Normalenrichtung) verläßt. Die Erscheinungen im Bereich außerhalb der Furche lassen sich auf diskrete 'Winkelordnungen' nach der Beziehung $n \cdot \lambda = 2d \cdot \cos \theta$ zurückführen. Bei bedampfter Furche weist die Interferenzerscheinung im Furchenbereich außer einem Hauptmaximum, das zur Richtung $\theta=0$ gehört, Nebenmaxima auf; die Lage der Nebenmaxima wird durch die Breite der Furche bestimmt.

Es wird kurz angedeutet, wie sich alle beobachteten Erscheinungen in einem Hohlleiter-Modell deuten lassen. Die ausführliche Behandlung dieses Modells ist einer zweiten Arbeit vorbehalten.

1. EINLEITUNG

Die Vielstrahlinterferometrie in der von S. Tolansky [1] entwickelten Form ist ein bedeutsames Verfahren zur Messung kleiner Höhendifferenzen an Oberflächen geworden. Ein typisches Objekt zeigt Abb. 1 (a). Es besteht aus zwei teildurchlässig verspiegelten Glaspatten, die sich mit den verspiegelten Flächen in einem Abstand der Größenordnung $1\text{--}10\ \mu$ gegenüberstehen. Die obere Platte ist durchweg eben; bei der unteren verläuft in einem ebenen 'Plateau' eine Furche von rechteckigem Profil. Wird dieses Objekt mit parallelem Licht beleuchtet und der Interferenzraum (d.h. der Luftspalt zwischen den Spiegeln) abgebildet, so entsteht in der Bildebene ein Interferogramm, wie es in Abb. 1 (a) neben dem Objekt angedeutet ist. Aus der Streifenversetzung kann man die Tiefe der Furche ablesen. Wegen der geringen Halbwertsbreite der Streifen gelangt man unter üblichen Bedingungen zu einer Genauigkeit der Einzelmessung von weniger als $1/100$ Wellenlänge.

Die Tiefe der Furche ist nicht das einzige, was man dem Interferogramm entnehmen kann: Die Länge des versetzten Streifenstücks gibt die Breite der Furche wieder. In jedem Interferogramm sind Aussagen über vertikale Differenzen am Objekt mit Aussagen über die laterale Ausdehnung der einzelnen Objektbereiche verknüpft. Es ist neuerdings die Frage nach der Grenze der lateralen Auflösung in der Vielstrahlinterferometrie aufgeworfen worden. Überlegungen von E. Ingelstam [2] und B. S. Thornton [3] führen auf eine

† Auszug aus der Dissertation des Verfassers: Nachweis und Deutung gebeugter Strahlung in der Vielstrahlinterferometrie, D 188, Freie Universität, Berlin, 1960.

Unschärfebeziehung: Eine Steigerung der vertikalen Auflösung (das ursprüngliche Anliegen der Vielstrahlinterferometrie) wird mit einer Verringerung der lateralen Auflösung erkauft; man kann für die Abbildung in der Vielstrahlinterferometrie im allgemeinen nicht das Auflösungsvermögen nach der Abbeschen Theorie erwarten. R. C. Faust [4] hat diese Verhältnisse an einem idealisierten Objekt diskutiert.

Das Vorbild der Abbeschen Theorie für die Abbildung des normalen mikroskopischen Objektes macht deutlich, daß laterale Auflösung und Beugung am Objekt miteinander verknüpft sind; nur ist es fraglich, wie man die Beugung am Objekt der Vielstrahlinterferometrie (dem Interferenzraum als ganzem) richtig zu beschreiben hat. Man denke sich in Abb. 1 (a) den oberen Spiegel parallel zum Plateau und zum Furchengrund des unteren Spiegels gestellt, was beim Verfahren der Streifen gleicher Farbbordnung (s. unten) möglich ist. Das Objekt werde von unten in Normalenrichtung mit einer ebenen Welle beleuchtet. Die elementare Behandlung der Vielstrahlinterferenz teilt die einfallende Welle in drei Bündel paralleler Strahlen (drei 'ebene' Teilwellen) auf, die entsprechend den Bereichen des Objektes durch die Ränder der Furche seitlich begrenzt sind. Jedes Strahlenbündel erleidet im Interferenzraum eine Zickzackreflexion; das führt zu resultierenden Strahlenbündeln, die den Interferenzraum mit ungeänderter Richtung verlassen.

Aus dieser Beschreibung läßt sich die Wiedergabe der Lateralstruktur in der Bildebene nicht ableiten. Zur Abbildung gehört ein Strahlenbündel (Wellenpaket) endlicher Apertur. Man muß die Beugung berücksichtigen, d.h. die Zerlegung der beleuchtenden ebenen Welle in ein solches Wellenpaket. Die Zerlegung kann nicht erst beim Austritt der Welle aus dem Interferenzraum einsetzen. Die Stetigkeitsforderungen für das elektromagnetische Feld machen es unmöglich, daß im Raum über der Furche und im Raum über dem Plateau Interferenzerscheinungen mit unstetiger seitlicher Begrenzung bestehen. Es ist eine Zerlegung der einfallenden Welle zu erwarten, die die Erscheinungen im Grenzgebiet benachbarter Interferenzräume miteinander koppelt.

Diese Überlegungen waren der Ausgangspunkt für einige Beugungsexperimente an einem vereinfachten Objekt.

2. OBJEKT UND VERSUCHSANORDNUNG

Abbildung 1 zeigt außer einem normalen Objekt mit Furche (a) die beiden untersuchten Objekte (b) und (c). Bei dem Objekt (a) verläuft die Furche in der Glasunterlage; Furchengrund und Plateau sind mit einer teildurchlässigen Silberschicht von 400 \AA bedampft, wie sie in der Vielstrahlinterferometrie üblich ist. Bei den Objekten (b) und (c) ist die Glasunterlage eben; die Furche verläuft in einer 'dicken' Silberschicht von 1100 \AA . Der Furchengrund ist im ersten Teil der Untersuchungen unbedampft (Objekt b), im zweiten Teil mit einer 400 \AA -Schicht bedampft (Objekt c). Die Objekte wurden von unten mit senkrecht einfallender Strahlung beleuchtet und die Interferenzerscheinungen im Durchlicht untersucht. Die Silberschichten von 1100 \AA , bzw. $1100 + 400\text{ \AA}$ sind fast undurchlässig. Dies ist für die Experimente von grundlegender Bedeutung: Die Strahlung, die bei dem normalen Objekt durch das Plateau direkt in den Interferenzraum eindringt, ist bis auf einen geringen Rest zugunsten der

Strahlung unterdrückt, die aus dem Furchenbereich durch Beugung in die Umgebung gelangt.

Es wurde das Verfahren der Streifen gleicher Farbordnung angewandt (vgl. [1], S. 96ff.), das Objekt also mit weißem Licht beleuchtet und auf den Spalt eines Spektrographen abgebildet. Der Spalt und das Bild der Furche kreuzten sich senkrecht. Die beiden Spiegel des Objektes waren in Parallelstellung, was besonders übersichtliche Verhältnisse für Beugungsexperimente schafft.

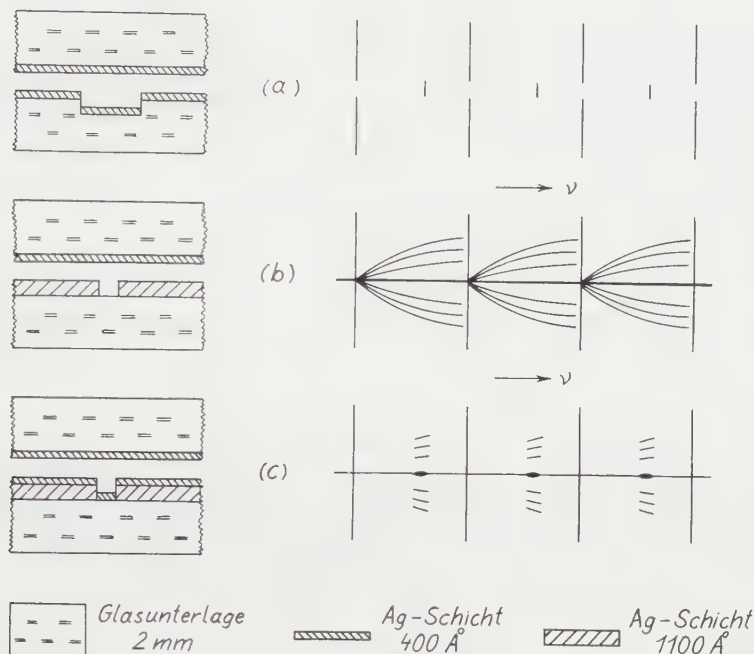


Abb. 1. Objekte, dazu Interferogramme gleicher Farbordnung.

(a) Normales Objekt mit breiter Furche. Im Interferogramm entsprechen die äußeren, langen Streifen den Plateaubereichen; das innere, versetzte Stück entspricht dem Furchenbereich.

(b) Unbedampfte schmale Furche in 'dicker' Silberschicht.

(c) Bedampfte schmale Furche in 'dicker' Silberschicht (durch Überdampfung von Objekt b entstanden).

Der obere Spiegel ist in allen Fällen eben.

Die Objekte b und c wurden im Rahmen dieser Arbeit untersucht; Furchenbreite 3–30 μ ; v : Wellenzahl.

In Abb. 2 ist die Versuchsanordnung schematisch dargestellt. Das genähert parallele Licht, das die Kollimatorlinse verläßt, wird über einen Umlenkspiegel von unten auf das Objekt gelenkt. Das Objektiv entwirft über einen weiteren Umlenkspiegel ein Bild des Objektes auf dem Spalt des Spektrographen. Die gestrichelten Linien im Objekt deuten die Furche an. In Abb. 2 ist durch einen gestrichelten Rahmen ferner die Brennebene des Objektivs bezeichnet. In diese Ebene wurden bei einigen Versuchen Blenden gelegt: entweder ein Streifen (s. linke Aperturhälfte) oder eine Schneide (s. rechte Aperturhälfte). Bei solchen

Ausblendungsversuchen war die Eintrittsblende des Kollimators rechteckig; ihre Stellung ist Abb. 2 zu entnehmen.

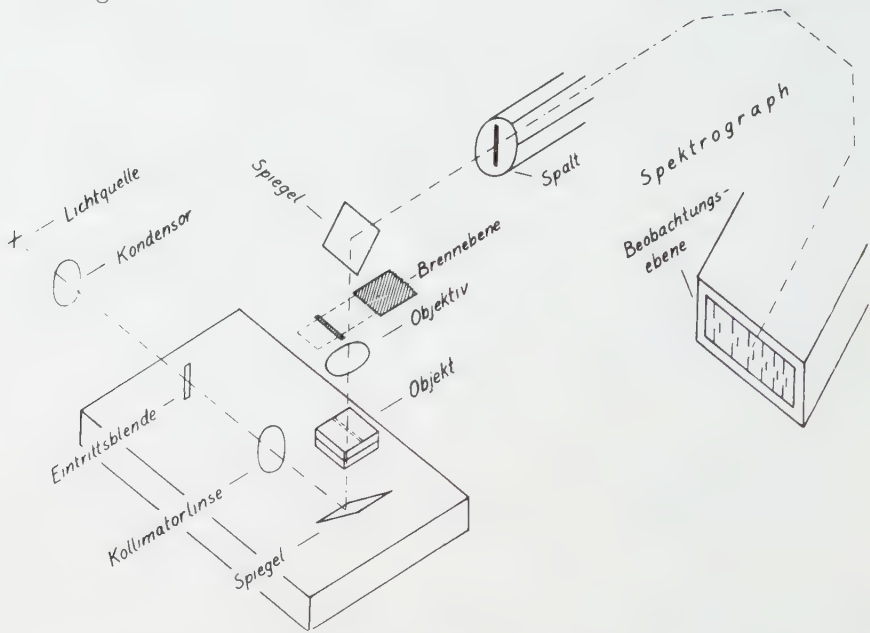


Abb. 2. Versuchsanordnung.

In einem Interferogramm gleicher Farbordnung variiert die Wellenlänge λ , bzw. die Wellenzahl $\nu = 1/\lambda$. Für diskrete Wellenzahlen ν hat der Interferenzraum ein Durchlässigkeitsmaximum; im Durchlicht entspricht dem das Maximum eines Streifens. Die Bedingung dafür ist:

$$n = 2d\nu \quad (1)$$

n : Ordnungszahl; d : Höhe des Interferenzraumes (Spiegelabstand).

So entsteht bei dem normalen Objekt nach Abb. 1 (a) ein Interferogramm, wie es im rechten Teil der Abbildung gezeichnet ist. Das Streifensystem im Furchenbereich ist gegenüber dem System im Plateaubereich zu kleineren Wellenzahlen ν versetzt, weil die Höhe d im Furchenbereich größer ist. Abb. 1 (a) zeigt die Versetzung maßstabgerecht für die Furchentiefe von 1100 \AA und den grünen Spektralbereich.

Mit den Interferogrammen zu den Objekten (b) und (c) sind grob schematisch die Ergebnisse der Untersuchungen vorweggenommen.

Lichtquelle war eine Quecksilber-Höchstdrucklampe Osram HBO 200. Das Spektrum dieser Lampe ist kontinuierlich, hat aber Maxima im Bereich der Quecksilberlinien $577/579, 561, 436 \text{ m}\mu$. Dadurch enthält ein einzelnes Interferogramm Teile, die bei erheblich verschiedener Belichtung entstanden. Man erkennt das an der Übersichtsaufnahme Abb. 3 (b).

Die rechteckige Eintrittsblende (s. Abb. 2) war 5 mm breit. Sofern es sich nicht um Ausblendungsversuche handelte, wurde auch eine kreisförmige Eintrittsblende von maximal 16 mm Durchmesser benutzt. Die Kollimatorlinse hatte 300 mm Brennweite. Daraus errechnet man für das eingestrahelte Lichtbündel maximale Öffnungswinkel von

$$(1/2) \cdot (5/300) = 0,008, \text{ bzw. } (1/2) \cdot (16/300) = 0,027.$$

Die quantitativen Untersuchungen der vorliegenden Arbeit erstreckten sich auf gebeugte Strahlung in einem Winkelbereich von 0,05 bis 0,22 (0,22 war der Aperturwinkel der verwendeten Objektive). Es ist nicht wahrscheinlich, daß irgendeiner der ausgewerteten Effekte durch die endliche Einstrahlungsapertur mitbedingt ist.

Zwei Objektive wurden benutzt: das Photoobjektiv Meyer Primoplan und eine Kombination zweier Achromate. Der Abbildungsmaßstab betrug 9,7 bzw. 6,7.

Typische Belichtungszeiten für die Aufnahmen waren bei unbedampfter Furche (Objekt 1b) 10 Min, bei bedampfter Furche (Objekt 1c) 40 Min. Das ist um einen Faktor 100 bis 1000 mehr, als—unter sonst gleichen Bedingungen—zur Aufnahme eines normalen Interferogramms nach Abb. 1 (a) benötigt wird.

3. UNBEDAMPFTE FURCHE

3.1. Mittlerer Spiegelabstand

Abbildung 3 zeigt eine Aufnahme an der unbedampften Furche. Der Spiegelabstand beträgt $23,5\mu$. Im Gesichtsfeld ist eine Furche der Breite $b = (3 \pm 1)\mu$. Der schmale Streifen (Abb. 3b) umfaßt das gesamte Interferogramm; damit soll vor allem die spektrale Intensitätsverteilung der Lichtquelle deutlich gemacht werden. Ein Ausschnitt ist darüber vergrößert dargestellt.

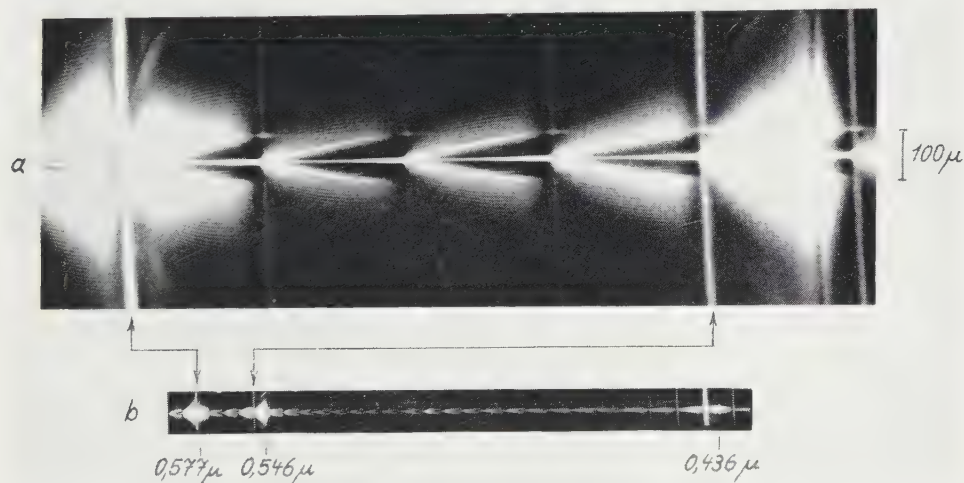


Abb. 3. θ -Interferenz bei unbedampfter Furche; Spiegelabstand $23,5\mu$;

(a) ein vergrößelter Ausschnitt, der durch die Linien bezeichnet wird; die Pfeile weisen auf Hauptstreifen;

(b) das gesamte Interferogramm mit Angabe einiger Wellenlängen (Hg-Linien). Furchenbreite 3μ ; Objektiv: Primoplan

Man erkennt in Abb. 3 zunächst vertikale Streifen. Sie werden wegen der endlichen, wenn auch geringen Durchlässigkeit des Plateaus von der dort senkrecht einfallenden Strahlung erzeugt. Es sind normale Streifen gleicher Farbordnung; sie sollen im folgenden als Hauptstreifen bezeichnet werden.

Zwischen je zwei Hauptstreifen ist eine Interferenzerscheinung anderer Art ausgebildet. Eine Folge von Streifen verläuft mit schwacher Krümmung horizontal. Längs einer Geraden senkrecht zur Furche findet man äquidistante Streifenmaxima. Die Intensität nimmt mit wachsender Entfernung von der Furche ab. Schon vor jeder quantitativen Erfassung zeigen Ausblendungsversuche, daß diese Erscheinung durch Strahlung entsteht, die das Objekt unter endlichen Winkeln θ verläßt; es soll abkürzend von θ -Interferenz gesprochen werden.

3.2. Deutung der θ -Interferenz

Blendet man durch einen Streifen in der hinteren Brennebene des Objektivs (s. Abb. 2) einen kleinen Winkelbereich aus, so wird die θ -Interferenz in einem streifenförmigen Teilgebiet senkrecht zur Furche gestört. Man kann so für das Interferogramm nach Abb. 3 experimentell feststellen, daß die Erscheinung in jeder Vertikalen zur Furche durch Strahlung entsteht, die das Objekt unter zwei diskreten Winkeln θ_1, θ_2 verläßt. Wirken beide Strahlungsanteile zusammen, so entsteht die periodische Folge der Maxima und Minima; sie verschwindet, sobald auch nur einer der beiden Anteile fehlt.

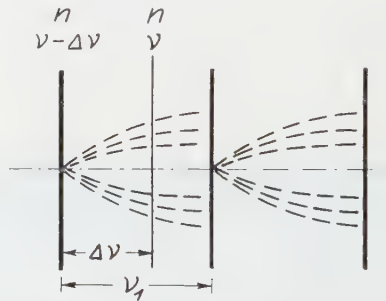


Abb. 4. Zur Ableitung des Zusammenhangs zwischen den Winkeln θ und dem Ort im Interferogramm. n : Interferenzordnung; $\nu, \nu - \Delta\nu$: Wellenzahlen. Hauptstreifen stark ausgezogen. Gestrichelte Linien deuten die θ -Interferenz an.

Die quantitative Auswertung zeigt, daß die Winkel θ_1, θ_2 durch die Formel

$$n = 2d\nu \cdot \cos \theta \quad (2)$$

bestimmt sind; d ist die Höhe des Interferenzraumes im Plateaubereich. Formel (2) ist die bekannte Bedingung für ein Durchlässigkeitsmaximum des Interferenzraumes bei endlichem Einfallswinkel θ der Strahlung. Durch (2) wird jedem Spiegelabstand d und jeder Wellenzahl ν , also jeder Vertikalen im Interferogramm nach Abb. 3, eine diskrete Folge von Winkeln $\theta_1, \theta_2, \theta_3, \dots$ zugeordnet, die zu Interferenzordnungen $n, n-1, n-2, \dots$ gehören. Unter den Bedingungen von Abb. 3 ist θ_3 überall größer als der Aperturwinkel des Objektivs. Die Auszeichnung der beiden verbleibenden Winkel θ_1, θ_2 entspricht einer Welle, die ein Gitter der Gitterkonstanten

$$g_{12} = \frac{\lambda}{\theta_2 - \theta_1} \quad (3)$$

abbildet ($\sin \theta$ durch θ ersetzt; λ : Wellenlänge). Durch (3) ist in der Tat für jede Stelle des Interferogramms der Streifenabstand bestimmt, den man längs einer Vertikalen mißt.

Für die Auswertung muß man die Winkel θ als Funktion des Ortes zwischen zwei Hauptstreifen darstellen. Als Koordinate wählt man zweckmäßig die Wellenzahl ν ; die Hauptstreifen haben dann voneinander den konstanten Abstand

$$\nu_1 = \frac{1}{2d}. \quad (4)$$

Es wird die normierte Größe

$$q = \frac{\Delta\nu}{\nu_1} \quad (5)$$

eingeführt (s. Abb. 4). Der Raum zwischen zwei Hauptstreifen wird überstrichen, wenn q von 0 bis 1 wächst.

An einer Stelle zwischen zwei Hauptstreifen sei die Wellenzahl ν ; der 'links' benachbarte Hauptstreifen habe die Wellenzahl $\nu - \Delta\nu$; die Ordnung sei n (s. Abb. 4). Es gilt dann für den Hauptstreifen

$$n = 2d(\nu - \Delta\nu) \quad (6)$$

und für die fragliche Stelle im Zwischenbereich nach (2)

$$n = 2d\nu \cdot \cos \theta_1. \quad (7)$$

Aus (6) und (7) erhält man, wenn man zur Näherung

$$\cos \theta \approx 1 - \frac{1}{2}\theta^2$$

übergeht, (4) und (5) benutzt und schließlich der besseren Anschauung wegen die Wellenlänge $\lambda = 1/\nu$ einführt:

$$\theta_1 = \sqrt{\left(q \cdot \frac{\lambda}{d}\right)}. \quad (8)$$

Anstelle von (7) lautet die Bestimmungsgleichung für θ_2 :

$$n - 1 = 2d\nu \cdot \cos \theta_2. \quad (9)$$

Daraus folgt bei sonst gleichen Schritten wie oben:

$$\theta_2 = \sqrt{\left[(q+1) \frac{\lambda}{d}\right]}. \quad (10)$$

Entsprechend erhält man

$$\theta_3 = \sqrt{\left[(q+2) \frac{\lambda}{d}\right]} \quad (11)$$

usw. Die Strahlungsanteile, die zu $\theta_1, \theta_2, \theta_3, \dots$ gehören, sollen als 1., 2., 3., ... Winkelordnung bezeichnet werden.

Dem vergrößerten Ausschnitt in Abb. 3 entspricht eine mittlere Wellenlänge $\lambda = 0,56 \mu$. Daraus errechnet man mit dem Spiegelabstand $d = 23,5 \mu$ als minimalen Wert ($q=0$) von θ_3 , bzw. maximalen Wert ($q=1$) von θ_2 :

$$\theta_3 (\min) = \theta_2 (\max) = \sqrt{\left(2 \cdot \frac{\lambda}{d}\right)} = 0,22. \quad (12)$$

Das ist gerade der Aperturwinkel des Objektivs. Die 3. Winkelordnung wirkt also hier bei der θ -Interferenz nicht mit.

Die Tabelle enthält Meßergebnisse, die an einem Streifensystem in Abb. 3 (a) (dem zweiten von rechts) gewonnen wurden. Die Streifenabstände auf der Photoplatte wurden durch den Abbildungsmaßstab des Objektivs

Streifenabstand g_{12} längs einer Vertikalen im θ -Streifensystem; $d = 23,5 \mu$; Bedingungen von Abb. 3 (a).

q	$g_{12}[\mu]$	
	gemessen	berechnet
0,4	$6,64 \pm 0,13$	$6,55 \pm 0,07$
0,7	$7,74 \pm 0,08$	$7,72 \pm 0,08$

dividiert (mit einer geringen Korrektur für die Abbildung im Innern des Spektrographen): So entstanden die Werte in Spalte 2. Den berechneten Werten liegt Formel (3) zugrunde; sie geht, wenn man θ_1 und θ_2 nach (8) und (10) einsetzt, in die folgende Beziehung über:

$$g_{12} = \sqrt{(\lambda d)[\sqrt{(q+1)} + \sqrt{q}]} \quad (13)$$

Der Spiegelabstand d wurde aus den Abständen der Hauptstreifen ermittelt.

Durch Ausblendungsversuche kann man den Zusammenhang zwischen θ und q für jede der Beziehungen (8) und (10) getrennt prüfen. Man erhält θ_1 , bzw. θ_2 aus der Brennweite des Objektivs und der Lage des Blendenstreifens in der hinteren Brennebene; diese Werte sind mit denen zu vergleichen, die sich aus q , λ und d ergeben (wobei q die gestörte Stelle im Interferogramm bezeichnet). Auch durch diese Messungen wurden die abgeleiteten Beziehungen —im Rahmen einer Fehlergrenze von 1,5 bis 3 Prozent—bestätigt.

3.3. Großer Spiegelabstand

Die Interferogramme von Abb. 5 und 6 wurden bei einem Spiegelabstand $d = 46 \mu$ aufgenommen; d ist also doppelt so groß wie bei Abb. 3. Der Aperturkegel des Objektivs erfaßt jetzt vier Winkelordnungen (Die Bezeichnung 'großer Spiegelabstand' soll andeuten, daß es mehr als zwei sind).

Die Aufnahme von Abb. 5 entstand ohne besondere Ausblendung. θ -Interferenz zeigt sich auch hier als eine Erscheinung mit Streifenstruktur; nur scheinen mehrere Streifensysteme nach Art von Abb. 3 miteinander

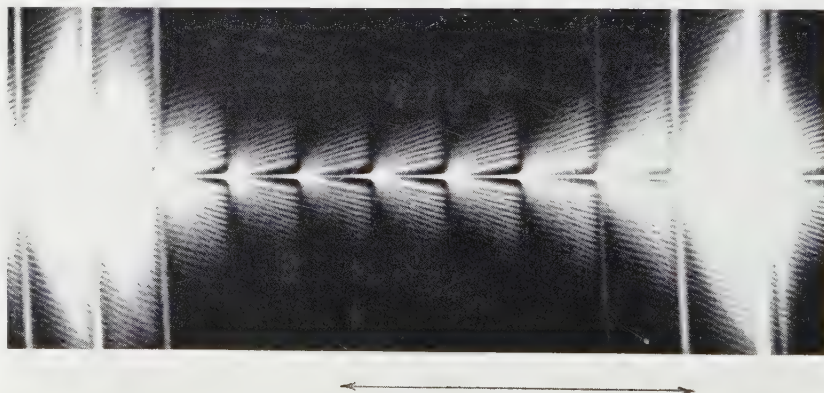


Abb. 5. θ -Interferenz bei unbedampfter Furche; Spiegelabstand 46μ . Spektralbereich, Furchenbreite, Objektiv wie bei Abb. 3 (a). Der Pfeil bezeichnet den Spektralbereich von Abb. 6.

verflochten zu sein. Ein einfaches Streifensystem mit periodischer Struktur in vertikaler Richtung wird daraus, wenn man durch Schneiden in der hinteren Brennebene des Objektivs die Apertur auf zwei Winkelordnungen begrenzt. Die Auswertung solcher Streifensysteme, wie sie an Hand der Tabelle beschrieben wurde, bestätigte wiederum Formel (3), bzw. (13). Wegen des verdoppelten Spiegelabstandes sind die Gitterkonstanten g_{12} hier um den Faktor $\sqrt{2}$ größer als in der Tabelle.

Blendet man durch einen Streifen in der hinteren Brennebene des Objektivs die 2. Winkelordnung für ein bestimmtes q -Intervall aus, so entsteht ein Interferogramm, wie es Abb. 6 zeigt. In dem erfaßten q -Intervall (also in

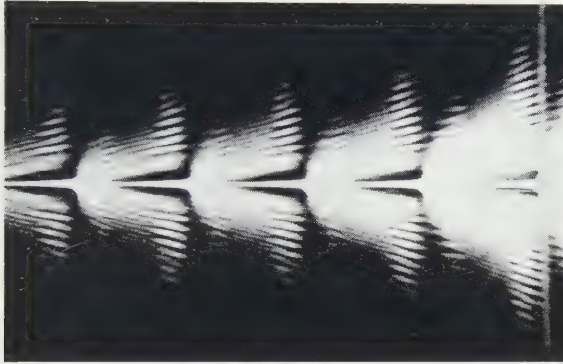


Abb. 6. Ausblendung der 2. Winkelordnung.

Zwei Blendenstreifen von 1 mm Breite liegen symmetrisch zur Aperturmitte in der hinteren Brennebene des Objektivs.

Bedingungen sonst wie in Abb. 5; Spektralbereich: s. Pfeil in Abb. 5. (Originalaufnahme auf härterer Photoplatte als Abb. 5.)

einem vertikalen Streifen des Interferogramms) beobachtet man eine periodische Folge von Maxima und Minima mit besonders kleiner Gitterkonstanten. Die Auswertung zeigt, daß es sich um das Zusammenwirken der 1. und 3. Winkelordnung handelt; die Gitterkonstante ist analog zu (3), bzw. (13) gegeben durch

$$g_{13} = \frac{\lambda}{\theta_3 - \theta_1} = \frac{1}{2} \sqrt{(\lambda d)} [\sqrt{(q+2)} + \sqrt{q}]. \quad (14)$$

Die 4. Winkelordnung, die außerdem im Aperturkegel war, scheint die periodische Struktur nach (14) nicht merklich zu beeinflussen; sie ist vermutlich zu schwach ausgeprägt.

Man kann auch die 1. Winkelordnung ausblenden und so ein Streifensystem erzeugen, das durch das Zusammenwirken der 2. und 3. Winkelordnung entsteht. Als Gitterkonstante ist zu erwarten:

$$g_{23} = \frac{\lambda}{\theta_3 - \theta_2} = \sqrt{(\lambda d)} [\sqrt{(q+2)} + \sqrt{(q+1)}].$$

Das Experiment bestätigte auch diese Beziehung.

3.4. Kleiner Spiegelabstand

Bei hinreichend kleinem Spiegelabstand d fällt nur die 1. Winkelordnung in den Aperturkegel des Objektivs. Für einen Aperturwinkel 0,22 und eine Wellenlänge $\lambda = 0,56 \mu$ leitet man aus (8) als Bedingung dafür ab: $d < 12 \mu$.

Es wurden Experimente bei $d=8\mu$ durchgeführt. Wie zu erwarten ist, gibt es keine periodische Folge von Maxima und Minima senkrecht zur Furche. Das θ -Streifensystem schrumpft zu einem einzigen ' θ -Streifen' zusammen.

An dem θ -Streifen bei kleinem Spiegelabstand zeigt sich ein Effekt, der—weniger übersichtlich—auch dem θ -Streifensystem bei größerem Spiegelabstand aufgeprägt ist: Der Verlauf des Streifens, d.h. seine Krümmung und sein Abstand von der Furche, sind durch die sphärische Aberration des Objektivs und die Scharfstellung bestimmt. Da dieser Effekt vielleicht allgemein einige Bedeutung für die Objektivprüfung hat, sollen die Ergebnisse in einer gesonderten Arbeit dargestellt werden.

Nach den Untersuchungen ist in Abb. 3, 5, 6 die Erscheinung in unmittelbarer Umgebung der Furche nicht typisch für die θ -Interferenz, sondern sie ist Ausdruck der merklichen sphärischen Aberration des Objektivs. Man vergleiche dazu das Interferogramm von Abb. 7 (a), das mit einem Objektiv geringerer sphärischer Aberration (der Achromatenkombination) aufgenommen wurde. Dort ist allerdings die Furchenbreite größer als bei Abb. 3, 5, 6; doch ist der Unterschied auch bei gleicher Furchenbreite deutlich zu bemerken.

3.5. θ -Interferenz und Spaltbeugung

Vielstrahlinterferenz wird meist nach der Summationsmethode behandelt. Es sei wiederum ein planparallel begrenzter (lateral hinreichend ausgedehnter) Interferenzraum ins Auge gefaßt, der von einer ebenen Welle beleuchtet wird. Summationsmethode bedeutet: Die einfallende Welle wird in eine Folge von Teilwellen aufgespalten, die durch sukzessive Reflexion an den Begrenzungsflächen entstehen; die Interferenzerscheinung wird als Überlagerung der Teilwellen berechnet.

Bei dem untersuchten Objekt (Abb. 1 b) ist der untere Spiegel—für sich allein betrachtet—ein Spalt. Stellt man sich die naheliegende Aufgabe, die Beugungserscheinungen in engem Anschluß an die bekannte Spaltbeugung zu behandeln, so wird man auch hier auf die Summationsmethode geführt: Von der Furche (als einer Spaltöffnung) geht eine gebeugte Welle aus und wird im Interferenzraum sukzessive reflektiert; zu berechnen ist die Überlagerung der Teilwellen.

Läßt man für die Reflexionen außer acht, daß der untere Spiegel die Furche enthält, denkt sich also das Plateau durchgehend, so folgt aus dem Ansatz unmittelbar die Existenz der Winkelordnungen, und es folgt weiter, daß die Charakteristik des Spaltbeugung als Einhüllende die Intensität der Winkelordnungen bestimmt (in Analogie zum Beugungsgitter, wo die Charakteristik des Elementarbereichs Einhüllende der Gitterordnungen ist).

Dieser Ansatz ist gewiß für eine erste Orientierung geeignet. Er gibt qualitativ ein Ergebnis richtig wieder, das sich aus dem Vergleich der θ -Interferenz bei verschiedenen Furchenbreiten (im Experiment 3— 30μ) ablesen ließ: Beim Übergang zu größeren Furchenbreiten treten hohe Winkelordnungen und große q -Werte (also Strahlung unter großem Winkel θ) relativ schwächer hervor. Eine weiter reichende Gültigkeit des Ansatzes ist kaum zu erwarten; denn es ist eine grobe Näherung, daß der untere Spiegel für die Reflexionen als durchweg eben betrachtet wird. Diese Näherung wird nur in dem Maße

zulässig sein, wie der Spiegelabstand groß gegen die Furchenbreite ist; sind Spiegelabstand und Furchenbreite von gleicher Größenordnung (wie bei den Untersuchungen der vorliegenden Arbeit und allgemein unter den praktisch interessanten Bedingungen der Vielstrahlinterferometrie), so müßte jede Reflexion am unteren Spiegel als ein eigener Beugungsvorgang in die Summation eingeführt werden.

Die Intensität der Winkelordnungen wurde zwar nicht gemessen; eine spezielle Folgerung aus dem diskutierten einfachen Ansatz ließ sich jedoch prüfen. Im Fraunhoferschen Beugungsdiagramm des Spaltes treten Minima auf unter Winkeln

$$\theta_1 = \frac{\lambda}{b}, \quad \theta_{II} = 2 \cdot \frac{\lambda}{b}, \dots \quad (15)$$

(b : Spaltbreite, bzw. Furchenbreite; λ : Wellenlänge; $\sin \theta \approx \theta$). Man kann abschätzen, daß diese Winkel für die untersuchten Furchenbreiten und Spiegelabstände (bis 53μ) in dem Bereich liegen, in dem θ -Interferenz beobachtet wurde. Wäre die Charakteristik der Spaltbeugung Einhüllende der Winkelordnungen, so müßten sich die Minima nach (15) als Unterbrechungen im Streifensystem der θ -Interferenz bemerkbar machen: Eine bestimmte Winkelordnung müßte an einer bestimmten Stelle q ausfallen. Ein solcher Effekt war nicht zu beobachten.

4. BEDAMPFTE FURCHE

In Abb. 7 (a, b) sind Aufnahmen an der unbedampften und an der bedampften Furche zum Vergleich untereinander gesetzt. Die Furchenbreite beträgt $(6,5 \pm 1,5) \mu$, der Spiegelabstand 53μ . Die Aufnahme an der bedampften Furche entstand bei sonst gleichen Bedingungen mit fünfmal größerer Belichtungszeit als die Aufnahme an der unbedampften Furche.

Bei bedampfter Furche bestehen für den Furchenbereich die normalen Bedingungen der Vielstrahlinterferenz, wenn man zunächst von einer möglichen Modifikation durch die geringe laterale Ausdehnung des Interferenzraumes absieht. Man erwartet ein Streifensystem, das entsprechend der Tiefe der Furche gegenüber dem System der Hauptstreifen im Plateaubereich zu größeren Wellenlängen verschoben ist (s. Abb. 1 a). Die Maxima dieses Streifensystems sollen als F-Hauptmaxima bezeichnet werden (F = Furche).

Es ist nach Abb. 7 (a, b) die entscheidende Änderung beim Übergang von der unbedampften zur bedampften Furche, daß θ -Interferenz auf ein kleines q -Intervall in der Umgebung des F-Hauptmaximums konzentriert wird. Schematisch ist das in Abb. 1 (c) gezeichnet. In Abb. 7 (b) ist allerdings nur ganz rechts, in einem Bereich hoher Leuchtdichte der Lichtquelle, ein Hauptstreifen des Plateaubereichs zu erkennen. Im übrigen fehlen die Hauptstreifen, weil die Durchlässigkeit des Plateaus durch die Überdampfung weiter herabgesetzt wurde. Auf dem Original jedoch kann man an mehreren Stellen des Spektrums Hauptstreifen erkennen; man kann ihre Lage auch aus der schwach ausgeprägten θ -Interferenz in der Umgebung der Stelle $q = 0$ erschließen (s. dazu ebenfalls den rechten Teil von Abb. 7 b). So läßt sich experimentell sicherstellen, daß die Aufnahmen 7 (a, b) mit gleicher Lage der Hauptstreifen untereinander stehen.

Abb. 7 (c), eine Aufnahme zur Furchenbreite $b = (14 \pm 2) \mu$ bietet im wesentlichen das gleiche Bild wie Abb. 7 (b). Doch bemerkt man im Bereich hoher

Leuchtdichte der Lichtquelle einen weiteren Effekt: Rechts neben dem einen vertikalen Streifen, in dem θ -Interferenz maximal ausgeprägt ist, gibt es einen 'Satellitenstreifen', das soll heißen einen schwächeren Streifen, der nicht am Ort eines F-Hauptmaximums liegt.

Dieser Effekt ist noch deutlicher an Abb. 8 zu erkennen, einer Aufnahme bei dem kleineren Spiegelabstand von 15μ . Man findet zunächst die aus Abb. 7(b, c) bekannten vertikalen Streifen maximaler θ -Interferenz, die von einem

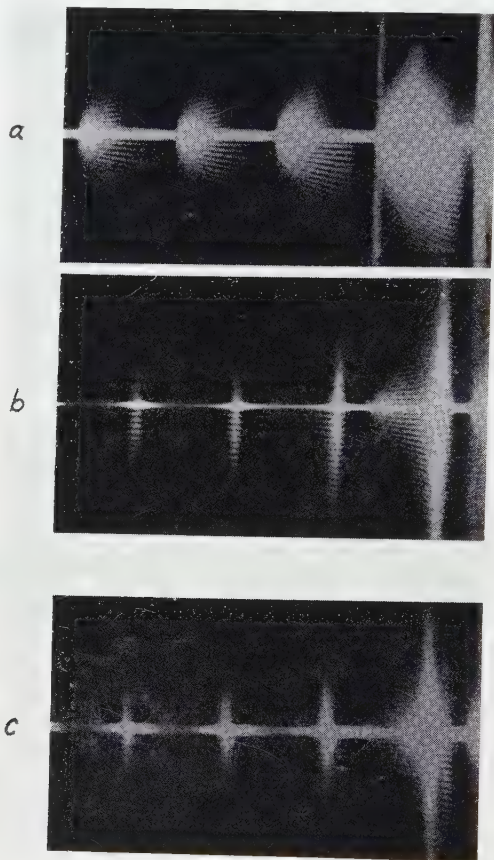


Abb. 7. Vergleich der θ -Interferenz bei unbedampfter und bei bedampfter Furche.

(a) Unbedampfte Furche; Breite $6,5\mu$.

(b) Bedampfte Furche; Breite $6,5\mu$.

(c) Bedampfte Furche; Breite 14μ .

Spektralbereich $\lambda = 0,559-0,546\mu$; Spiegelabstand 53μ ; Objektiv: Achromatenkombination.

Apertur durch Schneiden in der hinteren Brennebene des Objektivs unsymmetrisch begrenzt: 2. Winkelordnung wird in der oberen Gesichtsfeldhälfte bei $q=0,4$, in der unteren bei $q\approx 1$ abgeschnitten. Daher in der oberen Gesichtsfeldhälfte nur für $q<0,4$ θ -Interferenz mit Streifenstruktur.

F-Hauptmaximum herrühren. Einer dieser Streifen fällt in den Bereich hoher Leuchtdichte bei $\lambda=0,546\mu$. Hier (auf dem Original auch an anderen Stellen) erkennt man mehrere rechts benachbarte Satellitenstreifen. Der Abstand benachbarter Streifen ist bei der breiten Furche (unten) geringer

als bei der schmalen (oben); er wächst mit zunehmender Entfernung vom F-Hauptmaximum.

Den Satellitenstreifen entsprechen knotenartige Aufhellungen im Furchenbereich. Das zeigt bereits Abb. 8. Deutlicher tritt dieser Zusammenhang hervor, wenn man das Objektiv defokussiert. In Abb. 9 ist das Objektiv über die Scharfstellung der Furche hinaus vom Objekt entfernt. Die knotenartigen Aufhellungen im Furchenbereich sind zu Paaren von Knoten auseinandergerückt. Jedem der beiden Plateaubereiche entspricht eine eigene Folge von Knoten, die sich zu einem kurzen (genähert horizontal verlaufenden) 'Knotenstreifen' anordnen.

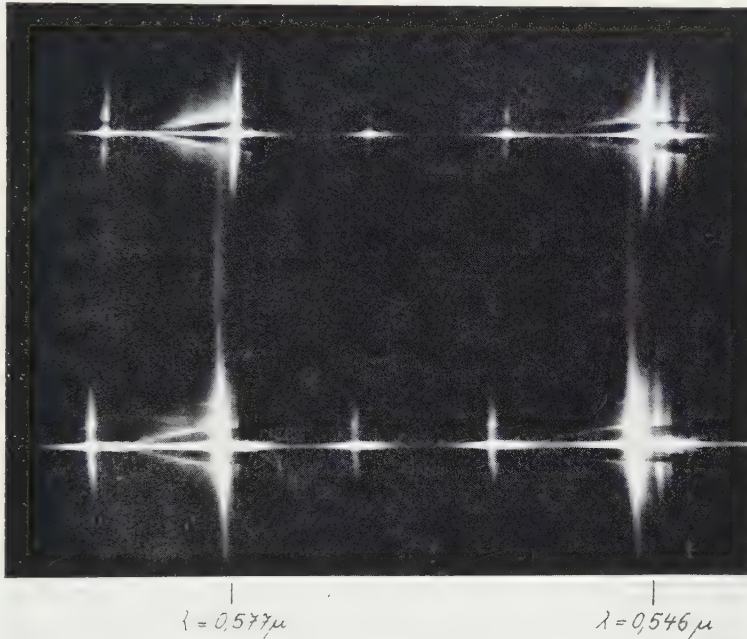


Abb. 8. Satellitenstreifen der θ -Interferenz bei bedampfter Furche; Spiegelabstand $15\ \mu$; oben: Furchenbreite $6,5\ \mu$; unten: Furchenbreite $14\ \mu$.

Weitere Einsicht bringen Ausblendungsversuche. Sie zeigen, daß die Knotenstreifen durch Strahlung entstehen, die unter endlichem Winkel θ aus dem Furchenbereich austritt, und zwar ist jeder Aperturhälfte einer der beiden Knotenstreifen zugeordnet. Die Knotenstreifen sind θ -Streifen des Furchenbereichs; sie stehen in Analogie zu den θ -Streifen des Plateaubereichs, die bei kleinem Spiegelabstand entstehen, wenn nur eine Winkelordnung im Aperturkegel ist (§ 3.4). Nur nimmt bei den θ -Streifen des Plateaubereichs die Intensität mit wachsendem θ monoton ab, während bei den Knotenstreifen einzelne Richtungen als Strahlungsmaxima (eben als 'Knoten') ausgezeichnet sind. Es liegt schon hier nahe (und wird durch die quantitative Deutung gerechtfertigt werden), die Knoten als F-Nebenmaxima zu bezeichnen, d.h. als Nebenmaxima der Interferenz im Furchenbereich.

Den Winkel θ , der einem F-Nebenmaximum zukommt, kann man wie früher aus dem Interferogramm bestimmen. Man denke sich in Abb. 4 die

gestrichelten Linien durch einen Knotenstreifen ersetzt. Dem Interferogramm entnimmt man q nach (5) und berechnet daraus θ nach (8). Anfangs- und Endpunkt der q -Skala ($q=0$ bzw. $q=1$) sind dabei jetzt zwei benachbarte F-Hauptmaxima.

Nach Abb. 8, 9 und weiteren Untersuchungen bei den Furchenbreiten 21, 14 und $6,5\mu$ ist die Lage der F-Nebenmaxima durch die Furchenbreite bestimmt. Bei den schmalsten untersuchten Furchen (Breite um 3μ) konnten keine F-Nebenmaxima beobachtet werden. Hier hört aber auch die Auszeichnung der Richtung $\theta=0$ durch ein scharfes F-Hauptmaximum auf. Mit abnehmender Furchenbreite werden die Erscheinungen an der bedampften Furche denen an der unbedampften Furche immer ähnlicher.

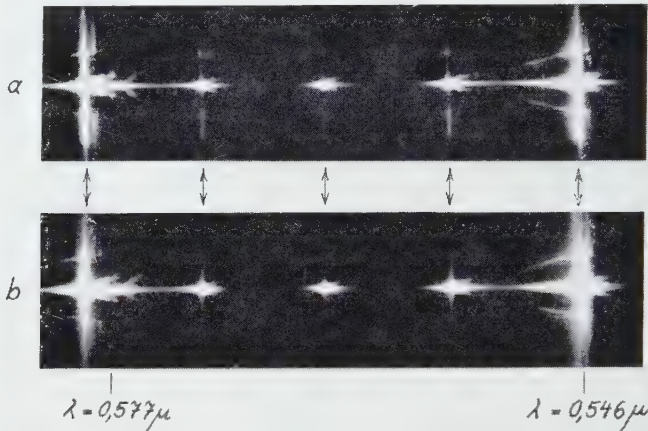


Abb. 9. Knotenstreifen bei bedampfter Furche. Die Pfeile weisen auf F-Hauptmaxima. Rechts daneben einige Paare von Knoten erkennbar (besonders bei $\lambda=0,577\mu$). Spiegelabstand 19μ .

(a) Furchenbreite 14μ .

(b) Furchenbreite 21μ .

Durch Auflichtmessungen an breiten Furchen in der gleichen Ag-Schicht wurde die Furchentiefe von 1100\AA bestimmt und damit die Lage der F-Hauptmaxima (ihre Versetzung gegenüber einem Hauptstreifen des Plateaubereichs), die bei einer breiten Furche unter normalen Bedingungen zu erwarten ist. Vergleicht man damit die Lage der vertikalen Streifen maximaler θ -Interferenz bei der Furche von $6,5\mu$ Breite (s. Abb. 7b), so zeigt sich als ein Effekt am Rande der Fehlergrenzen, daß diese Streifen nach rechts verschoben sind. Es ist danach zu vermuten, daß bei schmalen Furchen das F-Hauptmaximum in Richtung der F-Nebenmaxima verzerrt ist.

5. HOHLLEITER-MODELL

Wie am Schluß von Kap. 3 ausgeführt wurde, entstehen schon im Fall der unbedampften Furche Schwierigkeiten, wenn man die untersuchten Erscheinungen über die Summationsmethode aus der Spaltbeugung ableiten will. Diese Schwierigkeiten sind bei der bedampften Furche noch größer; insbesondere

ist nicht zu sehen, wie man auf diesem Wege zu einer Beschreibung der F-Nebenmaxima gelangen kann.

Eine Beschreibung aller beobachteten Erscheinungen liefert ein anderer Ansatz. Die Interferenzräume über dem Plateau sind als Hohlleiter anzusehen; der Interferenzraum über der Furche ist wegen der seitlichen Begrenzung einem Hohlraumresonator zu vergleichen. Die einfallende Strahlung erregt die Eigenwellen, bzw. Eigenschwingungen dieser Interferenzräume. Die Winkelordnungen des Plateaubereichs, die zur θ -Interferenz führen, lassen sich als stetige Fortsetzung der Eigenwellen in den Außenraum ansehen; jedes F-Nebenmaximum kann einer Eigenschwingung des Furchenbereichs zugeordnet werden.

Das soll in einer folgenden Arbeit näher ausgeführt werden.

ANERKENNUNGEN

Die vorliegende und die folgende Arbeit wurden im Rahmen einer Dissertation unter Anleitung von Herrn Prof. Dr. H. Lassen ausgeführt. Der Verfasser ist Herrn Prof. Lassen für viele Hinweise, Diskussionen und die gesamte Förderung der Arbeit zu großem Dank verpflichtet.

A groove having a width of 3 to 30 μ runs across an almost opaque silver layer on a flat glass substrate; above it—in a plane parallel position at distances of between 8 and 50 μ —there is a glass mirror covered by a partly transmitting evaporated layer. In the initial part of the experiments the bottom of the groove is not covered by any deposit; in the second part a partly transmitting layer is evaporated. This object is examined in transmitted light according to the method of fringes of equal chromatic order. Evidence is thereby provided of radiation which leaves the object under finite angles θ with the direction of the incident wave (normal direction). The phenomena within the region outside the groove can be ascribed to discrete 'angular orders' according to the relation $n\lambda = 2d \cos \theta$. In the case of the groove being covered by a layer the interference phenomenon within the region of the groove shows secondary maxima beside a principal maximum, which corresponds to the direction $\theta = 0$. The position of the secondary maxima is determined by the width of the groove.

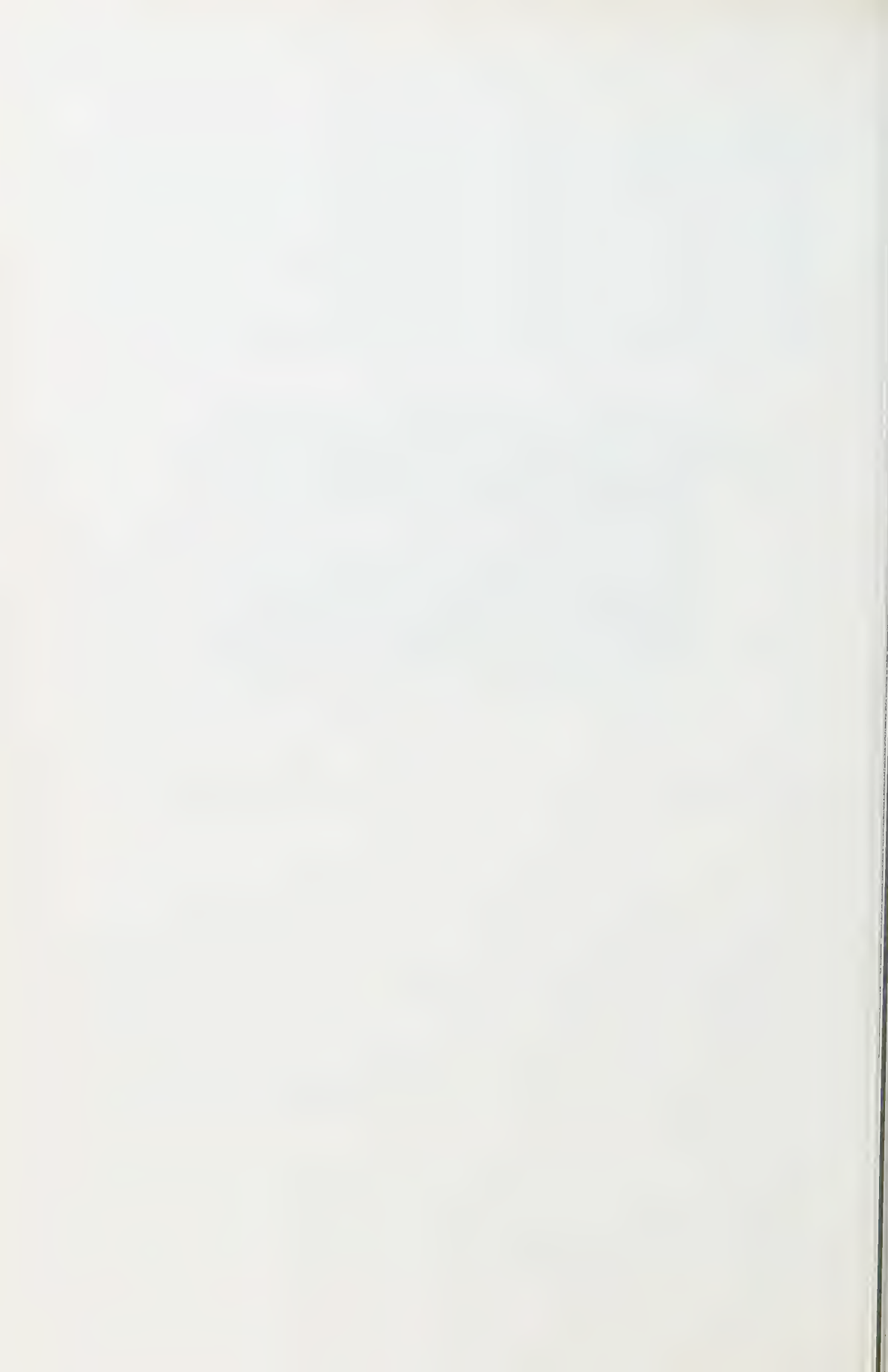
It is briefly indicated how all the phenomena observed could be explained by means of a waveguide model. A fuller treatment of this model is reserved for a second paper.

Dans un dépôt quasi opaque sur support de verre plan il y a un sillon de largeur comprise entre 3 et 30 μ . Par dessus se trouve, parallèle et à des distances comprises entre 8 et 50 μ , un miroir de verre sur lequel a été évaporée une couche semitransparente. Le fond du sillon est nu dans la première partie des recherches et il est recouvert d'une couche semitransparente dans la deuxième partie. Cet objet est examiné en lumière transmise suivant la méthode des franges d'égal ordre chromatique. On montre qu'il y a un rayonnement quittant l'objet sous un angle fini θ par rapport à la direction de l'onde incidente (direction normale). Les phénomènes observés dans la région extérieure au sillon se ramènent à des 'ordres angulaires' discrets, d'après la relation $n\lambda = 2d \cos \theta$. Lorsque le sillon est recouvert d'une couche mince, le phénomène interférentiel dans le domaine du sillon présente, en dehors d'un maximum principal correspondant à $\theta = 0$, des maxima secondaires dont la position est déterminée par la largeur du sillon.

On indique brièvement comment tous les phénomènes observés peuvent être expliqués par un modèle de guide d'onde. L'étude approfondie de ce modèle sera faite dans un deuxième travail.

LITERATUR

- [1] TOLANSKY, S., 1948, *Multiple beam interferometry of surfaces and films* (Oxford: Clarendon Press).
- [2] INGELSTAM, E., 1953, *Ark. Fys.*, **7**, 309.
- [3] THORNTON, B. S., 1957, *Opt. Acta*, **4**, 41.
- [4] FAUST, R. C., 1952, *Proc. roy. Soc. A*, **211**, 240.



Vielstrahlinterferenz als Hohlleiterproblem†

von GERHARD SIMONSOHN

I. Physikalisches Institut der Freien Universität, Berlin

(Received 29 August 1960)

In einer vorausgegangenen Arbeit wurden Beugungsexperimente an einem einfachen Objekt der Vielstrahlinterferometrie beschrieben: Durch eine schmale Furche in einem ebenen Spiegel wird der Interferenzraum zwischen zwei Spiegeln in drei planparallel begrenzte Teilräume aufgespalten, einen Furchenbereich und zwei angrenzende Plateaubereiche. Die Ergebnisse dieser Experimente waren der Anlaß, die elementare Beschreibung der Vielstrahlinterferenz zu erweitern.

Den Plateaubereichen läßt sich eine Folge von Hohlleiterwellen zuordnen, die von der einfallenden, in den Furchenbereich eindringenden Strahlung angeregt werden. Im Furchenbereich treten stehende Hohlleiterwellen auf. Wegen der Stetigkeit des elektromagnetischen Feldes sind die Hohlleiterwellen der Plateaubereiche an die Resonanzerscheinung im Furchenbereich gekoppelt.

Die Überlegungen führen zu einer richtigen Beschreibung der Meßergebnisse. Es ist darüber hinaus zu vermuten, daß Hohlleiter-Erscheinungen allgemein bei der Beugung in der Vielstrahlinterferometrie eine Rolle spielen.

1. EINLEITUNG

Es ist bekannt, daß man die Interferenz zwischen planparallelen, verspiegelten Flächen—also die Grunderscheinung der Vielstrahlinterferometrie—bei senkrechter Einfallrichtung der Strahlung als eine Resonanzerscheinung beschreiben kann (vgl. [1]). Der Interferenzraum, d.h. der Raum zwischen den verspiegelten Flächen, ist elektromagnetischer Eigenschwingungen fähig, die von der einfallenden Strahlung angeregt werden.

In dieser Darstellung besteht die Wirkungsweise eines Interferenzfilters darin, aus dem Spektrum der einfallenden Strahlung diejenigen Wellenlängen (samt einer kleinen Umgebung) auszusondern, die Eigenwellenlängen des Interferenzraumes sind. Die Strahlung dieser Wellenlängen führt zur Anregung von Eigenschwingungen, und das macht sich als Abstrahlung nach vorn—also als Durchlässigkeit des Filters—bemerkbar.

Die Eigenwellenlängen λ sind durch die Beziehung

$$n \cdot \lambda = 2d \tag{1}$$

(d : Höhe des Interferenzraumes; n : ganze Zahl) gegeben (wenn als Dielektrikum im Interferenzraum Luft mit dem Brechungsindex 1 angenommen wird). Die Eigenschwingungen lassen sich als Überlagerung zweier entgegengesetzt laufender ebener Wellen der Wellenlänge λ darstellen. Durch die Forderung (1) wird als einzige Randbedingung erfüllt, daß das elektrische Feld an den verspiegelten Flächen verschwindet. Die Lösung gilt streng nur für einen unendlich ausgedehnten Interferenzraum.

† Auszug aus der Dissertation des Verfassers: Nachweis und Deutung gebeugter Strahlung in der Vielstrahlinterferometrie, D 188, Freie Universität, Berlin, 1960.

In der Vielstrahlinterferometrie als Hilfsmittel der Oberflächenuntersuchung hat man es mit Objekten zu tun, bei denen die Höhe d des Interferenzraumes stetig oder unstetig variiert. Zum Beispiel wird in einem typischen Fall der Interferenzraum durch eine Furche in einem sonst ebenen Spiegel in drei Teilräume zerlegt, die durch die Ränder der Furche unstetig begrenzt sind. Stehen die beiden Spiegel parallel zueinander—was bei dem Verfahren der Streifen gleicher Farbordnung möglich ist—, so ist jeder Teilraum für sich ein Interferenzfilter. Es ist die übliche Näherung, für jedes dieser 'elementaren' Interferenzfilter die Eigenschwingung anzusetzen, die aus der des unendlich ausgedehnten Filters gleicher Höhe d durch unstetige seitliche Begrenzung entsteht. Damit ist eine grundlegende Forderung außer acht gelassen: die Stetigkeit des elektromagnetischen Feldes an der Grenze benachbarter Teilräume.

Die im folgenden mitgeteilten Überlegungen ließen sich allein unter dem Gesichtspunkt führen, das skizzierte Resonanzmodell für die Vielstrahlinterferenz so zu erweitern, daß diese Stetigkeitsforderung erfüllt werden kann. Entstanden sind sie zur Deutung der Ergebnisse einiger Beugungsexperimente, die in einer vorausgegangenen Arbeit [2] mitgeteilt wurden.

2. DAS BETRACHTETE OBJEKT

Das Objekt der Beugungsexperimente war aus zwei ebenen Glasspiegeln zusammengesetzt. Der obere Spiegel trug eine teildurchlässige Silberschicht, wie sie in der Vielstrahlinterferometrie üblich ist, der untere eine dickere, fast undurchlässige Silberschicht, in der eine Furche von einigen μ Breite freigelassen war (vgl. Abb. 1). Der Furchengrund war entweder unbedampft oder teildurchlässig bedampft. Die Spiegel waren parallel zueinander angeordnet; es wurde das Verfahren der Streifen gleicher Farbordnung angewandt. Die beleuchtende Strahlung fiel senkrecht von unten ein. Im Durchlicht wurde gebeugte Strahlung nachgewiesen.

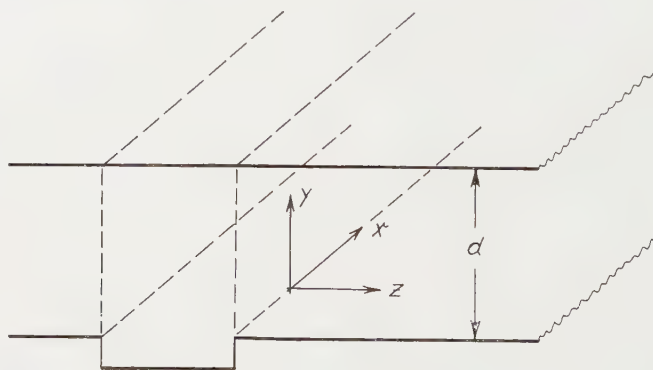


Abb. 1. Objekt (schematisch). Rechter Plateaubereich mit Achsenkreuz versehen.

Es soll hier nur dieses Objekt betrachtet werden; doch ist zu vermuten, daß die Überlegungen allgemeinere Bedeutung haben. Die drei planparallel begrenzten Interferenzräume, in die sich das Objekt zerlegen läßt, sollen als Furchenbereich, bzw. als Plateaubereiche bezeichnet werden. Die laterale Ausdehnung der Plateaubereiche lag bei 1 mm und war damit rund um einen Faktor 100 größer als Breite und Höhe des Furchenbereichs.

3. DIE PLATEAUBEREICHE ALS HOHLLEITER

3.1. Beziehung zur Mikrowellentechnik

Zwei ebene, parallele Platten hoher Leitfähigkeit bilden einen elektromagnetischen Hohlleiter. Man kann ihn als Grenzfall eines Hohlleiters von rechteckigem Querschnitt auffassen: Die Länge einer Seite ist unendlich.

Hohlleiter spielen in der Mikrowellentechnik eine große Rolle; ihre Eigenschaften sind in diesem Zusammenhang untersucht worden. Typische Abmessungen des Querschnitts sind 1 bis 10 cm bei einer Wellenlänge um 1 cm. Verringert man beide Werte um den Faktor 10^{-4} , schreibt also μ statt cm, so erhält man Bedingungen, wie sie in der Vielstrahlinterferometrie auftreten. Hohlleiterphänomene sind in der Optik bereits bei Untersuchungen zum Durchgang der Strahlung durch einen tiefen Metallspalt beobachtet worden ([3, 4, 5]).

Man kann nun die Plateaubereiche des untersuchten Objektes wegen der hohen Leitfähigkeit der Silberschichten als planparallel begrenzte Hohlleiter der Höhe d auffassen. In Abb. 1 ist der rechte Plateaubereich durch das eingezeichnete Achsenkreuz hervorgehoben. Es wird zunächst der Idealfall angenommen, daß der Hohlleiter in positiver z -Richtung unbegrenzt ist und die Wände unendliche Leitfähigkeit haben.

3.2. Homogene Hohlleiterwellen

Dem betrachteten Hohlleiter läßt sich eine Folge von Eigenwellen zuordnen, die durch eine geeignete Feldverteilung am Eingang ($z=0$) angeregt werden können. Zwei Wellentypen sind möglich: E-Wellen (TM-Wellen) und H-Wellen (TE-Wellen), das sind Wellen mit rein transversalem magnetischen, bzw. rein transversalem elektrischen Feld. Es werden nur H-Wellen betrachtet. Die hier in Frage kommenden allgemeinen Überlegungen lassen sich ohne weiteres auf E-Wellen übertragen.

Die Formeln sind nach Slater [6] zitiert. Der dort benutzte Winkel θ wurde entsprechend der Bezeichnung in der vorliegenden Arbeit durch das Komplement ersetzt. Für das Dielektrikum Luft zwischen den Wänden ist $\epsilon = \epsilon_0$, $\mu = \mu_0$ zu setzen, woraus folgt:

$$\omega \sqrt{(\epsilon_0 \mu_0)} = \frac{2\pi}{\lambda} = k.$$

Es existiert für jede 'Vakuumwellenlänge' λ eine diskrete Folge von H-Wellen, die zu 'Eigenwerten'

$$k_y = n \frac{\pi}{d}, \quad n = 1, 2, \dots \quad (2)$$

gehören. Die Komponenten der Feldstärken sind durch folgende Beziehungen gegeben:

$$\left. \begin{aligned} E_x &= H_0 \sqrt{\left(\frac{\mu_0}{\epsilon_0}\right) \frac{1}{\sin \theta}} \cdot \sin(k_y \cdot y) \\ H_y &= H_0 \cdot \sin(k_y \cdot y) \\ H_z &= H_0 \frac{\cos \theta}{j \sin \theta} \cdot \cos(k_y \cdot y) \end{aligned} \right\} \cdot \exp \left[2\pi j \left(\frac{t}{\tau} - \frac{z \cdot \sin \theta}{\lambda} \right) \right] \quad (3)$$

($\omega = 2\pi/\tau$).

Die Größe θ ist mit k_y durch die Gleichung

$$\cos \theta = \frac{k_y}{k} \quad (4a)$$

$$\text{bzw.} \quad \sin \theta = \frac{\sqrt{(k^2 - k_y^2)}}{k} \quad (4b)$$

verbunden. Schreibt man in den Formeln (3) als neue Konstante

$$\frac{H_0}{\sin \theta} = C$$

und führt die 'Rohrwellenlänge'

$$\Lambda = \frac{\lambda}{\sin \theta} \quad (5)$$

ein ([7], S. 14 f.), so erhält man:

$$\left. \begin{aligned} E_x &= C \sqrt{\left(\frac{\mu_0}{\epsilon_0}\right)} \cdot \sin(k_y \cdot y) \\ H_y &= C \cdot \sin \theta \cdot \sin(k_y \cdot y) \\ H_z &= C \cdot \frac{1}{j} \cdot \cos \theta \cdot \cos(k_y \cdot y) \end{aligned} \right\} \cdot \exp \left[2\pi j \left(\frac{t}{\tau} - \frac{z}{\Lambda} \right) \right] \quad (3a)$$

Das System (3a) stellt eine Welle dar, die sich in positiver z -Richtung ausbreitet; Λ ist der Abstand benachbarter Ebenen gleicher Phase.

Dabei ist vorausgesetzt, daß Λ reell, also nach (4b) $k_y \leq k$ ist. Unter dieser Bedingung, die nach (2) für eine endliche Zahl von Eigenwerten k_y erfüllt ist

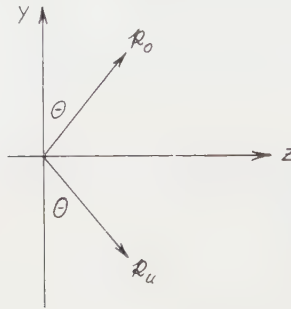


Abb. 2. Zur Zerlegung der Hohlleiterwelle (3a) in zwei ebene Wellen.

(für keinen Eigenwert, wenn $2d < \lambda$ ist), hat θ eine anschauliche Bedeutung. Die Welle (3a) läßt sich als Überlagerung zweier ebener Wellen darstellen, deren Wellenvektoren \mathbf{k}_o , bzw. \mathbf{k}_u den Betrag $k = 2\pi/\lambda$ haben; die Richtungen der Vektoren schließen mit der y -Achse den Winkel θ ein (s. Abb. 2). Setzt man (2) in (4a) ein, so erhält man für den Winkel θ , der zum n -ten Eigenwert gehört:

$$2d \cdot \cos \theta = n \cdot \lambda. \quad (6)$$

Das ist die bekannte Interferenzbedingung für schräg verlaufende Strahlung. Im Grenzfall $k_y = k$, also $\cos \theta = 1$, stellt (3a) die Eigenschwingung dar, die sich aus einer in y -Richtung einfallenden ebenen Welle und der entgegengesetzt laufenden Welle konstruieren läßt.

3.3. Deutung der Meßergebnisse

Die Experimente ([2], Kap. 3 und 4) hatten gezeigt, daß aus dem Plateaubereich Strahlungsanteile unter diskreten Winkeln θ austreten, die sich nach (6) berechnen lassen; diese Anteile wurden als Winkelordnungen bezeichnet. Wie die Zerlegung der Hohlleiterwelle in die beiden Teilwellen zeigt, sind die Winkelordnungen eng mit den Hohlleiterwellen verknüpft: Sie lassen sich als die nach oben gerichteten ebenen Teilwellen mit dem Wellenvektor \mathbf{k}_0 deuten, die sich wegen der endlichen Durchlässigkeit der Silberschicht schwach in den Außenraum fortsetzen. Man gelangt zu einer richtigen Beschreibung aller beobachteten Erscheinungen, wenn man sich zwei Schritte vorstellt:

Die einfallende Strahlung erregt im Furchenbereich eine Resonanzerscheinung. Diese Resonanzerscheinung bestimmt die Anregung von Eigenwellen der Plateaubereiche.

Bei bedampfter Furche hinreichender Breite weist die Resonanzerscheinung im Furchenbereich ausgeprägte Maxima auf. Ihnen entspricht eine maximale Anregung der Hohlleiterwellen der Plateaubereiche, die sich im Experiment an den Winkelordnungen ablesen läßt ([2], Abb. 7 und 8). Mit abnehmender Furchenbreite und beim Übergang zur unbedampften Furche verschwindet die Auszeichnung einzelner Stellen als Resonanzmaxima des Furchenbereichs; die Winkelordnungen der Plateaubereiche erscheinen dann annähernd gleichmäßig im Interferogramm

Es ist nun weiter zu fragen, wie man die Resonanzerscheinung im Furchenbereich zu beschreiben hat. Auch hier ist die Anwendung des Hohlleitermodells angemessen und führt zu einer quantitativ richtigen Deutung der beobachteten Nebenmaxima ([2], Abb. 7c, 8, 9). Das wird im folgenden Kapitel behandelt. Zuvor sollen noch die Aussagen über den Plateaubereich als Hohlleiter ergänzt werden.

3.4. Dämpfung durch endliche Leitfähigkeit der Wände

Die endliche Leitfähigkeit des Metalls, aus dem die Wände eines Hohlleiters bestehen, führt zu einem Energieverlust der Welle durch Joulesche Wärme. Beim Interferenzraum, wo mindestens die obere Begrenzung eine teildurchlässige Schicht ist, erscheint ein Teil der Energie, die der Welle entzogen wird, als austretende Strahlung. Wegen des Energieverlustes sind nur gedämpfte Hohlleiterwellen möglich. Bei schwachem Energieverlust, also hoher Leitfähigkeit der Wände, kann man erwarten, daß man die richtigen Lösungen genähert aus den Lösungen (3a) erhält, indem man sie mit einem Dämpfungsfaktor multipliziert ([7], S. 30 ff.). Heinze und Schmelzer [4] haben bemerkt, daß diese Näherung für E-Wellen von niedrigem Index n (s. (2)), die bei ihren Untersuchungen auftraten, ungültig ist. Bei der vorliegenden Arbeit kamen nur Wellen zu hohem Index n vor. Wegen der quantitativ richtigen Beschreibung der Winkelordnungen als Fortsetzungen der Wellen (3a) ist es wahrscheinlich, daß hier die Näherung gilt. Gelegentlich wurde ein Polarisationsfilter in den Strahlengang gebracht, ohne daß dadurch die beobachteten Erscheinungen beeinflußt wurden. Systematisch wurde aber nicht nach Polarisierungseffekten gesucht.

3.5. Inhomogene Wellen

Bisher wurden nur Wellen betrachtet, die der Bedingung $k_y \leq k$ genügen (s. (2)). Solche Wellen nennt man homogen (propagating modes); eine in

z -Richtung periodische Feldverteilung breitet sich mit einem Energietransport in dieser Richtung aus. Durch die Bedingung $k_y > k$ wird eine diskrete Folge von Hohlleiterwellen beschrieben, die man als inhomogene Wellen (evanescent modes) bezeichnet (s. [7], S. 16). Für $k_y > k$ wird die rechte Seite von Gleichung (4b) imaginär. Setzt man diesen imaginären Wert statt der bisher reellen Winkelfunktion $\sin \theta$ in (3) ein, so kann man die charakteristische Eigenschaft der inhomogenen Wellen ablesen: Die Phase ist unabhängig von z ; die Amplitude nimmt in z -Richtung exponentiell ab. Diese inhomogenen Wellen transportieren keine Energie ([7], S. 27); der Poyntingsche Vektor ist im zeitlichen Mittel Null.

Erst homogene und inhomogene Wellen zusammen bilden ein vollständiges System von Eigenwellen: Jede Feldverteilung in der Ebene $z=0$ (Furchenrand) kann durch eine Überlagerung dieser Wellen stetig in den Plateaubereich fortgesetzt werden. Es ist daher wahrscheinlich, daß im allgemeinen nicht nur homogene, sondern auch inhomogene Wellen durch die Strahlung im Furchenbereich angeregt werden. Inhomogene Wellen treten bei allen verwandten Problemen der Hohlleitertechnik auf: bei der Anregung durch vorgegebene Quellen ([7], S. 51 f.), bei der Reflexion an einer Blende ([7], S. 68 f.), bei un-stetiger Änderung des Hohlleiterquerschnitts ([6], S. 183 f.).

Ein experimenteller Beweis für die Existenz von inhomogenen Wellen ließ sich bisher nicht erbringen. Auch von den inhomogenen Wellen ist zu erwarten, daß sie sich wegen der endlichen Durchlässigkeit der oberen Silberschicht durch Abstrahlung bemerkbar machen. Erscheinungen, die in unmittelbarer Umgebung der Furche zu beobachten waren, könnten mit inhomogenen Wellen zusammenhängen; doch war bisher ein zuverlässiger Schluß nicht möglich. Der experimentelle Vorteil beim Nachweis der homogenen Wellen auf dem Wege über die Winkelordnungen ist die scharfe Auszeichnung einer Richtung. Dieser Vorteil besteht vermutlich für den Nachweis der inhomogenen Wellen nicht.

4. DER FURCHENBEREICH ALS HOHLRAUMRESONATOR

4.1. Stehende Hohlleiterwellen

Die Plateaubereiche sind lateral so weit ausgedehnt, daß sich eine homogene Hohlleiterwelle (3a) wegen der Dämpfung totlaufen kann. Deswegen kann man für die Plateaubereiche die Eigenwellen des einseitig unendlichen Hohlleiters ansetzen. Das gilt für den Furchenbereich nicht. Eine homogene Welle (3a), die sich im Furchenbereich ausbreitet, wird an den Rändern der Furche reflektiert. Die Überlagerung von hin- und rücklaufender Welle führt zu einer stehenden Welle, deren Knotenabstand in lateraler Richtung gleich der halben Rohrwellenlänge Λ nach (5) ist. Die stehende Welle 'paßt' in den Furchenbereich, wenn die Furchenbreite b ein ganzes Vielfaches m des Knotenabstandes ist. Das führt zu einer Bedingung für 'laterale Resonanz', die die Bedingung (6) für 'vertikale Resonanz' ergänzt:

$$m \cdot \Lambda = 2b$$

oder nach (5):

$$m \cdot \lambda = 2b \cdot \sin \theta. \quad (7)$$

Man kann den Furchenbereich einem Hohlraumresonator der Breite b und der Höhe d vergleichen, indem man sich an den Furchenrändern vertikale, reflektierende Wände denkt. Für den Idealfall, daß alle vier begrenzenden Ebenen unendliche Leitfähigkeit haben, sondert Formel (7) aus allen Wellen (3a),

die in einem unendlich ausgedehnten Hohlleiter der Höhe d möglich sind, diejenigen aus, die—als Kombination aus hin- und rücklaufender Welle—eine Eigenschwingung des Hohlraumresonators ergeben (vgl. [8]).

Zweierlei bedingt eine Abweichung von dem Idealfall:

(A) Die Leitfähigkeit der oberen und unteren Begrenzung des Furchenbereichs ist endlich.

(B) Die Reflexion, die durch die Querschnittsänderung am Furchenrand hervorgerufen wird, geschieht mit einem von 1 verschiedenen Reflexionsvermögen, d.h. die Randbedingung ist anders als bei einer leitenden Wand.

Sowohl (A) als auch (B) wirken sich als Abflachung der Resonanz aus. (B) läßt außerdem erwarten, daß die Bedingung (7) durch eine Funktion $\psi(\theta)$ korrigiert werden muß, die den Phasensprung bei der Reflexion einer Hohlleiterwelle am Furchenrand beschreibt:

$$m \cdot \lambda = 2b \cdot \sin \theta + 2\psi(\theta). \quad (7a)$$

Es bleibt hier zunächst offen, welchen weiteren Einfluß (A) hat.

4.2. Deutung der Meßergebnisse

Die Experimente ([2], Kap. 4) hatten gezeigt, daß auch aus dem Furchenbereich Strahlung unter endlichen Winkeln θ austritt. Bei Defokussierung war als ' θ -Streifen' die '1. Winkelordnung des Furchenbereichs' zu beobachten, also eine Erscheinung, bei der λ und θ nach (6) mit der Höhe d des Furchenbereichs zusammenhängen. Zum Unterschied von der entsprechenden Erscheinung im Plateaubereich waren hierbei einzelne Winkel θ als Knoten der θ -Streifen hervorgehoben. Diese Knoten wurden als F-Nebenmaxima bezeichnet (Nebenmaxima der Interferenz im Furchenbereich). Dem Winkel $\theta=0$ entspricht das F-Hauptmaximum, das man nach der elementaren Beschreibung als einziges Interferenzmaximum im Furchenbereich erwartet. Die Existenz der F-Nebenmaxima konnte auch indirekt aus der Anregung der Winkelordnungen des Plateaubereichs erschlossen werden ([2], Abb. 7c, 8).

Die Auswertung mehrerer Aufnahmen (s. Abb. 3) macht es wahrscheinlich, daß die beobachteten F-Nebenmaxima Maxima der lateralen Resonanz sind, die durch (7a) mit $m=1, 2, \dots$ beschrieben werden. Durch $m=0$ ist das F-Hauptmaximum festgelegt.

Im Zusammenhang mit den Experimenten war erläutert worden (s. [2], am Ende von Kap. 4), wie man den Winkel θ , der einem F-Nebenmaximum zukommt, über die Hilfsgröße q aus dem Interferogramm bestimmen kann. Zur Prüfung von (7a) muß jedem so bestimmten Winkel θ eine Ordnungszahl m zugeordnet werden. Die starke Schwärzung der Platten in der Nähe eines F-Hauptmaximums macht es ungewiß, ob das erste beobachtbare Maximum daneben zu $m=1$ oder einem größeren Wert gehört. Experimentelles Ergebnis ist aber dies: Ordnet man dem ersten beobachtbaren Nebenmaximum eine beliebige Ordnung $m=M$ zu, den jeweils benachbarten Nebenmaxima die Ordnungen $M+1, M+2, \dots$, so wird $m \cdot \lambda$ eine lineare Funktion von θ ; und weiter: Man kann M so wählen, daß die lineare Funktion mit guter Näherung eine Gerade durch den Nullpunkt wird. Mit dieser Zuordnung sind die Meßpunkte in die Darstellungen von Abb. 3 eingetragen. Im Rahmen der Meßgenauigkeit konnte $\sin \theta \approx \theta$ gesetzt werden.

Die Linearität der Funktion $m \cdot \lambda = f(\theta)$ bedeutet nach (7 a), daß $\psi(\theta)$ linear ist:

$$\psi(\theta) = \psi_0 + \psi_1 \cdot \theta.$$

Damit wird aus (7 a):

$$m \cdot \lambda = 2\psi_0 + 2(b + \psi_1) \cdot \theta. \quad (8)$$

Durch die Festsetzung für M wird ψ_0 zu Null gemacht (Bei anderer Zählung der Nebenmaxima erscheint $2\psi_0$ als ganzes Vielfaches einer Wellenlänge); man kann statt (8) schreiben:

$$m \cdot \lambda = 2(b + \psi_1) \cdot \theta. \quad (9)$$

In die graphischen Darstellungen sind je zwei Geraden eingetragen, zwischen denen die Meßpunkte liegen; der halbe Anstiegsfaktor, die Größe $b + \psi_1$, ist vermerkt.

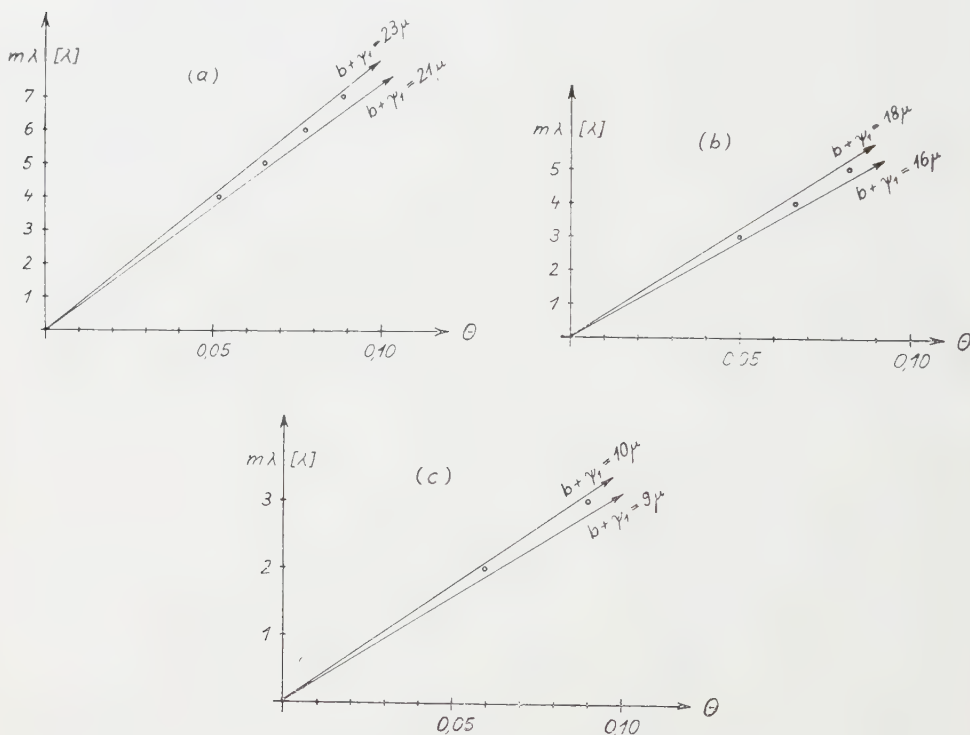


Abb. 3. Zur Deutung der F-Nebenmaxima durch Formel (9).

Jeder Meßpunkt entspricht einem beobachteten F-Nebenmaximum. Zum Vergleich ist je eine Gerade oberhalb und unterhalb der Meßpunkte eingetragen.

Typische Ergebnisse für drei Furchen; Spiegelabstand 19μ .

Es wurden drei Furchen bei Spiegelabständen $d=19$ und 14μ untersucht (die Furche mittlerer Breite auch bei $d=8\mu$). Die Interferogramme wurden im Wellenlängenbereich von $0,52$ bis $0,60\mu$ ausgewertet. Abb. 3 bringt als typisches Beispiel die Ergebnisse je einer Auswertung für $d=19\mu$.

Abb. 3 a gehört zur breitesten Furche. Die Meßpunkte lassen mit Hilfe der eingetragenen Geraden auf den Wert $b + \psi_1 = (22 \pm 1)\mu$ schließen. Die direkte Messung der Furchenbreite unter dem Mikroskop, die in der unsicheren

Beurteilung der Ränder eine erhebliche Fehlerquelle hat, ergab $b = (21 \pm 2) \mu$. Damit wäre es verträglich, daß ψ_1 in (9) gegenüber b zu vernachlässigen ist.

Bei der Furche mittlerer Breite (Abb. 3 b) war b nach direkter mikroskopischer Messung $(14 \pm 2) \mu$. Aus dem Anstieg der Geraden in Abb. 3 b schließt man auf $(b + \psi_1) = 17 \mu$.

Bei der schmalen Furche ließen sich höchstens zwei Nebenmaxima beobachten. Die Meßpunkte liegen zwischen den Geraden $(b + \psi_1) = 9 \mu$ und $(b + \psi_1) = 10 \mu$. Die direkte mikroskopische Messung ergab $b = (6,5 \pm 1,5) \mu$, so daß die Ergebnisse hier wie bei der Furche mittlerer Breite für einen endlichen Wert von ψ_1 sprechen, etwa $\psi_1 = 3 \mu$.

Die Phasensprungfunktion ψ wurde eingeführt, um die Abweichung vom Idealfall zu berücksichtigen, die oben (s. § 4.1) mit (B) bezeichnet wurde. Sie dürfte demnach wohl vom Spiegelabstand d , doch nicht von der Furchenbreite b abhängen. Wenn dennoch eine Abhängigkeit von der Furchenbreite zu bemerken ist, so könnte sich darin die Abweichung (A) ausdrücken: Die hin- und rücklaufenden Hohlleiterwellen, deren Überlagerung eine Eigenschwingung ergibt, sind gedämpft.

5. DAS ALLGEMEINE BEUGUNGSPROBLEM

5.1. *Fraunhofersche Beugung und ebene Wellen*

Die Fraunhofersche Beugung am flachen Objekt, z.B. am Spalt, wird meist nach dem Huygens-Fresnelschen Prinzip behandelt. Man kann auf einem anderen Wege zu dem gleichen Ergebnis gelangen [9]: Die gebeugte Welle wird als Entwicklung nach ebenen Wellen angesetzt; die stetige Anpassung der gebeugten Welle an die einfallende Welle in der beugenden Öffnung führt auf ein Fourier-Integral; es ist mit dem Beugungsintegral identisch, das—im Sinne des Huygens-Fresnelschen Prinzips—der mathematische Ausdruck für die Interferenz von Elementarwellen ist. Mit einer Erweiterung dieser 'Entwicklungsmethode' läßt sich eine Formulierung des Beugungsproblems geben, die nicht an der Voraussetzung hängt, daß das Feld in der beugenden Öffnung gleich dem der ungestörten einfallenden Welle ist [10].

5.2. *Übertragung der Entwicklungsmethode auf das Problem der Vielstrahlinterferometrie*

Ebene Wellen sind 'Eigenwellen' des freien Raumes. Sie sind der Aufgabe, das Feld im Objekt der Vielstrahlinterferometrie zu beschreiben, nicht angemessen. Die Analogie zur beschriebenen Entwicklungsmethode würde hier besagen: Das Feld wird nach den Eigenwellen bzw. Eigenschwingungen der Interferenzräume entwickelt; die Entwicklungskoeffizienten werden aus den Stetigkeitsforderungen für die Grenzen der einzelnen Interferenzräume und durch stetige Anpassung an die einfallende Welle bestimmt (Zur einfallenden Welle müßte vermutlich wie bei der erweiterten Methode für das flache Objekt [10] die reflektierte Welle hinzugenommen werden).

In Analogie zu den Verhältnissen beim flachen Objekt würde es auch stehen, wenn dabei inhomogene Wellen eine Rolle spielen. Inhomogene Wellen in der Form quergedämpfter, auslaufender Oberflächenwellen treten auch bei der Beugung am flachen Objekt auf ([11,12]; [10], S. 296). Die Entwicklungsmethode erhält ihre mathematische Geschlossenheit erst dadurch, daß in der

Entwicklung zu den ebenen Wellen solche inhomogenen Wellen hinzugenommen werden. Im Mikrowellenbereich ist der experimentelle Nachweis einer durch Beugung entstandenen inhomogenen Oberflächenwelle gelungen [13].

Die Entwicklungsmethode für das Objekt der Vielstrahlinterferometrie ist gewiß schwierig auszuführen. Die Ergebnisse der vorliegenden Arbeit können allenfalls ein Hinweis auf den realen physikalischen Gehalt der Methode sein. Abschließend werden einige Punkte erörtert, die bei der Ausarbeitung der Methode zu beachten wären. Damit wird zugleich der Wert der bisherigen experimentellen Erfahrung begrenzt.

5.3. Endliche Halbwertsbreite

Eine diskrete Folge von Hohlleiter-Eigenwellen erhält man nur in dem Idealfall, daß die Leitfähigkeit der Wände unendlich ist. Die endliche Durchlässigkeit der Silberschichten, die den Interferenzraum begrenzen, erzeugt nicht nur Dämpfung (vgl. §3.4), sondern führt dazu, daß aus einer einzelnen Eigenwelle eine kontinuierliche Verteilung in deren 'Umgebung' wird: Interferenzstreifen haben eine endliche Halbwertsbreite. Dieser Umstand dürfte eine erhebliche Erschwerung für die Entwicklungsmethode bedeuten.

5.4. Normales Objekt

Das untersuchte Objekt enthält eine durchlässige Furche, die von undurchlässigen Plateaubereichen begrenzt ist. Unter üblichen Bedingungen der Vielstrahlinterferometrie wären Furche und Plateau—überhaupt die einzelnen Bereiche der Spiegel—von gleicher Durchlässigkeit. Das Beugungsproblem ist dann schwieriger, weil die einfallende Welle auch direkt in den Plateaubereich eintreten kann.

Für die Praxis interessiert schließlich der allgemeinere Fall keilförmig begrenzter Interferenzräume.

5.5. Die Abbildung

Die Beugung am Objekt der Vielstrahlinterferometrie ist vor allem für die Frage des Auflösungsvermögens bei der Abbildung von Bedeutung. Die Feldverteilung im Interferenzraum selbst ist dafür nur von mittelbarem Interesse. Es kommt auf die Welle an, die vom Interferenzraum abgestrahlt wird und in der Bildebene interferiert. Zur vollständigen Lösung des Beugungsproblems würde es gehören, durch Anpassung an die Feldverteilung im Interferenzraum auch die abgestrahlte Welle zu bestimmen.

Für den Übergang zum normalen Objekt interessiert hier der Fall der bedampften Furche. Wie die Untersuchungen zeigten, kommen in der abgestrahlten Welle Anteile vor (die Winkelordnungen), die sich durch eine naheliegende Anpassung auf Hohlleiterwellen des Plateaubereichs zurückführen lassen. Doch ließen sich die Winkelordnungen des Plateaubereichs (als θ -Streifen und θ -Interferenz) nur durch Überbelichtung der Interferenzerscheinung im Furchenbereich auf der Photoplatte festhalten; es handelt sich um einen schwachen Effekt. Vermutlich machen sich die Eigenwellen des Plateaubereichs unter normalen Bedingungen nicht direkt in der abgestrahlten Welle bemerkbar. Sie könnten dennoch von entscheidender Bedeutung für

die Abbildung des Furchenbereichs sein, indem sie eine lateral begrenzte Resonanzerscheinung im Furchenbereich ohne Verletzung der Stetigkeit an den Furchenrändern möglich machen.

Durch die Deutung der Knoten im Interferogramm als Maxima der lateralen Resonanz im Furchenbereich wurden weitere Anteile der abgestrahlten Welle als direkte Fortsetzung von Hohlleiterwellen identifiziert; hier handelt es sich um stehende Hohlleiterwellen im Furchenbereich. Die Intensität der F-Nebenmaxima (Knoten) ist zwar schwach im Vergleich zur Intensität des F-Hauptmaximums, und es ist nicht wahrscheinlich, daß sie unter normalen Bedingungen eine wichtige Rolle spielen; doch bleibt selbst dann, wenn unter normalen Bedingungen keine Knoten im Interferogramm auftreten, eine Frage offen. Hand in Hand mit dem Auseinanderrücken der F-Nebenmaxima bei abnehmender Furchenbreite geht vermutlich eine Verbreiterung des F-Hauptmaximums; die Beobachtungen an den schmalsten untersuchten Furchen (Breite um 3μ) ordnen sich dem ein. Vielleicht äußert sich somit in dem Effekt der Hohlraumresonanz im Furchenbereich eine praktisch bedeutsame Verknüpfung von lateraler und vertikaler Auflösung: Geringe Furchenbreite ist nur mit einem flachen, breiten Interferenz- "Streifen" verträglich. Eine weitere Untersuchung dieser Zusammenhänge scheint angebracht.

ANERKENNUNGEN

Der Verfasser dankt Herrn Prof. Dr. H. Lassen, daß er auch diesen Teil seiner Dissertation mit wesentlicher Unterstützung im I. Physikalischen Institut der Freien Universität Berlin durchführen konnte.

A preceding paper described diffraction experiments on a simple object of multiple beam interferometry: a narrow groove in a flat mirror divides the interference space between two mirrors into three plane-parallel-limited regions, a groove region and two adjoining plateau regions. The results of these experiments gave rise to an extension of the elementary description of multiple beam interference.

The plateau regions permit attachment of a series of waveguide modes which are being excited by the incident radiation penetrating the groove region. In the groove region there appear standing waveguide modes. Due to the continuity of the electromagnetic field the waveguide modes of the plateau regions are coupled to the resonance phenomenon in the groove region.

These considerations lead to a correct description of the experimental results. It can be assumed that waveguide phenomena generally play a part in diffraction in multiple beam interferometry.

Dans un précédent travail, nous avons décrit des expériences de diffraction sur un objet simple de l'interférométrie à ondes multiples: à l'aide d'un sillon étroit tracé dans un miroir plan, l'espace interférentiel compris entre deux miroirs a été divisé en trois régions correspondant au sillon et aux deux plateaux. Les résultats de ces expériences nous ont fourni l'occasion d'étendre la description élémentaire des interférences à ondes multiples.

On associe aux 'plateaux' une suite d'ondes guidées (modes d'un guide d'onde) qui ont été excitées par le rayonnement incident pénétrant dans la région du sillon. Dans la région du sillon apparaissent des ondes guidées stationnaires. A cause de la continuité du champ électromagnétique, les ondes du 'plateau' sont couplées aux résonances dans la région du sillon.

Ces considérations conduisent à une description exacte des résultats expérimentaux. On peut donc supposer que les phénomènes relatifs aux guides d'onde jouent toujours un rôle dans la diffraction en interférométrie à ondes multiples.

LITERATUR

- [1] SOMMERFELD, A., 1950, *Optik*, 1. Aufl., Dietrich'sche Verlagsbuchhandlung Wiesbaden ; s. S. 56, 368, 375.
- [2] SIMONSOHN, G., 1961, *Opt. Acta*, **8**, 33.
- [3] THIESSEN, G., 1947, *Optik*, **2**, 266.
- [4] HEINZE, D., und SCHMELZER, CH., 1955, *Z. Phys.*, **142**, 133, 145.
- [5] SKOROBOGATOV, B. S., 1959, *Optics and Spectroscopy*, **7**, 482, 487.
- [6] SLATER, J. C., 1942, *Microwave Transmission*, 1. Aufl. (New York : McGraw-Hill), S. 124 ff.
- [7] HONERJÄGER, R., 1955, in Goubau, G., *Elektromagnetische Wellenleiter und Hohlräume* (Stuttgart: Wiss. Verlagsges. m.b.H.).
- [8] MÜLLER, R., 1955, in Goubau, G., *Elektromagnetische Wellenleiter und Hohlräume* (Stuttgart: Wiss. Verlagsges. m.b.H.), S. 149 ff.
- [9] SCHEFFERS, H., 1942, *Ann. Phys. Lpz.*, **42**, 211.
- [10] HÖNL, H., 1952, *Z. Phys.*, **131**, 290.
- [11] TORALDO DI FRANCIA, G., 1949, *Rev. Opt.*, **28**, s. S. 608 f.
- [12] LOHMANN, A., und WEGENER, H., 1955, *Z. Phys.*, **143**, 431.
- [13] SCHAFFNER, M., und TORALDO DI FRANCIA, G., 1949, *Nuovo Cim.*, **6**, 125.

Multiple diffraction by an aperture in a hard screen†

by SAMUEL N. KARP and JOSEPH B. KELLER

Institute of Mathematical Sciences, New York University, N.Y. 3, N.Y.

(Received 23 August 1960)

Two methods previously applied to diffraction by an aperture in a soft screen (one on which the field vanishes) are adapted to the case of a hard screen (one on which the normal derivative of the field vanishes). These methods are the geometrical theory of diffraction and the self-consistent field method. They are both applied to diffraction by an infinite slit and both yield the same result at distances greater than several wavelengths from the edges of the screen. The former is also applied to diffraction by a circular aperture. Expressions for the diffracted fields, the diffraction patterns and the transmission cross sections are obtained for the problems of the slit and the circular aperture. Graphs of the transmission cross sections are given for normal incidence.

1. INTRODUCTION

The present authors have previously presented two different methods for calculating the field diffracted when a wave hits an aperture in a thin screen [1, 2]. Both methods were applied to soft screens, i.e. screen on which the wave function vanishes. Some results were also given in [1] for hard screens on which the normal derivative of the wave function vanishes, but interaction between various parts of the edge of the screen was not taken into account. In the present article these two methods are extended to yield more complete results for hard screens, in that interaction is taken into account.

The geometrical theory of diffraction, described in reference [1], employs diffracted rays which are produced when a ray hits the edge of the screen. Some of the singly diffracted rays, which are produced by the incident rays, cross the aperture and hit the edge again, producing doubly diffracted rays, etc. The amplitude of the field on any diffracted ray is determined from that on the corresponding incident ray by means of a diffraction coefficient D which is given in [1]. In the case of a hard screen and an incident ray lying in the plane of the screen, D vanishes and the diffracted field is proportional to the normal derivative of the incident field at the edge. The proportionality factor is a new diffraction coefficient D' which has not been determined before. We will determine it and apply it to the diffracted fields produced by slits, circular apertures and other shaped apertures in hard screens.

The self-consistent field method described in [8] was applied in [2] to diffraction by an infinite slit. The field scattered by each edge of the slit was assumed to be produced by the incident field and by a cylindrical wave‡ emanating from the other edge. This assumption led to a pair of linear equations from which the amplitude of the field coming from each edge was

† This article is based upon Research Report No. EM-143 with the same title, November 1959, Institute of Mathematical Sciences, New York University. This work was supported in part by the Air Force Cambridge Research Center, under Contract No. AF 19(604)1717.

‡ i.e. the field of a line source.

determined. In the case of a hard screen it does not suffice to treat the field scattered from one edge to the other as being equivalent to the field of a line source, since then it would not interact with the second edge. Instead we consider this field to be that due to a line dipole. Then it does interact with the second edge and we can determine its strength as before. The resulting diffracted field coincides with that which we obtain by summing the fields on all the diffracted rays of the preceding method. This agreement lends support to both methods. The results also agree, where comparable, with those of Levine [3] and Millar [4] which were obtained by different methods.

The results of both methods given here do not apply to grazing incidence, although they can be modified to become applicable. The method in §3 applies to the calculation of both far and near fields, provided that the interedge spacing is large. For an example of its application to the calculation of higher order interactions between arbitrary cylinders, in terms of their non-interaction patterns, see [7]. On the other hand, the method in §2 is applicable at any fixed point, in the limit of *large frequency*. In particular, both methods are applicable in the far field.

2. THE GEOMETRICAL THEORY OF DIFFRACTION BY A HARD SCREEN

2.1. The diffraction coefficient

In the geometrical theory of diffraction the field u_e on a ray diffracted from an edge is given by ([1] equation (12))

$$u_e = D[s(1 + \rho_1^{-1}s)]^{-1/2} \exp(iks)u_i. \quad (1)$$

Here u_i denotes the incident field at the point of diffraction on the edge, s denotes distance from this point along the diffracted ray, ρ_1 denotes distance to the caustic of the diffracted rays and D is the diffraction coefficient. For a scalar field u satisfying the reduced wave equation and incident upon a hard screen, on which $\partial u / \partial n = 0$, D is given by ([1] equation (13))

$$D(\theta, \alpha) = -\frac{\exp(i\pi/4)}{2(2\pi k)^{1/2} \sin \beta} [\sec \tfrac{1}{2}(\theta - \alpha) - \csc \tfrac{1}{2}(\theta + \alpha)]. \quad (2)$$

The angles α and θ are defined by projecting the incident and diffracted rays onto the plane normal to the edge at the point of diffraction. The angles between these projections and the normal to the screen are α and θ respectively (see figure 1). The angle β is that between the incident ray and the edge. When the incident ray lies in the plane of the screen and $\alpha = \pi/2$, it follows from (2) that $D = 0$. In this case (1) must be replaced by ([1] equation (12'))

$$u_e = D'[s(1 + \rho_1^{-1}s)]^{-1/2} \exp(iks) \partial u_i / \partial n. \quad (3)$$

Here $\partial u_i / \partial n$ denotes the normal derivative of the incident field at the point of diffraction and D' is another diffraction coefficient. We will now determine D' for scalar fields satisfying the reduced wave equation. To do so we seek a two-dimensional field u satisfying $(\nabla^2 + k^2)u = 0$ and having a non-vanishing normal derivative on a half screen lying along the negative y axis. For the incident field u_0 we take a non-uniform plane wave travelling parallel to the screen and towards its edge. The simplest such field having a non-zero normal derivative on the screen is

$$u_0 = x \exp(-iky).$$

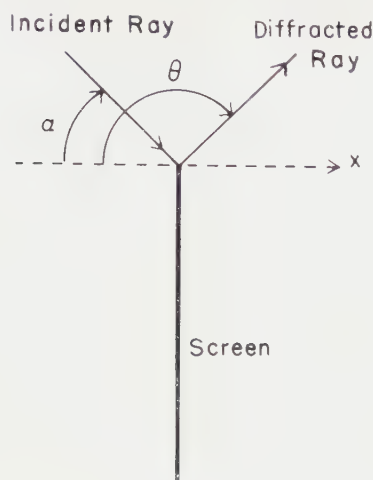


Figure 1. The projection of incident and diffracted rays into a plane normal to the edge. The angles α and θ are the angles between these projections and the negative x -axis, measured as shown in the figure. The diffracting edge, which is perpendicular to the plane of the figure, is the edge of the screen.

We note that u_0 can be expressed as the derivative of a plane wave with respect to its direction of propagation

$$u_0 = -\frac{1}{ik} \left[\frac{\partial}{\partial \alpha} \exp \{ ik(x \cos \alpha - y \sin \alpha) \} \right]_{\alpha=\pi/2}. \quad (4)$$

Let $v(\alpha)$ denote the solution of the half plane diffraction problem with the plane wave incident from the direction α . Then it follows from (4) that u is given by†

$$u = \frac{-1}{ik} v_{\alpha} \left(\frac{\pi}{2} \right). \quad (5)$$

We now apply (5) to the diffracted part of the field. Since $\partial u_0 / \partial x = 1$, it follows that

$$D'(\theta) = -\frac{1}{ik} D_{\alpha} \left(\theta, \frac{\pi}{2} \right). \quad (6)$$

If the incident ray makes the angle β with the edge then the factor k in (6) must be replaced by $k \sin \beta$. Then from (6) and (2) we obtain

$$D'(\theta) = -\frac{\exp(-i\pi/4)}{2(2\pi)^{1/2} k^{3/2} \sin^2 \beta} \frac{\sin(\pi/4 - \theta/2)}{\cos^2(\pi/4 - \theta/2)}. \quad (7)$$

Upon combining (3) and (7), we finally obtain for the field on an edge diffracted ray

$$u_c = \frac{\exp(iks - i\pi/4)}{2(2\pi k^3)^{1/2} \sin^2 \beta} \left[s \left(1 - \frac{s|\cos \delta + \rho \dot{\beta} \sin \beta|}{\rho \sin^2 \beta} \right) \right]^{-1/2} \frac{\sin(\pi/4 - \theta/2)}{\cos^2(\pi/4 - \theta/2)} \frac{\partial u_i}{\partial n}. \quad (8)$$

In (8) we have introduced the expression for ρ_1 given in equation (11) of reference [1]. The angle δ is that between the diffracted ray and the normal to the edge, $\dot{\beta}$ is the derivative of β with respect to arc length along the edge and ρ is the radius of curvature of the edge.

† For the application of this device in more general multiple scattering problems see [7].

If the edge has a corner then the field u_c on a corner diffracted is given by

$$u_c = C' \frac{\exp(iks)}{s} \frac{\partial u_i}{\partial n}. \quad (9)$$

This replaces equation (15) of reference [1] and C' is a new corner diffraction coefficient. From dimensional considerations we see that C' must be proportional to k^{-2} . We shall not consider this coefficient further.

The total field at a point is, as usual, the sum of the fields on all rays through the point. Let us now apply these results to some problems of diffraction through apertures.

2.2. Diffraction by a slit

Let us consider a plane wave incident upon a hard screen containing a slit of width $2a$ and of infinite length. The incident rays are assumed to be normal to the edges of the slit so the problem is essentially two-dimensional. The singly diffracted field has been computed in reference [1] by using (1) on each of the two singly diffracted rays through any point. In attempting to determine the doubly diffracted field, we find that the singly diffracted rays which produce it lie in the plane of the screen. Therefore (1) is no longer applicable and (3) or (8) must be used.

To apply (8) we note that in the present case $\beta = n/2$, $\beta = 0$, $\rho = \infty$ and $\rho_1 = \infty$. If the incident field is $\exp[ik(x \cos \alpha - y \sin \alpha)]$ and if the screen lies in the plane $x = 0$, application of (1) yields for the singly diffracted field

$$u_{e1} = D(\theta_1, -\alpha) r_1^{-1/2} \exp[ik(r_1 - a \sin \alpha)] + D(\theta_2, \alpha) r_2^{-1/2} \exp[ik(r_2 + a \sin \alpha)]. \quad (10)$$

In (10), r_1 and r_2 denote the distances of a point from the upper and lower edges $(0, \pm a)$ respectively. The angles θ_1 and θ_2 are determined by the corresponding rays as shown in figure 2. The field (10) was derived and examined in reference [1].

To determine the doubly diffracted field, let us consider that ray which is singly diffracted at the lower edge and which traverses the slit to the upper edge. The normal derivative of the field on this ray when it reaches the upper edge can be obtained from the second term in (10) by applying $(2a)^{-1} \partial / \partial \theta_2$ and then setting $r_2 = 2a$ and $\theta_2 = \pi/2$. Doing this yields

$$\frac{\partial u_{e1}}{\partial n} = - \frac{\exp(ika(2 + \sin \alpha) + i\pi/4)}{8(\pi ka^3)^{1/2}} \frac{\sin(\pi/4 - \alpha/2)}{\cos^2(\pi/4 - \alpha/2)}. \quad (11)$$

A similar expression with $-\alpha$ in place of α gives the normal derivative at the lower edge of the field on the ray singly diffracted at the upper edge. Insertion of either of these expressions into (8) yields the field on the doubly diffracted rays. Upon combining these two fields, we have for the doubly diffracted field

$$u_{c2} = - \frac{\exp(ika(2 + \sin \alpha) + ikr_1)}{16\pi(ka)^{3/2}(2kr_1)^{1/2}} \frac{\sin(\pi/4 - \alpha/2)}{\cos^2(\pi/4 - \alpha/2)} \frac{\sin(\pi/4 - \theta_1/2)}{\cos^2(\pi/4 - \theta_1/2)} \\ - \frac{\exp(ika(2 - \sin \alpha) + ikr_2)}{16\pi(ka)^{3/2}(2kr_2)^{1/2}} \frac{\sin(\pi/4 + \alpha/2)}{\cos^2(\pi/4 + \alpha/2)} \frac{\sin(\pi/4 - \theta_2/2)}{\cos^2(\pi/4 - \theta_2/2)}. \quad (12)$$

Far from the slit (12) simplifies in terms of polar coordinates r and ϕ . Then $r_1 \sim r - a \sin \phi$, $r_2 \sim r + a \sin \phi$, $\theta_1 \sim \pi + \phi$ and $\theta_2 \sim \pi - \phi$. Now (12) can be written as

$$u_{c2} = -(k/2\pi r)^{1/2} \exp(ikr + i\pi/4) f_d(\phi). \quad (13)$$

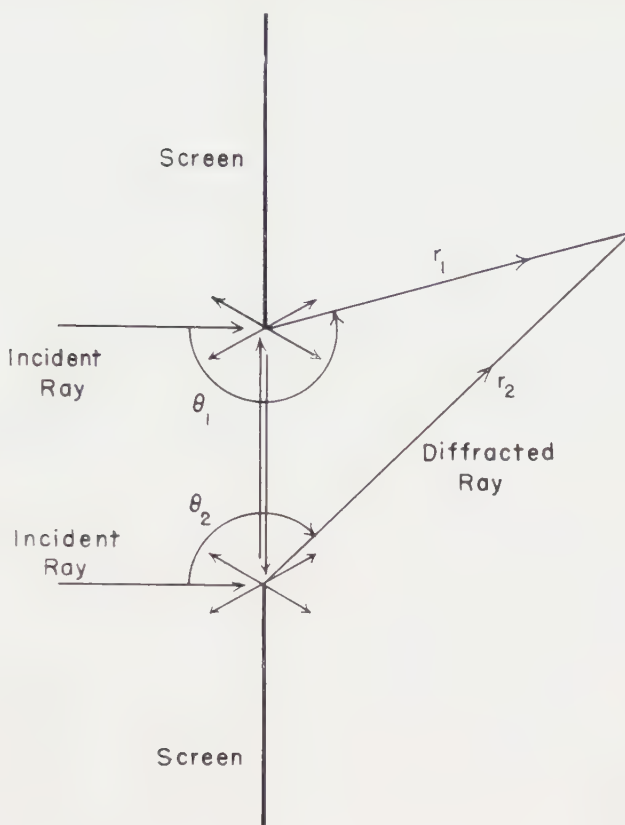


Figure 2. Diffracted rays produced when a normally incident plane wave hits a slit in a thin screen. Some singly diffracted rays are shown leaving each edge. Two of these rays are shown crossing the slit and hitting the opposite edge where they produce doubly diffracted rays.

In (13) $f_d(\phi)$ denotes the contribution of double diffraction to the radiation or diffraction pattern of the slit. From (12)

$$\begin{aligned}
 f_d(\phi) = & -\frac{\exp(2ika - i\pi/4)}{16\pi^{1/2}(ka)^{3/2}k} \left[\frac{\sin(\pi/4 - \alpha/2) \sin(\pi/4 + \phi/2)}{\cos^2(\pi/4 - \alpha/2) \cos^2(\pi/4 + \phi/2)} \right. \\
 & \times \exp[ika(\sin \alpha - \sin \phi)] + \frac{\sin(\pi/4 + \alpha/2) \sin(\pi/4 - \phi/2)}{\cos^2(\pi/4 + \alpha/2) \cos^2(\pi/4 - \phi/2)} \\
 & \left. \times \exp\{ika(-\sin \alpha + \sin \phi)\} \right]. \quad (14)
 \end{aligned}$$

The diffraction pattern due to single and double diffraction is $f_s(\phi) + f_d(\phi)$, where $f_s(\phi)$, which can be obtained from (10), is given by equation (23) of reference [1].

The contribution of double diffraction to the transmission cross section σ of the slit (per unit length) is equal to the imaginary part of $f_d(-\alpha)$, according to the cross-section theorem. This can be computed from (14) and added to $2a \cos \alpha$, which is the contribution of the transmitted and singly diffracted rays.

There results

$$\sigma = 2a \cos \alpha - \frac{2a}{32\pi^{1/2}(ka)^{5/2}} \left[\frac{\sin^2(\pi/4 - \alpha/2)}{\cos^4(\pi/4 - \alpha/2)} \sin [2ka(1 + \sin \alpha) - \pi/4] + \frac{\sin^2(\pi/4 + \alpha/2)}{\cos^4(\pi/4 + \alpha/2)} \sin [2ka(1 - \sin \alpha) - \pi/4] \right]. \tag{15}$$

In the case of normal incidence $\alpha=0$ and (15) becomes

$$\frac{\sigma}{2a} = 1 - \frac{\sin(2ka - \pi/4)}{8\pi^{1/2}(ka)^{5/2}}. \tag{16}$$

A graph of $\sigma/2a$ versus ka based on (16) is shown in figure 3 along with the exact values of $\sigma/2a$.

To determine the field on any multiply-diffracted ray we make repeated use of (8). In the table below we have enumerated the four types of multiply-diffracted rays. By referring to this table and using (8) we easily find that the

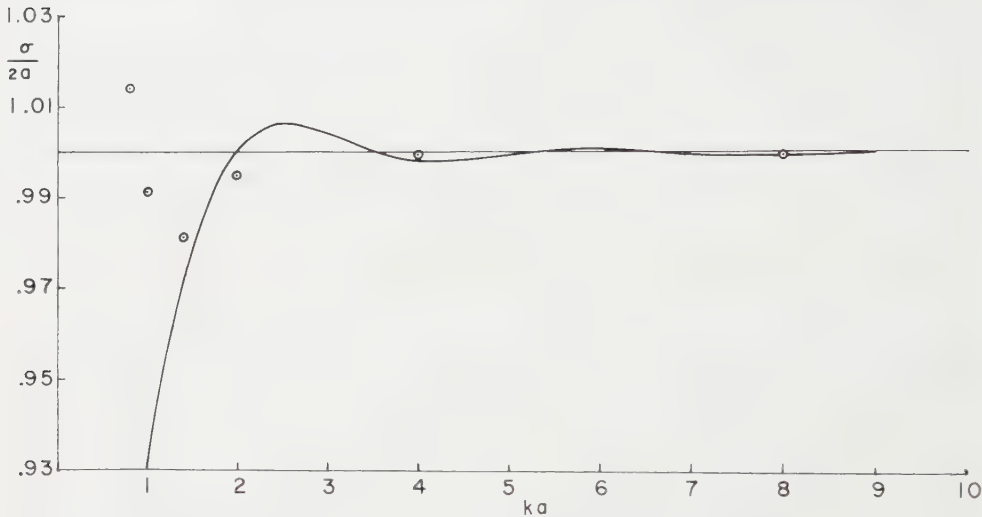


Figure 3. The transmission cross section per unit length for normal incidence on a slit of width $2a$ in a hard screen is shown as a function of ka . The ordinate $\sigma/2a$ is the transmission cross section σ divided by the geometrical cross section $2a$, and the abscissa is ka . The solid curve is based upon equation (16) which results from single and double diffraction. The encircled points are the exact values of $\sigma/2a$ computed by Skavlem [9]. Equation (23), which is based upon all orders of diffraction, yields a curve which is indistinguishable from the solid curve on the scale used here, except near $ka=1$ where one point (x) is shown.

Type	Initial diffraction	Number of diffractions at each edge		Final diffraction
		Lower	Upper	
A	Lower	$n+1$	n	Lower
B	Lower	n	n	Upper
C	Upper	n	$n+1$	Upper
D	Upper	n	n	Lower

field on a multiply diffracted ray of any type is given by one of the following expressions

$$\begin{aligned}
 (A) \quad & D'(\theta_2)r_2^{-1/2} \exp(ikr_2) \{ [D'_\theta(\pi/2)]^2 (2a)^{-3} \exp(4ika) \}^{n-1} \\
 & \times D'_\theta(\pi/2) D_\theta(\pi/2, \alpha) (2a)^{-3} \exp[ika(4 + \sin \alpha)]. \\
 (B) \quad & D'(\theta_1)r_1^{-1/2} \exp(ikr_1) \{ [D'_\theta(\pi/2)]^2 (2a)^{-3} \exp(4ika) \}^{n-1} \\
 & \times D_\theta(\pi/2, \alpha) (2a)^{-3/2} \exp[ika(2 + \sin \alpha)]. \\
 (C) \quad & D'(\theta_1)r_1^{-1/2} \exp(ikr_1) \{ [D'_\theta(\pi/2)]^2 (2a)^{-3} \exp(4ika) \}^{n-1} \\
 & \times D'_\theta(\pi/2) D_\theta(\pi/2, -\alpha) (2a)^{-3} \exp[ika(4 - \sin \alpha)]. \\
 (D) \quad & D'(\theta_2)r_2^{-1/2} \exp(ikr_2) \{ [D'_\theta(\pi/2)]^2 (2a)^{-3} \exp(4ika) \}^{n-1} \\
 & \times D_\theta(\pi/2, -\alpha) (2a)^{-3/2} \exp[ika(2 - \sin \alpha)].
 \end{aligned}$$

The total multiply-diffracted field u_m is obtained by adding together the fields on the four types of rays and summing with respect to n . The series to be summed is a geometric series given by

$$\sum_{n=1}^{\infty} \{ [D'_\theta(\pi/2)]^2 (2a)^{-3} \exp(4ika) \}^{n-1} = [1 - [D'_\theta(\pi/2)]^2 (2a)^{-3} \exp(4ika)]^{-1}. \quad (17)$$

Thus we obtain

$$\begin{aligned}
 u_m = & [1 - [D'_\theta(\pi/2)]^2 (2a)^{-3} \exp(4ika)]^{-1} [D'(\theta_1)r_1^{-1/2} \exp(ikr_1) \\
 & \times \{ D_\theta(\pi/2, \alpha) (2a)^{-3/2} \exp[ika(2 + \sin \alpha)] \\
 & + D'_\theta(\pi/2) D_\theta(\pi/2, -\alpha) (2a)^{-3} \exp[ika(4 - \sin \alpha)] \} \\
 & + D'(\theta_2)r_2^{-1/2} \exp(ikr_2) \{ D_\theta(\pi/2, -\alpha) (2a)^{-3/2} \exp[ika(2 - \sin \alpha)] \\
 & + D'_\theta(\pi/2) D_\theta(\pi/2, \alpha) (2a)^{-3} \exp[ika(4 + \sin \alpha)] \}]. \quad (18)
 \end{aligned}$$

The complete diffracted field $u_d = u_{e1} + u_m$ is given by (10) and (18). We have also obtained exactly this same result by the method of Part II.

Far from the slit (18) becomes

$$u = -(k/2\pi r)^{1/2} \exp(ikr + i\pi/4) f_m(\phi). \quad (19)$$

In (19) we have introduced $f_m(\phi)$, the diffraction pattern due to multiple diffraction. From (18) it is found to be given by

$$f_m(\phi) = F(\phi, \alpha) + F(-\phi, -\alpha). \quad (20)$$

Here $F(\phi, \alpha)$ is defined by

$$\begin{aligned}
 F(\phi, \alpha) = & -a \left[1 + \frac{i \exp(4ika)}{256\pi(ka)^3} \right]^{-1} \frac{\sin(\pi/4 + \phi/2)}{\cos^2(\pi/4 + \phi/2)} \\
 & \times \left\{ \frac{\exp[ika(2 + \sin \alpha - \sin \phi) - i\pi/4]}{16\pi^{1/2}(ka)^{5/2}} \cdot \frac{\sin(\pi/4 - \alpha/2)}{\cos^2(\pi/4 - \alpha/2)} \right. \\
 & \left. + \frac{i \exp[ika(4 - \sin \alpha - \sin \phi)]}{256\pi(ka)^4} \cdot \frac{\sin(\pi/4 + \alpha/2)}{\cos^2(\pi/4 + \alpha/2)} \right\}. \quad (21)
 \end{aligned}$$

When $\alpha = 0$, (20) simplifies to

$$\begin{aligned}
 f_m(\phi) = & -2a \left[1 + \frac{i \exp(4ika)}{256\pi(ka)^3} \right]^{-1} \left[\frac{\exp(2ika - i\pi/4)}{8\pi^{1/2}(ka)^{5/2}} + \frac{i \exp(4ika)}{128\pi(ka)^4} \right] \\
 & \times \frac{1}{\cos^2 \phi} [(\cos \phi/2 + \sin \phi \sin \phi/2) \cos(ka \sin \phi) - i(\sin \phi/2 \\
 & + \sin \phi \cos \phi/2) \sin(ka \sin \phi)]. \quad (22)
 \end{aligned}$$

The transmission cross section of the slit, per unit length, is the imaginary part of $f_s(-\alpha) + f_m(-\alpha)$. For normal incidence ($\alpha=0$) this yields

$$\frac{\sigma}{2a} = 1 - \left[\frac{\sin(2ka - \pi/4)}{8\pi^{1/2}(ka)^{5/2}} \left(1 + \frac{1}{256\pi(ka)^3} \right) + \frac{\cos(4ka)}{128\pi(ka)^4} \right] \times \left[1 - \frac{\sin(4ka)}{128\pi(ka)^3} + \frac{1}{(256\pi(ka)^3)^2} \right]^{-1}. \quad (23)$$

It should be noted that in the foregoing analysis, just as in that of reference [1], only the leading term in the expression for the field on a ray has been employed. Actually the field on any ray is given by a series in powers of k^{-1} . The coefficients of the various powers can be determined from the first term by solving the transport equations, supplemented by appropriate initial conditions. A method for obtaining these initial conditions and thence the higher terms, is presented in reference [5]. For the slit we can obtain the correction terms on the singly diffracted rays directly from the Sommerfeld solution for diffraction by a half-plane. The field (10), augmented by the first correction term on each ray is

$$u_{e1} = - \frac{\exp[ik(r_1 - a \sin \alpha) + i\pi/4]}{2\sqrt{(2\pi kr_1)}} \left[\sec \frac{1}{2}(\theta_1 + \alpha) \pm \csc \frac{1}{2}(\theta_1 - \alpha) \right] + \frac{\exp(-i\pi/2)}{4kr_1} \{ \sec^3 \frac{1}{2}(\theta_1 + \alpha) \pm \csc^3 \frac{1}{2}(\theta_1 - \alpha) \} - \frac{\exp[ik(r_2 + a \sin \alpha) + i\pi/4]}{2\sqrt{(2\pi kr_2)}} \left[\sec \frac{1}{2}(\theta_2 - \alpha) \pm \csc \frac{1}{2}(\theta_2 + \alpha) \right] + \frac{\exp(-i\pi/2)}{4kr_2} \{ \sec^3 \frac{1}{2}(\theta_2 - \alpha) \pm \csc^3 \frac{1}{2}(\theta_2 + \alpha) \}. \quad (24)$$

The lower sign in (24) applies to a hard screen; the upper sign, which applies to a soft screen, is included for completeness. Far from the screen (24) becomes

$$u_{e1} = - \frac{\exp(ikr + i\pi/4)}{\sqrt{(2\pi kr)}} \left\{ i \frac{\sin[ka(\sin \phi + \sin \alpha)]}{\sin \frac{1}{2}(\phi + \alpha)} \left[1 + \frac{1}{4ikr \sin^2 \frac{1}{2}(\phi + \alpha)} \right] \pm \frac{\cos[ka(\sin \phi + \sin \alpha)]}{\cos \frac{1}{2}(\phi - \alpha)} \left[1 + \frac{1}{4ikr \cos^2 \frac{1}{2}(\phi - \alpha)} \right] \right\}. \quad (25)$$

2.3. Diffraction by a circular aperture

Let us now consider a plane wave normally incident upon a circular aperture of radius a in a hard screen. The singly diffracted field consists of two terms, as in (10), and is given in reference [1], equation (36). To determine the doubly diffracted field we must calculate the normal derivative of the singly diffracted field on a ray which has crossed the aperture to the opposite edge. From [1] equation (36), we obtain for this derivative

$$\frac{\partial u_{e1}}{\partial n} = - \frac{\exp(2ika - i\pi/4)}{4(2\pi ka^3)^{1/2}}. \quad (26)$$

Now upon using (26) in (8), and taking account of the two doubly diffracted rays through any point not on the axis, we obtain for the doubly diffracted field

$$u_{e2} = - \frac{i \exp[ik(r_1 + 2a)]}{16\pi(k^4 a^3)^{1/2}} [r_1(1 - a^{-1}r_1 \cos \delta_1)]^{-1/2} \frac{\sin \delta_1/2}{\cos^2 \delta_1/2} - \frac{i \exp[ik(r_2 + 2a)]}{16\pi(k^4 a^3)^{1/2}} [r_2(1 - a^{-1}r_2 \cos \delta_2)]^{-1/2} \frac{\sin(\delta_2/2)}{\cos^2(\delta_2/2)}. \quad (27)$$

At points near the axis where $\delta_1 \approx \delta_2 \approx \delta = \tan^{-1}(x/a)$, we let ρ denote distance from the axis and x denote distance from the screen. Then (27) simplifies to

$$u_{,2} = - \frac{a^{1/2} \exp [ik(x \sin \delta + a \cos \delta + 2a) + i\pi/4]}{8\pi(k^4 a^3 \rho)^{1/2}(x^2 + a^2)^{1/4}} \frac{\sin(\delta/2)}{\cos^2(\delta/2)} \cos(k\rho \cos \delta - \pi/4). \quad (28)$$

The field (28) becomes infinite on the axis, which is a caustic of the diffracted rays. Upon applying the axial caustic correction (see [1]) to (28) it becomes

$$u_{,2} = - \frac{(a \cos \delta)^{1/2} \sin(\delta/2)}{8(2\pi k^3 a^3)^{1/2}(x^2 + a^2)^{1/4} \cos^2(\delta/2)} \exp(ik(x \sin \delta + a \cos \delta + 2a) + i\pi/4) \\ \times J_0(k\rho \cos \delta). \quad (29)$$

Far from the screen δ tends to $\pi/2$ and this becomes

$$u_{e2} = - \frac{aJ_0(ka \sin \phi)}{8x(\pi k^3 a^3)^{1/2}} \exp(ik(x + 2a) + i\pi/4). \quad (30)$$

To obtain the transmission cross section of the aperture we may apply the cross section theorem to $u_g + u_{e1} + u_{e2}$, where u_g denotes the geometrical optics field on the directly transmitted rays. From u_g and the leading term in u_{e1} we obtain the geometrical cross section πa^2 . From the second term in u_{e1} given in [5] we obtain the correction $-\pi/4k^2$. When we add these contributions to that of u_{e2} , which we find from (30), we obtain

$$\frac{\sigma}{\pi a^2} = 1 - \frac{1}{4(ka)^2} + \frac{\sin(2ka + \pi/4)}{4\pi^{1/2}(ka)^{5/2}}. \quad (31)$$

This result was previously obtained by Levine and Wu [6]. Additional terms can be obtained by considering further diffracted rays. A graph of $\sigma/\pi a^2$ versus ka based on (31) is shown in figure 4 along with the exact values of $\sigma/\pi a^2$.

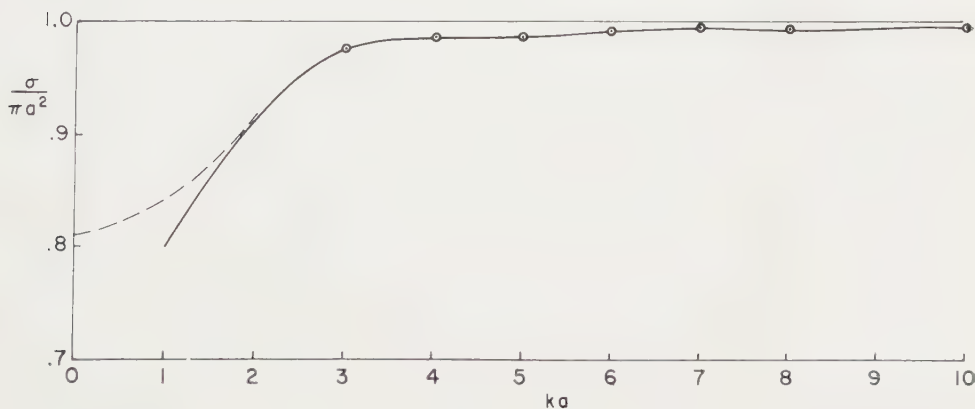


Figure 4. The transmission cross section σ for normal incidence on a circular hole of radius a in a hard screen is shown as a function of ka . The ordinate is $\sigma/\pi a^2$ and the abscissa is ka . The solid curve is based upon equation (31) which results from single and double diffraction. The encircled points and the dashed curve are the exact values computed by Bouwkamp [9].

3. THE SELF-CONSISTENT FIELD METHOD FOR A HARD SCREEN

3.1. *The method*

The self-consistent field method [8] of solving diffraction problems is a method which is applicable to diffraction by a collection of simple objects or by a composite object. In it the field is assumed to consist of the incident field and a number of scattered or diffracted fields, one emanating from each object. The self-consistency condition is that each scattered field must be that which the object from which it emanates would scatter in the absence of the other objects, when all the other fields are incident upon it. If this condition were fulfilled exactly, the assumed field would be the exact solution of the problem. The method becomes approximate, and at the same time practical, when the field scattered from each object can be assumed to have (in the neighbourhood of each other object) a specific form with an undetermined amplitude. For example, take the case when the spacing between objects is large compared to both the wavelength and the transverse body dimensions. Then, such a form is available. The field arriving from each other object is then, in fact, necessarily expressible as the field of a linear combination of a *finite* number of sources and multipoles. If in addition, the spacing is large compared to all other body dimensions, the above form reduces to a combination of plane waves, and derivatives of plane waves with respect to incidence angle. In either event, the consistency condition leads to a set of linear algebraic equations for the amplitudes of the scattered fields. The coefficient matrix of this system of algebraic equations is expressible in terms of the response of each isolated body to a source or to a plane wave, and also in terms of the derivatives of those responses with respect to source position or angle of incidence respectively. For another example, note that a similar simplification ensues when the condition of large spacing is replaced by the condition that all the objects are small compared to wavelength, since such bodies act like isotropic line sources or dipoles as far as their radiation is concerned.

In the case of a slit of infinite length in a thin hard screen, the simple objects referred to above are the two half-planes into which the slit divides the screen. The field is assumed to consist of an incident plane wave plus the two fields which the half-planes scatter when they are hit by a plane wave and an additional scattered wave emanating from each half-plane. Each of these latter waves, which arise because of interaction between the two half-planes, is assumed to be a wave of the form which the half-plane would scatter if hit by the field from a line dipole located at the edge of the other screen. The amplitudes of these two waves are then determined by the consistency condition.

In a previous application of this method [2] to diffraction by a slit in a soft screen, a simpler form of scattered wave was employed. This was the field scattered by a half-plane when hit by the field from an isotropic line source located at the edge of the other screen. Such an incident field is not scattered at all by a hard screen since it has a vanishing normal derivative on the screen. Therefore we must take into account a higher-order emanation from each screen, namely a line dipole field. Such a field does not have a vanishing normal derivative on the screen. Then a non-zero scattered field results.

Once the amplitudes are determined, the field is known at all points of space, provided the spacing is large. From it the diffraction pattern and the transmission cross section per unit length can be found.

3.2. Discussion

Let the screen be in the plane $x=0$ and let the edges of the slit be at $y = \pm a$. Let the plane wave $u_i = \exp [ik(x \cos \alpha - y \sin \alpha)]$ be incident from the left. We seek a field u which satisfies the reduced wave equation, has a vanishing normal derivative on the screen, is sufficiently regular at the edges and consists of u_i plus outgoing waves. To find u approximately, we assume that it has the form

$$u = u_i + w_1 + w_2 + c_1 v_1 + c_2 v_2. \quad (32)$$

The field w_1 is the field scattered by the upper half-plane when it is hit by u_i in the absence of the lower half-plane. Thus $u_i + w_1$ is the solution of the half-plane problem. The field v_1 is the field scattered by the upper half-plane when it is hit by the field from a unit (line) dipole located at the edge of the lower half-plane, $(0, -a)$, in the absence of that half-plane. The dipole moment is oriented normal to the screen, i.e. parallel to the x -axis. The constant c_1 is to be determined. The corresponding quantities with subscript 2 refer to the lower half-plane.

To determine c_1 and c_2 we shall impose the boundary condition $u_x = 0$ on each half-plane. From the definitions of w_1 and w_2 , it follows that $(u_i + w_1)_x = 0$ on the upper half-plane while $(u_i + w_2)_x = 0$ on the lower half-plane. Thus the boundary condition becomes

$$w_{2x} + c_1 v_{1x} + c_2 v_{2x} = 0, \quad x=0, \quad y > a, \quad (33)$$

$$w_{1x} + c_1 v_{1x} + c_2 v_{2x} = 0, \quad x=0, \quad y < -a. \quad (34)$$

Equations (33) and (34) are two linear equations for c_1 and c_2 . They have the solution

$$c_1 = (w_{1x}^- v_{2x}^- - w_{2x}^+ v_{2x}^-)(v_{1x}^+ v_{2x}^- - v_{1x}^- v_{2x}^+)^{-1}, \quad (35)$$

$$c_2 = (w_{1x}^- v_{1x}^+ - w_{2x}^+ v_{1x}^-)(v_{1x}^+ v_{2x}^- - v_{1x}^- v_{2x}^+)^{-1}. \quad (36)$$

In these equations a superscript $+$ means that $y > a$ and a superscript $-$ that $y < -a$.

These expressions for c_1 and c_2 depend upon the two values of y and therefore they are not constant. But if we use the asymptotic forms of the functions on the right sides of (35) and (36) then these expressions are constant. Therefore this is what we do. The asymptotic forms to which we refer are valid at points which are many wavelengths from the edge of either screen. Consequently our results will be applicable to slits which are wide compared to a wavelength. Analytically this means that ka must be large. But just as in the case of the soft screen, the results are very accurate even when a/λ is as small as unity (see figures 3 and 4).

If ρ is the distance from a fixed point to the edge of one of our screens, then the method in §2 requires large $k\rho$, in addition to large ka . Therefore the methods in §§1 and 2 should agree when $k\rho$ and ka are both large. They do agree in fact. Thus when the constants determined by (35) and (36), in the manner described above, are inserted into (33), then the asymptotic expansion (for large k) of the resulting formulas lead to the usual geometrical optics field plus a diffracted field. That diffracted field agrees with u_d as given by the sum of (10) and (18) in §2.

On décrit l'adaptation au cas d'un écran dur (sur lequel la dérivée normale du champ s'annule) de deux méthodes qui ont été appliquées déjà à l'étude de la diffraction par une ouverture dans un écran mou (sur lequel le champ s'annule). Ces méthodes sont: la théorie géométrique de la diffraction et la méthode du champ 'self-consistent'. Nous les avons appliquées au problème de la diffraction par une fente infinie et elles fournissent le même résultat à des distances des bords de l'écran plus grandes que quelques longueurs d'onde. La première méthode est appliquée aussi au cas de la diffraction par une ouverture circulaire. Pour le problème de la fente et de l'ouverture circulaire, on a obtenu des expressions pour les champs diffractés, les figures de diffraction et les sections efficaces de transmission. On présente des courbes donnant les sections efficaces de transmission dans le cas de l'incidence normale.

Zwei Methoden, die früher schon für die Beugung an einer Öffnung in einem weichen Schirm (an dem das Feld verschwindet) benutzt worden sind, werden nun auf den Fall eines harten Schirmes abgewandelt (an dem die senkrechte Ableitung des Feldes verschwindet). Diese beiden Methoden sind die geometrische Beugungstheorie und das Verfahren des self-consistent field. Sie werden beide auf die Beugung an einem unendlich langen Spalt angewendet und liefern das gleiche Ergebnis für Abstände von den Schirmkanten, die größer sind als mehrere Wellenlängen. Die erste Methode wird auch auf die Beugung an einer kreisförmigen Öffnung angewendet. Man erhält Ausdrücke für das abgelenkte Feld für die Beugungsfiguren und die Übertragung von Querschnitten bei spalt- und kreisförmiger Öffnung. Für den senkrechten Einfall sind auch die Übertragungen der Querschnitte gezeichnet.

REFERENCES

- [1] KELLER, J. B., 1957, *J. appl. Phys.*, **28**, 426. Also N.Y.U., Inst. Math. Sci., Div. EM Res., Report No. EM-92.
- [2] KARP, S. N., and RUSSEK, A., 1956, *J. appl. Phys.*, **27**, 886. Also N.Y.U., Inst. Math. Sci., Div. EM Res., Report No. EM-75.
- [3] LEVINE, H., N.Y.U., Inst. Math. Sci., Div. EM Res., Report No. EM-84.
- [4] MILLAR, R. F., 1958, *Proc. Camb. phil. Soc.*, **54**, 497.
- [5] BUCHAL, R. N., and KELLER, J. B., N.Y.U., Inst. Math. Sci., Div. EM Res., Report No. EM-131.
- [6] LEVINE, H., and WU, T. T., 1957, Tech. Report No. 71, Appl. Math. and Stat. Lab., Stanford University, July.
- [7] KARP, S. N., and ZITRON, N., N.Y.U., Inst. Math. Sci. Div. EM Res., Report No. EM-126.
- [8] KARP, S. N., 1959, McGill Symposium on Microwave Optics.
- [9] BOUWKAMP, C. J., 1954, *Rep. Prog. Phys.*, **17**, 35.

Interferometric methods for the photographic production of large gratings

by J. M. BURCH and D. A. PALMER

Communication from the National Physical Laboratory

(Received 11 August 1960)

The need for new types of coarse gratings for moiré fringe applications has aroused fresh interest in the possibility of using interferometry to generate gratings photographically. It is shown that this is now practical, and that certain commercially available emulsions have adequate resolving power and freedom from distortion.

A large two-beam interferometer has been constructed which is capable of producing gratings with between 1000 and 5000 lines per inch with an aperture 18 in. in diameter. The design and adjustment of the instrument are described. Large gratings of 1150 l.p.i. have been produced, and their application to stellar spectroscopy is being investigated. It is hoped to make the fringe spacing continuously variable, and this will open up further spectroscopic possibilities on the lines suggested by Connes [1].

1. INTRODUCTION

It has long been recognized [2] that it should be possible to use an interferometer to produce diffraction gratings photographically, but the method has always had the disadvantage that, even if a perfectly regular fringe pattern can be generated and recorded, the resultant grating may not have the light-grasp and homogeneity needed for serious spectroscopy. By 1957, however, a need had arisen for new types of coarse grating to be used in moiré fringe applications, and for these metrological gratings many of the usual spectroscopic tolerances were considerably relaxed. Since at this time research on colloidal photographic emulsions and on recording Lippmann-type interference patterns was already in progress at the National Physical Laboratory [3] it was decided to undertake an investigation of photographic methods which would supplement existing Merton-NPL methods for making fine gratings [4].

In order to find out whether a photographic emulsion would give sufficiently faithful recording, a preliminary study was made by means of direct interferometry [5]. Monochromatic light was divided at a semi-reflecting plane surface into two coherent beams, which were brought together again, by means of plane mirrors, so as to intersect at an oblique angle and form a pattern of fine interference fringes. Spacing of these fringes depended on the angle of inclination between the two interfering beams and was controlled by adjusting the mirrors. Earliest experiments were performed at 7500 lines per inch with a wedged type of Fizeau interferometer, but a more elaborate instrument was then built to produce between 11 000 and 60 000 fringes per inch localized across an aperture approximately three inches square.

2. RESULTS WITH PLANE MIRROR SYSTEMS

To photograph the fringes, a sensitive plate was held in the fringe pattern, a kinematic support being used to ensure precise location. After an exposure

lasting perhaps twenty minutes, the plate was developed and fixed in the normal manner to produce a photographic copy of the fringes, which could serve as a grating. Kodak Maximum Resolution emulsion was found to be very suitable for this purpose, because in addition to its high contrast and resolving power it was uniformly sensitive and exhibited very little emulsion shift under normal processing conditions. The interferometer itself provided complete information on the extent of this distortion, for by returning the processed plate to its original holder it was possible to observe a moiré pattern which delineated any difference between the original 'live' fringes and their photographically recorded copy.

The moiré fringe pattern shown in figure 1 was obtained in this way from a photographic plate containing approximately 57 000 lines per inch, and the fact that the moiré fringes are substantially straight demonstrates that the lateral distortion introduced by processing this thin gelatine emulsion was certainly less than two micro-inches. This information suggested that by photographic processes very accurate metrological gratings could be made available, but, because of the limited aperture and inconveniently fine pitch produced by the plane mirror interferometers, attention was then turned to non-interferometric methods of manufacture [6, 7].

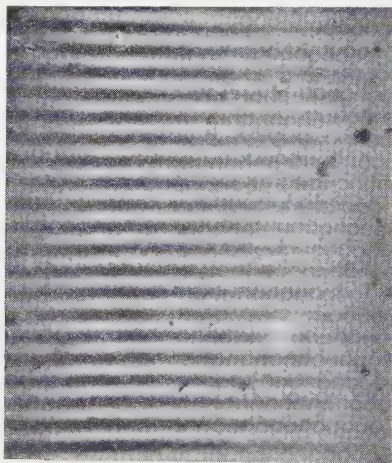


Figure 1. Moiré pattern formed between 57 000 l.p.i. grating, and original fringe pattern.

In 1958, however, both these disadvantages of the direct interferometric method were removed; following a suggestion by Dr. P. Fellgett, it was realized that, by locating a small interferometer near the focal plane of a single and large collimator, it would be possible to produce gratings of relatively coarse pitch and of very large aperture.

3. LARGE APERTURE SYSTEMS EMPLOYING A COLLIMATOR

Since an astronomical requirement had arisen for an objective grating to cover the aperture of a Schmidt telescope, it was at first proposed [7] to use the existing concave mirror of the Schmidt system as collimator for the new interferometer (figure 2). A beam splitting cube together with associated reflecting prisms would be placed at the solar focus of the mirror so as to produce two coherent images of the same monochromatic source which were separated

by approximately one inch (figure 3). Two collimated beams would then be reflected back from the mirror, inclined at a slight angle because of the separation of the source images, and under suitable conditions would interfere to produce fringes localized in the aperture of the telescope. Used in this way, the system allows the possibility of compensating for the aberration of the collimator, at least in the effect which it may have on the fringe pattern. A Schmidt mirror is spherical and therefore produces only spherical aberration in the two emerging beams. Provided that the photographic plate is located in the position at the centre of curvature of the mirror normally occupied by the aspheric corrector

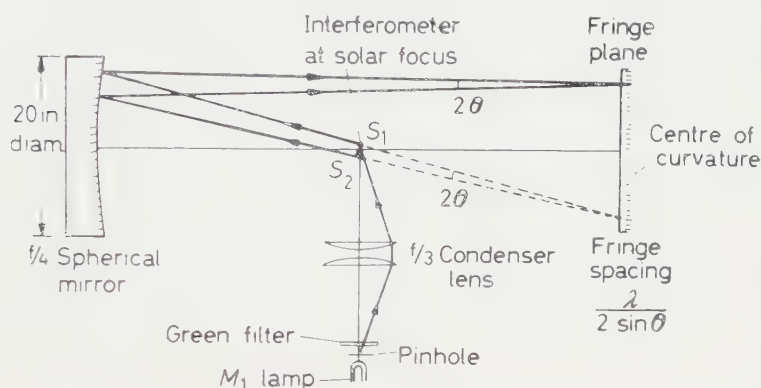


Figure 2. Reflecting arrangement for producing gratings of large aperture. S_1 and S_2 are coherent sources produced by the interferometer. (Reproduced from *Research* (1960), 13, 3.)

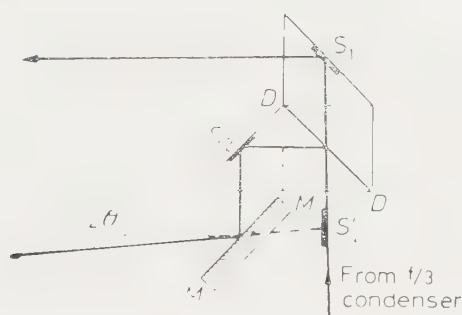


Figure 3. Cemented interferometer for producing a pair of coherent sources. Mirror is adjustable. (Reproduced from *Research* (1960), 13, 3.)

plate, the spherical aberration components in the two intersecting beams must be equal and free from lateral shear. Since the formation of interference fringes depends on the optical path difference between corresponding points in the two wave-fronts, and since the spherical aberration has merely added a similar fourth power phase term to each wavefront, the fringe spacing remains virtually unaffected. It can be shown that the residual sixth-order aberration which occurs in such an arrangement amounts to $N/2^{15}F^6$ fringes, where F is the focal ratio of the primary mirror and N the total number of fringes being produced. If for example an $f/2$ mirror is used to produce 100 000 fringes the error is still five times smaller than the Rayleigh limit.

As yet this purely catoptric system has not been constructed, but it would be possible to use it with very large apertures provided that it were housed in a suitable room. For the production of gratings with up to 18 in. aperture, however, it has been found more convenient to construct a corresponding dioptric system which employs a plano-convex lens as the collimator (figure 4). The use of a lens instead of a mirror has some advantage in that it shortens the tube length for a given focal length, and avoids obscuration of the central region of the fringe pattern by the shadow of the interferometer cube. Whether a reflecting or a refracting collimator is used, stability is more easily obtained than with a plane mirror interferometer of the same aperture, since the beam splitter is small, and all the critical adjustments are performed in its immediate vicinity.

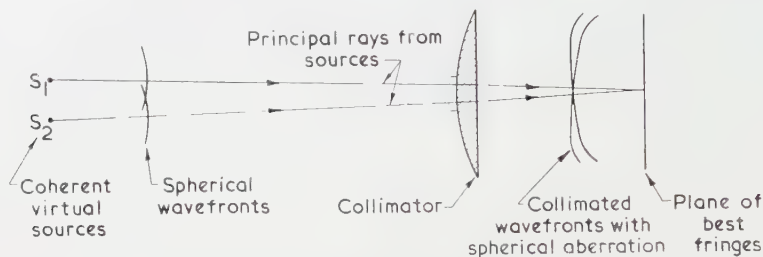


Figure 4. Alternative arrangement to that in figure 2 using plano-convex lens as collimator.

In the refracting version, the convex surface of the lens must face towards the interferometer, and the principal rays in each cone of light from the interferometer must pass through the surface normally, again in order to ensure that only spherical aberration is present in the collimated beams. The correct position for the photographic plate would be at the geometrical centre of curvature of the convex surface, were it not for refraction at the plane surface, which brings the best fringe plane nearer to the lens by a factor $1/\mu$. It is not difficult to show that this plane surface does not significantly affect the aberration, as the beams are collimated before they pass through it. The spherical aberration produced by the lens is, however, very much larger than for a mirror of similar focal ratio, to such an extent that, for the NPL collimator which has a focal length of 62 in. and a diameter of $18\frac{1}{2}$ in., only the central 15 in. can be considered free from aberration.

4. DESIGN OF INTERFEROMETER

A source of adequate spectral unity is obtained by under-running a mercury discharge lamp such as the Siemens MB/D or preferably miniature M1 lamp, the green line 5461\AA being isolated by means of a suitable filter. An extended source is essential to provide enough illumination for the relatively slow and fine-grained emulsion (Kodak V1056) which is needed to resolve fringe patterns containing up to 2500 lines per inch. In practice the size of the circular source is limited by the aperture available at the beam-splitting cube, and cannot exceed $\frac{3}{8}$ in. diameter without introducing vignetting. A more fundamental restriction, which applies to any interferometer of this type, is that the angular radius of the source must not exceed $N^{-1/2}$ radians where N is the total number of well-defined fringes required. Since the interferometer of figure 3 produces only 730 fringes per inch across a 15 in. aperture, a source over one inch in diameter would be

permissible, and the present instrument is from this point of view inefficient. Two other disadvantages of this first version are firstly that the cemented BiO beam-splitting film is strongly polarizing and produces fringes of good contrast only when used with a polarizing filter, and secondly that, unless the fully cemented construction is extremely accurate, one of the two emerging cones of light is slightly twisted with respect to the other.

For these reasons, and in order to obtain a more convenient variation of fringe spacing, the more adjustable form of construction shown in figure 5 is now preferred. The metallized beam-splitting cube together with one auxiliary reflector move together on a precision slide, between two larger adjustable reflectors which reflect the light towards the collimator and are nominally at 45° to the axis of the system. Thus the separation between the outgoing beams may be varied by moving the slide, and in this way continuous control of the grating spacing is provided. Two weak lenses placed in the emergent beams ensure that only slight adjustments, if any, will have to be made to the other controls if it is desired to adjust the grating spacing slightly.

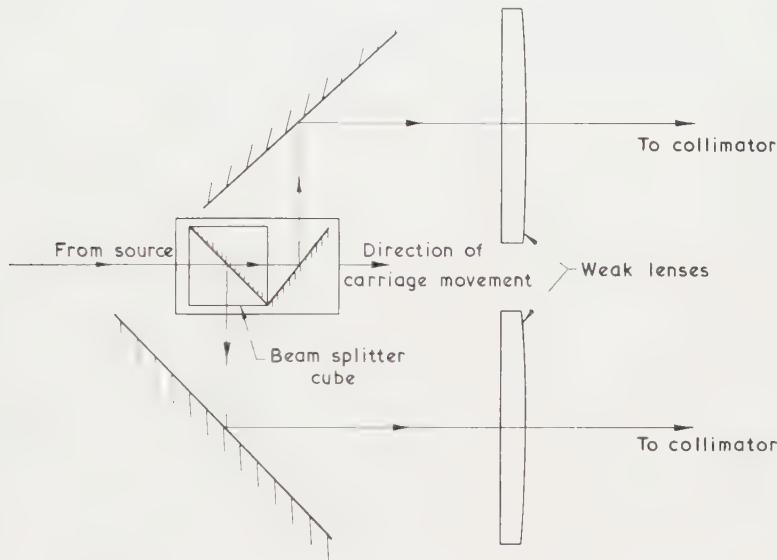


Figure 5. Preferred form of interferometer with slide for continuous adjustment of source separation.

5. ADJUSTMENT PROCEDURE

Initial adjustments to these interferometers are performed by the methods described below, but perhaps the most convenient method of making final adjustments is to observe their effect on the moiré fringes formed between a processed plate and the original fringe pattern. If observations are made with the processed plate returned to the kinematic holder, both in its original orientation and rotated through 180° , the deformation of the moiré pattern will indicate what adjustments if any are still needed.

The first adjustment is to locate the interferometer at the focus of the collimating lens as judged by autocollimation, and then to bring the plate-holder

into parallelism with the plane surface of the lens, again by obtaining auto-collimation. Axial adjustment of the plateholder with respect to the lens is obtained by placing a green illuminated slit centrally in the plane of the emulsion, and causing this slit to be imaged back on to itself by paraxial regions of the (unbloomed) convex surface of the lens. The exact separation of the interferometer from the collimator is not critical except for slight effects on vignetting and fringe spacing, but it is necessary that both images of the source be at exactly the same distance from the lens, since otherwise an objectionable difference of curvature is introduced between the two interfering wavefronts. This adjustment is accomplished by means of a fine tangent screw, which rotates the whole interferometer in azimuth until the auxiliary slit previously mentioned produces 'achromatic' fringes of shearing interferometer type across the aperture of the beam-splitter. A more satisfactory final check on this adjustment is to verify, by the reversal technique, that the gratings produced are free from progressive error.

Since a large source must be used to provide sufficient illumination, the fringes are strongly localized, and the region over which they exhibit good visibility is only about one-fifth of an inch deep. To cause the plane of optimum contrast to coincide with the plane of the photographic emulsion, a null technique is used, as with plane mirror systems, of observing enantiocyclic fringes [6] formed in the source plane. A fully aluminized auxiliary mirror is placed in the kinematic plateholder so as to coincide with the plane taken up by the emulsion during an exposure. Light from both images of the source is reflected in this auxiliary mirror, each beam returning along the track already traversed by its fellow on the outgoing journey. Thus two images of the source are focused back through the interferometer onto the original source plane, the light in the two beams having traversed the same cyclic path in opposite directions. By observing these returned images with a suitable semi-reflector inserted in the beam between the condenser and the interferometer, enantiocyclic fringes are seen as soon as the interferometer prisms are approximately adjusted. When these fringes seen in the source plane are 'fluffed out', and remain so from whatever direction they are viewed, all portions of the source are producing the same pattern of fringe intensity on the surface of the mirror. The latter is now removed and replaced by a sensitive photographic plate in order to make an exposure.

6. PRELIMINARY RESULTS OBTAINED

To check the optical theory of this interferometer, some preliminary experiments were carried out using the beam-splitting arrangement of figure 3 with a 4 in. aperture lens of 20 in. focal length. This combination gave about 2300 fringes per inch with mercury green light, and it was possible to obtain gratings accurate to about a quarter of a fringe over most of the lens aperture. Exposure time with Kodak V1056 emulsion was only a minute or so, and it was found that each such master could be copied on to MR emulsion with a useful gain in contrast and reduction of turbidity. Since the MR copies exhibited considerable corrugation of their gelatine surface, completely transparent phase gratings could then be obtained by the NPL polyester resin technique [8], and appeared to be suitable for the application to stellar spectroscopy which has been mentioned above.

With the experience gained with this small lens, the apparatus was rebuilt to use a plate-glass lens of full $18\frac{1}{2}$ in. aperture and 62 in. focal length. With a six-minute exposure on V1056 emulsion gratings were produced which were satisfactory except for marked local variations of fringe visibility introduced by striations within the material of the lens, and a corresponding component in optical glass was therefore ordered.

At this stage I. G. van Breda of Cambridge University Observatory was seconded to work with the interferometer during vacations. Following installation of the optical glass collimator and of a simplified version of the interferometer illustrated in figure 5, with slide and weak lenses omitted, gratings were produced with approximately 1150 lines per inch across a circular aperture 15 in. in diameter. Checks by reversal indicated that the regularity with which the fringes were spaced was well within the Rayleigh limit. Satisfactory copies were then obtained by printing through onto MR emulsion and finally on polyester resin replicas, the corrugation of the latter being chosen so as to concentrate as much light as possible into two equal first-order diffraction spectra. The astronomical possibilities of such objective gratings are now being evaluated at Cambridge by Mr. van Breda.

7. OTHER APPLICATIONS

While it is likely that one-dimensional or two-dimensional gratings of this size, with between 1000 and 5000 lines per inch, will find several metrological applications, there are two severe limitations to their usefulness in spectroscopy. The first of these is the poor blaze characteristic associated with simple symmetrical fringe records, which makes it difficult even with transparent resin gratings to concentrate more than about 30 per cent of incident light into a single diffracted order. The second disadvantage is the considerable aberration introduced into the wavefront of all orders by irregularity of the gelatine or resin layer and of its supporting glass plate. For a 15 in. diameter resin grating, carried on twin-ground plate glass $\frac{1}{4}$ in. thick, this aberration may amount in transmission to two or three fringes, and in reflection to perhaps a hundred fringes.

For spectroscopy of faint extended sources, however, an interesting escape can be found from these difficulties if a fringe-scanning method is adopted which allows a circular source to be used. A method is now envisaged whereby the 'frozen' fringe pattern which has been recorded photographically by one source will be compared on a subsequent occasion with the live optical fringes which are being generated by a second source. In the particular case, hitherto used for testing emulsion shift, where the same spectral line is used to generate both patterns, the moiré pattern which is produced can be analysed to obtain the autocorrelation function of the intensity spectrum. The spectral information contained in such moiré patterns is illustrated by figure 1, in which a marked lateral variation of fringe visibility is being produced by a slightly broadened natural mercury source.

In the slightly more general case where a known sharp line is cross correlated with a more complicated unknown spectrum, it should be possible to determine the latter. Depending on which of the two sources is used first, this technique would constitute either an analogue version of the digital methods used by Gebbie and others for Fourier Transform spectroscopy [9], or a single grating SISAM spectrometer working according to the elegant principles devised by

Connes [1]. It would seem to allow a photographic grating to achieve at short wavelengths a medium resolving power equal to the number of lines which it contains, coupled with a light grasp for very faint diffuse sources equivalent to a Fabry-Perot or Michelson of nearly the same aperture. Arrangement is being made to investigate this possibility.

ACKNOWLEDGMENTS

Special acknowledgment is due to Mr. I. G. van Breda for bringing the new interferometer into successful operation. The authors are also grateful to Dr. W. H. Stevens of Kodak Research Laboratories for advice on photographic emulsions and to Dr. H. A. Gebbie for discussions on correlation methods in spectroscopy. The work described forms part of the general research programme of the National Physical Laboratory, and this paper is published by permission of the Director of the Laboratory.

Les besoins de nouveaux types de réseau plus grossiers pour les applications des franges de moiré a renouvelé l'intérêt dans les possibilités d'utiliser l'interférométrie pour réaliser des réseaux par voie photographique. On montre que ceci est maintenant réalisable pratiquement, et que certaines émulsions existant dans le commerce ont un pouvoir résolvant suffisant tout en étant exemptes de distorsion.

On a construit un grand interféromètre à deux ondes qui peut servir à la fabrication de réseaux comportant 1000 à 5000 traits par pouce avec une ouverture de 18 pouces de diamètre. On décrit la réalisation et le réglage de l'instrument. On a fabriqué de grands réseaux de 1150 traits par pouce et on étudie maintenant leur application à la spectroscopie stellaire. On espère pouvoir rendre l'espacement des franges variable d'une manière continue et ceci ouvrira de nouvelles possibilités spectroscopiques suivant les suggestions de Connes [1].

Das Bedürfnis nach neuartigen groben Gittern für die Erzeugung von Moiréstreifen hat das Interesse an den Möglichkeiten neu geweckt, die die Interferometrie für die photographische Herstellung von Gittern bietet. Es zeigt sich, daß dies durchaus zweckmäßig ist und daß gewisse handelsübliche Emulsionen ein entsprechendes Auflösungsvermögen besitzen und frei von Verzerrungen sind.

Ein dafür gebautes Zweistrahl-Interferometer erlaubt es, Gitter mit 40 bis 200 Linien pro Millimeter bei einem Durchmesser von 450 mm herzustellen. Mit dem im Aufbau und in der Justierung beschriebenen Gerät wurden große Gitter von 45 Linien/mm hergestellt, deren Brauchbarkeit für Sternspektroskopie noch untersucht werden. Man darf hoffen, daß sich der Streifenabstand stetig verändern läßt. Damit erschließen sich weitere Möglichkeiten für die Spektroskopie in der von Connes [1] angeregten Richtung.

REFERENCES

- [1] CONNES, P., 1959, *Rev. Opt. (théor. instrum.)*, **38**, 157.
- [2] MICHELSON, A. A., 1927, *Studies in Optics* (Chicago: University Press).
- [3] CRAWFORD, B. H., 1954, *J. sci. Instrum.*, **31**, 333.
- [4] HALL, R. G. N., and SAYCE, L. A., 1952, *Proc. roy. Soc. A*, **215**, 536.
- [5] BURCH, J. M., 1960, *Photographic Production of Scales for Moiré Fringe Applications*, Brussels Colloquium on Optics in Metrology, May, 1958 (London: Pergamon Press).
- [6] BURCH, J. M., 1960, *The Possibilities of Moiré Fringe Interferometry*, NPL Symposium on Interferometry, June 1959 (London: Her Majesty's Stationery Office).
- [7] BURCH, J. M., 1960, *Research, Lond.*, **13**, 3.
- [8] DEW, G. D., 1952, *J. sci. Instrum.*, **29**, 277.
- [9] GEBBIE, H. A., 1958, *J. Phys. Radium*, **19**, 130.

Some factors in brightness discrimination with constraint of retinal image movement

by M. B. CLOWES

Physics Department, Reading University†

(Received 3 September 1960)

A study has been made of the discrimination of a luminance difference between the segments of a bipartite field, using the stabilized retinal image. It is shown that there is a simple correlation between the amplitude of retinal image motion and the level of visual discrimination measured by a time-average procedure. In the absence of retinal image motion, separation of the comparison stimuli further impairs discrimination. These phenomena are discussed in the light of recent electrophysiological studies of the mammalian eye.

1. INTRODUCTION

It has been shown by a number of workers [1-3] that the condition of voluntary fixation is accompanied by a characteristic regime of small eye movements. These involuntary movements include

- (i) a high frequency *tremor* of amplitude less than 0.5 min arc and frequencies up to 150 c/s;
- (ii) intermittent rapid *flicks* of up to 50 min arc occurring at irregular intervals (from 0.03 to 5 sec), and
- (iii) a slow motion drift at the rate of about 1 min arc/sec in the inter-flick periods.

Using optical techniques which eliminate or control retinal image motion, it has been shown that these involuntary movements play an important part in visual discrimination. Ditchburn and Ginsborg [3] and [4], Fender [5] and Krauskopf [6] have demonstrated that brightness discrimination is characteristically impaired when the subject views a test field whose retinal image is stabilized. Discrimination is intermittent and the effect is measured quantitatively as the percentage of the viewing period during which the subject signalled his ability to make the desired discrimination.

In this paper it is shown that brightness discrimination, measured in this way, is dependent upon retinal image motion in a more general way. The interpretation of these effects (Ditchburn [11]) has been in terms of the physiological characteristics of the visual pathways, and in particular, the heightened response to temporal changes in stimulation, as opposed to steady stimulation. Recent studies of the electrical activity of the vertebrate retina, have underlined the importance of another physiological process namely the lateral interaction of adjacent regions. This interaction takes the form of a decreased response from a retinal element, when an adjacent area is stimulated. Barlow *et al.* [15] point out the analogy between this lateral inhibition, and the perceptual phenomenon of spatial induction in the human discrimination of brightness.

† Now at the National Physical Laboratory, Teddington.

The stabilized image technique makes it possible to isolate purely spatial factors in visual discrimination and so to produce results of importance in connection with studies of spatial induction.

2. THE APPARATUS

The subject, wearing a tightly fitting contact lens to which is attached a mirror, views a target through an optical system which includes the eye mirror (figure 1). The optical system stabilizes the retinal image against translational movements of the eye, and also against rotations about a horizontal or vertical axis. The residual movements of the retinal image arising from rotations of the eye have been shown to be less than 0.3 per cent of those naturally occurring, in respect of a target viewed centrally in the system. A complete description of the optical system and its mode of operation has been given elsewhere [8].

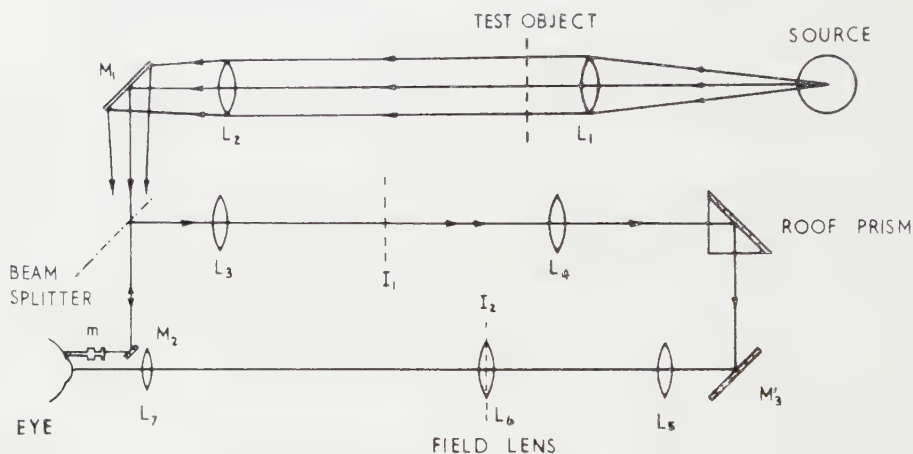


Figure 1. A test object is illuminated with parallel light from a tungsten strip filament lamp. An image of the test object is formed at infinity by L_2 and is reflected at normal incidence from the mirror on the contact lens. The image is passed through the telescopic system L_3 L_4 L_5 L_7 , with a magnification of $\times -\frac{1}{2}$, and is viewed by the subject with a relaxed eye. L_6 images the eye mirror and the source, upon the pupil.

3. EXPERIMENTAL METHOD

The standard stimulus used is a 1° circular field divided along a horizontal diameter (figure 2a). The luminance of either half may be varied independently by means of photometric wedges. The quantity $\text{time seen}/\text{time exposed} \times 100$ is calculated from a record of the subject's signals of the presence or absence of a brightness difference, and is called the Visibility (V). The exposure period is 90 sec. Signals during the first 30 sec are not included in the calculation of V , and an average value of V is calculated for the remaining period except when the temporal dependence of V is being investigated. In this case V is averaged over successive 20 sec periods to give a 'running' average.

Measurements of luminance are made with an S.E.I. photometer calibrated in foot lamberts on a logarithmic scale. It is convenient to express the luminance difference ΔB between the segments of the stimulus field simply as the difference between points measured on this scale. In all experiments one-half of the test field was maintained at a fixed luminance; the other half was adjusted to some

lower value. Throughout the investigations, the subjects were asked to maintain fixation upon the centre of the stimulus field.

Four types of constraint may be imposed upon the relationship between eye movements and retinal image movements, regarding unstabilized vision as constituting zero constraint. Measuring distance along the retina in terms of the equivalent visual angle, the four constraints are illustrated in table 1.



Figure 2.

Table 1

Constraint	Rotation of the eye		Displacement of retinal image	
	Horizontally	Vertically	Horizontally	Vertically
A (unstabilized)	θ	ϕ	θ	ϕ
B (stabilized)	θ	ϕ	0	0
C (exaggerated)	θ	ϕ	0	2ϕ
D (reversed)	θ	ϕ	$-\theta$	$-\phi$

Constraint C is obtained by inserting a Dove Prism between L_4 and the Roof Prism (figure 1) in the compensating system. Constraint D may be obtained by doubling the linear magnification of the telescopic compensating system, e.g. by halving the focal length of L_7 . In any one experiment two types of constraint are used alternately, but any systematic changes in the stimulus configuration (e.g. changes in luminance) are made in random order for both constraint situations separately. As expected, V increases with ΔB and the value of ΔB for which $V = 50$ per cent will be called the 50 per cent threshold (ΔB_{50}).

4. CONSTRAINTS A, B AND C

Using white light, with the luminance of the brighter half of the field at 20 foot lamberts, a detailed comparison of discrimination under constraints A and B has been made. The results are shown in figure 3. With constraint A, ΔB_{50} is 0.1, with constraint B, it is 0.3.

In conventional experiments on brightness discrimination with the unstabilized image (constraint A), the subject is not requested to fixate as in the above experiments, but is allowed to move his eyes freely. It is usually stated that the 'threshold' difference of luminance which is just perceived is about 0.02 log unit.

Some tests were made using 5 sec exposure and asking the subject to say whether the upper or the lower half of the field was brighter (no restrictions being placed upon voluntary eye movements). The subject gave nearly 100 per cent correct responses when ΔB was 0.012 and little more than a random proportion of correct responses when ΔB was 0.008 log units, indicating a threshold in the region of $\Delta B = 0.01$ log unit. This cannot be directly compared with our ΔB_{50} , because when the subject is allowed to move his eyes, vision is not intermittent. It does, however, indicate a performance much better than that attained with voluntary fixation. The implication is that the difference of threshold is due in large measure to the degree of fixation employed.

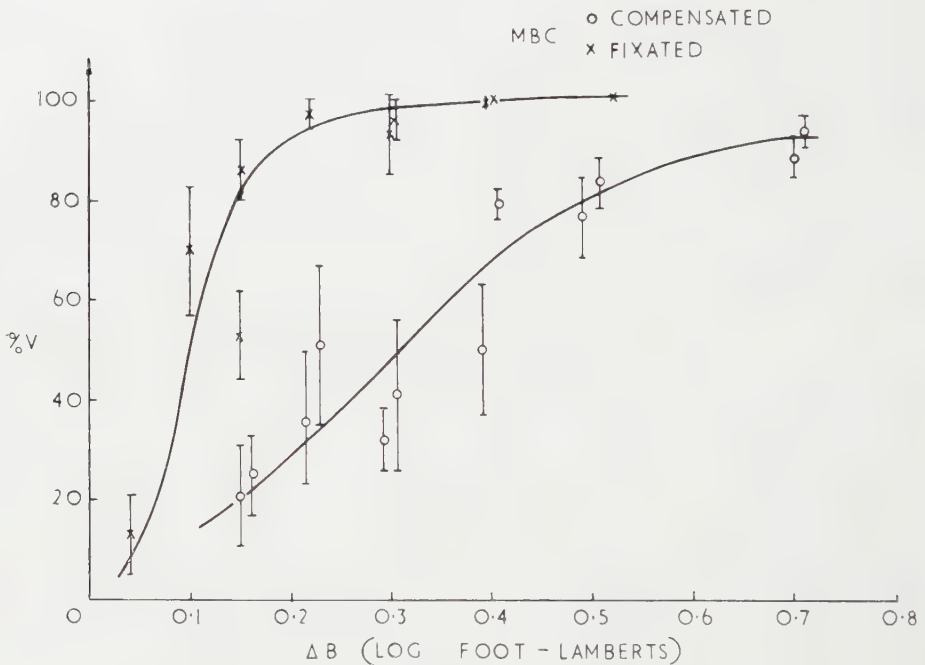


Figure 3.

Fender [5] using an apparatus in which the bipartite field was viewed via a ground-glass screen [7], measured the variation of V with luminance difference using constraint B only. Figure 4 shows his result (dotted) compared with values obtained in our measurements with three subjects. The considerable technical improvement between the two optical systems [8] has not been accompanied by any large shift in the visual threshold. From this it is possible to conclude that the curves in figure 4 are a satisfactory measure of the discrimination possible in the absence of retinal image motion.

Discrimination with constraints A and C have been compared using a stimulus illuminated with red light at a luminance of 1 lm/ft². Constraint C was applied to the vertical component of the retinal image movement (i.e. at right angles to the line dividing the bipartite field). The retinal image movement parallel to this line was subject to constraint B. These experiments form part of a group to

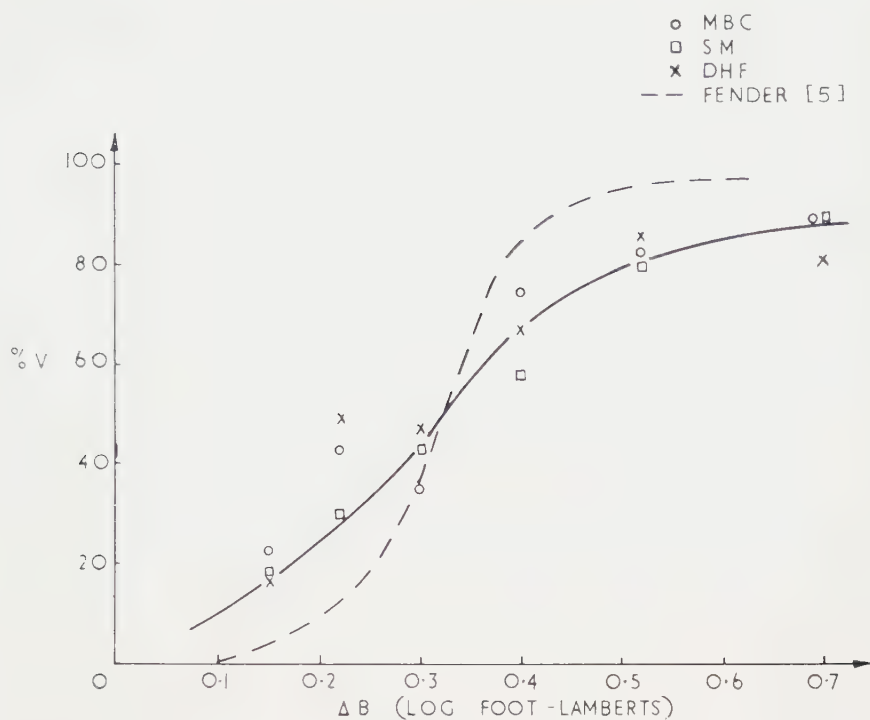


Figure 4.

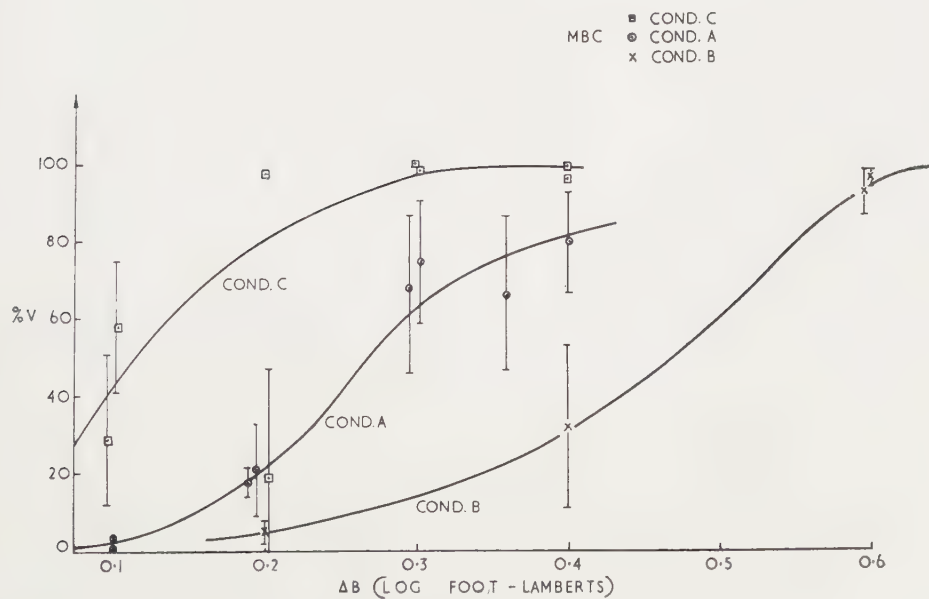


Figure 5.

investigate the properties of coloured stimuli under conditions of retinal image constraint. Figure 5 shows the results of two experiments on one subject. Included in the same graph are some results which show the visibility curve with constraint B, under these stimulus conditions. The movement of the constraint C curve, away from A and towards values appropriate to normal vision, must arise from the relative increase in retinal image motion.

Subjects report a 'locking-on' of eye movements in the vertical meridian. Recordings of the eye movements show that there is a reduction of $\times \frac{2}{3}$ in the amplitude of continuous movement, in both planes simultaneously, in spite of the asymmetry in the constraints applied to horizontal and vertical motion. The median flicks are also reduced. Table 2 shows this reduction measured in terms of the rotational displacement of the eye in successive 1 sec intervals, and also in terms of flick amplitude. This result is of considerable interest in relation to the theories of the control of eye movements as it suggests that the magnitude of the involuntary eye movements accompanying fixation are under central control. These modifications of the normal fixated eye movements complicate the interpretation of the relative positions of the C and the A Visibility curves. Further investigations will be required, possibly with an increased exaggeration, in order to decide which components of the retinal image movement are responsible for this effect.

Table 2

Displacement occurring in successive 1 sec intervals				
	Vertical		Horizontal	
	Constraint A	Constraint C	Constraint A	Constraint C
Mean	1.8 min arc	1.0 min arc	2.3 min arc	1.6 min arc
Median	1.5 " "	1.0 " "	1.8 " "	1.5 " "
Maximum	7.5 " "	3.5 " "	16.5 " "	6.5 " "
Minimum	0 " "	0 " "	0 " "	0 " "

Flick amplitude				
	Vertical		Horizontal	
	Constraint A	Constraint C	Constraint A	Constraint C
Mean	2.0 min arc	3.3 min arc	9.0 min arc	7.0 min arc
Median	1.8 " "	1.3 " "	9.0 " "	6.0 " "
Maximum	5.5 " "	14.5 " "	21.0 " "	17.5 " "
Minimum	0 " "	0 " "	1.0 " "	1.0 " "

5. REVERSED MOVEMENTS OF THE RETINAL IMAGE (CONSTRAINT D)

Observations in this condition have been made, although for reasons outlined below, quantitative studies are difficult. The stimulus field was first viewed under constraint A, and the luminance difference adjusted to be suprathreshold.

The stimulus was then viewed under constraint D when the subject reported that the appearance of the field was substantially unchanged, i.e. (1) the increment threshold was unchanged; (2) the brighter half of the field was correctly identified.

Since the *amplitude* of the retinal image motion bears the same relation to the eye movements as in normal vision we would not expect brightness discrimination to be affected, and this is borne out by the first observation above.

The modification of retinal image motion induced by this apparatus reverses the normal relation between the proprioceptive information from the extrinsic eye muscles, and the positional information from the retina. The second observation above suggests that the interpretive process which identifies the *direction* of the brightness increment in the test field does not rely upon proprioceptive information from the eye muscles. Quantitative measurements of visual thresholds under constraint D are hindered by the very large amplitude ($\pm 5^\circ$) eye movements which appear soon after the presentation of the stimulus. These movements resemble the pendular nystagmus reported by Ten Doeschate [9] and make fixation upon the target impossible.

6. BRIGHTNESS DISCRIMINATION WITH SEPARATED TEST FIELDS

In order to examine the contribution made by retinal image motion to spatial induction, the effect upon brightness discrimination, of separating the test fields

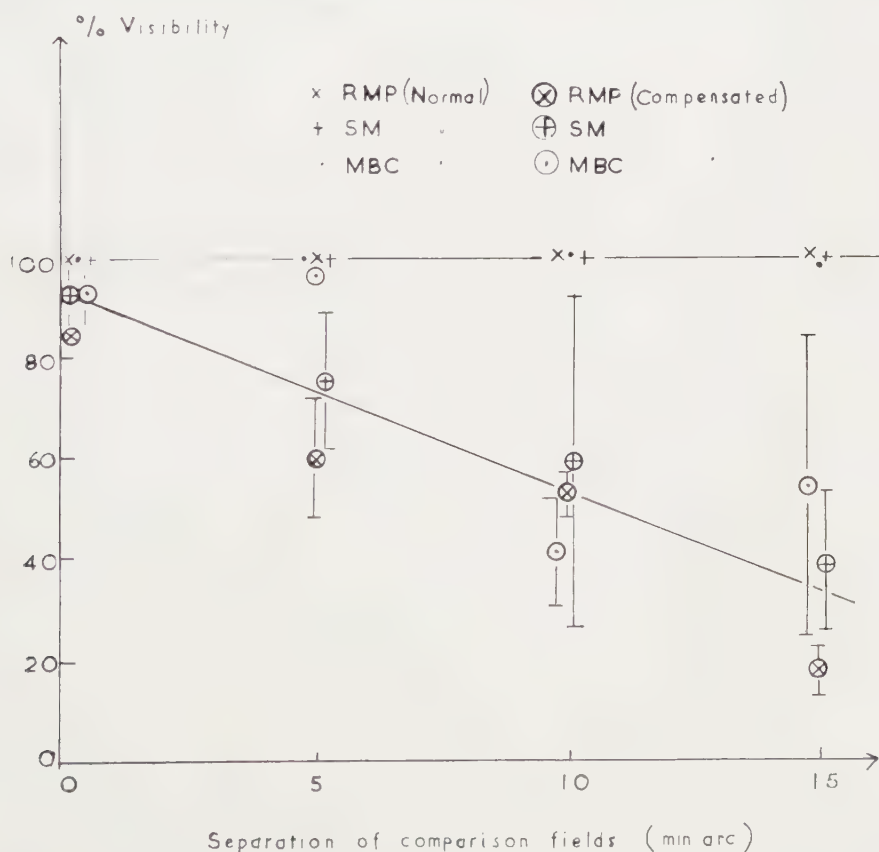


Figure 6.

is measured for constraints A and B. Discrimination of a brightness difference is measured for varying separations of the segments of the bipartite field (figure 2*b*), when the brighter segment is at a luminance of $0.0 \log (\text{lm/ft}^2)$ and the darker at $-0.6 \log (\text{lm/ft}^2)$ (red light). The subject fixates the centre of the stimulus field. The results for three subjects are shown in figure 6. Using constraint A there is a marginal fall-off in visibility for one subject (MBC). With constraint B, however, all three subjects record a decrease of visibility of the brightness difference with increasing separation.

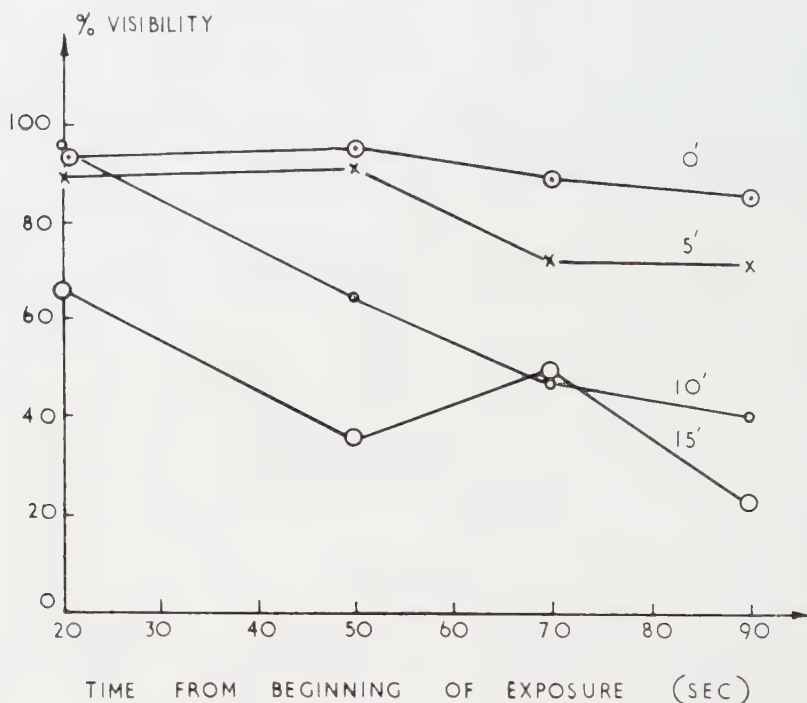


Figure 7.

An analysis of the results of the visibility measurements on the separated fields shows that this fall-off of visibility of the brightness difference with increasing separation contains a time-dependent element. The V measured in 20 sec intervals and including the interval 0–20 sec, is lower at the end of the exposure period than at the beginning. The results for any one observer are somewhat variable, but an average over the three observers employed in this experiment shows up the time-dependent element very well (figure 7). Four sets of results are obtained corresponding to each of the four separations used.

7. DISCUSSION

Modern interpretations of perceptual studies of vision have relied increasingly upon the physiological data supplied by micro-electrode studies of the retinæ of animals. The demonstration by Hartline [10] and others, of the 'on-off' system in sensory channels, was used by Ditchburn [11] to account for the early results obtained with the stabilized retinal image. He attributed the loss of

visual discrimination accompanying sustained absence of retinal image motion, to the decay of nervous activity in the optic tract, following the initial 'on' response. Ditchburn considered that the primary function of the involuntary eye movements, and particularly of the 'tremor', is to maintain post-retinal activity by subjecting receptors lying on the boundaries of the retinal image, to a continuously charging level of stimulation. Drift was assured to overcome local fatigue of the retinal elements, by moving the image to fresh zones, the retinal image being 'recentred' from time to time by a flick.

The time taken for the discrimination of brightness to fail in the stabilized condition (a few seconds), is an order of magnitude greater than the duration of the 'on' burst recorded by Hartline. This difference is to be expected if we identify the psychological phenomena with activity at a much higher level in the visual system, where EEG recordings demonstrate effects having durations of the right magnitude [12].

More recent microelectrode studies of the vertebrate retina, especially in the cat and the frog, have shown the 'on-off' system to be an aspect of a more complex situation. Kuffler [13] and others have shown that receptors in the retina of the cat are grouped in receptive fields having mutually inhibitory adjacent zones. The receptive fields of the large retinal ganglion cells have an essentially circular symmetry with a central zone stimulation of which produces a burst in the ganglion cell, either at 'off' or at 'on'. Correspondingly the peripheral zone will produce a burst at either 'on' or 'off'. The size of this field and its detailed behaviour depend upon the degree of light adaptation and the energy of the stimulus. Hubel [14], recording from cells in the visual cortex of the cat, has discovered receptive fields of different shapes. Both in the cat, and in the frog, it has been amply demonstrated that many of the receptor units are especially sensitive to moving stimuli [14, 18, 19].

This discovery of movement sensitivity is additional evidence to support Ditchburn's interpretation of the role of retinal image movement, in human brightness discrimination. The experiments described in § 4, in examining brightness discrimination with a number of different amplitude levels of retinal image movement, confirm this interpretation. The transition from non-fixated vision, to fixated vision with constraint C, with constraint A, and finally with constraint B, involves a progressive reduction in the amplitude of tremor motion of the retinal image. The accompanying impairment of discrimination (figure 5) is consistent with the view that the retina of the cat and of man have some organizational principles in common.

Barlow *et al.* [15] suggest that the 'lateral inhibition' sub-serving the zonal interaction in a receptive field could be the basis of the simultaneous contrast effects well known in psychological studies of vision. These contrast effects are of necessity present in all measurements of brightness discrimination. Since the lateral inhibition has a specific range, it should be possible to vary its contribution to brightness discrimination by separating the comparison fields in the test stimulus. The experiment described in § 6 was designed to test this hypothesis and at the same time to isolate the purely spatial factors involved, by eliminating retinal image movement. The decline of discrimination with separation of the comparison fields (figure 6) is in accordance with this physiological hypothesis. It suggests that brightness discrimination is based in part upon a 'comparison signal' generated by lateral inhibition, perhaps in the way suggested by Barlow

[16]. The time-dependence of the discrimination in this condition (figure 7) could arise (in terms of this hypothesis) from more complex temporal effects within receptive fields.

The experiments discussed in this paper underline the importance of the conditions of fixation in vision. The implication for experiments on visual discrimination is that consistent results can only be expected when reproducible patterns of fixation (or non-fixation) are used. This is essentially the conclusion reached by Thomson and Wright [17] in their experiments on foveal tritanopia. It seems indeed to have been recognized implicitly in the wide-spread use of 'glance' methods of colour matching and also the forced-choice short-exposure methods of measuring thresholds. The implication of an extension of these findings to colour vision has been borne out by some experiments by the author, to be reported elsewhere.

Further experiments on discrimination using controlled conditions of retinal image movement and continued research into the electro-physiological activity of the vertebrate retina, may be expected to establish the nature of the underlying nervous organization which gives rise to these effects.

ACKNOWLEDGMENTS

I would like to thank Professor R. W. Ditchburn for his advice and encouragement in this study, and the Director of the National Physical Laboratory for permission to publish this paper. I am grateful for many valuable discussions with Dr. D. H. Fender and Dr. Stella Mayne who, together with Dr. R. M. Pritchard, acted as subjects. The experimental work was supported by a research grant No. B-1233 from the Department of Health, Education and Welfare, Public Health Service, U.S.A.

Résultat d'une étude, à l'aide de l'image rétinienne stabilisée, de la discrimination d'une différence de luminances entre les deux moitiés d'un champ de vision. On montre qu'il y a une corrélation simple entre l'amplitude du mouvement de l'image rétinienne et le niveau de discrimination visuelle mesuré par une méthode de moyenne dans le temps. En absence de tout mouvement de l'image rétinienne, la séparation des stimuli de comparaison détériore la discrimination. Ces phénomènes sont discutés à la lumière d'études électrophysiologiques récentes de l'oeil des mammifères.

Das Unterscheidungsvermögen für den Helligkeitsunterschied zwischen den Segmenten eines zweiteiligen Feldes wurde mit Hilfe des stabilisierten Netzhautbildes untersucht. Es besteht eine einfache Beziehung zwischen der Bewegungsamplitude des Netzhautbildes und der visuellen Unterschiedshöhe, die durch eine Zeitmittelung gemessen wird. Beim Fehlen der Bewegung des retinalen Bildes erschwert die Trennung der Vergleichsreize die Unterscheidbarkeit. Diese Erscheinungen werden auf der Grundlage der neuen elektrophysiologischen Untersuchungen am Säugetierauge diskutiert.

REFERENCES

- [1] LORD, M. P., and WRIGHT, W. D., 1950, *Rep. Progr. Phys.*, **13**, 1.
- [2] RATLIFF, F., and RIGGS, L. A., 1950, *J. exp. Psychol.*, **40**, 687.
- [3] DITCHBURN, R. W., and GINSBORG, B. L., 1953, *J. Physiol.*, **119**, 1.
- [4] DITCHBURN, R. W., and GINSBORG, B. L., 1952, *Nature, Lond.*, **170**, 36.
- [5] FENDER, D. H., 1956, *Ph.D. Thesis*, Reading.
- [6] KRAUSKOPF, J., 1956, *J. opt. Soc. Amer.*, **47**, 740.

- [7] DITCHBURN, R. W., and FENDER, D. H., 1955, *Opt. Acta*, **2**, 128.
- [8] CLOWES, M. B., and DITCHBURN, R. W., 1959, *Opt. Acta*, **6**, 252.
- [9] DOESCHATE, J. TEN, 1954, *Ophthalmologica*, **127**, 65.
- [10] HARTLINE, H. K., 1940, *J. opt. Soc. Amer.*, **30**, 239.
- [11] DITCHBURN, R. W., 1955, *Opt. Acta*, **4**, 171.
- [12] ECCLES, J. C., 1953, *The Neurophysiological Basis of Mind* (Oxford: University Press).
- [13] KUFFLER, S. W., 1953, *J. Neurophysiol.*, **16**, 37.
- [14] HUBEL, D. H., 1959, *J. Physiol.*, **147**, 226.
- [15] BARLOW, H. B., FITZHUGH, R., and KUFFLER, S. W., 1957, *J. Physiol.*, **137**, 338.
- [16] BARLOW, H. B., 1959, *Mechanisation of Thought Processes*, **2**, 535 (London: H.M.S.O.).
- [17] THOMSON, L. C., and WRIGHT, W. D., 1947, *J. Physiol.*, **105**, 316.
- [18] BARLOW, H. B., 1953, *J. Physiol.*, **119**, 69.
- [19] LETTVIN, J. Y., MATURANA, H. R., McCULLOCH, W. S., and PITTS, W. H., 1959, *Proc. Instn. elect. Engrs*, **47**, 1940.



Diffraction of partially coherent light by a plane aperture

by GEORGE B. PARRENT, Jr. and THOMAS J. SKINNER

Electromagnetic Radiation Laboratory,
Air Force Cambridge Research Centre,
United States Air Force, Bedford, Massachusetts

(Received 18 July 1960)

Using the formulation of coherence theory as introduced by Wolf, the diffraction of partially coherent light is discussed. The mutual coherence function and the intensity distribution are computed for a plane slit illuminated by coherent, partially coherent and incoherent light. The results are plotted and discussed.

1. INTRODUCTION

Although considerable effort has been devoted to the study and development of coherence theory [1-6]. The question of what the diffraction pattern looks like for a system utilizing partially coherent light has not been adequately discussed. Furthermore, we find that in a strictly rigorous interpretation, both coherence and incoherence are unrealizable idealizations [6]. Thus, the determination of the diffraction pattern under the conditions considered here is of considerable practical importance. In the general formulation of coherence theory due to Wolf [7], it is found that in free space the mutual coherence function is propagated according to two wave equations; and these wave equations, of course, form the basis for the determination of the diffraction pattern. But, while these equations and their formal solutions [8] have proven very useful for further development of the theory, they have not been used as yet to solve the diffraction problem.

It is the purpose of this paper to determine the diffraction pattern of a slit illuminated by a partially coherent wave and it is hoped that, as with other developments in optical theory, the solution to this one-dimensional problem may, in addition to being interesting in its own right, provide some insight into the solution of the more general problems.

2. REVIEW OF THE GENERAL FORMALISM

The formulation of coherence theory as introduced by Wolf will be used exclusively in this paper. For the reader who may not be familiar with this general theory, a very cursory review of the principle definitions and pertinent theorems will be given here. For a more detailed discussion of the theory, one

should refer to the developmental papers [4, 6, 7, 8]. The fundamental entity in the theory is the mutual coherence function $\Gamma(\mathbf{x}_1, \mathbf{x}_2, \tau)$, which is defined as the complex† cross correlation of the disturbance, $V_1(t)$, at \mathbf{x}_1 , with the complex conjugate of the disturbance, $V_2^*(t)$, at \mathbf{x}_2 , i.e.

$$\Gamma(\mathbf{x}_1, \mathbf{x}_2, \tau) \equiv \Gamma_{12}(\tau) = \langle V_1(t + \tau) V_2^*(t) \rangle, \quad (1)$$

where the sharp brackets denote time average. The zero ordinate of the mutual coherence function, $\Gamma(\mathbf{x}_1, \mathbf{x}_2, 0)$, is termed the mutual intensity function; and the complex degree of coherence $\gamma_{12}(\tau)$ is defined as the mutual coherence function normalized by the square root of the product of the intensities at \mathbf{x}_1 and \mathbf{x}_2 , i.e.

$$\gamma_{12}(\tau) = \frac{\Gamma(\mathbf{x}_1, \mathbf{x}_2, \tau)}{\sqrt{[\Gamma_{11}(0)\Gamma_{22}(0)]}}. \quad (2)$$

By appealing to the Schwartz inequality, it may be shown that the modulus of $\gamma_{12}(\tau)$ is bounded by zero and one; and these extremes characterize incoherence and coherence, respectively.

One of the interesting features of the formulation is that in free space the mutual coherence is propagated according to the two wave equations:

$$\nabla_s^2 \Gamma_{12}(\tau) = \frac{1}{c^2} \frac{\partial^2 \Gamma_{12}(\tau)}{\partial \tau^2} \quad (s=1, 2). \quad (3)$$

Here the symbol ∇_s^2 denotes the Laplacian operator in the coordinates of \mathbf{x}_s ($s=1, 2$).

For diffraction by a plane aperture, it was shown by successive application of Green's theorem [6] that the mutual coherence function in the diffracted field is given by

$$\Gamma(\mathbf{x}_1, \mathbf{x}_2, \tau) = \frac{1}{(2\pi)^2} \iint \frac{\cos \theta_1 \cos \theta_2}{r_1 r_2} \Omega(r_1, r_2, \tau) \Gamma\left(S_1, S_2, \tau - \frac{r_1 - r_2}{c}\right) d\mathbf{s}_1 d\mathbf{s}_2 \quad (4)$$

where $\cos \theta_s = z/r_s$, z is the distance from the plane of the source to the plane of the diffracted pattern, \mathbf{S}_s are points in the diffracting aperture; \mathbf{x}_s are field points; r_s is the distance from \mathbf{x}_s to \mathbf{s}_s ; the integration is over the diffracting plane and Ω is the differential operator

$$\Omega = 1 + \frac{r_1 - r_2}{c} \frac{\partial}{\partial \tau} - \frac{r_1 r_2}{c^2} \frac{\partial^2}{\partial \tau^2}. \quad (5)$$

While the theory introduced by Wolf is completely general, we shall limit our attention to quasi-monochromatic fields. By quasi-monochromatic field we mean a field whose spectral width, $\Delta\nu$, is very much less than its mean frequency, $\bar{\nu}$, ($\Delta\nu \ll 1/\bar{\nu}$). This approximation allows us to ignore variations with frequency (evaluating all frequency dependent factors at the mean frequency) and to work with the mutual intensity function, $\Gamma_{12}(0)$, instead of the mutual coherence function. This approximation also limits the validity of the development to phenomenon involving path differences small compared to $c/\Delta\nu$. However, many problems of practical interest in both visible and micro-wave optics are covered by this approximation. When the quasi-monochromatic

† While the optical field is a real quantity, it proved to be convenient to formulate the theory in terms of carefully defined complex functions [7]. Thus the complex disturbance refers to the 'analytic signal' associated with the real field quantity.

approximation is imposed on (4), we obtain for the mutual intensity function in the field [6]

$$\Gamma(\mathbf{x}_1, \mathbf{x}_2, 0) = \frac{1}{(2\pi)^2} \iint (1 - i\bar{k}r_1)(1 + i\bar{k}r_2) \cos \theta_1 \cos \theta_2 \frac{\exp[i\bar{k}(r_1 - r_2)]}{r_1 r_2} \times \Gamma(\mathbf{S}_1, \mathbf{S}_2, 0) dS_1 dS_2 \quad (|\tau| \ll 1/\Delta\nu) \quad (6)$$

where $\bar{k} = 2\pi\nu/c$ is the mean wave number.

To conclude this brief review, we state two theorems (see Parrent [8]) concerning the coherent and incoherent limits of the mutual intensity function.

Theorem I. In the quasi-monochromatic approximation a coherent field is completely characterized by a complex wave function U which depends on the coordinate of one point only, and in terms of it the mutual intensity function is given by

$$\Gamma(\mathbf{x}_1, \mathbf{x}_2, 0) = U(\mathbf{x}_1)U^*(\mathbf{x}_2), \quad (7)$$

where U is a solution of the Helmholtz equation.

Theorem II. An incoherent quasi-monochromatic field cannot exist in free space. However, it is possible to define an incoherent *source* in such a manner as to be consistent with this theorem.

Before considering the general problem of the diffraction of partially coherent light, it will prove worthwhile in the interest of continuity of latter arguments to digress briefly and consider the singular case of incoherent illumination. Thus, §3 will treat this problem and in §4 we return to the general case.

3. THE FRAUNHOFER INTENSITY PATTERN OF A PLANE INCOHERENT QUASI-MONOCROMATIC SOURCE

As mentioned earlier, it may be shown that an incoherent *field* cannot exist in free space (Parrent [8]), although it is possible to *define* an incoherent source in such a manner as to be consistent with this result. While this definition gives consistent results for the diffraction and propagation problem, it is unsatisfactory in the sense that it destroys one of the properties of the mutual coherence function.

To illustrate this point, we recall from §2 that the mutual coherence function, $\Gamma_{12}(\tau)$, is defined by the relation

$$\Gamma_{12}(\tau) = \langle V_1(t+\tau)V_2^*(t) \rangle. \quad (8)$$

Setting $\mathbf{x}_1 = \mathbf{x}_2$ we obtain the self-coherence function $\Gamma_{11}(\tau)$ as

$$\Gamma_{11}(\tau) = \langle V_1(t+\tau)V_1^*(t) \rangle; \quad (9)$$

or evaluated at $\tau = 0$

$$\Gamma_{11}(0) = \langle V_1(t)V_1^*(t) \rangle = I(\mathbf{x}_1), \quad (10)$$

where $I(\mathbf{x}_1)$ is the intensity at \mathbf{x}_1 . Thus, an important property of the mutual coherence function is that when the two points coincide $\Gamma_{12}(0)$ collapses to the intensity. However, in order to obtain consistent results for the diffraction and propagation problems, it is necessary (following Blanc-Lappierre and Dumontet) to define an incoherent source as *a source for which the mutual coherence function for all pairs of points contained in the source is of the form*

$$\Gamma_{12}(\tau) = AI(\mathbf{x}_1, \tau)\delta(\mathbf{x}_1 - \mathbf{x}_2), \quad (11)$$

where A is the area of the source, I is the self coherence and δ is the Dirac delta function.

It is clear from (11) that $\Gamma_{11}(0)$ cannot represent the intensity for an incoherent source. Rather, for this singular case, the mutual coherence function must be interpreted as a density function, i.e. for incoherent sources

$$I(\mathbf{x}_1, \tau) = \frac{1}{A} \int_{\text{source}} \Gamma(\mathbf{x}_1, \mathbf{x}_2, \tau) d\mathbf{x}_2. \quad (12)$$

With these singularities in mind, we may now direct our attention to the determination of the diffraction pattern for incoherent light.

Indicating by \mathbf{S}_1 and \mathbf{S}_2 the vector positions of two typical points in the source plane, we can, in light of the foregoing discussion, describe an incoherent source by a mutual coherence function of the form.

$$\Gamma(\mathbf{S}_1, \mathbf{S}_2, \tau) = AI(\mathbf{S}_1, \tau) \delta(\mathbf{S}_1 - \mathbf{S}_2). \quad (13)$$

As stated in the introduction, we shall limit our attention to quasi-monochromatic fields. In this case [9] the mutual coherence function is of the form

$$\Gamma_{12}(\tau) \simeq \Gamma_{12}(0) \exp(-2\pi i \bar{\nu} \tau), \quad (|\tau| \ll 1/\Delta\nu); \quad (14)$$

thus combining (13) and (14), an incoherent quasi-monochromatic source is described by

$$\Gamma(\mathbf{S}_1, \mathbf{S}_2, \tau) \simeq AI(\mathbf{S}_1) \exp(-2\pi i \bar{\nu} \tau) \delta(\mathbf{S}_1 - \mathbf{S}_2), \quad (|\tau| \ll 1/\Delta\nu). \quad (15)$$

We note further that substituting from (14) into (3), the wave equations reduce to the two Helmholtz equations

$$[\nabla_s^2 + k^2] \Gamma_{12}(0) = 0, \quad (s = 1, 2), \quad (|\tau| \ll 1/\Delta\nu). \quad (16)$$

Hence the total solution is given by the solution to (16) with the boundary condition

$$\Gamma(\mathbf{S}_1, \mathbf{S}_2, 0) = AI(\mathbf{S}_1) \delta(\mathbf{S}_1 - \mathbf{S}_2), \quad (|\tau| \ll 1/\Delta\nu). \quad (17)$$

Substituting from (17) into the general solution, (6), we obtain

$$\begin{aligned} \Gamma(\mathbf{x}_1, \mathbf{x}_2, 0) = & \frac{A}{(2\pi)^2} \iint (1 - i\bar{k}r_1)(1 + i\bar{k}r_2) \cos \theta_1 \cos \theta_2 \frac{\exp[i\bar{k}(r_1 - r_2)]}{r_1 r_2} \\ & \times I(\mathbf{S}_1, 0) \delta(\mathbf{S}_1 - \mathbf{S}_2) d\mathbf{S}_1 d\mathbf{S}_2, \quad (|\tau| \ll 1/\Delta\nu). \end{aligned} \quad (18)$$

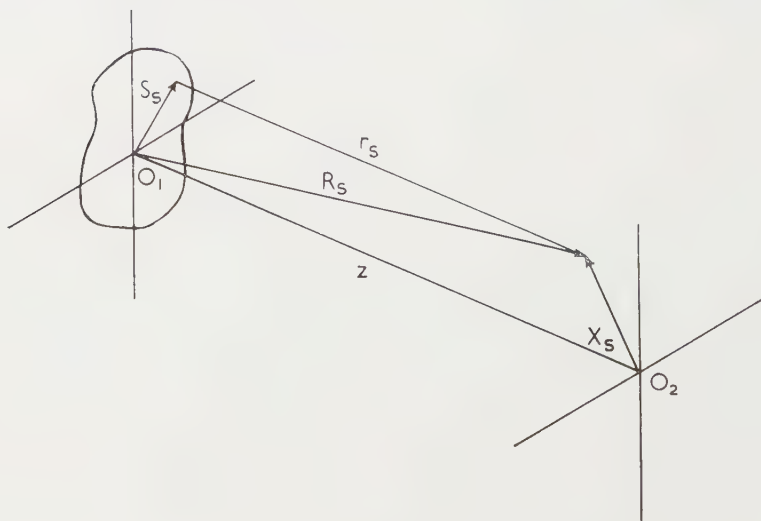


Figure 1.

To make the integral in (18) tractable, we introduce the approximation that the distances from the source points, \mathbf{S} , to the field points, \mathbf{x} , all be large compared to the maximum dimension of the source. To specifically utilize this approximation, consider the geometry illustrated in figure 1.

Let O_1 be a point on the source; z is the distance from O_1 , perpendicular to the source, to the field point O_2 ; \mathbf{S}_s and \mathbf{x}_s are the source and field position vector from O_1 and O_2 respectively; \mathbf{r}_s is the vector from the source point to the corresponding field point; and \mathbf{R}_s is the vector from the origin, O_1 , of the source to field point \mathbf{x}_s . Now

$$\mathbf{r}_s = \mathbf{z} + \mathbf{x}_s - \mathbf{S}_s, \quad (s=1, 2) \quad (19)$$

and squaring both sides of (19) we get

$$r_s^2 = R_s^2 + S_s^2 - 2\mathbf{S}_s \cdot \mathbf{x}_s, \quad (s=1, 2). \quad (20)$$

So, to a first-order approximation, $R_s = r_s$. This approximation is very good everywhere in the integral of (18) except in the argument of the exponential where we must evaluate $(r_1 - r_2)$ to second order. We have to second order from (20):

$$r_s = R_s \left(1 + \frac{S_s^2 - 2\mathbf{S}_s \cdot \mathbf{x}_s}{2R_s^2} \right), \quad (s=1, 2); \quad (21)$$

and therefore $(r_1 - r_2)$ becomes

$$r_1 - r_2 = (R_1 - R_2) + \left(\frac{S_1^2}{2R_1^2} - \frac{S_2^2}{2R_2^2} \right) + \frac{\mathbf{S}_2 \cdot \mathbf{x}_2}{R_2^2} - \frac{\mathbf{S}_1 \cdot \mathbf{x}_1}{R_1^2}. \quad (22)$$

Using these approximations, (18) becomes

$$\begin{aligned} \Gamma(\mathbf{x}_1, \mathbf{x}_2, 0) &= \frac{A}{(2\pi)^2} \frac{(1 - i\bar{k}R_1)(1 + i\bar{k}R_2)}{R_1 R_2} \exp[i\bar{k}(R_1 - R_2)] \cos\theta_1 \cos\theta_2 \\ &\times \int I\mathbf{S}_2 \exp \left\{ i\bar{k} \left[\frac{S_2^2}{2} \left(\frac{1}{R_1^2} - \frac{1}{R_2^2} \right) + \frac{S_2 \cdot \mathbf{x}_2}{R_2^2} - \frac{S_2 \cdot \mathbf{x}_1}{R_1^2} \right] \right\} d\mathbf{S}_2 \end{aligned} \quad (23)$$

It is clear by inspection that (23) is of the form

$$\Gamma(\mathbf{x}_1, \mathbf{x}_2, 0) = \text{constant} \times \cos\theta_1 \cos\theta_2 f(\mathbf{x}_1, \mathbf{x}_2) \quad (24)$$

where $f(\mathbf{x}_1, \mathbf{x}_2)$ is a function of the coordinate difference only, i.e.,

$$f(\mathbf{x}_1, \mathbf{x}_2) = f(x_1 - x_2, y_1 - y_2, z_1 - z_2). \quad (25)$$

To obtain the intensity distribution, it is necessary only to set $\mathbf{x}_1 = \mathbf{x}_2$ in (24); thus

$$I(\mathbf{x}) = \text{constant} \times \cos^2\theta, \quad (26)$$

since $f(\mathbf{x}_1, \mathbf{x}_2)$ is by virtue of (25) a constant when $\mathbf{x}_1 = \mathbf{x}_2$. However, (26) will be recognized as the intensity distribution of a Lambertian source. Thus, the following theorem has been proven: *At sufficiently large distances from a source large compared with the wavelength ($R \gg$ maximum dimension of the aperture) the intensity pattern of a plane incoherent source is Lambertian, independent of the source geometry.*

4. THE MUTUAL INTENSITY IN A FIELD ILLUMINATED BY A PARTIALLY COHERENT SLIT

Returning now to the more general problem of partial coherence, we have to choose a mutual intensity function. Since we are interested in trends and

not particular solutions, we shall introduce at this point certain simplifying constraints:

- (1) We assume the mutual intensity on the source to be a function of the difference $|\mathbf{S}_1 - \mathbf{S}_2|$ only.
- (2) We assume uniform illumination, i.e. $I(\mathbf{S}) = \text{constant}$.
- (3) We assume that mutual intensity function to be of the form

$$\Gamma_{12}(0) = A_{12} \exp\left(\frac{-|\mathbf{S}_1 - \mathbf{S}_2|}{\alpha}\right). \quad (27)$$

Here α is a constant termed the correlation interval.

As can be seen by examining the general solution of the propagation or diffraction problem, the first assumption covers a large class of physically interesting phenomena (see Parrent [8]). The second assumption is introduced to simplify the integration. The third assumption cannot be justified in general. However, in light of experimental evidence in the field of scatter communication an exponential correlation appears reasonable, and this particular form is easy to work with.

Using this restriction the mutual intensity distribution for a partially coherent source becomes

$$\Gamma_{12}(0) = \Gamma(\mathbf{S}_1, \mathbf{S}_2, 0) = I \exp\left(\frac{-|\mathbf{S}_1 - \mathbf{S}_2|}{\alpha}\right). \quad (28)$$

In (27) \mathbf{S}_1 and \mathbf{S}_2 are vector positions of points on the source; I is the constant intensity; and α is the coherence interval. The degree of coherence for points in the source is clearly

$$\gamma_{12}(0) = \exp\left(\frac{-|\mathbf{S}_1 - \mathbf{S}_2|}{\alpha}\right). \quad (29)$$

Clearly as $\alpha \rightarrow \infty$, the complex degree of coherence becomes identically equal to unity, i.e. as the coherence interval becomes infinite we obtain a coherent source. However, the mutual intensity function as given by (27) does not go over in a continuous way to the mutual intensity of an incoherent source; but this is not surprising in light of the singular nature of the incoherent source.

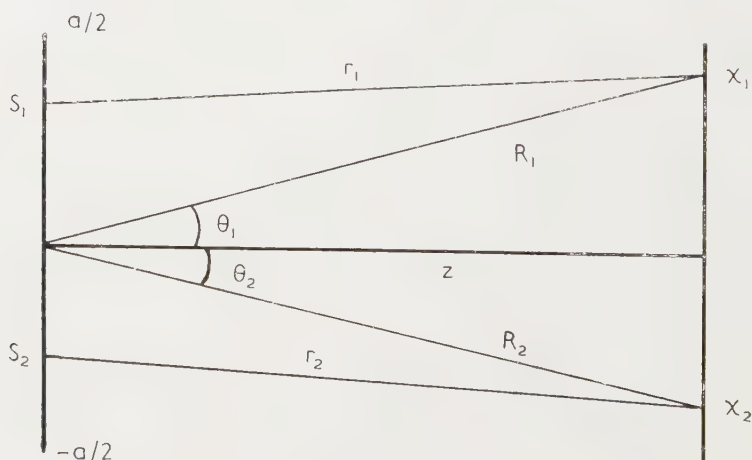


Figure 2.

We now consider a plane slit of width a (see figure 2) illuminated by quasi-monochromatic partially coherent light, such that over the slit the mutual intensity function is given by (27).

To find the diffraction pattern of the slit we have only to insert the form of the mutual intensity function over the source into (6). Doing this and also making the usual far field approximations (the same approximations as used in §2, plus the requirement that $\pi a^2/\lambda \ll R_s$ we get for the mutual intensity function in the far field

$$\Gamma_{12}(0) = \Gamma(\mu_1, \mu_2, 0) = c_{12} \int_{-a/2}^{a/2} \int_{-a/2}^{a/2} \exp\left(\frac{-|\mathbf{S}_1 - \mathbf{S}_2|}{\alpha}\right) \times \exp[i\bar{k}(\mu_2 S_2 - \mu_1 S_1)] dS dS_2, \quad (30)$$

$$\text{where} \quad c_{12} = I\bar{k}^2 \cos \theta_1 \cos \theta_2 \exp[i\bar{k}(R_1 - R_2)] \quad (31)$$

$$\text{and} \quad \mu_s = \frac{x_s}{R_s} = \sin \theta_s, \quad (s=1, 2). \quad (32)$$

The absolute value can be removed from the integrand of (30) by breaking the range of integration into two parts, one with $S_1 \geq S_2$ and one with $S_1 \leq S_2$. This yields for the mutual intensity function

$$\begin{aligned} \Gamma_{12}(0) = & c_{12} \int_{-a/2}^{a/2} \int_{-a/2}^{S_1} \exp\left[-\left(\frac{1}{\alpha} + i\bar{k}\mu_1\right)S_1\right] \exp\left[\left(\frac{1}{\alpha} + i\bar{k}\mu_2\right)S_2\right] dS_2 dS_1 \\ & + c_{12} \int_{-a/2}^{a/2} \int_{S_1}^{a/2} \exp\left[\left(\frac{1}{\alpha} - i\bar{k}\mu_1\right)S_1\right] \exp\left[-\left(\frac{1}{\alpha} - i\bar{k}\mu_2\right)S_2\right] dS_2 dS_1. \end{aligned} \quad (33)$$

Evaluating the integrals of (33) by straightforward but lengthy procedures we obtain

$$\begin{aligned} \Gamma_{12}(0) = & \frac{c_{12}}{(1/\alpha^2 + \bar{k}^2\mu_1^2)(1/\alpha^2 + \bar{k}^2\mu_2^2)} \left\{ \frac{a^2[1 + \exp(-a/\alpha)]}{2} \left(\bar{k}^2\mu_1\mu_2 - \frac{1}{\alpha^2} \right) \right. \\ & \times \bar{k}^2\mu_1\mu_2 \operatorname{sinc} \frac{\bar{k}\mu_1 a}{2} \operatorname{sinc} \frac{\bar{k}\mu_2 a}{2} \\ & + \frac{[2/\alpha^2 + \bar{k}^2(\mu_1^2 + \mu_2^2)]}{\alpha} a \operatorname{sinc} \frac{\bar{k}(\mu_2 - \mu_1)a}{2} \\ & - \exp(-a/\alpha) a \bar{k}^2(\mu_1 + \mu_2)^2 \operatorname{sinc} \frac{\bar{k}(\mu_1 + \mu_2)a}{2} \\ & \left. + 2[\exp(-a/\alpha) - 1] \left(\frac{1}{\alpha^2} - \bar{k}^2\mu_1\mu_2 \right) \cos \frac{\bar{k}\mu_1 a}{2} \cos \frac{\bar{k}\mu_2 a}{2} \right\}. \end{aligned} \quad (34)$$

To investigate the significance of the various terms in (34) we first examine the coherent limit. As shown in the foregoing, the coherent limit for the source is obtained by letting α go to infinity. If α is allowed to go to infinity in (34), we obtain for the far field mutual intensity function due to a coherently illuminated slit the following expression

$$\Gamma_{12}(0) = C_{12} a^2 \operatorname{sinc} \frac{\bar{k}\mu_1 a}{2} \operatorname{sinc} \frac{\bar{k}\mu_2 a}{2}. \quad (35)$$

We first note that the mutual intensity function is of the form predicted by Theorem I of §1; that is, it is characterized by a wave function which depends upon the coordinate of one point only, and is of the form $U(x_1)U(x_2)$, where $U(x_s) = a\bar{k}\sqrt{I} \cos \theta_s \sin \bar{k}\mu_s a/2$. If we let $\mu_1 = \mu_2 = \mu$ in (35), we get the far field intensity distribution of a coherently illuminated slit. That is

$$I(\mu) = a^2 \bar{k}^2 \cos^2 \theta \operatorname{sinc}^2 \frac{\bar{k}\mu a}{2}; \quad (36)$$

which is just the well known result for coherent illumination. Since (35) comes from just the first term of (34), we may associate this first term with the coherent contribution to the partially coherent field.

Since the form of the mutual intensity function chosen for the slit does not go continuously to an incoherent limit, we cannot take an incoherent limit of (34), but we can find the far field mutual intensity function of an incoherently illuminated slit and compare it with (34). If we put the incoherent mutual intensity function as defined by (11), into (6) for the field mutual intensity function and use the same geometry and approximations as used above in the derivation of the mutual intensity we obtain

$$\Gamma_{12}(0) = ac_{12} \int_{-a/2}^{a/2} \int_{-a/2}^{a/2} \delta(S_1 - S_2) \exp[ik(\mu_2 S_2 - \mu_1 S_1)] dS_1 dS_2, \quad (37)$$

where all quantities are as previously defined. Evaluation of this integral is straightforward and yields

$$\Gamma_{12}(0) = ac_{12} \text{sinc} \frac{\bar{k}(\mu_2 - \mu_1)a}{2}. \quad (38)$$

Since (38), the mutual intensity function due to an incoherent source, is of the form of the second term of (34), we may associate the second term of (34) with the incoherent contribution to the partially coherent field. In passing, we also note that the complex degree of coherence (as defined by (2)) of the far field produced by an incoherent slit is given by

$$\gamma_{12}(0) = \text{sinc} \frac{\bar{k}(\mu_2 - \mu_1)a}{2}. \quad (39)$$

Equation (39) illustrates Theorem II of §2; that an incoherent source gives rise to a partially coherent field.

By considering the coherent and incoherent limits, we see that the far field mutual intensity function due to a partially coherent slit contains a coherent term, an incoherent term and two mixed terms. This agrees with the intuitive notion of a mixing of coherent and incoherent light. However, (34) is still difficult to interpret in terms of the intensity distribution. To gain a better understanding of the effect of partial coherence on this distribution we now examine the intensity pattern.

5. FAR FIELD INTENSITY PATTERN OF A SLIT ILLUMINATED BY PARTIALLY COHERENT QUASI-MONOCROMATIC LIGHT

To obtain the far field intensity pattern of the slit, we have only to let $\mu_1 = \mu_2 = \mu$ in the expression for the far field mutual intensity function; thus we obtain

$$\begin{aligned} I(\mu) = & \frac{c}{(1/\alpha^2 + \bar{k}^2 \mu^2)^2} \left\{ \frac{a^2 [1 + \exp(-a/\alpha)]}{2} \left(\bar{k}^2 \mu^2 - \frac{1}{\alpha^2} \right) \bar{k}^2 \mu^2 \text{sinc}^2 \frac{\bar{k} a \mu}{2} \right. \\ & + \frac{2(1/\alpha^2 + \bar{k}^2 \mu^2)a}{\alpha} \\ & + 2[\exp(-a/\alpha) - 1] \left(\frac{1}{\alpha^2} - \bar{k}^2 \mu^2 \right) \cos^2 \frac{\bar{k} a \mu}{2} \\ & \left. - 4 \exp(-a/\alpha) \frac{a \bar{k}^2 \mu^2}{\alpha} \text{sinc} \bar{k} a \mu \right\}, \end{aligned} \quad (40)$$

where

$$c = I \bar{k}^2 \cos^2 \theta. \quad (41)$$

To facilitate the interpretation of (40), we now limit our attention to slits where $a/\lambda \gg 1$. In this case we know the first few fringes all occur within a small angle, θ , about the z axis. So within this limitation, we can set $\cos \theta = 1$ and $\mu = \sin \theta = \theta$. Introducing this limitation along with the change of variable $y = ka\mu = ka\theta$ into (40), we obtain for the intensity pattern of the slit

$$\begin{aligned}
 I(y) = \frac{1}{(a^2/\alpha^2 + y^2)^2} & \left[\left(\frac{1 + \exp(-a/\alpha)}{2} \right) \left(y^2 - \frac{a^2}{\alpha^2} \right) y^2 \operatorname{sinc}^2 y \right. \\
 & + \frac{a}{\alpha} \left(\frac{a^2}{\alpha^2} + y^2 \right) \\
 & + 2[\exp(-a/\alpha) - 1] \left(\frac{a^2}{\alpha^2} - y^2 \right) \cos^2 \frac{y}{2} \\
 & \left. - 4 \frac{a}{\alpha} y^2 \exp(-a/\alpha) \operatorname{sinc} y \right].
 \end{aligned} \quad (42)$$

Where we have normalized so that the intensity of the centre of the pattern is unity when $\alpha \rightarrow \infty$. This intensity pattern is plotted in figure 3.

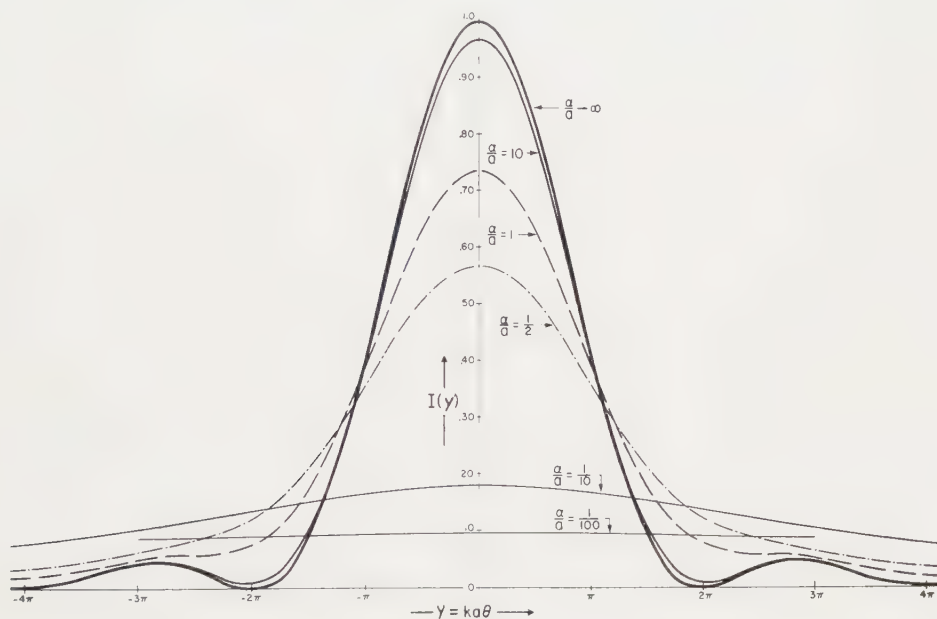


Figure 3.

By referring to this figure we see immediately the effect of partial coherence on the diffraction pattern of a slit. As we go from coherent to incoherent illumination, the intensity goes from the sinc function squared pattern of a coherent source to the cosine squared pattern of a Lambertian source. As we increase the number of coherence intervals in the aperture, the intensity of the central fringe decreases and the central fringe widens out. Also, the troughs between bright fringes are filled, so that with about one coherence interval in the aperture, the diffraction pattern consists of just one bright fringe falling off monotonically.

On discute la diffraction de la lumière partiellement cohérente en utilisant l'expression de la théorie de la cohérence introduite par Wolf. On calcule la fonction de cohérence mutuelle et la distribution d'intensité pour une fente plane éclairée en lumière cohérente, partiellement cohérente et incohérente. Les résultats sont représentés sur des graphiques et discutés.

Unter Benutzung der Formeln, die Wolf in die Kohärenztheorie eingeführt hat, wird die Beugung von partiell kohärentem Licht behandelt. Es werden die Kohärenzfunktion und die Intensitätsverteilung für einen ebenen Spalt berechnet, wenn er mit kohärentem, mit partiell kohärentem und mit inkohärentem Licht beleuchtet wird. Die graphisch aufgetragenen Ergebnisse werden diskutiert.

REFERENCES

- [1] VAN CITTERT, P. H., 1934, *Physica*, **1**, 201; 1939, *Ibid.*, **5**, 1129.
- [2] ZERNICKE, F., 1938, *Physica*, **5**, 785.
- [3] HOPKINS, H. H., 1951, *Proc. roy. Soc. A*, **208**, 263.
- [4] WOLF, E., 1954, *Proc. roy. Soc. A*, **225**, 96.
- [5] BLANC-LAPIERRE, A., and DUMONTET, P. M., 1954, *C. R. Acad. Sci., Paris*, **238**, 1005.
- [6] PARRENT, G. B., 1959, *J. opt. Soc. Amer.*, **49**, 787.
- [7] WOLF, E., 1955, *Proc. roy. Soc. A*, **230**, 246.
- [8] PARRENT, G. B., 1959, *Opt. Acta*, **6**, 285.
- [9] BORN, M., and WOLF, E., 1959, *Principles of Optics* (London: Pergamon Press), Chap. 10.

Nachtrag zu der Arbeit *Nachweis für die Überschreitbarkeit der von den Sampling-Expansion-Theoremen postulierten Informationsschranken* (1960, *Opt. Acta*, **7**, 53).

von HANS WOLTER

Institut für angewandte Physik der Universität Marburg/Lahn

Bei vollständiger Anwendung der in der Arbeit meist benutzten Normierung des Grundgebiets auf das Intervall $\langle -1; +1 \rangle$ müssen die Gleichungen (51), (58), (59) und (60) heissen:

$$|h_k| \leq \frac{C K^k}{k!}, \quad (51)$$

$$|a_n| \leq C \sum_{k=n}^{\infty} \frac{K^k}{k!}, \quad (58)$$

$$|a_n| \leq C \frac{e^K}{n!}, \quad (59)$$

$$C e^K \sum_{n=0}^{\infty} \frac{n/2+1}{n!} (2G'')^n. \quad (60)$$

Darin ist z.B. im Falle der Gleichung (33)

$$K = 2\pi W,$$

also $K = 2\pi$ bei der Normierung $W = 1$.

Dementsprechend muss es hinter Gleichung (58) heissen: Die Reihe in Gleichung (58) rechts ist ein Rest der Mac Laurin-Reihe für e^x mit $x = K$ und nach der Taylorschen Formel kleiner als das Taylorsche Restglied e^θ mit einem $0 \leq \theta \leq K$.

Auf das Ergebnis, weitere Formeln und den Text der Arbeit hat dieser Ersatz der 1 durch die Grösse K keinen Einfluss.

Colloquium on Optical Materials

Arranged by the International Commission of Optics and the
French Committee for Optics

Paris, 5-8 July 1961

A colloquium on Optical Materials will be held in Paris during the week preceding the London Conference on Optical Instruments and Techniques. The scope of this colloquium is the study of the relations between optical properties and physical structure of materials currently used in optical instruments. Various modern techniques for studying the structure of solids (x-ray diffraction, electron diffraction, electron microscopy, etc.) have now allowed a better knowledge of physical structures and better understanding of optical properties of materials. It seems desirable to compare results obtained in various laboratories on that subject.

The programme is:

- 5 July. Synthetic crystals and polarizing materials.
- 6 July. Vitreous materials (fused silica, glass, cements, fibres, etc.).
- 7 July. Thin layers (metallic and dielectric).
- 8 July. Techniques for testing materials.

A general introduction will be given for each of the four subjects and thereafter papers will be presented in one of the three languages, English, French, or German. The time allotted will be of the order of 15 minutes or more, whenever possible. A more detailed programme will be distributed as soon as possible.

Physicists or engineers interested in this colloquium should write before 15 March to:

Professor A. Maréchal, Institut d'Optique 3,
Boulevard Pasteur, Paris 15e, France,

and indicate (1) whether they would like to give a paper and if so, the title of the paper; (2) whether they intend to take part in the visits organized on Tuesday, 4 July, to research laboratories. Registration will cost 20 NF and will begin on Monday, 3 July.

Publication

Speakers will be asked to submit a summary (about two printed pages) not later than 15 April in order that a booklet of summaries can be made available before the conference. Full publication will be possible in *Optica Acta* for the papers, complying with the general rules of that journal. It would be useful if the full text of a paper could be distributed for use during the colloquium.

The transmission and degree of polarization of quarter-wave stacks at non-normal incidence†

by PHILIP BAUMEISTER

The Institute of Optics, University of Rochester, Rochester,
New York

(Received 10 August 1960)

The transmission and degree of polarization of a quarter-wave stack of non-absorbing films deposited on a transparent substrate is expressed in terms of two variables. One variable is a function only of the refractive indices of the layers, the incident medium, and substrate; the other variable depends on the angle of incidence. Several examples show how this theory furnishes insight into the behaviour of quarter-wave stacks at non-normal incidence and can also be utilized to design beam splitters, linear polarizers, and non-reflecting coatings.

1. INTRODUCTION

In the past two decades multi-layer filters have come into extensive use as narrow-band interference filters, colour filters, non-reflecting coatings, beam splitters, and polarizers. One of the disadvantages of a multi-layer optical filter over an absorption filter is that at non-normal incidence the former usually partially polarizes both the reflected and transmitted light. This polarization effect, however, is effectively utilized when a multi-layer is used as a linear polarizer. For example, in the ultra-violet region of the spectrum below a wavelength of 1800 Å and in certain portions of the infra-red spectrum all of the transparent optical substances are optically isotropic, which means that it is not possible to construct polarizers like Nicol and Glan-Thompson prisms. Thus thin film polarizers may become more important in these spectral regions. The question then arises as to what thin film combinations are best suited for use as polarizers. Several studies have been made of thin film polarizers [1, 2, 3] but they have usually been confined to the special cases of a single layer or where the multi-layer is surrounded by the same medium.

There is some interest in developing non-reflecting coatings which are effective at non-normal incidence. Pohlack [4] has made an extensive study of the reflectance of the single-layer non-reflecting coatings at non-normal incidence. Both he and others [5] have shown that at non-normal incidence it is impossible for a single-layer dielectric coating to completely non-reflect a dielectric surface. Quite a variety of two-layer coatings have been developed which will non-reflect a dielectric surface at normal incidence [6]. The question arises as to which of these combinations would function best at non-normal incidence.

Multi-layer beam splitters have been used in certain applications and have an advantage over conventional metal coatings in that their efficiencies can approach one. Even though the average transmission of both planes of polarization of a

† An epitome of this paper was presented at the October 1957 meeting of the American Optical Society.

beam splitter may be 50 per cent, it is often very desirable that the beam splitter should also transmit equally both components of polarization—that is, it should be non-polarizing. Although some beam splitters have been developed which have very nearly a 50-50 dividing ratio, there seems to have been few investigations into the problem of controlling the degree of polarization introduced into the beams.

It is a relatively simple task to compute the transmission of a multi-layer stack. In fact, numerous computer programmes are now in existence which will compute the transmission of a given multi-layer combination at normal incidence. It is also easy to compute the transmission in each plane of polarization at a non-normal incidence by replacing the refractive index of each medium by an 'effective index' and the thickness of each layer by an 'effective thickness'. In the remainder of this paper an expression will be derived for the average transmission and degree of polarization of a quarter-wave stack at non-normal incidence. Such a theory will enable us to gain some insight into performance of quarter-wave multi-layers and also provide a means of synthesizing designs which will produce a given transmission and degree of polarization.

2. THEORY

The *match point* of a quarter-wave stack of homogeneous, non-absorbing thin films occurs when the phase of retardation $\delta_i = 2\pi\mu_i t_i \sigma_0 \cos \theta_i$ of each of the layers, is equal to $\pi/2$. μ_i , t_i and θ_i are the index of refraction, geometrical thickness, and angle of refraction in the i th layer and σ_0 is the wave number of the incident light. In the remainder of this paper, we will restrict our attention to layers which are *matched*—that is, the δ_i of each layer is $\pi/2$ at all values of θ_i . As depicted in figure 1, a beam of parallel light is incident at an angle ϕ upon the multi-layer stack from a massive incident medium of index μ_0 . The first layer of the stack is next to the substrate of index μ_s and the last of the m layers is next to the incident medium. χ is the angle of refraction in the dielectric substrate.

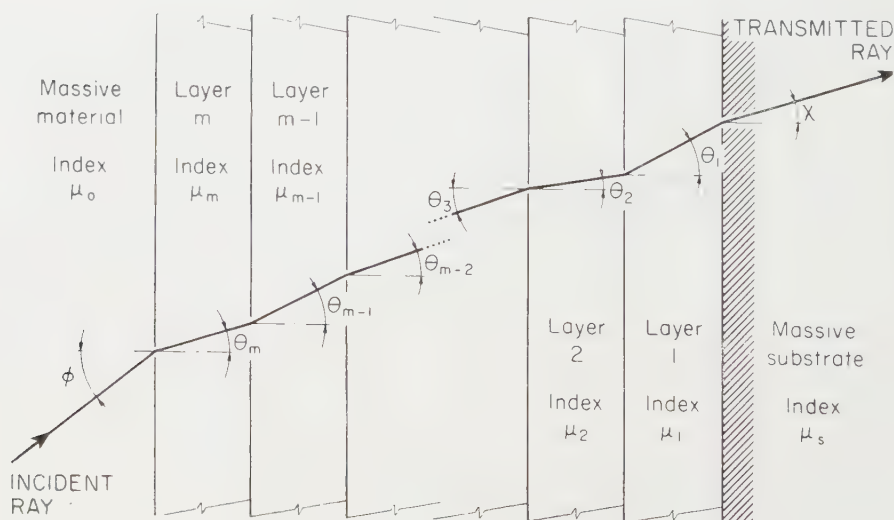


Figure 1. The path of a ray which traverses the multi-layer. For sake of clarity, the reflections which take place at each interface are not shown.

The reflectance of such a stack is calculated from the two-by-two *characteristic matrix* [7] of the stack. When $\delta_i = \pi/2$, the characteristic matrix becomes either diagonal or anti-diagonal and the formula for the reflected intensity, R , reduces to

$$R = 1 - T = 1 - \frac{4}{g_s g_0^{-1} G + g_0 g_s^{-1} G^{-1} + 2} \quad (1)$$

where

$$G = \left[\frac{g_2 g_4}{g_1 g_3} \dots \frac{g_m}{g_{m-1}} \right]^2, \quad m \text{ even},$$

$$G = \left[\frac{g_2 g_4}{g_1 g_3} \dots \frac{g_0}{g_m} \right]^2, \quad m \text{ odd}. \quad (2)$$

The quantities g_0 , g_s and g_i are defined in table 1 and depend on whether the electric vector is linearly polarized parallel (p polarization) or perpendicular (s polarization) to the plane of incidence.

Table 1. Definition of the quantities which appear in equation (2)

Symbol	Component of polarization	
	p	s
g_i	$\frac{\mu_i}{\cos \theta_i}$	$\mu_i \cos \theta_i$
g_0	$\frac{\mu_0}{\cos \phi}$	$\mu_0 \cos \phi$
g_s	$\frac{\mu_s}{\cos \chi}$	$\mu_s \cos \chi$

The variables X and Y are defined as:

$$X = \cos \chi \sec \phi (\sec \theta_1 \cos \theta_2 \sec \theta_3 \cos \theta_4 \dots \sec \theta_{m-1} \cos \theta_m)^2, \quad \text{for } m \text{ even}, \quad (3)$$

$$X = \sec \chi \sec \phi (\cos \theta_1 \sec \theta_2 \cos \theta_3 \sec \theta_4 \dots \sec \theta_{m-1} \cos \theta_m)^2, \quad \text{for } m \text{ odd},$$

$$Y = \mu_s \mu_0^{-1} (\mu_1^{-1} \mu_2 \mu_3^{-1} \mu_4 \dots \mu_{m-1}^{-1} \mu_m)^2, \quad \text{for } m \text{ even}, \quad (4)$$

$$Y = \mu_0^{-1} \mu_s^{-1} (\mu_1 \mu_2^{-1} \mu_3 \mu_4^{-1} \dots \mu_{m-1}^{-1} \mu_m)^2, \quad \text{for } m \text{ odd}.$$

The transmission T and reflectivity R in the two planes of polarization can be expressed in terms of X and Y :

$$T_p = 4/(XY^{-1} + X^{-1}Y + 2), \quad (5)$$

$$R_p = (XY^{-1} + X^{-1}Y - 2)/(XY^{-1} + X^{-1}Y + 2), \quad (6)$$

$$T_s = 4/(XY + X^{-1}Y^{-1} + 2), \quad (7)$$

$$R_s = (XY + X^{-1}Y^{-1} - 2)/(XY + X^{-1}Y^{-1} + 2). \quad (8)$$

The variables X and Y , as defined in equations (3) and (4) are always positive and greater than zero for $\phi < 90^\circ$. The quantity Y is a constant for a given multi-layer combination, whereas the variable X is one at normal incidence and depends upon the angle of incidence.

The condition that R_p should vanish is

$$X = Y, \quad (9)$$

whereas the condition that R_s should vanish is that

$$X = Y^{-1}. \quad (10)$$

For a given thin film combination in which μ_0 , μ_s , and μ_i are specified, it is always possible to find a value of the angle of incidence ϕ_p which satisfies either equation (9) or equation (10) provided that either of the following conditions is satisfied:

(1) The stack contains an odd number of layers.

(2) The incident medium and the substrate do not have the same refractive index—that is, $\mu_0 \neq \mu_s$. This angle of incidence ϕ_p which satisfies either equation (9) or equation (10) will be referred to as the *polarizing angle* and is usually the root of a polynomial in either $\cos \phi_p$ or $\sin \phi_p$, although in a few cases simpler solutions can be found.

3. AVERAGE TRANSMISSION

The average transmission T can also be conveniently expressed in terms of X and Y :

$$T = \frac{1}{2}(T_p + T_s) = (2X'Y' + 8)(X' + Y')^{-2} \quad (11)$$

where

$$X' = X + X^{-1} \quad \text{and} \quad Y' = Y + Y^{-1}.$$

It is noted that $T(X, Y)$ is unchanged if either X or Y is replaced by its reciprocal:

$$T(X, Y) = T(1/X, Y) = T(X, 1/Y) = T(1/X, 1/Y). \quad (12)$$

If we consider X' and Y' as variables and T as a parameter, equation (11) reduces to the equation of a conic section:

$$X'^2 + 2X'Y'(1 - T^{-1}) + Y'^2 = 8T^{-1}. \quad (13)$$

When T is greater than 0.5, equation (13) represents a family of ellipses of constant minor axis with their centres at the origin and inclined at 45° . The ellipses degenerate into two parallel straight lines inclined at 45° to the axes when $T = 0.5$. Equation (13) represents a family of hyperbolas when T is less than one-half. Figure 2 shows a plot of equation (13) as a function of X' and Y' for various values of the parameter T .

It is seen that when X gets large, $X' \sim X$, which means that the effect of using X and Y as variables in lieu of X' and Y' is to distort the region when X and Y' are close to one. The solid lines in figure 3 are contours of constant T as a function of the variables X and Y . Since the variables X and Y are directly computed from equations (3) and (4), figure 3 is more useful in practice than figure 2.

An interesting fact which can be seen from the figure 3 is that derivative $\partial T / \partial X$ at $X = 1$ can either be positive or negative. For example, it is seen that at $X = 1$, $Y = 2$, T decreases as X increases as Y remains constant, whereas the converse is true at $X = 1$, $Y = 6$. At the ordinate $Y_0 = 2 + \sqrt{3} = 3.73$ and $X = 1$, $\partial T / \partial X = 0$. At values of Y greater than Y_0 , T increases as X increases, attains a maximum, and then monotonically decreases. The loci of maximum of T as a function of the variables X and Y are plotted as a dotted line on figure 3 and are solutions of the equation

$$Y'^2 - X'Y' - 8 = 0. \quad (14)$$

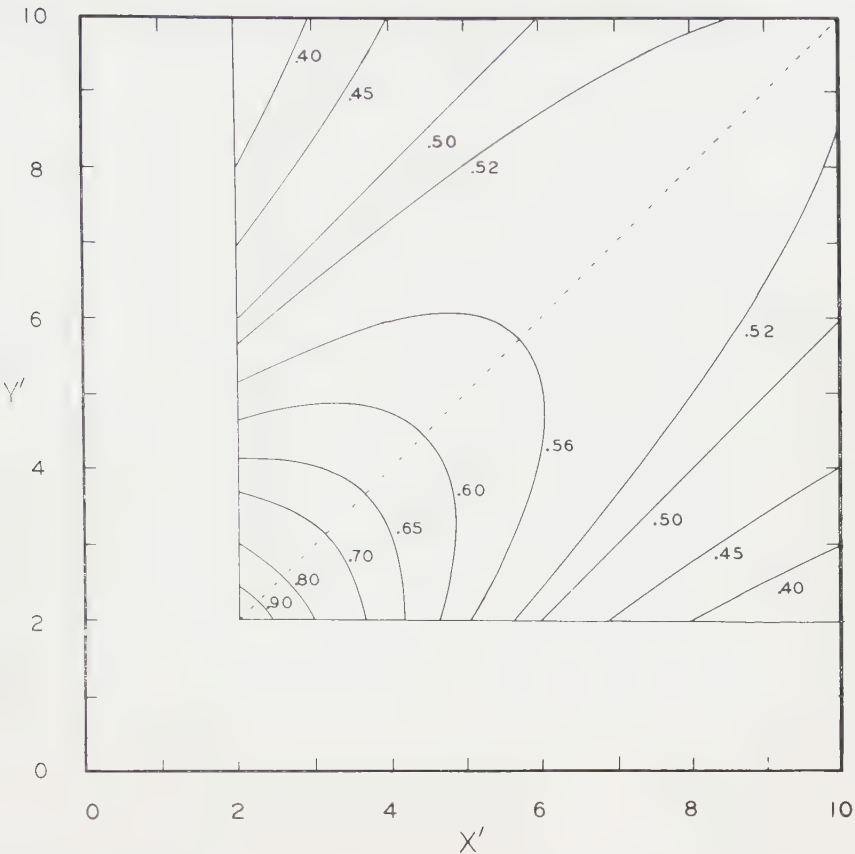


Figure 2. Contours of constant average transmission T as a function of X' and Y' .

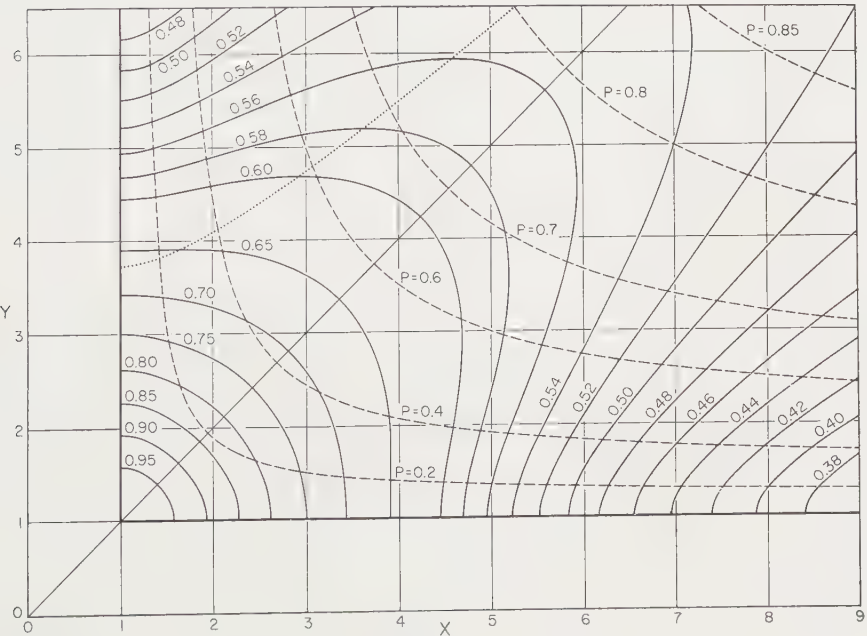


Figure 3. Contours of constant average transmission (solid lines) and degree of polarization (dashed lines) as a function of X and Y .

This fact that T attains a maximum when Y is greater than Y_0 has some practical consequences in the behaviour of quarter-wave multi-layers.

The average transmission can also be expressed in terms of the variables α and β which are defined as

$$\alpha = \ln X \quad \text{and} \quad \beta = \ln Y.$$

Then

$$T = \frac{1}{2}(\operatorname{sech}^2 \frac{1}{2}(\alpha + \beta) + \operatorname{sech}^2 \frac{1}{2}(\alpha - \beta)). \quad (15)$$

4. DEGREE OF POLARIZATION

The degree of polarization P of the transmitted light is also conveniently expressed in terms of X and Y :

$$P = \frac{T_p - T_s}{T_p + T_s} = \frac{(X^2 - 1)(Y^2 - 1)}{(X^2 + 1)(Y^2 + 1) + 4XY} = \frac{(XY + 1)^2 - (X + Y)^2}{(XY + 1)^2 + (X + Y)^2}. \quad (16)$$

A negative value of P will be taken to mean that more of the s component of polarization is transmitted than the p component. The quantity P , as defined in equation (16), is always positive for an air-dielectric interface. P is zero whenever either X or Y equals one. This fact will be used subsequently to design non-polarizing beam splitters.

If X and Y are regarded as variables and the quantity $\Delta = (1 - P)(1 + P)^{-1}$ as a parameter, lines of constant P are rectilinear hyperbolas and are shown as dashed lines in figure 3. It is seen from equation (16) that if Y remains constant as X becomes very large, the degree of polarization asymptotically approaches

$$P_{00} = (Y^2 - 1)(Y^2 + 1)^{-1}. \quad (17)$$

P has odd symmetry if X and Y are replaced by their reciprocals:

$$P(X, Y) = P(1/X, 1/Y) = -P(1/X, Y) = -P(X, 1/Y). \quad (18)$$

As a consequence of equations (10) and (18), it is only necessary to plot T and P in figure 3 for values of X and Y in the range $X \geq 1$ and $Y \geq 1$, although both X and Y as defined in equations (3) and (4) can attain fractional values. The degree of polarization can also be expressed in terms of α and β :

$$P = \sinh \alpha \sinh \beta (\cosh^2 \frac{1}{2}(\alpha + \beta) + \cosh^2 \frac{1}{2}(\alpha - \beta))^{-1}. \quad (19)$$

5. EXAMPLES

5.1. Air-dielectric interface

The simplest example is the transmission through an interface between air and a dielectric of index μ_s . Here the variables X and Y are simply $Y = \mu_s/\mu_0$ and $X = \cos \alpha \sec \phi$. Y is greater than one, provided $\mu_s > \mu_0$. The variable X is one at normal incidence and monotonically increases as the angle of incidence increases. It is easy to show that equations (5), (6), (7) and (8) reduce to the familiar Fresnel equations which appear in most textbooks on physical optics [8]. Equation (9) also reduces to the well-known relationship for Brewster's angle, $\phi_p = \arctan(\mu_s/\mu_0)$. Another interesting fact is that when the refractive index μ_s is greater than Y_0 , the dielectric plate should have a greater transmission at non-normal incidence. As shown in table 2, this effect should be observable in the infra-red at an interface between air and either germanium (refractive index 4.0) or tellurium (refractive index 5.0) although the effect is rather small and could

Table 2. Computed average transmission as a function of the angle of incidence, for an interface between air and dielectric materials of refractive index 4.0 and 5.0

Angle of incidence in degrees	Computed average transmission for refractive index	
	4.0	5.0
0	0.6400	0.5556
20	0.6400	0.5557
30	0.6402	0.5564
40	0.6407	0.5585
45	0.6412	0.5605
50	0.6417	0.5634
55	0.6421	0.5675
60	0.6420	0.5728
65	0.6404	0.5792
70	0.6343	0.5852
75	0.6167	0.5857
80	0.5684	0.5642
85	0.4323	0.4605

easily be masked by absorption. This effect, however, is very pronounced in the reflectance of radio waves from water, which has a refractive index of nearly nine [9]. Finally, we note that a single interface between air and glass of refractive index 1.50 will give a maximum degree of polarization $P_{00} = 0.385$ when X becomes very large as ϕ approaches 90° .

5.2. Multilayers

The degree of polarization P and average transmission T of multi-layers composed of quarter-waves can be found easily by calculating Y and tabulating the variable X at various angles of incidence. From these values of X and Y , T and P can be found from figure 3. Consider for example, the multi-layers whose designs are listed in table 3, in which H and L represent respectively films of quarter-wavelength optical thickness of high and low refractive index.

Figure 5 shows the average transmission T as a function of the angle of incidence ϕ for designs I and II. It is seen that as ϕ increases, the T of design I monotonically decreases, whereas for design II, T increases to a maximum and then monotonically decreases. Figure 4 shows that in both cases X increases monotonically with increasing ϕ . The fact that the T of design II attains a

Table 3. The index of refraction of each of the films of the multi-layers whose reflectance and transmission curves are shown in figures 5-11. H and L represent respectively a film of quarter-wave optical thickness of high and low refractive index

Design number	Number of layers	Design	Refractive index of					Comments
			Incident medium	Substrate	H	L	Y	
I	4	glass $LHLH$ air	1.00	1.52	1.62	1.35	3.15	Non-polarizing beam splitters at $\phi = 45^\circ$
II	8	glass $LHLHLHLH$ air	1.00	1.52	1.62	1.35	6.54	
III	3	glass LHL air	1.00	1.52	2.30	1.35	$(2.42)^{-1}$	
IV	5	glass $LHLHL$ air	1.00	1.52	2.30	1.35	$(7.03)^{-1}$	
V	2	glass HL air	1.00	1.52	4.48	1.50	$(5.828)^{-1}$	
VI	4	glass $HLHL$ air	1.00	1.52	3.13	1.82	$(5.828)^{-1}$	
VII	1	glass L air	1.00	1.52		1.35	1.199	Single-layer non-reflecting coating
VIII	3	glass LHL air	1.00	1.52	1.50	1.35	$(1.030)^{-1}$	Triple-layer non-reflecting coating
IX	5	glass $LHLHL$ air	1.00	1.52	1.50	1.35	$(1.271)^{-1}$	Five-layer non-reflecting coating

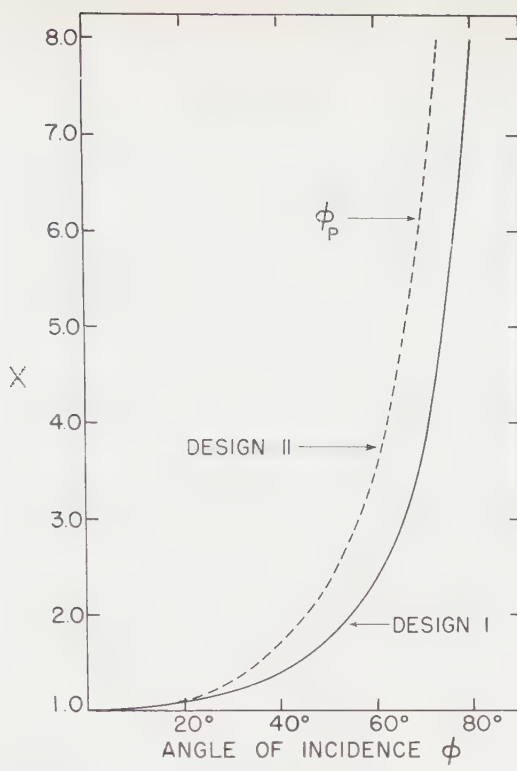


Figure 4. The variable X (defined in equation (3)) as a function of the angle of incidence ϕ for designs I and II. The designs are specified in table 3. The quantity ϕ_p is the polarizing angle.

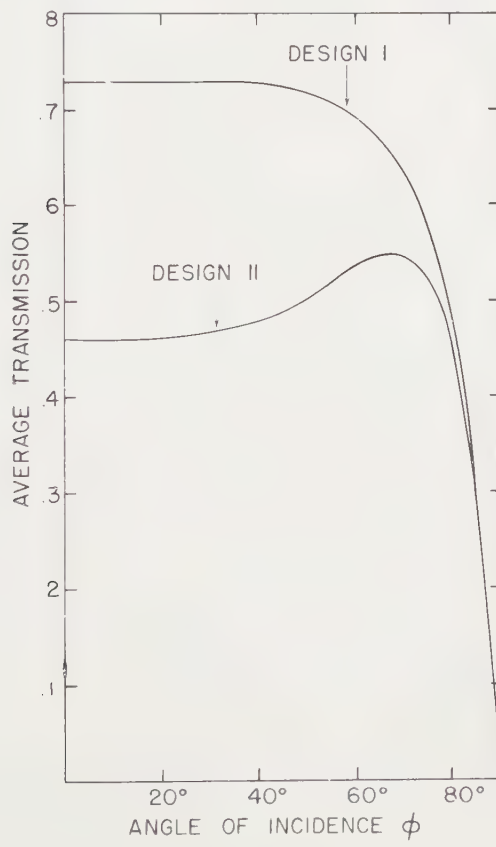


Figure 5. The average transmission T as a function of the angle of incidence ϕ for designs I and II.

maximum can simply be attributed to the fact that Y for design II is greater than Y_0 , whereas Y for design I is less than Y_0 . In the case of design II one can see from figure 3 that contours of larger T are crossed as X increases from one.

In both cases the degree of polarization monotonically increases and approaches P_{00} as ϕ approaches 90° . The degree of polarization is positive, like that produced by an air-glass interface. By inspection of figure 4 one can ascertain that the polarizing angle ϕ_p is close to 70° for design II at $X=6.15$. The fact that the degree of polarization is positive means that R_p is zero at ϕ_p .

A plot of X on a logarithmic scale versus ϕ is depicted in figure 6 for designs III and IV. In both cases X is less than one until the angle ϕ becomes large. However, the variable Y is also less than one and therefore the degree of polarization is positive when ϕ is small. X attains a minimum and then monotonically increases until it becomes greater than one and eventually becomes infinite as ϕ approaches 90° . At the point where X becomes one, i.e. at 61.5° for design III, the multi-layer is non-polarizing. For ϕ greater than 61.5° , the degree of polarization is negative, that is, $T_p < T_s$. The polarizing angle for design III occurs at $\phi = 82^\circ$. Here, however, it is the s component of polarization which has zero reflectance.

The average transmission as a function of ϕ is depicted in figure 7 for design III and in figure 8 for design IV. It appears that T is constant for $0 \leq \phi \leq 62^\circ$ for design III. Actually, T decreases slightly from a value of 0.8275 at normal incidence to 0.8269 at 45° where X is a minimum. T attains a minimum because Y^{-1} is greater than Y_0^{-1} . In contrast, T attains a maximum when X attains a minimum for design IV, due to the fact that in this case Y^{-1} is less than Y_0^{-1} . The sharp maximum in T at 88° is attributed to the fact that X' attains a value which satisfies equation (14).

5.3. Beam splitters

It is possible to use this theory to design beam splitters with specific characteristics. It was pointed out previously that there are many values of X and Y which lie along a given contour of T in figure 3. Thus it is possible to select a value of X and Y which will produce a certain T and P and then find what combination of layers will satisfy this value of X and Y .

As an example of this procedure, let us design a beam splitter of quarter-waves which at one wavelength not only has an average transmission of one-half at 45° incidence but is also non-polarizing. It is assumed that the layers are to be deposited upon a glass plate of refractive index $\mu_s = 1.52$ and that the incident medium is air. The additional polarization and loss in transmission introduced by the opposite side of the glass plate will be neglected. Let us also assume that the coating is composed of only two materials, i.e. the design is represented by

glass $(HL)^n$ air

where the integer n is number of times the basic building block of the stack HL is repeated. Let the refractive indices of the layers represented by H and L be μ_1 and μ_2 . It is necessary to solve two equations:

$$X = \mu_s \mu_0^{-1} \mu_1^{-2n} \mu_2^{2n}, \quad (20)$$

$$Y = \sec \phi (1 - \mu_0^2 \mu_s^{-2} \sin^2 \phi)^{1/2} (1 - \mu_0^2 \mu_1^{-2} \sin^2 \phi)^{-n} (1 - \mu_0^2 \mu_2^{-2} \sin^2 \phi)^n \quad (21)$$

in which X , Y , ϕ , μ_0 , μ_s and n are specified and μ_1 and μ_2 are the unknowns. The condition that $T=0.50$ and $P=0$ requires that $X=1$ and $Y^{-1}=3+\sqrt{8}$. Substituting these values into equations (20) and (21), it is found that when $n=1$,

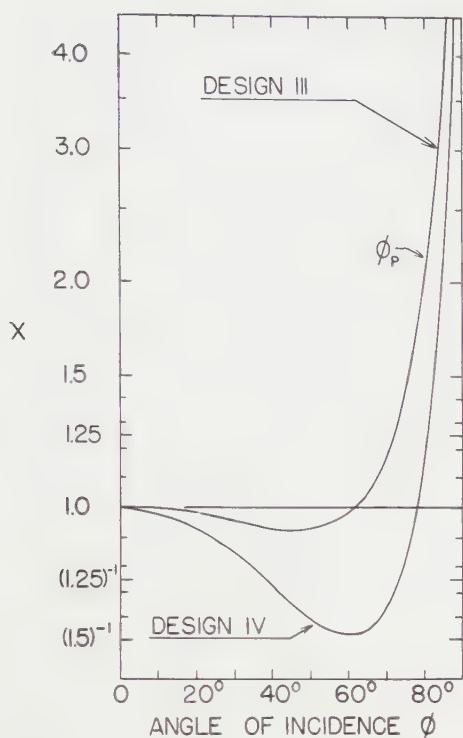


Figure 6. The variable X (defined in equation (3)) plotted on a logarithmic scale on the ordinate as a function of the angle of incidence ϕ . At the angle ϕ_p the reflected light is completely linearly polarized.



Figure 7. The average transmission T of design III as a function of the angle of incidence ϕ .

$\mu_1 = 4.48$ and $\mu_2 = 1.50$. In the case of a four-layer stack, i.e. $n=2$, $\mu_1 = 3.13$ and $\mu_2 = 1.82$. These values for μ_1 can only be attained in the infra-red region of the spectrum.

5.4. Non-reflecting coatings

For any thin film combination to be completely non-reflecting, two conditions must be simultaneously satisfied, namely that $X=1$ and $Y=1$. It is seen that a single dielectric layer can never non-reflect a dielectric substrate at non-normal incidence because the variable X is always greater than one. Thus we turn our attention to double-layer non-reflecting coatings. Here the relations expressed in equations (20) and (21) are utilized, specifying that $X=Y=1$. Solving for μ_1 and μ_2 leads to

$$\mu_2 = \mu_0 \sin \phi [\sec \phi \cos x - \mu_0 \mu_s^{-1}]^{1/2} [\cos x \sec \phi - 1]^{-1/2}, \quad (22)$$

$$\mu_1 = \mu_s^{1/2} \mu_0^{-1/2} \mu_2. \quad (23)$$

Equation (23) expresses the well-known fact that in a double-layer non-reflecting coating consisting of quarter-waves it is only necessary to specify the *ratio* of the refractive indices of the two layers [6]. However, it is also required that at normal incidence equation (22) be satisfied. This means that the index of the outer layer should be:

$$\mu_2 = \sqrt{2\mu_0(1 - \mu_0/\mu_s)^{\frac{1}{2}}(1 - (\mu_0/\mu_s)^2)^{-1/2}} = 1.097$$

for $\mu_0 = 1.0$ and $\mu_s = 1.511$. μ_2 decreases to one as ϕ approaches 90° . For example, at an angle of incidence of 45° the layer next to the glass should have a refractive index of 1.33 and the outer layer an index of 1.085, the latter obviously an impractical value. Thus, at any present stage of thin film technology any non-reflecting coatings for glass at non-normal incidence will be a compromise.

As an example of non-reflecting coatings which can be used at high angles of incidence consider designs VIII and IX. The average reflectance of these coatings at the *match point* is shown in figure 9. The reflectance of uncoated glass of refractive index 1.52 and the same glass coated with a single quarter-wave of cryolite (refractive index 1.35) are also shown in figure 9 for comparison. It

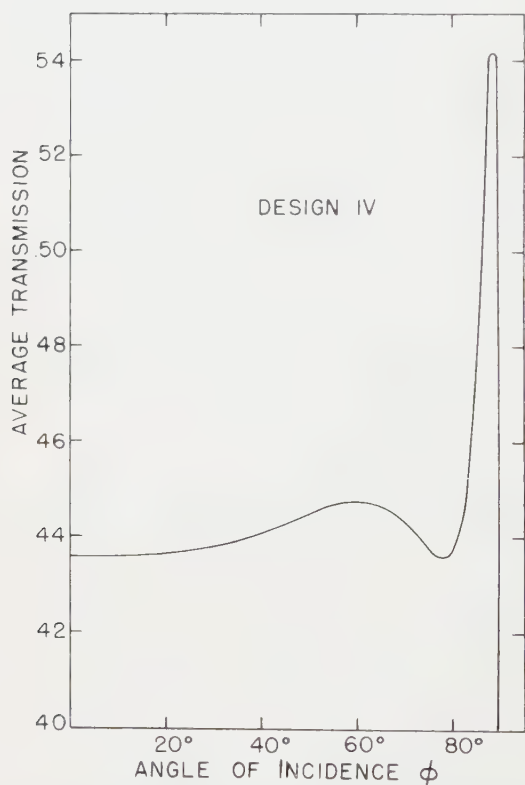


Figure 8. The average transmission T of design IV as a function of the angle of incidence ϕ .

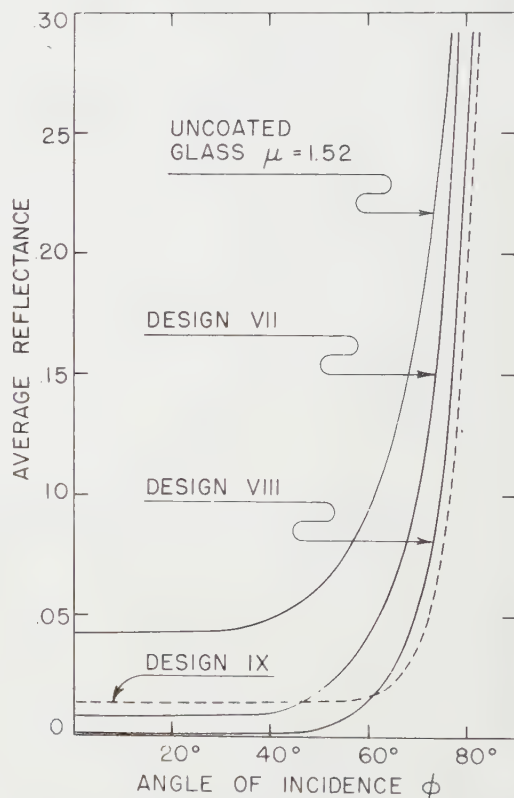


Figure 9. The average reflectance as a function of the angle of incidence for an air-glass interface, a non-reflecting coating consisting of a single quarter-wave film of index 1.35 (design VII) and three-layer and five-layer non-reflecting coatings whose designs are listed in table 3.

is seen that the three-layer coating (design VIII) is a better non-reflecting coating than the single-layer coating at the *match point* wave number at all angles of incidence. It is also seen that for angles less than 50° the five-layer coating (design IX) is not only comparable in performance to the single layer, but at higher angles has a lower reflectance than either the single layer (design VII) or the three-layer coating (design VIII).

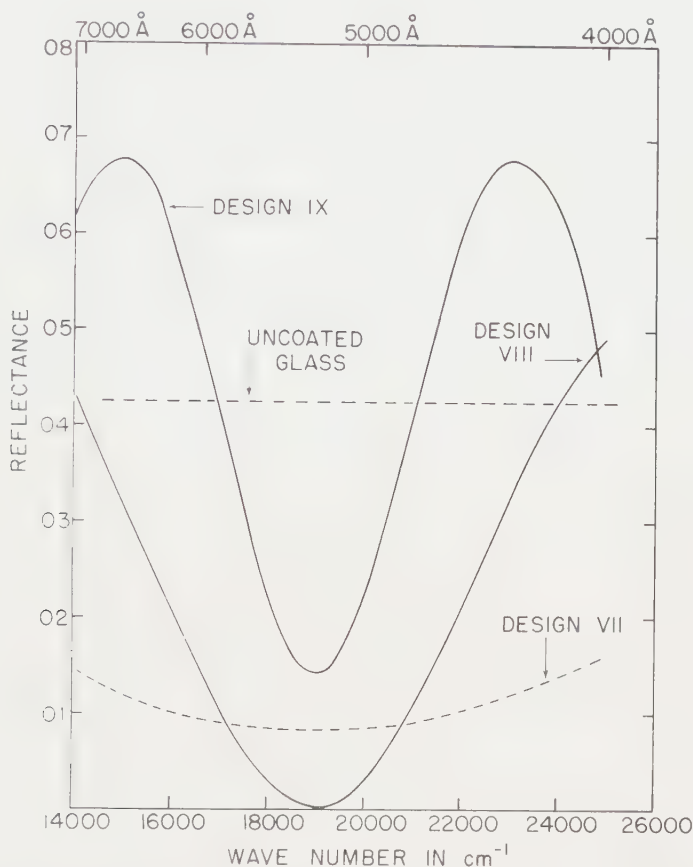


Figure 10. The reflectance as a function of wave number σ at normal incidence of multi-layers whose designs are listed in table 2.

However, figure 9 only shows the reflectance at the match-point wave number. Figure 10 shows the computed reflectance as a function of wave number σ at normal incidence for designs VII, VIII, and IX. One of the many advantages of using frequency (wave number) as the abscissa rather than wavelength is that the reflectance has even symmetry about σ_0 . The layers in designs VII, VIII, and IX all have a quarter-wave optical thickness at a wave number σ_0 of $19\,000\text{ cm}^{-1}$ in the green region of the spectrum. Figure 11 shows the computed reflectance of the same designs at $\phi = 60^\circ$, but with the thicknesses of all of the layers adjusted so that they are still 'matched' at σ_0 . It is seen that the three-layer stack (design VIII) has lower reflectance at both normal incidence and at $\phi = 60^\circ$. However, the price which has been paid for this lower reflectance at σ_0 is that the reflectance

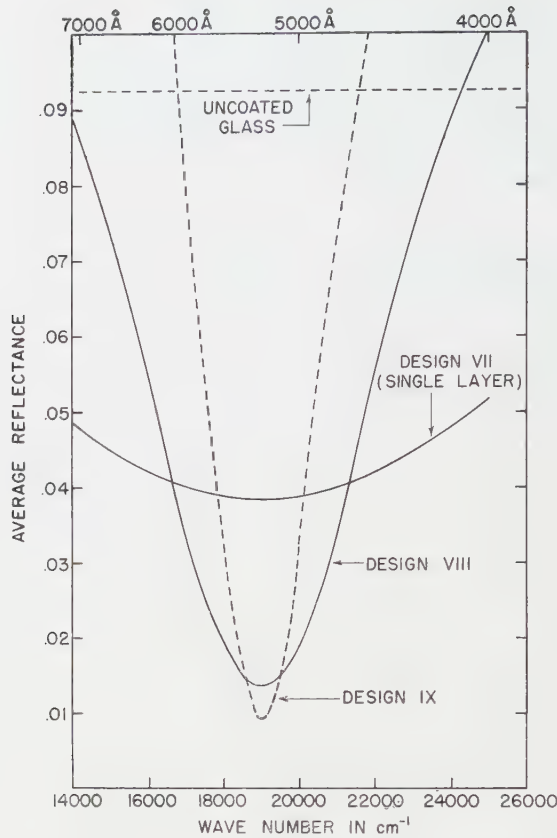


Figure 11. The average reflectance as a function of wave number σ at an angle of incidence of 60° , of the same multi-layer designs as in figure 10.

is considerably higher in both the red and blue spectral regions. Also, it is seen that even though the five-layer stack (design IX) has a higher reflectance than either designs VII or VIII at normal incidence, it has a lower reflectance at $\phi = 60^\circ$. If ϕ were increased to 70° , the advantage of the five-layer stack would be still greater, although the width of the spectral region over which the reflectance is low would now be even smaller.

6. DISCUSSION

The curves of reflection and transmission as a function of the angle of incidence ϕ which are shown in figures 5, 7, 8 and 9 can be computed quite easily, but unfortunately it would be a more difficult task to reproduce these curves experimentally. The difficulty lies in the fact that the curves are computed for multi-layers which are *matched* at all angles of incidence. For example, consider a multi-layer which contains more than one layer. Suppose that the thickness of each of the layers is adjusted so that each layer is *matched*; that is, the phase of retardation, δ_i , is exactly $\pi/2$ at some wave number σ_0 and angle of incidence ϕ_1 . Then at any angle of incidence other than ϕ_1 , although *some* of the layers may be *matched* at some particular wave number σ , there does not exist any value of σ at which *all* of the layers are matched. Thus in order to maintain the condition that the layers should be *matched*, at each angle of incidence it is necessary to

adjust the thickness of each of the layers. This can be accomplished in practice only by manufacturing a separate multi-layer for each angle of incidence.

Although this paper has considered only multi-layers which have a quarter-wave optical thickness†, the results are still useful. It can be shown that a quarter-wave stack has either a maximum or a minimum reflectance at σ_0 . Thus the reflectance at σ_0 gives either an upper or a lower bound. It has been seen in several examples that the reflectance may achieve the desired value at σ_0 , but the band width of the spectral region is rather small. It has been shown that the spectral transmission characteristics of multi-layers can be altered by adjusting the thicknesses of the layers by a relaxation process [10]. It is possible that similar techniques could be applied to some of the multi-layer devices which have been discussed in this paper.

On exprime en fonction de deux variables la transmission et le degré de polarisation d'un empilement de couches quart-d'onde non-absorbantes déposées sur un support transparent. L'une des variables n'est fonction que des indices de réfraction des couches, du premier milieu et du support; l'autre variable dépend de l'angle d'incidence. Plusieurs exemples montrent comment cette théorie fournit des renseignements sur le comportement d'empilements quart-d'onde en incidence oblique et peut être utilisée aussi pour calculer des séparateurs de faisceaux, des polariseurs linéaires et des traitements anti-réfléchissants.

Die Durchlässigkeit und der Polarisationsgrad einer eine viertel Wellenlänge dicken nicht absorbierenden Schicht, die auf einem durchsichtigen Träger niedergeschlagen ist, wird durch zwei Variablen ausgedrückt. Die eine Variable ist eine Funktion nur von dem Brechwert der Schicht, des ersten Mediums und des Schichtträgers; die andere Variable hängt vom Einfallswinkel ab. Einige Beispiele zeigen, wie diese Theorie einen Einblick in das Verhalten einer Viertel-Wellenlängen-Schicht bei schrägem Einfall bietet. Sie lässt sich auch auf die Strahlenteilung, auf lineare Polarisatoren und auf reflexmindernde Schichten anwenden.

Note added in proof.—P. G. Kard has published an article on multi-layer polarizers in *Proceedings of the Estonian Academy of Sciences*, **9**, 26 (1960).

REFERENCES

- [1] ABELÈS, F., 1950, *J. Phys. Radium*, **11**, 403.
- [2] SCHRÖDER, H., 1948, *Optik*, **3**, 499.
- [3] BANNING, M., 1947, *J. opt. Soc. Amer.*, **37**, 792.
- [4] POHLACK, H., 1952, *Jenaer Jahrbuch* (Jena: VEB Carl Zeiss), p. 103.
- [5] TURNER, A. F., 1941, *J. appl. Phys.*, **12**, 351.
- [6] COX, J., HASS, G., and ROWNTREE, R. F., 1954, *Vacuum*, **4**, 445.
- [7] BORN, M., and WOLF, E., 1959, *Principles of Optics* (London: Pergamon Press), p. 54.
- [8] *Ibid.*, p. 38.
- [9] HUND, A., 1952, *Short-Wave Radiation Phenomena* (New York: McGraw-Hill Book Company), Section 151.
- [10] BAUMEISTER, P., 1958, *J. opt. Soc. Amer.*, **48**, 955.

† The results apply equally well when $\delta_i = n(\pi/2)$, where n is an odd integer.

Visual recovery following local adaptation of the peripheral retina (Troxler's Effect)

by F. J. J. CLARKE

Technical Optics Section, Imperial College, London†

(Received 7 November 1960)

The course of recovery has been determined for two observers during the first five minutes after the removal of a bright extra-foveal stimulus, which had been made to disappear by steady fixation. The recovery curves show two linear portions when plotted on a log-time basis, the earlier portion having the steeper slope. The effects of testing different zones within the locally adapted area, of changing the size of test stimulus, of changing the luminance and the size of the conditioning field, of changing the degree of fixation, and of changing the retinal region have all been investigated. Results indicate that the early (rapid) phase of recovery represents recovery from Troxler's Effect, while the later (slower) phase represents recovery from normal light adaptation. The novel effects found are shown to be in accord with certain phenomena noticed by previous investigators, and are consistent with a boundary neutralization model for the visual organization of Troxler's Effect.

1. INTRODUCTION

It has long been known [1] that when a suitable target is viewed steadily without blinking and while trying to keep the eye free from movements, objects perceived by extra-foveal vision tend to 'fade out'. This phenomenon is termed *Troxler's Effect* after its original discoverer, and has also been referred to as *local adaptation*. This last makes a graphic description, for the effect is undoubtedly an adaptive process, and only seems to become manifest when an image is localized on the retina by steady fixation. Unfortunately these words (local adaptation) have sometimes been used in other connotations. The perceptual effects can be very marked, and under suitable conditions bright stimuli may disappear completely after only a few seconds. For this to happen the sensitivity within the stimulated area must be heavily depressed—Holth's term *stirreblindhet* (fixation blindness) was by no means inapt [2]. The investigation described in this paper consisted of experiments aimed at demonstrating the extent and distribution in space and time of this loss of sensitivity, leading if possible to a better understanding of the underlying processes.

Troxler's Effect depends in part on the continuity of the experimental conditions: if, for example, the luminance of the conditioning stimulus is changed by a significant amount the fading process is halted or reversed, while a stimulus that has been caused to disappear will promptly reappear. This makes any investigation of sensitivity within the stimulated area during the 'faded-out' phase very difficult, as the introduction of an additional probe field will tend to promote a reappearance of the conditioning stimulus as well: the experimental conditions are thus no longer those pertaining to the faded-out state. An alternative approach

† Now at National Physical Laboratory, Teddington, Middx.

is to avoid disturbing the adapted-out state by any additional test stimulus, but to measure the course of recovery of sensitivity following the removal of the conditioning stimulus. It is well known that the form of the recovery or dark adaptation curve depends on the effective strength of the previous adaptation. There is an extensive literature dealing with investigations of the relations between the recovery curve after normal light adaptation and the luminance, area or time of exposure of the adapting field. In this investigation the depression of sensitivity and recovery kinetics during the first five minutes of dark adaptation following removal of the stimulus have been used as a gauge of the extent and distribution of Troxler's Effect. There appear to be no previously published data on this particular topic, or even on the closely related phenomenon of the recovery following the removal of a stabilized retinal image.

When Troxler's Effect has set in and the conditioning stimulus has been made to disappear, it is found that a momentary interruption of the stimulus causes its reappearance. It can readily be demonstrated that the briefer the interruption, the dimmer is the reappearance. Further, rapidly flashing lights can be made to disappear. If the frequency is above the critical fusion frequency the fade-out can be readily performed, while as the frequency is lowered so does Troxler's Effect become more difficult to realize.

It will be seen from the above that the recovery of sensitivity following the removal of a locally adapted stimulus must be rapid, which in itself poses problems of measurement. The basic requirements are to provide a conditioning stimulus which can be caused to disappear, to cut this off quickly before a large eye movement causes an inadvertent reappearance, and to substitute another field configuration within the adapted area at suitable intervals of time, so that measurements of sensitivity can be made. Since complete disappearance becomes more difficult to achieve as the observations proceed, due to the onset of eye-strain during an observing session, it is clear that the field subtense must be less than the critical size that can just be made to disappear [3, 4, 5], and preferably much smaller, so as to make the 'fade-outs' as easy as possible. This means that a modest field size at a large eccentricity must be used for the conditioning stimulus. Further, in order to produce a significant depression of sensitivity, a fairly high brightness level must be employed [3].

There were many measuring techniques that could have been used to record the sensitivity, e.g. direct comparison at constant brightness, direct comparison with constant luminance (both using either foveal or neighbouring peripheral comparison patches), increment threshold or absolute threshold. The essential features were that the technique must involve rapid decisions, and must not of itself affect the sensitivity and thereby invalidate the results. For these reasons the absolute threshold method was chosen, so that the decisions made by the subject would not be ambiguous. Although it was thought possible that Troxler's Effect could occur at absolute threshold, or slightly above, the use of a slow flashing technique would prevent any such effect from occurring significantly.

2. EQUIPMENT AND CALIBRATION

The extra-foveal adaptometer described previously [4, 5] has been used throughout this investigation. The optical system is reproduced in figure 1 for convenience. The conditioning field was provided by a normal field aperture

placed at A_1 , giving a field subtense of 2° . The test field consisted of a photographic plate, suitably exposed, developed and mounted, which was readily fitted into the replacement field device Q . This could be swung into place in less than a second, so that recovery times of as short as 2 sec could be coped with. The photographic plate was made by masking, and had a relatively transparent circular area subtending $40'$ in the centre, the rest of the plate being fogged to high density. The transparent area was in fact exposed and developed to give some required density.

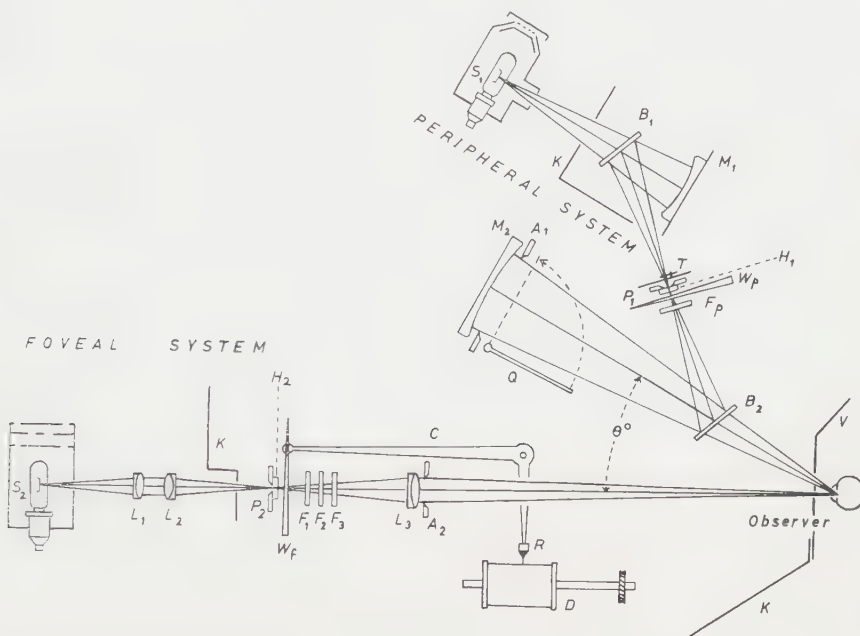


Figure 1. Optical system of the extra-foveal adaptometer [5]. The device Q enables a rapid change of both luminance and format to be accomplished.

The making of these plates presented certain problems. Thus the emulsion had to be processed in such a way as to avoid non-neutrality and undue scattering, as far as practicable. Then the density developed had to be controlled, since a well graduated set of densities from about 0.6 to about 2.0 was required. The density had also to be uniform and the edges had to be sharp. All plates had to be geometrically identical, since once the centring adjustments of Q were made, all plates in the set had to be positioned so that the test patch was truly concentric with the pre-adapting patch. Finally, a sound means of calibration had to be employed.

The manufacture of neutral filters to prescribed densities and with minimal scattering is an art acquired after long experience. The very best commercial filters made from photographic emulsions compare unfavourably with the colloidal carbon type, as regards scattering. The author was not fully able to solve the neutrality and scattering problem. Improvements were effected by using a slow fine-grain developer and fine-grain plates, yet the plates made were slightly blue in tone, and there was a certain amount of scattering. A large number of plates had to be used until a suitable set was available. Trouble with uniformity and

sharpness was initially caused by edge effects (Eberhard Effect and particularly halation) but improvements in masking and processing and the use of plates with an anti-halation backing proved effective. As a master plate was used for printing, it was easy to ensure that all plates were geometrically identical.

The plates were used in double transmission and the density had to be known therefore with some precision. A direct visual comparison method of calibration in the adaptometer was possible for these 40' circular patches, but not for certain other configurations described later. The plates were measured on a Hilger microphotometer, the mean density of each being taken from five measurements at various positions in the 40' patch. The Hilger microphotometer has ample precision for this purpose, but unfortunately it does not give the true density value for such filters, due to the presence of three sources of systematic error.

Firstly, the instrument measures only the emulsion density, since comparison is made with a dummy clean substrate. (If the substrate is omitted for the 'straight through' comparison, the optical system becomes defocused, leading to an invalid result.) Thus the instrument over-estimates the transmission by about 8 per cent (for 2 air/glass surfaces). Secondly the photo-cell used is a photovoltaic cell which is relatively more blue sensitive than the human eye. Both the peripheral adaptometer and the Hilger microphotometer use tungsten illumination, but the former uses a human detector whereas the latter uses the photovoltaic cell. Thus because of the slightly blue tone of the filters, the microphotometer again over-estimates the transmission. Finally the convergence and divergence of light is very small for a 40' field. The microphotometer however uses a relatively large numerical aperture for illuminating and collecting of light, a condition which leads to higher values of transmission where a filter scatters some light. Again, the transmission is over-estimated relative to the conditions holding in the adaptometer.

Thus the results of the microphotometer calibrations were expected to give lower values of density than those holding in the adaptometer. The only valid method is to calibrate such filters *in situ*. Four values of density were selected, and these were calibrated visually in the adaptometer by direct comparison with the foveal beam, with minimum separation and using alternate foveal glances. The difference between the visual and photoelectric values provided a small correction factor for each of the four densities selected. The complete set was then corrected appropriately. It should be noted that the precision of measurement was higher for the photo-electric than for the visual calibration. Thus although the absolute double densities were not known to closer than 0.06 units, the relative double densities of the various filters were known to 0.02 units. The presence of a little stray light scattered from residual dust on the beam-splitter B₂, see figure 1, prevented double densities greater than 4.0 being validly used.

3. OBSERVING CONDITIONS

The conditioning stimulus was presented at 30° of eccentricity in the upper meridian of the field of view, and was a 2° uniform field of source A illumination whose initial brightness, as seen by the dark adapted periphery, was adjusted until it matched that of an 8000 troland foveal patch subtending 1°, as viewed by the light adapted fovea. The luminance was 177 cd/sq.m for the main observer, giving a retinal illumination of 550 trolands. The test stimulus was a field of much lower luminance of subtense 40' and was presented at a position concentric

with that of the conditioning field. The field of view with the conditioning stimulus exposed is shown in figure 2 (a), while that during testing is shown in figure 2 (b).

In these experiments the total recovery time between 'fade-outs' was 10 min. Since a threshold method was being employed, a bright fixation patch was undesirable, due to the glare and scattered light that it would cause, so the foveal field was turned down as far as practicable without making the fixation target too dim to see clearly. The procedure was: (a) 10 min of dark adaptation, (b) conditioning field presented and fixation held until it had disappeared completely, (c) the field cut off and the replacement field aperture swung across, a stop-watch being started just as the field was cut off, and (d) the test stimulus presented in flashes of about $\frac{1}{2}$ sec, repeated about every 2 sec. The subject continued fixating until two successive flashes were 'seen', then pressed the stop-watch. This reading gave the time of reappearance T sec, appropriate to the density inserted in the conditioning stimulus by the replacement plate. For values of T less than about 12 sec the first flash 'seen' was taken as the reappearance time.

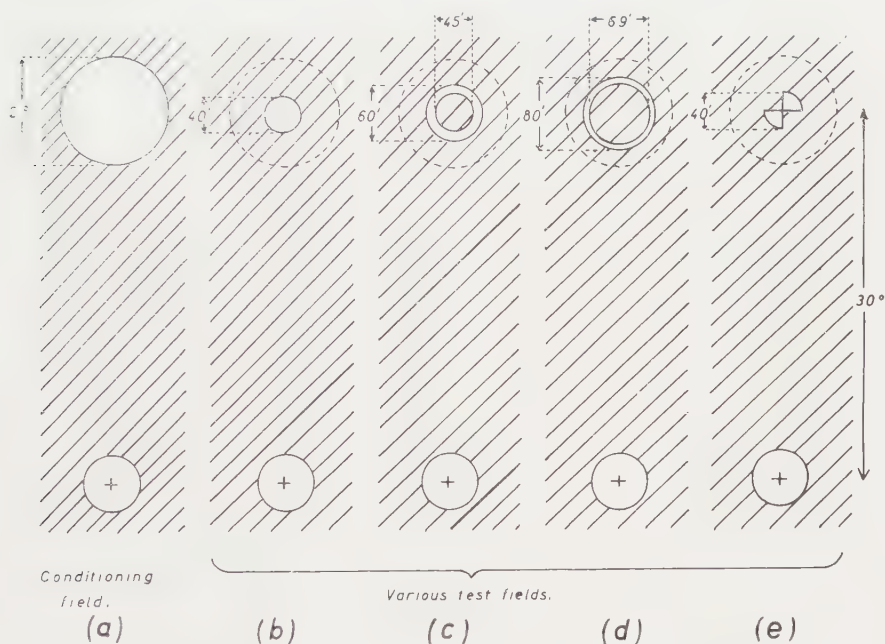


Figure 2. Fields of view. (a) during exposure to the conditioning field, (b)–(e) during recovery, with various test fields to determine the threshold sensitivity within the locally adapted area.

A most important aspect of this method of measuring the recovery curve is that a rigid and very accurate fixation is not required once the conditioning field has been made to disappear. This is because the edges of the test stimulus were nominally 40' inside the edge of the locally adapted area, figure 2 (b). During the recovery testing the observer blinked and moved his eyes as he pleased during the intervals between the flashes, which he controlled manually. As he operated the shutter he re-fixated each time just before a flash occurred. Repeated 'fade-outs' caused eye-strain and without these viewing techniques no such measurements could

have been made. Typically, 20 to 40 sec of fixation were required to cause the subjective disappearance of the 2° conditioning field, but this could occur within 15 sec when the observer managed to avoid a significant shift of fixation.

4. RESULTS

The time of reappearance T was plotted against the log threshold retinal illumination for the test stimulus, the mean results appearing on figure 3 (a), for the main observer (FC). It will be seen that the initial recovery is rapid and although a smooth curve can be drawn through the data, the curvature is sharp in the region of 25 sec. The data were replotted in terms of log threshold and log time, the results appearing in figure 3 (b). Nine long observing sessions were needed to make the 121 observations, the plotted points being mean values. Standard deviations, amended by Bessel's correction $\sqrt{(n/n-1)}$, are shown in a later diagram, figure 5.

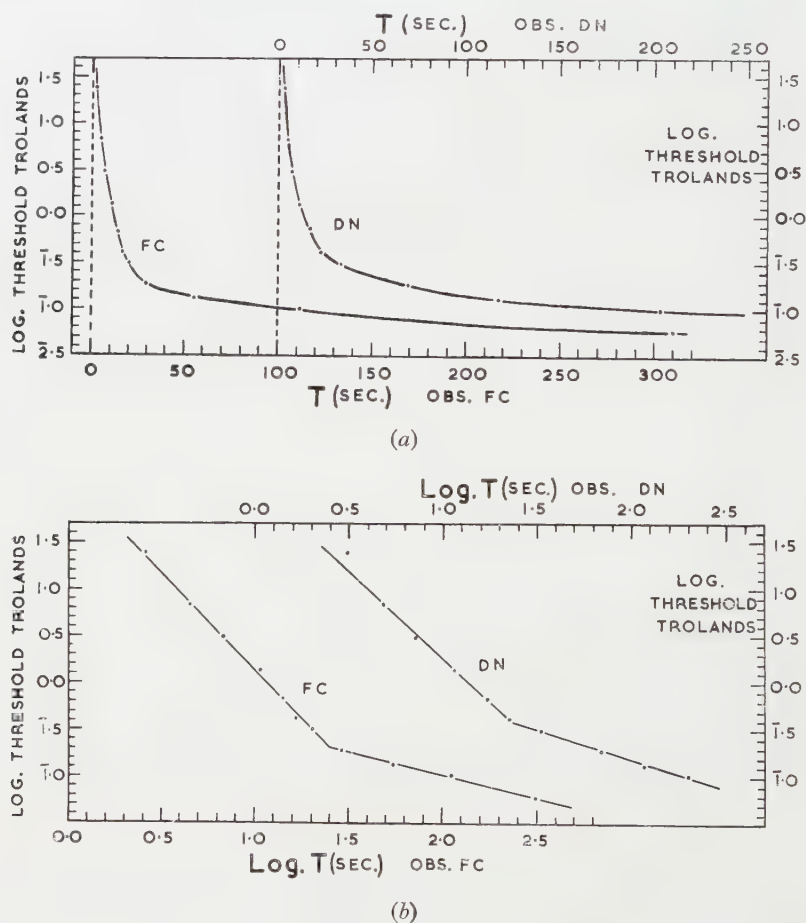


Figure 3. Recovery of sensitivity following local adaptation by a 2° field of 550 trolands, plotted (a) as a function of time, and (b) as a function of log time.

It will be seen that the recovery curve exhibits two linear portions, the early stages of recovery being rapid while the later stages are slower. The transition

occurs at about 25 sec. In this study the straight lines are drawn to fit the data concerned, rather than any preconceived notion.

4.1. Interpretation

When a normal recovery curve (i.e. a dark adaptation curve) is plotted on a linear time scale two portions are seen separated by a marked kink, if the conditioning stimulus is strong. If the conditioning stimulus is weak, the curve is smooth with no kink, and for various luminances, sizes and exposure times of pre-adapting field there are continuous families of dark adaptation curves. This

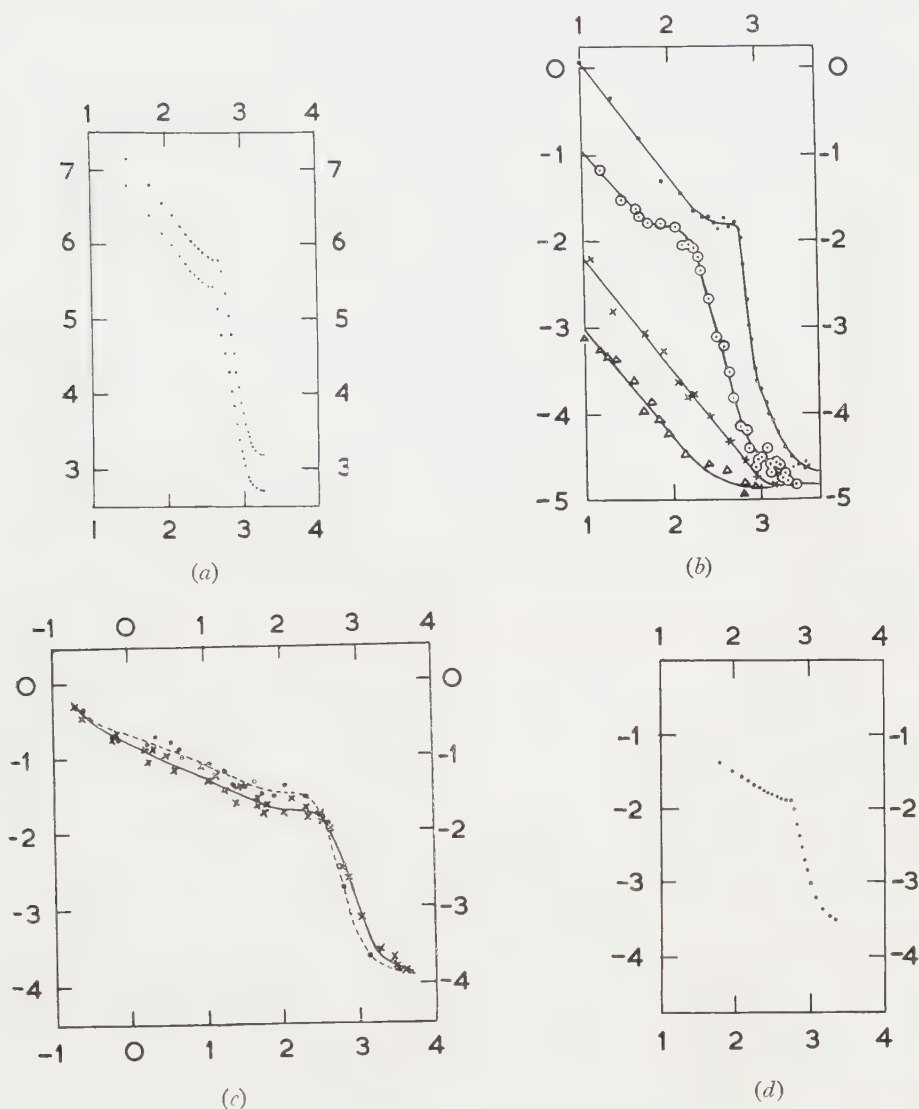


Figure 4. The normal course of dark adaptation for extra-foveal vision. (a) Data from 110 observers of Hecht and Mandelbaum [6]: points from their upper and lower limit curves containing 80 per cent of observations, replotted on a log time basis; (b) data of Mertens [7]; (c) data of Crawford [8]; (d) data of Winsor and Clark [9]: points from one of their curves replotted on a log time basis. Ordinates: log threshold. Abscissae: log time (sec).

has been a popular subject of research and it would be impractical to give here a history of such work. However, it appears that when the dark adaptation curve is plotted on a log threshold vs. log time basis the curves exhibit one or two linear portions, depending on the circumstances. To illustrate this, some data of Hecht and Mandelbaum [6], of Mertens [7], of Crawford [8] and of Winsor and Clark [9] have been collected in figure 4 and exhibited on a log time basis. It will be seen that the early 'cone' portion shows slower kinetics than the later 'rod' portion.

The author's data show quite a different state of affairs, for the early portion of the curve is steep, with a slope of 2.1, while the later part is less steep with a slope of 0.5. The interpretation proposed is that the initial portion showing rapid recovery represents recovery from Troxler's Effect, while the later portion represents recovery from 'normal' light adaptation, and is in fact the early portion of an orthodox dark adaptation curve. This is supported not only by the scale of time values involved, but by the fact that for the early portion of dark adaptation Hecht's and Mandelbaum's data (replotted) have a slope of 1.3, Merten's data have slopes ranging from 1.3 to 0.6, Winsor and Clark's data (replotted) have a slope of 0.6, while Crawford found slopes ranging from 0.9 down to 0.15, all depending on the various observing conditions used.

In view of these novel features of the recovery curve obtained from the main observer FC, it was felt desirable to determine the recovery of a second observer to serve as a guide as to how far these effects might be typical. Results obtained from 121 observations by observer DN are also shown in figure 3 (*a, b*) for comparison. It will be seen that when plotted on a log time basis the recovery curve of observer DN also showed two linear portions, slopes being 1.9 and 0.6 and the transition occurring at about 23 sec. Although some observer differences are apparent it is clear that recovery seems to proceed in two phases following local adaptation: a rapid recovery from a low level of sensitivity, which is succeeded after some time by a slower phase of recovery of more normal rate.

4.2. *Variation of test position within the locally adapted area*

It was desired to find how the Troxler Effect was distributed over the area stimulated by the conditioning field. Accordingly, two further sets of photographic plates were prepared and calibrated, these consisting of annular test fields 60' and 86' outside subtense and having a width such that the area of stimulation was constant. These gave fields of view as shown in figure 2 (*c, d*). The area was kept constant so as to enable thresholds to be realistically compared, but too little is known yet about the spatial integrating power of the retina to predict the correct thicknesses of annular rings to give constant physiological effect.

Results are shown in figure 5 for FC. It will be seen that the same slope and shape of recovery curve is obtained as before, for this observer, except that the transition time is delayed to about 34 sec and the thresholds are higher throughout. The delay of transition time (T_t sec) shows that the whole of the rapid recovery phase is delayed, i.e. the sensitivity is relatively depressed during the recovery from Troxler's Effect, meaning that Troxler's Effect is more marked towards the edge of the conditioned area and less marked towards the centre. The overall elevation of threshold is probably caused by the narrow annular rings not gaining as much by spatial integration as the solid area of the original 40' patch.

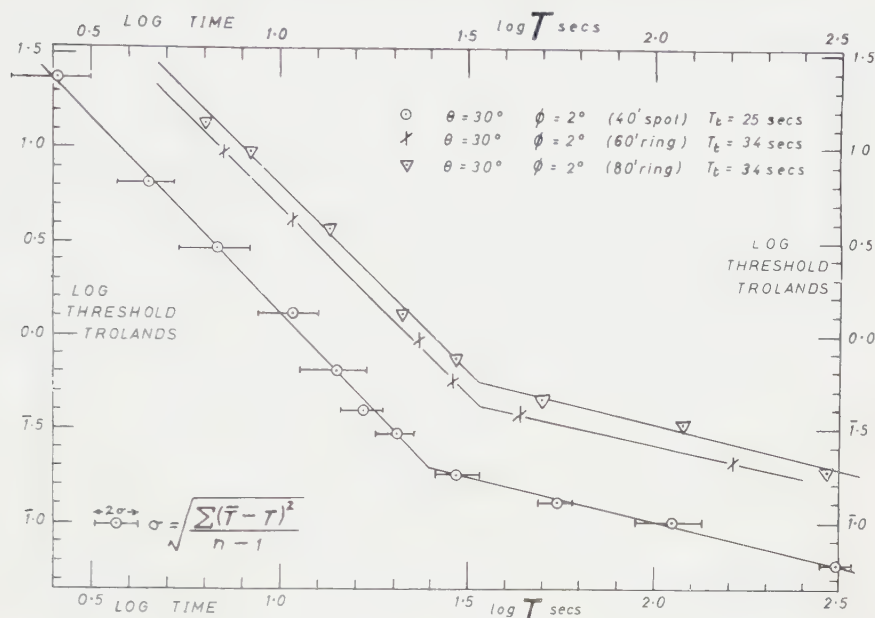


Figure 5. Course of recovery following local adaptation by a 2° field of 550 trolands. Effect of testing different zones within the locally adapted area.

4.3. Variation of area

In order to test this last point, an experiment was performed in which the effective area of test stimulus was reduced without altering the position in the pre-adapted area. This was achieved by 'quartering' the 40' test patch as shown in figure 2(e), the total area being halved. The result predicted on the above interpretations is that the threshold should be roughly doubled and the kinetics unaffected.

The results are shown in figure 6, with the original data for comparison. It is seen that within the limits of experimental error the predictions are fulfilled, supporting the interpretation. Thus in figure 5 the change of kinetics must have been caused by the change of position rather than change of effective test area.

4.4. Variation of conditioning luminance

A series of observations was made in which the conditioning field luminance was 1 log unit lower (giving 55 trolands), *ceteris paribus*. Results are shown in figure 7, the original data being shown for comparison. This diagram has ordinates to the same scale as before, but the units are the densities added to the conditioning stimulus. This enables the curves to appear reasonably juxtaposed for comparison without arbitrary adjusting. It will be seen that variation of conditioning luminance has not affected the kinetics of recovery in any significant way, a result which adds further weight to the interpretations.

4.5. Variation of retinal position

All recovery curves shown so far might be artifactual, due to the test area falling by chance on a blood vessel or on an unsuspected scotoma or pathological

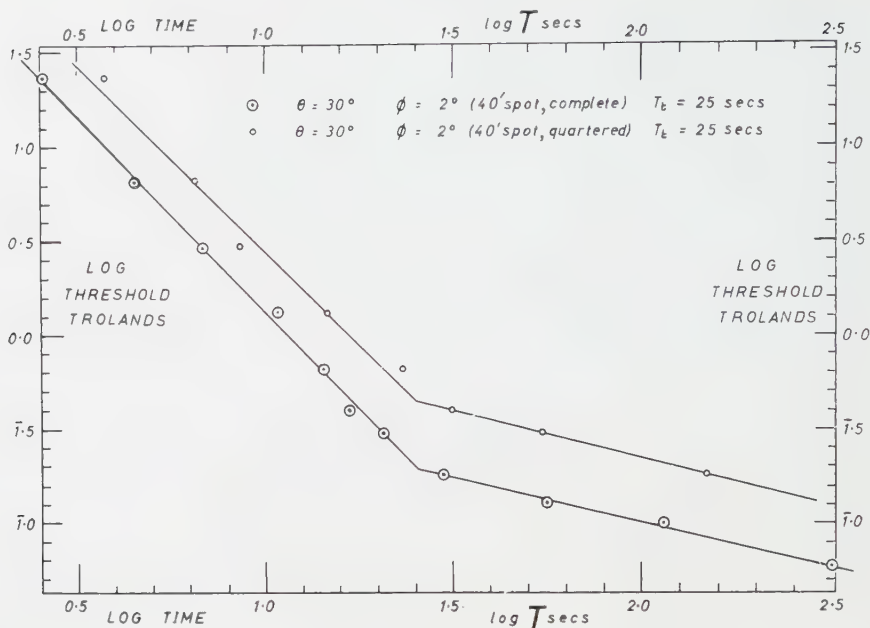


Figure 6. Course of recovery: effect of testing the same zone in the locally adapted area, but with a 50 per cent reduction of area.

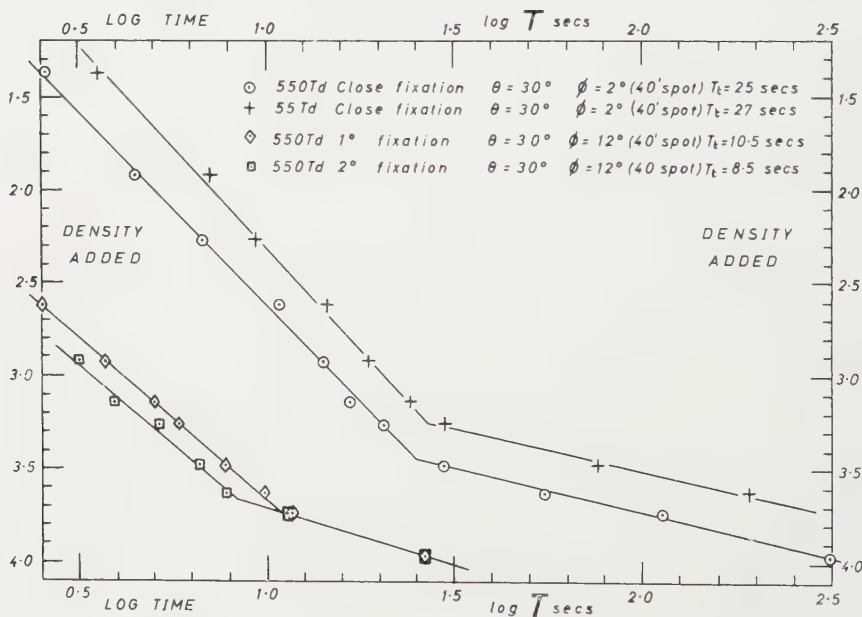


Figure 7. Course of recovery: effect of changing the luminance, size and degree of fixation of the conditioning stimulus.

anomaly. It was desirable to obtain confirmatory evidence and so another location was used at eccentricity $\theta = 25^\circ$. A smaller value of θ would not have been practicable with the repeated fade-outs necessary for these observations. The conditioning field was 2° and the test field was the 60' ring.

Results are shown in figure 8, the comparable data with $\theta = 30^\circ$ being shown also. It will be seen that the type of curve is identical, the slopes of the two portions being in good agreement. Thus the data reported are unlikely to be artifactual. It is interesting that the transition time is reduced from 34 sec at 30° to 20 sec at 25° . This supports the view on the above interpretations that Troxler's Effect is less marked as eccentricity is reduced, which is known already from the studies described previously [3, 5].

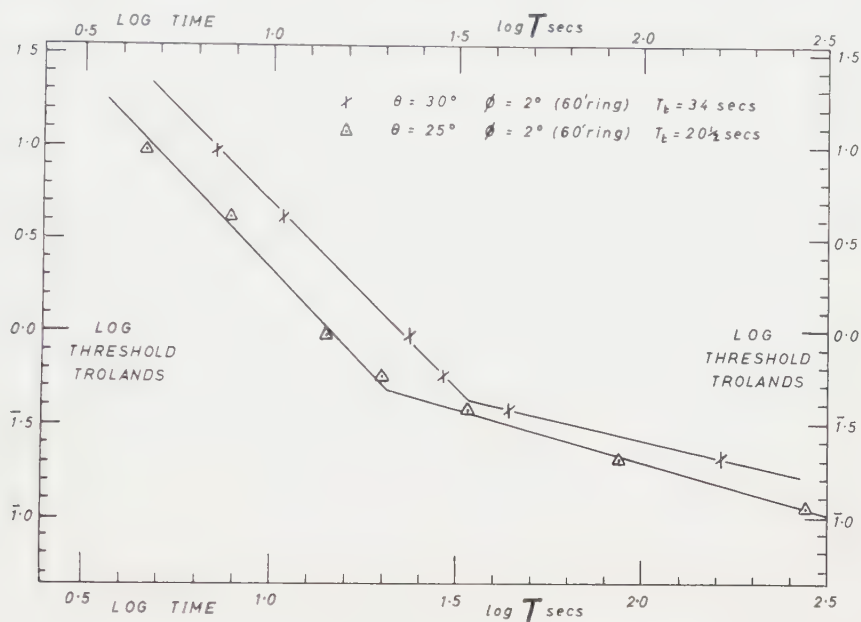


Figure 8. Course of recovery following local adaptation by similar stimuli at eccentricities of $\theta = 30^\circ$ and $\theta = 25^\circ$.

4.6. An experiment with normal light adaptation

In order to make a critical test of the hypothesis that the initial portion of the recovery curve represents recovery from Troxler's Effect, while the later portion is recovery from normal light adaptation, an attempt was made to eliminate Troxler's Effect while keeping as many conditions unchanged as possible. It has been shown in an earlier study [5] that increasing the conditioning area reduces Troxler's Effect. Yet it is also clear from figures 12 and 19 of that work that at 30° eccentricity a significant local adaptation (between 1 and 2 log units) must occur even with a 12° field. The other obvious way to decrease local adaptation is to keep the eye moving.

Using a 12° conditioning field at 30° eccentricity the fovea viewed a 1° field for 30 sec and fixation was directed every second to a fresh position on the edge of this foveal field, these being occupied in random order. The choice of 30 sec was simply to correspond to the average time of disappearance in the previous experiments, which is influenced by the occurrence of breaks of fixation as the eye becomes tired. The luminance was unchanged and the test area used was the $40'$ patch. Results are shown in figure 7 and three things are immediately seen:

(a) the type of curve seems to be the same, with two linear portions of approximately the same slope as previously found, (b) the whole curve shows a net lowering of threshold, and (c) the initial phase of rapid recovery now occupied less time, the transition time T_t being $10\frac{1}{2}$ sec only.

It is clear that on the interpretation suggested earlier in this paper this means that Troxler's Effect is much less marked, as expected. Yet the initial phase is definitely still present. In order to further reduce Troxler's Effect, more observations were made using the same technique, this time the fixation being directed from point to point on the edge of a 2° foveal patch. Results are shown on the same diagram, figure 7, the former being called ' 1° fixation' and these latter being called ' 2° fixation'. The only difference is that Troxler's Effect has indeed been further reduced, the transition time T_t now being $8\frac{1}{2}$ sec only.

5. DISCUSSION

The experiments described in this study have shown that when a continuously exposed peripheral stimulus is viewed while fixating a suitable target as steadily as possible, a local adaptation process sets in which causes a large depression of sensitivity to be manifest after the conditioning stimulus has been removed, and from which the visual system recovers fairly rapidly. In addition there must also occur the more familiar 'normal' light adaptation processes, which seem to be related more to the retinal illumination and time of exposure than to the degree of fixation practised by the observer. The recovery curves measured show two distinct phases, and suggest that the local adaptation effect is short-lived compared with the more normal light adaptation processes. The fact that reducing the eccentricity, increasing the conditioning area or increasing the eye-movements all separately cause the transition time to be shifted towards the origin, establishes a close correlation between the initial phase of recovery and Troxler's Effect.

The relationship between the local and 'normal' adaptation processes is probably rather complex, and is unlikely to be elicited while so little is known as yet about the 'normal' processes. Even in the relatively simple case of foveal vision, with only cone systems operative, the studies of Wright [10] by the binocular matching technique have revealed a wealth of interesting effects, most of which have yet to be explained. The question might well be raised that, as the Troxler Effect seems to be residually present in foveal vision [3], perhaps it has influenced experiments that are thought to deal with normal adaptation processes. As Wright tested foveal vision, used a 5° central adapting field and did not employ a fixation target (factors which would all be inimical to Troxler's Effect), one would not expect his recovery curves to show much of the initial rapid phase of recovery. Nevertheless a few of his curves do show such an effect in the first 5 sec.

It is interesting that orthodox dark adaptation curves only show one phase for foveal vision and two phases for extra-foveal vision. This author's attempt to obtain the early part of an orthodox curve by using a larger, 12° field and induced eye-movements gave a curve with the newly reported initial phase markedly reduced but still present. The reason for this appears three-fold: most workers have used small eccentricities in the paracentral region, larger pre-adapting fields and have not commenced testing until (typically) 10 to 60 sec have elapsed. Thus such workers have missed this initial phase of recovery. There are three notable exceptions to this, namely Wright [10] (see above), Crawford [8, 11] and Baker [12]. It will be seen from figure 4 that Crawford used short recovery times (1937)

and there is just a suggestion in the figure of an initial rapid phase. Yet Crawford used a cyclic method of presenting the adapting field and test field in turn for times less than 2 sec, which would inhibit Troxler's Effect. Further, the eccentricities were small, 0° , 5° and 14° , and the adapting field enormous (45° subtense) so that a significant local adaptation would not have been feasible.

More recently Crawford and Baker have measured the increment threshold during and after a long flash by different techniques, and data with exceedingly short recovery times have become available. Both used cyclic presentation (period 7.2 and 10 sec respectively), large fields (12° and 20° respectively) and small eccentricities (0° and 5° respectively), so that very little local adaptation could have set in. The published data are on a linear time scale. The author has replotted the data on a log time scale, using the cessation of the conditioning flash as origin. The results appear in figure 9 (*a, b*). It will be seen that there is indeed an initial phase of rapid recovery residually present. The slopes, varying from 1.0 to 1.74, are in reasonable agreement with the slopes of the author's data, figures 5 to 8, which are all very close to 2.0 for $\phi=2^\circ$ and 1.8 for $\phi=12^\circ$. Unfortunately the two studies [11, 12] reported above could equally well be described as measuring the recovery from the alpha-adaptation of Schouten and Ornstein [13]. The author cannot explain this, but a tentative hypothesis is that since alpha- and local adaptation are both almost certainly neutral in origin, the recovery kinetics could be common in rate.

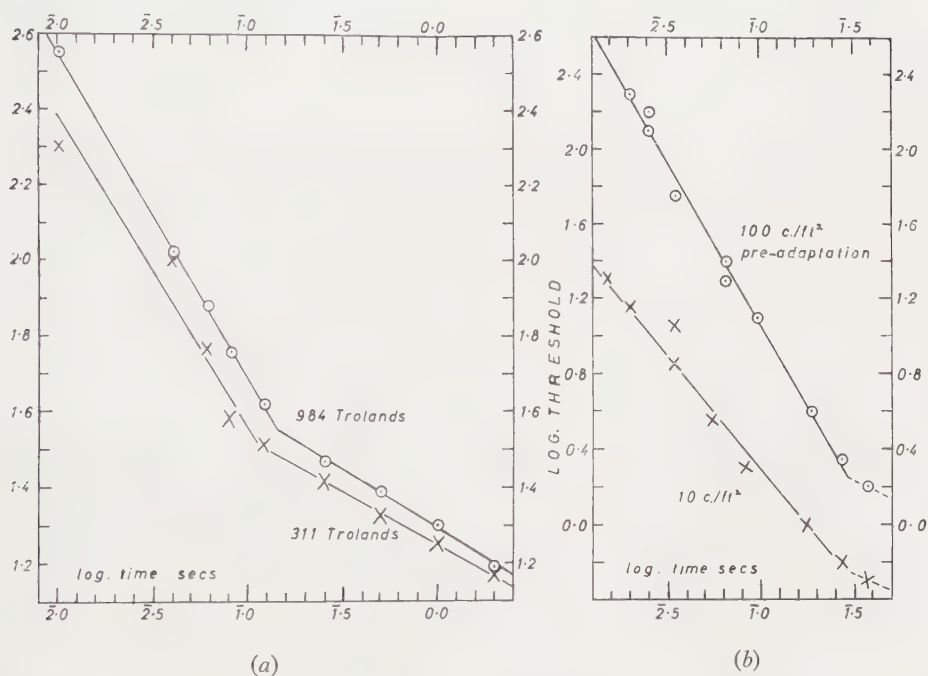


Figure 9. Very early stages of recovery from a light stimulus. Data of (*a*) Baker [12], and of Crawford [11], all replotted on a log time basis with the cessation of the conditioning stimulus as origin.

In order to account for previously obtained results [3, 5], two possible models of visual organization to explain Troxler's Effect have been discussed [4, 5]. In one case it was assumed that the effect was an *area* effect, being caused by massed

groups of receptors giving a 'constant light' signal for extended periods; at a late stage of the visual pathway such signals could become attenuated by some adaptive process such as *habituation* [14] or even straightforward neural accommodation. In the other case it was assumed that Troxler's Effect was a *boundary* effect, being caused by the boundaries of the retinal image remaining approximately stationary and becoming neutralized by some inductive process of adaptation. This could occur through the reduction of eye movements by fixation decreasing the amount of alternate stimulation and recovery of the sensory units on the optical boundary of the image; then the space-pattern information relayed to the cortex (largely by on- and off-receptors one supposes) would become drastically reduced.

The experiments with various test field configurations, figure 5, support the boundary model of local adaptation as this leads to the supposition that the sensory units in the conditioned area away from the boundary (i.e. in the centre) should not have their sensitivity depressed so much as those nearer. The effect shown in figure 5 now seems easy to understand. Moreover the relatively small amount of Troxler's Effect manifest at the centre of the large 12° field, figure 7, provides further evidence in favour of the boundary model.

Finally it should be noted that the overall depression of sensitivity with a 2° field as compared with a 12° field of the same luminance, shown in figure 7, appears to contradict the common notion that the larger the adapting field the more effective is the adaptation. The solution of this might well be found in the work of Kuffler [15], of Barlow [16] and of Brown and Wiesel [17] who have shown electro-physiologically that stimulation of a small retinal area inhibits the sensitivity of the surrounding region, and vice versa.

ACKNOWLEDGMENTS

The author is indebted to Professor W. D. Wright for his interest and encouragement throughout this work, and to Mr. D. Nightingale for undertaking some exacting observations. Thanks are due to the Beit Trustees for the award of a Research Fellowship.

L'évolution de la réadaptation a été déterminée pour deux sujets pendant les cinq premières minutes après la suppression d'un stimulus brillant et extra fovéal. On a fait disparaître ce stimulus en l'observant fixement. Les courbes de réadaptation montrent deux parties linéaires quand elles sont tracées en fonction logarithmique du temps, la première étant plus raide. On a étudié différentes zones du champ adapté, ainsi que les effets du changement de la grandeur du test stimulus, de la luminance et de l'étendue du champ conditionnant, du degré de fixation et de la région examinée de la rétine. Ces résultats montrent que la première phase de la réadaptation (phase rapide) représente la réadoption de l'Effet Troxler, tandis que la deuxième phase (lente) représente l'adaptation normale à la lumière. On a montré que les nouveaux effets trouvés sont en accord avec certains phénomènes observés par d'autres chercheurs et qu'ils sont compatibles avec l'idée de neutralisation des bords pour l'organisation visuelle de l'Effet Troxler.

Für zwei Beobachter wird während der ersten fünf Minuten nach dem Löschen eines hellen extrafovealen Reizes der Verlauf der Erholung bestimmt, wobei während des Löschens des Reizes die Fixierung aufrecht erhalten wird. Die Kurven der Erholung zeigen zwei gradlinige Stücke, wenn sie über logarithmischen Zeitabszissen aufgetragen werden. Die erste gradlinige Strecke zeigt eine größere Neigung. Die Untersuchung erstreckt sich auf den Einfluß der Prüfung in verschiedenen Zonen innerhalb des hell adaptierten Gebietes, auf den Einfluß einer Änderung der Größe des Prüfereizes, seiner

Helligkeit und der Größe des Adaptionsfeldes sowie auf Änderungen des Fixationsgrades und des Netzhautgebietes. Die Ergebnisse zeigen, daß die erste (schnelle) Phase der Erholung die Erholung vom Troxlereffekt darstellt, während die zweite (langsamere) Phase der Erholung von der normalen Helladaptation entspricht. Die gefundenen neuen Effekte stehen, wie sich zeigen läßt, in Übereinstimmung mit gewissen Erscheinungen, die frühere Forscher beobachtet haben und sie passen in eine Vorstellung von einer Grenzneutralisierung des visuellen Ablaufs des Troxlereffektes.

REFERENCES

- [1] See bibliography cited in references [4] and [5].
- [2] HOLTH, S., 1896, "Det normale Synsorgans indirekte Stirreblindhet og dens Betydning under Snysfeltundersøgelse", Norsk. Mag. for Laegevidenskaben, Kristiania (Tillaegshefte).
- [3] CLARKE, F. J. J., 1957, *Opt. Acta*, **4**, 69.
- [4] CLARKE, F. J. J., 1959, *Ph.D. Thesis*, London.
- [5] CLARKE, F. J. J., 1960, *Opt. Acta*, **7**, 219.
- [6] HECHT, S., and MANDELBAUM, J., 1939, *J. Amer. med. Ass.*, **112**, 1910.
- [7] MERTENS, J. J., 1955, *Opt. Acta*, **2**, 134.
- [8] CRAWFORD, B. H., 1937, *Proc. roy. Soc. B*, **123**, 69.
- [9] WINSOR, C. P., and CLARK, A. B., 1936, *Proc. nat. Acad. Sci., Wash.*, **22**, 283.
- [10] WRIGHT, W. D., 1946, *Researches on Normal and Defective Colour Vision* (London: Kimpton), p. 209.
- [11] CRAWFORD, B. H., 1947, *Proc. roy Soc. B*, **134**, 283.
- [12] BAKER, H. D., 1953, *J. opt. Soc. Amer.*, **43**, 798.
- [13] SCHOUTEN, J. F., and ORNSTEIN, L. S., 1939, *J. opt. Soc. Amer.*, **29**, 168.
- [14] JASPER, H. H., 1958, *Reticular Formation of the Brain* (Toronto: Little, Brown & Co.), p. 320.
- [15] KUFFLER, S. W., 1953, *J. Neurophysiol.*, **16**, 37.
- [16] BARLOW, H. B., 1953, *J. Physiol.*, **119**, 69.
- [17] BROWN, K. T., and WIESEL, T. N., 1959, *J. Physiol.*, **149**, 537.



The reflectivity of glass and aluminium gratings at grazing incidence below 1000 \AA †

by R. S. CRISP

Department of Physics, University of Western Australia, Nedlands, W.A.‡

(Received 23 September 1960)

Emission spectra of solids in the $40\text{--}1000 \text{ \AA}$ region may show a variety of different band shapes due to non-linear wavelength response of the diffraction grating used as dispersing element. It is concluded that aluminium is unsuitable as a grating material for use at grazing incidence and that glass is to be preferred.

Intensities predicted theoretically in various spectral orders do not agree with those observed for one particular glass grating. Where the ultimate in resolution is not required it is shown how to position a grating whose radius does not match the instrumental Rowland circle while still achieving good focus.

1. INTRODUCTORY AND INSTRUMENTAL

While the emission band spectra of a considerable number of solids have been published as the result of investigations using concave gratings at grazing incidence, little attention has been paid to any effect that the grating reflectivity may have had on the band shapes. O'Bryan [1] examined the response of a large number of gratings at normal incidence and more recently Sprague *et al.* [2] have given a theoretical treatment of grating reflectivity for grazing incidence and have verified some of their predictions experimentally. Other full treatments have been given by Mack *et al.* [3], Eckart [4], Beutler [5] and Stamm and Whalen [6].

The present instrument, which uses a 1 m radius concave grating mounted at an angle of incidence of 85° and a photomultiplier detector, has been described previously by Fisher *et al.* [7]. Spectra obtained, using two aluminium gratings, have been presented by the same authors and by Crisp [8]. Recent modifications have improved the working vacuum in the specimen chamber and the detection sensitivity. Spectra obtained under the new conditions and using a glass grating have been discussed by Crisp and Williams [9, 10] and Crisp [11].

Relevant dimensions and details of the two aluminium gratings and the one glass grating are contained in table 1.

The spectrometer was designed around grating A, and hence the machined Rowland circle has a radius of curvature of $1015.7/2 \text{ mm}$. The spectrometer and its contained grating were evacuated continuously to $2 \times 10^{-5} \text{ mm Hg}$ or better; while runs were actually being made liquid air in the spectrometer cold trap further reduced the pressure by a factor of 10. Gratings not in use were stored in air in the usual perspex containers. Where a grating was visibly dusty or its surface dull, it was cleaned with anaesthetic ether and swabs of grease-free cotton wool.

† The material in this article formed the basis of a paper given by the author at the Second Australian Spectroscopy Conference in Melbourne, June, 1959.

‡ Now at National Research Council, Ottawa.

Comparison of performance between the gratings was made by reference to the observed emission band shapes for $\text{Mg } L_{23}(250 \text{ \AA})$, $\text{Al } L_{23}(170 \text{ \AA})$ and $\text{Be } K(110 \text{ \AA})$. The shapes were assumed to be unaffected by the response of the photocathode whose sensitivity should not vary appreciably over the relatively small energy spread of a band. The validity of this assumption was checked for the case of aluminium L_{23} radiation by substitution of a Pt photocathode for the usual one of Cu-Be when the same band shape was observed.

Table 1. Grating data

Grating	Where ruled	Date ruled	Date installed	Material	Radius of curvature (mm)	Spacing (grooves per mm and \AA)
A (' N.P.L. ')	National Physical Laboratory, London	Feb. 1954	May 1955	Aluminium on glass	1015.7	567 17637
B (' Siegbahn ')	Nobel Institut Uppsala	Nov. 1956	Jan. 1957	Aluminium on glass	1016.3	1152 8681
C (' Glass ')	Nobel Institut, Uppsala	Pre 1953 See Rogers and Chalkin [12]	Feb. 1959	Glass	994.3	576 17361

2. RESULTS

The following is a brief historical summary of the salient experimental events :

May 1955.	Aluminium grating A installed.
November 1955.	First spectra obtained.
December 1955 to June 1956.	' Normal ' spectra from Mg, Al, Li, Cu and Be. No trace of intense $\text{C } K\alpha$ at 45 \AA .
July 1956	First distorted $\text{Al } L_{23}$ bands, rise in general background, decrease in reflectivity at 110 \AA .
December 1956 to January 1957.	Grating B gave normal spectra for $\text{Mg } L_{23}$ but very distorted band shapes for $\text{Al } L_{23}$.
June 1957 to January 1959.	Further deterioration of grating A with affected region extending beyond 250 \AA .
January 1959 to present.	Glass grating C in use with no distorted spectra except at 115 \AA .

2.1. The glass grating C

The band shapes for $\text{Mg } L_{23}$, $\text{Al } L_{23}$ and $\text{Be } K$ recorded using the grating C are shown in figure 1. Since the observed shapes for these bands were invariant when this grating was used, and since they agreed well with spectra published by

Skinner [13] and Cady and Tomboulion [14], the reflectivity curve of the 'glass' grating was assumed to be flat and was taken as a standard. The reflectivity curves for the other two gratings are then expressed not absolutely but relative to glass. One discontinuity occurs in the response of grating C at 115 Å. This is evident when the spectrum for Be K shown in figure 1 is compared with those shown in figure 2. Similar though less intense discontinuities have been observed previously [13] and ascribed to absorption by silicon L electrons.

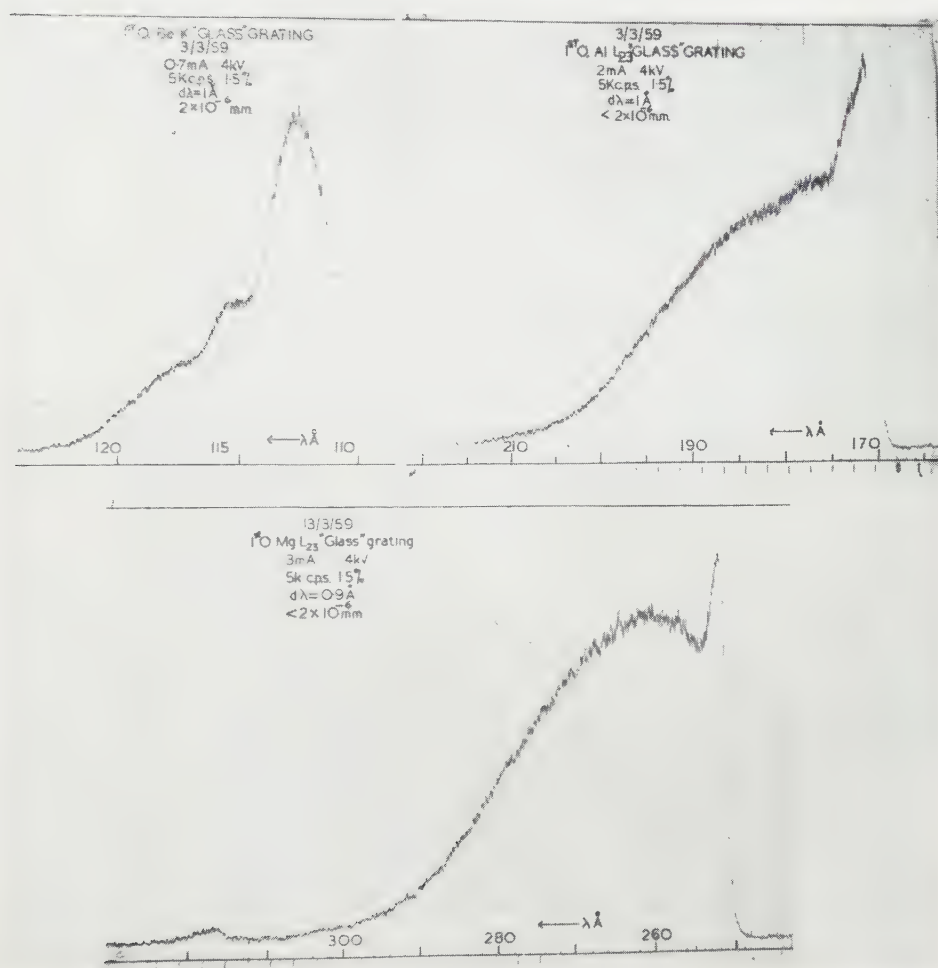


Figure 1. The Be K, Al L_{23} and Mg L_{23} band emission spectra recorded using grating C. The figure shows photographs of actual chart records. For each spectrum presented in this and succeeding figures, the date, order, spectrum, grating, target current and voltage, full scale counting range and error, optical resolution, target chamber pressure and an approximate wavelength scale are indicated on the chart. The chart speed was always one inch per minute.

A 'silicon absorption' curve constructed from the spectra of figures 1 and 2 resembles the absorption curve of Bedo and Tomboulion [15] only in the position

of an abrupt discontinuity at the silicon L absorption energy. Similar discontinuities due to characteristic absorption by other materials in the grating may be present but have not been observed, presumably because they do not happen to coincide with emission bands that have been examined. The continuum intensity is too low to reveal their presence.

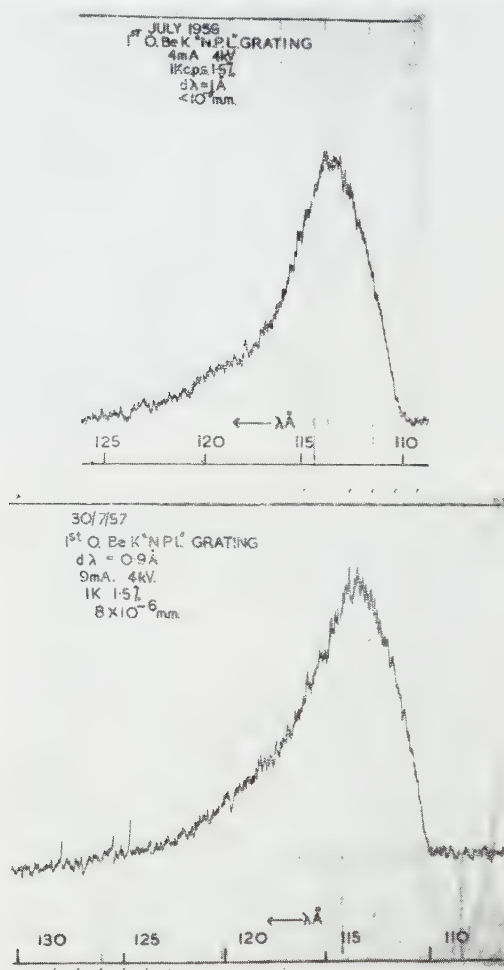


Figure 2. The Be K emission spectrum recorded on two occasions one year apart using grating A.

2.2. The aluminium grating A

Early spectra obtained with grating A have been published previously [7, 8]. Subsequent to July 1956, distorted AlL_{23} spectra were observed, accompanied by an increase in general background and a fall in spectrum intensity at 110 Å (cf. target powers and ratio of spectrum to background for the two Be K spectra shown in figure 2).

The grating was shown to be subject to 'contamination' by an unknown gas or vapour from the specimen chamber which entered the spectrometer via the

source slit, whose length and width were 1.2 cm and 50μ respectively. After the isolation valve had been opened for only an hour or so the shape of the Al L_{23} band was seen as shown in the upper left of figure 3, but it gradually changed to the shape shown in the lower left if the valve was left open for about six hours. This effect was observed irrespective of whether liquid air was used in the spectrometer cold trap or whether the gun was running or the beam was on the target. The specimen chamber cold trap was always used. Closing the isolation valve overnight allowed the grating to 'recover' to its earlier condition. The cycle

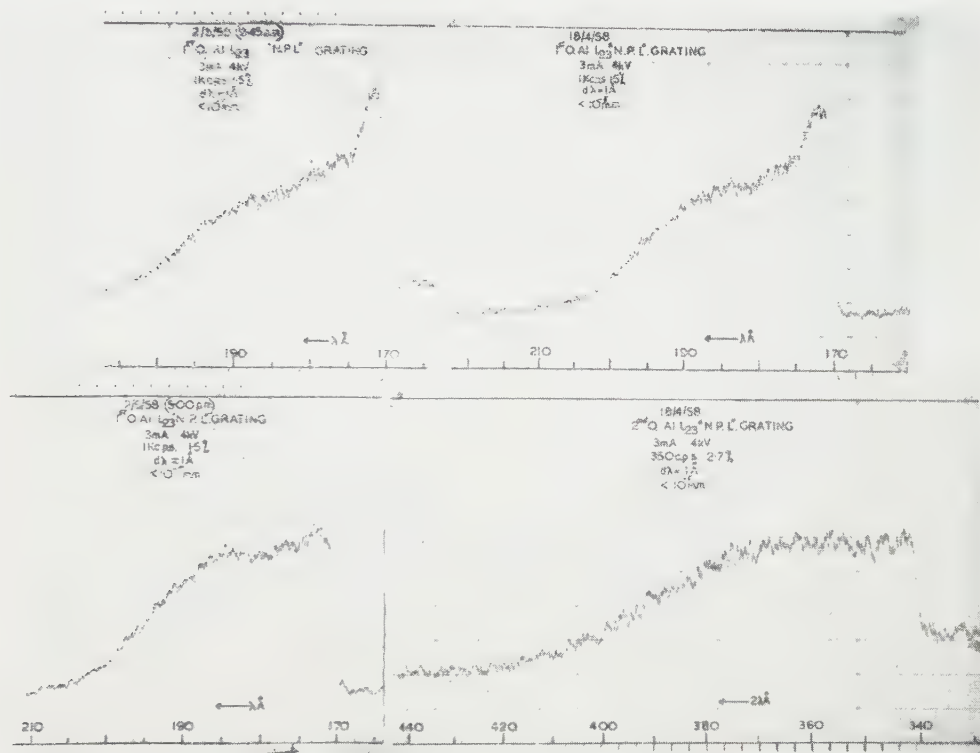


Figure 3. Examples of distorted Al L_{23} spectra recorded using grating A. For undistorted Al L_{23} recorded earlier using this grating see reference [7], figure 8.

was apparently repeatable indefinitely and was unaffected by subsequent improvements in specimen chamber vacuum and cold-trapping [10]. The two spectra on the right of figure 3 are for first and second order Al L_{23} , recorded within a few minutes of each other with the grating in its uncontaminated state. While the first order spectrum is not greatly distorted the second order shows no 'spike' at all. Figure 3 also illustrates the rise in general background between 18 April 1958 and 2 May 1958.

In the period between its installation and its replacement early in 1959, the response of grating A in the 250 Å region showed a gradual change which was evidenced by a modification of the observed band shape for Mg L_{23} . The ratio of the intensity of the peak at 250 Å to that of the hump at 265 Å has been used as

a measure of the shape of the band [8]. Figure 4 shows three Mg L_{23} spectra, two first order which illustrate the decrease in the measured value of the ratio over some months, as well as a typical second order spectrum which shows a high value for the ratio and which did not subsequently show the same change as the first order spectra. The observed spectra for Mg L_{23} did not show the short

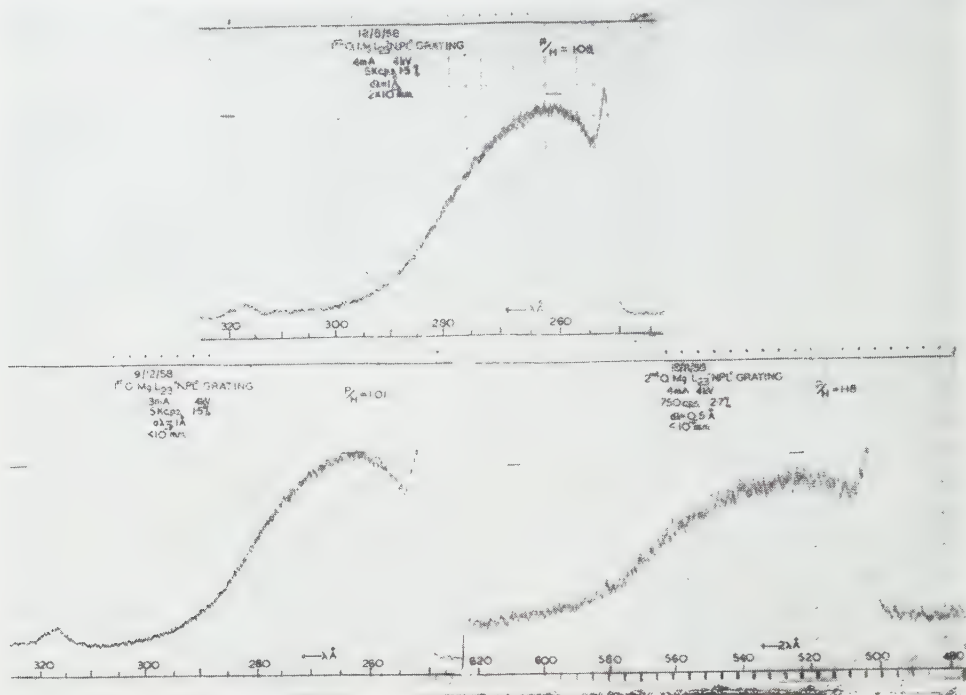


Figure 4. Mg L_{23} spectra recorded using grating A ($d\lambda$ in the spectrum on the lower right should be 1 Å not 0.5 Å).

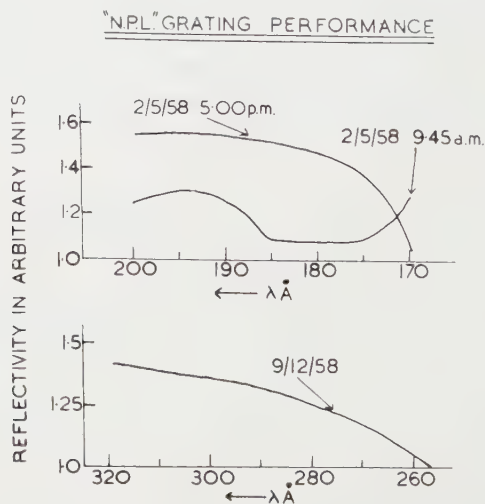


Figure 5. Reflectivity versus wavelength curves for grating A.

term contamination and recovery effects illustrated by the Al L_{23} bands in figure 3. Figure 5 shows reflectivity curves constructed for the 170 Å and 250 Å regions from spectra in figures 3 and 4.

2.3. The aluminium grating B

The grating B was substituted for grating A to obtain better resolution due to its greater dispersion. This grating gave a 'normal' Mg L_{23} spectrum ([7], figure 7), very low intensity at 110 Å for the Be K band and the utterly unrecognisable Al L_{23} spectra shown in figure 6. These are first and second order spectra recorded with the grating in each of the two possible orientations differing

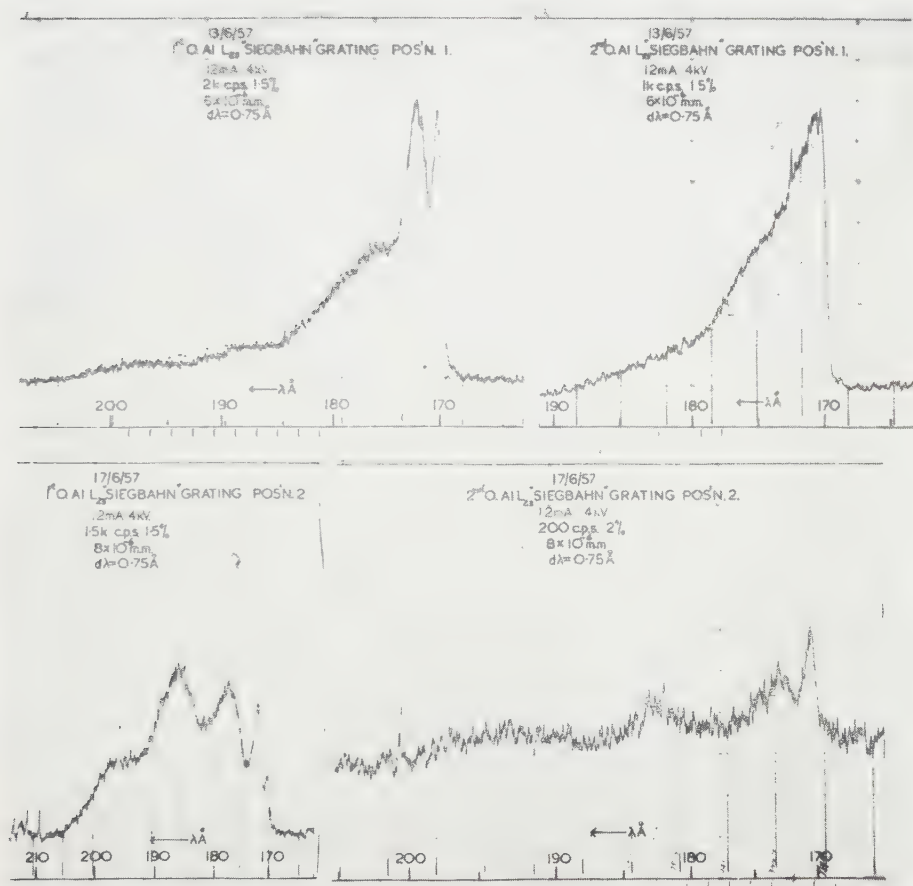


Figure 6. Distorted Al L_{23} spectra recorded using grating B.

from each other by 180° rotation about the normal. Reflectivity curves for three of these four spectra are shown in figure 7. The Mg L_{23} spectra observed with either of the two orientations agreed closely with the spectrum for Mg L_{23} in figure 1.

2.4. Background

Cady and Tombouliau [14] have quoted figures for the intensities of background relative to band spectrum for various metal targets. Table 2 contains

their data, those from the present measurements using the glass grating C and values obtained by measurement of the photometer curves published by Skinner [13]. Both aluminium gratings gave considerably higher backgrounds than the glass grating, as can be seen by inspection of figures 1, 2, 3, 4 and 6.

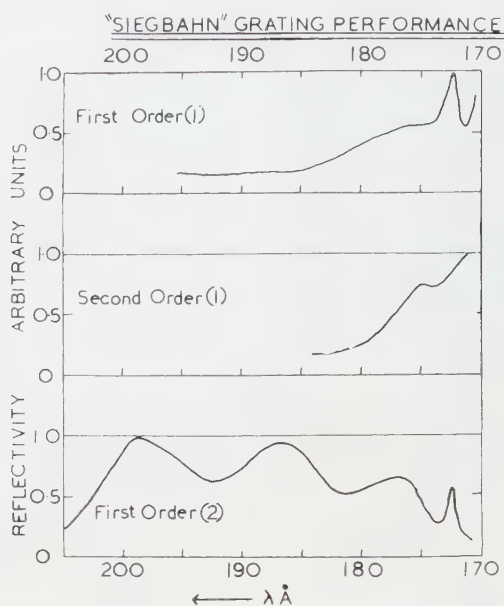


Figure 7. Reflectivity versus wavelength curves for grating B constructed from the spectra of figure 6.

Table 2. Ratio of band spectrum to background observed by various authors

Author	Na L_{23}	Mg L_{23}	Al L_{23}	Be K
Cady and Tomboulia [14]	1.7	7	11	—
Present (grating C)	25	26	30	63
Skinner [13]	1.7	3.9	3.2	3.4

The values for the present case are approximate in so far as they are critically dependent on the value of a *small* background.

3. THE DISTRIBUTION OF INTENSITY AMONG SPECTRAL ORDERS

It has been shown theoretically [2] that there is a short wavelength limit, λ_c , below which a particular spectral order should not be observed. It has also been shown that above this critical wavelength the intensity in a particular spectral order should increase smoothly as the wavelength increases.

While the intensity distribution among spectral orders for the aluminium grating A followed this picture qualitatively, that for the glass grating C did not. The peak intensities observed for the orders of CK (45 Å), BK (68 Å), BeK (110 Å), Al L_{23} (170 Å) and Mg L_{23} (250 Å) are shown in figure 8 where the intensities normalized to first order are plotted against the apparent wavelength. In figure 9 the data of figure 8 are replotted as reflectivity curves. With the

present set-up it was not convenient to measure the intensity of the direct image, nor was it possible to make absolute comparisons of reflectivity at different wavelengths, since this involves a knowledge of the true relative intensities of the emission bands.

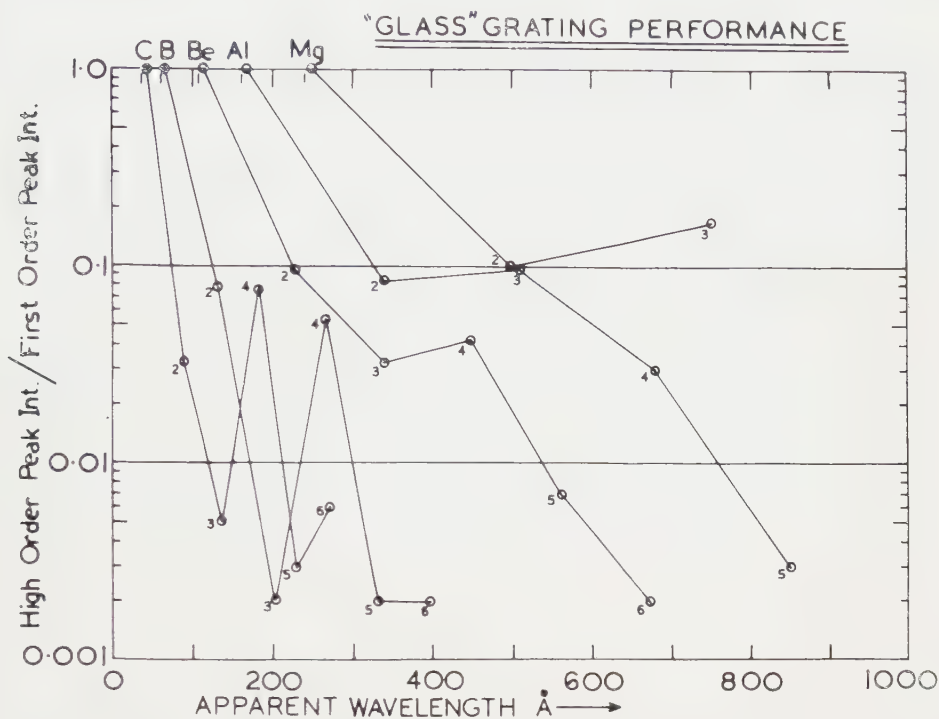


Figure 8. Plot of observed intensities versus apparent wavelength for spectral orders of grating C. The order is indicated by a figure near each plotted point while the emission bands used are indicated at the top of the figure.

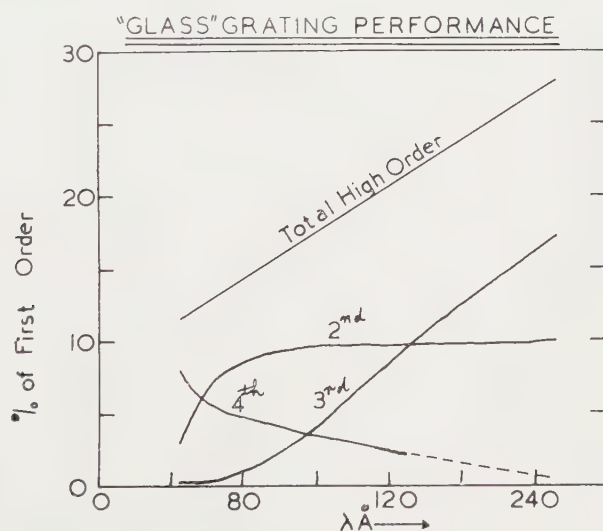


Figure 9. Data of figure 8 replotted to show variation of reflectivity as a function of order and wavelength for grating C.

4. DISCUSSION

The results detailed above illustrate how the performance of a concave grating, when used at grazing incidence, is strongly affected by the nature of the grating surface. Moreover, it is shown that the reflectivity of aluminium gratings is very variable and spectra obtained using such gratings should be viewed with caution. Glass as a grating material has the virtue of invariability of performance, and in the present cases a higher reflectivity at short wavelengths. This is in contrast to the usual preference for aluminium for use in the vacuum ultra-violet at normal incidence [16].

While no completely satisfactory explanation is forthcoming for the behaviours of the two aluminium gratings, the facts taken together show that the theoretical results when applied to real cases are likely to be modified by

- (i) Absorption and reflection coefficients of the grating material.
- (ii) The nature and distribution of any contaminant film.
- (iii) The presence of any ruling 'feathers' which may modify the intensity distribution in the diffracted radiation by means of selective absorption and reflection.

A partial explanation can be proposed which postulates a feather of the order of 1000 \AA high, but it is very difficult to visualize a mechanism which will be sufficiently sensitive to wavelength or diffraction angle, to explain for example the 'fine structure' in the spectra observed in figure 6. That the groove shape is intimately involved is shown by the profound effect that 180° rotation of the grating may have on the observed band shape.

The background observed in the present case is significantly lower than that observed by previous photographic workers. In the photographic case, the observed background consists of clear plate deflection, scatter from the grating, fogging by visible light (and possibly by stray electrons) together with a small contribution from the true x-ray continuum. For the photocathode of the detector used in the present case the photo-electric threshold is about 3000 \AA , while the multiplier has been rendered insensitive to charged particles by suitable selection of the operating potentials of the photocathode and shields. In addition, the background count rate due to electrical noise is zero, and hence the observed background will consist of true continuum plus scatter from the grating. The present figures indicate that the true continuum intensity is very low indeed, even lower than has been previously suggested. It is not possible to separate the two components due to continuum and scatter, but since irregularities in grating reflectivity (eg. at 115 \AA) are not visible in the background, the contribution by the continuum must be only a small percentage of the total. Skinner [13] has observed irregularities in grating reflectivity by means of the continuum. These observations were presumably made with very high target powers.

The reflectivity in various orders for the grating C displayed in figures 8 and 9 are different from the expected theoretical distribution [2] and show that the reflectivity at a particular diffracting angle is also a function of the true wavelength. The observed effects cannot be explained by a simple blaze. For instance at 510 \AA the relatively weak second order of 250 \AA coincides in diffracting angle with an enhanced intensity of the third order of 170 \AA . It is seen that the

summed curves of figure 9 give a straight line, whereas the theoretical result indicates a parabola-like variation. Apart from the anomalous relative intensities among orders, the critical wavelengths below which particular orders should not have appeared were not confirmed. The expressions for λ_c may be written explicitly as:—

$$\lambda_c = - \frac{\frac{N}{a\delta} \pm \sqrt{\left[\left(\frac{N}{a\delta}\right)^2 + 4\left(\frac{1 - \cos \phi}{\delta}\right)\right]}}{2}.$$

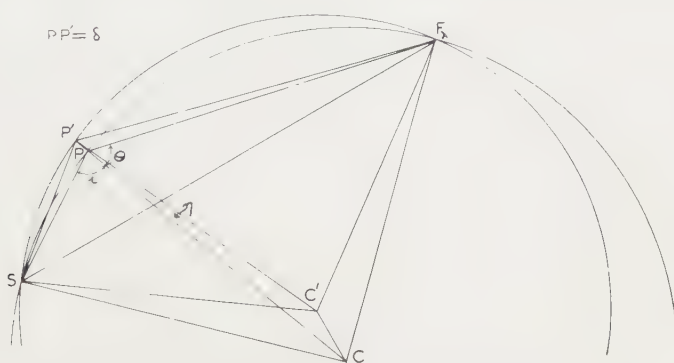
For the present constants and for values of N from 0 to -6 this gives λ_c values of 39 Å, 51 Å, 65 Å, 82 Å, 100 Å, 119 Å and 139 Å respectively. These predictions are not substantiated by figure 8, where for example, spectra as high as sixth order are seen for 45 Å radiation.

It is interesting to note that the important factor for determining the critical wavelength for *high* order spectra is the grating spacing, while for low and zero orders the angle of incidence is much more significant.

As with the anomalous behaviour of the aluminium gratings, a partial explanation for the intensities observed in various orders can be put forward which involves a ruling feather, although once again it is difficult to postulate a mechanism which is sufficiently and separately dependent on both the wavelength and the diffraction angle. It is unfortunate that time has not allowed the observation of intensities in spectral orders following 180° rotation of grating C about its normal.

5. GEOMETRY FOR CONCAVE GRATING OF 'WRONG' RADIUS

In a grazing incidence instrument the machined arc which defines the path of the photomultiplier (or to which the photographic plate is bent) must be made accurately with its radius of curvature half that of the grating. If several gratings are to be interchangeable in the one instrument, then their radii must be identical if a perfectly focused image of the source slit is to be produced on the machined circle for all wavelengths. However, by suitably positioning the grating pole a certain amount of mismatch of the two radii can be tolerated without serious loss of resolution. The Rowland circle of the grating and the machined circle of



GEOMETRY FOR FOCUSING GRATING WITH "WRONG" RADIUS

Figure 10. Geometry for positioning a grating of the 'wrong' radius of curvature in order to achieve focus at a selected wavelength.

different radii, may be so positioned that they intersect at any two selected points. For sharp focus the first of these must be chosen to be the source slit. The other may then be chosen to place the focus point of any desired wavelength λ on the machined circle. This will give a range of approximate focus for wavelengths on either side of λ .

In figure 10, P is the pole of a grating of correct radius R , located on the machined circle, centre C and radius $R/2$ such that the angle of incidence of radiation from the source slit S is i and the diffraction angle for radiation of the chosen wavelength λ , which focuses at F_λ , is θ . The pole P' of the grating whose radius is R' has been displaced a distance δ along the radius of the machined circle, after which the grating has been rotated through an angle η to make the two circles intersect at S and F_λ , and place the centre of the Rowland circle at C'. It is then required to determine δ and η in terms of R , R' and i where it is assumed that the two gratings have the same spacing. Figure 10 is drawn for the case $R' < R$. From simple geometry it may be shown that:

$$\sin \eta = \left[\frac{2CC' \sin(i - \theta)}{R'} \right] \sim \eta,$$

$$\delta = \frac{1}{2} \left[\frac{R' \sin(i - \theta + \eta)}{\sin(i - \theta)} - R \right]$$

where CC' is given by

$$CC' = \frac{1}{2} (R \sin(i + \theta - 90) - R' \sqrt{[1 - R \cos^2(i + \theta - 90)/R']}).$$

For $R' > R$ the same expressions hold with negative signs for δ and η , showing that the translation and rotation must be made in the opposite sense from those shown in figure 10. For the present case in order to fit the glass grating C to the machined circle and selecting $\lambda = 170 \text{ \AA}$, it was found that

$$\delta = 0.37 \text{ mm},$$

$$\eta = 5.6'.$$

The new angle of incidence, $SP'C'$ is found to be $84^\circ 51.4'$ whereas SPC was 85° . Under these conditions for $\lambda = 100 \text{ \AA}$, the focused image is displaced 0.13 mm outside the machined circle while for $\lambda = 250 \text{ \AA}$ it is displaced 0.15 mm inside, and the loss in resolution is only a few per cent of the 0.9 \AA achieved with slit widths of 45μ and defined by the criteria of Fisher [17]. In any case, the limit of resolution in instruments such as the present is set by the curvature of the source slit image and the length of the analyser slit, rather than by the slit widths. For a 1 m grating with 570 grooves per mm and a 1.2 cm analyser slit length, the limit is a little better than 1 \AA . If narrower slits are to be used for improved resolution then the analyser slit must be either shortened or curved, preferably the latter if good counting statistics are to be retained. It is a simple piece of mathematics to correct the calibration table [7] which was calculated for a grating which fitted the machined circle, to take account of the position, radius and spacing of the grating C.

ACKNOWLEDGMENTS

The author wishes to acknowledge the help and guidance of his supervisor, Dr. S. E. Williams, and of Professor C. J. B. Clews. Professor A. G. McLellan University of Canterbury, N.Z. kindly loaned the glass grating which has proved invaluable to the project. The receipt of a Postgraduate Research Studentship from the Australian Atomic Energy Commission is gratefully acknowledged.

Les spectres d'émission des solides dans la région comprise entre 40 et 1000 Å peuvent présenter des bandes de formes différentes dues à la réponse non-linéaire en longueurs d'onde du réseau de diffraction utilisé en tant qu'élément dispersif. On trouve que l'aluminium ne convient pas en tant que matériau pour réseaux utilisés en incidence rasante et que le verre doit lui être préféré.

Les intensités prévues théoriquement dans divers ordres spectraux ne correspondent pas aux intensités observées avec un certain réseau en verre. Lorsque la résolution extrême n'est pas nécessaire, on indique la façon dont il convient de placer un réseau dont le rayon ne correspond pas au cercle de Rowland de l'instrument, afin d'obtenir quand même une bonne mise au point.

Die Emissionsspektren fester Körper in dem Bereich zwischen 40 und 1000 Å können eine Vielzahl von verschiedenen Bandenformen zeigen. Sie hängen mit einer nicht-linearen Wellenlängenwiedergabe des Beugungsgitters zusammen, welches man als dispergierendes Element verwendet. Es ergibt sich, dass Aluminium als Gittermaterial wenig geeignet ist, wenn man es bei streifendem Einfall benutzt, und daß Glas vorgezogen werden sollte.

Die Intensitäten, die sich theoretisch für die verschiedenen Spektralordnungen ergeben, stimmen nicht mit denen überein, die man für ein bestimmtes Glasgitter beobachtet. Wenn nicht das Äußerste an Auflösung verlangt wird, so läßt sich angeben, wie das Gitter aufgestellt werden muß, wenn sein Radius nicht mit dem Rowlandkreis des Instrumentes übereinstimmt. Auf diese Weise kann man trotzdem eine gute Schärfe erhalten.

REFERENCES

- [1] O'BRYAN, H. M., 1931, *Phys. Rev.*, **38**, 32.
- [2] SPRAGUE, G., TOMBOULIAN, D. H., and BEDO, D. E., 1955, *J. opt. Soc. Amer.*, **45**, 756.
- [3] MACK, J. E., STEHN, J. R., and EDLEN, B., 1932, *J. opt. Soc. Amer.*, **22**, 245.
- [4] ECKART, C., 1933, *Phys. Rev.*, **44**, 12.
- [5] BEUTLER, H. G., 1945, *J. opt. Soc. Amer.*, **35**, 311.
- [6] STAMM, R. F., and WHALEN, J. J., 1946, *J. opt. Soc. Amer.*, **36**, 2.
- [7] FISHER, P., CRISP, R. S., and WILLIAMS, S. E., 1958, *Opt. Acta*, **5**, 31.
- [8] CRISP, R. S., 1958, *Aust. J. Phys.*, **11**, 449.
- [9] CRISP, R. S., and WILLIAMS, S. E., 1960, *Phil. Mag.*, **5**, 525.
- [10] CRISP, R. S., and WILLIAMS, S. E., *Phil. Mag.* (in the press).
- [11] CRISP, R. S., *Phil. Mag.* (in the press).
- [12] ROGERS, J. L., and CHALKLIN, F. C., 1954, *Proc. phys. Soc., Lond. B*, **67**, 348.
- [13] SKINNER, H. W. B., 1940, *Phil. Trans. A*, **239**, 95.
- [14] CADY, W. M., and TOMBOULIAN, D. H., 1941, *Phys. Rev.*, **59**, 381.
- [15] BEDO, D. E., and TOMBOULIAN, D. H., 1956, *Phys. Rev.*, **104**, 590.
- [16] HASS, G., HUNTER, W. R., and TOUSEY, R., 1957, *J. opt. Soc. Amer.*, **47**, 1070.
- [17] FISHER, P., 1954, *J. opt. Soc. Amer.*, **44**, 665.



Measurement of the horizontal extent of Panum's Area by a method of constant stimuli

by D. A. PALMER
Imperial College, London†

(Received 8 September 1960)

It has long been accepted that simultaneous stimulation of any pair of corresponding points in the retinas will give rise to a single perceived image. Many experiments also suggest that around each point there is a region wherein fusion is still possible with the corresponding point in the other retina. The extent of this region of fusion, sometimes called Panum's Area, has not often been measured in the central fovea, and there has not been very good agreement between the results.

For these reasons, a new determination has been made by using a method of constant stimuli, or 'forced-choice'. The observer made judgments on a flashed test spot which was variable in depth. The percentage of replies 'spot single' was plotted against the parallax at which the test spot had appeared. This technique allowed measurements to be made in the fovea, and was found to give repeatable results, with good agreement between three observers.

The test spot was $1.5'$ in subtense and was presented at various visual angles from 0° to 6° . In the fovea, the region of single vision was found to be $15'$ to $20'$ in extent. A vertical line $45'$ in height was also used, and with this the extent of the area was found to be $25'$. The results appeared to be unaffected by the duration of the appearance of the test spot at least for exposures greater than 0.01 sec. The figures obtained are slightly greater than the average for previous results, but fall within their spread.

1. INTRODUCTION

The experiments which are to be described arose in the course of some investigations involving the phenomenon of fixation disparity [1]. It was noted in that work that two similar objects could be separated in depth by a parallax difference of more than $15'$ of arc before either appeared to be double. On examination of the literature on this subject, it was found that there were very large variations between the estimations of the parallax range over which an object could move, without giving rise to diplopia, under conditions of steady binocular fixation. In view of the discrepancies, it was considered that it might be desirable to make a new investigation of the subject.

2. REASONS FOR MAKING A NEW MEASUREMENT

Before Wheatstone's work on the stereoscope [2] it was never very certain what occurred to the axes of the eyes when the observer attempted to fixate on two objects separated in depth. Aguillon [3], for example, considered that there was a plane—the horizontal section of which he called the horopter—passing through the point of fixation normally to the line of sight, on which objects would have to be placed in order to appear single. Any objects not on the horopter

† Now at the National Physical Laboratory, Teddington.

would appear to be double, until the necessary adjustment had been made in the convergence of the eyes.

From this type of consideration, Müller [4] built up the concept of 'corresponding points'. Every point in one retina was supposed to have its fellow in the other, and simultaneous stimulation of each pair of such corresponding points would give rise to a single perceived image. If two images fell on non-corresponding points, the perceived image would be double. Wheatstone's work however implied that around each corresponding point, there must be an 'area' wherein fusion was still possible with the corresponding point in the other retina. This concept was elaborated by many other workers, particularly Helmholtz [5], Volkmann [6] and Panum [7], the name of the last being often given to the areas of fusion.

These concepts made the corresponding point theory appear rather tenuous, and on that account the 'area' theory itself has not been accepted without reserve. Brewster [8], for example, considered that single vision of more than one object separated in depth was achieved by a scanning process involving fairly rapid changes in convergence. More recently, le Grand [9] has suggested that in view of the large variations found in the extent of the areas of fusion, they might not be proper physiological entities at all, but artefacts, arising for example from the inexperience of the observers. He compares the figures for Panum's Area outside the fovea with the figures for the monocular acuity as measured there, and from the reasonably good agreement, suggests that Panum's Area is merely the result of the binocular counterpart to the process responsible for setting a limit to the monocular acuity. This conclusion is perhaps aided by the absence of data for the central fovea, where the monocular acuity rises so greatly, and where comparison with the area of fusion would be most interesting.

This absence is largely due to the nature of the methods employed in measuring the area. The test objects are usually two vertical lines, which are arranged to appear side by side, with a horizontal separation corresponding to twice the visual angle at which the area is to be measured. It is possible to estimate the extent of the region of single vision, by separating the lines in depth until one appears to be double (see, for example, Volkmann [6], French [10], Ogle [11]). This arrangement has the great disadvantage that the images of the two lines as seen by one or the other eye may sometimes appear to cross over as the binocular parallax between the lines is being altered. This is confusing to the observer and can be avoided only if the angular separation between the lines is sufficiently large in comparison with the parallax changes which have to be made in the experiment. This implies that measurements cannot be made at a visual angle of much less than one degree.

Rösch [12] overcame this difficulty by arranging the two test objects, which were points in his experiment, to appear one above the other in the central fovea, and he found that the threshold of diplopia varied from about $7'$ to $33'$. This seems to be one of the very few results obtained in this way.

3. DISCUSSION OF PROPOSED METHOD

In view of this undesirable situation, it was decided to measure the area of fusion again, particularly in the fovea, by a method which was suggested from a remark of Ogle's [11] that the limits of single vision are not well defined and

are probably a gradient of some sort where the probable appearance of fusion increases in a statistical manner towards the centre of the areas. In order to carry out an investigation based on this principle, it was decided to use a method of constant stimuli, or 'forced-choice'. The observer would be required to fixate binocularly on a target. A test spot would then be flashed on, displaced in depth from the fixation target. The observer would indicate whether the test spot had appeared to be single or double. The percentage of replies 'test spot single' could then be plotted against the position of the test spot in depth. Such a curve would show a maximum when the test spot was at the same depth as the fixation mark, and would fall to zero as the spot was moved in front or behind the fixation mark. The extent of the area for single vision would be determined by the region over which the spot appeared to be single, or by some other suitable criterion.

This experimental method depends on the accuracy with which an observer can maintain binocular fixation. An experiment will be described which indicates that this is possible within the terms of the experiment, to within three or four minutes of arc. It is also necessary to eliminate the effect of any large convergence movements resulting from the presence of the test spot. Westheimer and Mitchell [13] have found that no reaction to a convergence stimulus is observed until 0.2 sec has elapsed from the first appearance of the stimulus, so that the time of exposure of the test spot should be kept below this figure.

4. EXPERIMENTAL PROCEDURE

For the experiments, the stereoscope which has already been described was employed [1, 14]. This was an optical instrument designed to facilitate the superposition of a number of binocular images, with provision for introducing small and measurable amounts of parallax between them. The parallax could be controlled by moving weak lenses in slides, which worked between the elements of the parts of the optical system which projected one set of images on to the other.

The field of the stereoscope was dark, except for two white fixation marks about 40' apart in the horizontal meridian. These were optically at infinity. The angular subtense between the marks was small enough to allow the observer to see both clearly at once. The space between the marks was left dark to provide an area for the appearance of the test spot. The observer was asked to direct his attention to this space, where after a word of warning, the test spot was flashed on by the operator. The binocular image of this test spot was formed by masking the filaments of two tungsten bulbs by means of knife edges, to form a square about 1.5' in subtense. The spot appeared for a duration of about 0.01 sec under the action of a shutter in the projection system of the stereoscope. The observer indicated whether the spot had appeared single or double. The experiment was repeated, whilst varying the parallax of the spot in a random way among chosen values, until enough replies had been obtained to plot a graph of the percentage of replies 'single' against the parallax (figure 1). A minimum of ten replies was obtained for each position of the spot; the actual number has been given in brackets after the words '% single' on the vertical axes of the graphs. A positive parallax indicates that the spot had appeared in front of the fixation marks.

This experiment was also repeated with the spot located at various visual angles up to about 6° in the periphery, on the left side of the fixation marks (results plotted in figures 1 and 2). In order to obtain a comparison with the results of some other workers, the effect of lengthening the spot into a vertical line $45'$ in height was also investigated in the fovea (figure 3). With the small test spot in the fovea, the presentation time was increased to 0.17 sec to see if the exposure

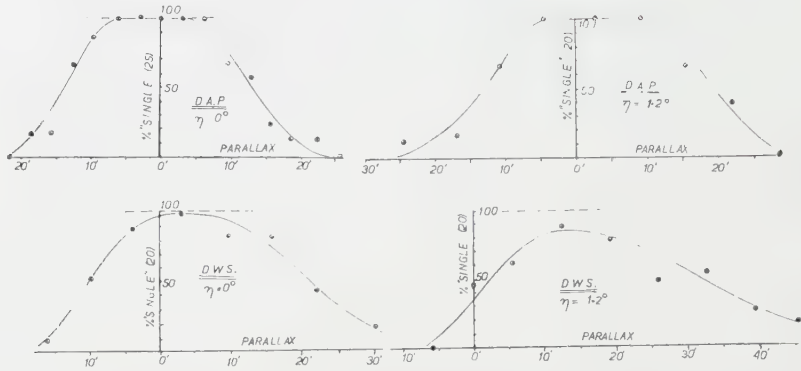


Figure 1. Percentage of replies 'spot single' plotted against parallax of spot in minutes of arc. Visual angle η , 0° and 1.2° . Exposure 0.01 sec.

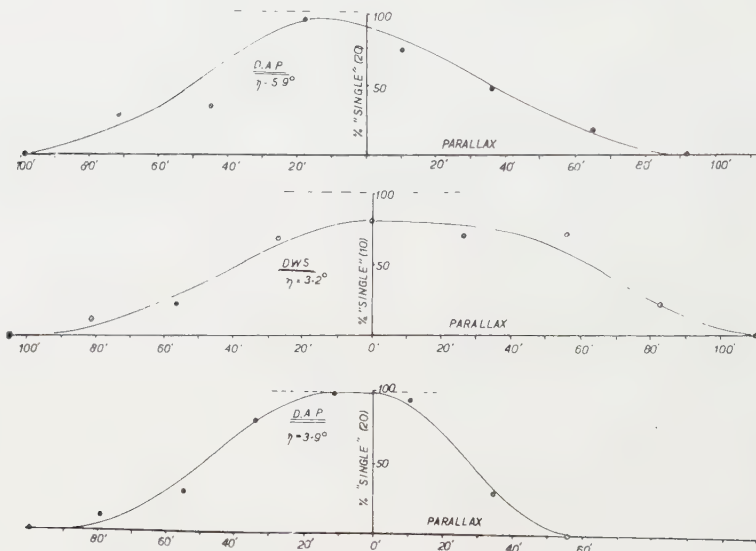


Figure 2. As figure 1, but with visual angles up to 6° .

had any effect on the results (figure 4). For this last experiment, the rest of the field was uniformly illuminated to produce about 10000 trolands of retinal illumination (2 mm pupils were used throughout all the experiments), to avoid a glaring appearance in the test spot. As the original bright fixation marks were now difficult to see, they were replaced by small black marks.

A 'monocular acuity' test was also arranged on the forced-choice principle, two spots similar to the binocular spot being employed, but visible to only one

eye, again for a presentation time of 0.01 sec. The percentage of replies 'single image' was plotted against the angular separation between the spots (figure 5), for comparison with the binocular results.

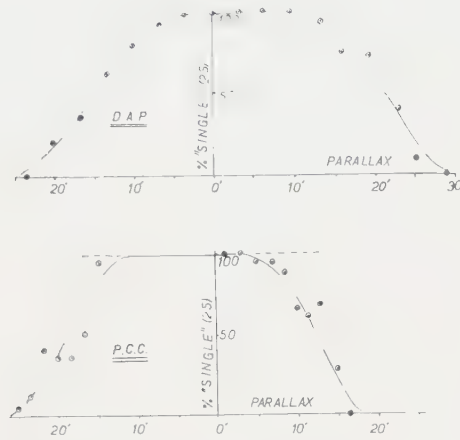


Figure 3. As figure 1, but with vertical line in fovea 45' in height.

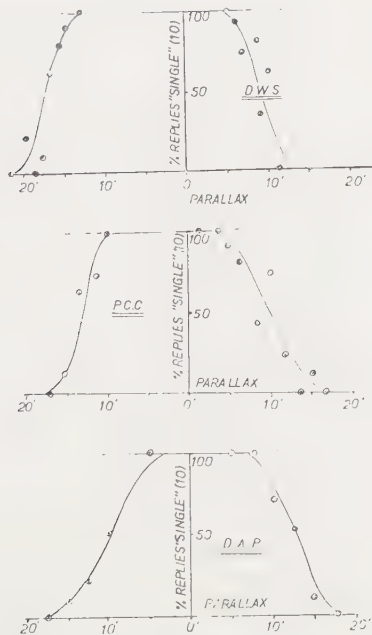


Figure 4. As figure 1, but with exposure increased to 0.17 sec.

D.A.P. also carried out an experiment with a continuously visible spot in the parafovea. It was found that the presence of the spot did not affect the binocular fixation by more than 2' or 3', provided that the visual angle was

greater than $1\frac{1}{2}^{\circ}$. (For this observation the convergence was measured by Ogle's [11] subjective technique.) It was thus possible to determine the extent of the region of single vision in the parafovea by moving the spot in depth and determining the points where the spot appeared to be just on the point of doubling. The results are plotted as circles in figure 6, which also contains all the results obtained by the forced-choice method, plotted as crosses for comparison. The criterion adopted in obtaining these figures will be discussed later, but briefly, the measurements were made between the points where the forced-choice curves had dropped to 83 per cent of their maxima.

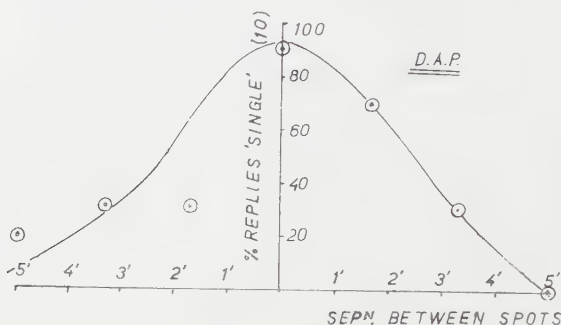


Figure 5. Monocular acuity experiment with two spots flashed in one eye for 0.01 sec. Percentage of replies 'image single' plotted against angular separation between spots in minutes of arc.

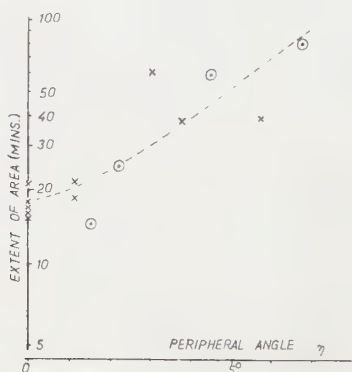


Figure 6. Extent of Panum's Area as estimated from all results plotted against visual angle η . Crosses represent results with flashed spot; circles, continuously visible spot.

As has been observed, the fixation targets had no detail in the central part of the field, to allow for an area in which the test spot could appear. To investigate how well binocular fixation could be maintained with such a target, a slightly modified form of the experiment was carried out, in which the two (monocular) images of the test spot were arranged to be separated in the vertical meridian, so that they could not be fused binocularly, and two images were always seen. A determination of the 'vernier acuity' with these two images was then performed, the parallax control being altered as before, except that this now varied

the alignment of the images, the test spots being flashed on for 0.01 sec. The observer was now asked to judge which spot had appeared to the right of the other. A graph was drawn of the percentage of replies 'upper spot to right of lower' against the physical angular separation between the spots (figure 7). The spread of this graph provides an estimate of the possible effect of convergence fluctuations.

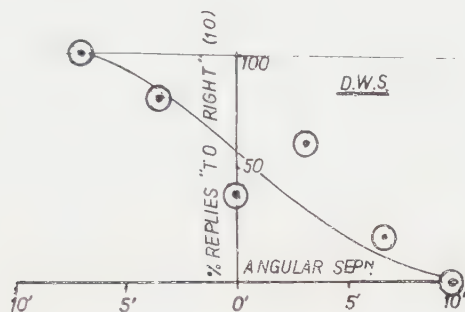


Figure 7. Effect of convergence fluctuations. Monocular images of spot separated vertically to prevent fusion. Percentage of replies 'upper image to right of lower' plotted against angular separation, in minutes, between images. Exposure time 0.01 sec.

5. DISCUSSION

Perhaps the most noteworthy aspect of the results is the good agreement between the three observers, especially in view of the large variability of previous investigations; as described by le Grand [9] for example; and no effects of 'training' were noticed. All the observers found the forced-choice experiments easy to perform, in the fovea at least.

It is not known whether any great significance should be attached to the position of the zero point on the parallax scale: whether for example, the area extends a greater distance in front than behind the fixation point. Probably the slight deviations shown in the mid-points of the graphs are due to the error in determining the point on the parallax scale where the test spot was equidistant with the fixation marks. This error does not affect the parallax scale itself, which was a relative measure, and was probably accurate to within 1'.

Before deciding on figures for the extent of Panum's Area from these results, it is necessary to consider some possible factors which might affect the measurements. It was possible for example, that convergence fluctuations in the eyes could influence the apparent extent of the area of fusion. As figure 7 shows however, fluctuations of this kind did not often exceed 3', which is a much smaller figure than that for the area.

It was also possible that the shortness of the presentation time, which was designed to arrest the effect of any convergence changes during observation, might nevertheless have some effect on its own account. For this reason, in some experiments the exposure was increased nearly twenty-fold to 0.17 sec (figure 4). There was no great difference to be found between the graphs for long and short presentation times, except for some sharpening up in the boundaries

of the area with the longer exposure, which was probably due to a greater confidence of the observers. The slope of the boundary of the area with the longer exposure has a magnitude which would be expected if the convergence movements were its only cause, so that it is possible that the boundaries are really quite sharp.

The finite size of the spot could also be a factor increasing the apparent size of the area, and for this reason, the subtense of the test spot was reduced to 1.5'. Figure 5 shows that any effect from this cause was small.

The area of single vision is thus of considerable extent, of the order of 10' in the fovea, but the statistical nature of the results makes it necessary to adopt some criterion in order to extract an exact figure. In the parafovea, the results are also somewhat confused by the curves obtained by D. W. S. (figures 1 and 2). This observer's graphs never reach the 100 per cent single level. On questioning D. W. S., it appeared that he had been disregarding the actual position of the spot in depth. D. A. P. on the other hand, who reaches the 100 per cent level more often, was influenced by the knowledge that when the test spot appeared to be level with the fixation mark, it ought also to be single, although he attempted to disregard this clue. The difference between the two observers' results is only slight and this indicates that the effect was not serious. In this region outside the central fovea, it was of course more difficult to make an estimation of the appearance of the spot, so that there was probably some guesswork, which would tend to dilute the results, and lower the level of the maximum.

It was decided to adopt the criterion that the area should be measured between the points where the curves had dropped to about 83 per cent of their maxima. This is the 'standard deviation' level of the Gaussian error function, and it seemed reasonable therefore, that at this value, the spot would be considered to be just on the point of diplopia. The agreement obtained by D. A. P. with the continuously visible spot using a similar criterion, seemed to justify this choice. The agreement between these two methods (figure 6) also supports the conclusion that the extent of the area is unaffected by the presentation time, at least for exposures longer than 0.01 sec.

With these considerations taken into account, the foveal value for Panum's Area would be about 15' to 20' for a spot as test object, and about 25' for a vertical line. These values are rather larger than some previous results: Ogle, [11], for example, quotes a figure of about 10' near the central fovea for vertical lines; but the present figures fall within the spread of the other investigators's results (see, for example, le Grand [9]).

Not all the previous results are strictly comparable, because of the differences in the experimental techniques, but it seems very possible that some of the variations found in the past may have been due to the statistical nature of this type of experiment and to the differing criteria which may therefore be adopted by various observers. The forced-choice method seems to be superior in the respect that it gave good agreement between the three observers, and also in that it allowed measurements to be made in the central fovea.

ACKNOWLEDGMENTS

The author wishes to thank Professor W. D. Wright for his encouragement and advice. The assistance of the observers, especially of Mr. D. W. Stonelake, is gratefully acknowledged.

Il a été admis pendant longtemps qu'en stimulant simultanément une paire de points correspondants sur les rétines on obtient une seule image perçue. Beaucoup d'expériences suggèrent aussi qu'autour de chaque point il existe une région où il est toujours possible d'obtenir la fusion avec le point correspondant de l'autre rétine. L'étendue de cette région de fusion, appelée parfois Aire de Panum, n'a pas été souvent mesurée dans la partie centrale de la fovea, et il n'y a pas eu très bon accord entre les résultats déjà obtenus.

Etant donné ceci, il a été procédé à une nouvelle détermination en utilisant une méthode de stimuli constants, ou 'choix forcé'. L'observateur devait porter des jugements sur une tache test variable en profondeur et présentée pendant une très brève durée. On traçait ensuite le pourcentage de réponses 'tache unique' en fonction de la parallaxe à laquelle la tache test était apparue. Cette technique permettait des mesures dans la fovea, avec des résultats reproductibles et un bon accord entre les trois observateurs.

La tache test avait une étendue angulaire de $1,5'$ et elle était présentée pour divers angles de vision depuis 0° jusqu'à 6° . Il a été trouvé que, dans la fovea, la région de vision unique était de $15'$ à $20'$. Il a été utilisé aussi un trait vertical de $45'$ de hauteur, et, dans ce cas, l'étendue de l'aire a été trouvée être de $25'$. Les résultats ne paraissent pas dépendre de la durée de l'apparition de la tache test, du moins pour des durées plus grandes que $0,01$ sec. Les nombres obtenus sont légèrement plus grands que la moyenne des résultats antérieurs, mais se situent à l'intérieur de leur dispersion.

Es steht seit langem fest, dass die gleichzeitige Reizung eines Paares korrespondierender Punkte auf der Netzhaut beider Augen nur einen einzigen Bildeindruck ergibt. Zahlreiche Versuche lassen auch vermuten, dass um jeden Punkt ein gewisses Gebiet liegt, innerhalb dessen eine Fusion mit dem korrespondierenden Punkt der anderen Netzhaut möglich ist. Die Ausdehnung dieses Verschmelzungsgebietes, das zuweilen Palmer-Bereich genannt wird, ist für die zentrale Fovea ziemlich wenig gemessen worden, und die Resultate zeigen keine gute Übereinstimmung.

Deswegen wurde eine neue Bestimmung mittels konstanter Reize unter einem 'Entscheidungszwang' durchgeführt. Der Beobachter traf seine Entscheidungen an einem aufblitzenden Prüffleck, der in seiner Tiefe veränderlich war. Der Prozentsatz der Antwort 'Einzelpunkt' wurde gegen die Parallaxe aufgetragen, unter der der Punkt erschien. Dieses Verfahren liess Messungen in der Fovea zu und lieferte fünf reproduzierbare Ergebnisse mit einer guten Übereinstimmung bei drei Beobachtern.

Der Prüffleck hatte eine Ausdehnung von $1,5'$ und wurde unter wechselnden Blickwinkeln zwischen 0° und 6° dargeboten. In der Fovea ergab sich für das Gebiet des Einzeldrucks eine Ausdehnung von $15'$ bis $20'$. Es wurde auch ein vertikaler Strich von $45'$ Höhe benutzt und damit ein Gebiet von $25'$ gefunden. Die Ergebnisse scheinen von der Dauer der Darbietung des Testes unabhängig zu sein, wenigstens bei Expositionen von mehr als $0,01$ sec. Die erhaltenen Zahlen sind nur wenig grösser als der Durchschnitt der früheren Ergebnisse, aber sie fallen noch in den Streubereich.

REFERENCES

- [1] PALMER, D. A., 1958, Ph.D. Thesis, University of London.
- [2] WHEATSTONE, C. W., 1838, *Phil. Trans.*, **2**, 371.
- [3] AGUILLON, F., 1613, *Opticorum Libri*, Vol. 6 (Antwerp).
- [4] MÜLLER, J., 1826, *Beiträge zur vergleichenden Physiologie des Gesichtsinns* (Leipzig), p. 71.
- [5] HELMHOLTZ, H., 1925, *Physiological Optics*, Vol. 3 (Optical Society of America), p. 400.
- [6] VOLKMANN, A. W., 1856, v. Graefes *Arch. Ophthalm.* II, 2, 1.
- [7] PANUM, P. L., 1858, *Physiologische Untersuchungen über das Sehen mit zwei Augen* (Kiel).
- [8] BREWSTER, D., 1856, *The Stereoscope, its History and Construction* (London).
- [9] LE GRAND, Y., 1956, *L'Optique Physiologique*, Vol. 3 (Paris : Editions de la Revue d'Optique), p. 211.
- [10] FRENCH, J. W., 1922-23, *Trans. opt. Soc., Lond.*, **24**, 226.
- [11] OGLE, K. N., 1950, *Binocular Vision* (Philadelphia : Saunders).
- [12] RÖSCH, J., 1943, *Actualités sci. industr.*, **944** and **945**.
- [13] WESTHEIMER, G., and MITCHELL, A. M., 1956, *Arch. Ophthalm.*, N.Y., **55**, 848.
- [14] PALMER, D. A., 1960, *Photogramm. Rec.*, **7**, 357.



Restitution des images aberrantes par le filtrage des fréquences spatiales

III. Restitution de l'image prise avec un filtre à deux foyers

par JUMPEI TSUJIUCHI
Institut d'Optique, Paris†

(Manuscrit reçu le 13 Juillet 1960)

On étudie la méthode de filtrage des fréquences spatiales pour rétablir la perte de contraste dans l'image due à l'emploi d'un filtre à deux foyers qui compense l'aberration de l'objectif de prise de vue. On constate que l'effet de l'aberration peut être parfaitement supprimé par ces deux procédés: mise d'un filtre compensant l'aberration et filtrage des fréquences spatiales, sans que l'influence de la partie zéro du facteur de transmission des fréquences spatiales de l'objectif de prise de vue se fasse sentir.

1. INTRODUCTION

Dans la deuxième partie de ces études [1], nous avons étudié la restitution de l'image formée par un objectif dont le facteur de transmission des fréquences spatiales comprend une partie négative et des zéros. Nous avons montré que la perte d'information à la prise de vue ne peut pas être retrouvée par cette méthode, et donc que la restitution n'est pas encore parfaite pour l'image dont la connaissance préalable de l'objet n'est pas suffisante pour compenser cette perte de l'information dans l'image restituée.

Si le but de la restitution est d'améliorer la qualité des images d'un objectif aberrant, ou d'augmenter la profondeur de champ, on peut envisager une méthode dans laquelle on utilise un filtre compensant l'aberration tel que le filtre à deux foyers employé lors de la prise de vue en éclairage incohérent [2]. Mais, l'image obtenue par cette méthode a un contraste très faible, et il n'est pas suffisant pour une image comme image photographique dans laquelle un grand contraste est nécessaire.

Nous avons donc essayé la combinaison de ces deux méthodes, c'est-à-dire la restitution de l'image obtenue par l'utilisation d'un filtre à deux foyers. On a une possibilité par cette méthode d'améliorer la qualité de l'image obtenue par un objectif aberrant sans souffrir de l'influence de la perte de l'information dans l'image.

2. CARACTÈRES DE L'IMAGE OBTENUE AVEC UN FILTRE À DEUX FOYERS

Soit x la coordonnée radiale normalisée dans le plan de pupille circulaire d'un objectif stigmatique définie par

$$x = X/L, \quad (1)$$

où X est la coordonnée géométrique dans ce plan et L le rayon de l'ouverture de la pupille, et soit $W(x)$ l'aberration de défaut de mise au point qui s'exprime par

$$W(x) = \frac{1}{2} \alpha^2 \delta x^2 \quad (2)$$

† Adresse présente: The Government Mechanical Laboratory, Suginami-ku, Tokio, Japon.

où δ est le défaut de mise au point et, si B est la distance entre le plan de pupille et le plan de l'image, α s'exprime par

$$\alpha = L/B \quad (3)$$

d'où la fonction pupillaire $f(x)$

$$f(x) = \exp ikW(x) \quad (4)$$

avec $k = 2\pi/\lambda$ (figure 1).

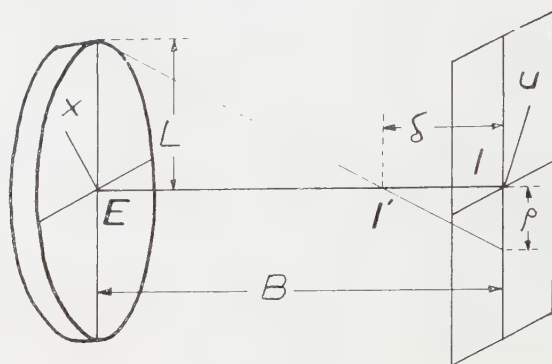


Figure 1.

Considérons maintenant un filtre à deux foyers [2] qui compense cette aberration. La transmission d'amplitude de ce filtre est

$$t(x) = \cos kW(x), \quad (5)$$

et la fonction pupillaire du système composé par un objectif avec un défaut de mise au point et le filtre devient

$$f_t(x) = f(x)t(x) = \left(\frac{1}{2}\right) [1 + \exp 2ikW(x)]. \quad (6)$$

Ce filtre est pratiquement préparé comme filtre déphasant dont le déphasage est donné par [2]

$$P(x) = 0 \quad \text{pour} \quad \cos kW(x) > 0 \\ = \pi \quad \text{pour} \quad \cos kW(x) < 0, \quad (7)$$

autrement dit, la fluctuation sinusoïdale d'amplitude $t(x)$ est remplacée par une fluctuation rectangulaire, l'équation (5) est donc exprimé par

$$t(x) = \frac{4}{\pi} \sum_{n=0}^{\infty} \frac{(-1)^n}{2n+1} \cos (2n+1) kW(x) \quad (8)$$

et la fonction pupillaire (6) devient

$$f_t(x) = f(x)t(x) = \frac{2}{\pi} \sum_{n=0}^{\infty} \frac{(-1)^n}{2n+1} \{ \exp [2(n+1)kW(x)] + \exp [-2nkW(x)] \}. \quad (9)$$

Si l'on considère une coordonnée radiale normalisée dans le plan de l'image comme

$$u = k\alpha U, \quad (10)$$

où U est la coordonnée géométrique dans ce plan; la répartition d'amplitude dans l'image d'un point est donnée, à un facteur constant près, par la transformée de Hankel de l'expression (9):

$$A(u) = 2 \int_0^{\infty} f_t(x) J_0(ux) x dx \\ = \frac{2}{\pi} \left[A_0(u) + \sum_{n=1}^{\infty} (-1)^{n-1} \left(\frac{1}{2n-1} - \frac{1}{2n+1} \right) A_{2n}(u) \right] \quad (11)$$

avec

$$\left. \begin{aligned} A_0(u) &= 2 \int_0^\infty J_0(ux) x dx, \\ A_{2n}(u) &= 2 \int_0^\infty \exp[i2nkW(x)] J_0(ux) x dx, \end{aligned} \right\} \quad (12)$$

où $A_0(u)$ correspond à la répartition d'amplitude dans l'image d'un point formée par l'objectif stigmatique et $A_{2n}(u)$, à celle d'un objectif dont l'aberration est $2n$ fois celle de l'objectif. La répartition d'intensité est donnée par :

$$\begin{aligned} I(u) &= |A(u)|^2 \\ &= \left(\frac{2}{\pi}\right)^2 \left[|A_0(u)|^2 + \sum_{n=1}^\infty \left(\frac{1}{2n-1} - \frac{1}{2n+1}\right)^2 |A_{2n}(u)|^2 \right. \\ &\quad + 2 \sum_{n=1}^\infty (-1)^{n-1} \left(\frac{1}{2n-1} - \frac{1}{2n+1}\right) A_0(u) A_{2n}(u) \\ &\quad \left. + \sum_{n=1}^\infty \sum_{n'=1, n' \neq n}^\infty (-1)^{n+n'} \left(\frac{1}{2n-1} - \frac{1}{2n+1}\right) \left(\frac{1}{2n'-1} - \frac{1}{2n'+1}\right) \times A_{2n}(u) A_{2n'}'(u) \right]. \end{aligned} \quad (13)$$

Dans ces conditions, si l'aberration $W(1) = W$ est assez grande, les termes en $A_n A_{n'}$ sont négligeables et

$$I(u) \doteq \left(\frac{2}{\pi}\right)^2 \left[|A_0(u)|^2 + \sum_{n=1}^\infty \left(\frac{1}{2n-1} - \frac{1}{2n+1}\right)^2 |A_{2n}(u)|^2 \right]. \quad (14)$$

La transmission des fréquences spatiales s'obtient en prenant la transformée de Hankel de l'expression (14)

$$\begin{aligned} H(x) &= 2 \int_0^\infty I(u) J_0(xu) u du / 2 \int_0^\infty I(u) u du \\ &= 2 \int_0^\infty I(u) J_0(xu) u du / 2 \int_0^\infty |f_1(x)|^2 x dx \\ &\doteq \left(\frac{2}{\pi}\right)^2 \left[H_0(x) + \sum_{n=1}^\infty \left(\frac{1}{2n-1} - \frac{1}{2n+1}\right)^2 H_{2n}(x) \right] \end{aligned} \quad (15)$$

avec

$$\left. \begin{aligned} H_0(x) &= 2 \int_0^\infty |A_0(u)|^2 J_0(xu) u du / 2 \int_0^\infty |A_0(u)|^2 u du, \\ H_{2n}(x) &= 2 \int_0^\infty |A_{2n}(u)|^2 J_0(xu) u du / 2 \int_0^\infty |A_{2n}(u)|^2 u du, \end{aligned} \right\} \quad (16)$$

c'est-à-dire que $H_0(x)$ est la transmission des fréquences spatiales de l'objectif stigmatique et $H_{2n}(x)$ celle de l'objectif ayant $2n$ fois plus d'aberration que l'original.

Mais, si l'on pose $x=0$ dans l'équation (15), on obtient

$$\begin{aligned} H(0) &= \left(\frac{2}{\pi}\right)^2 \left[1 + \sum_{n=1}^\infty \left(\frac{1}{2n-1} - \frac{1}{2n+1}\right)^2 \right] \\ &= 1 - \left(\frac{2}{\pi}\right)^2 < 1; \end{aligned}$$

ce résultat signifie que les composants interférentiels dans l'équation (13) ne sont pas négligeables tandis qu'ils ne dirigent guère la structure de l'image, et alors ils causent une distribution uniforme sur l'image dont le spectre correspond approximativement à $\delta(x)$. On peut donc écrire

$$H(x) = \left(\frac{2}{\pi}\right)^2 \left[1 + \sum_{n=1}^\infty \left(\frac{1}{2n-1} - \frac{1}{2n+1}\right)^2 H_{2n}(x) + \delta(x) \right]. \quad (17)$$

Comme W est assez grand, le calcul de (15) et (16) peut être fait dans l'approximation de l'optique géométrique. D'abord on peut considérer que

$$|A_0(u)|^2 = \delta(u), \quad (18)$$

on a donc

$$H_0(x) = 1, \quad (19)$$

et puis, en posant ρ le rayon étendu de l'image originale d'un point, on peut écrire

$$\begin{aligned} |A_{2n}(u)|^2 &= 1 & u < 2n\rho \\ &= 0 & u > 2n\rho. \end{aligned} \quad (20)$$

Alors, les équations (16) et (20) donnent [1]

$$H_{2n}(x) = \frac{2J_1(4nkWx)}{4nkWx} \quad (21)$$

et, par conséquent, l'équation (17) peut s'écrire

$$H(x) = \left(\frac{2}{\pi}\right)^2 \left[1 + \sum_{n=1}^{\infty} \left(\frac{1}{2n-1} - \frac{1}{2n+1} \right)^2 \frac{2J_1(4nkWx)}{4nkWx} + \delta(x) \right] \quad (22)$$

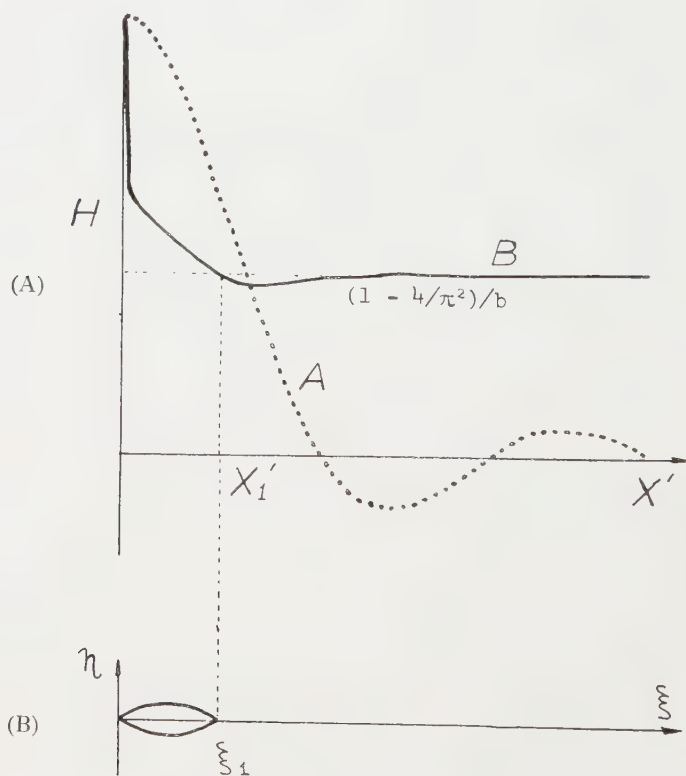


Figure 2. Spectre à restituer et courbes à dessiner.

(A) spectre à restituer: A spectre original et B spectre compensé par le filtre à deux foyers.

(B) Courbes à dessiner sur le disque tournant pour la préparation du filtre absorbant.

On trouvera dans la figure 2(A) une comparaison de $H(x)$ et la courbe originale. On peut constater qu'une forte décroissance de $H(x)$ dans la région des très

basses fréquences cause une perte de contraste dans l'image. On peut facilement trouver que la valeur de $H(x)$ reste toujours positive pour toute la région de fréquence, autrement dit, l'information de l'objet qui est perdue dans le système original peut être retrouvée par l'emploi de ce filtre lors de la prise de vue.

3. RESTITUTION

Puisque la transmission des fréquences spatiales de l'objectif muni d'un filtre à deux foyers est, comme on l'a vu dans ce qui précède, toujours positive, la restitution de l'image du système peut être faite par l'utilisation d'un filtre absorbant dans le restituteur [3]. En posant X' la coordonnée géométrique dans le plan du filtre dans le restituteur, on a

$$X' = (B'/B) Lx \quad (23)$$

où B' est la distance entre le cliché à restituer et le plan du filtre. La transmission d'amplitude du filtre qu'on met dans le restituteur devient [3]

$$F(X') = \frac{1}{b} \frac{i}{H(X')} \quad (24)$$

où b est une constante définie, en appelant D_0 la densité maximum du filtre, par

$$b = 10^{D_0/2}. \quad (25)$$

Pour la réalisation d'un filtre de restitution, on peut négliger le troisième terme $\delta(x)$ dans l'expression (16) si l'on utilise une émulsion ayant haut 'gamma' pour enregistrer l'image restituée. On peut aussi négliger les composants au-dessus de $n=2$ dans le deuxième terme puisque leur contribution à $H(x)$ est très faible. Le spectre à restituer devient alors

$$H(x) = \frac{1}{\pi^2/4 - 1} \left[1 + \frac{4}{9} H_2(x) \right]. \quad (26)$$

On a donc, d'après (24) et (26)

$$F(X') = \frac{\pi^2/4 - 1}{b} \frac{1}{1 + \frac{4}{9} H_2(X')}. \quad (27)$$

Ce filtre absorbant est préparé par un procédé photographique dans lequel on utilise un disque tournant [1]. Appelons maintenant, comme on l'a vu dans la deuxième partie de ces études [1], $\eta = g(\xi)$ la courbe qu'on dessine sur ce disque à l'aide des coordonnées rectangulaires (ξ, η) , on a

$$\begin{aligned} g(\xi) &= \left(\frac{b}{\pi^2/4 - 1} \right)^{\gamma/2} \xi \left[1 + \frac{4}{9} H_2(\xi) \right]^{\gamma/2} \\ &\doteq \left(\frac{b}{\pi^2/4 - 1} \right)^{\gamma/2} \left[\xi + \frac{4}{9} \frac{\gamma}{2} \xi H_2(\xi) \right]. \end{aligned} \quad (28)$$

Le premier terme de cette équation donne une distribution uniforme d'absorption sur le filtre. En fait, pratiquement, on n'a besoin d'atténuer le spectre que pour $X' < X'_1$, où X'_1 est la première racine de $H_2(X') = 0$. Avec les données numériques de [1] on trouve

$$X'_1 = 0,30 \text{ mm}, \quad (29)$$

et d'après l'équation (27)

$$b = \pi^2/4 - 1 = 1,47 \quad (30)$$

et enfin, d'après l'équation (25)

$$D_0 = 0,33. \quad (31)$$



Figure 3. Image restituée: (A) image originale, (B) image obtenue par la mise du filtre à deux foyers et (C) image restituée à partir de (B).

Dans ces conditions, le premier terme de la courbe (28) peut être négligé et on a finalement, d'après (21), (28) et (29)

$$g(\xi) = a' J_1(\xi) \quad \text{pour} \quad \xi \leq \xi_1' \quad (32)$$

où ξ_1' est la première racine de $J_1(\xi) = 0$ et a' une constante (figure 2 B).

Nous avons dessiné quatre paires des courbes

$$\pm \eta = \pm a' J_1(\xi), \quad \pm \xi = \pm a' J_1(\eta)$$

sur un disque noir en gardant blanches les régions comprises entre chaque paire de courbe. Nous l'avons photographié de telle façon que le rayon de la partie blanche corresponde exactement à X_1' et que la densité maximum soit 0,33 environ. L'émulsion que nous avons choisie est 'Collodium' de Guillemot.

Le cliché à restituer est préparé en photographiant l'objet à l'aide d'un objectif photographique ($f = 200$ mm, 1:6, 3, $B = 216$ mm) avec un filtre à deux foyers (for 10,8 λ pour une ouverture de 11 mm) sur une émulsion 'Panatomic' de Kodak développé par D78 avec $\gamma \div 1$.

Le filtre et le cliché ainsi obtenus sont également immergés respectivement dans chaque lame de phtalate de buthyle entre deux plaques de verre bien polies pour éviter le déphasage de la surface d'onde qui traverse ces émulsions dans le restituteur.

4. RÉSULTATS DE LA RESTITUTION

Dans la figure 3, nous avons montré les résultats de l'expérience. (A) est l'image originale avec un défaut de mise au point de 10,8 λ prise sans filtre à deux foyers, (B) l'image prise avec le filtre à deux foyers, et (C) l'image restituée de (B) par le filtre absorbant dans le restituteur.

On peut reconnaître dans ces résultats que l'image (B) est très améliorée sur (A), mais le contraste est très faible. Dans l'image (C), le contraste est bien augmenté par la restitution et on ne peut pas reconnaître la décroissance de la fidélité de l'image à l'objet comme on l'a vu dans la restitution directe de (A) et dans l'augmentation simple de contraste de l'image photographique [4].

5. CONCLUSION

La perte de contraste dans l'image fournie par l'objectif muni d'un filtre à deux foyers est rétablie à l'aide d'un filtre absorbant placé dans le restituteur. L'image ainsi obtenue est parfaitement nette, et la fidélité de l'image à l'objet n'est pas abimée. L'augmentation du contraste de l'image photographique est déjà étudiée par une méthode analogue [4], mais, pour l'image dont le contraste est abimé par un filtre à deux foyers, la restitution peut être faite plus raisonnablement.

On peut constater que la même méthode de restitution est valable pour l'image obtenue à l'aide d'un filtre compensant une aberration quelconque de l'objectif de prise de vue en utilisant de nouveau la fonction $H_2(X')$ dans chaque cas.

Cette méthode est un autre aspect du problème de la 'restitution' de l'image aberrante, mais, comme on l'a vu dans ce qui précède, si le but de la restitution est d'améliorer la qualité de l'image d'un objectif dont la compensation d'aberration est très difficile, elle sera une solution très efficace pour améliorer son image. On le rencontrera au moment de la photographie d'un objet bougeant avec une grande profondeur de champ en éclairage faible, ou au moment d'une prise de vues en éclairage infrarouge ou ultraviolet.

REMERCIEMENTS

Ces études, la deuxième et la troisième, ont été faites sous la direction de Monsieur le Professeur André Maréchal en tant que travail d'attaché de recherches du Centre National de la Recherche Scientifique en France. Je tiens à exprimer ma gratitude à Monsieur A. Maréchal qui a bien voulu m'instruire au cours de ces études, et également aux chercheurs de l'Institut d'Optique pour leurs nombreux conseils.

A study has been made of a method of spatial frequency filtering to restore the contrast in the image formed by means of a two-focus filter compensating the aberration of the taking objective. It is shown that the effect of the aberration can be completely removed by these two processes, using a filter to compensate the aberration and then spatial frequency filtering, without loss from the zero part of the response function of the taking objective.

Man kann die Aberrationen eines Aufnahme-Objektives durch die Verwendung eines Bifokalfilters herabsetzen und den Kontrastverlust im Bilde durch eine Frequenzfilterung wiederherstellen. Auf diese Weise kann der Einfluß des Aberrationen durch diese beiden Schritte vollkommen unterdrückt werden: Beseitigung der Aberration und Filterung der Linienfrequenzen. Der Einfluß des Null-Bereichs der Kontrastübertragungsfunktion des Objektivs bleibt dabei unmerklich.

RÉFÉRENCES

- [1] TSUJIUCHI, J., 1960, *Opt. Acta* (à paraître).
- [2] TSUJIUCHI, J., 1958, *Rev. d'Opt.*, **37**, 1.
- [3] TSUJIUCHI, J., 1960, *Opt. Acta*, **7**, 243.
- [4] MARECHAL, A., CROCE, P., et DIETZEL, K., 1958, *Opt. Acta*, hors série, 256.

ERRATA

Opt. Acta, 1960, **7**, 243.

Restitution des images aberrantes par le filtrage des fréquences spatiales

par JUMPEI TSUJIUCHI

Institut d'Optique, Paris

p. 243 après le titre, insérer un sous-titre :

(I) Restitution de l'image dont le spectre reste positif

p. 244 dans les équations (2), au lieu de $u_1 = k\alpha_1 U_1 / m_{12}$ et

$$v_1 = k\alpha_1 V_1 / m_{12}, \text{ lire } u_1 = k\alpha_1 U_1, v_1 = k\alpha_1 V_1 \text{ et } U_2 / U_1 = V_2 / V_1 = m_{12}.$$

p. 246 dans les équations (16), au lieu de $u_4 = k\alpha_4 m_{34} U_4$ et

$$v_4 = k\alpha_4 m_{34} V_4, \text{ lire } u_4 = k\alpha_4 U_4, v_4 = k\alpha_4 V_4 \text{ et } U_4 / U_3 = V_4 / V_3 = m_{34}.$$

The optical performance of windows with axial temperature gradients

by J. V. RAMSAY

Division of Physics, National Standards Laboratory, C.S.I.R.O.,
Sydney

(Received 2 August 1960)

The effect of an axial temperature gradient on the optical performance of a plane parallel window is discussed. It is shown theoretically that an incident plane wave front is not deformed significantly on traversing the window. However, appreciable angular deviation can occur, leading to distortion in the image of an extended object.

Experiments which support these results are described and a method is indicated for reducing the effect of air turbulence arising at the window surfaces.

1. INTRODUCTION

In solar telescopes image deterioration is often caused by turbulence in the optical path on the image side of the objective. One possible method of overcoming this trouble might be to control the temperature of the image space using the objective or a specially inserted window as a thermal barrier between the image and object spaces. A similar set of thermal conditions is encountered with windows used in aerial mapping and reconnaissance. It is therefore of interest to consider the performance of windows when their surfaces are at different temperatures.

Related problems have been discussed previously. Couder [1] has discussed the deformation produced in large mirrors, and more recently Sliusarev [2] has considered the case of a radial temperature gradient in a window. Miskin [3] in an unpublished report has considered the deviation of rays traversing a window having an axial temperature gradient.

1.1. Terminology

In this paper the term *deformation* is restricted to a variation in the shape of the wave front, *angular deviation* to a change in the direction of the normal to the wave front, *bending* to the change in the shape of the window and *distortion* to a variation in magnification across the image of an extended object.

2. BASIC THEORY

Consider a plane parallel window one face of which is maintained at a temperature T_1 and the other at T_2 . It can be shown (Love [4]) that this results in pure bending, the surfaces of the window taking up the form of concentric spheres having radii

$$\left. \begin{aligned} R_1 &= \frac{t}{\alpha(T_2 - T_1)} \\ R_2 &= R_1 + t, \end{aligned} \right\} \quad (1)$$

and

where α is the linear coefficient of thermal expansion and t the thickness of the window.

It follows that, for unit temperature difference between the faces, such a window introduces a deviation δ radians in the rays traversing it given by

$$\begin{aligned}\delta &= -\alpha[\tan I - \tan I'] \\ &= -\alpha \left[\tan I - \frac{\sin I}{(n^2 - \sin^2 I)^{1/2}} \right],\end{aligned}\quad (2)$$

where I and I' are respectively the angles of incidence and refraction at the first surface and n the refractive index; this result was first obtained by Miskin. Values of δ/α obtained from (2) are plotted in figure 1 as functions of I for several refractive indices.

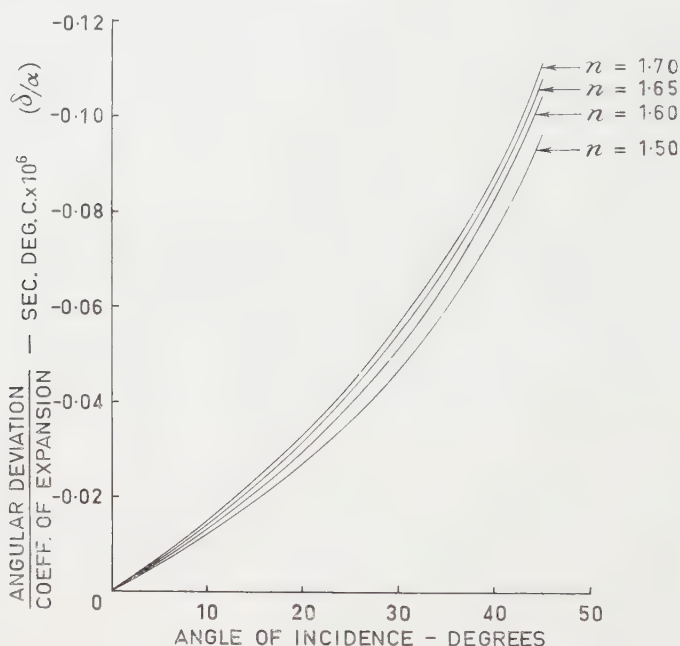


Figure 1. Deviation, for unit temperature difference, of a ray traversing a window subject to an axial temperature gradient for various refractive indices n .

In all practical cases the bending of the window is so small that, for a parallel beam, the angle of incidence, and hence the deviation, is effectively constant across the surface. For example, for $I=45^\circ$, the maximum variation in δ is 0.01 sec over a 10 cm aperture crown glass window 1 cm thick with a temperature difference of 50°C between the surfaces and with $\alpha = 6 \times 10^{-6} \text{ per } ^\circ\text{C}$. Therefore an incident plane wave emerges as a plane wave, though suffering a small deviation. Consequently the only effect of such a window on the performance of an optical system of which it may be considered a part is to cause distortion in the image of an extended object.

In design problems the window surface temperatures need to be estimated and this may be done by the usual heat transfer methods (Brown and Marco [5]).

Equation (2) shows that the total angular deviation is dependent only on the total temperature drop across the glass of the window. This temperature drop can be reduced by the use of a double air-spaced window. For example, in the case of a single window of a borosilicate crown glass, 2.26 cm thick with an airflow of 200 cm/sec across one face and 700 cm/sec across the other face, the total temperature drop across the window for a difference of 28°C in the air temperature on either side of the window is 4.5°C. For a double window made of two pieces of the same glass 1.13 cm thick, separated by an enclosed air space 0.5 cm thick and subjected to the same airflow across the outside faces as above, the temperature drops across the two glass components add to only 2.4°C.

3. EXPERIMENTAL PROCEDURE

3.1. Experimental arrangement

Some of the above results have been tested experimentally using a window in the wall of a temperature-controlled enclosure, the air in which could be maintained at some 35°C above the outside room air, this being controlled to a nominal 20°C. The experimental arrangement is shown diagrammatically in figure 2. E is the temperature-controlled enclosure, in one wall of which is

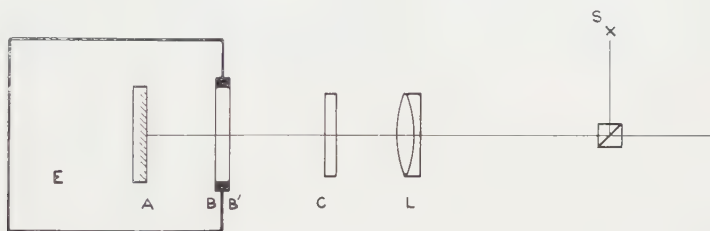


Figure 2. Schematic diagram of the interferoscope used to examine the bending of a window by an axial temperature gradient. For details consult § 3.1 of the text.

inserted a circular window BB' having a wedge angle of approximately 2 sec, a diameter of 12.5 cm and a thickness of 2.26 cm. The window is mounted so that its edge is thermally insulated from the mount by a piece of felt 0.7 cm thick. Provision is made for introducing a forced airflow across each face of the window. A and C are reference flats and L a lens which converts the system into an interferoscope. The light source is a water-cooled electrodeless ^{198}Hg lamp. Fizeau type fringes can be observed

- (1) between A and B indicating the shape of B,
- (2) between B and B' indicating the shape and parallelism of B and B',
- (3) between B' and C indicating the shape of B', and
- (4) between A and C showing any deformation of the wave front traversing the window.

Attempts to measure the surface temperatures with thermo-couples attached to the faces were unsuccessful, the heat transfer coefficients derived from the indicated temperatures showing poor agreement with published values (Brown and Marco). The surface temperatures have been measured more accurately by making a laminated window with the thermocouples inserted in the laminations

and extrapolating the temperatures so measured to the surface. This method gives results in fair agreement with published data.

3.2. *Experimental results*

Interference fringes between the faces B' and C are difficult to observe on account of turbulence arising near face B' due to the difference in temperature between the air and the face. Experimentally it is found that the fringes are steady if the air in the room is quite stagnant; if, as is usually the case, the room air is moving, steady fringes are obtained if a stream of air of sufficient velocity is directed across the face. The necessary velocity can be expressed very approximately as

$$V \geq 150 + 100T,$$

where V is in cm per sec and T is the temperature difference in $^{\circ}\text{C}$ between the air and the surface of the window. This relation holds for air velocities in the room up to 150 cm/sec.

Figure 3 shows interferograms illustrating the form of the surfaces and the optical quality of the window. The interferograms are arranged so that those marked (a) are the fringes between faces A and B, (b) between B and B', (c) between B' and C, and (d) between A and C. The fringes labelled (a) appear broken; this is the result of three-wave interference, the waves arising at A, B and B'. The relevant interference fringes, those due to waves arising at A and B only, are concentric with the fringe which is heavily marked. Analogous remarks apply to those labelled (c). Group 1 shows the interferograms when the enclosure E (figure 2) is at room temperature, Group 2 when the enclosure is 24.7°C above room temperature with no forced airflow across B but with an airflow of 1000 cm/sec across B', and Group 3 when the enclosure is 28.2°C above room temperature with a forced air stream of approximately 200 cm/sec across B and 1000 cm/sec across B'. The interferograms marked (a) and (c) show the increase in the curvature of the surfaces B and B' respectively under the influence of a temperature gradient which increases in the order Groups 1, 2 and 3. Those marked (b) show that the two surfaces of the window, B and B', remain approximately parallel with increasing temperature gradients whilst those marked (d) show the deformation of the wave front traversing the window. This latter effect is seen to be small, the asymmetry of the deformation being attributed to non-uniformities in the forced air streams, in particular that across B', which would introduce temperature variations across the face of the window. This view is based on the following demonstration.

Part of the non-uniformity in the airflow across B' arises from the presence of the test plate C. In order to achieve a more uniform flow, plate C was removed and the system tested by placing an autocollimated shearing interferometer at the focus of the lens L. The interferograms so obtained are shown in figure 3, Group 4; (f), (g) and (h) correspond respectively to the same thermal and air velocity conditions as in 1, 2 and 3 except that the airflow across B' is now more uniform. The asymmetry has disappeared for no airflow across B (4(g)). The introduction of an airflow across B causes an asymmetry to reappear. This is particularly noticeable in the two fringes at the top of the interferogram 4(h). These experiments have not been taken further as it has been found impracticable to improve the airflow uniformity inside the enclosure E.

Measurements of the interferogram 3*a* show the form of the surface to be spherical to within the limits of measurement ($\lambda/10$) and to have a radius of 5.5×10^4 cm. The use of published heat transfer data (Brown and Marco) and the thermal conductivity of BK7 glass (Morey [6]) gives a value of 6.1×10^4 cm for the radius, in fair agreement with that obtained experimentally.

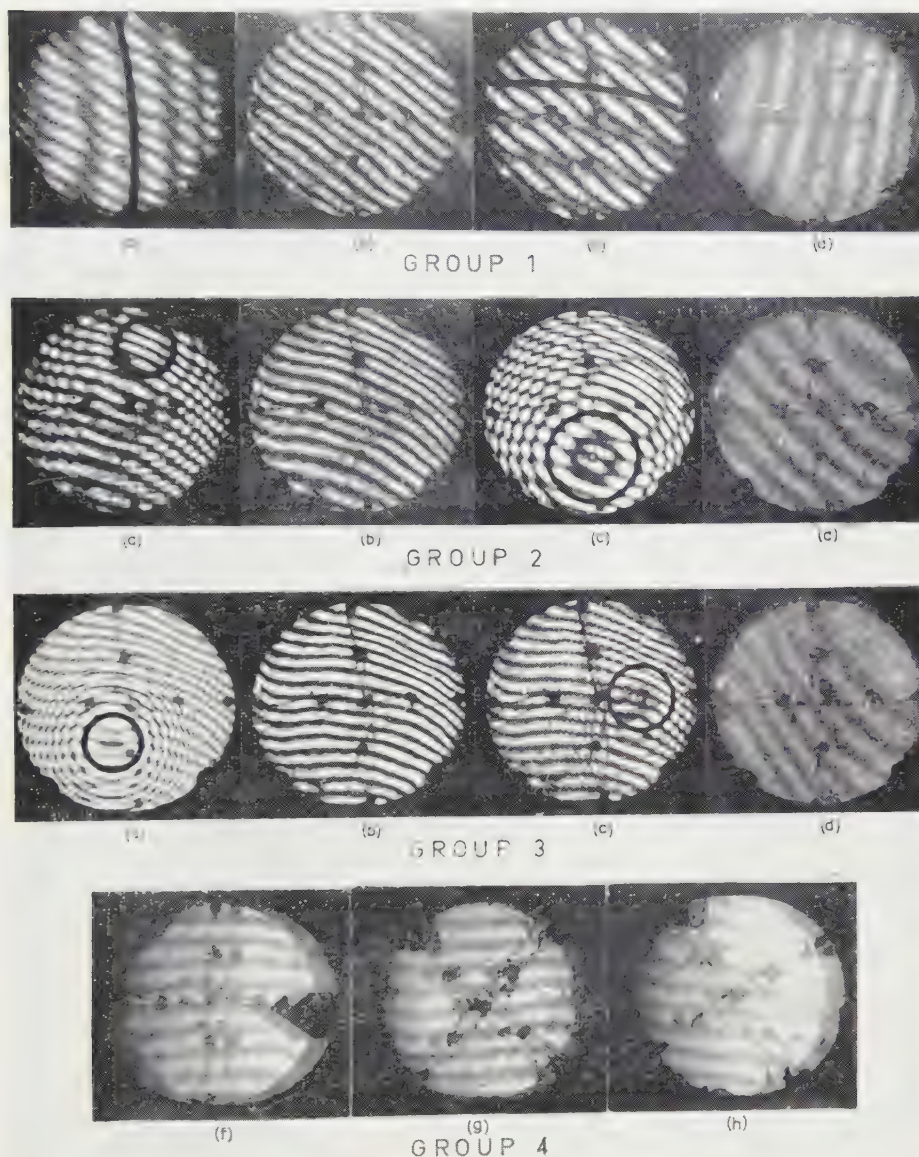


Figure 3. Interferograms showing the bending of a window used as a thermal barrier. Group 1 corresponds to zero temperature difference between inside and outside air, 2 and 3 to the temperature distributions discussed in § 3.2. Group 4 are sheared interferograms corresponding to conditions similar to 1, 2 and 3. (a) is the interferogram between A and B of figure 2, (b) between B and B', (c) between B' and C, and (d) between A and C. In (a) and (c) the relevant interference fringes are concentric with those heavily marked.

4. CONCLUSION

It has been shown that wave fronts traversing a window having an axial temperature gradient suffer an angular deviation but no deformation; the angular deviation amounts to 0.45 sec per °C temperature difference between the faces for waves inclined at 40° to the axis for a crown glass window. A double air-spaced window can be used to decrease this deviation. Turbulence arising at the faces of the window can be reduced to insignificant proportions if a uniform stream of ambient air of sufficient velocity is directed across the outer faces.

ACKNOWLEDGMENTS

The suggestion by Dr. R. G. Wylie and Mr. W. A. Caw to use a forced air stream to reduce turbulence is gratefully acknowledged.

On discute l'effet d'un gradient de température axial sur la qualité optique d'une fenêtre plan-parallèle. On montre théoriquement qu'une onde plane incidente n'est pas déformée de façon sensible à la traversée de la fenêtre. Toutefois, il peut y avoir une déviation angulaire appréciable, provoquant la distorsion de l'image d'un objet étendu.

On décrit des expériences qui confirment ces résultats et on indique une méthode pour réduire l'effet de la turbulence de l'air aux faces de la fenêtre.

Der Einfluss eines axial verlaufenden Temperaturgefälles auf die optische Güte eines planparallelen Glasfensters wird untersucht. Die Theorie ergibt, dass eine einfallende parallele Wellenfront beim Durchsetzen des Fensters nur unbeträchtlich gestört wird. Es kann jedoch eine merkliche Winkelabweichung auftreten, die zu einer Verzerrung des Bildes eines ausgedehnten Objektes führt.

Es werden die Versuche zur Bestätigung dieser Theorie mitgeteilt, und es wird ein Weg gezeigt, um den Einfluss der Luftbewegung in der Nähe der Fensterflächen zu verringern.

REFERENCES

- [1] COUDER, M. A., 1931, *Bull. astr. Mem. Varieties*, **7**, 201.
- [2] SLIUSAREV, G. G., 1959, *Optika i Spektroskopia*, **7**, 134.
- [3] MISKIN, E. A., 1957, British Ministry of Supply unpublished report.
- [4] LOVE, A. E., 1944, *Treatise on Mathematical Theory of Elasticity*, 4th edition (New York: Dover Publications).
- [5] BROWN, A. I., and MARCO, S. M., 1942, *Introduction to Heat Transfer* (New York and London: McGraw-Hill Book Co.).
- [6] MOREY, G. W., 1954, *The Properties of Glass*, 2nd edition (New York: Reinhold Publishing Corp.).

CORRESPONDENCE

Approximate synthesis of a prescribed diffraction pattern by means of different aperture distributions

by LUIGI CAPRIOLI†, ANNA MARIA SCHEGGI
and GIULIANO TORALDO DI FRANCIA

Centro di Studi per la Fisica delle Microonde, Firenze, Italia

(Received 5 October 1960)

It is well known, both in optics and in antenna theory, that one and the same power radiation pattern can be obtained by means of different phase and amplitude distributions over a radiating aperture. This is due to two reasons. In the first place the phase distribution of the prescribed radiation pattern is not specified, and can be chosen at will; in the second place one can have different source distributions which differ from one another for non-radiative terms (evanescent waves).

For some practical applications, it is useful to determine the aperture distribution which can be realized in the easiest way and in particular to require the phase of this distribution to present no discontinuity or even to show the smallest possible variations over the aperture. For this purpose we have applied an approximate method which is especially suitable for numerical computations. This method is related to the sampling theorem [1, 2] and takes advantage of the fact that the phase of the prescribed pattern is inessential; it is substantially analogous to the method described by Woodward [3] for the determination of an amplitude and phase distribution over a finite one-dimensional aperture which yields an approximation to a specified radiation pattern.

Let x be the abscissa on a one-dimensional aperture (the extension to the two-dimensional case is straightforward), D the width of the aperture, α the sine of the radiation angle and $A(\alpha)$ the complex amplitude at infinity. We will consider a set of sampling points α_n equi-spaced by λ/D , where λ is the wavelength. Let $A(\alpha_n)$ represent the value of the prescribed radiation pattern for $\alpha = \alpha_n$. The expression

$$\bar{A}(\alpha) = \sum A_n \frac{\sin[\pi(D/\lambda)(\alpha - \alpha_n)]}{\pi(D/\lambda)(\alpha - \alpha_n)} \quad (1)$$

with

$$A_n = A(\alpha_n) \exp(i\varphi_n) \quad (2)$$

and φ_n arbitrary, will be considered as an approximation to the prescribed power pattern. The aperture distribution $a(x)$ corresponding to (1) is

$$a(x) = \frac{\lambda}{D} \sum A_n \exp\left(-i \frac{2\pi}{\lambda} \alpha_n x\right). \quad (3)$$

In our numerical application we prescribed a rectangular radiation pattern, which is sometimes of interest in radar technique. The angular width of the pattern was $10\lambda/D$. We considered a set of eleven sampling points (five on

† Istituto Matematico, Università' Bologna, Italia.

each side of the central sampling point $\alpha=0$). The phase parameter φ_n was given the form $\varphi_n=n\varphi$, where n takes all the integral values in the range $-5 \dots +5$.

The radiation patterns and the associated aperture distributions were computed for a number of values of the parameter φ . From a comparison of these diagrams with those relative to $\varphi=0$ it appeared that the most convenient cases are those corresponding to about $\varphi=25^\circ, 30^\circ$; in fact for these values of φ the radiation patterns are close enough to that corresponding to $\varphi=0$ and at the same time the phase of the aperture varies smoothly in a small range. Figure 1 shows the diagrams at infinity for $\varphi=0^\circ, 25^\circ, 30^\circ$, while figures 2, 3, 4 show the corresponding aperture distributions.

The calculations were extended to the case of a two-dimensional square aperture. The distributions along the sides turns out to be identical to the previous one. We therefore plotted the distribution along the diagonal. It was found that in this case the most convenient value for φ is about $\varphi=30^\circ$. Figure 5 shows the amplitude distributions at infinity along the diagonal for $\varphi=0^\circ, 30^\circ$. Figures 6, 7 show the corresponding amplitude and phase distributions.

In conclusion, our computations show that it is quite possible to eliminate the sudden jumps of the phase in the aperture distribution, while having an approximation to the rectangular Fraunhofer pattern at least as good as that obtained by applying the conventional sampling technique.

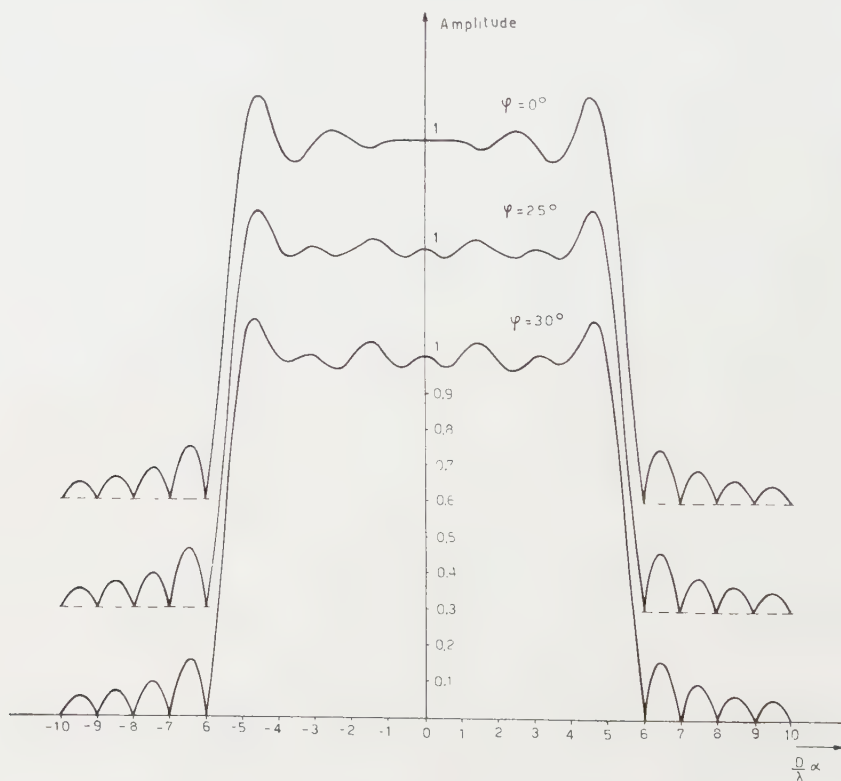


Figure 1. Radiation pattern for different values of φ .

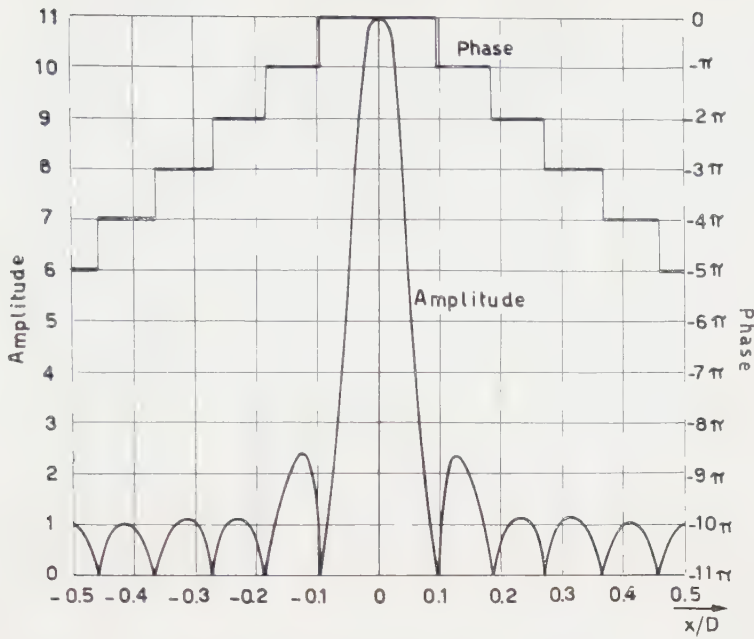


Figure 2. Amplitude and phase distribution on the aperture for $\varphi = 0^\circ$.

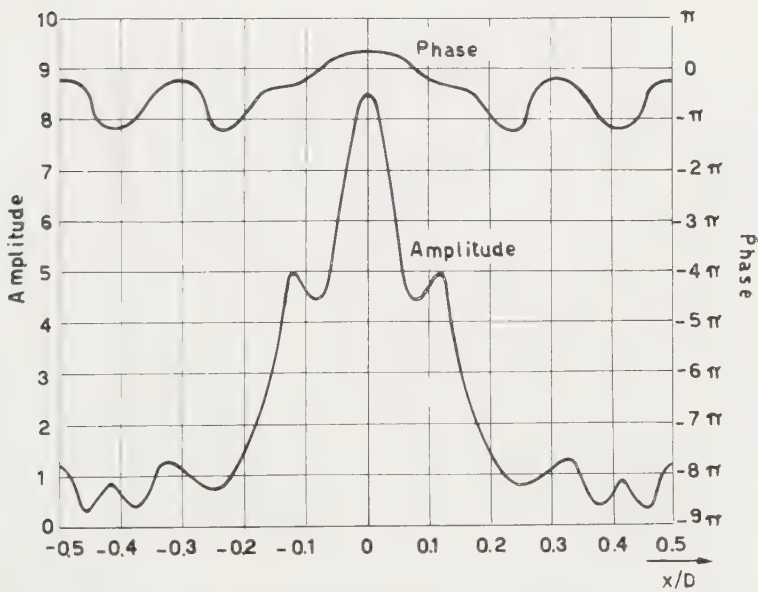


Figure 3. Amplitude and phase distribution on the aperture for $\varphi = 25^\circ$.

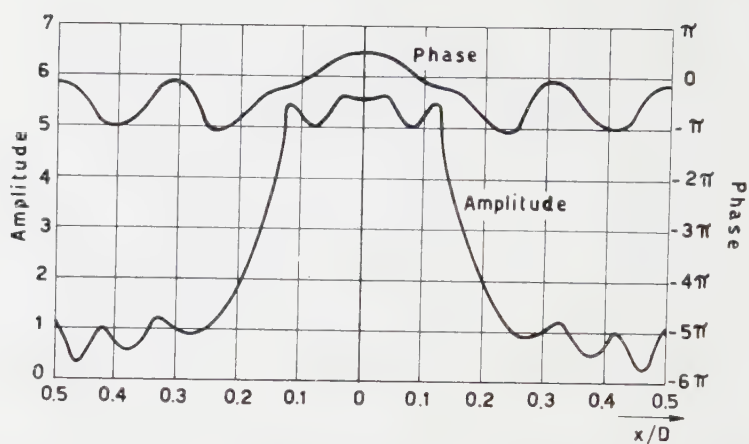


Figure 4. Amplitude and phase distribution on the aperture for $\varphi = 30^\circ$.

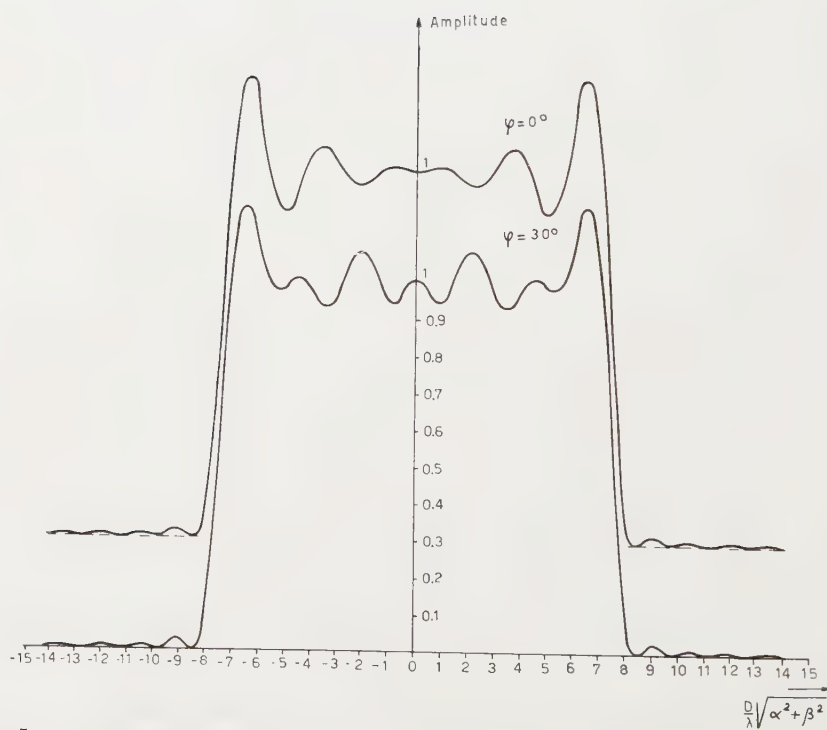


Figure 5. Amplitude distribution on the diagonal at infinity for different values of φ .

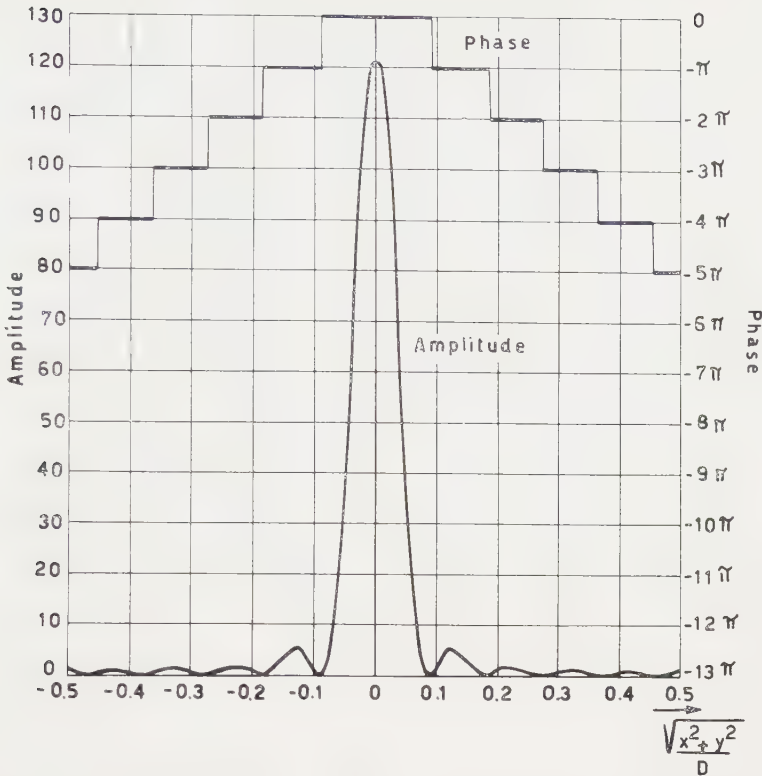


Figure 6. Amplitude and phase distribution on the diagonal of the aperture for $\varphi = 0^\circ$.

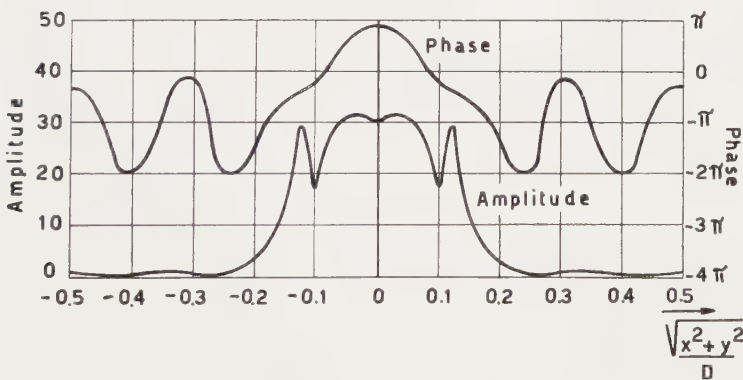


Figure 7. Amplitude and phase distribution on the diagonal of the aperture for $\varphi = 30^\circ$.

REFERENCES

- [1] TORALDO DI FRANCIA, G., 1958, *La Diffrazione della Luce*, ed. Sc. Einaudi (Torino), p. 13.
- [2] SHANNON, C. E., 1949, *Proc. Inst. Radio Engrs, N.Y.*, **37**, 10.
- [3] WOODWARD, P. M., 1946, *J. Instn elect. Engrs*, **93**, 1554.



REVIEWS

Principles of Optics. By MAX BORN and EMIL WOLF. (Pergamon Press, 1959.) [Pp. 803.] £6 0s. 0d.

THIS comprehensive and brilliant treatise is intended to fill the same place in the English-speaking world as Max Born's *Optik* has held for German readers. It is, however, a considerably better book. Optics is, in fact, a more interesting subject today than it was when Born's classic was written, and there can be no doubt that the present work will rank as a classic in its turn. Professor Wolf, now established in the University of Rochester, made outstanding contributions to British optics while he was in this country and the sections describing these are among the most interesting in the book. But the whole text bears the marks of his clear and accurate style.

After a historical introduction, the properties of electromagnetic fields are derived in Chapter I as consequences of Maxwell's equations. Reflection and refraction are discussed in terms of 'smoothed' media in the orthodox classical way, and the chapter also includes an account of low-reflection coatings and of multilayer coatings. The same treatment is carried further in Chapter II, which also covers elementary dispersion theory. Geometrical optics is introduced in Chapter III as a limiting case of the wave theory; the geometrical theory of optical images is developed in Chapters IV and V. The treatment here is based on Hamilton's methods, which are described as "a very powerful tool for systematic analytical investigations of the general properties of optical instruments". This assessment seems a little misjudged from the practical point of view. Hamilton's methods do indeed provide a powerful tool for the investigation of the general properties of optical systems. But an optical instrument is usually a highly atypical optical system analytically. It is a system in which the residual wave-aberrations are unusually small in some sense which corresponds to the practical needs of the user; less than one-quarter wavelength over 40 per cent of the aperture, for example. Its value depends on special properties, rather than on general ones. This may explain why Hamilton's methods have not found much direct application to the design of optical instruments; their very generality unfits them to some extent for this purpose.

Chapter IV, on image-forming instruments, was contributed by Dr. P. A. Wayman. It is written on a lower level than the others, but gives useful references to more specialized texts. Chapter VII, by Dr. W. L. Wilcock, is concerned with the elements of the theory of interference and with interferometers. One of the plates (Fabry-Perot fringes from absorption lines in the solar spectrum) reproduces a pioneer photograph published by Babcock in 1927.

With Chapter VII we reach diffraction theory. Many readers will find this and the three following chapters the best in the book. Starting with Fresnel's zone construction and Kirchhoff's diffraction theory, the authors give a masterly survey of the field, in which Professor Wolf has himself made outstanding contributions. Especially noteworthy, because so seldom found in text-books, are the sections on the relation between the scalar theory and the electromagnetic theory, on Zernike's phase-contrast technique, on phase-distribution near focus in an aberration-free image, and on Gabor's method of imaging by reconstructed wave-fronts. The diffraction theory of aberrations is developed in much the same way as in Nijboer's well-known Thesis (Groningen, 1942) where point images are being discussed; images of extended objects are considered by the spatial-frequency techniques originating with Duffieux and Lansraux.

Chapter X discusses interference and diffraction with partially coherent light, correlation functions of light beams, the Zernike-van Cittert theory of degree of coherence, and its application by Hopkins and Barham to investigate the influence of the condenser on resolution in a microscope. Rigorous diffraction theory, on the basis of Maxwell's equations together

with specified boundary conditions, is the subject of Chapter XI, contributed by Dr. P. C. Clemow (who also prepared the valuable Appendix III on methods of steepest descent and stationary phase). A short chapter follows on the diffraction of light by ultrasonic waves.

The last two chapters, on the optics of Metals and the Optics of Crystals, are based on the corresponding chapters of *Optik*, revised and extended with the help of Professor A. M. Taylor and Dr. A. R. Stokes respectively. The treatment is on a classical (pre-quantum) basis.

Nine appendices, occupying 68 pages, conclude the intellectual feast. A good author index (10 pages) and subject index (19 pages) are provided. The book is beautifully printed by the Pitman Press and is worth more than its price.

E. H. LINFOOT.

Jenaer Jahrbuch 1960. Wissenschaftliche Veröffentlichungen. Herausgeber: Prof. Dr. PAUL GÖRLICH, Jena. 1. Teil. Mit 192 Bildern und 31 Tabellen im Text. 319 Seiten. 2. Teil mit 277 Bildern, 6 Faksimiles und Tabellen im Text. 694 S. 16,7 × 24 cm. 1960. Lederin. Jeder Teil 25.-DM. Gustav Fischer Verlag Jena.

1. Teil.

FÜR die Durchrechnung eines Strahles durch eine Folge von brechenden, sphärischen Flächen stellt F. Franke einen Formelsatz in Speerkoordinaten zusammen und vergleicht den Rechenaufwand bei der Benutzung dieser Formel mit dem bei der Verwendung eines Formelsystems vektoriellen Aufbaus. H. Zöllner stellt Spiegel- und Linsenobjektive für photographische Zwecke einander gegenüber. Die Vorteile der Spiegelsysteme kommen nur dann voll zur Geltung, wenn es sich um langbrennweitige Systeme mäßigen Öffnungsverhältnisses und Bildfeldes handelt. Andernfalls und namentlich bei hochgeöffneten Systemen zeigen sich die reinen Linsenarrangements überlegen. H. Maenz, R. Tiedeken und R. Wanke stellen neue Projektionsobjektive für Kinomaschinen vor. Der Einfluß verschiedener Wärmeschutzfilter auf die Lichtleistung und auf die Temperaturbelastung der Dias bei Projektionsapparaten wird von E. Helbig untersucht. Einen sehr ausführlichen Bericht über die Perspektivbedingung und ihre Realisierung an Entzerrungsgeräten gibt O. Weibrecht. H. Moenke stellt an einer Reihe von Absorptionsspektren im Infrarot fest, daß dieses Verfahren geeignet ist, über die Herkunft der Mineralien Aufschluß zu geben. Mit dem elektrooptischen Effekt an zwei synthetischen Kristallen und ihrer Eignung zur Lichtsteuerung und Bildschreibung befaßt sich eine Arbeit von S. Rissmann und Vosahlo. K. Pabst untersucht die Lichtausbeute fester Szintillatoren bei Anregung mit α , β , γ -Strahlen. Und C. Fritzsche beschäftigt sich mit der Abhängigkeit der Leuchtdichte von der anregenden Spannung bei elektro-lumineszierenden ZnS-Phosphoren. Vorangeschickt sind einige historische Ergänzungen zu den Abbeschen Abhandlungen, und schließlich sei noch eine elektronenoptische Arbeit von K. H. Schmidt über den elektrolytischen Keiltrog erwähnt.

Der 2. Teil

beginnt mit einer Fortführung der historischen Betrachtungen über die Stereoauto-graphen aus dem Jahre 1911 und 1914. Ch. Hofmann greift die Frage der Zentrierungen in optischen Systemen auf. Die Dezentrierung einer sphärischen Einzellinse wird danach einwandfrei nur durch 3 Parameter definiert: Die beiden Flächenkipnungen und das Azímut. C. Frischmuth behandelt die Auswertung von Luftbildpaaren, wenn die Brennweiten bei der Projektion der Luftbilder eine andere ist als bei der Aufnahme. H. und L. Moenke berichten über quantitative spektralphotometrische Untersuchungen im Infrarot, um die Brauchbarkeit dieser Methode für geologische Zwecke zu prüfen. Eine sehr ausführliche Arbeit von H. Hora behandelt die Polarisationsabhängigkeit der Photo-emission bei zusammengesetzten Kathoden von Cs_3Sb und Cs_2O . Es lassen sich daraus Schlüsse über die Anregungsvorgänge im Inneren der Kathoden ziehen. Th. Tuchscheerer zeigt, daß Natriumalicolat einen hervorragenden Lichtwandler im Ultravioletten darstellt. Allerdings scheint die empfohlene Korngröße von 0,02 mm doch noch ein wenig grob. Von F. Franke stammt eine Verallgemeinerung eines Reduktionssatzes über Umkehrmatrizen. —Außerdem enthält der Band noch eine Arbeit über Röntgen-Kristallanalyse und eine über Ferroelektrika.

GG. FRANKE.

Ziffern-Rechenautomaten. Elektronisches Rechnen und Regeln. WILHELM KÄMMERER. Bd. 1, 303 S., mit 156 Bild. Berlin: Akademie-Verlag. DM. 29,—

Das Werk kommt einem im deutschen Sprachgebiet bestehenden dringenden Bedürfnis nach einer breiteren Darstellung über den grundsätzlichen Aufbau numerischer Rechenautomaten entgegen. Die lebhaft entwickelte Entwicklung auf diesem Gebiet macht eine Behandlung der Ziffer-Rechenmaschinen in Vorlesungen notwendig, außerdem aber auch in Buchform für alle diejenigen, die schon länger in der Praxis stehen und denen als Mathematiker und Techniker heute die Aufgabe zufällt, mit dem neuen Handwerkszeug umzugehen. Das Werk ist nicht als Handbuch gedacht sondern als Wegweiser, um in die Grundlagen einzudringen und über die reine Technik des Programmierens hinaus zu einem Verständnis der einzelnen Aggregate zu kommen. Gerade für diese Aufgabe muß das Buch besonders empfohlen werden; es berührt alle wesentlichen Fragen, wenn sie auch nicht erschöpfend dargelegt werden können, weil das den Rahmen eines Lehrbuches sprengen würde. Der Verfasser bezieht sich hauptsächlich auf drei Maschinentypen, die in Jena unter seiner Mitarbeit entwickelte Maschine 'Oprema', die in erster Linie für die Berechnung optischer Systeme gedacht war, ferner auf die Z 22 von der Firma Zuse in Hersfeld und auf eine russische Maschine. Diese konkreten Vorstellungen bewahren den Verfasser, in die geradezu uferlose Breite der modernen Entwicklung zu versinken, ohne dabei das Typische im Aufbau einer Rechenmaschine zu verlieren. Besonders dankbar wird man es begrüßen, daß eine gut verständliche Einführung in die algebraische Logik gegeben wird. Selbstverständlich ist auch der Programmierung ein umfangreicher Abschnitt von rund 100 Seiten eingeräumt worden.



On some degenerate cases of thin film interference

by PAUL G. KARD

State University of Tartu, Estonian SSR, USSR

and ZDENĚK KNITTL

Meopta Research Institute of Optics and Fine Mechanics,
Prerov, Czechoslovakia

(Received 15 November 1960)

The theory of a metallic interference film is scrutinized in peculiar situations brought about by performing various mathematical limiting processes on the refractive indices. Special attention is paid to geometric degeneration of the layer to a single boundary in such conditions. The relation of the discussion to some real layers is indicated.

1. INTRODUCTION

Interference in a thin film, treated on the basis of the multiple-reflection model, leads to an apparently clear idea of the process of building up the resultant waves. Its essence lies in the interplay of Fresnel amplitudes governed by the phase shifts inside the film. The application of these methods is not obviously valid in certain special cases. Generally speaking, these cases arise during various mathematical limiting processes performed on the parameters of the reflectivity and transmissivity formulae for an interference film. The present authors were both engaged in certain discussions of this kind previously [1, 2], and have since embarked jointly on a systematic study of such singular cases.

The limits in question are of two general types. One of them concerns the refractive indices, i.e. $n \rightarrow 0$ or $n \rightarrow \infty$, where n may denote any of the indices pertaining to the layer. The other type of limit is $h \rightarrow 0$, i.e. the film degenerates to a single boundary through its thickness tending toward zero. This case is particularly interesting if it is performed as a second stage operation, the first stage being a limit on the refractive index.

From the technological point of view these limits are of course objectionable, but considering them is not illogical and means applying certain tests to the theory, which it should stand. It will be seen later that some physically interesting conclusions emerge from such mathematical considerations.

A thorough analysis of degenerate interference must of course resort to the electromagnetic theory of the layer, but the multiple-reflection model will also be followed where possible.

2. FUNDAMENTAL FORMULAE AND THE CONDITIONS OF DEGENERACY

This study is concerned with a thin metallic film sandwiched between two dielectrics according to the scheme $n_0/n_1 = \eta_1 - i\kappa_1/n_2$, the thickness of the layer being h . The complex reflectivity and transmissivity of such a system are given by the well-known expressions

$$\rho = \frac{r' + r'' \exp(-2ix)}{1 + r'r'' \exp(-2ix)}, \quad \theta = \frac{d'd'' \exp(-ix)}{1 + r'r'' \exp(-2ix)}, \quad (1a, b)$$

where

$$r' = \frac{n_0 - n_1}{n_0 + n_1}, \quad r'' = \frac{n_1 - n_2}{n_1 + n_2}, \quad d' = \frac{2n_0}{n_0 + n_1}, \quad d'' = \frac{2n_1}{n_1 + n_2}, \quad (2)$$

$$x = \alpha - i\beta, \quad \alpha = k\eta_1 h, \quad \beta = k\kappa_1 h, \quad k = \frac{2\pi}{\lambda} \quad (3)$$

are the Fresnel coefficients at the simple boundaries and the phase shift, respectively. Light is supposed to travel from medium n_0 to n_2 and normal incidence is considered only. No special symbols are introduced for complex numbers.

The above formulae pertain to the electric components of the electromagnetic waves. Since we are going to study degenerate states, due attention must also be paid to the magnetic component in order to see the behaviour of the electromagnetic field as a whole. The corresponding formulae are identical with (1 *a, b*), but the Fresnel coefficients (2) are replaced by

$$r_M' = -r', \quad r_M'' = -r'', \quad d_M' = \frac{2n_1}{n_0 + n_1}, \quad d_M'' = \frac{2n_2}{n_1 + n_2}. \quad (4)$$

Notes: (i) In order to obtain a clear comparison with the **E**-vector, the **H**-coordinate axis is supposed not to change orientation upon reflection.

(ii) Once the incident electric amplitude has been chosen as 1, the corresponding magnetic amplitude is then n_0 and the reflected one $\rho_M n_0$. All subsequent expressions follow this convention.

The expressions (1) satisfy the relations

$$\lim_{h \rightarrow 0} \rho = \frac{r' + r''}{1 + r' r''} = \frac{n_0 - n_2}{n_0 + n_2}, \quad (5a)$$

$$\lim_{h \rightarrow 0} \theta = \frac{d' d''}{1 + r' r''} = \frac{2n_0}{n_0 + n_2}, \quad (5b)$$

describing the physically obvious fact that "with the vanishing of the layer separating the first and third media, the classical Fresnel formulae obtain". For the purpose of this study the equations (5 *a, b*) will be referred to as the conditions of degeneracy†.

Discussion of the more complicated cases of layer degeneration also requires knowledge of the electromagnetic field inside the film. The appropriate formula is less well known, but equally simple to derive as (1 *b*), namely

$$E_1(\xi) = \frac{d' \exp(-i\phi)}{1 + r' r'' \exp(-2ix)} = \frac{d' \exp[i(x - \phi)]}{\exp(ix) + r' r'' \exp(-ix)} \quad (6)$$

for the electric amplitude of the positive-going wave at a distance $\xi = \phi/kn_1$ from boundary n_0/n_1 , and

$$E_1'(\xi) = E_1(\xi) r'' \exp[-2i(x - \phi)] \quad (7)$$

for the negative-going wave at the same distance.

The magnetic amplitudes are

$$H_1(\xi) = n_1 E_1(\xi), \quad H_1'(\xi) = -n_1 E_1'(\xi). \quad (8)$$

In the subsequent discussion the second form of (6) is of advantage.

† More precisely "of geometric degeneracy". Since no such term will be coined for the other type of degeneracy ($n \rightarrow 0$, $n \rightarrow \infty$), which might correspondingly be called optical, the above given concise wording will be used throughout this study.

Omitting the elementary but tedious algebra, the entire field inside the layer can be found to be

$$E_{1s} \equiv E_1 + E_1' = D^{-1} 2n_0 \exp(-k\kappa_1\xi) \{ [n_1(1+P) + n_2(1-P)] \cos(\alpha - X) + i[n_1(1-P) + n_2(1+P)] \sin(\alpha - X) \} \quad (9a)$$

where

$$D = [n_1(n_0 + n_2)(1 + N^2) + (n_1^2 + n_0n_2)(1 - N^2)] \cos \alpha + i[n_1(n_0 + n_2)(1 - N^2) + (n_1^2 + n_0n_2)(1 + N^2)] \sin \alpha,$$

$$P = \exp[-2k\kappa(h - \xi)], \quad X = k\eta_1\xi, \quad N = \exp(-\beta)$$

and

$$H_{1s} = H_1 + H_1' = n_1 \times \text{expression (9a), where } P \text{ is replaced by } -P. \quad (9b)$$

Similarly, converting the expressions (1a, b) to a form homogeneous in $\exp(\pm ix)$, one obtains for the entire field on the first and second boundary, measured in medium n_0, n_2 respectively

$$E_{0s} = E_0 + E_0' = \text{expression (9a), where } \left. \begin{array}{l} \xi = X = 0, \\ P = N^2, \end{array} \right\} \quad (10a)$$

$$H_{0s} = H_0 + H_0' = \text{expression (9b), where } \left. \begin{array}{l} \xi = X = 0, \\ P = N^2, \end{array} \right\} \quad (10b)$$

$$E_2 = E_1(\xi = h), \quad d'' = D^{-1} 4n_0n_1N, \quad H_2 = n_2E_2. \quad (11a, b)$$

It is convenient not to split up the complex n_1 into its Gaussian components in these formulae.

With finite values of the material constants the boundary conditions

$$\left. \begin{array}{l} E_{0s} = E_{1s}(0), \quad E_{1s}(h) = E_2 \\ H_{0s} = H_{1s}(0), \quad H_{1s}(h) = H_2 \end{array} \right\} \quad (12)$$

are satisfied for all values of h , including the limit $h \rightarrow 0$. In some of the optically degenerate cases this is at times not the case, which in turn entails a violation of the degeneracy conditions.

Our aim is now to investigate the behaviour of the electromagnetic field of a plane monochromatic wave in the three media $n_0/n_1/n_2$ with respect to various limits performed on the refractive indices and to check in these circumstances the validity of the degeneracy and boundary conditions.

It will be advantageous to deal first with the less important limits concerning the outer media and then concentrate on the layer itself. The equations of this section will often be used without special reference.

3. DEGENERACY OF OUTER MEDIA

$$(1a) \quad n_0 \rightarrow \infty$$

In accordance with the physical necessity that all vectors at any time should be finite, we must suppose in this case $\mathbf{E} \rightarrow \mathbf{0}$ so that a purely magnetic wave of finite amplitude is incident on boundary one. This means that the incident energy flux tends towards zero and the case loses its physical significance. However, it is possible to carry on the discussion purely formally using the amplitude concept. In fact, the degeneracy conditions are concerned with amplitude relations only. (The same remark holds for case (1b)).

From (4) it follows that $r_M' = -1$, $d_M' = 0$ and no field (either magnetic or electric) exists behind the first boundary. The magnetic wave is totally reflected.

The degeneracy condition may be regarded as fulfilled, e.g. for the magnetic reflectance

$$\lim_{h \rightarrow 0} \lim_{n_0 \rightarrow \infty} \rho_M = \lim_{h \rightarrow 0} (-1) = -1 = \lim_{n_0 \rightarrow \infty} \left(-\frac{n_0 - n_2}{n_0 + n_2} \right)$$

and similarly for the other cases.

(1 b) $n_0 \rightarrow 0$

In this case $\mathbf{H} \rightarrow \mathbf{0}$ in the incident wave, so that a purely electric wave with no energy transport must be supposed to exist in the first medium. For this wave $r' = -1$, $d' = 0$ and again no field exists behind boundary one. The degeneracy conditions can be seen fulfilled as under (1 a).

(2 a) $n_2 \rightarrow \infty \Rightarrow r'' = -r_M'' = -1$, $d'' = 0$, $d_M'' = 2$

In the last medium there exists only the magnetic disturbance. The electric one is totally reflected at the second boundary, but the layer as a whole may yield various reflectivities. The difference $1 - |\rho|^2$ may be interpreted as absorption in the film.

The degeneracy conditions are fulfilled, since

$$\lim_{h \rightarrow 0} \lim_{n_2 \rightarrow \infty} \rho = -1 = \lim_{n_2 \rightarrow \infty} \frac{n_0 - n_2}{n_0 + n_2},$$

and similarly for transmission.

The relation $\lim_{h \rightarrow 0} \rho = 1$ is in conformity with the necessity that absorption should tend to zero simultaneously with h .

(2 b) $n_2 \rightarrow 0 \Rightarrow r'' = -r_M' = 1$, $d'' = 2$, $d_M'' = 0$

The situation is analogous to that of (2 a) but in this case the purely magnetic disturbance in the third medium is replaced by the electric one.

In all the cases 1 to 2 the boundary conditions are fulfilled.

4. DEGENERACY OF LAYER MEDIUM

$$(3 a) \quad \eta_1 \rightarrow \infty, \kappa_1 \geq 0, \text{ finite} \Rightarrow r' = -r_M' = -1, d' = 0, d_M' = 2, \\ r'' = -r_M'' = +1, d'' = 2, d_M'' = 0$$

It is easily seen that for all $h \neq 0$ the reflected electric amplitude now identically equals -1 , the transmitted one 0. For the magnetic vector these coefficients are 1 and 0 respectively. All the incident energy is reflected on boundary one, with only a wattless magnetic disturbance penetrating behind it. There is no field in the third medium.

When investigating the degeneracy conditions, one must bear in mind that unless more detailed assumptions are made, the limit $h \rightarrow 0$ now does not imply $\text{Re}(x) \rightarrow 0$ since $\eta_1 \rightarrow \infty$. Some difficulties arise with respect to our original convention that the limit $\eta_1 \rightarrow \infty$ is performed first and the limit $h \rightarrow 0$ second. As a matter of fact, both limits are performed simultaneously. Each of these variables may have a convergence rate of its own with the result that $\eta_1 h$ tends to some value.

The following two principal cases must be distinguished:

- (i) $\eta_1 h = \text{constant}$, different from zero or integral multiple of $\lambda/2$
- (ii) $\eta_1 h = l\lambda/2$, $l = 0, 1, 2$

Case (i) (with $\alpha \rightarrow \text{const} \neq l\pi$) is equivalent to the simple limit $\eta_1 \rightarrow \infty$ already discussed. The degeneracy conditions are obviously not fulfilled, because the limits $-1, 0$ are not equal to the right-hand sides of equations (5). Similarly for the magnetic vector.

Regarding the degenerate double-boundary as one surface, one may investigate how far the Maxwell boundary conditions are fulfilled on it for the case in question. In terms of the reflectivity and transmissivity coefficients, these conditions are written as $1+r=d$. While this is true of the electric vectors ($1-1=0$), the magnetic vectors show a discrepancy in that $1+1=2 \neq 0$. (Since $H_0=n_0$, the discontinuity of H is $2H_0$.)

Let us now study in more detail how the boundary conditions are violated. Presumably, this violation may be in connection with the existence of surface currents, so that we shall start out from the fourth Maxwell equation, which is satisfied by a monochromatic plane wave in the following way

$$\text{curl } \mathbf{H} = \frac{4\pi}{c} (\mathbf{j}_c + \mathbf{j}_d)$$

where

$$\mathbf{j}_c = \sigma \mathbf{E}, \quad \mathbf{j}_d = \frac{i\omega\epsilon}{4\pi} \mathbf{E}, \quad (13 a, b)$$

are the convection and displacement currents, respectively. Further

$$\epsilon = \eta_1^2 - \kappa_1^2, \quad \frac{2\pi\sigma}{\omega} = \eta_1\kappa_1. \quad (14 a, b)$$

For the application of these formulae it is necessary to know the entire field inside the degenerate layer, i.e. to adapt equations (9 a, b) to our case. For this purpose it is necessary to note the following:

The field inside the layer is dependent on X , where by definition $0 \leq X \leq \alpha$. However, this dependence loses its real meaning if $h \rightarrow 0$ in such a way that $\eta_1 h = k^{-1}\alpha = \text{const} \neq 0$. The interval $\langle 0, \alpha \rangle$ then remains finite, although from the geometrical point of view the inside of the layer degenerates to a simple plane. The exact values of the field vectors in such a case must be identical with the mean values over the optical path, which permits the elimination of X from the expressions (9 a, b). Since the integration variable is only present in the numerators, the result is quickly achieved by using the formulae

$$\frac{1}{\alpha} \int_0^\alpha \cos(\alpha - X) dX = \frac{\sin \alpha}{\alpha}, \quad \frac{1}{\alpha} \int_0^\alpha \sin(\alpha - X) dX = \frac{1 - \cos \alpha}{\alpha}.$$

Special attention must be paid to evaluating the mean of the expression $n_1(1-P)\sin(\alpha-X)$, where $|n_1| \rightarrow \infty$, $1-P \sim 2k\kappa_1(h-\xi) \rightarrow 0$. It can be shown to be

$$\frac{2\kappa_1 n_1}{\alpha \eta_1} \int_0^\alpha \sin(\alpha - X) \cdot (\alpha - X) dX = \frac{2\kappa_1}{\alpha} (\sin \alpha - \alpha \cos \alpha).$$

Moreover, performing in the denominator the limit

$$\lim_{\eta_1 \rightarrow \infty} n_1(1-N^2) = 2k\eta_1\kappa_1 h = 2\kappa_1 \alpha \quad (15)$$

one obtains

$$\bar{E}_{1s} = \frac{2n_0 \eta_1 \sin \alpha + i[n_2(1 - \cos \alpha) + \kappa_1(\sin \alpha - \alpha \cos \alpha)]}{\alpha \eta_1 (n_0 + n_2 + \kappa_1 \alpha) \cos \alpha + i\eta_1 \sin \alpha}. \quad (16)$$

(The corresponding expression for \bar{H}_{1s} can be dispensed with.)

It is now possible to evaluate the currents according to (13) and (14). In the case under consideration $\epsilon \sim \eta_1^2$. Since according to (16) $\tilde{E}_{1s} \sim 2n_0/i\eta_1\alpha$, we can infer

$$j_c = -i \frac{2n_0\kappa_1 c}{\alpha\lambda}, \quad j_d = \frac{c}{4\pi} \frac{2n_0}{h}. \quad (17 a, b)$$

If now linear density of surface current is introduced by the formula $s = (j_c + j_d)h$, it is easily seen that for $h \rightarrow 0$ there remains a non-zero displacement surface current $cH_0/4\pi$ in the boundary. This corresponds to a discontinuity of H by $2H_0$ as established above.

Case (ii) requires special treatment in that it is necessary to consider the rate of convergence $\alpha \rightarrow l\pi + \alpha_1$, where α_1 is infinitesimally small of some order. We may then put $\sin \alpha = (-1)^l \alpha_1$, $\cos \alpha \approx (-1)^l (1 - \alpha_1^2/2)$ and equations (10), (11) assume the forms

$$E_{0s} = \frac{2n_0}{n_0 + g}, \quad H_{0s} = E_{0s}g, \quad (18 a, b)$$

$$E_2 = (-1)^l E_{0s}, \quad H_2 = n_2 E_2 = (-1)^l \frac{n_2}{g} H_{0s} \quad (19 a, b)$$

where

$$g = n_2 + \kappa_1 \alpha + i\eta_1 \alpha_1 \quad (20)$$

and use is again made of limit (15).

Equation (16) now yields, for l even,

$$\tilde{E}_{1s} = \frac{2n_0 \alpha_1 \eta_1 - i\alpha \kappa_1}{\alpha \eta_1 \quad n_0 + g} \quad (21 a)$$

and for l odd

$$\frac{2n_0 \alpha_1 \eta_1 - i(2n_2 + \kappa_1 \alpha)}{\alpha \eta_1 \quad n_0 + g}. \quad (21 b)$$

The limiting values of the Fresnel reflection coefficients are best deduced from (18 a, b) as

$$\rho \equiv E_{0s} - 1 = \frac{n_0 - g}{n_0 + g} = -\rho_M \equiv \frac{H_{0s}}{n_0} - 1. \quad (22)$$

The transmission coefficients are given by (19 a, b) as $\theta = E_2$, $\theta_M = H_2/n_0$.

The values of all these Fresnel coefficients depend on the rate of convergence α_1 and on the multiple of π towards which α is converging. Moreover, a change of sign of the transmission coefficient can occur if l is odd. Case (ii) gives therefore ample opportunity for the degeneracy conditions not to be fulfilled, which is accompanied by violation of the Maxwell boundary conditions.

Indeed, the electric vector satisfies the boundary conditions on the degenerate boundary or not, according as l is even or odd. The magnetic vector behaves normally if (and only if) $l=0$, $\alpha_1 \eta_1 \rightarrow 0$. For all other cases the boundary conditions for H are not satisfied†.

The degeneracy conditions in their turn are only fulfilled if $l=0$ (for $\kappa_1=0$ suffices l even) and $\alpha_1 \eta_1 = 0$.

As compared with (i), case (ii) has introduced a new discontinuity, namely that of the electric vector. From the third Maxwell equation it follows that ($\mu = 1$)

$$E_{2s} - E_{0s} = -kiH_{1s}h \quad (23)$$

† For $\kappa_1=0$ this statement becomes: if l is odd, or if with an even $l \neq 0$, $\alpha_1 \eta_1 \neq 0$ H is discontinuous.

which can be verified by (18 *a*) and (19 *a*) with l odd. It is interesting that this discontinuity never occurs without that of H , while H may violate the boundary conditions alone both in (i) and (ii).

It remains to calculate the surface currents connected with the discontinuity of H . We may proceed according to the pattern set under (i), but equations (21 *a, b*) are now appropriate for E_{1s} instead of (16), which leads to some qualitatively new results.

Let us begin with $l = \alpha/\pi$ odd. Then

$$s_d = \frac{i\omega}{4\pi} \eta_1 \frac{2n_0}{n_1 - \frac{c}{4\pi} \frac{h}{\eta_1}} [\alpha_1 \eta_1 - i(2n_2 + \kappa_1 \alpha_1)] = \frac{c}{4\pi} \frac{2n_0}{n_1 + \frac{c}{4\pi} \frac{h}{\eta_1}} [2n_2 + \kappa_1 \alpha + i\alpha_1 \eta_1] \quad (24)$$

$$s_c \approx s_d \eta_1^{-1} \rightarrow 0.$$

Owing to the resemblance of (21 *a*) and (21 *b*), all the other cases may be formally involved in (24), if the term $2n_2$ is replaced by $[1 - (-1)^l]n_2$. The resulting formula then gives the values of the displacement surface currents for $l = 0, 1, 2, \dots$ and $\alpha_1 \eta_1 =$ zero or non-zero. These will easily be verified to be equal to $c/4\pi \times$ discontinuity of H for the case in question.

In conclusion of this section it should be explicitly stressed that, for the degeneracy conditions to be fulfilled (this occurring only for $l = 0$, $\alpha_1 \eta_1 = 0$), the convergence $h \rightarrow 0$ must be of the type $0(\eta_1^{-2})$. Indeed, $l = 0$ implies $\alpha = \alpha_1$ so that $\alpha_1 \eta_1 = \alpha \eta_1 = k \eta_1^2 h$.

$$(3b) \quad \kappa_1 \rightarrow \infty, \eta_1 \geq 0, \text{ finite}$$

This limit has the same effect upon the Fresnel coefficients as that discussed under (3 *a*). Moreover, $\beta \rightarrow \infty$ and the purely magnetic disturbance penetrating into the layer is immediately attenuated so that practically no electromagnetic wave exists behind boundary one.

As far as performing the limit $h \rightarrow 0$ is concerned, the reasoning is analogous to that of § (3 *a*). Since the attenuation exponential is not periodic, we have to distinguish simply between $\kappa_1 h \rightarrow$ non-zero constant and $\kappa_1 h \rightarrow$ zero.

In deriving the mean value corresponding to (16) we meet with procedures of the type

$$n_1 \exp(-Y)(1-P) \sin(\alpha - X) \approx n_1 [\exp(-Y) - N^2 \exp(Y)] k \eta_1 (h - \xi) \\ \approx i \eta_1 [\exp(-Y) - N^2 \exp(Y)] (\beta - Y), \quad Y = k \kappa_1 \xi,$$

which expression is then averaged over the interval $0 \leq Y \leq \beta$. \tilde{E}_{1s} can be found to be

$$\frac{2n_0}{-i\kappa_1\beta - i\kappa_1(1-N^2) + (n_0 + n_2 + \eta_1\beta)(1+N^2)} \frac{(n_2 - i\kappa_1)(1-N^2) + \eta_1\beta(1+N^2)}{\quad} \quad (25)$$

In the first case $\tilde{E}_{1s} = 2n_0 / -i\kappa_1\beta$, which leads to a non-zero displacement surface current

$$s_d \equiv h j_d = \frac{i\omega}{4\pi} \frac{-\kappa_1^2 h}{-i\kappa_1\beta} 2n_0 = \frac{c}{4\pi} 2H_0, \quad (26)$$

corresponding to the discontinuity of H after degeneration.

If $\beta \rightarrow 0$, $N \rightarrow 1$ and this may have some effect on the value of the term $-i\kappa_1(1-N^2)$. In fact it converges to $-2ik\kappa_1^2 h$, formula (25) assumes the form

$$\tilde{E}_{1s} = \frac{2n_0}{n_0 + n_2 - i\beta\kappa_1}$$

and the corresponding surface current is

$$s_d = \frac{-ic}{4\pi} \frac{2n_0}{n_0 + n_2 - i\beta\kappa_1} \beta\kappa_1. \quad (27)$$

By finding the limiting values of the Fresnel coefficients for the case $\beta \rightarrow 0$, namely

$$\rho = \frac{n_0 - n_2 + i\beta\kappa_1}{n_0 + n_2 - i\beta\kappa_1} = -\rho_M, \quad \theta = \frac{2n_0}{n_0 + n_2 - i\beta\kappa_1} = \frac{n_0}{n_2} \theta_M \quad (28)$$

(27) may be verified to correspond to the discontinuity of H , E being continuous.

Again, if the convergence $h \rightarrow 0$ is of the type $0(\kappa_1^{-2})$, $\beta\kappa_1 \rightarrow 0$ and the degeneracy conditions are satisfied.

$$(3c) \quad \eta_1 \rightarrow \infty, \kappa_1 \rightarrow \infty, \kappa_1/\eta_1 \neq 0, \eta_1/\kappa_1 \neq 0$$

For $h \neq 0$ the situation resembles (3b). For further study let us write down the above given assumptions in the following form: $\eta_1 = a\zeta$, $\kappa_1 = b\zeta$, a, b finite, non-zero; $\zeta \rightarrow \infty$. Then $\alpha = a\psi$, $\beta = b\psi$, where $\psi = k\zeta h$. Writing $b/a = p$ so that $Y = pX$, the averaging process may be carried out by means of the formulae

$$\begin{aligned} \frac{1}{\alpha} \int_0^\alpha \exp(\pm pX) \sin(\alpha - X) dX &= \frac{\exp(\pm p\alpha) - \cos \alpha \mp p \sin \alpha}{\alpha(1 + p^2)} \\ \frac{1}{\alpha} \int_0^\alpha \exp(\pm pX) \cos(\alpha - X) dX &= \frac{\sin \alpha \pm p[\exp(\pm p\alpha) - \cos \alpha]}{\alpha(1 + p^2)} \end{aligned}$$

The resulting expression for \tilde{E}_{1s} is

$$\begin{aligned} \tilde{E}_{1s} &= \frac{2n_0}{\alpha(1 + p^2)} \\ &+ \frac{n_1[(1 + N^2) \sin \alpha + p(1 - N^2) \cos \alpha] + n_2[(1 - N^2) \sin \alpha + p(1 + N^2) \cos \alpha - 2pN] +}{n_1\{[(n_0 + n_2)(1 + N^2) + n_1(1 - N^2)] \cos \alpha +} \\ &+ i\{n_1[p(1 + N^2) \sin \alpha - (1 - N^2) \cos \alpha] + n_2[p(1 - N^2) \sin \alpha - (1 + N^2) \cos \alpha + 2N]\}} \\ &+ i[(n_0 + n_2)(1 - N^2) + n_1(1 + N^2)] \sin \alpha \} \end{aligned} \quad (29)$$

For $\zeta \rightarrow \infty$ it simplifies to

$$\tilde{E}_{1s} = \frac{2n_0}{\alpha(1 + p^2)} \frac{p - i}{\zeta(a - bi)}. \quad (30)$$

The corresponding surface currents for $\zeta \rightarrow \infty, h \rightarrow 0$ in such a way that $\psi \neq 0$ are

$$s_d = \frac{c}{4\pi} \frac{a^2 - b^2}{a^2 + b^2} \frac{1 + pi}{1 - pi} 2n_0, \quad s_c = \frac{-ic}{4\pi} \frac{2ab}{a^2 + b^2} \frac{1 + pi}{1 - pi} 2n_0 \quad (31a, b)$$

their sum amounting to

$$s = s_c + s_d = \frac{c}{4\pi} 2H_0. \quad (32)$$

This result is in conformity with that of the previous two cases: for $\zeta h \neq 0$ $\rho_M = -\rho = -1$ and the magnetic vector jumps by $2H_0$, E being here also continuous.

This is the first time, however, that a non-zero convection current appears alongside s_d . For $a = b$ (i.e. for the same rate of convergence $\eta_1, \kappa_1 \rightarrow \infty$) it even takes over the whole responsibility for the discontinuity.

Let now $\psi \rightarrow 0 \Rightarrow \alpha, \beta \rightarrow 0$. Then

$$s_d = \frac{i\omega}{4\pi} (a^2 - b^2) \tilde{E}_{1s} \zeta^2 h, \quad s_c = \frac{\omega}{2\pi} ab \tilde{E}_{1s} \zeta^2 h \quad (33 a, b)$$

where

$$\tilde{E}_{1s} = \frac{2n_0}{n_0 + n_2 + i\psi(a^2 - b^2 - 2abi)} \quad (34)$$

and it may be concluded that—again—for $\zeta^2 h \rightarrow 0$, continuity of H is established together with the validity of the degeneracy conditions.

For $\zeta^2 h = \text{const} \neq 0$ ($\zeta h \rightarrow 0$), the reflection and transmission coefficients are

$$\rho = -\rho_M = \frac{n_0 - g'}{n_0 + g'}, \quad \theta = \frac{n_0}{n_2} \theta_M = \frac{2n_0}{n_0 + g'} \quad (35 a, b)$$

where

$$g' = n_2 + i\psi\zeta(a^2 - b^2 - 2abi), \quad (36)$$

E being therefore continuous, the discontinuity of H conforming with $(4\pi/c)s$.

In all the three cases (3a, b, c) it has thus been shown that the degenerate states of the layer often lead to discontinuities of the \mathbf{H} -vector, sometimes even of the \mathbf{E} -vector, all of which are always accompanied by the existence of surface currents. The degenerate double-boundary becomes an object physically different from a simple Fresnel boundary and cannot therefore be expected to converge with $h \rightarrow 0$ to a state characterized by the Fresnel coefficients. The degeneracy conditions quite necessarily fail to be satisfied.

(4a) $\eta_1 \rightarrow 0, \kappa_1 \neq 0$

This limit implies $|r'| = 1 = |r''|$, but the phase angles of these Fresnel coefficients may assume arbitrary values dependent on κ_1 :

$r' = \exp(i\delta')$, $r'' = \exp(i\delta'')$. Also $\text{Re}(x) = 0$ so that

$$\lim_{\eta_1 \rightarrow 0} \rho = \frac{\exp(i\delta') + N^2 \exp(i\delta'')}{1 + N^2 \exp[i(\delta' + \delta'')]}, \quad \lim_{\eta_1 \rightarrow 0} \theta = \frac{d' d'' N}{1 + N^2 \exp[i(\delta' + \delta'')]} \quad (37 a, b)$$

The same holds true of the magnetic vectors, which will not therefore be discussed explicitly.

It is evident that (37) may yield quite general results, particularly that $|\rho|^2$ may deviate from unity. In the formally simplest case $n_0 = n_2$ the difference $1 - |\rho|^2$ can be shown to be

$$\left[1 + \left(\frac{1 - N^2}{2N} \right)^2 \text{cosec}^2 \delta' \right]^{-1}.$$

For $\kappa_1 \rightarrow 0$ or ∞ it tends to zero, while its maximum is given by the condition $\kappa_1 = n_0 \Rightarrow \delta' = \pi/2$, yielding

$$1 - |\rho|^2 = \frac{4N^2}{(1 + N^2)^2} > N^2.$$

Thus it can be estimated, e.g. for $\kappa_1 h \approx 1/20\lambda$, $1 - |\rho|^2 > 0.5$.

This is the first (and only) time in this study that we meet a case where a unit reflection coefficient at the first boundary is not accompanied (before degenerating $h \rightarrow 0$) by 100 per cent reflection of energy on the whole layer.

Considering the first boundary isolated, the limit $\eta_1 \rightarrow 0$ results in complete reflection of energy, while a wattless electromagnetic wave continues to travel behind it. This follows from the relations

$$d' = \frac{2n_0}{n_0 - i\kappa_1} \neq 0, \quad \text{energy transmission} = \frac{\eta_1}{n_0} |d'|^2 = 0.$$

In a metallic layer, however, this total reflection of energy on the first boundary is frustrated and electromagnetic energy infiltrates through the film into the third medium, as shown above. This closely resembles the case of frustrated total reflection on a boundary between two dielectrics[†].

There arises the question of how energy may pass through the film, if the Poynting vector—in metals proportional to $\eta_1|E|^2$ —is zero owing to $\eta_1 \rightarrow 0$. However, this is only true in a half-infinite space behind the first boundary. Inside a layer, where there are two encountering waves, the orthodox Poynting vector in metals is not the only carrier of energy. A new energy-flux vector arises depending on the amplitudes of both the incident and reflected waves and vanishing with κ_1 , see e.g. [3]. Along the depth of the layer this vector generally changes according to the sine function. In our special case $\eta_1 = 0$ it becomes a constant vector (depending perhaps on the thickness of the layer, but not on the depth coordinate inside it), pointing in the positive direction. It is this vector that represents the whole energy transport across the optically degenerate film.

Another remark may be made about the physical significance of this case. Suppose we ignore the concept of interference and treat the problem from the point of view of Newtonian emanation theory, using the model of multiple reflections. We should then have to state that a boundary having a metallic medium behind it with $\text{Re}(n_1) = 0$ represents an insurmountable obstacle for the light corpuscles, whatever the design of other boundaries behind it may be. The wave-theoretical treatment, on the contrary, shows that, in a way, light exists behind the boundary and even predicts the transmission of energy, if the metallic medium becomes a layer.

This somewhat resembles the behaviour of a particle with respect to a potential barrier, as treated in classical physics and by wave mechanics[‡].

A further point perhaps worth mentioning is that $\eta_1 \rightarrow 0$ implies absorption of metallic film $\rightarrow 0$, although $\kappa_1 \neq 0$. This follows immediately from the explicit formula for absorption derived in [3]. It could also be deduced indirectly by putting $A = 1 - |\rho|^2 - (n_2/n_0)|\theta|^2$.

Finally let us proceed to the second limit $h \rightarrow 0$. The conditions of degeneration are evidently fulfilled, because $N \rightarrow 1$ and equations (37 a, b) essentially yield the left-hand sides of (5).

$$(4b) \quad \kappa_1 \rightarrow 0$$

This limit renders the layer dielectric, which by itself presents no difficulties and clearly fulfills the degeneracy conditions. Moreover, an interesting sub-case may be created by limiting $\eta_1 \rightarrow 0$.

$$(4b1) \quad \kappa_1 = 0, \eta_1 \rightarrow 0$$

The result is obtained with advantage from the reflectivity and transmissivity formulae corresponding to (9 a, b). Replacing the sine by its arc one obtains

$$\lim_{\eta_1 \rightarrow 0} \rho = \frac{g'' - n_2}{g'' + n_2}, \quad \lim_{\eta_1 \rightarrow 0} \theta = \frac{2n_0}{g'' + n_2} \quad (38)$$

[†] This has already been stated in [1], but the implication based on this result should be used in the reversed sense.

[‡] In essence this amounts to no more than the well-established everyday experience that interference in a film changes the original reflecting power of the boundaries. However, if the change is effected on a 100 per cent original reflection, the case gains in attractiveness and becomes surprising in the light of older theories.

where

$$g'' = n_0 + i k n_0 n_2 h. \quad (39)$$

The degeneracy conditions are obviously fulfilled.

It is important also to ascertain which of the apparently natural assumptions is misleading here. One might be tempted to use the well-known rule that in optics it is the optical path that counts, and say limiting $\eta_1 \rightarrow 0$ is equivalent to limiting $x \rightarrow 0$ which would lead to the result

$$\rho - \frac{r' + r''}{1 + r' r''} = \frac{0}{0} = \frac{n_0 - n_2}{n_0 + n_2}$$

independent of h .

This would mean that an interference layer (dielectric or absorbing) might not only degenerate through its geometric thickness tending towards zero, but that, retaining finite depth, it might also become optically insignificant through its refractive index $n_1 = \eta_1 - i\kappa_1$ assuming the value zero in both of its components.

However, a detailed analysis shows this is not the case.

5. EXAMPLES

The limiting values of the refractive indices and thicknesses considered throughout this study may at first sight seem to rule out the practical application of such considerations, but it may be pointed out that e.g. case (4a) is quite near reality with a thin magnesium, gold, silver and especially sodium film, where $\eta \ll \kappa$.

Moreover, a class of multilayer dielectric films, namely those symmetrical with respect to the outer media, are equivalent to a simple hypothetical layer, [4, 5]. Operating on the design data of the real system may lead to quite extraordinary values of the equivalent layer parameters, so that in this sense there are well-founded reasons for the single-layer model to work in all situations.

A brief example will show what we mean.

Let there be a three-layer dielectric system $n_0/n_1/n_2/n_3/n_4$, symmetrical with respect to the outer media so that $n_1 = n_3 = \nu$, ($n_2 = n'$), $h_1 = h_3 = h$. Denoting simply $\cos \alpha = C$, $\sin \alpha = S$, the interference matrix of this system is (for normal incidence)

$$M = \prod_{\nu=1}^3 \begin{bmatrix} C_\nu & \frac{i}{n_\nu} S_\nu \\ i n_\nu S_\nu & C_\nu \end{bmatrix} = \begin{bmatrix} Q & iP \\ iT & Q \end{bmatrix}.$$

For simplicity we choose $n_2 h_2 = \lambda/4 \Rightarrow C_2 = 0$, $S_2 = 1$. Then

$$Q = -\frac{n'^2 + n^2}{n'n} CS, \quad P = \frac{1}{n'n^2} (n^2 C^2 - n'^2 S^2), \quad T = \frac{1}{n'} (n'^2 C^2 - n^2 S^2). \quad (40 a, b, c)$$

Furthermore in general $Q^2 + PT = 1$.

For the parameters of the equivalent layer it follows by comparison that

$$\cos \alpha_e = Q, \quad n_e = \frac{\sin \alpha_e}{P} = \frac{\sqrt{(1 - Q^2)}}{T} = \sqrt{(T/P)} \quad (41 a, b)$$

so that in the given case

$$n_e = \sqrt{\left(\frac{n'^2 C^2 - n^2 S^2}{n^2 C^2 - n'^2 S^2} \right)}. \quad (42)$$

It is now possible to make $n_e \rightarrow \infty$ "by purely technological means" letting $P \rightarrow 0$, i.e. $\tan \alpha \equiv S/C \rightarrow n/n'$.

In order to avoid undue formal complications, we shall confine ourselves to the following case $n' > n$, $0 < \bar{\alpha} = \arctg n/n' < 45^\circ$. Only the limit $\alpha \rightarrow \bar{\alpha} -$, i.e. $h \rightarrow \bar{\alpha}/kn \equiv \bar{h}$ from the left (with n constant) will be investigated.

Let us put $h = \bar{h} - \epsilon$, $\epsilon > 0$, small. Then

$$\sin \alpha = \sin \bar{\alpha} - kn\epsilon \cos \bar{\alpha} = \frac{n}{\sqrt{(n'^2 + n^2)}} (1 - kn'\epsilon) \quad (43)$$

and similarly for $\cos \alpha$, so that by (40 a), (41 a)

$$\cos \alpha_e = - \left(1 - k \frac{n'^2 - n^2}{n'} \epsilon \right)$$

from which relation it follows that

$$\alpha_e = l\pi + \alpha_1, \quad l \text{ odd}$$

where

$$\alpha_1 = \pm \sqrt{\left(2k \frac{n'^2 - n^2}{n'} \epsilon \right)} \quad (43)$$

is the rate of convergence of α_e towards $l\pi$.

Since P can be shown to be $2k\epsilon > 0$, the plus or minus sign associated with α_1 determines the sign of $n_e \leq 0$, which corresponds to an ambiguity of the choice in α_e in the third or second quadrant. Inserting (43) into (42) we find

$$|n_e| = \sqrt{\left(\frac{1}{2k} \frac{n'^2 - n^2}{n'} \frac{1}{\epsilon} \right)}$$

and in both cases

$$\alpha_1 n_e \equiv \alpha_1 \eta_e = - \frac{n'^2 - n^2}{n'} \neq 0.$$

We are therefore concerned with a case of the type (3 a (ii)) where $\kappa_1 = 0$ and may immediately write the result by (22) as

$$\rho = \frac{n_0 - n_4 + i \frac{n'^2 - n^2}{n'}}{n_0 + n_4 - i \frac{n'^2 - n^2}{n'}}.$$

This can be verified by direct calculation with the three-layer system.

The example has shown that quite normal real films may indeed lead to extraordinary situations in the domain of the equivalent layer, which the theory has to tackle if the equivalence theorem is to be general.

6. CONCLUSION

The classical electromagnetic theory of a thin metallic film has been applied to various limiting cases of refractive indices and thicknesses $(\infty, 0)$. The concept of mathematical limit, particularly that of convergence rate, has been found to exert substantial influence, both quantitative and qualitative, upon the resulting reflectivities and transmissivities. All the cases of degenerate interference can be logically classified and explained within the framework of the present theory of the metallic film so that, contrary to some opinions [7], there is no reason for its revision from this point of view. The material presented also contributes to the usefulness of the concept of equivalent layer.

On examine la théorie d'une lame mince interférentielle dans des cas particuliers qui se présentent lorsqu'on effectue certains passages à la limite mathématique sur les indices de réfraction. Dans ces conditions on examine avec une attention particulière la dégénérescence géométrique de la couche en une seule surface. On indique la relation qui existe entre les cas discutés et des lames réelles.

Die Theorie der metallischen Interferenzschichten wird auf die besonderen Verhältnisse ausgedehnt, die vorliegen, wenn man mit dem Brechwert zu verschiedenen mathematischen Grenzen geht. Die geometrische Entartung zur Dicke Null der Schicht, also zu einer einzelnen Grenzfläche unter den angegebenen Umständen wird besonders behandelt. Der Zusammenhang dieser Betrachtung mit einigen realisierten Schichten wird mitgeteilt.

REFERENCES

- [1] KNITTL, Z., 1958, *Czech. J. Phys.*, **8**, 131.
- [2] KARD, P. G., 1958, *Bull. Acad. Sci., U.R.S.S.*, **7**, 283.
- [3] KNITTL, Z., 1959, *Czech. J. Phys.*, **9**, 133.
- [4] ROZENBERG, G. V., 1958, *Optika tonkoslojnych pokrytij* (Thin Film Optics) (Moscow), p. 211.
- [5] HERPIN, A., 1947, *Comptes Rendus*, **225**, 182.
- [6] EPSTEIN, L. I., 1952, *J. opt. Soc. Amer.*, **42**, 806.
- [7] VAŠIČEK, A., 1960, *Optics of Thin Films* (Amsterdam: North-Holland), p. 325.



Colorimetric daylight illuminant with high ultra-violet content

by B. HISDAL

The Royal Norwegian Council for Scientific and Industrial Research,
Blindern, Norway

(Received 11 January 1961)

For colorimetry of daylight fluorescent materials, a daylight illuminant of higher ultra-violet energy content than that of source C is needed. In an earlier paper it was shown that an increase in ultra-violet energy can be obtained by supplementing source C with another source containing a tungsten lamp and an ultra-violet transmitting filter. Newer data indicate that the ultra-violet content of average daylight may be considerably higher than that assumed in the previous paper. The purpose of this investigation is to see what kind of approximation to this type of ultra-violet energy distribution is possible, using the same arrangement as before.

It is shown that an approximation, satisfactory for all cases of daylight fluorescent colorimetry can probably not be obtained with only one supplementary source, using conventional filters and reasonable (tungsten) lamp intensities. A satisfactory solution for the type of ultra-violet distribution involved seems to require at least two supplementary sources. Examples of spectral energy distributions obtainable with one and with two supplementary sources are shown.

1. INTRODUCTION

A number of fluorescent dyes in common use today absorb radiation in the near ultra-violet and emit part of this absorbed energy as light. These dyes are often used to give a material a certain colour under daylight conditions. To measure this colour it is necessary to have an artificial illuminant whose relative spectral energy distribution is equivalent to that of daylight both in the visible and in the ultra-violet. As the daylight sources B and C are deficient in ultra-violet energy, the CIE has recommended that the question of finding a more suitable illuminant for fluorescent colorimetry be taken up for investigation.

It is possible to obtain an illumination at the sample surface, whose relative spectral energy distribution is approximately representative of average daylight also in the ultra-violet, by supplementing source C by another source, radiating only in the ultra-violet. This is one of the methods recommended for further investigation by the CIE [1].

In a previous paper [2] an arrangement was described where the supplementary source consisted of a tungsten lamp and an ultra-violet transmitting filter. In this arrangement the illumination from source C was incident on the sample at an angle of 45° with the normal, and the radiation from the ultra-violet source was incident at the same angle, from the other side. The radiation reflected (and emitted) in the direction of the normal to the sample was measured by means of a spectrophotometer. A schematic diagram of such an arrangement is shown in figure 1.

The tungsten lamp in the ultra-violet source is operated at a colour temperature of 2854°K (CIE source A), which is the same as the temperature of the lamp in source C. Except for the ultra-violet filter, the lamps, filters and geometry

used in the two sources have the characteristics recommended by the CIE. As the ultra-violet filter does not transmit in the visible, the energy distribution in this region is the same as for source C. The usual tables and procedures for colour computation can therefore be used.

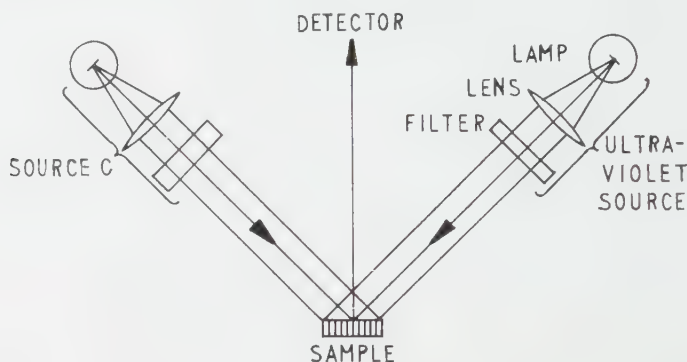


Figure 1. Illumination arrangement for a daylight fluorescent sample.

For measuring purposes the two sources in the above arrangement can be used to illuminate the fluorescent sample either in front of the entrance slit of a spectrophotometer, or in a photoelectric tricolorimeter. It can of course also be used as an illuminant for the visual inspection of fluorescent samples, but has the disadvantage that the level of illumination is rather low for a somewhat larger area.

Concerning the visible and ultra-violet energy distribution in daylight, Middleton [3] has suggested a distribution for colorimetric use, based on the published results of a number of observers. This distribution agrees reasonably well with some measurements of noon-time daylight from overcast sky made by the author during the summer and early autumn, on the outskirts of Oslo, Norway. The results of these two investigations show a much higher energy content for daylight than was used in the previous work. In order to find what kind of approximation to this type of energy distribution is possible, using the same arrangement as before, the design of the ultra-violet source will be reconsidered. The re-design will be carried through both for lamps with the tabulated energy distribution of source A, and also for tungsten ribbon filament lamps with a spectral variation in emissivity as found by DeVos [4]. The effect of selective transmission by the lamp envelope will be considered.

It is in many cases possible to obtain a satisfactory geometry of illumination with an arrangement containing more than two sources. This will allow the use of more than one ultra-violet source, which may give a better approximation in spectral energy distribution, and have certain advantages as far as the choice of filters and lamp intensities is concerned. On the other hand the number of lamps should be kept small for technical and economical reasons. Therefore only the cases of using one and two supplementary ultra-violet sources will be considered here.

In the following the supplementary ultra-violet source will be referred to as source C_{uv} and its energy distribution as E_{uv} . The energy distribution of source C will be referred to as E_C , and the resulting distribution of the two sources combined, as E_T . The corresponding quantities when a ribbon lamp with quartz

window is used will be designated by the additional subscript Q, and when this lamp has a glass envelope, with the additional subscript G. The fluorescent colours of the type mentioned above will be called daylight fluorescent colours.

2. ULTRA-VIOLET ENERGY IN DAYLIGHT

To find a representative ultra-violet energy distribution for the type of daylight represented by source C, the following procedure was chosen:

First the sum of the tabulated energy distribution values for every $10\text{ m}\mu$ from 420 to $560\text{ m}\mu$ was found for source C. The energy distribution suggested by Middleton was then normalized to give the same total energy between 420 and $560\text{ m}\mu$. This distribution is shown in figure 2 (marked 'Adopted distribution') together with the tabulated distribution of source C.

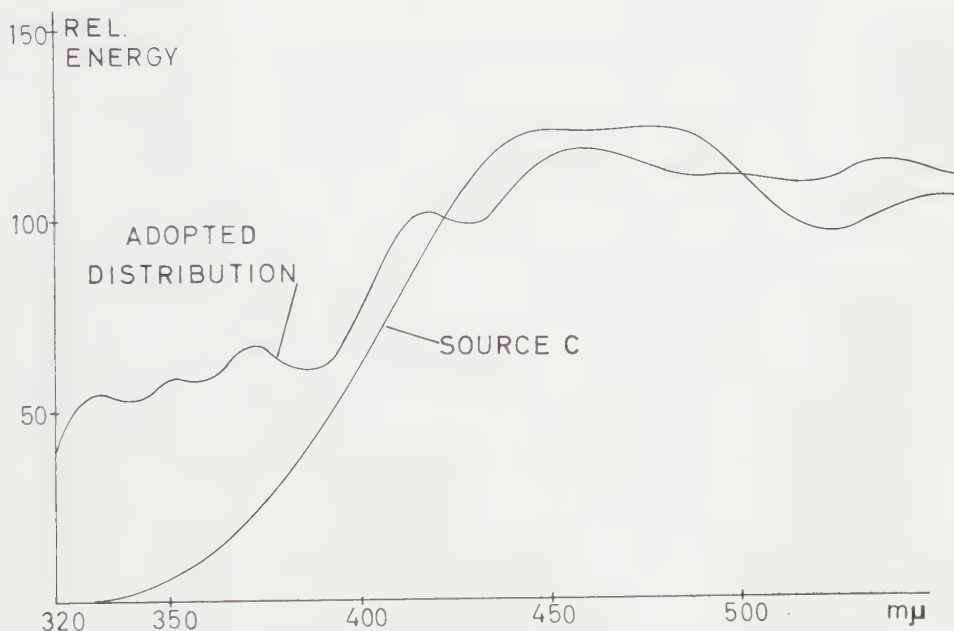


Figure 2. Adopted distribution-spectral energy distribution of daylight as suggested by Middleton, when normalized to give the same total energy between 420 and $560\text{ m}\mu$, as CIE source C.

For the purpose of this investigation it is assumed justified to adopt the normalized data below $390\text{ m}\mu$ as a representative ultra-violet distribution for source C. The adopted data are given in table 1, column two, up to $380\text{ m}\mu$. From $390\text{ m}\mu$ the data are the same as those tabulated for source C.

The normalized distribution curve of figure 2 represents an average smoothed curve where the Fraunhofer absorption lines and bands do not appear. However, in regions with many strong absorption lines, dips will occur in the smoothed curve. For instance, the dip near $390\text{ m}\mu$ is mainly caused by the strong absorption bands in this region of the calcium and hydrogen gases in the solar atmosphere. From figure 2 it is also seen that the ultra-violet energy in daylight drops off rather rapidly below $330\text{ m}\mu$.

Table 1. Ultra-violet energy distribution

Wavelength (m μ)	Adopted distribution E_T	Source C E_C	Source C _{uv} E_{uv}	Source A $E_A = E_C/T_C$
320	39.5	0.01	39.5	12.3
330	55.2	0.4	54.8	17.0
340	52.9	2.7	50.2	22.8
350	58.8	7.0	51.8	30.2
360	58.8	12.9	45.9	39.1
370	68.0	21.4	46.6	49.9
380	62.9	33.0	29.9	62.5
390	47.4	47.4	0	77.1

The data of column two, table 1, give the relative energy E_T to be approximated by the combination of sources C and C_{uv}. To find the relative energy E_{uv} to be supplied by source C_{uv} alone, the energy E_C supplied by source C must be subtracted. The tabulated values of E_C are given in column three and the ideal distribution of E_{uv} in column four. The energy distribution E_A for source A, obtained by multiplying the values of E_C by $1/T_C$ (where T_C is the transmittance of the Davis-Gibson filter for source C [5]), is given in column five.

3. TRANSMITTANCE OF THE IDEAL ULTRA-VIOLET FILTER

From the data given in table 1, the transmittance of the ideal ultra-violet filter can be computed. (The ideal filter transforms the energy distribution of source A into the ideal distribution for source C_{uv} given in column four of table 1.) However, as the relative energy values of source A below 370 m μ are lower than the values required for E_{uv} (compare columns four and five of table 1), it follows that the intensity of the lamp in source C_{uv} must be higher than that of the lamp in source C. The transmittance of the ideal filter has therefore been computed for the case where the lamp in source C_{uv} has four times the intensity of the lamp in source C. The values of source A, from column five, table 1, when multiplied by four, are given in table 2, column two. In column three are given the transmittance values of the corresponding ideal filter (i.e. the product of corresponding terms in columns two and three is equal to the values of E_{uv} in column four of table 1).

Table 2. Transmittance (T) of ideal ultra-violet filter, when a lamp with the spectral energy distribution of source A is used both in source C and in source C_{uv}. The lamp in source C_{uv} has four times the intensity of the lamp in source C

Wavelength (m μ)	$4 \times E_A$	T (per cent)
320	49.2	80.3
330	68.0	80.6
340	91.2	55.0
350	120.8	42.9
360	156.4	29.3
370	199.6	23.3
380	250.0	12.0
390	308.4	0

The values in table 2 refer to lamps of spectral characteristics as tabulated for source A, i.e. a non-selective radiator. However, because of the spectral variation in emissivity of the tungsten filament and the selective transmission of the lamp envelope, the spectral energy distribution of actual tungsten filament lamps will deviate from that tabulated for source A. The deviation in the visible may not be big enough to be important in practical colour measurements, with the accuracies commonly obtainable today. But in the ultra-violet, the effect of the deviations may become significant and must be taken into consideration when computing the ultra-violet filter needed for such lamps.

The radiation characteristic of a specified type of tungsten ribbon filament has been thoroughly studied by DeVos [4]. From his data the ultra-violet energy distribution for a given temperature can be computed. As lamps with this type of filament and a window of known transmission are commercially available, the energy distribution and the associated ideal filter will be computed for these lamps. (It should be noted that there is a certain temperature variation along the ribbon filament and that the computed spectral energy distribution therefore strictly refers only to the radiation from the central part used during the calibration of the lamp.)

In table 3, column two, the spectral transmittance in the ultra-violet of the quartz window of a particular lamp is given. It is assumed that the transmittance of the quartz window is constant over the visible region. Column three shows the spectral energy distribution E_{AQ} of the radiation from this lamp up to $390\text{ m}\mu$, when operated to give the best colour match with source A (according to Judd [6]). The distribution for the ribbon lamp (E_{AQ}) has here been multiplied by the normalization factor obtained for source C_Q , when this has been normalized so as to give the same total energy between 420 and $560\text{ m}\mu$, as source C.

Table 3. Transmittance (T_Q) of ideal ultra-violet filter, when a ribbon filament lamp with quartz window and filament emissivity as found by DeVos, is used both in source C and in source C_{uv} . The lamp in source C_{uv} has four times the intensity of the lamp in source C

Wavelength ($\text{m}\mu$)	Transmittance Quartz window	Ribbon lamp E_{AQ}	Source C_Q E_{CQ}	T_Q (per cent)
320	92.1	11.1	0	89.3
330	92.3	15.5	0.4	88.5
340	92.6	21.2	2.5	59.3
350	92.7	28.4	6.6	45.9
360	92.8	37.2	12.2	31.2
370	92.8	47.9	20.6	24.7
380	92.8	60.4	32.0	12.8
390	92.6	74.9	46.1	0.4

Column four gives the energy distribution E_{CQ} for this lamp in connection with the Davis-Gibson filter for source C. The transmittance of the ideal filter is given in column five. It is here assumed that the lamp used in source C_{uvQ} has four times the intensity of the lamp in source C_Q . With these relative lamp intensities, and the ideal ultra-violet filter, the sum of the energies from source C_{uvQ}

and source C_Q , will at each wavelength be equal to the value E_T given for the adopted daylight in table 1, column two.

In table 4, the corresponding data are given for a ribbon filament lamp with a glass window of transmittance as shown in column two. (The transmittance values of the glass window, as well as the above quartz window have been supplied by the manufacturer.) The transmittance of some glass bulbs belonging to lamps used as standards for visual colorimetry has been measured and gave values essentially similar to those in column two (although in one case considerably lower). The transmittance values of column two are therefore assumed to be fairly representative of the transmittances that can be found in ordinary glass envelopes. The operating conditions for this lamp are the same as those of the lamp in table 3.

Table 4. Transmittance (T_G) of ideal ultra-violet filter, when a ribbon filament lamp with glass window and filament emissivity as found by DeVos, is used both in source C and in source C_{UV} . The lamp in source C_{UV} has four times the intensity of the lamp in source C

Wavelength ($m\mu$)	Transmittance Glass window	Ribbon lamp E_{AG}	Source C_G E_{CG}	T_G (per cent)
320	49.5	6.1	0	> 100
330	65.9	11.4	0.2	> 100
340	76.4	18.0	2.1	70.4
350	82.9	26.1	5.7	50.9
360	86.2	35.6	11.8	33.1
370	88.5	47.0	20.2	25.4
380	89.3	59.8	31.6	13.1
390	89.8	74.6	46.0	0.5

As shown, the transmittance of the ideal filter would have to be larger than 100 per cent at 320 $m\mu$ and 330 $m\mu$. The approximations obtainable at these wavelengths will therefore be very bad. From this it is concluded that the approximations obtainable, using lamps with ordinary glass envelopes, will be rather unsatisfactory, and they are therefore not suited for use in source C_{UV} .

4. PRACTICAL ULTRA-VIOLET FILTERS

Various filters have been investigated to find combinations giving a good approximation to the ideal filters of tables 2 and 3. Filters to be used with light sources of the tabulated distribution of source A will be considered first. It will then be shown how the data of these filters must be changed in order to give the best result when used with ribbon filament lamps.

Among the liquid filter solutions investigated, solutions of $NiSO_4 \cdot 6H_2O$ and $KCr(SO_4)_2 \cdot 12H_2O$ had very satisfactory ultra-violet transmission characteristics. The appreciable transmission in the blue-green part of the spectrum could be removed by means of an aqueous solution of $CoSO_4 \cdot 7H_2O$. All these solutions are stable and easily prepared, according to investigations made by Kasha [7]. The real problem however is to remove the transmission in the red part of the spectrum, without influencing the transmission in the ultra-violet. This problem could not be solved by any of the solutions investigated, and therefore no completely satisfactory filter using only liquid solution components has

been found. The data for the combination giving the best transmittance are listed in table 5, column two.

Table 5. Transmittance of experimental ultra-violet filters

Wavelength (m μ)	All liquid filter	2 mm UG11 NiSO ₄ 50 g/l	2 mm UG11 KCr(SO ₄) ₂ 19 g/l	5.2 mm UG11 glass	10 mm UG5 KCr(SO ₄) ₂ 19 g/l
320	38.1	71.9	66.5	68.5	63.7
330	38.9	70.0	65.9	67.8	67.0
340	38.5	64.4	60.8	65.1	57.0
350	32.5	56.5	52.8	59.2	50.2
360	24.8	40.1	39.7	44.5	37.5
370	14.5	17.6	22.0	18.8	23.3
380	7.1	3.2	6.0	1.3	10.7
390	3.0	0.1	0.2	0	1.5
400	1.8	0	0	0	0
660	0.1	0	0	0	0
680	0.3	0	0.1	0	0.1
700	0.9	1.8	3.9	0.1	1.2
720	1.6	3.0	6.2	0	9.8

This filter consists of three 1 cm long glass cells with quartz windows, built together in one unit and containing the following (freshly made) aqueous solutions:

I. $\text{KCr}(\text{SO}_4)_2 \cdot 12\text{H}_2\text{O}$ 40 g/l;

II. $\text{CoSO}_4 \cdot 7\text{H}_2\text{O}$ 450 g/l;

III. An aqueous ammonia solution of copper sulphate, $\text{CuSO}_4 \cdot 5\text{H}_2\text{O}$ 12 g/l plus 200 cm³/l of a 25 per cent solution of NH_3 . [The latter solution is not very satisfactory as the ammonia attacks the glass of the cells and also evaporates if the cells are not hermetically sealed [8].

Better results can be obtained when the liquid filters are combined with glass filters of high ultra-violet, and low visible transmission. Column three of table 5 gives the transmittance of a combination of a Schott UG11 filter 2 mm thick and an aqueous solution of $\text{NiSO}_4 \cdot 6\text{H}_2\text{O}$ 50 g/l. The transmittance of the same glass filter with a solution of $\text{KCr}(\text{SO}_4)_2 \cdot 12\text{H}_2\text{O}$ 19 g/l is given in column four. In both cases the solution is contained in a 1 cm thick cell with quartz windows. In column five is given the transmittance of a UG11 filter, 5.2 mm thick. Table 5 also shows the transmittances of these filters in the visible region.

A slightly better approximation in spectral distribution is obtained with a Schott UG5 filter of 10 mm thickness in connection with the same solutions. The data for this filter in connection with the $\text{KCr}(\text{SO}_4)_2 \cdot 12\text{H}_2\text{O}$ solution, are shown in column six of table 5. Also a 23.5 mm thick UG5 filter could be used instead of the 5.2 mm UG11 filter.

The data of table 5 (except for the all liquid filter in a three-compartment cell) are obtained from measurements with a Cary recording spectrophotometer calibrated in density units. The photometric scale of the instrument was checked with glass standards of spectral transmittance. The chemicals used were all of P.A. grade, and the data for all the glass filters refer to the specific samples measured.

The thicknesses and concentrations of the filters in table 5 are chosen such that these filters in connection with a source A of the appropriate intensity, will give a source C_{uv} of nearly the same total energy output in the range 330 to 390 m μ as the adopted daylight (within ± 1 per cent of the sum of the values in column four of table 1). The appropriate intensity of the lamp in source C_{uv} is four times the intensity of the lamp in source C for all filters, except the all liquid filter. Here the intensity of the lamp would have to be six times that of

Table 6. Ultra-violet energy distribution E_{uv} obtained with the experimental filters, when a lamp with the spectral energy distribution of source A and four times the intensity of the lamp in source C is used in source C_{uv}

Wavelength (m μ)	E_{uv} (ideal)	2 mm UG11 + NiSO ₄ 50 g/l	2 mm UG11 + KCr(SO ₄) ₂ 19 g/l	5.2 mm UG11	10 mm UG5 + KCr(SO ₄) ₂ 19 g/l
320	39.5	35.4	32.7	33.7	31.3
330	54.8	47.6	44.8	46.1	41.5
340	50.2	58.7	55.4	59.4	52.0
350	51.8	68.3	63.8	71.5	60.6
360	45.9	62.9	62.1	69.6	58.7
370	46.6	35.1	43.9	37.5	46.5
380	29.9	8.0	15.0	3.3	26.7
390	0	0.3	0.6	0	4.6
Sum	318.7	316.3	318.3	321.1	321.9

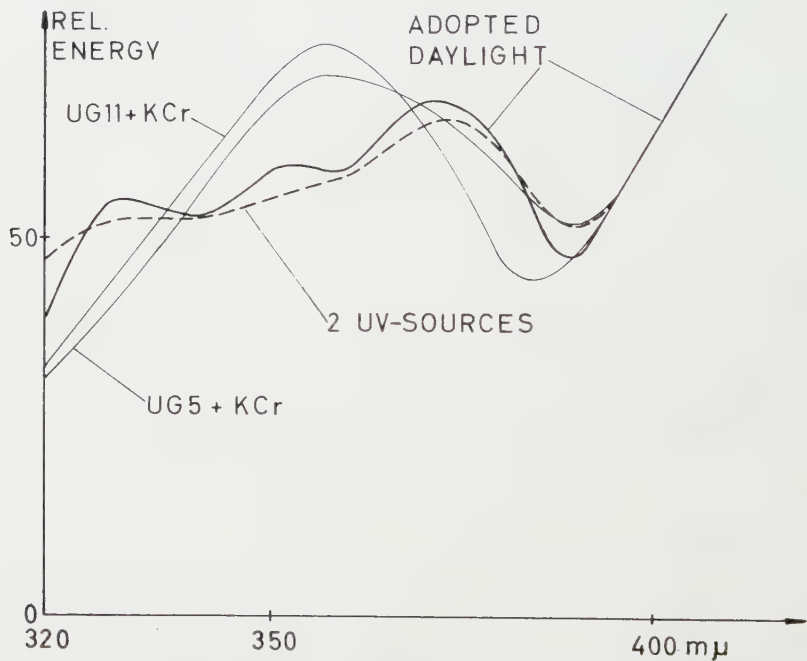


Figure 3. Adopted ultra-violet energy distribution (heavy solid curve) and approximations obtainable with one source (thin solid curves) or two supplementary sources (broken curve).

the lamp in source C. As this lamp intensity is rather high, and the filter also has a somewhat high transmission in the visible, this source C_{uv} is not considered suitable for colorimetric use.

The resulting ultra-violet energies have been computed and are given in table 6, columns three to six.

The ultra-violet energy distributions of the combined sources (E_T), when the ultra-violet sources of columns four and six are used, are shown in figure 3.

The filters of table 5 were computed for use with light source A. As the ultra-violet energy output of the ribbon lamp is somewhat lower than that of the tabulated source A, the transmittance of the associated ultra-violet filter must be higher (compare last columns of tables 2 and 3). It is therefore necessary to reduce the thickness of the UG11 filter from 2 to 1.5 mm, and the thickness of the UG5 filter from 10 to 6.7 mm, in the glass-liquid filter combinations. For the UG11 filter used alone, the thickness has to be reduced from 5.2 to 4.5 mm. When these changes are made, very nearly the same total ultra-violet energies are obtained as those shown at the bottom of columns three to six of table 6.

It is usually possible to obtain filters suitable for ribbon filament lamps by similar modifications of the filters computed for source A. The complete computation of filters is therefore only carried through for the latter type of distribution.

Other makes of glass filters can of course also be used. Among these are the Chance OX 1, the Corning 9863 and the Wratten 18B. However, for the latter two types, the thicknesses would have to be even larger than for the UG5 filter, in order to reduce the visible transmission sufficiently.

5. TWO ULTRA-VIOLET SOURCES

With two separate ultra-violet sources, one having its maximum near the short wavelength end, and the other near the long wavelength end of the ultra-violet region, it should be possible to obtain a better overall approximation. The main thing is to improve the distribution near the short wavelength end. For this purpose a filter with a transmission peak of at least 40 per cent in the region 320 to 330 m μ and very low transmission above 350 m μ is needed. A satisfactory glass filter with this type of transmission characteristic has not been found. However, a liquid-glass filter combination using a 1 cm path of an aqueous solution of $\text{NiSO}_4 \cdot 6\text{H}_2\text{O}$ and a 2 mm UG11 filter has a very suitable type of transmission. The resulting ultra-violet energy distribution obtained when this filter, with a concentration of 250 g/l of NiSO_4 , is used with a lamp of intensity $4.3 \times E_A$ in one source C_{uv} and a 5 mm UG2 filter with a lamp of intensity $2.1 \times E_A$ is used in the other source C_{uv} , is shown in column two of table 7.

In column three is given the resulting distribution when one source has the same type of filter as the first source above, but now with a concentration of 500 g/l of NiSO_4 and a lamp of intensity $4 \times E_A$ and the other source uses a 12.5 mm UG5 filter with a lamp of intensity $1.9 \times E_A$. This distribution has been drawn as the broken curve in figure 3. The transmittance curves of the filters used are shown in figure 4 (the data of the NiSO_4 solution include the reflection losses of the particular quartz windows used).

As before, all the glass-filter thicknesses and lamp intensities have been adjusted so that the sum of each column is nearly the same as the sum of the adopted daylight distribution in column two of table 6.

Table 7. Energy distribution with two ultra-violet sources

Wavelength (mμ)	Source 1	Filter	Lamp in source C _{uv}	Filter	Lamp in source C _{uv}
		2 mm UG11 + NiSO ₄ 250 g/l	$4.3 \times E_A$	2 mm UG11 + NiSO ₄ 500 g/l	$4 \times E_A$
	Source 2	5 mm UG2	$2.1 \times E_A$	12.5 mm UG5	$1.9 \times E_A$
320		35.4		47.0	
330		44.9		51.9	
340		53.9		50.0	
350		57.6		48.2	
360		50.4		45.3	
370		43.4		43.5	
380		28.8		29.1	
390		3.4		4.4	
Sum		317.8		319.4	

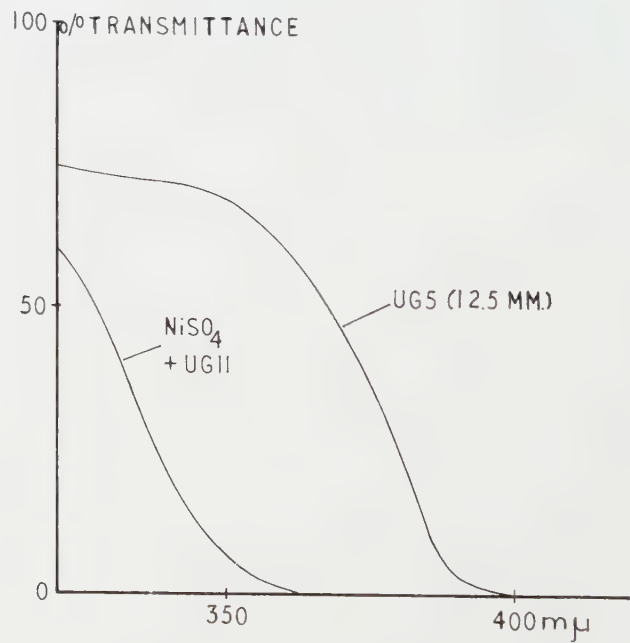


Figure 4. Transmittance curves for the filters in the supplementary sources used to give the resulting energy distribution shown by the broken curve of figure 3.

6. DISCUSSION

The results obtained in the previous sections indicate what kind of approximation to the adopted distribution can be obtained when source C is supplemented by one or two sources C_{uv} using glass or liquid filters and a source A or a ribbon filament lamp of reasonable intensity. Due to uncertainties in the recorded

data, small variations in cell transmittances or variations in transmission of the glass filters from one melt to another, it probably will be necessary to make adjustments in filter thicknesses, concentrations or lamp intensities in order to get a close reproduction of the data given.

As shown by figure 3, the approximation in spectral energy distribution, using only one source C_{uv} , is not very good. If we could have used lamps of higher intensities in source C_{uv} , and therefore filters with lower transmission, it would have been possible to obtain a much better approximation. However, as the intensity of the lamp is increased, the effect of even a small visible transmission in the ultra-violet filter (especially in the red region) becomes more and more important. Also the increased heating may be troublesome. For these reasons we have only investigated the approximations obtainable with lamp intensities in source C_{uv} up to about four times that of the lamp in source C. (A better approximation could probably also have been obtained with a high pressure Xenon lamp in source C_{uv} . This possibility has not been investigated here.)

The criterion used in the design of the lamp-filter combinations for source C_{uv} was, that they must give the same total ultra-violet energy in the region 320 to 390 $m\mu$ as the adopted distribution. This criterion is satisfied by all the combinations of tables 6 and 7. The combination which, at the same time, gives the closest approximation in spectral distribution without significant transmission in the visible, will then represent the best solution.

Because of the narrow wavelength range of source C_{uv} , it is possible to adjust its total ultra-violet energy output somewhat, without significant changes in spectral energy distribution, by varying the filament temperature of the lamp. This possibility can be used for fine adjustment and for correcting changes that occur due to ageing of the lamps. In this way the above criterion can always be satisfied by practical sources, even if the initial lamp intensities are not quite correct.

For daylight fluorescent colours with a fairly even absorption over a broad band, the colorimetric results obtained with an illuminant that satisfies the above criterion, will ordinarily be representative of those obtained in the adopted daylight (for colours where the whole fluorescent spectrum is excited by any wavelength within the absorption band). This will also usually be the case when colours of the same, or nearly the same type of more selective absorption are compared. However, when comparing colours with strongly selective absorption, and where the absorption maxima lie in different parts of the ultra-violet region, discrepancies may occur. The approximations obtained with one source C_{uv} will therefore not be satisfactory for all cases of fluorescent colorimetry (in the type of daylight considered).

It should be kept in mind that the ultra-violet content and distribution in daylight vary considerably, and that the adopted distribution may not be the one most representative of average daylight. Some measurements indicate a lower energy content and an intensity distribution that falls off more rapidly towards shorter wavelengths [9]. For this type of distribution there should be a good chance of obtaining a much better approximation, using only one source C_{uv} . The question of whether a satisfactory approximation is obtainable with one supplementary source or not will therefore in the end depend on the type of ultra-violet distribution that is adopted as representative.

The approximation to the adopted distribution when two sources C_{uv} are used (as shown in figure 3) is probably good enough in most cases of colorimetric measurements. It should also be possible to reproduce this distribution quite well, even with filters having transmittances somewhat different from those used here. This is so, because the resulting energy distribution can be adjusted considerably by choosing suitable lamp intensities, by varying the filament temperatures (for the lamps in C_{uv}) and by adjusting the filter thicknesses and concentrations.

The relative intensities of the lamps in the different sources can also be varied by using condenser lenses of suitable apertures. As the cross section of all the beams should preferably be the same, this means that shorter focal length lenses will have to be used in source C_{uv} .

According to the data of the manufacturer, the ultra-violet transmittance of the glass filters UG11 and UG5 may change after being exposed to intense radiation. From tests on samples of these glasses in our laboratory it seems that this change is small at wavelengths above $320\text{ m}\mu$. Also it takes place rather slowly with the light sources and illumination levels usually encountered in colorimetric instruments. The same type of effect has been reported for the Corning 9863 filter (Kasha [7]).

Liquid filters are not very well suited for use in commercial types of colorimetric instruments. In the case of two separate ultra-violet sources, the liquid filter could have been avoided if an interference filter, with a transmission suitable for the source C_{uv} with maximum energy output near the short wavelength end, had been available. This filter would have to be of the broad-band type (half-width at least $25\text{ m}\mu$) and with a maximum transmission of about 40 per cent in the region 325 to $330\text{ m}\mu$. Such a filter probably can be made†, but is so far not commercially available. With the number of parameters that can be varied in the two ultra-violet sources, it will be possible to reproduce a given energy distribution quite well, even if the transmission characteristic of the interference filter should vary somewhat from one filter to another.

When properly operated, the ribbon filament lamp, with emissivity as found by DeVos [4], has a well known spectral energy distribution. Lamps, as described by DeVos, are commercially available, and they can be operated at 2854°K . Therefore this is the only practical source for which filter data have been indicated. However, as such lamps should preferably not be operated above 2600°K for long periods, they are not well suited for continuous use in a colour measuring instrument. For this purpose, a projection type lamp, with a coiled tungsten filament and an envelope or window of quartz, or glass of high ultra-violet transmission and with a well-known spectral energy distribution might be used.

When a lens is used to make the radiation from source C_{uv} unidirectional before reaching the filter and the sample, the lens material must not show significant selective absorption in the ultra-violet. For source C an ordinary achromatic lens is often used and the absorption below $350\text{ m}\mu$ may then be quite high. On the other hand, the energy contribution of source C at these wavelengths is also rather low, and this effect can therefore often be neglected. As the absorption is mainly due to the concave flint component of the lens the absorption will vary across the beam. This results in an uneven spectral distribution across the sample. These effects of lenses in the ultra-violet should be taken into

† Private communication from Schott and Gen., Mainz.

consideration when designing filters and computing the resulting energy distribution (E_T) of the combined sources.

7. CONCLUSION

For the type of ultra-violet distribution considered, and with the adopted limitation on lamp intensities, the following conclusions seem to be justified:

The approximations obtainable with source C and one supplementary ultra-violet source of the type described may be satisfactory for many, but not all cases of daylight fluorescent colorimetry. To obtain a generally satisfactory approximation in distribution, at least two supplementary sources will have to be used. From a practical point of view the illumination arrangement is not ideal, but it allows a useful solution of the problem by means of components that are cheap and easily available.

ACKNOWLEDGMENTS

I am indebted to the Royal Norwegian Council for Scientific and Industrial Research for supporting this investigation, and to the Central Institute for Industrial Research for the use of their facilities.

Pour la colorimétrie des matériaux fluorescents à la lumière du jour, on a besoin d'une source qui fournisse davantage d'énergie ultra-violette que la source C. Il a été montré dans un précédent article qu'il est possible d'obtenir une augmentation de l'énergie ultra-violette en ajoutant à la source C une autre contenant une lampe à tungstène et un filtre qui transmet l'ultra-violet. Des données plus récentes indiquent que le contenu ultra-violet de la lumière du jour moyenne peut être beaucoup plus important que ce qui a été supposé dans l'article précédent. Le but de cette étude est de voir quelle sorte d'approximation est possible pour ce type de distribution d'énergie ultra-violette, en utilisant le même montage que précédemment.

On montre qu'une solution, satisfaisante pour tous les cas de colorimétrie de substances fluorescentes à la lumière du jour, ne peut probablement pas être obtenue avec une seule source supplémentaire, en utilisant des filtres conventionnels et des intensités raisonnables pour la lampe (à tungstène). Une solution satisfaisante pour le type de distribution ultra-violette nécessaire semble nécessiter au moins deux sources supplémentaires. On montre des exemples de distributions spectrales d'énergie pouvant être obtenus avec une et deux sources supplémentaires.

Für die Kolorimetrie von Materialien, die im Tageslicht fluoreszieren, benötigt man eine Tageslichtbeleuchtung, die aber einen höheren Betrag an Ultraviolett enthält als die Lichtquelle C. In einer älteren Untersuchung war gezeigt worden, daß man eine Zunahme der Ultraviolett-Energie dadurch erreichen kann, daß man zusätzlich zur Lichtquelle C eine andere Wolframlampe in Verbindung mit einem ultraviolett-durchlässigen Filter benutzt. Neure Zahlenangaben aber zeigen, daß der Ultraviolettgehalt des durchschnittlichen Tageslichtes doch beträchtlich höher sein kann, als es in der früheren Untersuchung angenommen war. Diese Untersuchung soll prüfen, wie weit diese Verteilung der Ultraviolett-Energie angenähert werden kann, wenn man dieselbe Anordnung wie vorher benutzt.

Es zeigt sich, daß eine Annäherung, die für alle Fälle der Fluoreszenz-Kolorimetrie im Tageslicht wahrscheinlich nicht befriedigend erreicht werden kann, wenn man nur eine zusätzliche Lichtquelle, die üblichen Filter und eine noch erträgliche Intensität der Wolframlampe verwendet. Eine befriedigende Lösung für die gewünschte Art des Ultraviolettanteils scheint wenigstens zwei zusätzliche Lichtquellen erforderlich zu machen. Es werden Beispiele der spektralen Energieverteilung gezeigt, die man mit einer und mit zwei zusätzlichen Lichtquellen erhalten kann.

REFERENCES

- [1] COMMISSION INTERNATIONALE DE L'ECLAIRAGE, 1955, Proceedings 13th Session, Zürich.
- [2] HISDAL, B., 1956, *Opt. Acta*, **3**, 139.
- [3] C.I.E. TECHNICAL COMMITTEE 1.3.1., Colorimetry, 1955, Report of Secretariat United States Committee.
- [4] DEVOS, J. C., 1953, Doctor's Thesis, The Free University of Amsterdam.
- [5] DAVIS, R., GIBSON, K. S., and HAUPT, G. W., 1953, *J. Res. nat. Bur. Stand.*, **50**, 31.
- [6] JUDD, D. B., 1936, *J. opt. Soc. Amer.*, **26**, 421.
- [7] KASHA, M., 1948, *J. opt. Soc. Amer.*, **38**, 929.
- [8] DAVIS, R., and GIBSON, K. S., 1931, *Nat. Bur. Stand. Misc. Publ.*, No. 114, 27.
- [9] SCHULZE, R., 1951, Commission Internationale de l'Eclairage, Proceedings 12th Session, Stockholm.

Definitionshelligkeit und Kontrastübertragung

von F. I. HAVLIČEK

Ljubljana-Prule, Jugoslavija

(Received 10 April 1961)

Mit Hilfe der Definitionshelligkeit wird das gebeugte Licht in Zentrallicht und Streulicht aufgeteilt, und für Streifensysteme beliebiger Streifenzahl wird mit Näherungsformeln die Kontrastübertragung berechnet.

Im Idealfall der Beugung an einer kreisrunden Oeffnung ist die Beleuchtungsintensität I in einer auf der Achse senkrechten Entfernung ρ vom Konzentrationspunkt

$$I = \left(\frac{2I_1(y)}{y} \right)^2; \quad y = \frac{2\pi}{\lambda} \rho \sin \theta.$$

$I_1(y)$ ist eine Zylinderfunktion, λ die Wellenlänge und θ der halbe Oeffnungswinkel des Strahlenbündels. Die Gesamtintensität, die auf das zentrale Beugungsscheibchen und auf die begleitenden Ringe fällt, ist

$$Q_{n, n+1} = \int_{y_n}^{y_{n+1}} 2\pi y I dy; \quad y_n = 0; 3,83; 7,02; 1,17; \dots$$

$$Q_{n, n+1} = 10,3; 0,96; 0,35; \dots$$

Die mittlere Intensität im Beugungsscheibchen ist also $10,3/3,83^2\pi = 0,225$. Als asymptotische Entwicklung der obigen Zylinderfunktion gilt [1]

$$I_1(y)^2 \frac{\cos(y - \frac{3}{4}\pi)}{\sqrt{(\frac{1}{2}\pi y)}}, \quad \text{also } I \sim \frac{4}{\pi y^3} \text{ mit } \cos^2_{\text{mitt.}} = \frac{1}{2}.$$

Mit dieser Approximation werden die Gesamtintensitäten im ersten und zweiten Ring 0,95 und 0,35 und die Gesamtintensität ausserhalb des zentralen Beugungsscheibchens 2,09 bzw. reduziert auf die Fläche des Beugungsscheibchens 0,0453. Die Gesamtintensität verteilt sich also im Idealfall mit 83 Prozent auf das Beugungsscheibchen und mit 17 Prozent auf die begleitenden Ringe.

Haben wir nun einen langen hellen Streifen der Breite X , dessen einzelne Punkte Aufpunkte obiger Beugungsscheibchen sind, so wird in einer Entfernung Z vom Rande des hellen Streifens die Beleuchtungsintensität R durch das Streulicht der begleitenden Ringe um die Zentren der Beugungsscheibchen im Sinne obiger asymptotischer Entwicklung

$$R_v = \frac{8}{\pi} \left(\frac{1}{Z} - \frac{1}{Z+X} \right) \quad \text{sein.}$$

Für einen Punkt innerhalb des hellen Streifens in der Entfernung Z vom Rand ist die Intensitätserhöhung durch Streulicht

$$R_u = \frac{8}{3,83} - \frac{8}{\pi} \left(\frac{1}{Z} - \frac{1}{X-Z} \right).$$

Haben wir nun nicht nur einen hellen Streifen der Breite X , sondern 2, 4, 6, ... und dazwischen dunkle Streifen der gleichen Breite X und betrachten wir einen

Punkt in der Mitte der dunklen Streifen mit $Z=X/2$, dann wird die reduzierte Intensität der Beleuchtung in diesem Punkt r_v

$$r_v = \frac{64}{3,83^2 \pi^2} \frac{1}{X} \left(\frac{1}{1,3} + \frac{1}{5,7} + \frac{1}{9,11} + \frac{1}{13,15} + \frac{1}{17,19} + \dots \right)$$

progressiv:

$$r_v = \frac{1}{X} (0,148; 0,161; 0,166; 0,168; 0,1694; \dots; 0,174).$$

Für die Erhöhung der Beleuchtungsintensität in der Mitte der hellen Streifen, die den mittlerem Dunkein begleiten (Asymmetrie) erhält man die reduzierten Intensitäten r_u für 2, 4, 6, ... helle Streifen

$$r_u = 0,0455, -\frac{0,208}{X}; -\frac{0,1892}{X}; -\frac{0,1811}{X}; -\frac{0,1816}{X} \dots; -\frac{0,174}{X}.$$

Ist nun die Definitionshelligkeit $D.I.$ so bedeutet das, dass die Höhe des Maximums des Beugungsscheibchens proportional reduziert ist und damit auch praktisch proportional die Gesamtintensität, die in das Beugungsscheibchen fällt. Die Intensität die auf das Streulicht entfällt erhöht sich also um den Faktor C

$$C = (1 - 0,83 D.I.)/0,17.$$

Da sich nun durch Superposition jede feinere Struktur praktisch ausmittelt, erhält man z.B. in Fall von sechs hellen Streifen die Kontrastübertragung $P.K.$

$$P.K. = \{0,255 D.I. + (r_u - r_v)C\} / \{0,225 D.I. + (r_u + r_v)C\} \\ = (0,27X - 0,35C) / (0,27X - 0,018C),$$

bezw. die Tabelle von $P.K.$ für verschiedene Werte von X und $D.I.$

$3,83/X$	X	$D.I. = 1,0$	0,8	0,6	0,4	0,2
0,766	5	0,75	0,50	0,24	0,044	-0,29
0,383	10	0,87	0,75	0,63	0,53	0,38
0,192	20	0,94	0,87	0,82	0,77	0,69
0,077	50	0,97	0,95	0,93	0,90	0,88
0,038	100	0,99	0,97	0,96	0,95	0,94

Inversionen, bei denen die Intensität im ursprünglich dunklen Streifen grösser ist als im ursprünglich hellen, beginnen also um X gleich 5 und $D.I.$ 0,2. Ferner ist:

$$X = 7,65 \cdot (1 - 0,051 P.K.) \cdot (1 - 0,83 D.I.) / (1 - P.K.).$$

Um einen konkreten Anschluss an übliche optische Systeme zu finden, setzen wir den Fall von $D.I.$ 0,6 und $P.K.$ 0,8 voraus; es ist dann $3,83/X$ gleich 0,2 also $X=18,4$. Für Fotoobjektive üblicher relativer Oeffnungen bei λ gleich 0,0006 mm:

$F : 1,4$	$\sin \theta = 0,336$	$\frac{2\pi}{\lambda} \sin \theta = 3520$	$\rho = X \frac{2\pi}{\lambda} \sin \theta = 0,0052$	$1/2\rho = 96$
: 2	0,242	2540	0,0073	68
: 2,7	0,182	1910	0,0096	52
: 4	0,124	1300	0,0142	35
: 5,6	0,089	935	0,0197	25
: 8	0,062	653	0,0281	18

Die letzte Kolonne rechts gibt die entsprechende Linienzahl für den mm, die wegen parasitärem Licht etc. auf rund die Hälfte zu reduzieren ist.

Rosenhauer und Rosenbruch [2] geben Messungen u.a. an einem Fotoobjektiv einer Brennweite von 50 mm und einer relativen Oeffnung $F:2,8$. Schätzen wir für diesen Fall die $D.I.$ mit 0,5, so folgen für vorgeschriebene $P.K.$ die folgenden Linienzahlen im mm; nämlich:

$$\frac{2\pi}{\lambda} \sin \theta = 1910; \quad D.I. = 50 \text{ Prozent}; \quad F:2,8; \quad f = 50 \text{ mm.}$$

$P.K.$	3,83/ X	X	$\rho = X/1910$	Linienzahl im Millimeter		
				$1/2\rho$	gemessen[2]ca	$D.I. = 1$
0,8	0,18	21,20	0,0110	45	25	165
0,6	0,36	10,65	0,0056	89	37	305
0,4	0,54	7,10	0,0037	135	50	—
0,2	0,71	5,4	0,0028	179	120	—
0	0,95	4,02	0,0021	224	(Inversion)	—

Für den Idealfall $D.I. = 1$, erhalten wir hier um rund 15 Prozent höhere Werte, als [2] angegeben wurde, was grössenordnungsweise verständlich ist, da hier ja nur sechs helle Streifen, also merklich weniger Streulicht berücksichtigt ist.

Ueber die Definitionshelligkeit ist man also nach obigem in der Lage, schnell auf die Kontrastübertragung zu schliessen oder aber umgekehrt für eine gewünschte Kontrastübertragung auf die hiezu nötige Definitionshelligkeit. Beim Korrigieren von optischen Systemen [3]† wird man also auch in diesem Belange in der Definitionshelligkeit einen sehr brauchbaren Hilfwert finden.

The refracted light is divided into central light (rays) and stray light by means of definition luminosity, and the contrast sensitivity for band systems of any given number of bands is calculated with the aid of approximation formulae.

A l'aide de l'éclairement au centre de la tache de diffraction on décompose la lumière diffractée en lumière centrale et lumière diffractée et l'on calcule, à l'aide de formules approchées, le facteur de contraste pour des systèmes à traits comportant un nombre quelconque de traits.

LITERATUR

- [1] JAHNKE, E., und EMDE, F., 1948, *Tafeln höherer Funktionen* (Leipzig: Teubner).
- [2] ROSENHAUER, K., und ROSENBRUCH, K. J., 1960, *Optik*, **17**, 274.
- [3] HAVLIČEK, F. I., 1960, *Einführung in das Korrigieren optischer Systeme* (Stuttgart: Wissenschaftliche Verlagsgesellschaft).
- [4] HAVLIČEK, F. I., 1951, *Nature, Lond.*, **168**, 743.
- [5] HAVLIČEK, F. I., Demnächst in *Zeitschrift fuer Instrumentkunde*.

† Die hier gebrachte Bestimmung der Definitionshelligkeit gilt für den praktischen Fall der Debye'schen fernen Kugel streng, da man man einerseits aus der Wellenfläche [4] und der, der fernen Kugel die Wellenaberrationen als Funktion des Tangens des Einfallswinkels der Strahlen auf der Achse bestimmen kann und man andererseits dieselben Wellenaberrationen erhält, wenn man in

$$\int_0^\theta \Delta S_k' d(\lambda - \cos \theta) \text{ den } \cos \theta$$

in eine Tangensreihe entwickelt; die gebrachte graphische Behandlung der Definitionshelligkeit ist also für beliebige Oeffnungen berechtigt, solange das Beugungsintegral für die Debye'sche ferne Kugel gilt [5].

Optical alignment devices based on a two-mirror system

by J. DYSON

A.E.I. Ltd., Research Laboratory, Aldermaston Court, Aldermaston, Berks

(Received 16 December 1960)

The requirements to be satisfied by an optical alignment system are indicated, and a two-mirror system is described. The elementary form of this is restricted in its field of application, but it can be converted into a very sensitive interferometer for toolroom or labor \pm tory use. Its errors and coherence conditions are examined.

Modifications of the simple system suitable for more practical conditions are described, and their errors are investigated. It is shown that very high accuracies can be obtained without excessive demands on the optical workmanship.

The effects of atmospheric irregularities are indicated, and test results are described briefly.

1. INTRODUCTION

The accurate alignment of mechanical parts is becoming of increasing importance in engineering. An obvious example is that of a large turbo-alternator set which has a number of bearings which must be aligned accurately in a horizontal plane and which must depart from alignment in a vertical plane by calculated amounts in order that the rotating parts may have a sag of the correct magnitude to give minimum alternating forces at the couplings.

Another typical application is that of a linear accelerator, the various apertures of which must be accurately aligned in both planes.

2. REQUIREMENTS FOR A SATISFACTORY OPTICAL ALIGNMENT DEVICE

In applications of the type described above, alignment is in principle required with respect to a line defined by two fixed points, rather than, for example, the axis of rotation of a machine tool. It is therefore necessary that the line defined by the optical system (the 'reference axis') should coincide with the above line and not be affected by small tilts of the apparatus.

It is evident that a system in which the line is defined by optical apparatus at one end only of the line will necessarily be sensitive to small tilts, such as may be caused by thermal effects or settling of foundations of that apparatus. Such a system may be compared with a straight rigid rod clamped at one end only. What is required is the optical analogue of a weightless string stretched between two fixed points. It is interesting to note that a stretched string is widely used in practice for this purpose, but unfortunately no real string is weightless and the accurate detection of its position without disturbing it is not very easy under workshop conditions.

The reference axis must, of course, be straight to within the accuracy of measurement required and this accuracy should be attainable without the use of inconveniently small tolerances in the workmanship. Further, one set of apparatus must be capable of use, with simple adjustments, over varying lengths of line.

It is also convenient if the setting accuracy is constant at all points of a line of given length, though in most cases it is acceptable if the error of setting is proportional to the overall length of line.

3. THE ELEMENTARY TWO-MIRROR SYSTEM

The devices to be described herein are based on the optical system shown in figure 1. Two identical concave spherical mirrors M_1 , M_2 are separated by their common radius of curvature so that the centres of curvature C_1 , C_2 of M_1 and M_2 lie respectively on the surfaces of M_2 and M_1 . An axis is now defined by the line C_1C_2 . It can easily be shown that a small object O on C_1C_2 gives rise, after successive reflections at the two mirrors, to an image I which has the same axial position as O , is of unit magnification, and is inverted.

It is evident that that part of the object which lies on the axis will be imaged on to itself. Consequently, if the object is suitably illuminated and viewed so as to see both object and image simultaneously, the distance from any selected point of the object to the axis C_1C_2 is equal to one-half the distance between that selected point and its image.



Figure 1. Basic two-mirror system.

This suggests a method for using the system shown in figure 1 as an alignment device. The object O may conveniently be a graticule in the form of a divided scale. The mirrors M_1 , M_2 are set up in suitable positions at the two ends of the system to be aligned and C_1C_2 then constitutes the reference axis. The graticule is placed in turn at each of the points to be aligned and the distance between the zero of the divided scale and its image is read directly at each point. From the readings so obtained, the errors of alignment may be calculated in an obvious manner. This system, however, suffers from a number of disadvantages. The points C_1 and C_2 which define the reference axis are themselves determined by the mirrors M_1 , M_2 which are separated from those points by a distance equal to the whole accessible length of the reference axis. It follows that a small tilt of either mirror will displace the reference axis by a relatively large amount. Consequently this system is of practical utility only for small lengths and when used in carefully controlled conditions such as are found in, for example, a measuring room. A further disadvantage lies in the fact that, for moderate angular apertures, the concave mirrors will have noticeable aberrations, thereby reducing the setting accuracy. Spherical aberration is zero for points at the ends of the reference axis and rises to a maximum in the centre.

4. THE ALIGNMENT INTERFEROMETER

The presence of spherical aberration suggests that it might be useful to make the instrument into a two-beam interferometer, for, if the two beams are inclined at equal angles to the axis, they will then suffer equal path length changes due to

spherical aberration so their relative path-difference due to this effect will be zero. This may be done in a variety of ways, but that illustrated in figure 2 seems to be the most convenient. The two mirrors M_1 , M_2 are pierced by small central holes, and a beam of plane-polarized light enters from the left. It is intercepted by a Wollaston prism, modified from the usual form by dividing one of the birefringent wedges and placing one-half on either side of the other wedge to give a symmetrical structure, which divides it into two beams each making an angle α with the axis. The two beams follow the path shown and, because of the symmetry of the prism, emerge parallel with the axis. As the prism has appreciable thickness the two emergent beams do not coincide but are mutually displaced by a short distance. They enter a telescope fitted with an analyser and fringes may be observed in its focal plane.

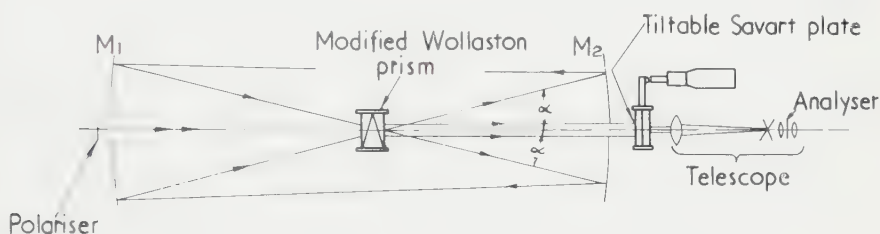


Figure 2. Alignment interferometer.

If the Wollaston prism moves through a distance d at right angles to the axis and in the plane of the diagram, it is easy to show that a path difference $p = 4d \sin \alpha$ is introduced between the two emergent beams. This result is true if the Wollaston prism is replaced by any symmetrical afocal system with the same general properties of splitting and deflecting the incident light, regardless of its particular mechanism of operation. The fringe system seen in the telescope, therefore, moves by a number n of fringes given by

$$n = (4d \sin \alpha) / \lambda \quad (1)$$

where λ is the wavelength of the light used. The motion of the Wollaston prism can be measured by counting the number of fringes which pass the cross-hairs and applying equation (1). However, it is more convenient to use white light, giving a recognizable white or black central fringe, and for every measurement return this to the cross-hairs by means of a compensator.

A Savart plate, mounted to allow it to be tilted through an angle determined by a lever and micrometer screw, forms a suitable compensator. This requires the planes of polarization to make angles of 45° with the vertical, whereas the two beams emerging from the Wollaston prism are polarized vertically and horizontally. A half-wave plate is therefore placed between these components, suitably oriented to rotate the planes of polarization through 45° .

The compensator can also be made to fulfil another function. The two beams emerging from the Wollaston prism are separated in the vertical plane by a few tenths of a millimetre, giving rise to fringes in the telescope which are inconveniently close together. The Savart plate also gives rise to a separation and the two separations can, by suitable design, be arranged partially or wholly to cancel

each other, thereby increasing the width of the fringes and allowing the use of lower magnification.

5. COHERENCE CONDITIONS IN THE ALIGNMENT INTERFEROMETER

The fringe contrast is determined by the coherence of the two interfering beams which contribute to any given point of the fringe pattern. As this pattern is formed at infinity in the optical space just after the prism, this coherence is determined by the difference in wave-front distortion of the two waves formed by a single plane wave incident on the system from the left. As all the surfaces of the prism are plane, the 'conoscopic' figures formed by the crystalline material of the prism are at infinity and will not give rise to any such relative wave-front distortion. Hence, only the effects of the two mirrors need be considered.

These effects may be evaluated as follows. Two surfaces, Σ_1 and Σ_2 , are constructed normal to C_1C_2 and coinciding respectively with the aperture of the prism and the mirror M_2 . Rectangular coordinates x, y and X, Y are taken in Σ_1 and Σ_2 as shown. A typical ray PQR of a parallel pencil meets Σ_1, Σ_2 in points Q and R with coordinates x, y and X, Y . The primary wave-front aberration is given by a well-known formula and is equal to

$$\text{Wave-front aberration} = \frac{(X^2 + Y^2)^2}{4L^3}. \quad (2)$$

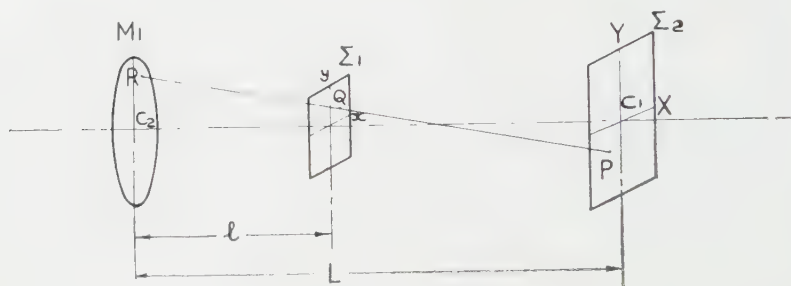


Figure 3. Aberrations of the two-mirror system.

If the ray PQR makes angles α and β with the planes C_2C_1X and C_2C_1Y , then, assuming that α and β are small,

$$X = x - \beta(L-l), \quad Y = y - \alpha(L-l). \quad (3)$$

Substituting these values into (2) gives

$$\text{Aberration} = \{[x - \beta(L-l)]^2 + [y - \alpha(L-l)]^2\} / (4L^3). \quad (4)$$

As the angular field of the telescope will always be small against the magnitude of the deviation produced by the prism it is reasonable to set β equal to zero and to take α as being equal to the deviation produced by the prism. This gives a result strictly true only for the centre of the field.

With this simplification (4) now becomes

Wave-front aberration

$$= [(x^2 + y^2)^2 - 4y(x^2 + y^2)\alpha(L-l) + 2(x^2 + 3y^2)\alpha^2(L-l)^2 - 4y\alpha^3(L-l)^3 + \alpha^4(L-l)^4] \cdot 1/(4L^3). \quad (5)$$

The fourth term in (5) indicates that the reference surface with respect to which the aberrations are calculated is inclined to the surface normal to the principal

ray through the centre of the prism by an angle $\alpha^3(L-l)^3/L^3$. As, at this stage, only the aberrations referred to this latter surface are required, this term is dropped in what follows.

The differential aberration P_1 between the two interfering wave-fronts produced by M_1 alone is then given by the difference between the right-hand side of (5) and a similar expression obtained by writing $-\alpha$ for α . This gives

$$P_1 = 2y(x^2 + y^2)\alpha(L-l)/L^3. \quad (6)$$

The contribution from M_2 is obtained by writing l for $L-l$ in (6) and reversing the signs of x and y , giving a total aberration of

$$P_1 + P_2 = 2y(x^2 + y^2)\alpha(L-2l)/L^3. \quad (7)$$

For good fringe visibility the value of $P_1 + P_2$ must be small as compared with a wavelength. If the radius of the prism aperture is a_1 the maximum value of $P_1 + P_2$ is given by

$$(P_1 + P_2)_{\max} = 2a_1^3\alpha/L^2 \quad (8)$$

and arises when the prism is situated at one end of the reference axis, with an equally large but negative value when the prism is at the other end.

The above discussion gives the distortion of one wave-front relative to the other. The two wave-fronts may, however, be tilted or shifted relative to each other, this effect being produced by the aberrations of the principal rays.

The spherical aberration of a pencil of rays of semi-aperture α , diverging from the prism and converging to it again, can be calculated by standard formulae. The interesting result is obtained that the primary spherical aberration contributions P_{s1} , P_{s2} from M_1 and M_2 are equal, and are given by

$$P_{s1} = P_{s2} = \frac{l^2(l-R)^2\alpha^4}{4R^3}. \quad (9)$$

The tilts of the wave-fronts produced by this aberration can be calculated and turn out to be zero in first approximation. This indicates that the fringes are formed at infinity for all axial positions of the prism.

There is, however, a resultant shift S in the vertical plane between the two-wave-fronts. This can easily be calculated from (9) as

$$S = 2l^2(l-R)^2\alpha^3/R^3. \quad (10)$$

The effect of this is to vary the spacing of the fringes seen in the focal plane of the telescope, but not to affect their visibility. If the cross-hairs are at the centre of the field no systematic error will be introduced by this effect.

If the mirrors M_1 and M_2 are not separated by the correct distance the magnification of the system will not be unity and the emerging wave-fronts will be tilted with respect to each other by an amount depending on the axial position of the prism. The effect of this is that the fringes will not be formed at infinity, and re-focusing of the telescope will be necessary for each position of the prism.

A similar effect is obtained if the radii of curvature of M_1 and M_2 are not identical.

6. EXPERIMENTAL RESULTS WITH THE ALIGNMENT INTERFEROMETER

A model of this device has been made with mirrors of 20 in. radius of curvature and 3 in. diameter, using a Wollaston prism of $\frac{3}{8}$ in. aperture, made of Iceland spar, which gave a value of α of approximately $1/16$ radian. For these values,

the maximum value of $P_1 + P_2$ was 2.1×10^{-6} in., or about $\lambda/10$, and could be ignored. The shift S between the wave-fronts is 6.1×10^{-4} in. As the separation of the beams at the telescope objective is approximately 0.040 in., this additional shift is negligible. The Savart plate used as a compensator was also made of Iceland spar. The apparatus could be used over a length of about 14 in., the extreme ends of the reference axis being unusable because of obstruction of the return beam by the prism. Readings could be taken to 0.1 fringe, corresponding to an error of alignment of 8 micro-in.

The prism was supported in a carriage running on guide rails, being so arranged that the vertical position of the prism was controlled by a probe sliding in a vertical guide. The lower end of the probe rested on the surface of which the flatness was to be checked. Measurements were made on a 10 in. diameter optical flat of which the profile was known from optical measurements, and it was found that the readings obtained did not deviate from the correct values by more than the 8 micro-in. mentioned above.

The accuracy of reading could be increased by a very large factor by using polarimetric methods of ascertaining the fringe position, but this does not seem worth while, in view of the very great mechanical stability of the apparatus which would be required to give significance to such readings. However, it is worth noting that by fixing the prism and mirrors in a rigid frame, with the prism midway between M_1 and M_2 , a very accurate instrument could be made which could fulfil a function similar to that of Rayleigh's interferometer.

The experimental model described above and several mechanically improved successors have been applied to the checking of surface plates of small machine slides and of the sealing ring of a large axial flow compressor.

7. SYSTEMS BASED ON TWO VIRTUAL MIRRORS

The disadvantage of the extreme sensitivity to tilt of the two mirrors of the system described above led to a search for systems not having this disadvantage. It was found that it could be avoided if virtual mirrors were used. The system

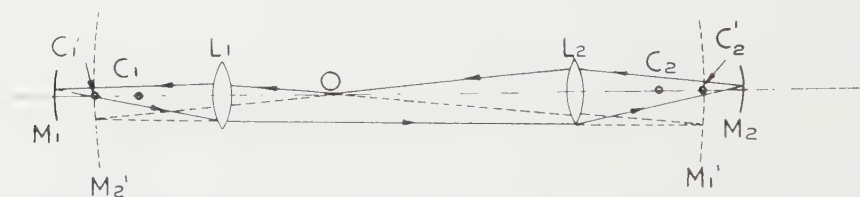


Figure 4. System using virtual mirrors.

is shown in figure 4. At each end of the reference axis is a lens L_1 , L_2 of relatively short focal length, each with a small mirror M_1 , M_2 placed just beyond its prime focus. It can then easily be verified that, if light emanates from an object O on the axis, the ray paths in the space between L_1 and L_2 are the same as if the imaging were by two virtual mirrors M_1' , M_2' . The positions of the poles and centres of curvature C_1' , C_2' of these mirrors are those of the images formed by the lenses L_1 , L_2 of the poles and centres of curvature C_1 , C_2 of the mirrors M_1 , M_2 . In figure 4 the ray paths are completed by dotted lines to illustrate the imaging by the (dotted) virtual mirrors.

The positions of C_1' , C_2' , which define the reference axis, are determined by the positions of C_1 , C_2 and L_1 , L_2 and can, by suitable design, be made to fall very close to or actually between the material objects which define them. Hence, the sensitivity to tilt is very greatly reduced. It can in fact be made zero if the point of support is arranged to fall immediately below the virtual centres of curvature.

A further advantage of this type of system is that the same apparatus may be used for widely differing lengths of reference axis by varying the distance between the lenses and the mirrors. In view of this facility, it is not appropriate to use this system as an interferometer, as to do so would mean the provision of a separate Wollaston prism for each length of reference axis in view of the necessary variation of the angle of deviation in order to keep the two beams within the aperture of the lenses. For this reason the system just described has been used only as an imaging device.

8. CHROMATIC ABERRATION

The outstanding aberration in the above system is the secondary chromatic aberration of the lenses. If the focal length of each lens be f and its diameter a , then, taking Conrady's [1] figure of $f/2500$ for the chromatic difference of focus for the spectrum between the C and F lines, the wave-front aberration amounts to $a^2/(2 \times 10^4 f)$. As four passages of the light through a lens are involved in a complete circuit, the total aberration is four times this. If the convergence angle at the image is α , the resulting disc of confusion at the C and F focus has a radius of $4a^2/(10^4 f \alpha)$. The ratio of this to the radius of the Airy disc is $8a^2/(10^4 f \lambda)$ which, for $a = 2$ in., $f = 12$ in., $\lambda = 2 \times 10^{-5}$ in. has the value 13.3. Hence a very considerable deterioration of the image sharpness will be observed.

This state of affairs cannot be greatly improved by the use of special glasses, and the lenses are generally too large to allow the use of fluorite. A radically different approach was tried, using catadioptric systems.

9. THE MAKSTOV SYSTEM

Maksutov [2] has described a telescopic system in which the converging power is given by a spherical mirror, the aberrations of which are corrected by a weak meniscus lens of deep curvature. According to Maksutov the residual chromatic aberration is 500 to 800 times smaller than that of an achromatic objective of similar power, so this appeared likely to be a satisfactory alternative to the lens-mirror system described above.

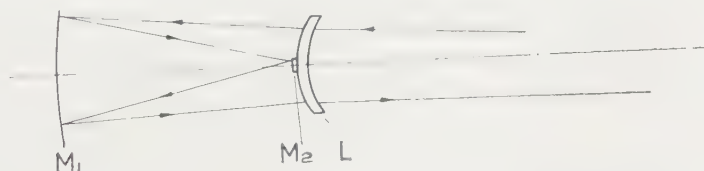


Figure 5. The Maksutov system.

The system used is shown in figure 5. The design differs somewhat from that of Maksutov in that the meniscus lens L is moved somewhat closer to the primary mirror M_1 and is re-designed in order to maintain satisfactory correction

of the aberrations. A small mirror M_2 is mounted on the centre of L and plays a part similar to that of M_1 in figure 4. The light is reflected from M_2 and re-traverses the system, the external ray-paths being the same as in figure 4.

The use of this system effected a striking improvement in the image, chromatic aberration being quite unnoticeable. An additional loss of light is of course involved as a total of four extra reflections is required, but this was a very reasonable price to pay for the better image quality.

The mirror M_2 can be made as a small silvered spot on the convex surface of L , and the point corresponding to C_1' in figure 4 is then somewhat to the right of L . However, if this is done a sharp image of the central obstruction caused by M_2 appears within the usable length of the reference axis, which is inconvenient. Accordingly, M_2 is made as a separate glass disc which is cemented to L . The curvature of M_2 is of some importance and will be discussed later.

Focusing for varying lengths of reference axis is effected by varying the separation of the lens and the mirror M_1 .

10. SPHERICAL ABERRATION

The Maksutov telescopes can, of course, only be corrected for a single object distance, whereas the object may lie at any point along the reference axis. The length of this axis will also vary, depending on the particular application. The system at either end may be treated as a back-to-back combination of two nearly telescopic systems, each corrected for a large object distance L' , the length of the reference axis being L . Considering only the left-hand end of the system the long conjugate for the first traverse is l (the distance of the object) and for the second traverse is $Ll/(2l-L)$. The equivalent focal length of the telescopic system is taken as f and the angular semi-aperture in the object space as α . The convergence angle on the short conjugate side is taken as $\beta = ld/f$ very nearly, β being fairly small.

Using formulae developed by Hopkins [3] the spherical aberration P_1 contributed by the first passage of the Maksutov system is given by

$$P_{\text{Mak}_1} = \frac{f^2 \beta^4}{8} \left(\frac{1}{l} - \frac{1}{L'} \right) \quad (11)$$

and the aberration P_{Mak_2} produced by the second passsge is

$$P_{\text{Mak}_2} = \frac{f^2 \beta^4}{8} \left(\frac{2l-L}{lL} - \frac{1}{L'} \right). \quad (12)$$

giving a total aberration for this end of the system of

$$\begin{aligned} P_{\text{Mak}_1} + P_{\text{Mak}_2} &= \frac{f^2 \beta^4}{4} \left(\frac{1}{L} - \frac{1}{L'} \right) \\ &= \frac{l^4 \alpha^4}{4f^2} \left(\frac{1}{L} - \frac{1}{L'} \right). \end{aligned} \quad (13)$$

The contribution from the other end is obtained by writing $L-l$ for l in (13), giving the total aberration as

$$P_{\text{tot}} = \frac{\alpha^4}{4f^2} [l^4 + (L-l)^4] \left(\frac{1}{L} - \frac{1}{L'} \right). \quad (14)$$

In general, α will vary with l ; thus, if α is limited by the apertures of the lenses, it will be equal to $a/[2(L-l)]$, where a is the diameter of the lens aperture,

for values of l between zero and $L/2$, and $a/(2l)$ for values between $L/2$ and L . Writing the former of these two values for α into (14) gives

$$P_{\text{tot}} = \frac{a^4}{64f^2} \left[\frac{l^4}{(L-l)^4} + 1 \right] \left(\frac{1}{L} - \frac{1}{L'} \right) \quad (15)$$

valid for $0 \leq l \leq L/2$. This indicates that the spherical aberration measured as a wave-front distortion is twice as great at the mid-point of the system as it is at either end.

The radius r_c of the minimum disc of confusion is then given by

$$r_c = \frac{a^3}{32f^2} \left[\frac{l^4}{(L-l)^3} + L - l \right] \left(\frac{1}{L} - \frac{1}{L'} \right). \quad (16)$$

This expression does not vary much over the range $0 \leq l \leq L/2$; it has equal values for $l=0$ and $l=L/2$, and a minimum of 0.70 of this value at $l=0.347L$.

The foregoing analysis assumes that L is very large against f , and so is approximate only. The approximation is worse for the end closer to the object position, but the contribution from this end is always smaller than that from the more distant end because of the smaller incidence-height of the limiting rays. Consequently the worst effects of the lack of exactness are avoided.

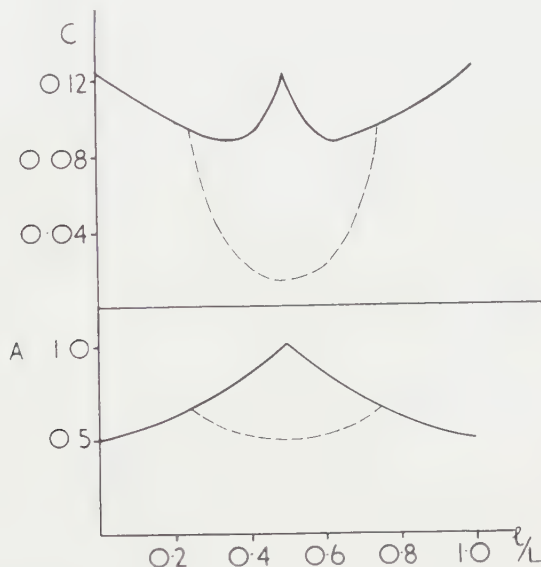


Figure 6. Variation of aperture (A) and disc of confusion (C) with distance. Broken lines indicate modification due to use of a stop fixed to the observing head.

The angular aperture may be restricted to a constant value of $a/(2L)$ by placing a stop of diameter $a/2$ at the mid-point of the reference axis. This, however, is inconvenient, as it will obstruct the passage of the observing head. It is more practical to fix the stop to the observing head itself, in which case the value of α varies from $a/(2L)$ at either end and at the centre of the reference axis to $2a/(3L)$ at points one-quarter of the length of the reference axis from each end. This has the effect of holding the illumination more nearly constant and greatly reducing the radius of the disc of confusion near the centre of the reference axis.

These results are plotted in figure 6 where the values plotted are those of the non-dimensional quantities

$$\left. \begin{aligned} A &= L\alpha/a, \\ C &= \frac{4r_c f^2}{a^3 L [(1/L) - (1/L')]} \end{aligned} \right\} \quad (17)$$

From the above analysis it can be seen that, if the Maksutov systems are designed to have zero spherical aberration for a long conjugate equal to the length of the reference axis, the spherical aberration will be zero in first approximation for an object point at any position along that axis.

A practical example will show the magnitude of the aberration to be expected if the above condition is not met. Assuming $a=2$ in., $f=8$ in., $L=120$ in., $L'=240$ in., the maximum value of the radius of the disc of confusion in the absence of a stop is given by (16) as 0.002 in.

The corresponding wave-front distortion is approximately 1.5 wavelengths. If a stop fixed to the observing head is used as described above, the disc of confusion near the ends of the reference axis is unchanged in size, but near the centre of the reference axis its radius is diminished to 0.00025 in. As the radius of the Airy disc under these conditions is 0.0013 in., the aberration can be neglected in this region.

In fact, even without the stop, the value of aberration calculated above is not likely to have a very serious effect on the image sharpness when diffraction is taken into account, but rather to reduce the contrast somewhat.

11. THE EFFECT OF COMA

One way of using the alignment system is to mount both object and eyepiece graticules together in a mount which can be displaced in two directions normal to the reference axis by means of micrometer drives. The image of the object graticule is made to coincide with the eyepiece graticule by means of these drives and the alignment error is then read off the micrometers. This converts the device into a 'null reading' instrument. If the centres of both graticules are arranged to lie on the reference axis when set for coincidence, they can be so designed as to avoid the introduction of any error due to oblique coma in the system.

However, the Maksutov system can readily be designed so as to be free from oblique coma, and coma is not very sensitive to changes of conjugates [3].

Central coma, due to faulty centring, inaccurate surfaces or inhomogeneous glass introduces an error directly, due to the resulting lateral shift of the centre of gravity of the image of each object point.

Taking Cartesian coordinates x, y in a plane normal to the reference axis and some distance from the image, the origin of coordinates being on the reference axis, the wave-front distortion due to coma may be represented by

$$p_c = P_c r^{-3} x(x^2 + y^2) \quad (18)$$

when r is the radius of the circular cross section of the beam at this plane. The lateral shift of the centre of gravity of the image pattern is then given by

$$S_c = P_c / \alpha \quad (19)$$

where α is the angle of convergence of the peripheral rays at the image. In the case of the practical example mentioned above, where $\alpha=1/120$ radians, the

wave-front aberration P_c for an error of 10^{-4} in. is given by (19) as 0.83×10^{-6} in. It is evident that central coma must be kept to a very low value indeed.

Fortunately, the close approach to symmetry of the Maksutov systems for large object distances leads to a partial cancellation of central coma which eases the problem considerably.

Considering first the effect of faulty centring, the n th surface encountered by the light will give rise to primary spherical aberration of amount P_{sn} .

If O_n is the centre of curvature of the n th surface, the peripheral rays intersect a plane through O_n normal to the axis in a circle of radius r_n centred on the reference axis. It is assumed that O_n is displaced from the reference axis by an amount δ_n . The comatic part of the aberration is given by

$$P_{cn} = 4P_{sn}\delta_n/r_n. \quad (20)$$

The total coma given rise to by this surface will then be

$$P_{cn} + P_{cn}' = 4\delta_n [P_{sn}/r_n - P_{sn}'/r_n'] \quad (21)$$

where the quantities with primes refer to the second passage of the light through this surface. In general, the primed quantities differ from the unprimed ones.

The radii r_n and r_n' will be equal if O_n (referred to the image space) coincides with C_2 , the centre of curvature of M_2 in figure 5 and corresponding with C_1' in figure 4, both referred to the image space.

For the mirror M_1 the right-hand side of (21) can be calculated giving to the first approximation

$$P_{cM_1} = \frac{2l^2\alpha^3}{LR^3} (L-l)(3S-R)\delta_{M_1} \quad (22)$$

where R is the mirror radius and S is the distance of C_2 from the mirror M_1 . To this degree of approximation, P_{cM_1} is independent of the strength of the lens L if, as is the case in practice, L is weak as compared with M_1 . The lateral shift of the image due to central coma is then given by

$$\text{Shift}_M = \frac{2l^2\alpha^2}{LR^3} (L-l)(3S-R)\delta_{M_1} \quad (23)$$

and will be zero in first approximation at all points if $S=R/3$; otherwise, it is zero at either end of the axis and rises to a maximum at $l=2L/3$.

The aberrations of the mirror M_2 can be neglected in practical cases in view of the small incidence-height thereon.

The constants of the lens L are given, for a given focal length and aperture ratio, by Maksutov [2] for the case of an object at infinity, and are not greatly departed from in the system described above. The spherical aberrations for the two lens surfaces are opposite and nearly equal, and do not vary greatly for a given incidence-height of the peripheral ray on the plane through the centre of curvature and normal to the axis, with small variation of the convergence angles. These aberrations are best determined by calculation from a ray-trace in any practical case.

The distance from the centres of curvature of the lens surfaces to the point C_2 are both taken as t , since these centres of curvature nearly coincide. The spherical aberration for a parallel beam of aperture α is denoted by P_1 , P_2 for the concave and convex surfaces respectively. The lateral image-shift for a displacement $\delta_{1,2}$ of the centre of curvature of either surface is then given by

$$\text{Shift}_{L1,2} = 384P_{1,2}l^2t\alpha^2\delta_{1,2}(l-L)/(La^4). \quad (24)$$

A displacement of the centre of curvature of one surface only corresponds to an error of edging of the lens; an error of centring of the lens as a whole corresponds to setting $\delta_1 = \delta_2$ and gives

$$\text{Shift}_L = 384(P_1 + P_2)l^2 t \alpha^2 \delta_1 (l - L) / (La^4). \quad (25)$$

The most sensitive surface to errors of figure is that of the mirror M_1 , for a given error will produce about four times the wave-front error in this surface than in either lens surface. Furthermore, flexure of the mirror produces its full effect on the wave-front, whereas the effect of flexure of the lens is largely compensated by the complementary deformations of the two surfaces. To obtain an indication of the degree of cancellation to be expected, the asymmetrical part of the error of figure of the mirror surface expressed as wave-front distortion may be rendered in first approximation by the expression

$$P_m = 8P_m x(x^2 + y^2)/a^3 \quad (26)$$

where x, y are Cartesian coordinates taken in a plane tangent to the mirror pole and a is the aperture of a parallel incident ray just filling the system. The lateral shift due to the error of figuring can then be shown to be

$$\text{Shift}_F = 16P_m S l^2 (L - l) x^2 / (a^3 L) \quad (27)$$

where S has the same meaning as in (23).

The effect of errors of figuring or inhomogeneity of the glass of the lens L is given by an expression similar to (27) replacing S by t as in (24).

It will be seen from the foregoing that any one of the effects of errors of centring or figuring can be reduced to zero in first approximation by suitable choice of the position of C_2 , and the choice of which of these effects should be so eliminated depends on practical considerations.

To illustrate the orders of magnitude involved, the system described previously with $L = 120$ in., $a = 2$ in., $R = 16$ in., may be considered, the small mirror M_2 being assumed to be flat. Then $S = 8$ in. in (23). The maximum image shift is taken as 10^{-4} in., occurring at $L = 2/3L$. Equation (23) then gives $\delta_{M_1} = 0.17$ in. for the allowable separation between the reference axis and the centre of curvature of M_1 . In (24), $t = 3$ in. approximately and $P_1 = 11 \times 10^{-4}$ in., giving δ_1 as 0.0085 in. for the accuracy of centring of one lens surface with respect to another, whereas (25) gives 0.13 in. as the accuracy of centring of the lens as a whole. From (27) the allowable error of figuring of the form indicated in (26) is given as 0.4×10^{-4} in., or about two fringes. The allowable errors of the lens surfaces are, of course, considerably greater.

The final disturbing factor to be taken into account is the eccentricity of the limiting stop. It is easy to show that, if this stop is placed at the position of C_2 , its eccentricity is without effect on the central coma. If the surface of M_2 is flat, as in the example to which the above numerical results relate, the position of this point does not change with respect to the mirror M_1 , and so the stop can be fixed in position. If a stop fixed to the measuring head is used, it must be carefully centred with respect to the object and image gratitudes. If the total wave-front spherical aberration at any point on the reference axis is P_s and the radius of the stop is r , the image shift due to a stop eccentricity δ_s is given by

$$\text{Shift}_{\text{stop}} = 4P_s \delta_s / (\alpha r). \quad (28)$$

The effect of this is most severe when $l=L/4$ or $3L/4$, and, in the case of the example cited above, the tolerance on the concentricity is then 0.006 in. for an image shift of 10^{-4} in.

The tolerances given above do not take into account the effects of higher order aberrations, which would impose sharper restrictions, but in Maksutov systems of moderate focal ratios higher-order aberrations are not prominent. Errors of figuring are likely to contain higher-order terms, but these are most marked towards the edge and can largely be avoided by making the component somewhat larger than is required and edging down to the desired diameter.

Further, in the numerical calculations given above the aperture angle α has been taken constant at $1/120$ radian, whereas, as has been described previously, it may rise above this value for some values of l . The object of the calculations is, however, to show that the necessary tolerances are comfortably within what is possible in high-grade optical work.

It will be seen that, as α and L vary inversely for different lengths of reference axis, the tolerances are practically unchanged with increasing L for a given amount of image shift.

The image shift of 10^{-4} in. is considerably less than what would be allowable in routine alignment measurements except for machine tool applications. The error introduced into the alignment measurements is, of course, one-half of the image shift.

12. OTHER ABERRATIONS

The aberrations which cause symmetrical expansion of the image point, such as astigmatism or curvature of field, do not cause any systematic error, and need only be kept to a value low enough to avoid noticeable deterioration of the image quality.

Distortion, if symmetrical about the centre of the field, also causes no error when using a suitably designed graticule. If, due to any of the causes which also give rise to central coma, the centre of distortion does not coincide with the reference axis, an error is introduced, but this is always smaller than that due to central coma.

13. ATMOSPHERIC REFRACTION

All optical measurements in the atmosphere are affected by variations in the refractive index of the air. These may be of widely differing types. Small-scale variations, due to turbulence, produce blurring of the image and also image shifts of rapidly varying amounts. With the small apertures envisaged here image blurring is rarely severe and results only in a small reduction in sensitivity. Image shifts cause errors which may, by averaging over a period, often be reduced to small amounts. This is especially true if electronic means are used for detection of the image position. Large-scale variations may be idealized into two types; air prisms, giving a refractive index which, over a short length of the reference axis, varies linearly with distance in a direction transverse to that axis, and stratification, where the refractive index is constant in planes parallel with the reference axis and with each other but varies linearly in a direction normal to those planes.

It is easy to show that an air prism gives its greatest effect when it coincides with the object and image. If the air prism produces a deviation θ , the image shift is given by

$$\text{Shift}_{\text{air}} = \frac{2\theta l(L-l)}{L} \quad (29)$$

and its maximum value, at $l=L/2$ is $\theta L/2$. The resulting error of alignment is thus $\theta L/4$. This error is the same as would be obtained by an alignment telescope if the apparent position of the target is compared instantaneously with that of a fixed target at the end of the range, and is one-quarter of the maximum error if this is not done. (In the case of the alignment telescope the error is a maximum if the air prism is adjacent to the telescope.) In the case of stratification the image shift obeys a relationship with l similar in form to (29) and the above comparison with an alignment telescope also holds.

14. EXPERIMENTAL RESULTS

A model has been made with constants similar to those used for the numerical calculations above. The object and image planes were made accessible by the use of two plane-parallel, partially reflecting glass plates placed at 45° with the axis, and the fitting holding these, the lamp, graticules and eyepiece, was provided with micrometer adjustments in two directions at right angles to each other and to the reference axis.

This model has been tested with distances between the two ends varying between 6 ft and 95 ft. At the shortest distance the effect of spherical aberration was obtrusive, but from 15 ft upwards setting accuracies were obtained corresponding roughly to $\pm 10^{-5}$ in. per foot of length of reference axis. This sensitivity was obtained with various types of graticule, but the best has seemed to be one in which the ends of two broad lines, one on each graticule, are set into coincidence.

Further development and application of this system is continuing. Photo-electric means for detecting the image position and giving an electrical signal indicative of this position are also being developed.

15. CONCLUSIONS

A two-mirror optical system forms a useful basis for an optical alignment device. The simplest system can be made into an interferometer which is capable of very high sensitivity, but this is only suitable for a laboratory or measuring room instrument.

A more complex system using virtual concave mirrors forms an instrument capable of wider and more practical application. A particularly convenient form uses a modified Maksutov system at each end of the reference axis.

The disturbing factors which limit the degree of straightness of the line so defined have been examined, and it is shown that adequate accuracy for practical applications can be obtained using tolerances which present little difficulty to a good optical workshop.

This system has been tried out in practice and setting accuracies of 10^{-5} in. per foot have been obtained with lengths of reference axis from 15 to 95 ft.

ACKNOWLEDGMENTS

The author wishes to thank Cooke, Troughton and Simms Limited for the construction and mounting of the optical parts of the experimental models; Dr. W. Hirst for encouragement in pursuing the development; Dr. A. W. Crook and Mr. R. J. Tillen for design and construction of auxiliary equipment and extensive testing under workshop conditions; and Dr. T. E. Allibone, F.R.S., Director of the Laboratory, for permission to publish this paper.

Les conditions à satisfaire par un système optique d'alignement sont indiquées et un système à deux miroirs est décrit. La version élémentaire d'un tel système à un champ d'application restreint, mais elle peut être transformée en interféromètre très sensible pour l'atelier ou le laboratoire. On étudie ses défauts et les conditions de cohérence.

Des modifications du système simple, en vue d'applications pratiques sont décrites et leurs défauts sont étudiés. On montre que l'on peut atteindre de très hautes précisions sans exigences excessives sur la réalisation.

Les effets des irrégularités atmosphériques sont indiqués et des résultats de contrôles sont décrit brièvement.

Es werden die Bedingungen aufgestellt, die ein optisches Fluchtungsgerät erfüllen muss, und es wird eine Anordnung aus zwei Spiegeln beschrieben. In der einfachen Form ist diese Anordnung in ihrem Anwendungsbereich beschränkt, aber sie kann in ein sehr empfindliches Interferometer für Werkstatt und Prüfraum umgewandelt werden. Seine Fehler und Kohärenzbedingungen werden geprüft.

Ausserdem werden Modifikationen der einfachen Anordnung, die sich für mehr praktische Bedingungen eignen, beschrieben und ihre Fehler untersucht. Man kann damit sehr hohe Genauigkeiten erreichen, ohne an die optische Herstellung übertriebene Forderungen zu stellen.

Es werden die Einflüsse atmosphärischer Störungen angegeben und die Prüfergebnisse kurz mitgeteilt.

REFERENCES

- [1] CONRADY, A. E., 1929, *Applied Optics and Optical Design* (Oxford: University Press), p. 157.
- [2] MAKSUTOV, D. D., 1944, *J. opt. Soc. Amer.*, **34**, 270.
- [3] HOPKINS, H. H., 1946, *Proc. phys. Soc. Lond.*, **58**, 100.

Focal tolerances and best focal setting for model photographic images with primary spherical aberration

by E. H. LINFOOT
University of Cambridge

(Received 20 December 1960)

The question of focal depth and best focal setting in photographic images is of importance to optical designers because of its connection with the problem of obtaining a satisfactorily flat field, and it would evidently be a great convenience to be able to predict, without constructing a trial model, the best focal surface and the focal depth in different parts of the field of a photographic design working with a specified emulsion. Recent developments in optical theory and in computing techniques suggest that this old problem could now be attacked again with better hope of success. A combined attack from the theoretical and experimental sides seems to be needed. A beginning on the theoretical side is attempted in the present paper, in which the dependence of focal depth and best focal setting on photographic spread and noise is examined computationally in selected model photographic images with 0, 1, 2 and 4 wavelengths respectively of primary spherical aberration. Two different model emulsions are used to receive each image.

The criterion of focal depth adopted is that the image quality (in a precisely defined sense) shall not fall below 80 per cent of that at best focus; the curves given in figures 6, 7 and 8 also allow the focal depths corresponding to other percentage criteria to be read off for the images considered.

Three different measures of image quality are used and compared. The first is a generalization of the Strehl intensity ratio (§§ 2.1, 2.2); the second is a measure of the discriminating power (§ 3) of the model photographic system, used on a random object set of specified mean contrast; the third evaluates the quality of the image by means of its normalized structural resolution, (§ 4).

Only the second of these evaluations is sufficiently refined to take account of the fact that the focal depth of the system and the position of best focus may change when the noise-level in the receiving surface is altered. One of the results of the present investigation is that these changes are of little practical consequence provided the amount of fourth-power aberration does not exceed two wavelengths. The three different image-quality evaluations then lead to nearly the same conclusions and it seems that we can predict the focal depth sufficiently well from a knowledge of the focal ratio, the aberrations, and the contrast transfer function of the receiving surface, without specifying the ratio of object contrast to emulsion noise.

In systems with four wavelengths of spherical aberration, the focus of best discrimination may change considerably, and the focal depth appreciably when the noise-level in the receiving surface is varied. In all the cases examined the focal depth depends rather sensitively on the image spread in the receiving surface. It appears that one wavelength of primary spherical aberration (the Rayleigh limit) can lower the image quality at best focus appreciably even when photographic spread is large compared with diffraction spread and the image is noisy.

1. INTRODUCTION

In the present paper contrast-transmission functions are used to examine the effect of spread and noise in the receiving surface on focal tolerances and on the

position of the best focal setting for aberration-free images and for images with primary spherical aberration.

Because of its connection with practical problems (inexpert focusing is probably the commonest error in the actual use of optical systems) the question of the best focal setting in a system with spherical aberration has received a good deal of attention in the optical literature. Papers by Conrady [3, 4], Flügge [8], Huber [16], Dupouy-Camet [5], Kingslake [19] and Kämmerer [17], in which they report the results of experimental investigations, are of especial interest on the practical side. Theoretical investigations were published by Strehl [34, 36], Conrady [2], Väisälä [37], Richter [29] and Wang Ta-hang [38]. More recently Kuwabara [20, 21] has attacked the problem both theoretically and experimentally and an important paper on diffraction images with spherical aberration has been published by Focke [9].

Only a few of the above papers (those by Strehl, H. G. Conrady, and Dupouy-Camet) were concerned exclusively or mainly with primary spherical aberration. Richter, A. E. Conrady, Väisälä, Wang-Ta-Hang, and Kuwabara considered primary spherical aberration in the course of more general investigations, directed usually to the question of the best balancing of a mixture of sixth- and eighth-power aberration by controlled primary spherical aberration and focal adjustment. Focke, Huber, Kingslake and Kämmerer were not concerned at all with pure fourth-power wave errors but with balanced mixtures of primary and higher-order aberration, such as are found in the axial images of camera lenses. Some brief comments on their approach seem relevant, nevertheless, in the present context.

All but four of the experimental investigations (those by Flügge, Huber, Kingslake and Kämmerer) and all the theoretical ones were explicitly concerned with the properties of the aerial diffraction image. Kingslake [19] and Kämmerer [17] used photography to record this image after magnification by re-imaging, thus ensuring that the effect of photographic spread on the recorded images was small in comparison with that of the wave aberrations, but leaving the non-linear photographic response. Huber [16] used a modified F/1.8 triplet objective of focal length 10 cm, "so that the spherical aberration always has a greater effect on the resolution than does the photographic emulsion". Later he notes that the small grain size of the emulsion used "leaves the resolution obtained by the objective almost unaffected". He developed to a contrast $\gamma=1$, and criticizes Flügge for not having done the same; his discussions, however, are on a purely ray-theoretic basis. In each of these cases the experimental arrangements ensured a strong mismatch between the optical spread in the aerial image and the photographic spread in the emulsion which recorded it, the photographic spread being the smaller.

Flügge's investigation, on the other hand, included microphotometer measurements of edge-profiles in photographic images in which the effects of optical spread and of the diffusion of light in the emulsion layer are of the same order of magnitude, and he points out that the quality of a photographic lens should be judged by the photographic images which it produces under normal conditions of use. However, his proposed measure of the unsharpness of photographic images with spherical aberration by means of a single parameter, the effective edge-spread, has not found general acceptance. Some of its defects were pointed out by Huber ([16], p.334).

On the theoretical side, the later investigations of the effects of spherical aberration on image equality and on the best focal setting seem to have been largely influenced by the earlier ones, which had derived their incentive from problems connected with the design of microscopes and astronomical telescopes for visual use. In these systems with very small aberrations, the *Strehl intensity ratio* (Definitionshelligkeit) was found to provide a useful indication of the subjectively judged image quality. Strehl [34] had shown that the central light intensity in point diffraction images by a system with primary spherical aberration takes equal values at equidistant focal settings on either side of mid-focus, although of course the structure of the two point diffraction images at these two focal settings may be quite different. He concluded that, in systems with small amounts of primary spherical aberration, the mid-focus was the best focus when the quality of the image was 'evaluated' by means of its Strehl intensity ratio. Richter [29] showed that this remains true for amounts of fourth-power aberration up to a little more than two wavelengths†. Kuwabara [21] showed that as the amount of fourth-power aberration increases through a certain value (about 2.4 wavelengths) there is a jump transition of the position of best focus, in the above sense, to a position about 0.3 of the way from paraxial to marginal focus, and that the image at the symmetrically related focal setting on the other side of mid-focus, though its Strehl intensity ratio is the same as that at 'best' focus, has an inferior structure because its central disc contains a much smaller proportion of the total light. Figure 1, which is similar to one given by Kuwabara ([21], figure 3)‡, shows the variation of Strehl intensity ratio with focal setting for selected amounts of fourth-power aberration. Isophote diagrams computed by A. Maréchal and published in *Recent Advances in Optics* ([22], pp. 60–61) show the three-dimensional light-distribution in point diffraction images with 3, 4, 6 and 10 wavelengths of fourth-power aberration; from these diagrams it is easy to read off the two focal settings of maximum Strehl definition and the structure of the diffraction images at these two focal settings§. In particular, it is clear from the first two isophote diagrams that the value of the Strehl intensity ratio does not, in a point diffraction image with three or four wavelengths of fourth-power aberration, determine even approximately the amount of light in the central disc of the point diffraction image, or the size of this disc. A knowledge only of the focal ratio and of the Strehl intensity ratio is therefore insufficient for evaluating the performance of such a system used in conjunction with a photographic emulsion of known spread and granularity. In particular, it is not possible to discuss the position of the best photographic focal setting, or the way in which this setting may be influenced by changes in photographic spread and granularity, in terms only of the Strehl intensity ratio and the properties of the photographic emulsion.

To discuss these questions we need more detailed information about the image structure, such as is provided by isophote diagrams or, in a more convenient form, by the contrast-transmission function (ct-function) of the optical system.

† An account of Richter's analysis is given in J. Picht's book *Optische Abbildung*, 1941, pp. 165–184.

‡ Kuwabara's figure covers 21 cases, 17 of which are not included in figure 1. His curves are less detailed than those given here. A rather inaccurate version of the curve for $A=8$ was given in a previous paper ([26], figure 5).

§ In the first of these diagrams, 2300 should read 2500.

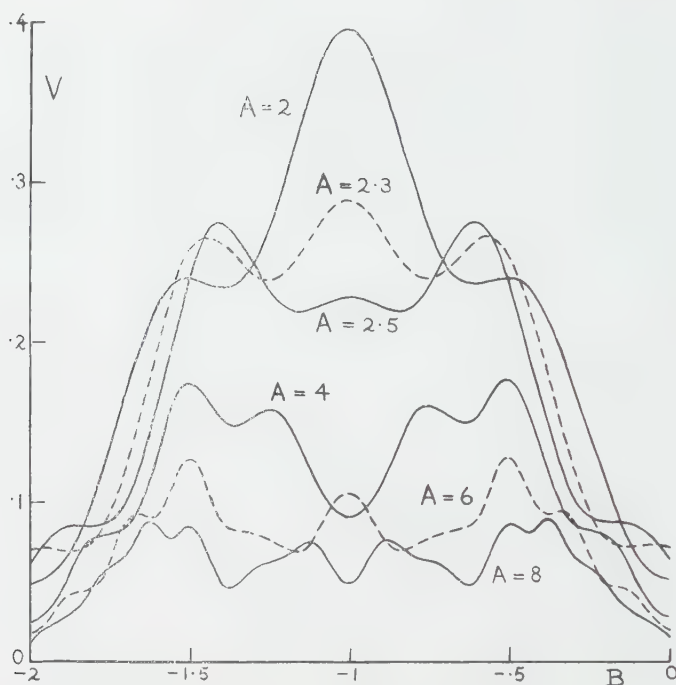


Figure 1. Strehl intensity ratio V in monochromatic diffraction images with selected amounts of primary spherical aberration, each over a range of focal settings. The parameter A gives the amount of fourth-power aberration in wavelengths; B specifies the focal setting in accordance with (1) (see text). At the paraxial focus $B=0$; at the marginal focus $B=-2$. For $A < 2.35$ the Strehl intensity ratio is greatest at the mid-focal setting $B=-1$. Each curve is symmetrical about the line $B=-1$.

2. SYSTEMS WITH PRIMARY SPHERICAL ABERRATION

2.1. Aerial diffraction images

The wave distortion function ϕ for a system with a primary spherical aberration can be written in the form

$$\phi(r) = A\lambda(r^4 + Br^2), \quad (1)$$

where r is a polar variable which runs from 0 at the centre of the aperture to 1 at its edge, λ the wavelength of the light, A the amount of fourth-power aberration measured in wavelengths, and B a parameter which specifies the focal setting. At the paraxial focus $B=0$, at the marginal focus $B=-2$, at the mid-focal setting $B=-1$.

As is well known, the isoplanatic image of a small, incoherently lit sinusoidal test grating by a system with wave-aberration (1) shows a sinusoidal intensity distribution similar to that in the grating itself, but with reduced or reversed contrast. The ratio of the contrast in the image to that in the object grating varies with the line spacing, and measures the absolute value of the contrast-transmission function of the system. Figures 2 and 3 display this function for a small-field monochromat in the cases $A=1$ and $A=4$, over a range of focal settings in each case. Corresponding figures for $A=0, 2, 8$ have been published elsewhere [24, 25, 26].

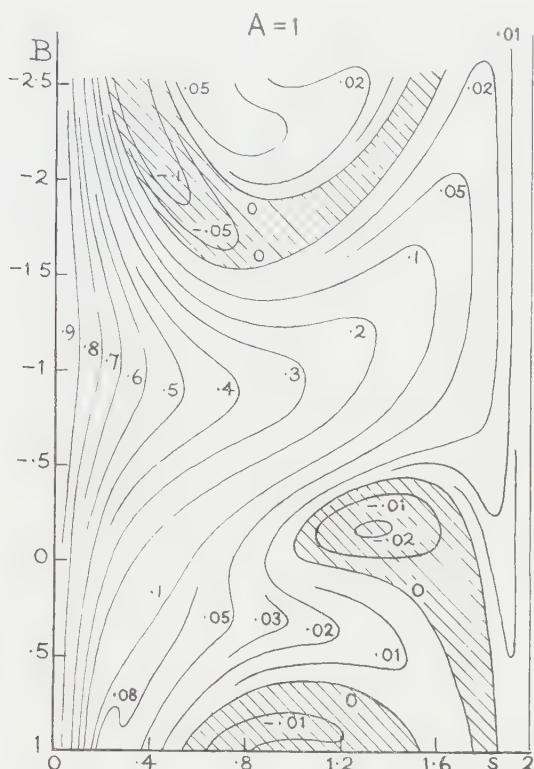


Figure 2. Contrast transmission τ of a monochromat with one wavelength of primary spherical aberration at different focal settings. The abscissa s is the reduced line-frequency $2\lambda F\omega$, which takes the value 2 at the cut-off frequency $(F\lambda)^{-1}$. The ordinate B specifies the focal setting, in accordance with (1) (see text). At the paraxial focus $B=0$, at the marginal focus $B=-2$. The numbered curves give the values of τ as a function of s and B . In the shaded areas $\tau < 0$ (contrast reversal). The values of τ along each horizontal line $B = \text{const.}$ represent the ct -function $\tau(s)$ of the system at the corresponding focal setting.

In each of figures 2 and 3, the abscissa s represents the reduced line-frequency [14] in the image surface; that is to say $s = 2\omega F\lambda$, where ω is the line frequency in the image, F is the focal ratio and λ is the wavelength of the light. The ordinate B specifies the focal setting as already explained. The numbered curves in the figures indicate the values of the contrast transmission τ as s and B vary. Along each horizontal line $B = \text{constant}$, the values of $\tau = \tau(s)$ define the optical contrast-transmission function of the system at the corresponding focal setting. In the shaded regions $\tau < 0$ and a sinusoidal grating is imaged with reversed contrast. Along each vertical line $s = \text{constant}$, the values of τ show the variation of contrast transmission with focal setting for a sinusoidal test-grating of image-line frequency $\omega = s/(2F\lambda)$. The point on each vertical line at which the contrast transmission τ attains its greatest value gives the best focal setting $B = B^*$ for a sinusoidal test object of image line frequency ω . This best focal setting B^* is different for sinusoidal test objects of different line-frequencies, but since the ct -function of a photographic system is, for low-contrast images in light of given wavelength, simply the product of τ with the photographic contrast

transfer function τ_1 , the best focal setting is the same for low-contrast photographic images as for the aerial image. It is shown for $A = 1, 2, 4, 6, 8$ in figure 4†.

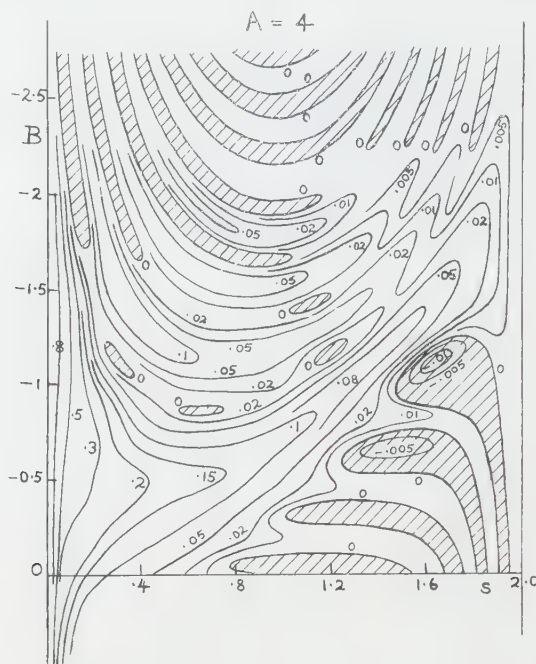


Figure 3. Contrast transmission τ of a monochromat with four wavelengths of primary spherical aberration at different focal settings. The abscissa s and the ordinate B have the same meaning as in figure 3. The numbered curves give the values of τ as a function of s and B . In the shaded area $\tau < 0$ (contrast reversal).

It will be seen that each of the quasimonochromatic sinusoidal components into which a polychromatic extended object can be analysed possesses its own best focus, namely the focus of greatest image-contrast, the position of which is the same for aerial and photographic images. In systems with spherical aberration the best focal setting for the object as a whole can be regarded as a compromise between these individual best foci. In general, the best focal setting will be different for different types of object detail, a fact well known in aerial photography. Further, the meaning of the term 'best focal setting' will depend on the criterion of image quality adopted.

This complicated situation is usually dealt with in a rather summary way by setting up a definition of the quality of the image of a point object, and then defining the quality of an optical system as the average quality of the images of point objects in different parts of its working field. We shall apply this procedure to images formed by monochromats with primary spherical aberration (1), taking the coefficients A, B in (1) as constant over the working field, so that the imaging is isoplanatic. (The value of B is altered, however, when the focal setting is varied.)

† A less accurate diagram was given for the cases $A = 1, 2, 4$ in a previous paper ([1], figure 8).

Since the aberrations are radially symmetrical, the Strehl intensity ratio V here satisfies the equation [15]

$$V = 2 \int_0^2 \tau(s) s ds \quad (2)$$

whenever the intensity in the diffraction image is greatest at its centre. In particular, (2) holds for $A = 1, 2, 4$; $-2 < B < 0$.

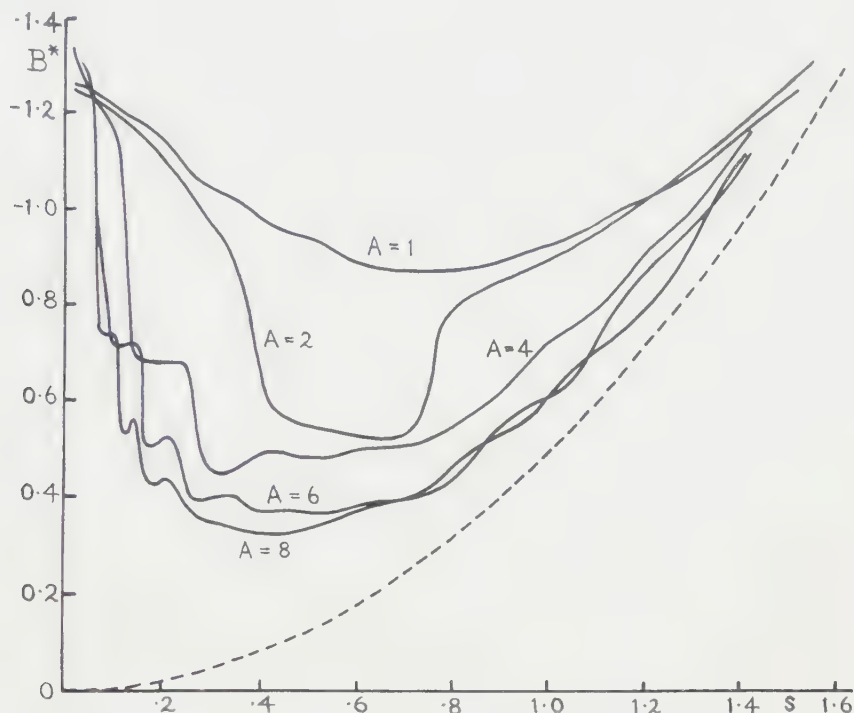


Figure 4. Variation of best focus B^* with line frequency of a sinusoidal test object imaged by monochromats with selected amounts of primary spherical aberration. s is the reduced line-frequency in the image (see text) A measures the amount of fourth-power aberration in wavelengths. The dotted curve is the parabola $s^2 = 2B^*$.

When V is used as an image-quality evaluation, the best focal setting is interpreted as the one which maximizes (2). An equivalent formulation is that it maximizes the (u, v) -mean of $\tau = \tau(u, v)$ over the spatial frequency pass-band $u^2 + v^2 < 1/(F\lambda)^2$ of the system, outside which τ is everywhere zero. In fact, the spatial frequency (u, v) in the image-surface is connected with the reduced line-frequency s by the equation

$$s = 2F\lambda\sqrt{(u^2 + v^2)}. \quad (3)$$

Thus if $\tau(u, v)$ denotes the physical quantity τ considered as a function of (u, v) , we have in the radially symmetrical cases

$$\text{Mean}_{u^2 + v^2 < 1/(F\lambda)^2} \{ \tau(u, v) \} = \frac{F^2 \lambda^2}{\pi} \int_0^{2\pi} d\psi \int_0^{1/F\lambda} \tau(\omega \cos \psi, \omega \sin \psi) \omega d\omega,$$

where $u = \omega \cos \psi$, $v = \omega \sin \psi$, $\omega = +\sqrt{(u^2 + v^2)}$,

$$\begin{aligned}
&= \frac{1}{4\pi} \int_0^{2\pi} d\psi \int_0^2 \tau(s) \cdot s \, ds \\
&= \frac{1}{2} \int_0^2 \tau(s) \cdot s \, ds \\
&= \frac{1}{4} V.
\end{aligned}$$

2.2. Model photographic systems

In a low-contrast photograph of an extended object with complex fine structure, the fine detail in a small area of the photographic image can be well represented by convoluting the intensity distribution in the diffraction image at the front surface of the emulsion with the local photographic spread function and then adding a suitably defined stochastic function to represent the emulsion noise [7]. We call this approximate representation a *model photographic image*, and it seems a safe assumption that the quality of a photographic lens can be estimated more realistically in terms of the quality of the model photographic images which it produces than in terms of its aerial diffraction images, even when the model used involves some over-simplification. The verisimilitude of the model is improved by the fact that the fine detail in a photographic image is mainly rendered by silver grains near to the front surface of the developed emulsion (Scheffer, [33]). If we disregard for the present the effect of emulsion noise on the image quality (this will be considered later), the analogue for model photographic images of the quality evaluation(2) (Strehl definition) is the *photographic Strehl definition* V_1 , given (in systems with spherical aberration) by the equation

$$V_1 = 2 \int_0^2 \tau(s) \tau_1(s) \cdot s \, ds, \quad (5)$$

in which $\tau_1(s)$ denotes the photographic contrast transfer at the reduced spatial frequency s^\dagger . In an emulsion of the ordinary kind, the photographic process can be regarded as approximately linear for low-contrast images, but there are other effects, for example adjacency effects and the effect of finite emulsion thickness (about 10 or 15 μ), which are ignored in the corresponding model emulsion. Sayanagi [31] and Kelly [18] have given reasons for believing that, in low-contrast images, a small adjacency effect can be taken account of sufficiently well by a change in the photographic ct-function τ_1 . The unreality involved in ignoring the effects of finite emulsion thickness at high apertures can be reduced by measuring τ_1 at the same focal ratio F as that of the system forming the images. According to Frieser [11] the measured values of τ_1 show no dependence on F when $F \geq 5$. For reasons outlined elsewhere ([1], p. 525) not very much is lost by restricting the discussion to the imaging of low-contrast fine detail.

In attempting to extend Strehl's and Richter's investigations so as to take quantitative account of photographic spread, the most obvious procedure is therefore to begin by adopting V_1 in place of V as an image quality evaluation and to examine the effect of photographic spread in model emulsions on the position of the V_1 -maximizing focal setting and on the focal tolerance, in selected special cases. This is done in §2.3 for aberration-free images and for images

[†] Sayanagi's 'two-dimensional information volume' [30] is $\pi V_1/4F^2\lambda^2$. Because $s = 2\omega F\lambda$, the value of $\tau_1(s)$ which corresponds to a given value of s depends on the focal ratio F .

with selected amounts of primary spherical aberration, and the extent to which the same results may be expected to hold for actual emulsions of finite thickness is also considered.

However, it is not photographic spread alone which reduces the quality of a photographic image; in scientific photography granularity is likewise of importance, because it limits the accuracy of the conclusions which can be drawn from measurements of the photographic density. In § 3 the combined effects of photographic spread and noise on the focal tolerance of model photographic images, and on the position of best focal setting, are examined in the same selected special cases. In order to be able to do this it is necessary to adopt, in place of V_1 , a definition of image quality which takes account both of photographic spread and of emulsion noise (granularity), as well as of the optical aberrations and of diffraction. The quality evaluation adopted is one which measures the discriminating power of the system; that is to say the effectiveness with which small object-differences can be distinguished in the 'noisy' photographic images.

Finally, in § 4, the effect of spread in the receiving surface on the focal tolerance and on the best focal setting in the same model photographic images is calculated according to a third evaluation, originally proposed by Schade [32] and Fellgett [6], and the results are compared with those of §§ 2 and 3.

2.3. Computed special cases

Making use of some computational results already applied to a different purpose elsewhere [27] and of others obtained at the same time, we consider the values of V_1 over a range of focal settings in three F/4 systems with the selected amounts 0, λ , 2λ , 4λ of fourth-power aberration, imaging near-monochromatic light of wavelength $\lambda = 500 \text{ m}\mu$ onto two model emulsions E1 and E2.

Model emulsion E1 has the acceptance factor τ_1 shown in figure 5; it is the 'model emulsion 10' already used in an earlier paper [1]. Model emulsion E2 has twice the spread of E1; its acceptance factor τ_2 is obtained from the first by a simple change of scale, according to the equation

$$\tau_2(\omega) = \tau_1(2\omega),$$

where ω denotes the line frequency in the image-surface†. The value of $\tau_1(\omega)$ is taken as zero for $\omega > 300$ lines per mm. In both model emulsions the noise can be prescribed at will; its properties do not affect the value of V_1 .

An idea of the relation in which the model emulsions E1 and E2 stand to two well-known emulsion types is given by the measured ct-values (acceptance factors) also included in figure 5. The plotted points near the τ_2 -curve refer to Tri-X Miniature emulsion. They were kindly supplied by Mr. P. G. Powell of Kodak Limited. The measurements were made on images of sinusoidal gratings by an F/5 lens working with Wratten filters No. 25, 58 and 47, which gave mean wavelengths $\lambda \simeq 625 \text{ m}\mu$, $530 \text{ m}\mu$ and $440 \text{ m}\mu$ respectively. The contrast in the object-gratings was about 0.5. Development was carried out in such a way as to keep adjacency effects small. The variation of the ct-values with wavelength λ is seen to be fairly small, as was also found by Hendeberg ([12], figures 22 and 23) for the Afga emulsions IFF and IU.

† The effect on the computed values of V_1 of doubling the emulsion spread is the same as that of having the focal ratio. But the effects of finite emulsion thickness are more pronounced at F/2 than at F/4 and the model emulsion correspondingly less realistic.

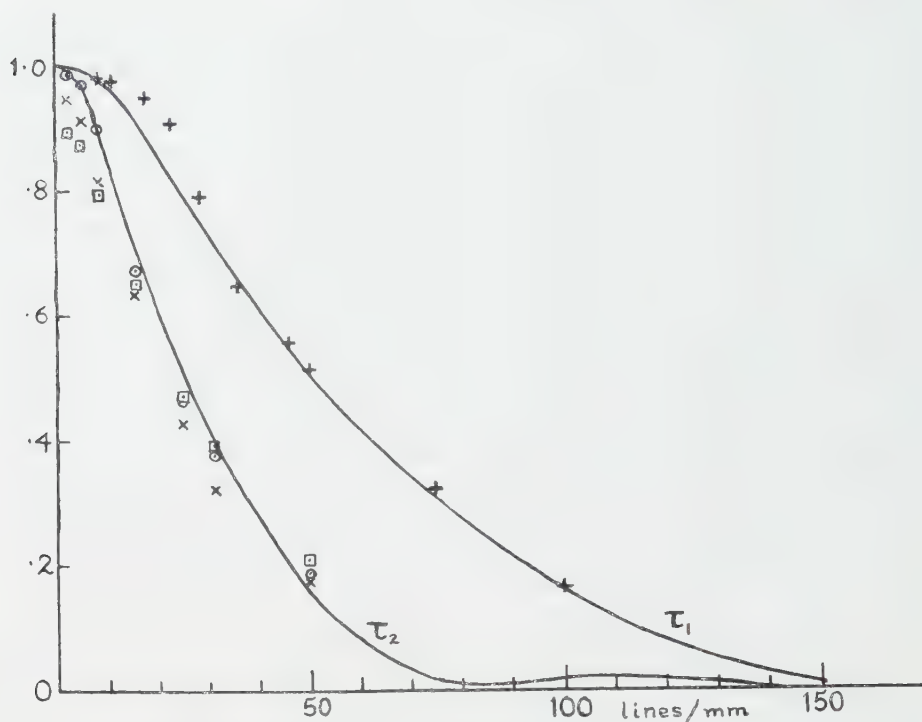


Figure 5. Sine-wave response factors of photographic receiving surfaces. The abscissae give the image-line frequency ω .

Solid curves: τ_1 (model emulsion E1) and τ_2 (model emulsion E2) at line frequencies $\omega < 150$ lines/mm.

Plotted points \circ , \times , \square : Kodak Tri-X Miniature emulsion at wavelengths near 625 m μ , 530 m μ , 440 m μ respectively (Powell, private communication).

+ : Kodak Microfile Pan near 546 m μ , developer D158, 3 min, 20°C with continuous brushing [13].

The plotted points near the τ_1 -curve are measured values found by Hendeborg [13], (figure 7) for Kodak Microfile Pan emulsion with developer D158 (3 min, 20°C) and continuous brushing of the emulsion surface, in light of mean wavelength 546 m μ (half-value width of the λ -range: 35 m μ). Evidently the model emulsion E1 ('emulsion 10') can be made to represent this emulsion-developer combination rather closely by suitably adjusting the noise. The most obvious discrepancy is the upward deviation of the plotted points from the τ_1 -curve in the range 10–40 lines/mm. However, a smooth distortion of the τ_1 -curve in this range, making it pass through the plotted points, would not alter the value of V_1 calculated from (5) by more than 3.2×10^{-4} , which is less than 3.2 per cent of its value near best focus in an F/4 system with up to four fringes of primary spherical aberration (see figure 6). A further discrepancy, less easy to estimate, arises from the fact that Hendeborg's sinusoidal exposure-distributions were recorded at F/2, not at the focal ratio F/4 at present under consideration. The effects of finite emulsion thickness on the contrast transmission will not be the same in the two cases.

In figure 6 (a) the dotted curve, which gives the values of the expression $\sin^2 \pi b / (\pi b)^2$ for $-1 < b < 1$, represents for $-0.8 < b < 0.8$ the classical Strehl definition of an aberration-free system at different focal settings specified by the parameter b . The value of b specifies the focal setting through the wave-aberration function $\phi(r) = b\lambda r^2$ †. The linear scale in microns of the corresponding focal settings in an F/4 system is also shown, the value of λ being taken as $500 \text{ m}\mu$. The two remaining curves give the normalized photographic Strehl definition for the system working with the model emulsions E1 and E2 respectively. V_1 and V_2 in the figure denote the photographic Strehl definition (5) in these two special cases; to obtain the two curves, its value has been normalized to 1 at the best focal setting. The size of the normalizing constants, 14.5 for E1 and 50.1 for E2, shows what a large reduction in quality the intervention of even a

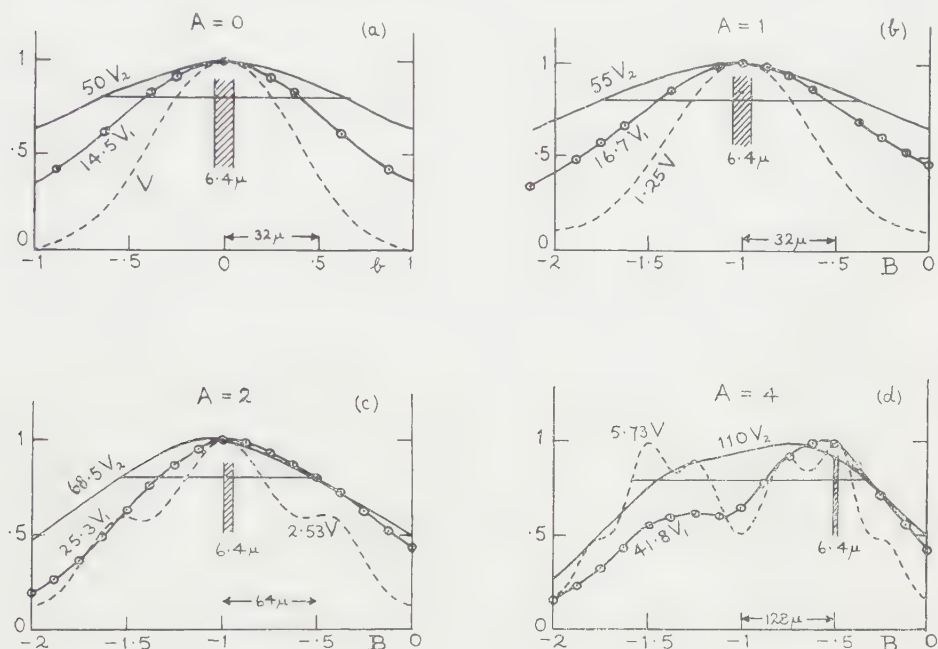


Figure 6. 'Best' focal setting and focal tolerances in F/4 monochromats ($\lambda = 500 \text{ m}\mu$) with 0, 1, 2, 4 wavelengths of fourth-power aberration, determined from the Strehl definition. The dotted curves refer to the aerial image, the solid curves to model photographic images with emulsions E1, E2 respectively. The abscissa B in the cases $A=1, 2, 4$ specifies the focal setting in accordance with (1) (see text). The abscissa b in the case $A=0$ specifies the focal setting by means of the wave distortion $\phi(r) = b\lambda r^2$ ($0 < r < 1$) in the exit pupil. V_1 and V_2 denote the photographic Strehl definition in the images with emulsions E1, E2 respectively. V denotes the Strehl intensity ratio in the aerial images when $A=1, 2, 4$ when $A=0$, V denotes the value of the integral on the right of (2) (see text), which is equal to the Strehl intensity ratio when $-0.8 < b < 0.8$. The parts of the curves lying above the horizontal lines correspond to 'acceptable' images of quality at least 80 per cent of that at best focus. The shaded vertical strips indicate the thickness of a high-resolution emulsion layer such as Kodak Microfile Pan.

† As $|b|$ increases from 0.8 to 1, the central bright spot in the diffraction image gradually disappears (see for example [22], figure 10) and the Strehl intensity ratio is no longer given by (2).

high-resolution emulsion produced in the images of an F/4 system with negligible aberrations. Of course this is due to the fact that the emulsion and the optical system are strongly mismatched. To match an aberration-free F/4 system we should need an emulsion with a spread half-width of 2 or 3 microns.

The shaded vertical strip of thickness 6.4μ represents a section of a typical high-resolution emulsion layer on the same scale. In the model emulsions E1 and E2 the emulsion thickness is treated as negligible, and we can read off from the curves the focal tolerances corresponding to a given percentage drop in the value of V_1 . We here adopt, somewhat arbitrarily, a 20 per cent drop in V_1 as tolerance basis. The extent to which the resulting focal tolerances may need to be changed when emulsion thickness is taken into account is considered later. For the model emulsions E1 and E2 their values are 54μ and 85μ respectively. For the aerial image, the focal tolerance corresponding to a 20 per cent drop in V (the 'Rayleigh tolerance') is 33μ .

Figure 6(b) shows the corresponding curves for an F/4 system with 1λ of fourth-power aberration; that is, with aberration function $\phi(r) = \lambda(r^4 + Br^2)$. The vertical scale of each curve is adjusted so that its maximum ordinate is 1. The parameter B specifies the focal setting as explained in §1. The distance from paraxial focus ($B=0$) to marginal focus ($B=-2$) is 128μ in the F/4 system. At the mid-focal setting ($B=-1$) the system just satisfies the Rayleigh quarter-wave criterion. This is the best (V -maximizing) focal setting for the aerial image; to a sufficient accuracy it can also be regarded as the best (V_1 -maximizing) focal setting for the two model photographic images, though in fact the V_1 -maximum is very slightly displaced towards marginal focus in the E2 image.

It is interesting to note that the introduction of 1λ of fourth-power aberration, which reduces V by 20 per cent at best focus, has also reduced V_1 by as much as 13 per cent at best focus in the E1 images and by 9 per cent in the E2 images, although the central disc in the diffraction image is much smaller than the photographic spread in each case. This shows that, in the image with aberration, the light lost from the central disc is fairly widely distributed among the inner Airy rings. It is well known that the size of the disc and the positions of the rings are almost unaffected at best focus by 1λ of fourth-power aberration.

The focal tolerances corresponding to a 20 per cent drop in V_1 are now 58μ and 92μ respectively for the model emulsions E1 and E2.

In figure 6(c) the amount of fourth-power aberration has been increased to 2λ . The aberration function is $\phi(r) = 2\lambda(r^4 + Br^2)$. The distance from paraxial focus ($B=0$) to marginal focus ($B=-2$) is now 256μ in the F/4 system; the horizontal scale is half that of figure 6(b), so that the shaded vertical strip appears only as half wide as in figure 6(a) and (b). The focal tolerances are now 51μ in the aerial image, 109μ with model emulsion E1, 130μ with E2. The best focus is shifted 10μ from mid-focus towards marginal focus with model emulsion E2, and about 6μ from mid-focus towards paraxial focus with E1; these shifts are too small to change the normalized value of V_1 appreciably at mid-focus, but it is interesting that they are in opposite directions. The optical spread is less than the image-spread of E1, but the optical ct-function is comparable with τ_1 in the spatial frequency range $0 < \omega < 75$ lines/mm.

In figure 6(d) the amount of fourth-power aberration has been increased to four wavelengths. The distance between paraxial focus ($B=0$) and marginal focus ($B=-2$) is 512μ ; the horizontal scale is half that of figure 6(c). The

dotted curve shows the variation in the Strehl definition V of the aerial image as B is varied, the other two curves the variation in the photographic Strehl definition V_1 when the image is received on the model emulsions E1 and E2. The maximum ordinate on each curve is normalized to 1 as before.

For the aerial image there are two ranges, each of length 108μ and symmetrically situated with respect to mid-focus, in which V is nowhere less than 80 per cent of its maximum value. In the range nearer paraxial focus the image has a well-marked core-and-halo structure, in which the bright core contains up to 40 or 50 per cent of the total light (compare [26], figure 6, curves 4, 4a). In the range near marginal focus the bright core contains much less light [20, 21] and the images of extended objects are far less satisfactory to the eye. We therefore take the focal tolerance as 108μ , ignoring the axicon-type images near the secondary focus $B = -1.5$.

The focal tolerance in the model photographic images is now 141μ for E1 and 288μ for E2. The latter is *more* than twice the values for the system with 2λ of fourth-power aberration (figure 6 (c)). The explanation is, of course, that the structure of the image near best focus is now quite different. The best focus, which in the aerial image was almost exactly one quarter of the distance from paraxial to marginal focus, is shifted 64μ towards marginal focus in the E1 image; in the E2 image the shift is practically zero, although the photographic spread is twice as great.

It is natural to ask how far these results, obtained for model emulsions in which the thickness of the emulsion layer is treated as negligible, may be expected to hold also for actual emulsions of the same effective spread and noise characteristics, recording low-contrast images at a focal ratio $F/4$. As an example, we consider Kodak Microfile Pan, for which the thickness of the emulsion layer is given by Hendeberg [13] as about 6μ . The curves of figure 6 suggest that even in the cases $A=0$ and $A=1$ the focal tolerances could hardly be changed by as much as 8 per cent if the model were altered so as to take account of the finite emulsion thickness. In the cases $A=2, 4$ the changes could hardly exceed 4 per cent. In Tri-X Miniature, a double-coated emulsion of total thickness about 15μ †, the changes would of course be larger. Using the E2 curves as a rough guide we can make the upper estimates of 20 per cent in the cases $A=0, 1$; 10 per cent in the case $A=2$, and 5 per cent in the case $A=4$.

The last three error estimates are probably too high, because low spatial frequencies contribute very little to the photographic Strehl definition‡, while it may be concluded from Scheffer's experimental results already referred to that the remaining spatial frequencies are rendered mainly by silver grains near to the front surface of the emulsion layer. But even focal tolerance predictions with an inaccuracy of 20 per cent would, if they could be computed for practical lens systems as art of the optical design procedure, provide useful data needed for the appropriate designing of the mechanical parts. Although the special cases discussed in the present paper are insufficient for even a preliminary discussion of this more complex problem, they give some indication of what can be expected in high quality astrographic systems such as Schmidt cameras.

† I am indebted to Mr. Powell for this information.

‡ The contribution from the spatial frequencies $\omega < 10$ lines/mm is, by (5), less than 0.0016 in an $F/4$ system with $\lambda = 500 m\mu$.

3. DISCRIMINATING POWER

A measure of the quality of a photographic system which takes account of emulsion noise (granularity) as well as of aberrations can be based on its *discriminating power*, that is to say on the extent to which its images allow us to distinguish one object-intensity distribution from another. More precisely, the discriminating power of a system is defined as the logarithm of the effective number of distinguishable images [7] which it forms when presented with a random low-contrast object set of prescribed spatial power spectrum. It agrees in value with the statistical mean information content of an image for the given object set.

Discriminating power in this sense evidently depends on the characteristics of the object set, as well as on the optical design and on the choice of photographic emulsion. The dependence is unavoidable if discriminating power is to be measured realistically, but it is an unwelcome complication. Moreover, photographic systems are usually designed without prior knowledge of the statistics of the object set on which they will be used. In the absence of this knowledge, it is possible to simplify the definition of discriminating power at little cost in realism.

We can do so by using a restricted type of object-set for the evaluation, namely a random low-contrast set with flat spatial power spectrum in the optical pass band \mathcal{F} . On the assumption that the emulsion noise is gaussian, we obtain after calculation the quality evaluation

$$5.30 \int_0^2 \log_e \{1 + |\tau \tau_1|^2 R\} s \, ds \quad (6)$$

for photographic systems with circular aperture and radially symmetrical aberrations†, where s is the reduced line-frequency (3) and R is the 'signal-to-noise' ratio in \mathcal{F} ; more precisely, the ratio of statistical mean object-structure power density in spatial frequency to emulsion-noise power density in spatial frequency. In the model emulsions E1 and E2, the emulsion noise is taken as gaussian and assigned a flat power-spectrum in \mathcal{F} †. Then R is constant throughout the optical pass band \mathcal{F} of the photographic system; a constant value $R=100$ in \mathcal{F} corresponds to fairly 'clean' images, a value $R=8$ in \mathcal{F} to noisy ones. In actual emulsions it may be presumed that the noise is nearly gaussian and measurements of the Agfa emulsions IFF, IF, ISS and Ultra published by Zeitler ([39], figure 15) show a nearly flat noise-power spectrum in the spatial frequency range 5–100 lines per mm. But it seems ([10], figure 15) that this only holds over a restricted range of photographic densities for emulsion Isopan ISS.

We can examine the effect of a change in emulsion noise-level on the image quality (6) by assigning different constant values to R in the passband \mathcal{F} . In the present section we are mainly concerned with the effects of changes in emulsion spread and noise-level on the focal tolerance according to the evaluation (6), and on the position of best focus.

† See refs. [1], [7]. With the normalization here adopted, (6) measures the statistical mean information content per image in bits per Airy disc. When the aberrations are not radially symmetrical, (6) is replaced by the expression

$$\frac{5.30}{2\pi} \int_0^{2\pi} d\psi \int_0^2 \log_e \{1 + |\tau \tau_1|^2 R\} s \, ds,$$

in which τ is a function of the azimuth ψ as well as of s .

† It would be enough to suppose the power spectrum flat over the (smaller) region \mathcal{F}_1 in which $\tau_1 \neq 0$.

In figure 7 are shown the results of applying the evaluation (6) to the same model photographic images as before, with the constant values 100 and 8 assigned to the signal-to-noise parameter R . The four diagrams (a), (b), (c), (d) refer to F/4 systems with 0, λ , 2λ , 4λ wavelengths of fourth-power aberration respectively, each over a range of focal settings. The abscissae b and B specify the focal setting in the same way as in figure 6. Along each curve the ordinate represents the discriminating power (6), expressed as a fraction of its value at 'best' focus, when the systems are used with model emulsions E1 (curves 3 and 4) and E2 (curves 1 and 2) in light of wavelength $\lambda = 500 \text{ m}\mu$. In curves 1 and 3 of each diagram, the value of R is 8; in curves 2 and 4 the value of R is 100. As already noted, these values correspond to noisy and 'clean' images respectively.

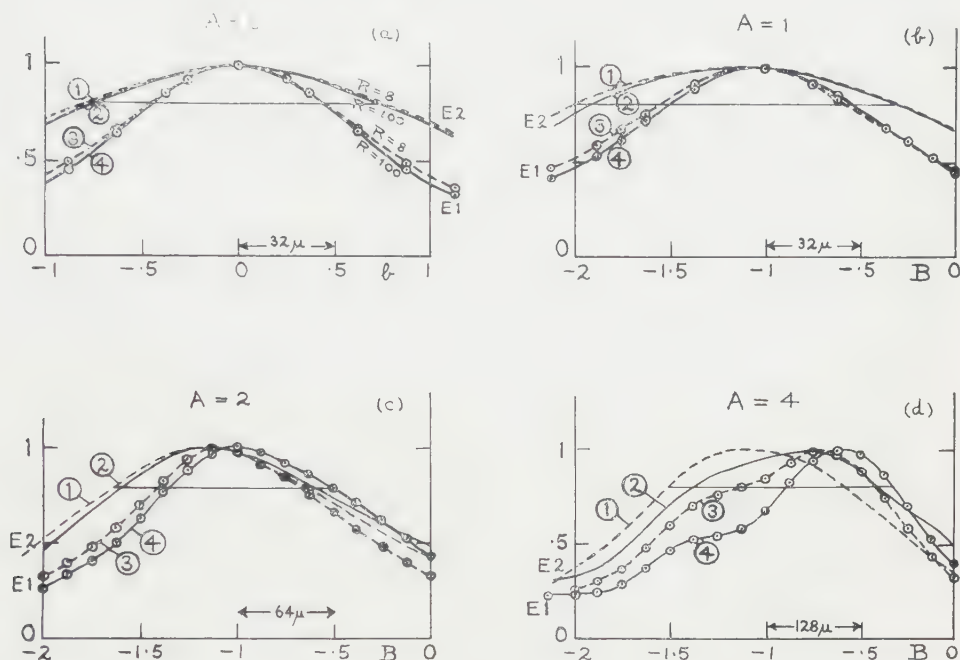


Figure 7. Effect of changes in emulsion spread and noise on best focal setting and on focal tolerances, in F/4 monochromats ($\lambda = 500 \text{ m}\mu$) with 0, 1, 2, 4 wavelengths of fourth-power aberration, when the image quality is evaluated by means of the discriminating power of the system (see text). The abscissae b , B specify the focal setting as in figure 6. The curves —○—○— and —○— —○— in each diagram give the normalized discriminating power of the system with emulsion E1; the curves ——— and — — — that with emulsion E2. The maximum ordinate of each curve is normalized to 1. On the solid curves the signal-to-noise parameter R has the value 100; on the dotted curves, $R=8$. The normalizing factors (reciprocals of the discriminating power at best focus) for the curves labelled 1, 2, 3, 4 are respectively 12.4, 3.26, 3.48, 0.91 when $A=0$; 13.2, 3.51, 4.07, 1.05 when $A=1$; 15.8, 4.19, 6.19, 1.58 when $A=2$; 27.0, 6.71, 13.0, 2.65 when $A=4$. The parts of the curves lying above the horizontal lines correspond to 'acceptable' images of quality at least 80 per cent of that at best focus.

The values of the discriminating power in bits per Airy disc are obtained on multiplying the ordinates read off from the curves of figure 7 by the appropriate constants, named in the figure caption.

Inspection of the curves reveals the interesting fact that in the cases $A=0, 1, 2$, where the amount of fourth-power aberration does not exceed 2λ , the focal tolerances, position of 'best' focus, and percentage variation in discriminating power with focal shifts are almost the same in the clean images with $R=100$ as in the noisy images with $R=8$. When $A=4$, on the other hand, they differ considerably between clean and noisy images. Further, when $A=0, 1, 2$ the normalized discriminating-power curves (figure 7 (a), (b), (c)) show a remarkably close resemblance to the corresponding curves (figure 6 (a), (b), (c)) of normalized photographic Strehl definition. In particular, the focal tolerances corresponding to a 20 per cent drop in discriminating power are not very different from those corresponding to a 20 per cent drop in photographic Strehl definition (see table).

A	Emulsion	Focal V -tolerance	Focal V_1 -tolerance	Focal discrimination tolerance		Focal T_1 -tolerance
				$R=8$	$R=100$	
0	E1	$33\ \mu$	$54\ \mu$	$58\ \mu$	$58\ \mu$	$64\ \mu$
0	E2		$85\ \mu$	$101\ \mu$	$94\ \mu$	$106\ \mu$
1	E1	$34\ \mu$	$58\ \mu$	$64\ \mu$	$64\ \mu$	$64\ \mu$
1	E2		$92\ \mu$	$109\ \mu$	$104\ \mu$	$112\ \mu$
2	E1	$52\ \mu$	$109\ \mu$	$96\ \mu$	$110\ \mu$	$93\ \mu$
2	E2		$131\ \mu$	$128\ \mu$	$131\ \mu$	$128\ \mu$
4	E1	$108\ \mu$	$141\ \mu$	$182\ \mu$	$147\ \mu$	$250\ \mu$
4	E2		$288\ \mu$	$241\ \mu$	$256\ \mu$	$284\ \mu$

Focal tolerances of F/4 monochromats. V denotes the Strehl intensity ratio; V_1 the photographic Strehl definition, T_1 the photographic structural resolution (§ 4). Each focal range represents a 20 per cent tolerance in the corresponding evaluation.

In the cases $A=0, 1, 2$ the aerial image has of course not yet developed a marked core-and-halo structure, and the focus of best discriminating power (figure 7 (a), (b), (c)) is near mid-focus. When $A=4$, this best focus varies its position considerably (figure 7 (d)) as spread and noise are varied, and the normalized discriminating power-curves no longer resemble the normalized V_1 -curves (figure 6 (d)) so closely.

To sum up: For the set of 16 cases considered, namely monochromats with

$$A=0; \quad -1 < b < 1;$$

$$A=1, 2, 4; \quad -2 < B < 0,$$

imaging at F/4 on to model emulsions E1, E2, each at the two signal-to-noise ratios $R=8, R=100$, it appears that the position of the focus of best discrimination and the focal tolerance corresponding to a specified percentage fall in discriminating power are very insensitive to a change in the value of the signal-to-noise parameter R when the aberrations do not exceed twice the Rayleigh tolerance limit (cases $A=0, 1, 2$).

The discriminating power is decreased quite noticeably by only 1λ of fourth-power aberration, even when the emulsion spread is five or six times the diameter

of the bright central nucleus of the diffraction image and the image is noisy. With emulsion E1 the decrease is 14 per cent for $R=8$, 13 per cent for $R=100$. With emulsion E2 it is 6 per cent for $R=8$, 7 per cent for $R=100$.

The last result is of considerable interest, because it indicates that *a reduction of the wave aberrations to values well below the quarter-wave limit may be of practical importance even when the system is to be used with a fast, noisy emulsion.*

In the case $A=4$ (figure 7(d)) on the other hand, the shift of best focal setting when R increases from 8 to 100 is about 100μ in the E2 images, while the focal tolerance (based on a 20 per cent drop in discriminating power) decreases by 21 per cent. In the E1 images, where the photographic spread is smaller, the dependence of focal tolerance on noise level is less sensitive; changing R from 8 to 100 leaves the 20 per cent focal tolerance practically unaltered.

4. PHOTOGRAPHIC STRUCTURAL RESOLUTION

When $R \ll 1$, the evaluation (6) takes the limiting form

$$5 \cdot 30 R \int_0^2 |\tau \tau_1|^2 s \, ds. \quad (7)$$

In the cases $A=0, 1, 2$ of figure 7, where the curves are only weakly dependent on R , it makes little practical difference to the focal tolerances, or to the choice of best focus, whether the image quality is assessed by (6) or by (7). Even in the case $A=4$, the change in the focal tolerances is not large (see table), though the change in the position of best focus may be considerable, when the basis of the quality assessment is changed from (6) to (7).

The image evaluation (7) still depends on the mean object contrast through the signal-to-noise parameter R , but we can derive from it a 'figure of merit' for the system, essentially the same as one proposed by Schade [32] and Fellgett [6], by taking the ratio T_1 of the value of (7) for the given system to its value for an aberration-free system of the same aperture and focal length, imaging on to a surface with negligible spread and with the same value of R . We call T_1 the *structural resolution factor* of the photographic system at the given focal setting; an easy calculation shows that it satisfies the equation

$$T_1 = 4 \cdot 36 \int_0^2 |\tau \tau_1|^2 s \, ds. \quad (8)$$

The 20 per cent focal tolerances of the system and the position of best focal setting according to (7) or (8) depend only on the optical design, the spread in the model receiving surface, the focal setting, and the wavelength of the light. Like the photographic Strehl definition V_1 , the photographic structural resolution factor T_1 defined by (8) is a figure of merit for the system which lacks full realism but has the practical merit of simplicity.

In figure 8 are shown the results of applying the quality evaluation (8) to the same images as were examined in figures 6 and 7; as before, each curve gives the evaluation as a fraction of its value at best focus. The solid curves refer to the model photographic images; the structural resolution factors of the F/4 systems working with model emulsions E1 and E2 are denoted in this figure by T_1 and T_2 respectively. The constants by which T_1 and T_2 have been multiplied to obtain

the plotted ordinates are shown on the curves. The dotted curves give, in the same way, the structural resolution factor T of the aerial images, which can be treated as the special case $\tau_1 \equiv 1^\dagger$.

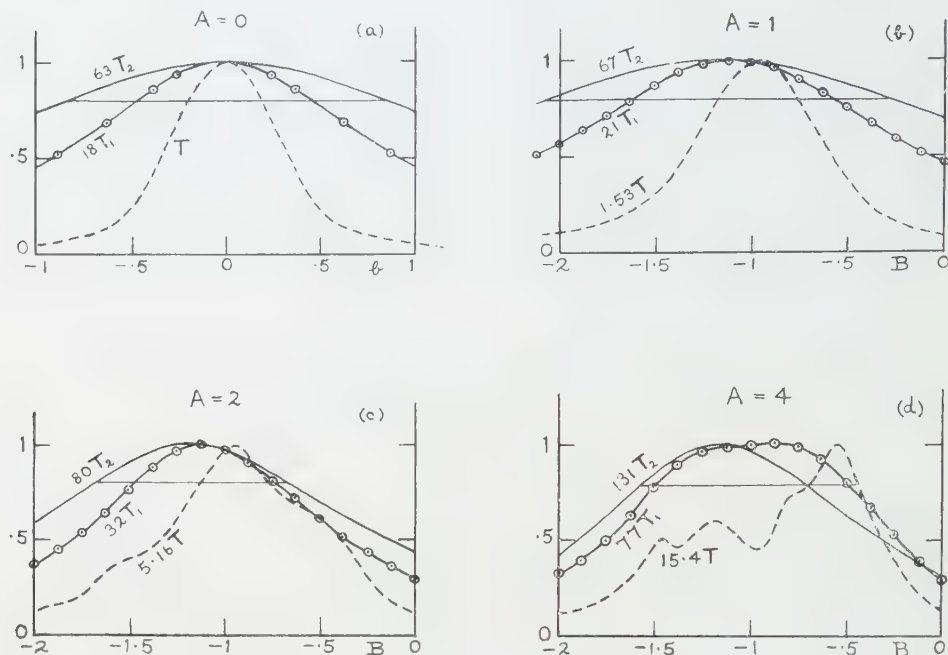


Figure 8. Best focal settings and focal tolerances evaluated from the structural resolution. The special cases examined are the same as in figure 6. The dotted curves show the normalized structural resolution in the aerial image over a range of focal settings, the solid curves show the normalized photographic structural resolution in the images received on model emulsions E1 and E2; the maximum of each curve is normalized to unity. The normalizing constants are shown on the curves. T_1 and T_2 denote the photographic structural resolution factor (8) with emulsions E1, E2 respectively; T the structural resolution factor of the aerial diffraction image. The parts of the curves lying above the horizontal lines correspond to 'acceptable' images of quality at least 80 per cent of that at best focus.

From a comparison of figures 6, 7 and 8 it appears that in the cases $A = 0, 1, 2$ the focal tolerances corresponding to a specified percentage fall in photographic structural resolution agree closely with those corresponding to the same percentage fall in discriminating power at $R = 8$ or at $R = 100$. The position of best focus shows an appreciable shift, however, on passing from one evaluation to the other, in the case $A = 2$. In the case $A = 4$, the photographic structural resolution diverges appreciably from the other evaluations.

From the run of the curves in figure 6, 7 and 8 it appears that the effect of finite emulsion thickness on the focal tolerances may be expected to be of about the same size whether these tolerances are based on photographic Strehl definition, on discriminating power, or on photographic structural resolution. Upper estimates of the effect in the first case were given at the end of §2.3.

† The general notion of structural resolution was discussed in a previous paper [23], where the 'local structural resolution' $R_{x,y}$ yields the quantity T on multiplication by $10.60 F^2 \lambda^2 / \pi$.

ACKNOWLEDGMENTS

My grateful thanks are due to the Cambridge University Mathematical Laboratory, and in particular to Mr. P. Swinnerton-Dyer, for carrying out the computations on which figures 1, 2, 3, 4, 6, 7, 8 are based. Also to Mr. P. G. Powell and Dr. G. C. Farnell of the Kodak Research Laboratories for measured contrast-transfer values of photographic emulsions, some of which are shown in figure 5, and for helpful discussions.

La question de la profondeur de foyer et de la mise au point optimum dans les images photographiques est importante pour les calculateurs opticiens à cause de sa relation avec le problème de l'obtention d'un champ plan satisfaisant, et il serait très désirable de pouvoir prédire, sans construire de modèle d'essai, la meilleure surface focale et la profondeur de foyer dans différentes régions du champ d'un projet de système photographique travaillant avec une émulsion donnée. Les développements récents de la théorie des images et des méthodes de calcul suggèrent que ce vieux problème soit maintenant attaqué avec de meilleures chances de succès. Une attaque combinée à la fois du côté théorique et du côté expérimental semble être nécessaire. Une étude théorique est tentée dans la présente publication, et l'on étudie par le calcul les variations de profondeur de foyer et de mise au point optimum en fonction de la diffusion photographique et du bruit dans des images photographiques types affectées de 0, 1, 2 et 4 longueurs d'onde d'aberration sphérique du 3^e ordre. Deux modèles d'émulsions sont utilisées pour recevoir chaque image.

Le critère de profondeur de foyer adopté est que la qualité de l'image (définie avec précision) ne doit pas descendre au-dessous de 80 pour cent de la valeur au meilleur foyer; les courbes données sur les figures 6, 7, 8 permettent de connaître les profondeurs de foyer correspondant à d'autres pourcentages pour les images considérées. Trois mesures différentes de la qualité de l'image sont utilisées et comparées. La première est une généralisation du critère de rapport d'intensité de Strehl (§§ 2.1, 2.2); le second est une mesure du pouvoir de discrimination (§ 3) du système photographique, utilisé pour un ensemble d'objets aléatoires de contraste moyen donné; le troisième évalue la qualité de l'image au moyen de sa 'résolution structurelle normalisée' (§ 4).

Seule la seconde méthode d'évaluation permet de tenir compte du fait que la profondeur de foyer et la mise au point du système sont susceptibles de changer lorsque le niveau de bruit dans la surface réceptrice change. L'un des résultats du présent travail est que ces variations ont peu d'importance pratique si l'aberration sphérique n'excède pas 2 longueurs d'ondes. Dans ces conditions les trois méthodes d'évaluation de la qualité des images, conduisent à des conclusions très voisines et il semble que l'on puisse assez bien prédire la profondeur de foyer à partir du nombre d'ouverture, des aberrations, et de la fonction de transfert de contraste du récepteur, sans avoir à spécifier le rapport du contraste de l'objet à la valeur du 'bruit' de l'émulsion.

Dans les systèmes entachés de 4 longueurs d'ondes d'aberration sphérique la mise au point de meilleure discrimination peut changer considérablement et la profondeur de foyer de façon appréciable quand le niveau de bruit dans l'émulsion varie. Dans tous les cas examinés la profondeur de foyer est assez sensible à la diffusion de l'image par la surface réceptrice. Une longueur d'onde d'aberration sphérique (limite de Rayleigh) peut abaisser la qualité de l'image au meilleur foyer de façon appréciable même lorsque la diffusion photographique est grande par rapport à la tache de diffraction et que l'image présente du 'bruit'.

Die Frage der fokalen Tiefe und besten Einstellung bei photographischen Bildern ist für optische Rechner von Bedeutung, weil sie mit der Aufgabe einer befriedigenden Bildebnung zusammenhängt; es würde offensichtlich eine grosse Annehmlichkeit bedeuten, wenn man ohne die Herstellung eines Musterstückes vorhersagen könnte, welches die beste Einstellebene und fokale Tiefe in verschiedenen Teilen des Feldes eines photographischen Objektivs bei der Benutzung einer bestimmten Emulsion ist. Neuere Entwicklungen der Theorie und der Rechenverfahren lassen erwarten, dass man dieses alte Problem nun mit

besseren Aussichten auf Erfolg wird angehen können. Es scheint nötig, dass man die Frage zugleich von der theoretischen und experimentellen Seite anzugreifen hat. Von Seiten der Theorie soll die vorliegende Arbeit einen ersten Versuch darstellen. Dabei wird die Abhängigkeit der fokalen Tiefe und der besten Einstellung auf die photographische Streuung und den Schleier bei ausgewählten photographischen Modellbildern mit 0, 1, 2 bzw. 4 Wellenlängen primärer sphärischer Aberration berechnet. Als Bildempfänger werden zwei verschiedene Modell-Emulsionen benutzt.

Das Kriterium für die angenommene Tiefenschärfe besteht darin, dass die Bildgüte (in einem genau definierten Sinn) nicht unter 80 Prozent des Wertes bei bester Einstellung sinken darf. Die in den Figuren 6, 7 und 8 gezeigten Kurven erlauben für die untersuchten Abbildungen auch die fokale Tiefe entsprechend anderen Prozent-Kriterien abzulesen.

Es werden drei verschiedene Masse der Bildgüte benutzt und verglichen. Das erste ist eine Verallgemeinerung des Strehlschen Intensitätsverhältnisses (§§ 2.1, 2.2). Das zweite ist eine Messung der Trennschärfe (§ 3) des photographischen Modellsystems, benutzt bei einer zufälligen Objektserie von besonderem mittleren Kontrast. Das dritte beurteilt die Bildgüte mittels seiner normierten Strukturauflösung (§ 4).

Nur die zweite dieser Bewertungen ist fein genug, um die Tatsache zu berücksichtigen, dass die fokale Tiefe des Systems und der Ort bester Einstellung sich verschieben kann, wenn das Schleierniveau der Empfängerfläche sich ändert. Eines der Ergebnisse der vorliegenden Untersuchung ist, dass diese Änderungen von geringer praktischer Bedeutung sind, vorausgesetzt der Betrag der Aberrationen vierter Ordnung übersteigt nicht zwei Wellenlängen. Die drei verschiedenen Bewertungen der Bildgüte führen dann zu fast den gleichen Schlüssen, und es scheint, dass wir die fokale Tiefe genügend gut voraussagen können aus einer Kenntnis des Brennweitenverhältnisses, der Aberrationen und der Kontrastübertragungsfunktion der Empfängerfläche, ohne auf das Verhältnis des Objekt-contrastes zu dem Emulsions-Schleier einzugehen.

Bei Systemen mit vier Wellenlängen sphärischer Aberration können sich der Ort der besten Auflösung beträchtlich und die fokale Tiefe merklich verschieben, wenn das Schleier-Niveau in der Auffangfläche sich ändert. In allen untersuchten Fällen hängt die fokale Tiefe recht empfindlich ab von der Bildstreuung in der Auffangfläche. Es scheint, dass eine Wellenlänge primärer sphärischer Aberration (die Rayleigh-Grenze) die Bildgüte bei der besten Einstellung merklich herabsetzen kann, auch wenn die photographische Streuung gross ist gegenüber der Beugungsstreuung und das Bild schleierig ist.

REFERENCES

- [1] BLACK, G., and LINFOOT, E. H., 1957, *Proc. roy. Soc. A*, **239**, 522.
- [2] CONRADY, A. E., 1919, *Non. Not. R. astr. Soc.*, **79**, 575.
- [3] CONRADY, H. G., 1926, *Photogr. J.*, **66**, 9.
- [4] CONRADY, H. G., 1926, *Proc. Opt. Convention*, p. 830.
- [5] DUPOUY-CAMET, C., 1953, *Rev. d'Opt.*, **32**, 454.
- [6] FELLGETT, P. B., 1953, *J. opt. Soc. Amer.*, **43**, 371.
- [7] FELLGETT, P. B., and LINFOOT, E. H., 1955, *Phil. Trans. A*, **247**, 369.
- [8] FLÜGGE, J., 1926, *Z. InstrumKde*, **46**, 333, 289.
- [9] FOCKE, J., 1956, *Opt. Acta*, **3**, 110.
- [10] FRIESER, H., 1958, *Mitt. Forschungslab. Agfa*, **2**, 249.
- [11] FRIESER, H., 1959, *Photogr. Korr.* (3. Sonderheft), 25.
- [12] HENDEBERG, L. O., 1960, *Ark. Fys.*, **16**, 417.
- [13] HENDEBERG, L. O., 1960, *Ark. Fys.*, **16**, 457.
- [14] HOPKINS, H. H., 1955, *Proc. roy. Soc. A*, **231**, 91.
- [15] HOPKINS, H. H., 1957, *Proc. phys. Soc. Lond. B*, **70**, 1162.
- [16] HUBER, S., 1943, *Z. InstrumKde*, **63**, 333, 369.
- [17] KÄMMERER, J., 1957, *Optik*, **14**, 399.
- [18] KELLY, D. H., 1960, *J. opt. Soc. Amer.*, **50**, 269.
- [19] KINGSLAKE, R., 1954, *NBS Circular* 526, 259.
- [20] KUWABARA, G., 1955, *J. opt. Soc. Amer.*, **45**, 309.
- [21] KUWABARA, G., 1955, *J. opt. Soc. Amer.*, **45**, 625.

- [22] LINFOOT, E. H., 1955, *Recent Advances in Optics* (Oxford: Clarendon Press).
- [23] LINFOOT, E. H., 1957, *Opt. Acta*, **4**, 12.
- [24] LINFOOT, E. H., 1959, Proc. 1958 Summer School, Imperial College, London.
- [25] LINFOOT, E. H., 1960, *Qualitätsbewertung optischer Bilder* (Brunswick: Fr. Vieweg).
- [26] LINFOOT, E. H., 1960, *Opt. Acta*, **7**, 65.
- [27] LINFOOT, E. H., 1960, *Proc. phys. Soc. Lond.*, **76**, 870.
- [28] PICT, J., 1931, *Optische Abbildung* (Brunswick: Fr. Vieweg).
- [29] RICHTER, R., 1925, *Z. InstrumKde*, **45**, 1.
- [30] SAYANAGI, K., 1956, *J. appl. Phys*, Japan, **25**, 193 (in Japanese).
- [31] SAYANAGI, K., 1960, *J. opt. Soc. Amer.*, **50**, 185.
- [32] SCHADE, O. H., 1952, *JMPTE*, **58**, 182.
- [33] SCHEFFER, W., 1910, *Brit. J. Photogr.*, **57**, 24.
- [34] STREHL, K., 1894, *Theorie des Fernrohrs* (Leipzig: Barth).
- [35] STREHL, K., 1895, *Z. InstrumKde*, **15**, 364.
- [36] STREHL, K., 1902, *Z. InstrumKde*, **22**, 213.
- [37] VÄISÄLÄ, Y., 1922, *Ann. Univ., Fenn. Amboensis*, B, **1**, No. 2.
- [38] WANG TA-HANG, 1941, *Proc. phys. Soc. Lond.*, **53**, 157.
- [39] ZEITLER, E., 1958, *Mitt. Forschungslab. Agfa*, **2**, 217.



Thin-lens aberration theory

by C. G. WYNNE

Optical Design Group, Imperial College, London

(Received 6 February 1961)

The general theory of the primary aberrations of thin lenses, including the primary aberrations of pupil imagery, is developed in a form adapted to its application to optical designing problems, and the methods of this application are discussed, with some examples.

1. THE SIGNIFICANCE OF THIN-LENS ABERRATION THEORY

For most optical systems of practical interest a complete analytic treatment of the aberrations is not possible. The primary aberrations, obtained by considering the aberration function to be expanded as a polynomial in the aperture and field angles or related quantities and neglecting all but the lowest power terms, can be calculated numerically, but here again an analytic treatment is generally not possible. For a system having rotational symmetry the primary aberration terms are seven in number, two relating to chromatic aberrations and five (the Seidel aberrations) to monochromatic aberrations. Owing to the presence of significant high-order terms in the expansion, the seven primary aberrations generally give a quite inadequate description of the performance of a corrected optical system, but they are of value in optical designing because their reduction to small values is a necessary, though not a sufficient, condition for good correction; so that in principle the search for well-corrected optical systems can be restricted to that range of values of the design parameters for which first-order correction is possible, thereby effectively reducing the number of parameters of the system by seven. But since the primary aberrations are fairly complicated functions of the design parameters, it is not generally possible to define explicitly the ranges of values of these parameters that correspond to the range of first-order solutions. It is at this point that thin lens aberration theory becomes relevant to the optical design problem. This paper is an attempt to formulate and extend this theory so as to facilitate its application to the problems of optical designing.

For lenses of zero axial thickness the two primary chromatic aberrations and one of the Seidel terms (the Petzval sum) are invariant as the lens shape is altered, keeping its power constant. The other four Seidel terms relating to spherical aberration, coma, astigmatism and distortion, vary with the lens shape, but if these aberrations arising at the two surfaces of the thin lens be taken together, higher-power terms in the design parameters arising at the two surfaces cancel, the total aberration coefficient of the thin lens reducing in each case to a quadratic function of the shape, suitably defined, leading to a considerable simplification of the analysis. A system of thin lenses having first-order correction may therefore be designed by choosing a set of lens powers and separations having the required total power and satisfying the three shape-invariant conditions, the remaining four primary aberrations being corrected by appropriate changes of shape, commonly described as 'bending'. The components of actual lens systems are rarely all sufficiently thin for the effects of thickness on the aberrations

to be negligible, but some components often are. For lenses of moderate thickness the aberrations follow the general trend given by thin-lens theory, so that these methods are of considerable value in finding systems having first-order correction and in subsequent modifications of them to reduce higher-order aberrations while maintaining first-order correction. Equations for the primary spherical aberration, coma, astigmatism and distortion of thin lenses have been given by a number of authors, the earlier literature having been reviewed by Taylor [1] and von Rohr [2], but the striking geometrical regularities given below, which greatly facilitate their application, do not appear to have been discussed.

In addition to the aberrations of the image, lens systems also have aberrations of the pupil. Although these do not directly affect the image quality, they are of importance for several different reasons: the variation of the image aberrations with conjugates can be expressed in terms of them (see, for example [3]); since they affect the path of light through the system, some higher-order image aberrations can be considered as arising from them; and one of them, the coma of the pupil, can be used to increase the effective pupil size for oblique imagery relative to that on the axis, thus compensating to some extent for the decrease of illumination with obliquity which normally occurs [4]. The field curvature term is identical for image and pupil imagery, and the other primary monochromatic aberrations of pupil imagery are simply related to those of normal imagery, and display the same types of regularity, as is shown below.

2. THIN-LENS ABERRATION THEORY

Using a notation similar to that given by Hopkins [5], for a single spherical refracting surface the primary aberration coefficients of spherical aberration (S_I), coma (S_{II}), astigmatism (S_{III}) and distortion (S_V) may be written

$$\left. \begin{aligned} S_I &= A^2 y \Delta(u/n), & S_{II} &= (\bar{A}/A) S_I, \\ S_{III} &= (\bar{A}/A) S_{II}, & S_V &= (\bar{A}/A) (S_{III} + PH^2) \end{aligned} \right\} \quad (1)$$

where y is the intersection height on the surface of a paraxial ray at the conjugates considered, u is its angle with the lens axis, $A = ni$ where i is the angle of incidence in a medium of refractive index n , H is the Smith-Helmholz-Lagrange invariant, Δ denotes the change on refraction, P is the Petzval field curvature $[-(1/r)\Delta(1/n)]$, r is the radius of curvature, and a bar over a symbol denotes that it relates to a paraxial principal ray through the stop centre instead of to a paraxial ray from the object. \bar{A}/A may be expressed as $H[E + (1/Ay)]$, using Seidel's difference formula, where

$$E = \sum \frac{d_{j,j+1}}{n_{j,j+1} y_j y_{j+1}},$$

$d_{j,j+1}$ being the axial separation between the j th and $(j+1)$ th surfaces from the stop, in medium of refraction index $n_{j,j+1}$, and the summation is taken surface by surface from a value $E=0$ at the stop. The primary aberration coefficients of pupil imagery are of course precisely the same as those given above, with symbols with and without bars interchanged, but they are more readily calculated using relationships given, in this notation, by Wynne [3]:

$$\left. \begin{aligned} \bar{S}_I &= HE(S_V + PH\bar{A}\bar{y}), & \bar{S}_{II} &= S_V + H\Delta\bar{u}^2, \\ \bar{S}_{III} &= S_{III} + H\Delta u\bar{u}, & \bar{S}_V &= S_{II} + H\Delta u^2. \end{aligned} \right\} \quad (2)$$

S_I varies with the fourth power of the aperture, S_{II} and \bar{S}_V with the third power of the aperture and the first power of the field, S_{III} and \bar{S}_{III} with the square of

aperture and field, S_V and \bar{S}_{II} with the first power of the aperture and the cube of the field, and \bar{S}_I with the fourth power of the field angle.

Thin lens formulae have generally been given for a lens in air ($n=1$); if this limitation is not imposed they are equally applicable to a thin air-space between two components of the same refractive index, which often occurs in lens systems, so that the general case will be treated here of a thin lens of refractive index $n_0 n$, in a medium of refractive index n_0 .

2.1. Symmetrical variables

If the paraxial ray from the object make angles u_1 and u_2' with the axis before and after refraction by the lens, it is convenient to introduce the symmetrical variable $U = u_1 + u_2'$ to express the relationship between the conjugates at which the lens is working, U being invariant as the lens shape is changed; since $u_2' - u_1 = yk$ where k is the power of the lens, the magnification of the lens

$$M = \frac{u_2'}{u_1} = \frac{U + yk}{U - yk},$$

and $M = -1$ at $U = 0$. Similarly, if α_1 and α_2 be the angles between the axis and the normals to the two surfaces at the height y of the paraxial ray incidence, the shape of the lens may be expressed in terms of the variable $\Lambda = \alpha_1 + \alpha_2$, $\Lambda = 0$ describing an equi-convex or equi-concave lens.

Equations (1) and (2) may be expressed in terms of these variables, using simple Gaussian optics, giving after considerable reduction the primary aberration coefficients for the thin lens, which are the sum of the two surface coefficients, as

$$\left. \begin{aligned} S_I &= \frac{1}{4} y^2 k n_0 \left[y^2 k^2 \left(\frac{n}{n-1} \right)^2 + \frac{n+2}{n} (\Lambda - U)^2 - 2U(\Lambda - U) \right], \\ S_{II} &= HES_I + \frac{1}{2} Hyk \left[(\Lambda - U) \frac{n+1}{n} - U \right], \\ \bar{S}_V &= HES_I + \frac{1}{2} Hyk \left[(\Lambda - U) \frac{n+1}{n} + U \right], \\ S_{III} &= (HE)^2 S_I + H^2 E y k \left[(\Lambda - U) \frac{n+1}{n} - U \right] + H^2 k / n_0, \\ \bar{S}_{III} &= (HE)^2 S_I + H^2 E y k \left[(\Lambda - U) \frac{n+1}{n} \right], \\ S_V &= (HE)^3 S_I + \frac{3}{2} H^3 E^2 y k \left[(\Lambda - U) \frac{n+1}{n} - U \right] + H^3 E \frac{k}{n_0} \left(3 + \frac{1}{n} \right), \\ \bar{S}_{II} &= (HE)^3 S_I + \frac{3}{2} H^3 E^2 y k \left[(\Lambda - U) \frac{n+1}{n} - \frac{U}{3} \right] + H^3 E \frac{k}{n_0} \left(1 + \frac{1}{n} \right), \\ \bar{S}_I &= (HE)^4 S_I + 2H^4 E^3 y k \left[(\Lambda - U) \frac{n+1}{n} - \frac{U}{2} \right] + H^4 E^2 \frac{k}{n_0} \left(3 + \frac{2}{n} \right). \end{aligned} \right\} \quad (3)$$

Equations equivalent to those above for S_I , S_{II} , S_{III} and S_V have been given by a number of authors, using a variety of variables. In the earlier German literature reviewed by von Rohr [2] the shape variable used was the first radius, and the coordinate variable the object distance. Symmetrical variables, different from

those used here, were introduced, in a more limited range of application, by Coddington [6] and applied generally by Taylor [1]. Argentieri [7] used a coordinate variable $\psi = U/y$, and a combined shape and coordinate variable $\mu = (\Lambda - U)/y$. Hopkins [5] has given a general discussion of the equation for S_I , and those for S_{II} , S_{III} and S_V for a lens at the stop. For this case ($E=0$), S_{II} becomes a linear function of Λ , having a value of zero at $\Lambda = U(2n+1)/(n+1)$, a shape near to that at which $|S_I|$ has its minimum value, $\Lambda = U(2n+2)/(n+2)$ (see below); S_{III} has a constant value of $H^2 k n_0$, and S_V a constant value of zero for all values of Λ ; S_V , like S_{II} , becomes a linear function of Λ , while S_{III} , \bar{S}_{II} and \bar{S}_I are zero for all shapes of lens. Equations equivalent to all eight of equations (3) were given, with some discussion by Wynne [8].

2.2. General properties of thin-lens equations

For the general case of a thin lens not at the stop, equations (3) show that the variation of each S with shape (Λ) is parabolic, the axis of the parabolae lying parallel to the S axis. By simple geometry, $1/n_0 y E = \tan \phi = T$, say, where ϕ is the angle subtended by the pupil semi-diameter at the thin lens; and by differentiation, the vertices of the various parabolae occur at lens shapes as follows:

$$\left. \begin{aligned} \text{For } S_I, \text{ the vertex is at } \Lambda &= \frac{n+1}{n+2} 2U, \\ \text{for } S_{II} \text{ and } \bar{S}_V \text{ ,, ,, ,, } \Lambda &= \frac{n+1}{n+2} (2U - T), \\ \text{for } S_{III} \text{ and } \bar{S}_{III} \text{ ,, ,, ,, } \Lambda &= \frac{n+1}{n+2} (2U - 2T), \\ \text{for } S_V \text{ and } \bar{S}_{II} \text{ ,, ,, ,, } \Lambda &= \frac{n+1}{n+2} (2U - 3T), \\ \text{for } \bar{S}_I \text{ ,, ,, ,, } \Lambda &= \frac{n+1}{n+2} (2U - 4T), \end{aligned} \right\} \quad (4)$$

i.e. the vertices are equally spaced along the shape axis, occurring at shapes successively more concave to the stop down the list given above. The spacing between successive vertices, $T(n+1)/(n+2)$, is independent of the power and the conjugates of the lens, and varies only slowly with n .

The 'steepness' of a parabola is conveniently defined by the reciprocal of its semi-latus rectum, which for the parabolae of equations (3) is given by

$$\left. \begin{aligned} \frac{d^2 S_I}{d\Lambda^2} &= \frac{1}{2} y^2 k n_0 \frac{n+2}{n}, \\ \frac{d^2 S_{II}}{d\Lambda^2} = \frac{d^2 S_V}{d\Lambda^2} &= H E \cdot \frac{1}{2} y^2 k n_0 \frac{n+2}{n}, \\ \frac{d^2 S_{III}}{d\Lambda^2} = \frac{d^2 S_{III}}{d\Lambda^2} &= (H E)^2 \cdot \frac{1}{2} y^2 k n_0 \frac{n+2}{n}, \\ \frac{d^2 S_V}{d\Lambda^2} = \frac{d^2 \bar{S}_2}{d\Lambda^2} &= (H E)^3 \cdot \frac{1}{2} y^2 k n_0 \frac{n+2}{n}, \\ \frac{d^2 S_2}{d\Lambda^2} &= (H E)^4 \cdot \frac{1}{2} y^2 k n_0 \frac{n+2}{n}. \end{aligned} \right\} \quad (5)$$

The 'steepness' of the various parabolae are therefore simple multiples of that of the S_I parabola and HE raised to the power corresponding to the various aberrations' dependence on field angle. For a lens at the stop ($E=0$, $T=\infty$) the latera recta of the curves of aberrations of oblique imagery become infinite, the

vertices occur at physically unrealizable shapes $\Lambda = \infty$ and the curves degenerate into the straight lines already discussed for this case.

For the general case, the 'steepness' of the eight parabolae of equations (3) are given simply by equation (5), their location along the Λ axis by equations (4), so that it only remains to define their position along the S axis. For some purposes this is most conveniently done by using expressions for the value of each S at the vertex of its parabola (equations (7) below); rather simpler algebraically are the expressions giving the value of each coefficient at the shape making $|S_I|$ a minimum (equation (4)). If the value of each coefficient at this lens shape be denoted by an asterisk,

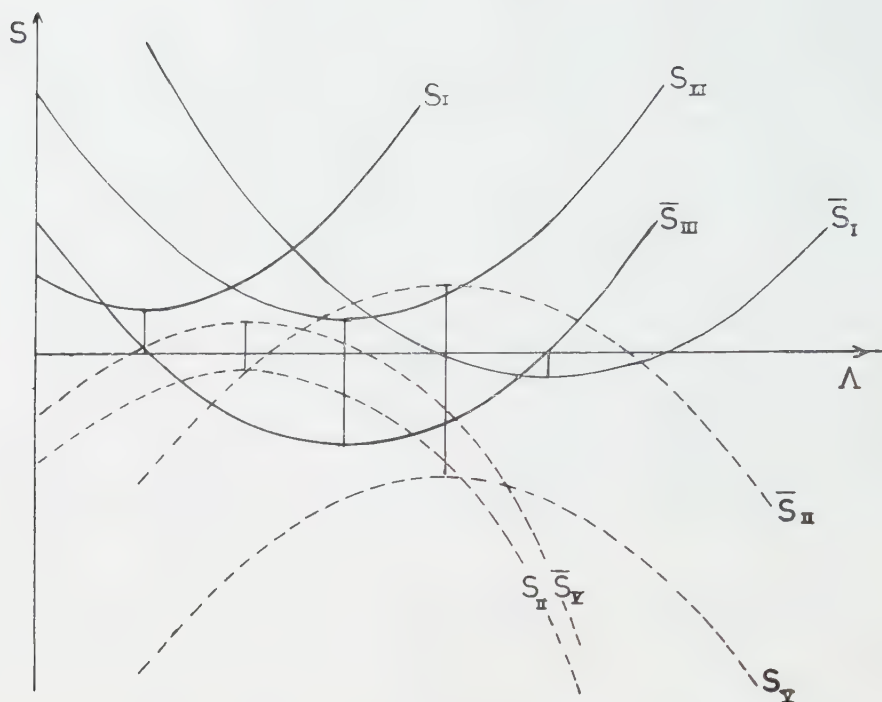
$$\left. \begin{aligned} S_I^* &= \frac{1}{4} y^2 k n_0 \left[y^2 k^2 \left(\frac{n}{n-1} \right)^2 - \frac{n}{n+2} U^2 \right], \\ S_{II}^* &= HE S_I^* - \frac{1}{2} \frac{HykU}{n+2}, \\ \bar{S}_V^* &= HE S_I^* + \frac{1}{2} HykU \frac{2n+3}{n+2}, \\ S_{III}^* &= (HE)^2 S_I^* - \frac{H^2 EykU}{n+2} + H^2 k/n_0, \\ \bar{S}_{III}^* &= (HE)^2 S_I^* + \frac{1}{2} H^2 EykU \frac{2n+2}{n+2}, \\ S_V^* &= (HE)^3 S_I^* - \frac{3}{2} \frac{H^3 E^2 ykU}{n+2} + H^3 E \frac{k}{n_0} \left(\frac{3n+1}{n} \right), \\ \bar{S}_{II}^* &= (HE)^3 S_I^* + \frac{1}{2} H^3 E^2 ykU \frac{2n+1}{n+2} + H^3 E \frac{k}{n_0} \left(\frac{n+1}{n} \right), \\ \bar{S}_I^* &= (HE)^4 S_I^* + \frac{nH^4 E^3 ykU}{n+2} + H^4 E^2 \frac{k}{n_0} \left(\frac{3n+2}{n} \right). \end{aligned} \right\} \quad (6)$$

The eight equations for the thin-lens primary aberrations, which in the form of equations (3) show considerable algebraic complexity, can therefore be considered as representing the variations of the aberrations coefficients with lens shape as a set of eight parabolae with axes parallel to the S axis, with vertices spaced at equal intervals along the shape axis, the pairs of curves for S_{II} and \bar{S}_V , for S_{III} and \bar{S}_{III} and for S_V and \bar{S}_{II} being coaxial and of identical steepness, the steepness of the curves at the successive vertex positions increasing as successive powers of HE , and having S values at the shape of minimum spherical aberration given by the regularly changing equations (6) (figure). Considered in this way they are more readily applicable to first-order designing.

From the first of equations (3) and (6) it follows that S_I for large values of Λ has the same sign as k , i.e. is positive for convergent lenses and negative for divergent ones, and that this is also true at the Λ value making $|S_I|$ a minimum, and hence for all values of Λ , except for values of U such that

$$\left(\frac{U}{yk} \right)^2 \geq \frac{n(n+2)}{(n-1)^2},$$

i.e. for a range of virtual object or image positions, one conjugate being substantially shorter than the equivalent focal length of the thin lens. The locus of the vertices



of the S_I parabolae for different values of U is the parabola given by equation (6) for S_I^* , $|S_I^*|$ being a maximum, and therefore stationary, at $U=0$ (cf. Hopkins [5]).

The loci of the vertices for the other aberration coefficients may be treated similarly; the vertex values of each of these coefficients, obtained by substituting shape values Λ , from equations (4) into equations (3), show the same kind of regularity as equations (5), but are slightly more complicated. For the purpose of defining the loci of the vertices, they may conveniently be expressed in the form:

$$\left. \begin{aligned}
 S_{II \min} &= \frac{1}{4} \frac{Hyk}{T} \left[\left(\frac{ykn}{n-1} \right)^2 - \frac{n}{n+2} \left(U + \frac{T}{n} \right)^2 - T^2 \right], \\
 \bar{S}_{V \min} &= \frac{1}{4} \frac{Hyk}{T} \left[\left(\frac{ykn}{n-1} \right)^2 - \frac{n}{n+2} \left\{ U - \frac{T}{n} (2n+3) \right\}^2 + T^2 \left(3 + \frac{4}{n} \right) \right], \\
 S_{III \min} &= \frac{1}{4} \frac{H^2k}{n_0 T^2} \left[\left(\frac{ykn}{n-1} \right)^2 - \left(\frac{n}{n+2} \right) \left(U + \frac{2T}{n} \right)^2 \right], \\
 \bar{S}_{III \min} &= \frac{1}{4} \frac{H^2k}{n_0 T^2} \left[\left(\frac{ykn}{n-1} \right)^2 - \frac{n}{n+2} \left\{ U - \frac{T}{n} (2n+2) \right\}^2 \right], \\
 S_{V \min} &= \frac{1}{4} \frac{H^3k}{n_0^2 y T^3} \left[\left(\frac{ykn}{n-1} \right)^2 - \frac{n}{n+2} \left(U + \frac{3T}{n} \right)^2 + T^2 \left(3 + \frac{4}{n} \right) \right], \\
 \bar{S}_{II \min} &= \frac{1}{4} \frac{H^3k}{n_0^2 y T^3} \left[\left(\frac{ykn}{n-1} \right)^2 - \frac{n}{n+2} \left\{ U - \frac{T}{n} (2n+1) \right\}^2 - T^2 \right], \\
 \bar{S}_I \min &= \frac{1}{4} \frac{H^4k}{n_0^3 y^2 T^4} + \left[\left(\frac{ykn}{n-1} \right)^2 - \frac{n}{n+2} (U - 2T)^2 \right].
 \end{aligned} \right\} \quad (7)$$

For a given stop position (T) the loci of the vertices of the various aberration parabolae are therefore a set of parabolae, having vertices at the conjugates given by:

for S_I , $U = 0$	at a shape	$\Lambda = 0$,
,, S_{II} , $U = -\frac{T}{n}$,, ,, ,,	$\Delta = -\frac{n+1}{n} T$,
,, S_{III} , $U = -\frac{2T}{n}$,, ,, ,,	$\Lambda = -\frac{n+1}{n} \cdot 2T$,
,, S_V , $U = -\frac{3T}{n}$,, ,, ,,	$\Lambda = -\frac{n+1}{n} \cdot 3T$,
for \bar{S}_I , $U = 2T$,, ,, ,,	$\Lambda = 0$,
,, \bar{S}_{II} , $U = T\left(2 + \frac{1}{n}\right)$,, ,, ,,	$\Lambda = \frac{n+1}{n} T$,
,, \bar{S}_{III} , $U = T\left(2 + \frac{2}{n}\right)$,, ,, ,,	$\Lambda = \frac{n+1}{n} 2T$,
,, \bar{S}_V , $U = T\left(2 + \frac{3}{n}\right)$,, ,, ,,	$\Lambda = \frac{n+1}{n} 3T$.

From equations (3) it follows that for large positive or negative values of A , S_{III} , \bar{S}_{III} and \bar{S}_I , like S_I , have the same sign as k , and S_{II} , S_{II} , S_V and S_V have the same sign as Ek . It was shown above that S_I always has the same sign as k unless

$$U^2 \geq \frac{n(n+2)}{(n-1)^2} (yk)^2.$$

The corresponding values for U which make the various S parabolae reach zero values follow directly from equations (7); this for S_{II} to have zeros,

$$\left(U + \frac{T}{n}\right)^2 \geq \frac{n+2}{n} \left[\left(\frac{ykn}{n}\right)^2 - T^2\right]$$

with similar expressions from the rest of equations (7).

These equations are less directly interpreted than that for S_I , both because of the additional variable T , and because T increases toward infinity as the lens approaches the stop, so that the vertex values of S_{II} , S_{III} , etc., to which these equations refer, occur at values of the shape factor Λ which also approach infinity, i.e. at extreme shapes where the two radii of curvature approach the value zero. These equations are only useful therefore for lenses well removed from the stop. Inserting reasonable values of U corresponding to what is commonly encountered in actual lenses, it is found that for S_{II} (which changes sign near the shape giving a minimum value to $|S_I|$ for a lens at the stop), and for \bar{S}_{II} (which is zero for all shapes for a lens at the stop), both positive and negative values may be reached at physically realizable shapes for all stop positions removed from the lens; S_{III} , (which has a constant value of H^2k/n for a lens at the stop), and \bar{S}_{III} (which is zero for a lens at the stop), may reach small values of sign opposite to that of k over a limited range of shapes; while S_V , with a constant value of zero for a lens at the stop, normally has the same sign as Ek for lenses removed from the stop except at extreme conditions of refraction (large values of U).

Equations (7) also give the variations of the various aberrations as a function of T . One application of these is to the forms of wide-angle objective employing a

front divergent element to introduce coma of the entrance pupil in order to increase the effective aperture for oblique pencils of light [4, 9]. For such a lens in front of the stop, the maximum increase of oblique aperture occurs at the vertex of the \bar{S}_{II} parabola, and differentiation of the equation for \bar{S}_{II} in (7) gives the T value, and hence the distance from the stop of the front divergent lens to give maximum \bar{S}_{II} for given values of yk , n and U . This application is discussed in detail below.

3. APPLICATIONS OF THIN-LENS THEORY

The general type of procedures required for the design of optical systems having first-order correction follows from the theory given above.

It follows directly from equations (3) that a system of thin lenses of finite total power in contact (and therefore having the same value of E) cannot have $\sum S_I$, $\sum S_{II}$ and $\sum S_{III}$ for the complete system simultaneously reduced to zero; for if $\sum S_I$ is zero, $\sum S_{II}$ is the sum for all the lenses of the second term of S_{II} in equations (3), and if this and $\sum S_I$ are zero, $\sum S_{III} = \sum H^2 k / n_0$. For correction of these three aberrations, either a system of thick lenses, or of separated thin lenses, must therefore be used. For such a system of thin lenses, since the steepness of the parabolae for the aberrations S_{II} , S_{III} and S_V increases as successively higher powers of stop distance (equations (5)), changes to S_V will tend to be most readily made on lenses furthest removed from the stop, where the rate of change is greatest, and changes to S_{II} on lenses nearer the stop, where S_{III} and S_V change relatively more slowly, or are stationary for lenses at the stop. Again, a system of separated thin lenses normally has a stop inside the lens, some components being in front of the stop and some behind it; since for lenses before and behind the stop the parabolae for S_{II} and S_V are inverted relative to those for S_I and S_{III} , S_{III} can normally be corrected simultaneously with S_V by the appropriate choice of bendings of lenses before and behind the stop.

These considerations lead to a reasonably systematic procedure for first-order correction in systems of thin lenses. A system of thin lenses is first found having the required total power and satisfying the three shape-invariant aberration conditions; for a variety of reasons, some connected with primary aberration correction and some with higher-order aberrations, almost all lens systems covering at all large field angles are of an approximately symmetrical form (see, for example, Wynne [10]), consisting either of outer convergent parts (single lenses or system of lenses) on either side of a central divergent lens or lenses near to the stop, or more rarely the reverse arrangement of outer divergent systems with a central convergent component. The simplest case of the former arrangement, the Cooke triplet, consists of three single lenses; in more complicated forms either of the outer convergent lenses may be replaced by a cemented doublet (Tessar) or replaced by two single convergent lenses, or in the Celor form of lens the central divergent lens of the triplet may be replaced by two divergent lenses.

3.1. The Cooke triplets

The Cooke triplet of three separated thin lenses, of given glass types, has five shape-invariant design parameters (the powers of the three lenses, and their two separations) to satisfy four shape-invariant conditions (the equivalent focal length of the combined system, the Petzval sum, and the two primary chromatic conditions). Let the spare parameter be assigned initially in some arbitrary

way, and a lens system set up to satisfy the shape-invariant conditions, with each thin lens initially of the shape to make its $|S_I|$ a minimum, the aberrations being calculated for the whole system with the stop at the central divergent lens. In general none of the shape-dependent aberrations will then be corrected. From the discussion given earlier, it follows that the S_{III} total of either of the outer lenses will be reduced as they are bent more concave to the central stop, the S_V changes in the two cases being of opposite sign; an appropriate combination of bendings of these two lenses will therefore reduce S_{III} and S_V for the system simultaneously to zero or required small values. S_{II} for the system will not generally then be corrected, but this changes linearly with the shape of the central lens, S_{III} and S_V being invariant, so that an appropriate bending of the central lens will give a lens form having S_{II} , S_{III} and S_V corrected. For the simple triplet all the shape variables have now been used, so that if S_I is not corrected, that is if the positive S_I of the two convergent lenses is not approximately balanced by the negative S_I of the divergent lens, a different choice must be made of the free parameter in the initial lay-out of the system, and the process repeated, giving a different S_I total when the other primary aberrations are corrected. Interpolation or extrapolation from these two values will generally lead to a corrected system for S_I .

For more complicated systems, similar procedures are used, but the greater complexity, giving a larger number of variables than conditions to be satisfied, leads to a range of solutions having first-order correction. For example, if one of the single convergent lenses of the triplet be replaced by two convergent lenses in contact having a combined power equal to that of the original single lens, then the distribution of power between them gives an additional design parameter in the initial setting-up to satisfy the shape-invariant conditions. If each of these two thin lenses be given initially the shape to make $|S_I|$ a minimum, $\sum S_I$ for the pair will be lower than for the original lens. The process of correcting S_{III} and S_V for the system by bending the back and front may now take the form of combining the bending of the back with a bending of one or other of the two front lenses, giving another spare design parameter. Combination of all the design parameters will in this case lead to an infinite number of first-order corrected systems. The choice among these will depend on their higher-order aberrations, determined by ray-tracing.

3.2. The double-Gauss objective

Apart from the triplet lens and its derivatives, characterized by the central divergent part consisting of one or more divergent (generally biconcave) lenses, the other main group of lens forms in common use, the double-Gauss form, has the central divergent part in the form of an air-space between two thick meniscus lenses both concave to the central stop; in its simplest forms, a single convergent lens is placed adjacent to the outer convex surface of each meniscus lens. For such thick meniscus lenses of relatively low power, thin-lens theory is of negligible value; but having set up a system satisfying the shape-invariant conditions and calculated the aberrations surface by surface, thin-lens theory may then usefully be applied to sections of the system which are relatively thin to attain correction of the complete system. As in the case of the simple triplet, S_{III} and S_V can be corrected simultaneously by appropriate combinations of bends either of the front and rear convergent lenses, or the front and rear air spaces between these convergent

lenses and the meniscus lenses; and S_{II} can be corrected by bending the central air-space, which is commonly thin enough for the S_{III} and S_V changes here to be small. The choice available in the variables for correcting S_{III} and S_V allows S_I to be corrected simultaneously with the other primary aberrations, again with an infinite number of solutions.

3.3. *Pupil coma*

In addition to leading to general systematic procedures for securing first-order correction of complete optical systems, thin-lens theory is applicable to many more specific problems. For example, in the form of wide-angle lens referred to above in which a large front divergent lens is used to employ the Slussareff effect, whereby coma of the entrance pupil is introduced to increase the field illumination, thin lens theory may be applied to give the optimum shape and position for this front lens. Since pupil coma is not corrected, the primary pupil coma coefficient \bar{S}_{II} gives a good approximation to the actual value, and the problem is therefore to obtain the largest possible negative value of \bar{S}_{II} , this being the sign required to increase marginal illumination.

From equations (3), the value of S_{II} at extreme lens shapes (large Λ) has the same sign as Ek , which is positive for a divergent lens in front of the stop, so that the largest negative value of S_{II} will occur at the vertex of the S_{II} parabola, at a shape given by equations (4). At this shape, the value of \bar{S}_{II} is given by equations (7). For the usual case of an object at infinity, $U=yk$; substituting this into equation (7) for $\bar{S}_{II \min}$ gives a cubic equation in yk/T , the ratio of the numerical aperture of the first lens to the angle the stop subtends at it. Differentiating this equation with respect to yk/T and equating to zero gives a quadratic equation in yk/T whose roots, the values of yk/T required to maximize $-\bar{S}_{II}$, are a rather complicated function of n . These two roots are of opposite sign, the negative one corresponding to the largest negative value of \bar{S}_{II} for a converging lens behind the stop, or a diverging lens in front of the stop; this is therefore the required value of yk/T . For a given field angle \bar{u} and refractive index of the front lens, the pupil coma \bar{S}_{II} depends only on the ratio yk/T , so that the analysis leads to a family of solutions, all having equal pupil coma; for forms of lens with smaller values of numerical aperture of the front lens, the distance of the lens from the stop will be greater (T smaller), hence for a given field angle the lens diameter will be larger. The choice from among the family of solutions will depend on the general aberrations correction of the complete lens.

4. LENSES OF FINITE THICKNESS

For lenses of finite thickness, which are necessary for physical realization, the primary aberration coefficients are of much greater complexity; for example, the S_I variation of a thick lens with bending depends on powers of the shape factor up to the fourth. But for lenses of moderate thickness the general trend of the aberrations is similar to that given by the thin-lens theory. Some plausibility may be given to this assertion by the following considerations.

If a lens of finite thickness be derived from one of zero thickness by keeping the first surface fixed, and moving the second to a finite distance from it, altering

its curvature so as to maintain the power of the lens, then from the first of equations (1) the value of S_I for the thickened lens will be the same as that of the thin lens:

- (a) when the shape is such that the paraxial ray within the lens is parallel to the axis,
- (b) when the shape is such that the refraction at the second surface is aplanatic,
- (c) when the shape is such that the paraxial ray is incident normally on the second surface ($A=0$): in this case there is a double coincidence of the S_I curves for the thin and thick lenses.

The S_I curve for the thick lens therefore intersects that of the thin lens from which it is derived at the shapes corresponding to (a) and (b), and the two curves osculate at the shape corresponding to (c).

Similar sets of coincidences occur for the thin and thick lens curves of the other primary aberrations.

La théorie générale des aberrations du 3^e ordre des lentilles minces (y compris les aberrations de l'imagerie pupillaire) est développée sous une forme adaptée à ses applications aux problèmes de calcul optique; les méthodes d'application sont étudiées et illustrées par quelques exemples.

Die allgemeine Theorie der primären Aberrationen dünner Linsen einschliesslich der Pupillenabbildung lässt sich in eine Form bringen, die sie für ihre Anwendung bei Aufgaben der optischen Durchrechnung geeignet macht. Die Methoden dieser Anwendung werden durch einige Beispiele ergänzt.

REFERENCES

- [1] TAYLOR, H. D., 1906, *A System of Applied Optics* (Macmillan & Co. Ltd.).
- [2] ROHR, M. VON, 1920, *The Formation of Images in Optical Instruments* (H.M.S.O.).
- [3] WYNNE, C. G., 1952, *Proc. phys. Soc. Lond. B*, **65**, 429.
- [4] SLUSSAREFF, G., 1941, *J. Phys., U.S.S.R.*, **4**, 537.
- [5] HOPKINS, H. H., 1950, *Wave Theory of Aberrations* (Oxford: University Press).
- [6] CODDINGTON, H., 1829, *A Treatise on the Reflection and Refraction of Light* (London: Simpkin, Cambridge and Marshall).
- [7] ARGENTIERI, D., 1942, *Ottica Industriale* (Milan: Ulrico Hoepli).
- [8] WYNNE, C. G., 1953, *Thesis*, University of London.
- [9] ROOSINOV, M. M., 1950, British Patent Specification No. 640, 232.
- [10] WYNNE, C. G., 1956, *Rep. Prog. Phys.*, **19**, 298.



Interpretation des aspects particuliers des images obtenues dans une expérience de détramage

par Mme M. MARQUET et J. TSUJIUCHI†
Institut d'Optique, Paris

(Manuscrit reçu le 29 décembre 1960)

Les aspects particuliers des images obtenues dans une expérience de détramage, tels que: obtention en négatif de certaines régions du cliché, formation de liserés, etc. sont expliqués par la théorie de la diffraction. On montre que ces aspects dépendent essentiellement de la loi de tramage, c'est-à-dire du rapport entre les parties opaques et les parties transparentes dans une surface élémentaire, rapport qui, après tramage, traduit les demi-teintes du cliché initial avant tramage.

1. INTRODUCTION

Nous nous proposons d'interpréter les aspects particuliers des images observées dans une expérience de détramage précédemment décrite et réalisée avec le montage à double diffraction schématisé sur la figure 1 (Mme Marquet, *Opt. Acta*, 1959, 6, 404).

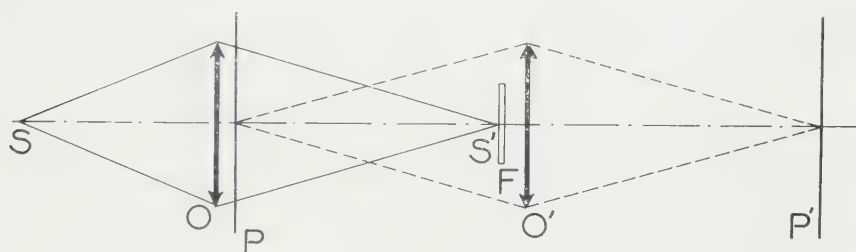


Figure 1.

Il est indispensable de rappeler au préalable quelques notions sur le tramage des clichés photographiques.

2. RAPPEL DU PRINCIPE DE TRAMAGE

Le but du tramage est de permettre la traduction des demi-teintes par un procédé qui, tel que l'impression typographique, ne donne que deux tonalités la couleur de l'encre appliquée par la matière avec une épaisseur constante et la couleur du papier nu.

Les clichés tramés transparents utilisés en photogravure sont obtenus par reproduction par contact, en lumière ponctuelle et sur émulsion très contrastée d'un cliché normal. La reproduction se fait au travers d'une trame composée de deux séries de traits équidistants de période a représentée figure 2 (a); les deux séries de traits sont perpendiculaires et font en général un angle de 45° avec les bords du format initial.

Après développement, le cliché tramé se présente sous forme d'une série de petites taches noires, centrée sur un quadrillage de maille a (figure 2 (b)). La

† Adresse actuelle: The Government Mechanical Laboratory, Sugunami-ku, Tokyo, Japon.

forme et la dimension de ces taches dépendent en partie des lois de diffraction (la trame et le cliché à tramer sont à une petite distance l'un de l'autre) et pour la grande part du coefficient de diffusion de l'émulsion utilisée pour le tramage;

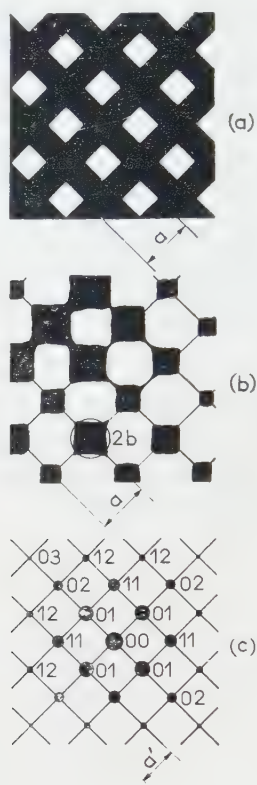


Figure 2.

les taches sont d'autant plus grandes que la région correspondante du cliché initial, est plus transparente; en première approximation ces taches sombres peuvent être assimilées à des éléments sensiblement circulaires de rayon b (figure 2 (b)).

2.1. Loi de tramage

Si l'on pose $t = 2b/a$, les variations de t en fonction des densités correspondantes du cliché initial caractérisent la loi de tramage. En général, on ne détermine pas cette loi de tramage; on peut seulement dire qu'en pratique t est compris entre 0 et une valeur voisine de l'unité ($t=0$ pour les parties claires du cliché tramé t légèrement supérieur ou égal à 1 pour les parties sombres).

La photographie tramée originale que nous avons utilisée était un négatif, le pas de la trame étant de 3 mm^{-1} , une portion est représentée agrandie figures 3 et 6. Nous en avons tiré un contretype positif dont une portion est représentée figure 7 et dans lequel les éléments sombres sont remplacés par des éléments circulaires transparents. Or, dans l'application des lois de la diffraction, en raison du théorème de Babinet, ces éléments jouent la même rôle qu'ils soient opaques ou clairs à la diffusion près; on pourra donc prendre indifféremment pour valeur de $2b$ la diamètre d'un élément sombre (dans le cas du négatif 6) ou le diamètre d'un élément clair (dans le cas du positif 7). Il s'en suit que pour une région

donnée $t = 2b/a$ aura approximativement même valeur qu'il s'agisse du négatif ou de sa copie positive.

3. NATURE DU SPECTRE D'UN CLICHÉ TRAMÉ

3.1. *Etude expérimentale*

Les variations de transparence du cliché original sont traduites sur le cliché tramé par des variations de grandeur d'éléments circulaires caractérisés par une valeur t définie plus haut. Ces éléments circulaires, analogues à des cellules, sont disposés selon un quadrillage à maille carrée de pas a , ainsi que le montrent les figures 2 (b), 6 et 7. Chaque cellule du cliché tramé placée en P dans le montage

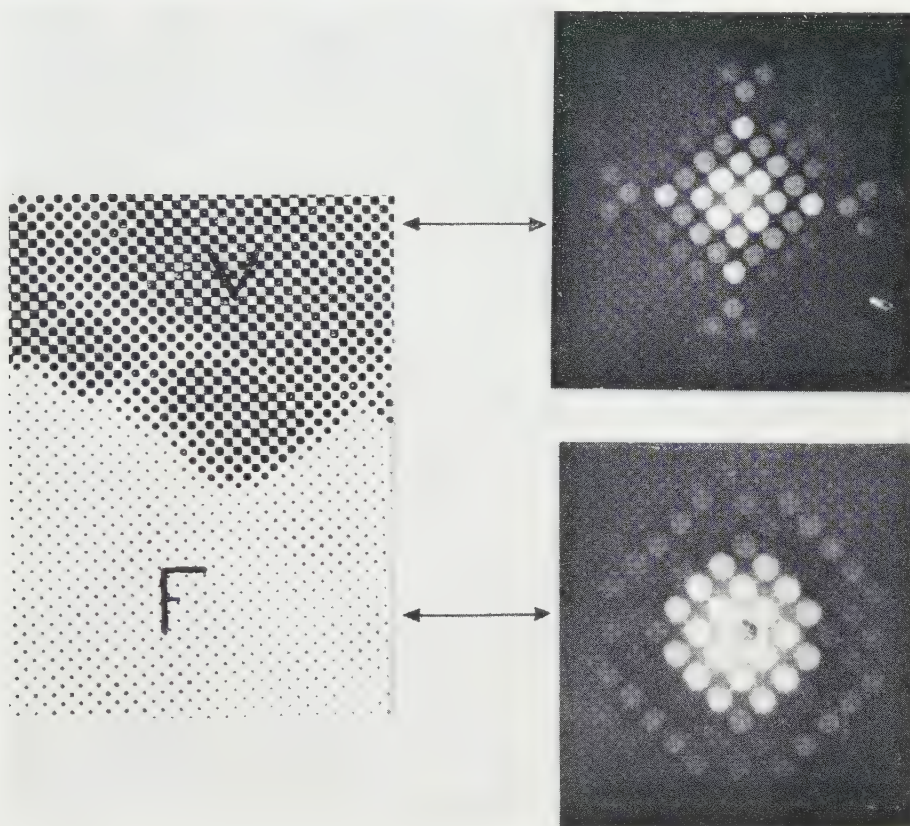


Figure 3.

à double diffraction (de la figure 1) diffracte dans toutes les directions ; l'amplitude diffractée est fonction de la dimension de la cellule donc de t , ainsi qu'on peut le mettre en évidence en isolant de petites régions uniformes du cliché tramé : la figure 3 reproduit les spectres relatifs aux régions V et F du négatif tramé, pour lesquelles on a

$$t_v = 0,8 ; \quad t_f = 0,25.$$

Ces spectres ont été obtenus en impressionnant une plaque photographique dans le plan F ; on peut constater que les répartitions d'intensités des spectres élémentaires sont très différentes.

Lorsque l'on utilise le format total du cliché tramé, un point quelconque de F reçoit de la lumière diffractée provenant de chacune des cellules du cliché tramé, or ces cellules étant disposées selon une loi périodique, il est évident que les points du plan F correspondant aux spectres élémentaires du quadrillage formé par les cellules jouiront de propriétés particulières.

3.2. Etude théorique

Mathématiquement, pour une région sensiblement uniforme, c'est-à-dire ayant une valeur de t à peu près constante le cliché tramé peut être considéré comme le produit de convolution d'une cellule de diamètre $2b$ avec un quadrillage de points de maille a (figure 4). Dans le plan F le spectra de diffraction relatif à la portion de cliché considérée est alors le produit du spectre d'une cellule par le spectre T du motif carré formé par les 2 trames initiales.

Le spectre D_b relatif à une cellule est une tache d'Airy dont l'amplitude maximum dépend essentiellement du diamètre $2b$. Le spectre T discontinu correspond au produit de convolution de deux trames rectangulaires de même période : c'est un ensemble de points lumineux disposés selon un quadrillage de maille a' de même direction que les trames composantes.

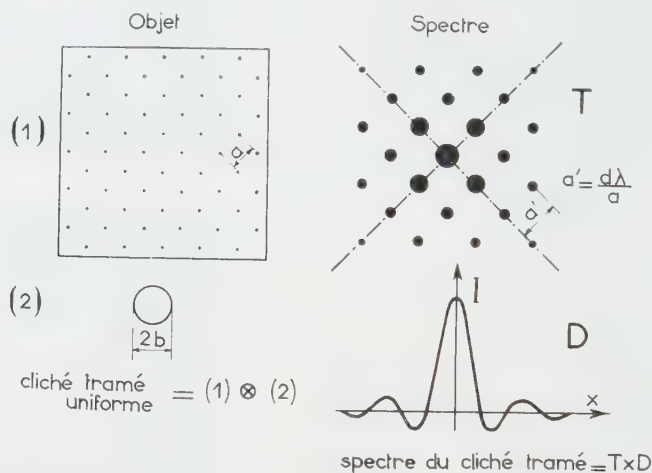


Figure 4.

On a $a' = d\lambda/a$, d distance PF, λ longueur d'onde éclairante. Ainsi que nous l'avons mis en évidence expérimentalement dans le paragraphe précédent, l'aspect géométrique du spectre résultant $S = T \times D_b$ reste identique quelle que soit la valeur de b ; seule l'intensité de chacune des taches élémentaire du spectre est fonction de l'amplitude diffractée par la cellule de diamètre $2b$. Le spectre relatif à la totalité du cliché tramé s'obtient par la superposition de tous les spectres S_b correspondant à chaque valeur de b comprise entre 0 et a

$$S = \sum_0^a D_b \times T = T \sum_0^a D_b$$

ce qui signifie pratiquement que le spectre du cliché tramé sera un spectre discontinu coïncidant avec le spectre des trames composantes. Les amplitudes, et par conséquent les intensités, seront nulles, sauf pour les points du spectre correspondant au spectre T; en ces points, pour une région du cliché déterminée par le

diamètre $2b$ des cellules composantes, l'intensité sera proportionnelle à l'intensité diffractée par une cellule de diamètre $2b$ dans la direction correspondant au spectre élémentaire considéré.

4. CALCUL DES INTENSITÉS DIFFRACTÉES

Le calcul des valeurs relatives des intensités diffractées se fait de façon approchée en assimilant les éléments transparents du cliché tramé à des cercles: c'est le cas du positif de la figure 7, copie du négatif obtenu par tramage direct. Il suffit d'appliquer la loi de diffraction relative aux amplitudes de lumière diffractée par une ouverture circulaire pour les directions correspondant aux spectres élémentaires. L'amplitude diffractée dans une direction $\alpha\beta$ définie comme il est

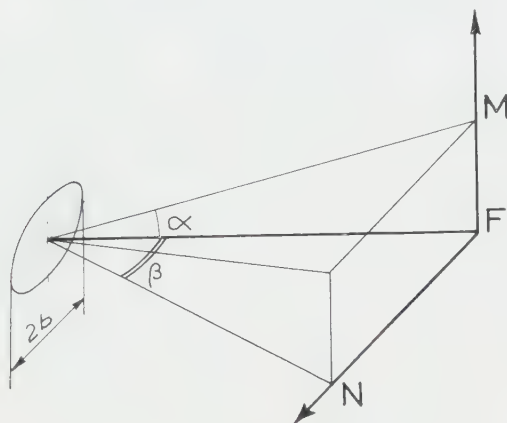


Figure 5.

indiqué sur la figure 5 est donnée par :

$$A_{\alpha\beta} = \frac{2n}{\lambda} A_0 b^2 \frac{J_1[bk\sqrt{(\alpha^2 + \beta^2)}]}{bk\sqrt{(\alpha^2 + \beta^2)}} ;$$

A_0 amplitude incidente, k constante telle que $k = 2n/\lambda$:

$$I = |A_{\alpha\beta}|^2 = A_0^2 b^4 \left(\frac{n}{\lambda}\right)^2 \left[\frac{2J_1 bk\sqrt{(\alpha^2 + \beta^2)}}{bk\sqrt{(\alpha^2 + \beta^2)}} \right]^2 .$$

Si m et n sont les coordonnées de la direction $\alpha\beta$ avec le plan F en prenant $a' = d\lambda/a$ pour unité et S' image géométrique de S pour origine on a

$$\alpha_m = \frac{ma'}{a} = \frac{m\lambda}{a}, \quad \beta_n = \frac{na'}{a} = \frac{n\lambda}{a}$$

d'autre part

$$t = \frac{2b}{a} 2b, \quad b = \frac{a}{2} t.$$

En remplaçant α , β , b par leur valeur en fonction de m , n et t on obtient pour valeur des intensités diffractées

$$\begin{aligned} I_{mn} &= A_0^2 b^4 \left(\frac{n}{\lambda}\right)^2 \left[\frac{2J_1 nt\sqrt{(m^2 + n^2)}}{nt\sqrt{(m^2 + n^2)}} \right]^2 \\ &= A_0^2 \left(\frac{n}{\lambda}\right)^2 \frac{a^4}{16} t^4 \left[\frac{2J_1 nt\sqrt{(m^2 + n^2)}}{nt\sqrt{(m^2 + n^2)}} \right]^2 . \end{aligned} \quad (1)$$

4.1. Cas où m et $n \neq 0$

A l'aide de la formule précédente, nous avons tracé les courbes donnant I en fonction de t pour les spectres élémentaires 0,1, 0,2, 1,1, 1,2, 2,2. Ces courbes

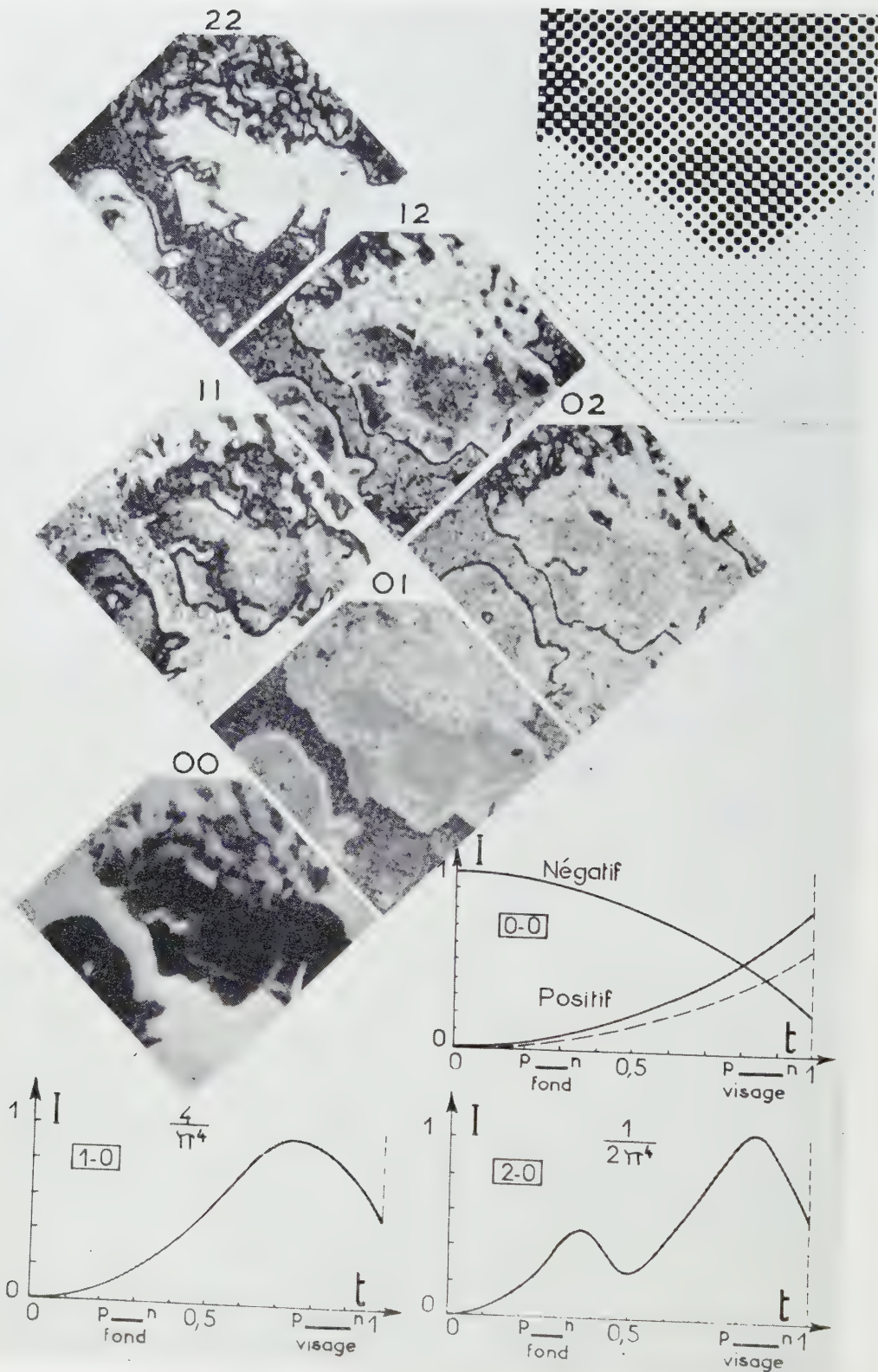


Figure 6.

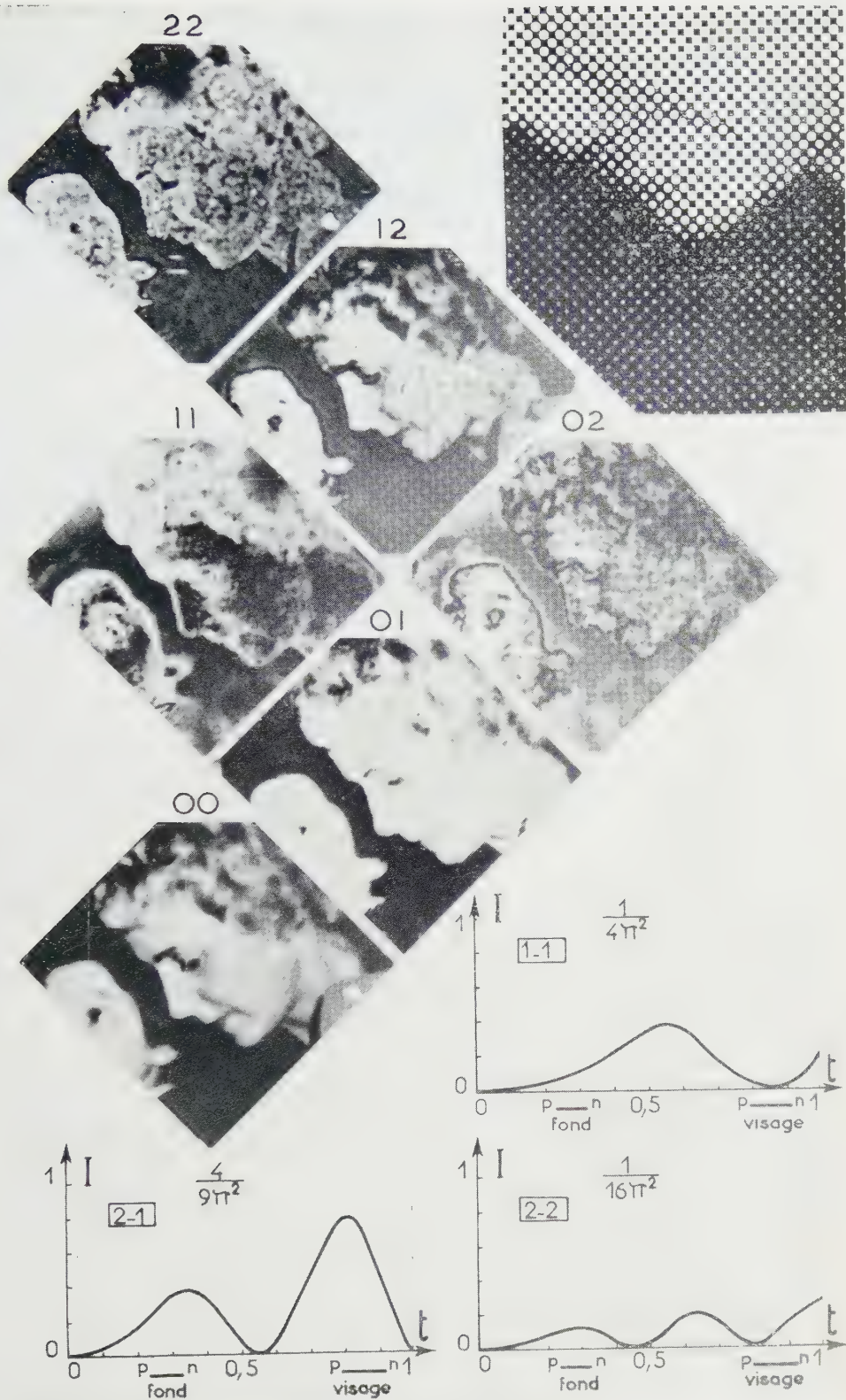


Figure 7.

figurent sur les figures 6 et 7 ; les ordonnées sont à multiplier par le facteur indiqué à gauche ; la valeur unitaire correspond à l'intensité de l'image géométrique lorsque la surface du cliché est entièrement transparente. En raison du théorème de Babinet, le calcul précédent s'applique lorsque les éléments circulaires transparents sont remplacés par des éléments sombres : les courbes tracées sont donc valables dans le cas du négatif tramé figure 6 et dans le cas de sa copie positive figure 7, les valeurs de t étant approximativement égales pour des régions correspondantes.

4.2. Cas de l'image centrale (m et $n=0$)

L'intensité diffractée devient

$$I_{00} = A_0^2 \left(\frac{n}{\lambda} \right)^2 \frac{a^4}{16} t^4$$

(courbe représentée en pointillé sur la figure 6).

Cette formule, valable lorsque la dimension de S' est petite par rapport à S , ne s'applique que dans le cas des éléments circulaires transparents (positif). Dans tous les autres cas on peut appliquer en première approximation les lois de l'optique géométrique qui indiquent que l'intensité au point S est proportionnelle au rapport de la surface transparente de la région du cliché considéré à la surface totale.

Dans le cas du négatif $2b$ est le diamètre des taches noires

$$I = C \frac{a^2 - nb^2}{a^2} = C \left(1 - \frac{nb^2}{a^2} \right)$$

$$t = \frac{2b}{a}, \quad I = C \left(1 - \frac{nt^2}{4} \right). \quad (2)$$

Dans le cas du positif $2b$ est le diamètre des éléments transparents

$$I = C \frac{nb^2}{a^2} = C \frac{nt^2}{4}. \quad (3)$$

Des courbes relatives aux équations (2) et (3) précédentes, ainsi que celles déduites de l'application de la formule (1) ont été tracées sur les figures 6 et 7 ; d'une façon générale, on obtient des courbes monotones croissante dans le cas de la copie positive du cliché tramé, décroissante dans le cas du négatif tramé.

5. EXPÉRIENCE

Si dans le montage de la figure 1 on isole successivement par un diaphragme sélecteur chacun des spectres élémentaires 0,0, 0,1, 0,2, 1,1, 1,2, 2,2 on observe en P' dans chacun des cas une image détramée, car en ne laissant passer qu'un élément de spectre on détruit la périodicité.

Les résultats représentés sur la figure 6 sont relatifs au cliché tramé négatif placé dans le reconstituteur ; les photographies reproduites correspondent à ce que l'on peut observer visuellement en P' .

Sur la figure 7 on a reproduit d'une façon analogue les aspects visuels obtenus avec la copie positive du négatif précédent.

Les aspects des images obtenues sont très variables avec la position du diaphragme sélecteur ; ils peuvent être schématisés par :

(a) la valeur relative des intensités obtenues pour différentes régions du cliché ayant des valeurs de t déterminées ;

Négatif $t_f=0,32, \quad t_v=0,92$					
	Intensités		Aspects		
	Observation	Théorie	Observation	Théorie	
0-0	$V < F$	$F=0,92$ $V=0,34$	F négatif V négatif	F négatif V négatif	
0-1	$V > F$	$F=0,12$ $V=0,72$	F négatif V = 0	F négatif V positif	sans liseré
0-2	$V = F$	$F=0,50$ $F=0,60$	F négatif V positif	$F=0$ $V \geq 0$	liseré noir liseré blanc faible
1-1	$V \leq F$	$F=0,12$ $V=0,10$	F négatif V négatif	F négatif V négatif	liseré noir liseré blanc
1-2	$V = F$	$F=0,34$ $V=0,30$	$F=0$ V négatif	$F=0$ V = négatif	liseré noir
2-2	$V > F$	$F=0,41$ $V=0,95$	$F=0$ C positif	$F=0$ V positif	2 liserés noirs 1 liseré blanc
Positif $t_f=0,24, \quad t_v=0,80$					
0-0	$V > F$	$F=0,04$ $V=0,50$	F positif V positif	F positif V positif	
0-1	$V > F$	$F=0,05$ $V=0,95$	$F=0$ V positif	$F=0$ V positif	sans liseré
0-2	$V > F$	$F=0,20$ $V=0,80$	F positif $V \geq 0$	F positif $V \leq 0$	liseré noir liseré blanc
1-1	$V = F$	$F=0,05$ $V=0,05$	F positif $V \leq 0$	F positif $V \leq 0$	liseré blanc
1-2	$V > F$	$F=0,18$ $V=0,80$	F négatif $V \geq 0$	positif $V=0$	liseré noir
2-2	$V \geq F$	$F=0,10$ $V=0$	$F=0$ $V \leq 0$	$F \geq 0$ $V=0$	liseré bl. } faibles liseré noir }

(b) l'aspect local, c'est-à-dire le sens de la variation aux alentours d'une valeur de t selon que l'on a l'impression d'un cliché négatif ou positif;

(c) la présence de liserés sombres ou clairs.

Le tableau résume les aspects observés pour les régions du visage et du fond déjà considérés (figure 5), pour lesquelles les valeurs de t sont approximativement

$$\begin{array}{ll}
 \text{Positif} & \left\{ \begin{array}{ll} \text{fond} & t=0,24 \\ \text{visage} & t=0,8 \end{array} \right. \\
 \text{Négatif} & \left\{ \begin{array}{ll} \text{fond} & t=0,32 \\ \text{visage} & t=0,92 \end{array} \right.
 \end{array}$$

6. PRINCIPE DE L'INTERPRÉTATION

Dans l'observation visuelle d'un cliché tramé, lorsque la dimension de la trame est inférieure à la limite de résolution de l'oeil, on peut considérer que l'impression lumineuse relative à une région donnée est proportionnelle au rapport des surfaces transparentes à la surface totale. C'est ainsi que, dans le cas du négatif tramé ($2b$ diamètre des taches sombres), l'intensité perçue par l'oeil I est donnée par

$$I = C \frac{a^2 - nb^2}{a^2} \quad \text{si } t = \frac{2b}{a} \quad \text{on a } I = C \left(1 - \frac{nt^2}{4}\right).$$

Dans le cas du positif $2b$ diamètre des taches claires

$$I = C \frac{nt^2}{4}.$$

Lorsque t varie, on retrouve des courbes analogues à celle donnant les intensités du spectre élémentaire OO, obtenues en appliquant les lois de l'optique géométrique. C'est ainsi que, dans l'observation du négatif, l'intensité décroît avec t et, dans l'observation du positif, l'intensité croît avec t . Dans l'expérience de détramage, le diaphragme sélecteur I sert de pupille d'entrée à l'objectif d'observation O' (figure 8); le flux lumineux émis par une cellule du cliché tramé et

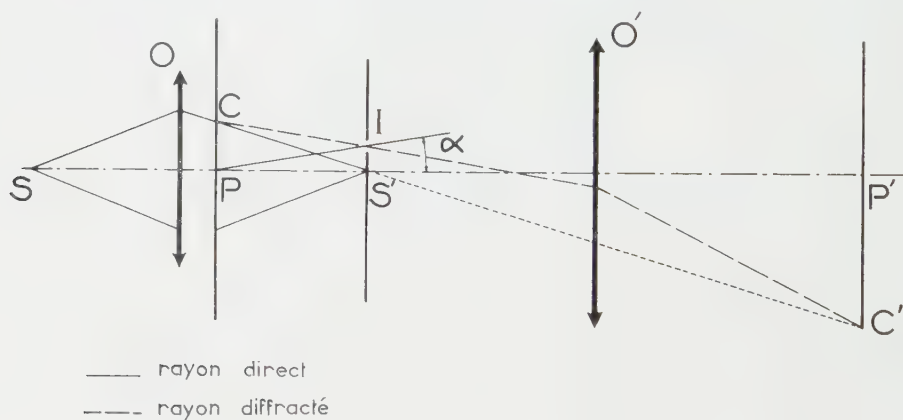


Figure 8.

impressionnant l'oeil observant en P' est constitué uniquement par le flux diffracté par le cellule C dans la direction CI, flux égal au flux diffracté par une cellule de même dimension placée en P, diffractant dans la direction PI définie précédemment par m et n . L'intensité du flux diffracté est donnée par les courbes $I_{mn} = f(t)$; il est donc possible d'expliquer les changements d'aspects des figures 6 et 7 à l'aide de ces courbes.

(a) Les valeurs relatives des intensités des régions V et F sur les clichés détramés doivent correspondre aux valeurs de I déterminées sur les courbes I_{mn} pour les valeurs de t correspondantes.

Sur le tableau on a porté les valeurs de I ainsi trouvées.

(b) Si, pour une région correspondant à un petit intervalle $(t, t + \Delta t)$, la courbe I_m , varie dans le même sens que la courbe I_{00} l'aspect de la région détramée obtenu en laissant passer le spectre élémentaire m et n sera celui du cliché tramé, c'est-à-dire positif si le cliché observé est positif, négatif s'il est négatif.

Si la variation est de sens contraire, le cliché détramé sera positif pour un cliché tramé négatif; c'est le cas pour le visage du cliché négatif figure 6 détramé en utilisant le spectre 22, le visage du cliché positif correspondant figure 8 restera positif car la courbe $I_{(22)}$ croît pour $0,8 < t < 1$.

(c) Lorsque les courbes $I_{(m,n)}$ présentent un minimum, on devra observer un liseré sombre pour les contours séparant deux régions pour lesquelles les valeurs de t encadrent ce minimum. D'une façon analogue, on observera un liseré clair lorsque les courbes présenteront un maximum. Pour le fond on a t voisin de 0,3, pour le visage t voisin de 0,85; la courbe I_{20} présente un minimum pour 0,6 on constate sur le cliché détramé 2,0 un liseré sombre bordant le visage, de même pour I_{21} . Sur le cliché 2,2 (figure 7), on voit très bien le double liseré sombre et le liseré clair correspondant aux 2 minima $t=0,45$ et $t=0,8$ et au maximum $t=0,6$.

7. DISCUSSION

Ainsi qu'on peut le constater par l'étude des figures 6 et 7, et du tableau, l'accord est satisfaisant entre la théorie et l'expérience. Nous allons étudier les principales causes d'erreurs. Tout d'abord on peut constater que l'accord est meilleur pour le négatif direct que pour la copie positive; or le négatif direct a été obtenu sur support mince, alors que le positif a été tiré sur une émulsion à support d'épaisseur double. Les clichés n'ayant pas été immergés, il apparaît des irrégularités sur le positif dues en partie au gonflement de la gélatine autour des grains d'argent et en partie aux différences d'épaisseur entre les parties transparentes et les parties noires l'image argentique faisant surépaisseur. D'autre part, dans la théorie nous avons uniquement tenu compte de la diffraction mais il y a une diffusion due à la nature même des clichés photographiques et de leur support, diffusion qui peut entraîner des modifications dans la répartition des intensités dans le plan F. D'autre part, nous avons supposé que les éléments sombres du négatif pouvaient être assimilés à des cercles, ce qui n'est qu'une approximation; en réalité, les formes sont intermédiaires entre le carré et le cercle, d'où imprécision sur la valeur de t .

En résumé, cette expérience de détramage nous a permis d'expliquer par les lois de la diffraction et par le théorème de Babinet des aspects de détramage avariés, analogues à ceux que l'on peut observer dans d'autres domaines: télévision par exemple.

Some particular aspects are discussed of the images obtained by a process of removal of dot structure. Such effects as contrast reversal in some regions, edge effects, etc., are explained by diffraction theory. It is shown that these aspects depend essentially on the law of dot-formation, that is to say the relationship between opaque and transparent regions on an elementary surface, the relationship which, in the process of dot formation, transforms half-tones present in the original.

Die besonderen Erscheinungen an Bildern, die man beim Versuch einer Entrasterung erhält, lassen sich durch die Beugungstheorie erklären. Solche Erscheinungen sind u. a. die Umwandlung gewisser Bereiche des Klisches ins Negative und das Auftreten einer Bewandung. Sie hängen wesentlich von der Art der Rasterung ab, d. h. von dem Verhältnis der undurchlässigen zu den durchlässigen Teilen eines Flächenelementes, welches nach der Rasterung die Halbtöne des Anfangsklisches vor der Rasterung umkehrt.



REVIEWS

The Electron Microscope: The present state of the Art. By M. E. HAINE, including a chapter written in collaboration with V. E. COSSLETT. [Pp. 282.] 105 Illus. Price £2 15s. 0d.

THE technique of production of the electron microscope and the manipulation of this instrument is entirely different from that of the light microscope. The optical conceptions, however, which are used for the design, are identical in both cases. For this reason, the present monograph should appeal to anybody interested in optics.

The book starts with the geometric optical properties of electron microscope lenses, then discusses the wave nature of the electron rays, leading to problems of resolving power and image contrast. Limiting factors to the performance of the instrument, e.g. lens errors, and practical design considerations are explained in detail. A chapter on specimen techniques, written in collaboration with V. E. Cosslett concludes the book.

The author remarks in his preface that the literature on electron microscopes has become enormous; also there exist already several good books on the subject. The present monograph, however, must be considered as a valuable contribution which contains much new information not available in the older books. Moreover, it should appeal particularly to practising electron microscopists who wish to have a better understanding of their instruments, and to scientists in general who want to read a compact survey in order to obtain the necessary information on how this powerful new tool is best applied to their particular problems.

O. KLEMPERER.

ERRATA

Colour correction in optical systems and a new dispersion formula

by MAX HERZBERGER

Research Laboratories, Eastman Kodak Company, Rochester, N.Y., U.S.A.

In *Op. Acta*, 6, 197, July, 1959, certain inconsistencies have been noted in the paper bearing the above title. They can be corrected as follows:

Page 202, matrix at foot of page. Columns 1 and 4 should be interchanged; likewise columns 2 and 3.

Page 203, table headings. For " $a_1 \dots a_4$," read " $a_4 \dots a_1$ ".

Line above equation (3.1). For " $\lambda=0.5983$," read " $\lambda=0.5893$ ".



Scattering of evanescent waves by cylindrical structures†

by LAURA RONCHI, VERA RUSSO, GIULIANO TORALDO
DI FRANCIA and CORRADO ZACCAGNINI

Centro di Studio per la Fisica delle Microonde, Firenze, Italia

(Received 3 December 1960)

This paper is concerned with the diffraction of an electromagnetic evanescent wave by an infinitely conducting half-plane (§ 2) and by an infinitely conducting cylinder of circular cross section (§ 3). General formulae are given for the near and far fields. Scattering patterns are shown in several particular cases.

1. INTRODUCTION

It has been shown [1] that the field generated by a charged particle in uniform straight motion can be expanded into a set of evanescent waves of different frequencies. The evanescent waves may be made to impinge on a plane diffraction grating parallel to the path of the particle. Some of the diffracted waves turn out to be ordinary plane waves, which carry energy away from the grating (Smith and Purcell effect [2, 3, 4, 5]).

It would be of interest to find the best grating structure which allows to produce the greatest possible amount of energy for a prescribed frequency. As a first step, it may be useful to study the diffraction of an evanescent wave by a single scattering element. This will probably suggest what type of elements should be arranged in an array in order to build a suitable grating. Accordingly, we have started by investigating the diffraction of an evanescent wave by a simple cylindrical obstacle with generators perpendicular to the direction of propagation.

In this paper we will give some results for the case of (1) an infinitely conducting half-plane with the rim perpendicular to the direction of propagation of the incident wave, and (2) an infinitely conducting cylinder of circular cross section.

The physical meaning of the scattering of an evanescent wave may need some clarification, due to the necessary presence of a material surface in the neighbourhood of the scattering obstacle. To this end, we will refer to a concrete physical situation (figure 1). An infinite plane surface SS separates a transparent medium with refractive index $n > 1$ from free space. An incident plane wave O in the first medium is totally reflected at SS , giving rise to a plane reflected wave O' and an evanescent wave E which penetrates into free space. The evanescent wave impinges on a cylindrical obstacle C (scatterer), with the generators parallel to SS †, and gives rise to a scattered field. We will assume that the distance h from SS to the scatterer C is made to increase indefinitely, while the amplitude of the evanescent wave at C remains constant; as a consequence, the intensity of O must increase exponentially with h .

† The research reported in this document has been sponsored in part by the Air Research and Development Command, United States Air Force, under Contract AF 61 (052)-67, through the European Office ARDC.

‡ An analogous discussion could be made in the case of a finite non-cylindrical obstacle.

The field scattered into the half-space above C can be expanded into a set of real plane waves and of evanescent waves (attenuated in the upward direction). The real plane waves, at a great distance from C , form a cylindrical wave. When the cylindrical wave and the evanescent waves impinge on SS , they are partially refracted into medium n and partially reflected downwards. However, the reflected cylindrical wave arrives at C with an intensity inversely proportional to h , while the evanescent waves vanish exponentially with increasing h . Therefore secondary scattering can be neglected.

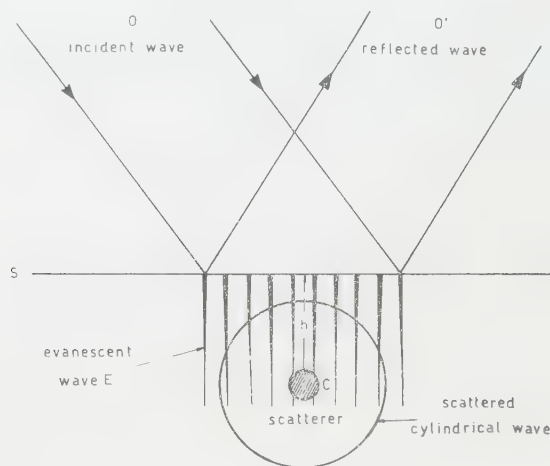


Figure 1. The evanescent wave E originated by total reflection at SS and the cylindrical wave scattered by the cylindrical obstacle.

Among the evanescent waves there is one, $E'\dagger$, having the same attenuation (in an opposite direction) as the incident wave E and travelling in the same direction.

As is well known, interference of E and E' can give rise to a pumping of energy across SS . Of course, this is the power which is subtracted from O' and goes into the scattered cylindrical wave; it is easily seen that this power is constant when h increases.

In the sequel, when talking of the scattering of an evanescent wave, we will have in mind the physical situation described above. However, in some practical applications, multiple scattering may not be negligible.

2. SCATTERING BY A PERFECTLY CONDUCTING HALF-PLANE

2.1. The total field

Let us refer to a system of rectangular coordinates x, y, z (figure 2) such that the screen occupies the half-plane $z=0, y>0$; or, alternatively, to a system of cylindrical coordinates x, ρ, θ , such that $y=\rho \sin \theta, z=\rho \cos \theta$.

Let the direction of propagation of the incident wave be parallel to the y -axis and make an angle θ^i with the z -axis.

\dagger For the sake of simplicity, we talk here as if the set of scattered waves were discreet. But, of course, it is a continuous set.

Two cases will be considered separately: (1) the incident wave is polarized parallel to the rim of the screen, so that the electric field has the sole component E_x (TE case); (2) the incident wave is polarized perpendicular to the rim of the screen, so that the magnetic field has the sole component H_x (TM case).

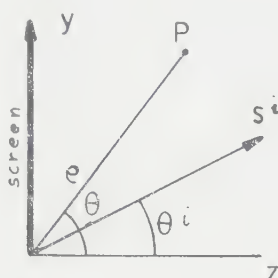


Figure 2. Rectangular and cylindrical coordinates in a plane normal to the edge of the screen.

In the case of a real incident wave, Sommerfeld's solution [6, 7] can be written in the form

$$E_x = f_1(\rho, \theta) - f_2(\rho, \theta) \quad (1)$$

for the TE case, and

$$H_x = f_1(\rho, \theta) + f_2(\rho, \theta) \quad (2)$$

for the TM case, where

$$f_1 = \frac{\exp[-i(\pi/4)]}{\sqrt{\pi}} \exp[ik\rho \cos(\theta - \theta^i)] \int_{-\infty}^{-\sqrt{(2k\rho) \sin(\theta - \theta^i)/2}} \exp(it^2) dt \quad (3)$$

and

$$f_2 = \frac{\exp[-i(\pi/4)]}{\sqrt{\pi}} \exp[-ik\rho \cos(\theta + \theta^i)] \int_{-\infty}^{-\sqrt{(2k\rho) \cos(\theta + \theta^i)/2}} \exp(it^2) dt. \quad (4)$$

The 'physical' Riemann sheet is defined by $-3\pi/2 \leq \theta \leq \pi/2$.

The other components of the fields can be found by means of the Maxwell equations.

One can verify that this solution holds good also when θ^i is a complex angle.

Let us now replace θ^i by $\theta^i + i\chi$ into (3) and (4); we will stipulate that $\chi > 0$ in order to have the incident wave attenuated towards the screen. The attenuation constant will turn out to be $\alpha = k \sinh \chi$.

From (3) it is readily obtained

$$f_1 = \frac{\exp[-i(\pi/4)]}{\sqrt{\pi}} \exp(ik\xi \cosh \chi - k\eta \sinh \chi) \int_{-\infty}^{a_1 + ib_1} \exp(it^2) dt \quad (5)$$

where $\xi = \rho \cos(\theta - \theta^i)$, $\eta = \rho \sin(\theta - \theta^i)$ and

$$\left. \begin{aligned} a_1 &= -\sqrt{(2k\rho) \sin \frac{\theta - \theta^i}{2}} \cosh \frac{\chi}{2}, \\ b_1 &= \sqrt{(2k\rho) \cos \frac{\theta - \theta^i}{2}} \sinh \frac{\chi}{2}. \end{aligned} \right\} \quad (6)$$

Analogously, from (4), one obtains

$$f_2 = \frac{\exp[-i(\pi/4)]}{\sqrt{\pi}} \exp(-ik\xi' \cosh \chi - k\eta' \sinh \chi) \int_{-\infty}^{a_1 + ib_1} \exp(it^2) dt \quad (7)$$

where $\xi' = \rho \cos(\theta + \theta^i)$, $\eta' = \rho \sin(\theta + \theta^i)$, and

$$\left. \begin{aligned} a_2 &= -\sqrt{(2k\rho)} \cos \frac{\theta + \theta^i}{2} \cosh \frac{\chi}{2}, \\ b_2 &= \sqrt{(2k\rho)} \sin \frac{\theta + \theta^i}{2} \sinh \frac{\chi}{2}. \end{aligned} \right\} \quad (8)$$

Equations (5) and (7) in conjunction with (1), (2) represent the total (incident plus scattered) field.

2.2. Asymptotic expressions of f_1 and f_2

It is interesting to note that if the total field is split into incident plus scattered field, the scattered field at a large distance can be represented as a cylindrical wave. This is possible because the incident wave is an evanescent wave attenuated towards the screen. The same property does not hold when the incident wave is an ordinary plane wave.

In order to find the distribution of the far field scattered by the screen, one has to investigate the asymptotic behaviour of an integral of the type

$$I(a+ib) = \int_{-\infty}^{a+ib} \exp(it^2) dt \quad (9)$$

for either $|a|$ or $|b|$ or both tending to infinity.

By well-known methods, one can find the following asymptotic expressions:

$$\int_{-\infty}^{a+ib} \exp(it^2) dt = \sqrt{\pi} \exp\left(i\frac{\pi}{4}\right) - \frac{i}{2} \frac{\exp[i(a+ib)^2]}{a+ib} \quad (10)$$

for $a > 0$;

$$\int_{-\infty}^{a+ib} \exp(it^2) dt = -\frac{i}{2} \frac{\exp[i(a+ib)^2]}{a+ib} \quad (11)$$

for $a < 0$;

$$\int_{-\infty}^{ib} \exp(it^2) dt = \sqrt{\pi} \exp\left(i\frac{\pi}{4}\right) - \frac{1}{2b} \exp(-ib^2) \quad (12)$$

for $b \rightarrow +\infty$, and

$$\int_{-\infty}^{ib} \exp(it^2) dt = -\frac{1}{2b} \exp(-ib^2) \quad (13)$$

for $b \rightarrow -\infty$. Note that (12) and (13) coincide with (10) and (11) respectively, evaluated for $a = 0$.

By recalling (7), f_1 may be written as

$$f_1 = \frac{1}{\sqrt{\pi}} \exp\left(-i\frac{\pi}{4}\right) \exp(ik\xi \cosh \chi - k\eta \sinh \chi) I(a_1 + ib_1) \quad (14)$$

where a_1 and b_1 are given by (6).

For $\rho \rightarrow \infty$, $|a_1|$ tends to infinity, except that for $\theta = \theta^i$. In this case $a_1 = 0$ and $b_1 \rightarrow +\infty$. Accordingly, the asymptotic expression of f_1 is obtained by introducing into (14) the expressions (10) and (11). One finds

$$f_1 = \exp(ik\xi \cosh \chi - k\eta \sinh \chi) \left[1 - \frac{\exp[i(\pi/4)] \exp[i(a_1 + ib_1)^2]}{2\sqrt{\pi}(a_1 + ib_1)} \right] \quad (15)$$

for $a_1 \geq 0$, $(-3\pi/2 \leq \theta \leq \theta^i)$, and

$$f_1 = -\exp(ik\xi \cosh \chi - k\eta \sinh \chi) \frac{\exp[i(\pi/4)] \exp[i(a_1 + ib_1)^2]}{2\sqrt{\pi}(a_1 + ib_1)} \quad (16)$$

for $a_1 < 0$, $(\theta^i < \theta \leq \pi/2)$.

Analogously, one obtains for f_2 the following expressions

$$f_2 = \exp(-ik\xi' \cosh \chi - k\eta' \sinh \chi) \left[1 - \frac{\exp[i(\pi/4)] \exp[i(a_2 + ib_2)^2]}{2\sqrt{\pi}(a_2 + ib_2)} \right] \quad (17)$$

for $a_2 > 0$, $(-3\pi/2 \leq \theta < -\pi - \theta^i)$, and

$$f_2 = -\exp(-ik\xi' \cosh \chi - k\eta' \sinh \chi) \frac{\exp[i(\pi/4)] \exp[i(a_2 + ib_2)^2]}{2\sqrt{\pi}(a_2 + ib_2)} \quad (18)$$

for $a_2 \leq 0$, $(-\pi - \theta^i \leq \theta \leq \pi/2)$.

In order to visualize the situation, let us consider figure 3 where \mathbf{s}^i indicates the direction of propagation of the incident wave, and \mathbf{s}^r the direction symmetric to \mathbf{s}^i with respect to the screen.

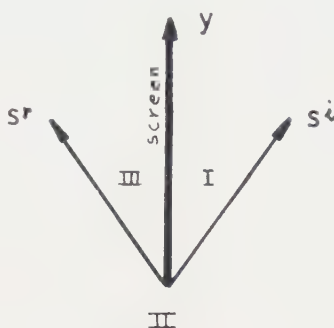


Figure 3. Domains of validity for the different expressions of f_1 and f_2 .

The three directions \mathbf{s}^i , \mathbf{s}^r , y , divide the plane into three sectors, denoted in figure 3 by I, II, III, respectively. It can be seen that the expression (15) holds in the sectors II and III, while the expression (16) holds in sector I. Analogously, the expression (17) holds in the sector III, while (18) holds in the sectors I and II.

The expressions of f_1 and f_2 may then be interpreted as follows.

Expression (15) gives f_1 in the form of the incident wave plus a cylindrical wave; in the sector I the expression (16) of f_1 does not contain the incident wave, but only the cylindrical wave. However, this does not matter very much, since in the sector I the incident wave vanishes exponentially at infinity and is negligible with respect to the scattered field.

Analogously, expression (17) of f_2 , holding in sector III, contains a term which can easily be interpreted as an evanescent wave reflected by the screen, in the sense of geometrical optics, plus a cylindrical wave. However, the appearance of the reflected wave in sector III does not matter for our purpose, since such wave vanishes exponentially at infinity and does not contribute to the far field. The reflected evanescent wave is not present in sectors I and II, where it would increase exponentially.

In the case of a perfectly conducting screen, the field is represented by one of the combinations of f_1 and f_2 , given by (1) and (2) respectively. The scattered field will be represented by the corresponding combination of the cylindrical waves appearing in the expressions of f_1 and f_2 .

2.3. The scattered fields

From (1), (15), (16), (17) and (18), with the help of (6) and (8), one obtains for the scattered field E_x^s in the TE case

$$|E_x^s| = \frac{1}{\sqrt{(2\pi k\rho)}} \sqrt{\left(\frac{(1 - \sin \theta)(\cosh \chi + \sin \theta^i)}{[\cosh \chi - \cos(\theta - \theta^i)][\cosh \chi + \cos(\theta + \theta^i)]} \right)} \quad (19)$$

and

$$\begin{aligned} \sin \phi_E &= -\frac{\sqrt{2}}{\sqrt{(k\rho)}} \frac{\sinh \chi/2}{|E_x^s|} \left\{ \frac{\cos(\theta - \theta^i)/2}{\cosh \chi - \cos(\theta - \theta^i)} - \frac{\sin(\theta + \theta^i)/2}{\cosh \chi + \cos(\theta + \theta^i)} \right\} \\ \cos \phi_E &= -\frac{\sqrt{2}}{\sqrt{(k\rho)}} \frac{\cosh \chi/2}{|E_x^s|} \left\{ \frac{\sin(\theta - \theta^i)/2}{\cosh \chi - \cos(\theta - \theta^i)} - \frac{\cos(\theta + \theta^i)/2}{\cosh \chi + \cos(\theta + \theta^i)} \right\} \end{aligned} \quad (20)$$

where ϕ_E indicates the phase of E_x^s .

Analogously, in the TM case, one obtains

$$|H_x^s| = \frac{1}{\sqrt{(2\pi k\rho)}} \sqrt{\left(\frac{(1 + \sin \theta)(\cosh \chi - \sin \theta^i)}{[\cosh \chi - \cos(\theta - \theta^i)][\cosh \chi + \cos(\theta + \theta^i)]} \right)} \quad (21)$$

and

$$\begin{aligned} \sin \phi_H &= -\frac{\sqrt{2}}{\sqrt{(k\rho)}} \frac{\sinh \chi/2}{|H_x^s|} \left\{ \frac{\cos(\theta - \theta^i)/2}{\cosh \chi - \cos(\theta - \theta^i)} + \frac{\sin(\theta + \theta^i)/2}{\cosh \chi + \cos(\theta + \theta^i)} \right\}, \\ \cos \phi_H &= -\frac{\sqrt{2}}{\sqrt{(k\rho)}} \frac{\cosh \chi/2}{|H_x^s|} \left\{ \frac{\sin(\theta - \theta^i)/2}{\cosh \chi - \cos(\theta - \theta^i)} + \frac{\cos(\theta + \theta^i)/2}{\cosh \chi + \cos(\theta + \theta^i)} \right\}, \end{aligned} \quad (22)$$

where ϕ_H indicates the phase of H_x^s .

From (19) and (21) one can derive that both in the TE and TM cases, the amplitude of the scattered field is symmetric with respect to the y -axis. It is interesting to note that $|E_x^s(\chi, \theta, \theta^i)|$ of the TE case is proportional to $|H_x^s(\chi, \theta - \pi, \theta^i - \pi)|$ of the TM case.

From (20) and (19) one derives that the phase of E_x^s on both sides of the sheet differs by π . The same holds for the phase of H_x^s in the TM case, as can be derived from (22) and (21).

It is an easy matter to prove the following properties. In the TE case, $|E_x^s|$ vanishes for every value of θ^i and χ , at $\theta = \pi/2$, except for $\chi = 0$ and $\theta^i = \pi/2$. In this case $|E_x^s|$ becomes infinite, however the case $\chi = 0$ cannot be treated in the present approximation. On the other hand, if $\cosh \chi - \sin \theta^i < 2$, $|E_x^s|$ presents a minimum at $\theta = -\pi/2$, and two maxima at $\theta = \theta_1, \theta_2$, such that

$$\sin \theta_1 = \sin \theta_2 = 1 - (\cosh \chi - \sin \theta^i).$$

If $\cosh \chi - \sin \theta^i \geq 2$, $|E_x^s|$ has a single maximum at $\theta = -\pi/2$. In the TM case, $|H_x^s|$ vanishes at $\theta = -\pi/2$ for every value of χ and θ^i (the case $\theta^i = -\pi/2$ is of no interest, since it cannot occur). If $\cosh \chi + \sin \theta^i < 2$, there is a minimum at $\theta = \pi/2$ and two maxima at θ_1 and θ_2 such that

$$\sin \theta_1 = \sin \theta_2 = -1 + \cosh \chi + \sin \theta^i.$$

If $\cosh \chi + \sin \theta^i \geq 2$, there is a single maximum at $\theta = \pi/2$.

2.4. Scattering patterns and scattering factor

For practical purposes we are chiefly interested in the computation of the scattering pattern $\rho S^s/P^i$, where ρ is the distance from the rim of the screen,

S^s is the Poynting vector of the scattered field and P^i the power incident on the screen per unit length of the rim. Of course P^i has a meaning for $\theta^i \neq \pi/2$ only.

Equation (19) yields in the TE case

$$S^s = \frac{1}{2Z} EE^* = \frac{1}{Z4\pi k\rho} \frac{(1 - \sin\theta)(\cosh\chi + \sin\theta^i)}{[\cosh\chi - \cos(\theta - \theta^i)][\cosh\chi + \cos(\theta + \theta^i)]} \quad (23)$$

and equation (21) yields in the TM case

$$S^s = \frac{Z}{2} HH^* = \frac{Z}{4\pi k\rho} \frac{(1 + \sin\theta)(\cosh\chi - \sin\theta^i)}{[\cosh\chi - \cos(\theta - \theta^i)][\cosh\chi + \cos(\theta + \theta^i)]}. \quad (24)$$

As regards the power incident on the screen per unit length, consider first the TE case. The electric field of the incident wave has been assumed to be (see equation (15)):

$$E_x = \exp(ik\xi \cosh\chi - k\eta \sinh\chi).$$

Hence the Poynting vector is readily found and the value of P^i turns out to be

$$P^i = \frac{1}{4kZ} \cotanh\chi. \quad (25)$$

In the TM case P^i is found to be

$$P^i = \frac{Z}{4k} \cotanh\chi.$$

There follows

$$\rho \frac{S^s}{P^i} = \frac{1}{\pi} \tanh\chi \frac{(1 - \sin\theta)(\cosh\chi + \sin\theta^i)}{[\cosh\chi - \cos(\theta - \theta^i)][\cosh\chi + \cos(\theta + \theta^i)]} \quad (26)$$

in the TE case, and

$$\rho \frac{S^s}{P^i} = \frac{1}{\pi} \tanh\chi \frac{(1 + \sin\theta)(\cosh\chi - \sin\theta^i)}{[\cosh\chi - \cos(\theta - \theta^i)][\cosh\chi + \cos(\theta + \theta^i)]} \quad (27)$$

in the TM case.

The asymptotic value of the quantity $\rho S^s/P^i$ when the attenuation tends to infinity (i.e. $\chi \rightarrow \infty$) may be easily found in both TE and TM cases. In the TE case one has

$$\lim_{\chi \rightarrow \infty} \rho \frac{S^s}{P^i} = \frac{1 - \sin\theta}{\pi \cosh\chi}. \quad (28)$$

and in the TM case

$$\lim_{\chi \rightarrow \infty} \rho \frac{S^s}{P^i} = \frac{1 + \sin\theta}{\pi \cosh\chi}. \quad (29)$$

The quantity $\rho S^s/P^i$ has been evaluated for the following values of θ^i and of the attenuation per wavelength:

$$\theta^i = \pi/2; \quad \pi/4; \quad 0; \quad -\pi/4$$

attenuation = 5.62; 12.58; 18.22; 38.58; 48.13 dB/ λ .

The numerical results are shown in the diagrams of figures 4-7, where $\rho S^s/P^i$ is plotted for various values of attenuation as a function of θ .

The *scattering factor* of the screen will be defined as the ratio of the total scattered power to the geometrically incident power:

$$\sigma = \frac{1}{P^i} \int_0^{2\pi} S^s \rho d\theta.$$

By a laborious but not difficult integration one finds both in the TE and TM case

$$\sigma = \frac{2}{\cosh \chi} = \frac{2}{\sqrt{1 + \alpha^2/k^2}}$$

where $\alpha = k \sinh \chi$ is the attenuation constant.

It is interesting to note that for $\alpha \rightarrow 0$, $\sigma \rightarrow 2$, which value as is well known, represents the scattering factor of any finite screen for an ordinary incident plane wave.

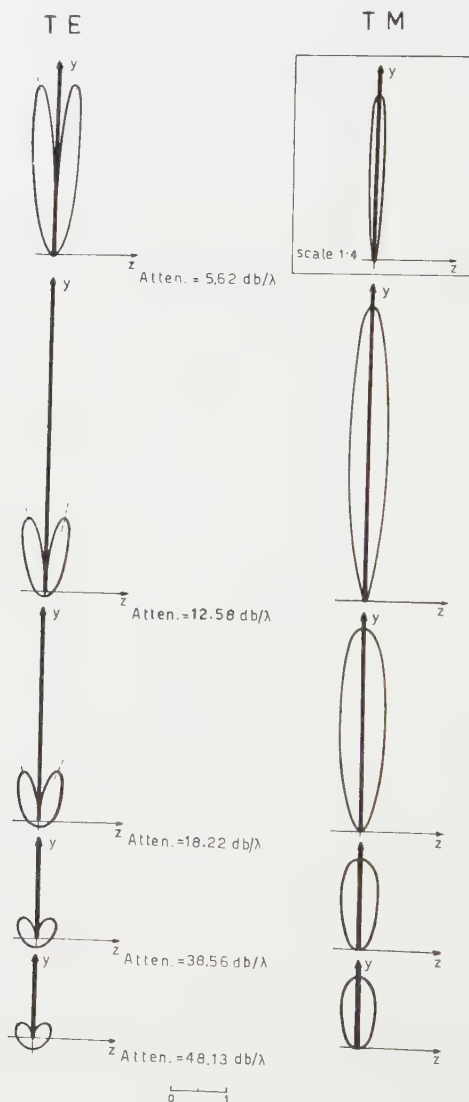


Figure 4. Scattering patterns in both TE and TM cases for $\theta^i = \pi/2$ and a number of values of the attenuation of the incident wave (power). Broken lines show the directions of maximum scattering.

3. SCATTERING BY AN INFINITELY CONDUCTING CYLINDER OF CIRCULAR CROSS SECTION

3.1. Incident waves of TE_c and TM_c types

We will study the scattering of an evanescent wave by a perfectly conducting cylinder of infinite length and circular cross section. The direction of attenuation will be assumed to be perpendicular to the axis of the cylinder.

We shall carry out the treatment as an extension of the well-known case of an ordinary plane wave.

We recall [8] that it is possible to define an electric and a magnetic Hertz vector $\mathbf{\Pi}$ and $\mathbf{\Pi}'$, both satisfying the vector wave equation

$$(\nabla^2 + k^2)\mathbf{\Pi} = 0. \quad (30)$$

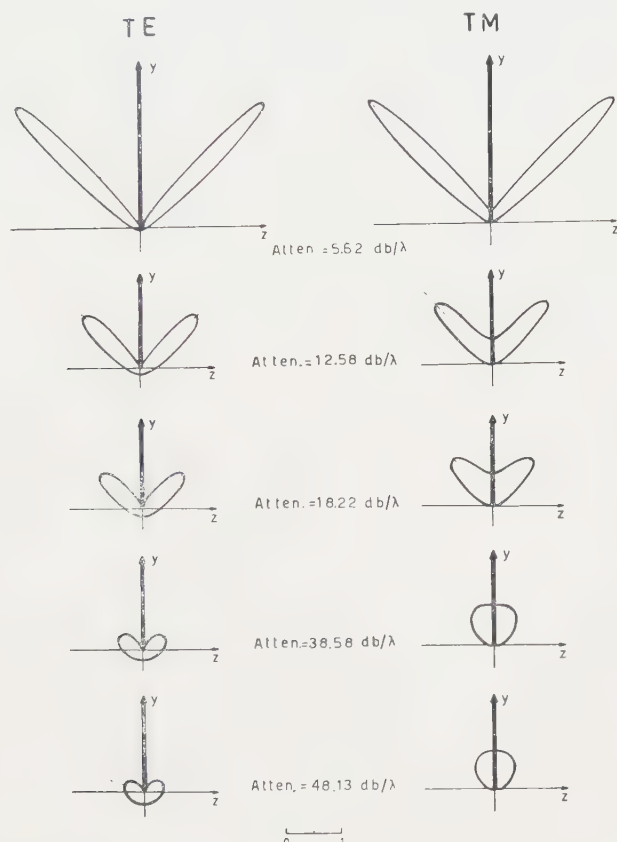


Figure 5. Scattering patterns in both TE and TM cases for $\theta^i = \pi/4$ and a number of values of the attenuation of the incident wave (power). Broken lines show the directions of maximum scattering.

The components of the electromagnetic field are given, in the former case, by

$$\mathbf{H} = i\omega\epsilon_0 \nabla \times \mathbf{\Pi}, \quad \mathbf{E} = \nabla \times \nabla \times \mathbf{\Pi} \quad (31)$$

and in the latter case by

$$\mathbf{H} = \nabla \times \nabla \times \mathbf{\Pi}', \quad \mathbf{E} = -i\omega\mu_0 \nabla \times \mathbf{\Pi}'. \quad (32)$$

In the case of a homogeneous charge-free medium, it is possible to express an electromagnetic field of the most general kind by means of two independent scalar functions. It is sufficient to put

$$\Pi = \Pi \mathbf{a}, \quad \Pi' = \Pi' \mathbf{a}. \quad (33)$$

We will deal separately with the case when the incident wave has a vanishing component of the E -vector parallel to the cylinder axis, and with the case when the incident wave has a vanishing component of the H -vector parallel to the cylinder axis. Conventionally, we will term these cases TE_c and TM_c respectively.

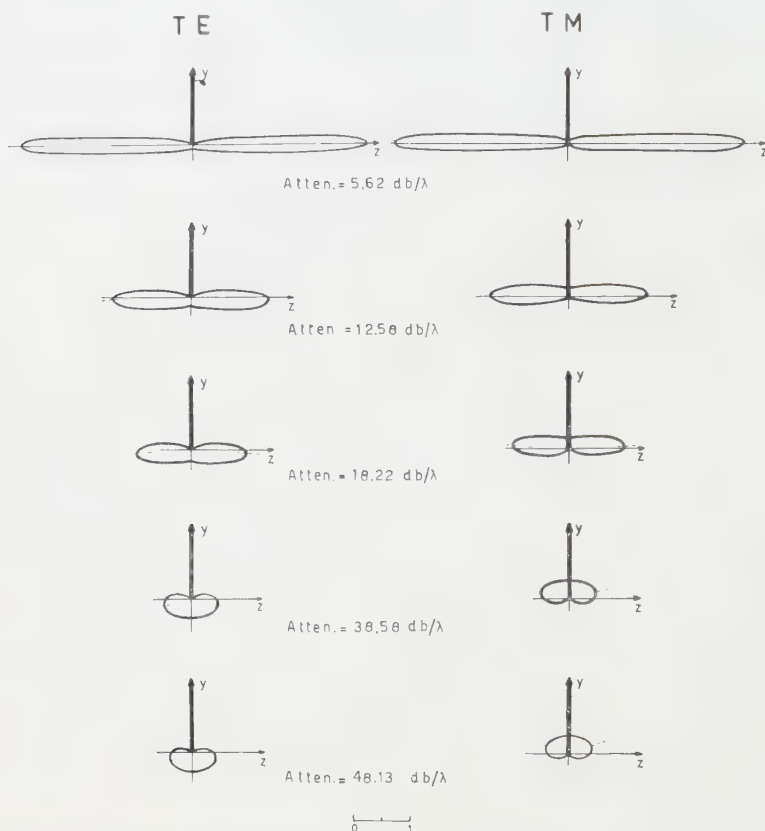


Figure 6. Scattering patterns in both TE and TM cases for $\theta_i = 0$ and a number of values of the attenuation of the incident wave (power). Broken lines show the directions of maximum scattering.

We will refer to rectangular axes x, y, z with y coincident with the axis of the cylinder.

To start with, let us consider an ordinary plane wave, whose direction of propagation is specified by the angles ϕ^i, θ^i shown as positive in figure 8.

Plane waves of the TE_c and TM_c types can be represented by the Hertz vectors

$$\Pi' = \mathbf{i}_y A \exp [ik(x \sin \phi^i \sin \theta^i + y \cos \phi^i + z \sin \phi^i \cos \theta^i)], \quad (34)$$

$$\Pi = \mathbf{i}_y B \exp [ik(x \sin \phi^i \sin \theta^i + y \cos \phi^i + z \sin \phi^i \cos \theta^i)], \quad (35)$$

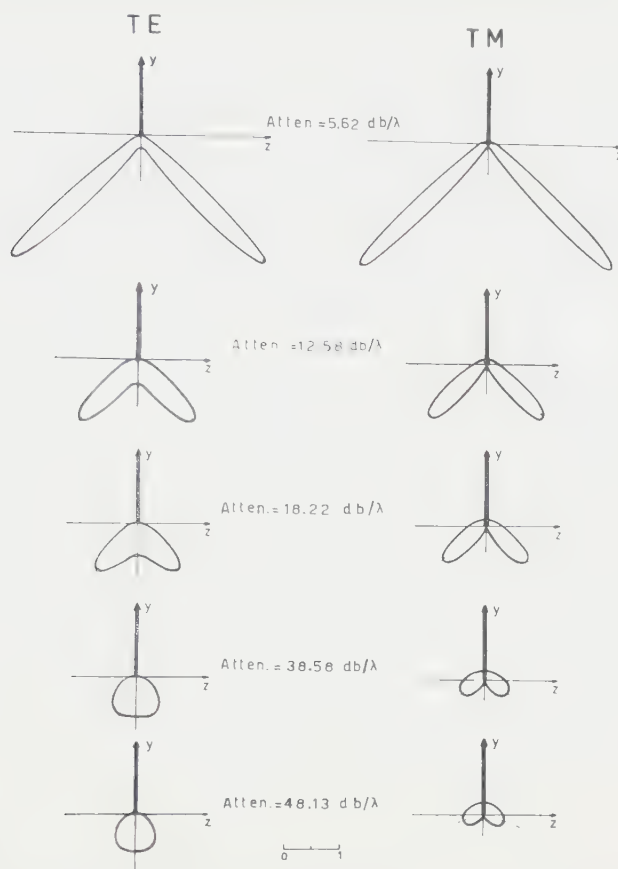


Figure 7. Scattering patterns in both TE and TM cases for $\theta^i = -\pi/4$ and a number of values of the attenuation of the incident wave (power). Broken lines show the directions of maximum scattering.

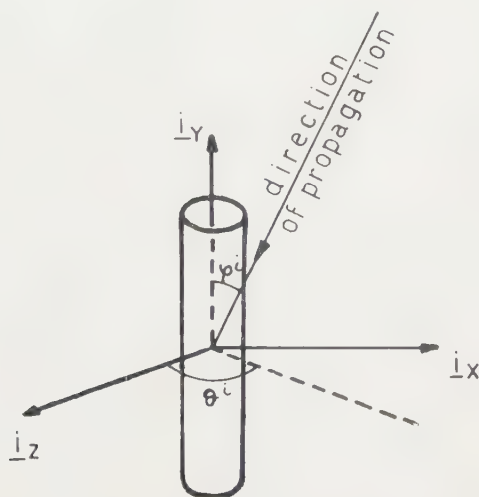


Figure 8. The cylindrical scatterer referred to a system of rectangular coordinates.

respectively. Equations (34) and (35) can also be written as [8]

$$\Pi' = \mathbf{i}_y A \exp(iky \cos \phi^i) \sum_{-\infty}^{\infty} i^n J_n(k\rho \sin \phi^i) \exp[in(\theta - \theta^i)], \quad (36)$$

$$\Pi = \mathbf{i}_y B \exp(iky \cos \phi^i) \sum_{-\infty}^{\infty} i^n J_n(k\rho \sin \phi^i) \exp[in(\theta - \theta^i)] \quad (37)$$

in terms of the cylindrical coordinates defined by $x = \rho \sin \theta$, $z = \rho \cos \theta$, $y = y$. Here J_n denotes the Bessel function of first kind and order n .

Equations (34) and (35) can represent evanescent waves attenuated in the direction of positive z , if either ϕ^i or θ^i or both ϕ^i and θ^i are made to assume suitable complex values. Precisely, $\sin \phi^i \sin \theta^i$ and $\cos \phi^i$ must remain real quantities, while $\sin \phi^i \cos \theta^i$ must become a purely imaginary quantity iQ , with $Q > 0$. This can be obtained in two different ways. From the condition for $\cos \phi^i$ to be real, one has that ϕ^i can be chosen either real (case 1) or imaginary $\phi^i = -i\beta$ (case 2). Without loss of generality, we will assume $\beta > 0$. In case 1, since $\sin \phi^i \sin \theta^i$ must be real and $\sin \phi^i \cos \theta^i$ imaginary, one derives that θ^i must be chosen complex, and precisely

$$\theta^i = \frac{\pi}{2} - i\chi$$

with χ real and positive. Conversely, in case 2, one has to choose θ^i complex

$$\theta^i = \pi - i\chi'$$

with χ' real.

Accordingly, equation (34) becomes, in case 1,

$$\Pi'_i = \mathbf{i}_y A \exp(-kz \sin \phi^i \sinh \chi) \exp[ik(x \sin \phi^i \cosh \chi + y \cos \phi^i)] \quad (38)$$

and in case 2

$$\Pi'_i = \mathbf{i}_y A \exp(-kz \sinh \beta \cosh \chi') \exp[ik(x \sinh \beta \sinh \chi' + y \cosh \beta)]. \quad (39)$$

Both (38) and (39) may be used to represent a TE_c evanescent wave attenuated in the positive direction of z . Analogously, equation (35) becomes, in case 1,

$$\Pi_i = \mathbf{i}_y B \exp(-kz \sin \phi^i \sinh \chi) \exp[ik(x \sin \phi^i \cosh \chi + y \cos \phi^i)] \quad (40)$$

and in case 2,

$$\Pi_i = \mathbf{i}_y B \exp(-kz \sinh \beta \cosh \chi') \exp[ik(x \sinh \beta \sinh \chi' + y \cosh \beta)]. \quad (41)$$

The last two equations represent TM_c evanescent waves attenuated in the positive direction of z .

Let us call ψ the angle between the y -axis and the direction of propagation of the phase, which is parallel to the xy -plane. One has, in case 1,

$$\tan \psi = \tan \phi^i \cosh \chi \quad (42)$$

and in case 2,

$$\tan \psi = \tanh \beta \sinh \chi'. \quad (43)$$

The parameters of the evanescent wave, which have an immediate physical meaning, are ψ and the attenuation constant α , which equals $k \sin \phi^i \sinh \chi$ in case 1 and $k \sinh \beta \cosh \chi'$ in case 2; ϕ^i and χ or β and χ' are instead more convenient for numerical computations. One can easily express ϕ^i , χ and β , χ' in terms of α and ψ , obtaining

$$\left. \begin{aligned} \sin \phi^i &= \sqrt{\left(\sin^2 \psi - \frac{\alpha^2}{k^2} \cos^2 \psi \right)}, \\ \sinh \chi &= \frac{1}{\sqrt{\left(\frac{k^2}{\alpha^2} \sin^2 \psi - \cos^2 \psi \right)}}, \end{aligned} \right\} \quad (44)$$

$$\left. \begin{aligned} \sinh \beta &= \sqrt{\left(\frac{\alpha^2}{k^2} \cos^2 \psi - \sin^2 \psi\right)}, \\ \cosh \chi' &= \frac{1}{\sqrt{\left(\cos^2 \psi - \frac{k^2}{\alpha^2} \sin^2 \psi\right)}}. \end{aligned} \right\} \quad (45)$$

It is readily seen from (44) and (45) that case 1 holds for

$$\frac{\alpha}{k} \leq |\tan \psi| \quad (46)$$

and case 2 for

$$\frac{\alpha}{k} \geq |\tan \psi|. \quad (47)$$

As a consequence, case 1 describes completely the case of normal incidence $\psi = \pi/2$.

By convention, case 1 will be termed the case of 'small attenuation' and case 2 the case of 'large attenuation'.

3.2. The scattered field for small attenuation

Let us first consider the case of small attenuation.

It is possible to show that the expressions (36), (37) hold also in the case of complex angles. Accordingly, one can write

$$\Pi_i' = \mathbf{i}_y A \exp(iky \cos \phi^i) \sum_{-\infty}^{\infty} i^n J_n(k\rho \sin \phi^i) \exp\{in[(\theta - \pi/2) + i\chi]\} \quad (48)$$

for the TE_c case, and

$$\Pi_i = \mathbf{i}_y B \exp(iky \cos \phi^i) \sum_{-\infty}^{\infty} i^n J_n(k\rho \sin \phi^i) \exp\{in[(\theta - \pi/2) + i\chi]\} \quad (49)$$

for the TM_c case. The Hertz vector for the scattered field will be written in the form

$$\Pi_s' = \mathbf{i}_y A \exp(iky \cos \phi^i) \sum_{-\infty}^{\infty} a_n H_n^{(2)}(k\rho \sin \phi^i) \exp\{in[(\theta - \pi/2) + i\chi]\} \quad (50)$$

for the TE_c case, and

$$\Pi_s = \mathbf{i}_y B \exp(iky \cos \phi^i) \sum_{-\infty}^{\infty} b_n H_n^{(2)}(k\rho \sin \phi^i) \exp\{in[(\theta - \pi/2) + i\chi]\} \quad (51)$$

for the TM_c case. Here $H_n^{(2)}$ indicates the Hankel function of the second kind and order n .

The constants a_n and b_n must be determined by means of the boundary conditions. One finds, in the TE_c case

$$a_n = -i^n \frac{J_n'(ka \sin \phi^i)}{H_n^{(2)'}(ka \sin \phi^i)} \quad (52)$$

where primes indicate derivation with respect to the argument and a denotes the radius of the cylinder, and in the TM_c case

$$b_n = -i^n \frac{J_n(ka \sin \phi^i)}{H_n^{(2)}(ka \sin \phi^i)}. \quad (53)$$

By substituting (52) and (53) into (50) and (51), we obtain

$$\begin{aligned} \Pi_s' = & -i_y A \exp(iky \cos \phi^i) \sum_{n=-\infty}^{\infty} i^n \frac{J_n'(ka \sin \phi^i)}{H_n^{(2)}(ka \sin \phi^i)} \\ & \times H_n^{(2)}(k\rho \sin \phi^i) \exp\{in[(\theta - \pi/2) + i\chi]\} \end{aligned} \quad (54)$$

in the TE_c case, and

$$\begin{aligned} \Pi_s = & -i_y B \exp(iky \cos \phi^i) \sum_{n=-\infty}^{\infty} i^n \frac{J_n(ka \sin \phi^i)}{H_n^{(2)}(ka \sin \phi^i)} \\ & \times H_n^{(2)}(k\rho \sin \phi^i) \exp\{in[(\theta - \pi/2) + i\chi]\} \end{aligned} \quad (55)$$

in the TM_c case.

From (48) and (54) by means of (32) we can now calculate the incident and scattered fields for the TE_c case. For the TM_c case one must make use of (49) (55) and (31). Straightforward computations yield the following expressions of the scattered fields for large values of ρ .

TE_c case

$$E_\rho = E_y = 0, \quad E_\theta = k^2 Z \sin \phi^i \Pi_s', \quad (56)$$

$$H_\theta = 0, \quad H_\rho = k^2 \cos \phi^i \sin \phi^i \Pi_s', \quad H_y = k^2 \sin^2 \phi^i \Pi_s' \quad (57)$$

where

$$\begin{aligned} \Pi_s' = & -A \sqrt{\left(\frac{2}{\pi k}\right)} \exp(i\pi/4) \frac{\exp[ik(y \cos \phi^i - \rho \sin \phi^i)]}{\sqrt{(\rho \sin \phi^i)}} \\ & \times \sum_{n=-\infty}^{\infty} (-1)^n \frac{J_n'}{H_n^{(2)'}} \exp\{in[(\theta - \pi/2) + i\chi]\}. \end{aligned} \quad (58)$$

In equation (58) the Bessel and Hankel functions are intended to be evaluated for the value of the argument $ka \sin \phi^i$.

TM_c case

$$E_\theta = 0, \quad E_\rho = k^2 \cos \phi^i \sin \phi^i \Pi_s, \quad E_y = k^2 \phi^i \Pi_s, \quad (59)$$

$$H_\rho = H_y = 0, \quad H_\theta = -(1/Z) k^2 \sin \phi^i \Pi_s \quad (60)$$

where

$$\begin{aligned} \Pi_s = & -B \sqrt{\left(\frac{2}{\pi k}\right)} \exp(i\pi/4) \frac{\exp[ik(y \cos \phi^i - \rho \sin \phi^i)]}{\sqrt{(\rho \sin \phi^i)}} \\ & \times \sum_{n=-\infty}^{\infty} (-1)^n \frac{J_n}{H_n^{(2)}} \exp\{in[(\theta - \pi/2) + i\chi]\}. \end{aligned} \quad (61)$$

In equation (61) the Bessel and Hankel functions are intended to be evaluated for the value of the argument $ka \sin \phi^i$.

3.3. The scattered field for large attenuation

In the case of large attenuation, that is, when (47) is satisfied, one can repeat step by step the procedure followed in the preceding section. The resulting expressions of the fields coincide, as could be expected, with the expressions which would be obtained from equations (56) to (61) by simply substituting $i\beta$ for ϕ^i and $i\chi'$ for $i\chi + \pi/2$.

From (58) and (61) one derives that, for attenuation constants satisfying (47), the radiative field vanishes. This is related to the fact that the constant of propagation k_y in the direction of the cylinder axis is larger than the constant of propagation k in free space, according to the relation

$$k_y = k \cosh \beta$$

Accordingly, the radiative field vanishes for the value of the attenuation constant corresponding to $\beta=0$, that is, from (45) or (44), to

$$\frac{\alpha}{k} = |\tan \psi| \quad (62)$$

and remains zero for any value of α/k larger than $|\tan \psi|$.

3.4. The Poynting vector of the scattered field in the TE_c and TM_c cases

From (56) and (57) we can now evaluate in a straightforward manner the asymptotic value of the complex Poynting vector $\mathbf{S}^s = (\mathbf{E} \times \mathbf{H}^*)/2$ of the scattered field in the TE_c case. We obtain

$$\mathbf{S}^s = \frac{1}{2} k^4 Z [-\sin^2 \phi^i \cos \phi^i \mathbf{i}_y + \sin^3 \phi^i \mathbf{i}_\rho] \Pi_s' \Pi_s'^* \quad (63)$$

The Poynting vector turns out to be a real quantity.

From (58) and (63) it is an easy matter to evaluate the power P^s carried by the scattered field per unit length of the cylinder

$$P^s = \int_0^{2\pi} S_{\rho\rho} d\theta. \quad (64)$$

One finds

$$P^s = 2k^3 Z \sin^2 \phi^i |A|^2 \sum_{n=-\infty}^{\infty} \frac{(J_{n-1} - J_{n+1})^2}{[H_{n-1}^{(2)} - H_{n+1}^{(2)}]^2} \exp(-2n\chi). \quad (65)$$

P^s is a function of the attenuation, of the incidence angle ψ and of the radius a of the cylinder measured in wavelengths. If a is made to vanish, P^s vanishes, too. The most significant terms of series (65) correspond to $n=0$ and $n=1$, and tend to zero as a^4 .

Analogously one derives the complex Poynting vector of the scattered field in the TM_c case. One finds, from (59) and (60),

$$\mathbf{S}^s = \frac{1}{2} \frac{k^4}{Z} [-\sin^2 \phi^i \cos \phi^i \mathbf{i}_y + \sin^3 \phi^i \mathbf{i}_\rho] \Pi_s \Pi_s^* \quad (66)$$

and

$$P^s = 2 \frac{k^3}{Z} \sin^2 \phi^i |B|^2 \sum_{n=-\infty}^{\infty} \frac{J_n^2}{[H_n^{(2)}]^2} \exp(-2n\chi). \quad (67)$$

For a tending to zero, P^s tends to zero as $1/\ln^2 a$, therefore much less rapidly than in the preceding case.

3.5. The TE_p and TM_p cases

We shall call TE_p an evanescent wave whose E -vector is normal to the direction of propagation of the phase, and TM_p an evanescent wave whose H -vector is normal to the direction of propagation of the phase.

It is an easy matter [9] to decompose a TE_p or a TM_p wave into a TE_c and a TM_c wave:

$$TE_p = -\frac{i}{k^2 Z} \frac{\sinh \chi}{\sin \phi^i} TE_c - \frac{1}{k^2} \frac{\cosh \chi}{\sin \phi^i \cos \phi^i} TM_c, \quad (68)$$

$$TM_p = -\frac{1}{k^2 Z} \frac{\cosh \chi}{\sin \phi^i \cos \phi^i} TE_c + \frac{i}{k^2} \frac{\sinh \chi}{\sin \phi^i} TM_c \quad (69)$$

where TE_p and TM_p represent, conventionally, the complex amplitudes of the corresponding waves, and TE_c , TM_c are the expressions (38), (40) for $A=B=1$. On the other hand, one can show by means of (56), (57), (59) and (60) that, asymptotically, a TE_c and a TM_c scattered wave are orthogonal to one another and transport their powers independently of one another. Accordingly, the Poynting vector of the total scattered field for a TE_p or TM_p wave may be

evaluated as the sum of the Poynting vectors of the TE_c and the TM_c component waves taken separately.

It is interesting to evaluate the scattering pattern and the scattering factor defined by

$$f(\theta) = \rho S_\rho^s / P^i, \quad \sigma = P^s / P^i$$

respectively, where S_ρ^s is the radial component of the asymptotic Poynting vector of the scattered field, and P^i the power incident on the cylinder per unit length of the cylinder axis. Of course, it will be noted that the incident TE_c and TM_c components are not orthogonal to one another, consequently the incident power must be evaluated for the compound TE_p or TM_p wave.

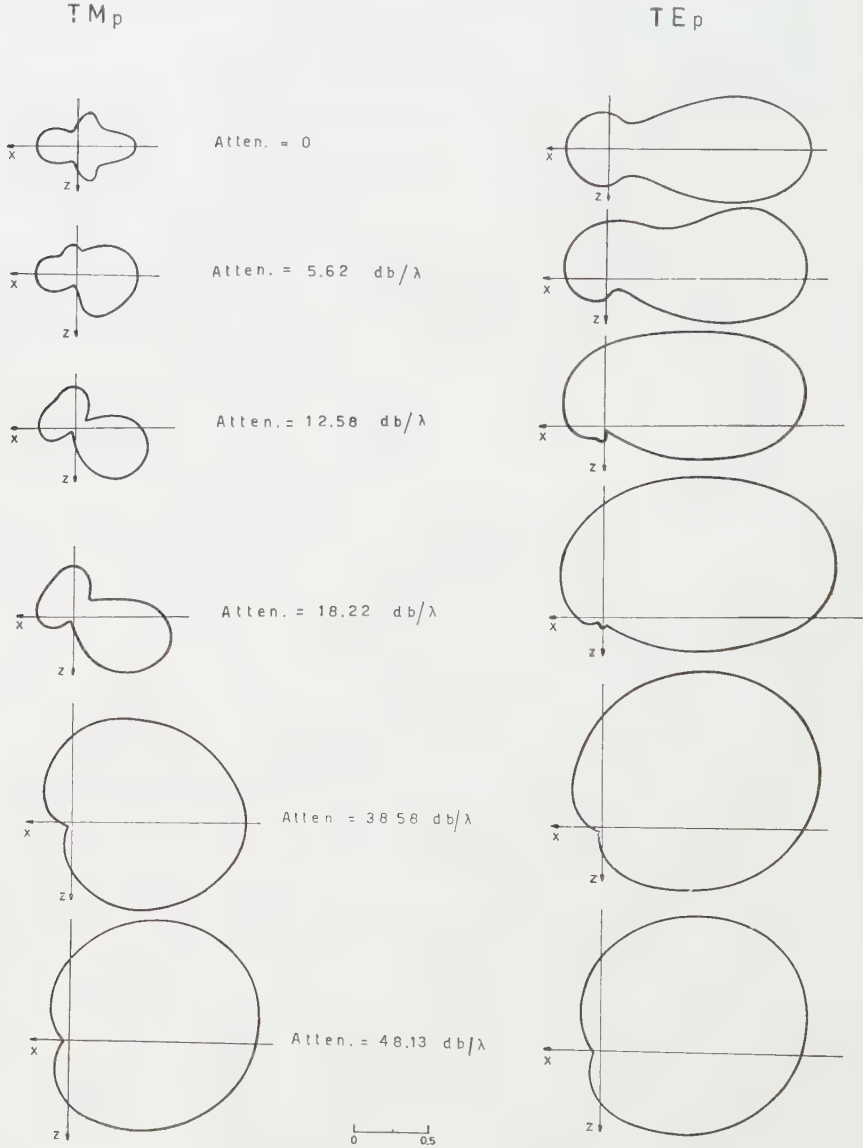


Figure 9. Scattering patterns in the TM_p and TE_p cases, for $\psi = \pi/4$ and $ka = 3$ for a number of values of the attenuation of the incident wave (power). The incident wave is supposed to travel from left to right and to be attenuated downwards.

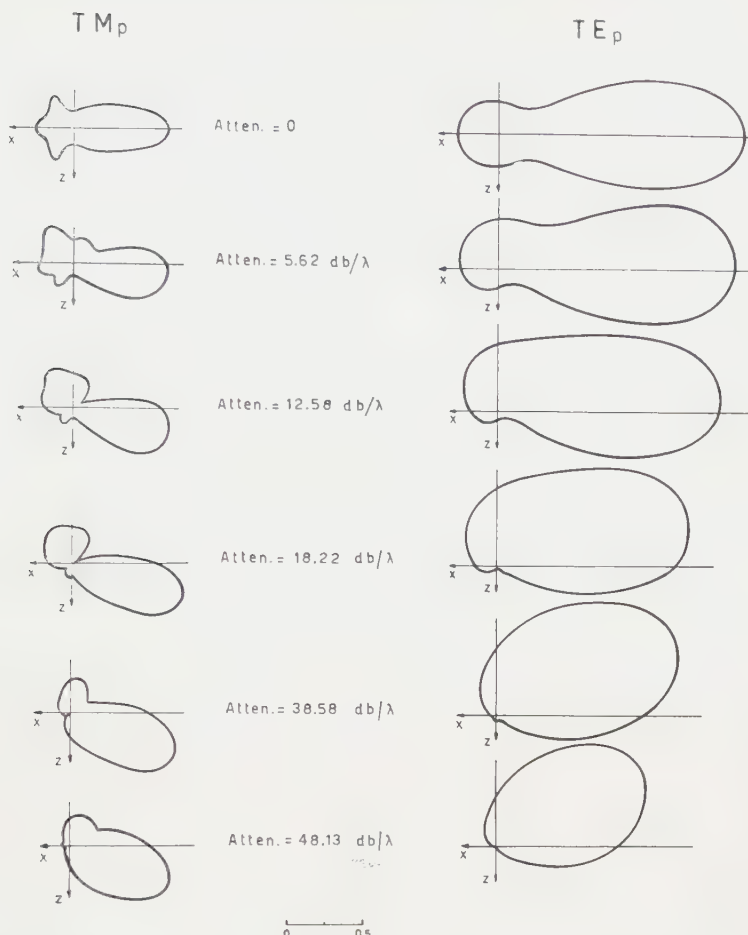


Figure 10. Scattering patterns in the TM_p and TE_p cases for $\psi = \pi/2$ and $ka = 3$ for a number of values of the attenuation of the incident wave. The incident wave is supposed to travel from left to right and to be attenuated downwards.

In figures 9, 10, 11 the scattering pattern is plotted versus θ both in the TM_p and TE_p cases, for the following sets of values of the parameters ψ and ka

$$\begin{aligned} \psi &= \pi/4, \quad ka = 3, \\ \psi &= \pi/2, \quad ka = 3, 0.75, \end{aligned}$$

and for the following values of the attenuation of the incident wave (power) in the direction of z , expressed in decibels per wavelength

$$\text{attenuation: } 0, 5.62, 12.58, 18.22, 38.58, 48.13 \text{ dB}/\lambda.$$

The incident wave is supposed to travel from left to right and to be attenuated downwards.

Figure 12 shows the scattering factor versus the attenuation in the case $\psi = \pi/2$ and $ka = 0.75, 1.5, 3, 6$ respectively. It is interesting to note that the scattering factor presents some sort of resonance phenomena for increasing attenuation.

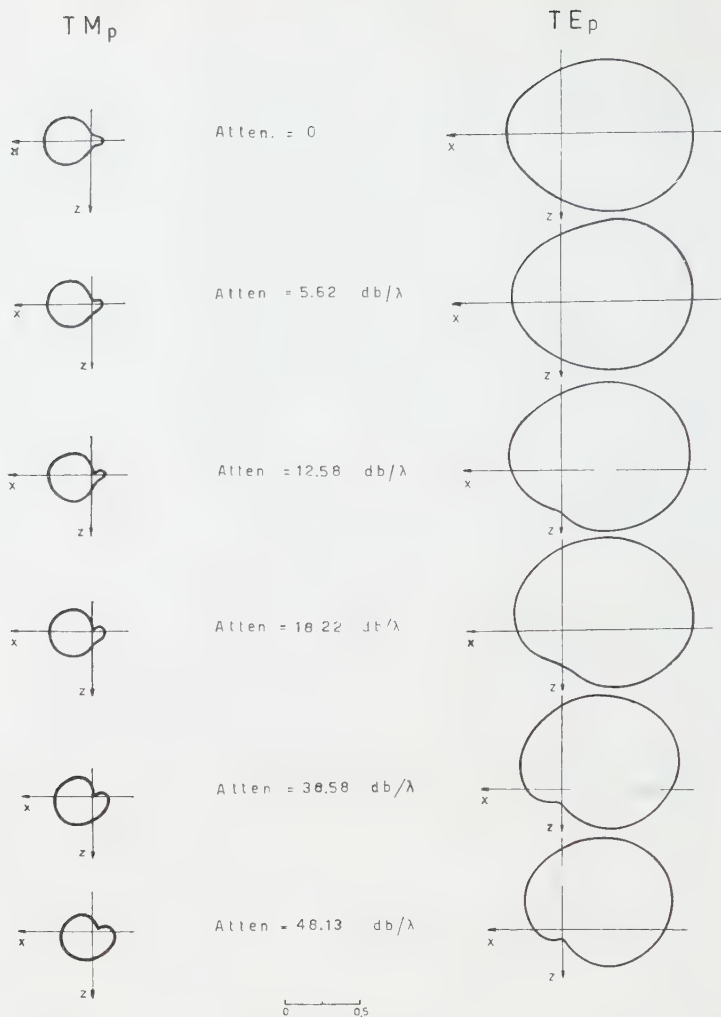


Figure 11. Scattering patterns in the TM_p and TE_p cases for $\psi = \pi/2$ and $ka = 0.75$ for a number of values of the attenuation of the incident wave. The incident wave is supposed to travel from left to right and to be attenuated downwards.

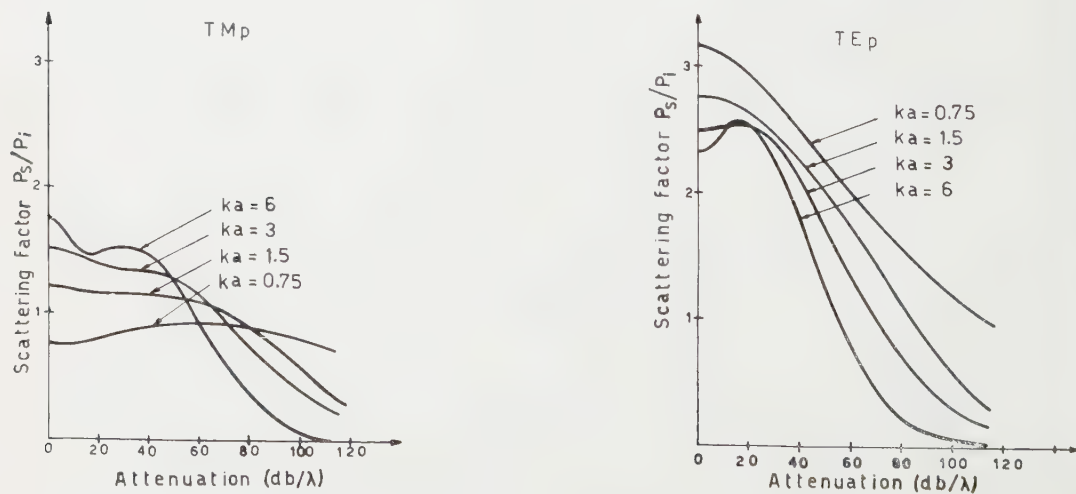


Figure 12. The scattering factor versus attenuation for $\psi = \pi/2$ and various values of the radius of the cylinder ($ka = 0.75, 1.5, 3, 6$) in the TM_p and TE_p cases.

4. CONCLUSION

The diffraction of an evanescent wave by a conducting half-plane and by a conducting cylinder has been investigated.

It is interesting to note that, unlike the case of an incident real wave, one can split the total field into an incident wave and a scattered cylindrical wave also when the scatterer is a half-plane. In this case, if the attenuation is not too large, there are two pronounced directions of scattering, symmetrical with respect to the half-plane. When the attenuation per wavelength exceeds a certain value, the two maxima disappear and there remains a $1 \pm \sin \theta$ pattern (see figures 4, 5, 6, 7).

In the case of the circular cylinder, the scattering cross section per unit length of the cylinder shows some sort of resonance for increasing attenuation.

For oblique incidence, the scattering cross section vanishes above a given value of the attenuation.

Cet article est relatif à la diffraction d'une onde électromagnétique évanesciente par un demi-plan infiniment conducteur (§ 2) et par un cylindre de section circulaire infiniment conducteur (§ 3). On donne des formules générales pour les champs au voisinage des surfaces et à grande distance de celles-ci. On montre des figures de diffusion dans certains cas particuliers.

Die Arbeit behandelt die Beugung einer quergedämpften Welle an einer unendlich ausgedehnten leitenden Halbebene (§ 2) und an einem ebensolchen Kreiszyylinder (§ 3). Es werden die allgemeinen Formeln für das Feld in naher und großer Entfernung mitgeteilt. Für einige besondere Fälle sind die Streucharakteristiken dargestellt.

REFERENCES

- [1] TORALDO DI FRANCIA, G., 1960, *Nuovo Cim.*, **16**, 61.
- [2] SMITH, S. J., and PURCELL, E. M., 1953, *Phys. Rev.*, **92**, 1069.
- [3] SMITH, S. J., 1953, *Thesis*, Harvard University, Cambridge, Massachusetts.
- [4] KASTLER, A., 1955, *Nuovo Cim.*, Suppl., **3**, 761.
- [5] ISHIGURO, K., and TAKO, T., 1959, Fifth Meeting and Conference of C.I.O., Stockholm.
- [6] SOMMERFELD, A., 1896, *Math. Ann.*, **47**, 317.
- [7] TORALDO DI FRANCIA, G., 1956, *Introduction to the Modern Theory of Electromagnetic Diffraction* (Florence: Ist. Naz. di Ottica), p. 21.
- [8] MENTZER, J. R., 1955, *Scattering and Diffraction of Radio Waves* (London: Pergamon Press), p. 56.
- [9] RONCHI, L., RUSSO, V., TORALDO DI FRANCIA, G., and ZACCAGNINI, C., 1960, Tech. Note No. 8 of Contract AF 61 (052)-67, Centro Microonde, October.

On the reversibility of light beams in conducting media

by IVAN ŠANTAVÝ

Technical University, Brno, Czechoslovakia

(Received 3 November 1960)

A theorem is derived stating that it is possible to reverse light beams in a system of conducting layers in the sense of the classical Stokes' principle, provided that proper adjustments are made to the amplitude of the reflected and transmitted ray. It is shown that the generalized theorem of reversibility includes as special cases the Stokes' principle and its extension to homogeneous dielectric films.

1. INTRODUCTION

In the optics of thin films relations are often used resulting from the possibility of reversing light beams. This is the so-called principle of reversibility (see, for example, [1]). Mostly known as Stokes' principle, it states the following: Let us reverse both the reflected and refracted rays originated from a light ray incident with amplitude A_0 from medium 1 on the boundary between two dielectric media 1 and 2 (figure 1). Each of these rays in its turn gives rise to a reflected and a refracted ray. Then the two rays travelling in the medium 1 in the direction to the left interfere, summing up to a ray with an amplitude A_0 . The two rays travelling to the right within the medium 2 give a zero field. Denoting the relative complex amplitudes of the reflected and refracted rays by the symbols r , t , respectively, one obtains the two equations

$$r_R r_R^* + t_R t_L^* = 1, \quad (1)$$

$$r_R t_R^* + t_R r_L^* = 0. \quad (2)$$

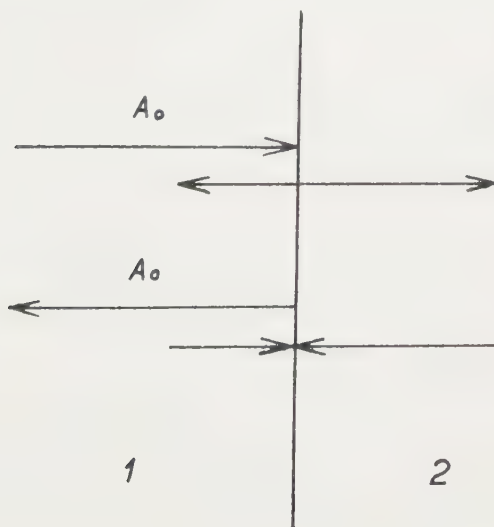


Figure 1.

The indices R, L denote propagation of the light to the right and left, respectively. The asterisks designate complex conjugate quantities.

If the original ray travels from the right to the left, the same consideration gives

$$r_L r_L^* + t_L t_R^* = 1, \quad (3)$$

$$r_L t_L^* + t_L r_R^* = 0. \quad (4)$$

These relations are due to Stokes who considered a simple boundary between two dielectrics. They are also valid for a system of dielectric films, as was shown by Knittl [2].

The problem of light reversal in conducting media was considered by Fragstein [3], Knittl [4] and others, who all gave attention to the energetic situation on the boundary between a dielectric and a metal. From their considerations it follows that Stokes' principle of reversibility generally loses its validity there.

In the case of a simple dielectric-metal boundary the Fresnel amplitudes satisfy the equations

$$r_R r_R + t_R t_L = 1, \quad (5)$$

$$r_R t_R + t_R r_L = 0, \quad (6)$$

$$r_L r_L + t_L t_R = 1, \quad (7)$$

$$r_L t_L + t_L r_R = 0. \quad (8)$$

These relations are analogous to equations (1)–(4) and admit an interpretation as a kind of reversibility, but not in the Stokes sense. It is possible to obtain from equations (1)–(4) much useful information about the amplitudes r , t (see [2]), whilst the equations (5)–(8) are not so rich in consequences. Equations (1)–(4) and (5)–(8) are identical in the case of a simple boundary between two dielectrics, all the r and t amplitudes being real in that case.

For a system of conducting layers no relations analogous to equations (1)–(4) or (5)–(8) have so far been known. The purpose of this paper is to examine the relation between equations (1)–(4) and equations (5)–(8) from the standpoint of the Maxwell theory. It will be shown they not only have a similar form, but that there is an intrinsic connection between them. They are special cases of equations representing a general reversibility theorem for a system of arbitrary conductive or non-conductive films, to be deduced in the following.

2. PRELIMINARY REMARKS ON MAXWELL EQUATIONS

Let us consider a system of isotropic and conducting or non-conducting films. Let the characteristic parameters ϵ , μ , σ of the film media be arbitrary functions of x only (see figure 2) and let the media on the both sides of the system be homogeneous and isotropic.

If an electromagnetic wave is incident on such a system, the Maxwell equations for conducting media

$$\left. \begin{aligned} \text{curl } \vec{E} &= -\mu \frac{\partial \vec{H}}{\partial t}, & \text{div } (\epsilon \vec{E}) &= \rho, \\ \text{curl } \vec{H} &= \sigma \vec{E} + \epsilon \frac{\partial \vec{E}}{\partial t}, & \text{div } (\mu \vec{H}) &= 0, \end{aligned} \right\} \quad (9)$$

hold for the vectors \vec{E} , \vec{H} everywhere but at the discontinuity regions of the quantities ϵ , μ , σ , where corresponding boundary conditions resulting from equations (9) are satisfied.

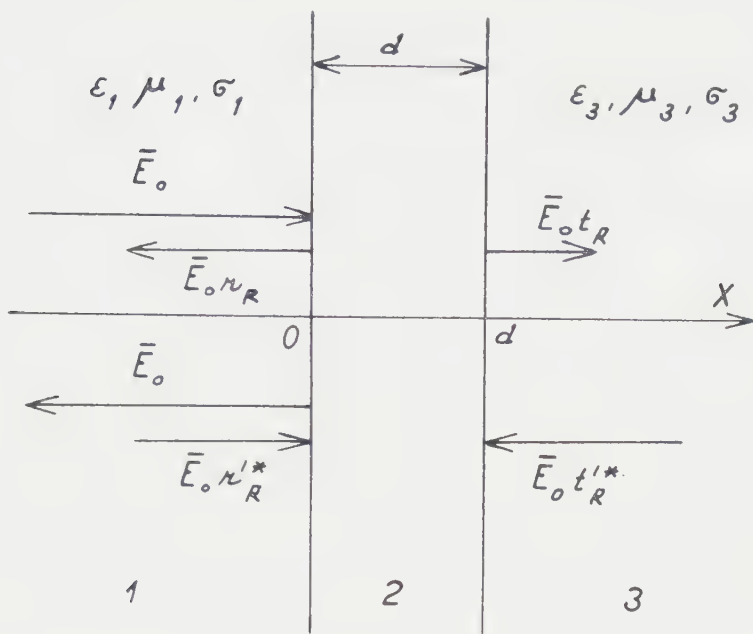


Figure 2.

The Maxwell equations for non-conducting media are known to be invariant with respect to the change of variables defined by

$$\bar{E}' = \bar{E}, \quad \bar{H}' = -\bar{H}, \quad t' = -t, \quad \rho' = -\rho,$$

or by

$$\bar{E}' = -\bar{E}, \quad \bar{H}' = \bar{H}, \quad t' = -t, \quad \rho' = -\rho$$

(see [5], p. 43). It is evident that the invariance of Maxwell's equations will be maintained even for conducting media, if in addition to the above stated transformations the conductivity is changed according to the rule $\sigma' = -\sigma$. This means that equations (9) are invariant to the transformations

$$\bar{E}' = \bar{E}, \quad \bar{H}' = -\bar{H}, \quad t' = -t, \quad \rho' = \rho, \quad \sigma' = -\sigma \quad (10)$$

or

$$\bar{E}' = -\bar{E}, \quad \bar{H}' = \bar{H}, \quad t' = -t, \quad \rho' = -\rho, \quad \sigma' = -\sigma. \quad (11)$$

To derive the theorem of reversibility equation (10) will be used, equation (11) leading to the same result.

3. THE THEOREM OF REVERSIBILITY

Let a plane harmonic electromagnetic wave be incident on the system of films in the direction from the left to the right. For the sake of simplicity it will be supposed to be linearly polarized and propagating along the Ox axis. Then, outside the layer system, the electromagnetic field is given by the equations

$$\bar{E}_1 = \bar{E}_0 \{ \exp [i(k_1 x - \omega t)] + r_R \exp [i(-k_1 x - \omega t)] \} \quad \text{for } x < 0, \quad (12)$$

$$\bar{E}_3 = \bar{E}_0 t_R \exp [i(k_3 x - \omega t)] \quad \text{for } x > d. \quad (13)$$

Here, \bar{E}_0 denotes a real constant vector and $k_i^2 = \epsilon_i \mu_i \omega^2 + i \mu_i \sigma_i \omega$. The formulae for the vector \bar{H} are analogous and may be omitted here. Since the equations (9)

are invariant with respect to the transformation (10), the functions given by formulae

$$\bar{E}_1' = \bar{E}_0 \{ \exp [i(k_1'x + \omega t)] + r_R' \exp [i(-k_1'x + \omega t)] \}, \quad (14)$$

$$\bar{E}_3' = \bar{E}_0 t_R' \exp [i(k_3'x + \omega t)], \quad (15)$$

also are solutions of the Maxwell equations. Here, the quantities k_i' , r_R' , t_R' are obtained by changing the signs of all the conductivities σ in the corresponding quantities k_i , r_R , t_R . For example,

$$k_1' = \sqrt{(\epsilon_1 \mu_1 \omega^2 - i \mu_1 \sigma_1 \omega)}.$$

In the same way the formulae for the vectors \bar{H}_i are obtained. Now, passing to vectors complex conjugate to \bar{E}' , \bar{H}' , we have the solution

$$\bar{E}_1'^* = \bar{E}_0 \{ \exp [-i(k_1'^*x + \omega t)] + r_R'^* \exp [-i(-k_1'^*x + \omega t)] \},$$

$$\bar{E}_3'^* = \bar{E}_0 t_R'^* \exp [-i(k_3'^*x + \omega t)].$$

It follows from the formula for k_i that $k_i' = k_i^*$ or $k_i'^* = k_i$, so that the last formulae assume the form

$$\bar{E}_1'^* = \bar{E}_0 \{ \exp [i(-k_1x - \omega t)] + r_R'^* \exp [i(k_1x - \omega t)] \}, \quad (16)$$

$$\bar{E}_3'^* = \bar{E}_0 t_R'^* \exp [i(-k_3x - \omega t)]. \quad (17)$$

The individual terms of these equations have the following significance: The second term of formula (16) represents a wave with the amplitude $\bar{E}_0 r_R'^*$ falling on the system from the left, whilst formula (17) stands for a wave incident on the system from the right and having the amplitude $\bar{E}_0 t_R'^*$. The first term of equation (16) represents a wave with the amplitude \bar{E}_0 propagating out of the layer system in the direction to the left. This means: *Reversing the reflected ray with a simultaneous change of its amplitude from $\bar{E}_0 r_R$ to $\bar{E}_0 r_R'^*$, and reversing at the same time the refracted ray with a change of its amplitude from $\bar{E}_0 t_R$ to $\bar{E}_0 t_R'^*$, one obtains the reversed original ray propagating with the amplitude \bar{E}_0 in a direction inverse to that of the original ray, whilst the field on the right of the system equals zero.* In this way, it is possible to reverse rays in conducting media.

To derive equations corresponding to the relations (1)–(4) or (5)–(8), respectively, we write the total field of the reversed refracted ray given by formula (17) in the form

$$\bar{E}_{1t} = \bar{E}_0 t_R'^* t_L \exp [i(-k_1x - \omega t)], \quad (18)$$

$$\bar{E}_{3t} = \bar{E}_0 t_R'^* \{ \exp [i(-k_3x - \omega t)] + r_L \exp [i(k_3x - \omega t)] \}. \quad (19)$$

Index t indicates the field of the transmitted ray to be under consideration. Likewise the total field of the reversed reflected ray given by the second term of the formula (16) has the form

$$\bar{E}_{1r} = \bar{E}_0 r_R'^* \{ \exp [i(k_1x - \omega t)] + r_R \exp [i(-k_1x - \omega t)] \}, \quad (20)$$

$$\bar{E}_{3r} = \bar{E}_0 r_R'^* t_R \exp [i(k_3x - \omega t)]. \quad (21)$$

Comparing the formulae (16)–(21) leads to the equations

$$r_R'^* r_R + t_R'^* t_L = 1, \quad (22)$$

$$r_R'^* t_R + t_R'^* r_L = 0. \quad (23)$$

For the case of the original ray falling on the system from the right-hand medium, quite analogous relations are obtained:

$$r_L'^* r_L + t_L'^* t_R = 1, \quad (24)$$

$$t_L'^* t_L + t_L'^* r_R = 0. \quad (25)$$

It is possible to put equations (22)–(25) into yet another form, corresponding to that of equations (1)–(4). The operations of applying dashes and asterisks being commutative, it holds $r'^* = r^{**}$; further we have $r'' = r$, $r^{**} = r$, etc. By a suitable distribution of these operations over the terms of equations (22)–(25) we get

$$r_R r_R'^* + t_R t_L'^* = 1, \quad (26)$$

$$r_R t_R'^* + t_R r_L'^* = 0, \quad (27)$$

$$r_L r_L'^* + t_L t_R'^* = 1, \quad (28)$$

$$r_L t_L'^* + t_L r_R'^* = 0. \quad (29)$$

Any of these equivalent forms represents a generalization for conducting media of the known principles of reversibility. Equations (1)–(4) and (5)–(8) follow as special cases thereof:

(a) For a simple dielectric–dielectric boundary $\sigma = 0$, $r' = r$, $r^* = r$, etc., so that equations (26)–(29) assume the form (5)–(8).

(b) In the case of simple metal–dielectric or metal–metal boundary it follows from the Fresnel coefficients $r'^* = r$, etc. Thus, equations (26)–(29) come into the form (5)–(8).

(c) In the case of a system of dielectric layers embedded in dielectric media $\sigma = 0$, $r' = r$, $r'^* = r^*$, etc. Equations (26)–(29) assume the form (1)–(4).

It will be noticed that it is possible to obtain the relations (26)–(29) directly from the formulae representing electromagnetic waves without deriving equations (22)–(25), by applying the dash and asterisk operations to the formulae (18)–(21) instead to (12), (13) and comparing the resulting solutions of Maxwell's equations with equations (12) and (13).

From the reversibility equations it is possible to derive the interesting relations

$$\frac{t_R'^*}{t_R} = \frac{t_L'^*}{t_L},$$

$$r_R r_R'^* = r_L r_L'^*.$$

It is of some importance to note a common origin was chosen on the Ox axis for both of the outside media, i.e. the amplitudes of all the rays have been referred to the point $x = 0$. If, instead of formula (13), another expression for the wave travelling in the medium 3 were chosen, viz.

$$\bar{E}_3 = \bar{E}_0 t_R \exp \{i[k_3(x-d) - \omega t]\}$$

and correspondingly in the subsequent equations, the relative amplitudes t_R , r_L would now be measured at the point $x = d$. All the relations for r , t so far derived also hold in this case.

4. CONCLUSIONS

The possibility of reversing light in conducting media has been considered from the standpoint of the invariance of the Maxwell equations. A theorem has been arrived at, stating that, contrary to, or as an extension of, the existing opinions, it is formally possible to reverse light rays even in conducting media and make them interfere in the sense of the classical Stokes principle of reversibility, provided that proper adjustments are made to the reflection and transmission coefficients of the reversed rays. In addition to taking their complex conjugate values, as claimed by Stokes, these adjustments consist in changing the signs of all the conductivities σ , explicitly or implicitly involved in the classical formulae for optical boundaries and thin films (an operation denoted in this paper by dashing).

The general theorem on reversibility, expressed by equations (22)–(25), or (26)–(29), and valid for homogeneous as well as inhomogeneous stratified conducting media, includes as special cases the Stokes principle and its extension by Knittl to homogeneous dielectric multilayers. It also throws light on a problem pointed out by the latter in connection with reversibility on metal–dielectric boundary.

For the sake of simplicity a linearly polarized wave and perpendicular incidence have been considered only, but the results maintain their validity even in the general cases.

Since the Maxwell equations have been taken as the starting point of the present paper, the possibility of reversing rays is formulated as a theorem, not a principle. It is to be interpreted as a formal result, valid within the framework of the macroscopic electromagnetic theory, with no claims on the real mechanism of energy dissipation inside conducting media. However, it is of importance for the macroscopic theory of stratified media, which is the present-day theoretical basis for most of the applications of thin film optics.

ACKNOWLEDGMENT

The author is indebted to Dr. Knittl for drawing his attention to the problem of reversibility in optics and for exchanging views on the subject. The results the latter has obtained on the basis of the generalized principle will be given in a separate paper to follow.

Nous établissons un théorème d'après lequel il est possible de renverser le sens des rayons lumineux dans les milieux absorbants au sens du principe classique de Stokes après modification convenable des amplitudes des rayons réfléchi et réfracté. Nous démontrons que le principe de Stokes et son extension pour les couches diélectriques homogènes ne sont que des cas spéciaux de notre théorème général de réversibilité.

Es wird ein Theorem abgeleitet, welches die Möglichkeit der Umkehrung der Lichtstrahlrichtungen in beliebigem System von leitenden Schichten im Sinne des Stokesschen Reversibilitätsprinzips beweist. Es wird gezeigt, dass die Amplituden des reflektierten und des durchgegangenen Strahles dabei in geeigneter Weise modifiziert werden müssen. Es wird ebenfalls bewiesen, dass das Stokessche Reversibilitätsprinzip und dessen Erweiterung für Systeme von dielektrischen Schichten als Spezialfälle des allgemeinen Reversibilitätstheorem angesehen werden können.

APPENDIX

In using the theorem of reversibility in thin films optics the case of normal incidence on a system of homogeneous layers is most often considered. The application on the relative amplitudes r, t of the operation denoted by dashing offers no difficulties in this case. In the case of oblique incidence, however, some care must be taken in the dashing, since expressions such as $\sqrt{(k_t^2 - k_m^2 \sin^2 \alpha_m)}$ occur in the formulae.

To show which of the two possible roots should be taken after applying the dash, let us suppose that in the situation indicated by figure 2 at least one of the wave numbers k_1, k_3 is complex and that the angle of incidence α_1 is not equal to zero. Let one of the angles α_1 and (refraction angle) α_3 be real, say α_1 . Then, the refraction angle α_3 is generally complex and the wave in the medium 3 inhomogeneous. Consider a linearly polarized incidence wave with \vec{E} normal to the plane of incidence. After applying the operation of dashing on the vectors

of the electromagnetic field, one deduces by the same method as in the case of normal incidence equations analogous to the equations (14), (15):

$$\bar{E}_1' = \bar{E}_0 \{ \exp [i(k_1' \cos \alpha_1 x + k_1' \sin \alpha_1 z + \omega t)] + r_R' \exp [i(-k_1' \cos \alpha_1 x + k_1' \sin \alpha_1 z + \omega t)] \} \quad (a)$$

$$\bar{E}_3' = \bar{E}_0 t_R' \exp \{ i[(k_3 \cos \alpha_3)' x + (k_3 \sin \alpha_3)' z + \omega t] \}, \quad (b)$$

where

$$k_3 \sin \alpha_3 = k_1 \sin \alpha_1, \quad k_3 \cos \alpha_3 = \sqrt{(k_3^2 - k_1^2 \sin^2 \alpha_1)},$$

so that

$$(k_3 \sin \alpha_3)' = k_1' \sin \alpha_1, \quad (k_3 \cos \alpha_3)' = \sqrt{(k_3'^2 - k_1'^2 \sin^2 \alpha_1)}.$$

The expression $\sqrt{(k_3'^2 - k_1'^2 \sin^2 \alpha_1)}$ admits two values: $K_1 = [\sqrt{(k_3'^2 - k_1'^2 \sin^2 \alpha_1)}]^*$ and $K_2 = -[\sqrt{(k_3'^2 - k_1'^2 \sin^2 \alpha_1)}]^*$, since $k_1' = k_1^*$, $k_3' = k_3^*$ and since $\sin \alpha_1$ is real. It is possible to insert any of the two K_1 's, K_2 's into equation (b), the vectors \bar{E}_1' , \bar{E}_3' together with the corresponding \bar{H}_1' , \bar{H}_3' not ceasing to fulfill the Maxwell equations. The choice of the appropriate root is given by the condition that the complex conjugate value of the expression (b) may represent the reverted transmitted wave. This will be reached by inserting K_1 . Since the relations

$$(k_3 \sin \alpha_3)^* = k_1 \sin \alpha_1, \quad (k_3 \cos \alpha_3)^* = k_3 \cos \alpha_3$$

are then valid, the vector $\bar{E}_3'^*$ does represent a wave propagating in a sense opposite to that of the transmitted wave.

The case of real k_1 's, k_3 's must be considered as the limit of the foregoing for $\sigma_1 \rightarrow 0$, $\sigma_3 \rightarrow 0$. When applying the dash on the now real or pure imaginary expression $\sqrt{(k_3^2 - k_1^2 \sin^2 \alpha_1)}$, the root $K_1 = [\sqrt{(k_3^2 - k_1^2 \sin^2 \alpha_1)}]^*$ must be taken to obtain the reverted wave. So, one has in each case $(k_3 \cos \alpha_3)^* = k_3 \cos \alpha_3$. For real k_1 's, k_3 's it might seem more natural to put $\sqrt{(k_3'^2 - k_1'^2 \sin^2 \alpha_1)} = \sqrt{(k_3^2 - k_1^2 \sin^2 \alpha_1)}$ instead of $\sqrt{(k_3'^2 - k_1'^2 \sin^2 \alpha_1)} = [\sqrt{(k_3^2 - k_1^2 \sin^2 \alpha_1)}]^*$. That, however, would lead to the root K_2 which does not give a wave propagating in the appropriate sense.

Of particular interest in this sense is the case of total reflection on a simple boundary. Since $\sigma = 0$ here, and the Fresnel coefficients are known to be complex, one might consider equations (1)-(4) as the appropriate expression of the reversibility principle. However, proceeding along the lines of this appendix, we are led to equations (5)-(8). Both the p - and the s -components of the Fresnel amplitudes may be found to satisfy these relations.

We restricted our consideration to a real α_1 without loss of generality, as all the inhomogeneous waves propagating within the layer-system originate from homogeneous waves incident on the first layer. Thus, it is possible to replace the expression $k_1 \sin \alpha_1$ by $k_0 \sin \alpha_0$, α_0 being a real angle. All that has been said about $k_3 \cos \alpha_3$ maintains its validity for $k_l \cos \alpha_l$, where l is a suffix characterizing an arbitrary film of the system.

A similar analysis could be made for an incident wave which is polarized in the plane of incidence.

REFERENCES

- [1] VAŠÍČEK, A., 1960, *Optics of Thin Films* (Amsterdam).
- [2] KNITTL, Z., 1957, *Czech. J. Phys.*, **7**, 427.
- [3] FRAGSTEIN, C., 1950, *Phys. Blätter*, **6**, 153.
- [4] KNITTL, Z., 1959, *Czech. J. Phys.*, **9**, 133.
- [5] VLASOV, A., 1955, *Macroscopic Electrodynamics* (Moscow) (in Russian).



A simple after image method demonstrating the involuntary multidirectional eye movements during fixation

by F. J. VERHEIJEN

Laboratory of Comparative Physiology, University of Utrecht,
The Netherlands

(Received 20 July 1960)

An after image method is described with which the following features of the eye movements during fixation can be demonstrated in an easy way to a large audience: (a) the drifts; (b) the flicks and the inhibition of vision during the flicks; (c) the multidirectional character of both drifts and flicks; (d) the coordination of the movements in both eyes; and (e) the order of magnitude of the movements.

It was observed early in the study of visual fixation that it is impossible to keep an after image motionless, and it has been concluded that during fixation on a small target the human eyes are not stationary but in constant motion (see e.g. Dodge [1], Öhrwall [2]). At that time it was suggested that the function of these movements is to prevent adaptation in the receptors and to keep an image on the fovea.

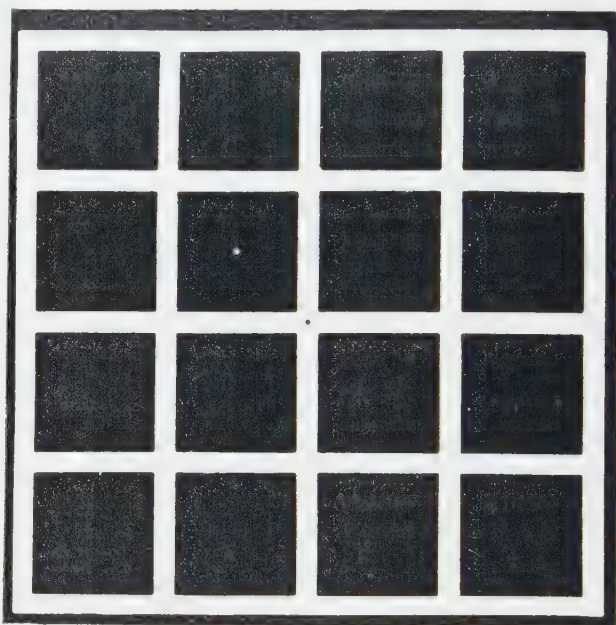
Recently these movements have been recorded and analysed (Ratliff and Riggs [3], Ditchburn and Ginsborg [4], Drischel and Lange [5], Ditchburn [6, 7], and others). The old suggestion about the function of these micro-ocular movements are confirmed by this recent work: the stabilization of the retinal image results in a strong impairment of perception both with respect to quantity—form—(Ditchburn and Ginsborg [8], Riggs *et al.* [9], Cornsweet [10], Ditchburn *et al.* [11], and with respect to quality—colour—(Ditchburn [12, 7]), while the movements are, at least partly, controlled by foveal feedback (Ditchburn and Ginsborg [4], Cornsweet [10], Drischel and Lange [5], Nachmias [13]).

In view of the basic significance of these movements it was thought desirable to have a simple method for demonstrating them to a large group of persons, for instance during a laboratory course. The simple after-image method reported in the present paper demonstrates some features of the micro-ocular movements in an impressive way.

Use is made of the stimulus pattern often used for the demonstration of the simultaneous brightness contrast phenomenon. As shown in the figure a black point is added at the central crossing of the middlemost horizontal and the middlemost vertical white line; a white point is placed in the centre of an adjacent dark square. The dimensions of the white lines and the dark squares are more or less arbitrary. The black and the white point should be as small as possible provided they are visible. The stimulus pattern is viewed under average daylight or artificial illumination conditions. Sufficient immobilization of the head is obtained by supporting it by both hands while the elbows are resting on a table.

If the eyes look steadily for some tens of seconds at the black point, and be then directed at the white point, the dark negative after image of the white line pattern will be seen. Closer examination will show that the dark line pattern of the after image is not stationary but that it is moving about irregularly in spite of the fact that the white point is steadily fixated. After some time the after image becomes indistinct. If the fixation of the white point is further continued for some seconds, and if after that the gaze be turned back towards the black point, the after image will reappear, moving about as before.

The phenomenon can be easily demonstrated to a large audience by projecting a slide of the stimulus pattern. The intensity contrast between the white lines and the dark squares should not be too strong: dark grey for the squares generally proves to provide the best conditions.



Pattern for demonstrating the micro-ocular movements during fixation. Proceed as follows: first look for some tens of seconds at the central black point, then transfer the gaze and look at the white point in one of the adjacent dark squares. The dark after image of the white line pattern should be seen in constant motion. For further details see text.

Some features of the micro-ocular movements that have been demonstrated in the above mentioned recent work can easily be perceived.

(a) The drifts manifest themselves by a continuous shift of the after image pattern. More details of these movements can be detected by paying attention, for instance, to the changing position of the small dark square, formed by the after image of the crossing of the middlemost horizontal and the middlemost vertical white line, relative to the white fixation point: the dark square appears to change its position relative to the white fixation point in an irregular but continuous way.

(b) The flicks require closer observation of the above mentioned small dark square and the white fixation point. It will be discovered that, at time intervals of one or more seconds, their mutual position is abruptly changed. The movement causing this sudden position change is a frequently hardly perceptible interruption of their continuous changes of position. Ditchburn [6] demonstrated an inhibition of vision during the flicks.

(c) The drifts and the flicks occur in all directions.

(d) The fact that the movements are identical whether they are observed with one eye or with both eyes demonstrates that the drifts and flicks of both eyes are coordinated.

(e) The order of magnitude of the micro-ocular movements can be estimated by increasing the distance at which the pattern is viewed until the mutual movements of the after image and the fixation point are so large that the relative position changes of the fixation point sweep over the whole width of the dark after-image bands. With a band width of three mm this is generally found to be the case at a distance of about one metre, indicating an order of magnitude of the micro-ocular movements of about ten minutes of arc.

On décrit une méthode par images consecutives avec laquelle on peut montrer facilement à une nombreuse assistance les caractères suivants des mouvements des yeux pendant la fixation: (a) les drifts (dérive); (b) les flicks (les mouvements rapides) et l'inhibition de la vision pendant ceux-ci; (c) le caractère désordonné (directions multiples) des drifts et des flicks; (d) la coordination des mouvements des deux yeux; (e) l'ordre de grandeur des mouvements.

Es wird eine Nachbildmethode beschrieben, mit der man die folgenden Eigenschaften der Augenbewegung während des Fixierens in einfacher Weise einem grossen Hörerkreise vorführen kann: (a) Die Deviationen (drifts); (b) die Rucke (flicks) und die Hemmung des Sehens während der Rucke; (c) die ständige Richtungsänderung der Deviationen und Rucke; (d) die Koordinierung der Bewegung beider Augen und (e) die Grössenordnung der Bewegungen.

REFERENCES

- [1] DODGE, R., 1907, *Psychol. Rev.*, Suppl. 8, No. 4; 1909, *Z. Psychol.*, **52**, 321 (German translation).
- [2] ÖHRWALL, H., 1912, *Skand. Arch. Physiol.*, **27**, 65.
- [3] RATLIFF, F., and RIGGS, L. A., 1950, *J. exp. Psychol.*, **40**, 687.
- [4] DITCHBURN, R. W., and GINSBORG, B. L., 1953, *J. Physiol.*, **119**, 1.
- [5] DRISCHEL, H., and LANGE, C., 1956, *Pflüg. Arch. ges. Physiol.*, **262**, 307.
- [6] DITCHBURN, R. W., 1955, *Opt. Acta*, **1**, 171.
- [7] DITCHBURN, R. W., 1959, 20th Thomas Young Oration: Physical Society Year Book, p. 56.
- [8] DITCHBURN, R. W., and GINSBORG, B. L., 1952, *Nature, Lond.*, **170**, 36.
- [9] RIGGS, L. A., RATLIFF, F., CORNSWEET, J. C., and CORNSWEET, T. N., 1953, *J. opt. Soc. Amer.*, **43**, 495.
- [10] CORNSWEET, T. N., 1956, *J. opt. Soc. Amer.*, **46**, 987.
- [11] DITCHBURN, R. W., FENDER, D. H., MAYNE, S., and PRITCHARD, R. M., 1956, *Proc. phys. Soc. Lond. B*, **69**, 1165.
- [12] DITCHBURN, R. W., 1957, Paper No. 15, Symposium, Visual Problems of Colour.
- [13] NACHMIAS, J., 1959, *J. opt. Soc. Amer.*, **49**, 901.



The sensitivity performance of the eye, in the presence of various limiting mechanisms of different origin

by M. v. MENTS

Ministry of Defence, Scientific Department,
Hakirya, Tel-Aviv, Israel

(Received 16 June 1961)

The eye is able to distinguish two neighbouring domains of comparable luminance, only if the signal to noise ratio, under well specified conditions, exceeds a certain minimum value. The noise can be due to different sources. The class of cases, wherein the statistical fluctuations in the number of messages sent from the retina inwards set a natural limit to perceptibility, has received ample attention.

In looking at a scene with the aid of an intermediate device (e.g. an image intensifier), at least two other phenomena may still restrict the perceptibility. The first phenomenon is a kind of amplifier noise, manifesting itself as a noise background on the ultimate viewing screen. The second phenomenon is the occurrence of a low number of events in one of the intermediate stages of the compound vision process in question.

These two kinds of noise are elucidated and the sensitivity performance of the eye in their presence is calculated.

1. INTRODUCTION

It has been established, that Statistical Fluctuations in the Primary Photoprocess[†] make a very significant contribution to the limitations in visual perceptibility[‡] at low or fairly low, light levels [1-3]. On the basis of both experimental and theoretical studies, relationships have been established between the luminance (L), the angular size (α) of a test object, and the lower limit of perceptible contrast (C) [4-7].

However, actual results bring to light, especially in the region of low contrast and small angles of perception, other mechanisms, which also limit perceptibility, such as optical defects, effects of memory, and the finite sizes of the cells in the retina of the eye.

But, to quote Rose [6]: "The match between the eye and an ideal device also provides at minimum a good first approximation to an understanding of the performance of the eye in terms of fluctuations in the primary photo process. Depending mostly on how well further independent measurements of the quantum efficiency of the eye agree with the quantum efficiencies deduced in this paper, the analysis of performance in terms of fluctuations may be appreciably better than a first approximation."

[†] Under 'Statistical Fluctuations in the Primary Photoprocess' may be understood the statistical fluctuations in the arrival of photons at the retina of the eye. This will henceforth be referred to as: The S.F.P.P. mechanism.

[‡] Perceptibility may be defined as the ability of the eye to distinguish two neighbouring 'patches' of almost equal luminance.

On the basis of these statements one might endeavour to treat visual problems as being based on an idealized† eye, and, at a certain stage, introduce corrections in order to adapt the idealized to the real eye.

So far it has been assumed that the scene is observed with the naked eye. But as soon as a scene is viewed with the help of intermediate devices (as in the case of television), complications arise in determining the factors which limit the eye's perceptibility [6]. For in case of such an 'armed' eye, new limiting mechanisms may enter the picture and intermingle with those previously mentioned with respect to the naked eye.

A general scheme of relationships between L , α and C would be quite impossible for any 'armed' eye, if one could not start from a simplified theory with regard to the naked eye.

The most obvious way is again to use the idealized eye. It will be demonstrated in the following sections that this will enable the eventual effects of new limiting mechanisms, as caused by the nature of the intermediate device(s), to be introduced in a smooth way.

In the last resort one may, in discussing the armed eye, switch over from the idealized to the real eye in the same way as is usual for the naked eye. There is a strong justification for this sequence of manipulations in the previously mentioned good match between the real eye and the idealized eye, and, moreover, in the ultimate results obtained in this way for the armed eye, which agree remarkably well with reality.

2. GLOSSARY OF VARIOUS TERMS RELATING TO EYE BEHAVIOUR

In the previous section, various sorts of 'scientific eyes' have been mentioned, and definitions have been added in the text.

In order to facilitate a quick reading, they are repeated here with further definitions to be used in the following sections:

Naked eye:	eye looking directly at a scene.
Armed eye:	eye, looking at a scene with the help of an intermediate auxiliary device (such as television).
Idealized eye:	eye, whose perceptibility is limited by the S.F.P.P. mechanism only.
Real eye:	the ordinary human eye as it actually sees and distinguishes.
Simplified eye:	eye, whose pupil diameter and integration time do not vary with the scene luminance or with the size of the object.
Perceptibility:	ability of the eye to distinguish two neighbouring 'patches' of almost equal luminance.
S.F.P.P.:	statistical fluctuations in the primary photo process, meaning the statistical fluctuations in the arrival of photons on the retina of the eye.
A.N.:	amplifier noise, being introduced in one or more of the stages of a compound vision amplification process.
L.N.E.I.:	lowest number of events in one of the intermediate stages of a compound vision amplification process.
Vision amplification:	every action which ultimately helps the eye to distinguish more details.

† An idealized eye is an eye whose perceptibility is limited by the S.F.P.P. mechanism only.

3. THE CONNECTION BETWEEN THE PROPERTIES OF THE IDEALIZED EYE AND THE REAL ARMED EYE

For an idealized eye, that is moreover simplified (constant diameter of the pupil and a constant integration time t) Rose [5] arrived, on a purely mathematical basis, at the relation:

$$L \alpha^2 C^2 = ct. \quad (1)$$

Because of very obvious deviations of the real eye from this idealized eye, this relation may be used to indicate only the trend of the connection among the magnitudes involved. This is dealt with in the same basic article [5], where results for the real eye are represented by graphs obtained with the help of experiments. One of these graphs is depicted in figure 1.

However, it should be borne in mind that all these properties of both the idealized and the real eye apply strictly for the naked eye only.

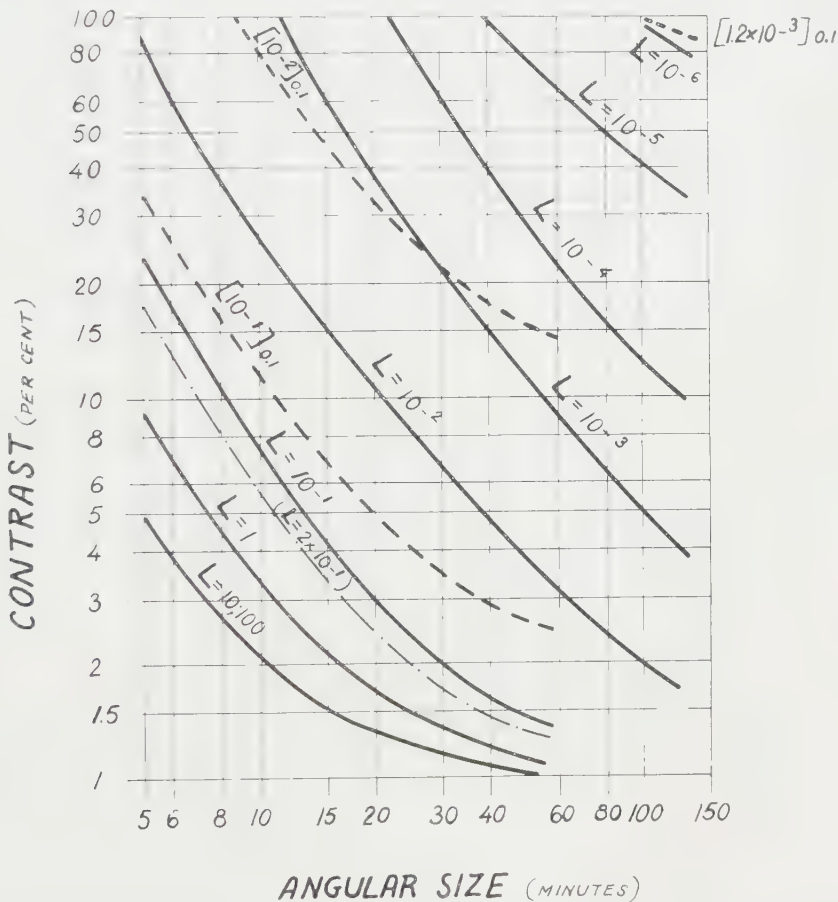


Figure 1. Performance data for the eye, with the luminance L (in foot lambert) as a parameter (full lines). The dotted lines apply to the presence of a noise background of 0.1 foot lambert.

As soon as intermediate devices are used, resulting in the creation of the armed eye, the principles underlying the simple theory of the naked eye cease to be the only valid ones.

Some well-known intermediate devices are a fluoroscopic x-ray device, an image converter, an image intensifier, a television kinescope, a telescope or a photograph with or without the help of an additional magnifying optical instrument.

By applying any such intermediate device, a situation may be created in which the final perceptibility is limited by 'Amplifier Noise' (A.N.) being introduced in one or more of the stages of the compound vision amplification process, especially if electronic devices are used. An example of 'A.N. limited vision' is an image on an image converter screen with excessive fading caused by field emission current. Although such A.N. mechanisms have been extensively dealt with in the field of electronic amplification and the associated noise problems, its effects in the case of vision are dealt with only rather superficially [6, 8, 9].

Another limiting mechanism can be the 'Lowest Number of Events occurring during the integration time of the eye in one of the Intermediate stages' (L.N.E.I.) of the compound vision amplification process. An example of 'L.N.E.I. limited vision' may be experienced when watching a film from the front row of a cinema. Causes of L.N.E.I. limiting mechanisms have already received attention elsewhere [10, 11].

When neither L.N.E.I. nor A.N. mechanisms is present, the 'Statistical Fluctuations in the Primary Photoprocess' determine the sensitivity performance of the idealized eye (S.F.P.P. mechanism)[†].

The counterpart in electronics of the S.F.P.P. mechanism would be the case where noise in the indicating instrument is the limiting factor.

This is an unfavourable situation, which should be avoided wherever possible. The desired improvement is most frequently achieved by increased 'noiseless' amplification.

The same is very often true of vision. In a majority of cases where the eye and its properties constitute the limiting elements in a certain case of vision, the conditions can also be improved by 'amplification'[‡].

The means of accomplishing this visual amplification may be subdivided into two distinct groups:

- I. 'Perfect noiseless amplification', to be accomplished either
 - (a) by the diminution of the distance between the eye and the object, or
 - (b) by better lighting of the object. Note that (b) increases the light per unit area of the retina while (a) does not.

The perceptibility after the amplification, remains described by a relation as depicted in figure 1; one has only to switch over to the new α or L value, to determine the new values of the lower limit of perceptible contrast C .

- II. Amplification, obtainable with the aid of an intermediate relaying, magnifying, and/or intensifying device of the optical and/or electron optical type.

The second group represents the type of amplification which creates the armed eye, and some examples have already been dealt with at the beginning of this section.

[†] The L.N.E.I. mechanism becomes identical with the S.F.P.P. mechanism, when the stage of relaying impressions from the retina inwards, is the one with the 'lowest number of events'.

[‡] In the field of vision, useful amplification may be defined as every action which ultimately helps the eye to distinguish more details.

It may or may not introduce its inherent noise, giving rise to the limiting A.N. and L.N.E.I. mechanisms already defined.

From all these considerations, it appears that the results of figure 1 are true only for the S.F.P.P. class (the naked eye, or Group I amplification). As soon as A.N. and/or L.N.E.I. mechanisms are involved (Group II amplification), the sensitivity performance may be worse than figure 1 leads to believe. In these comparisons, the parameter L in figure 1 should be related generally to the final image as it is viewed by the eye, and not to the luminance of the scene before the vision amplification.

The purpose of the simple theory outlined in the following sections is to illustrate ultimately the relationship between L , α and C , both theoretically and graphically, for the Group II amplification.

4. GENERAL THEORY OF THE S.F.P.P. LIMITING MECHANISM

The number of quanta N_e , effectively relayed by the retina of the eye during the integration time t_i , was derived by Rose [5] to be

$$N_e = \frac{m}{4} \theta t_i \alpha^2 D^2 L, \quad (2)$$

where

m = number of quanta per second corresponding with one lumen of the light used;

θ = quantum yield of the eye;

α = angular size of the object (radians);

D = diameter of the eye pupil (ft);

L = Luminance of the scene (foot lambert).

The lowest perceived contrast is defined by

$$C = \frac{\Delta L}{L} = \frac{\Delta N_e}{N_e} = \frac{k \sqrt{(\Delta^2 N_e)}}{N_e} = \frac{k \sqrt{(N_e)}}{N_e}, \quad (3)$$

where k is the threshold signal-to-noise ratio, and ΔL the lowest possible luminance difference allowing for the distinguishing of two neighbouring patches of luminance L and $L + \Delta L$ respectively.

By combining equations (2) and (3), one obtains

$$L \alpha^2 C^2 = \frac{4k^2}{m \theta t_i D^2} = S(L, \alpha). \quad (4)$$

This relation implies—in contrast with equation (1) and the assumptions leading to it—that the factors k , θ , t_i and D are all functions of L and α . So, although the relation (4) arose from S.F.P.P. considerations, it is sufficiently general to represent the real (naked) eye. A practical representation of equation (4), valid for a special set of conditions, is depicted by figure 1 (full lines). This theory and its practical results only hold in the case of S.F.P.P. class vision, i.e. for the naked eye and for the Group I amplification.

It holds for the Group II amplification† only when the following two conditions are fulfilled (see figure 2).

† Although the Group II amplification also includes cases where there is no screen, terms relating to the cases where there is a screen are used for reasons of convenience. This is because more precise expressions such as: ‘the ultimate image the eye is looking at’ do not at all contribute to a better comprehension.

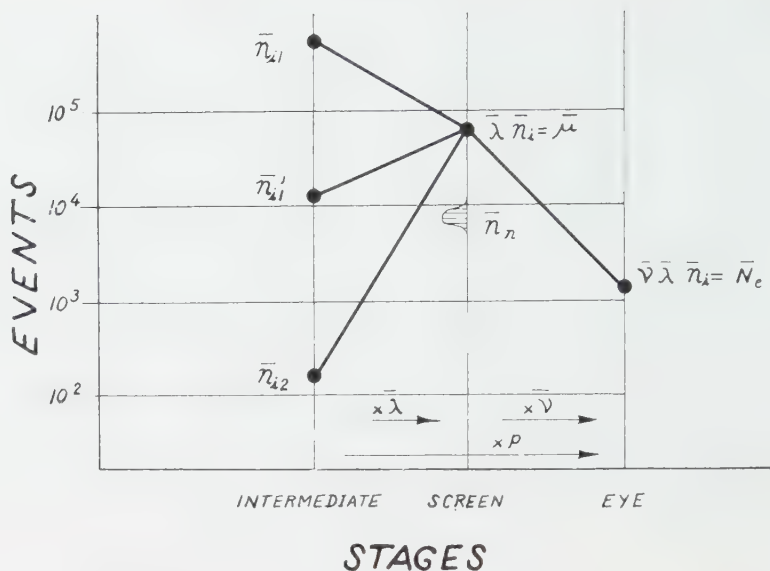


Figure 2. Schematic illustration of possible agents that may limit the sensitivity performance of the eye: the Statistical Fluctuations in the Primary Photoprocess (S.F.P.P.) represented by the number of events $\bar{v}\bar{\lambda}\bar{n}_i = \bar{N}_e$; the Amplifier Noise events n_n on the screen (A.N.), and/or the Lowest Number of Events \bar{n}_{i2} in an Intermediate stage (L.N.E.I.).

- (1) The number N_e , as defined by equation (1), is much smaller than the smallest number of events (occurring during the integration time t_i) in any one of the intermediate stages, the scene included [7].

Briefly: there is no L.N.E.I. mechanism limiting the perceptibility.

- (2) The noise background level on the screen is much smaller than the corresponding image level [10].

Briefly: there is no A.N. mechanism limiting the perceptibility.

In all cases of Group II amplification, let:

$[t_i]$ = notation for 'occurring during the integration time t_i ';

s.l.n. = stage with lowest number of events $[t_i]$: only those stages preceding the screen are considered;

N_e = number of events relayed from the retina inwards $[t_i]$;

n_i = number of events in s.l.n., in general, $[t_i]$;

n_{i1}, n_{i1}', n_{i2} = number of events in s.l.n., in particular cases, $[t_i]$;

n_{noise}, n_n = number of noise events on the screen $[t_i]$;

and further:

λ = multiplication of events from s.l.n. to screen;

ν = multiplication of events from screen to stage behind retina;

$p = \bar{\lambda}\bar{\nu}$ = multiplication of events from s.l.n. to stage behind retina;

μ = number of events on screen $[t_i]$.

As the eye catches only a small part of all photons emerging from the screen, and as further θ (quantum yield of the eye) is always *far less than unity*, it follows that

$$\nu \ll 1; \quad \overline{\Delta^2 \nu} = \nu. \quad (5)$$

It is further seen from figure 2 that the above-mentioned first condition implies:

$$\overline{N_e} \ll \overline{n_i} \quad \text{or} \quad \overline{n_i} \geq \overline{n_i'};$$

or

$$\lambda \bar{\nu} \ll 1. \quad (5a)$$

The second condition implies:

$$\bar{n}_{\text{noise}} \ll \bar{\mu} \quad \text{or} \quad \bar{n}_{\text{noise}} \leq \bar{n}_n. \quad (5b)$$

The r.m.s. value of N_e is generally a complicated function of $\overline{\Delta^2 n_i}$, $\overline{\Delta^2 \lambda}$ and $\overline{\Delta^2 \nu}$. Mandel [8] derived an expression for a special application, but the above magnitudes n_i , λ and ν were purposely defined in such a way, that his general expression for $\overline{\Delta^2 N_e}$ also holds in the present case:

$$\overline{\Delta^2 N_e} = \bar{\nu}^2 \bar{\lambda}^2 \overline{\Delta^2 n_i} + \bar{\nu}^2 \bar{n}_i \overline{\Delta^2 \lambda} + \bar{n}_i \bar{\lambda} \overline{\Delta^2 \nu}. \quad (5)$$

Furthermore [8]

$$\overline{\Delta^2 n_i} = \overline{n_i}; \quad \overline{\Delta^2 \lambda} \lesssim \bar{\lambda}. \quad (7)$$

By inserting (5), (5a) and (7) into (6), one obtains:

$$\overline{\Delta^2 N_e} \approx \bar{\lambda} \bar{\nu} \bar{n}_i \approx \overline{N_e}. \quad (8)$$

It was upon this equation (8), the condition relation for the S.F.P.P. class, that the last step of the basic relation (3) was founded.

5. THE THEORY OF LIMITATIONS AS CAUSED BY THE A.N. MECHANISM

If only the first condition mentioned in the previous section is fulfilled, but the second one is not, the noise background on the screen L_n (as caused by \bar{n}_n ; see figure 2), is comparable with or higher than, the fluctuations in the image level L (as caused by $\bar{\lambda} \bar{n}_i$).

Corrections have then to be applied to the previous set-up of relations between L , α and C , i.e. equations (2), (3) and (4). By the very reason of the limitations for the idealised eye being caused by the S.F.P.P. mechanism, one may easily verify the following new set of equations:

$$N_e' = \frac{m}{4} \theta' t_1' \alpha^2 D'^2 (L + L_n), \quad (9)$$

$$\Delta N_e' = \frac{m}{4} \theta' t_1' \alpha^2 D'^2 \Delta L' = k' \sqrt{(N_e')}, \quad (10)$$

and

$$C' = \frac{\Delta L'}{L} = \frac{\Delta N_e'}{N_e'}. \quad (11)$$

The prime refers to the situation in which the noise background L_n is present. By simple manipulations, one finds, on combining the last three equations:

$$\frac{L^2}{L + L_n} C'^2 \alpha^2 = \frac{4k'^2}{m\theta' t_1' D'^2}. \quad (12)$$

With the help of equation (4) one may write for the real eye:

$$\frac{4k'^2}{m\theta' t_1' D'^2} = S(L + L_n, \alpha) = (L + L_n) \alpha^2 C_{L+L_n}^2. \quad (13)$$

By inserting the result of equation (13) into equation (12) one obtains

$$C' = C_{L+L_n} \frac{L+L_n}{L}. \quad (14)$$

This relation simply implies that the increase in the lower limit of perceptible contrast is found by multiplying a fictitious contrast C_{L+L_n} by the factor $(L+L_n)/L$. In a rough approximation, it may be seen with the help of equation (1) that:

$$C' \approx C \sqrt{\left(\frac{L+L_n}{L}\right)}.$$

By way of example, a case will be dealt with in which a noise-background of 10^{-1} foot lambert is present on the screen. (It is assumed that the eye would otherwise have been the restricting element† and that the L, α, C relationship would have been as depicted by the full lines of figure 1.) The result of this A.N. situation is illustrated by the dotted lines in figure 1. It is obvious that the curves for 1 and 10 or 100 foot lamberts are hardly influenced. However, the new curve for 10^{-1} foot lambert, $[10^{-1}]_{0.1}$, is already shifted considerably higher than its position $L = 10^{-1}$ in the case of the S.F.P.P. mechanism without the noise-background. This curve has been obtained by multiplying the curve for $L = 2 \times 10^{-1}$ by two, according to equation (14).

As there is no distinguishable difference between the curves for $L = 10^{-1}$ and $L = 1.1 \times 10^{-1}$, the curve $[10^{-2}]_{0.1}$ has been obtained by multiplying the $L = 10^{-1}$ curve by eleven. Finally, one may find with the help of equation (14), that the lowest perceptible luminance in this case is about 1.2×10^{-3} foot lambert. At this luminance a 100 per cent contrast can be distinguished if the size of the object is of the order of 100 min or more.

6. THE THEORY OF LIMITATIONS AS CAUSED BY L.N.E.I. ALONE OR BY L.N.E.I. AND A.N. MECHANISMS TOGETHER

If the first condition for the S.F.P.P. class is not fulfilled, implying $\bar{n}_{i2} < N_e$ (see figure 2), the noise relation (6) does not change into the simple relation (8), because

$$\bar{\lambda}\bar{\nu} > 1, \quad (5c)$$

in contrast to the result of equation (5a).

By inserting the results of (5), (5c) and (7) into (6), one obtains

$$\Delta^2 N_e \approx (\bar{\lambda}\bar{\nu} + 1) N_e \approx (p + 1) N_e. \quad (15)$$

The magnification factor p , is defined by

$$p = \bar{\lambda}\bar{\nu} \quad (16)$$

and is in fact the amplification of events from the stage with the lowest number of events, to the stage behind the retina.

Under these conditions, and if, moreover, the noise background cannot be neglected, one obtains the following new set of relations:

† N.B. Such a condition is not relevant to the image intensification apparatus of Teves and Tol [10]. In their case, the statistical fluctuation in the number of x-ray quanta absorbed in the fluoroscopic screen restricts the quality of the vision, as may be seen in their figure 6. Such a typical L.N.E.I. case will be treated in the next section.

$$N_e'' = \frac{m}{4} \theta'' t_i'' \alpha^2 D''^2 (L + L_n), \quad (17)$$

$$\Delta N_e'' = \frac{m}{4} \theta'' t_i'' \alpha^2 D''^2 \Delta'' L = k'' \sqrt{(\Delta^2 N_e'')}, \quad (18)$$

$$\overline{\Delta^2 N_e''} = \frac{m}{4} \theta'' t_i'' \alpha^2 D''^2 [(p+1)L + L_n], \quad (19)$$

and

$$C'' = \frac{\Delta'' L}{L}. \quad (20)$$

The double prime refers to the situation in which the noise background L_n is present and, moreover, a L.N.E.I. limiting mechanism hampers the perceptibility.

Equation (19) is obtained by adding the squares of uncorrelated noise quantities, which follow from the results of equations (9) and (15).

Combination of equations (18), (19) and (20) yields:

$$\frac{4k''^2}{m\theta'' t_i'' D''^2} = \frac{C''^2 L^2 \alpha^2}{(p+1)L + L_n}. \quad (21)$$

But again, for the real eye one may put as a result of equation (4):

$$\frac{4k''^2}{m\theta'' t_i'' D''^2} = (L + L_n) \alpha^2 C_{L+L_n}^2. \quad (13 a)$$

Inserting (13 a) in (21), yields:

$$C'' = C_{L+L_n} \sqrt{\left(\frac{(L + L_n)(L + L_n + pL)}{L^2} \right)}, \quad (22)$$

and if, for instance,

$$L_n \ll L \quad \text{and} \quad p \gg 1,$$

simply

$$C'' \approx (\sqrt{p})C. \quad (23)$$

In the L.N.E.I. type image intensifier of Teves and Tol [10] (their figure 6), the events amplification factor p amounts to approximately ten.

For $p=0$, equation (22) is reduced to (14) as is to be expected.

7. CONCLUSION

Previous investigators established and explained the relationship between the luminance of a scene (L), the angular size of an object (α), and the lowest perceptible contrast (C), if the eye is not aided by colour differences. The theory outlined in the present paper may be considered as an extension of these ' L, α, C ' relations, in the presence of various well-defined noise mechanisms of different origin, appearing if vision amplification is applied with the aid of intermediate devices.

It should be emphasized that this theory applies likewise to a variety of ' L, α, C ' relations and that it is obviously not restricted to as special a relationship as depicted by figure 1. A practically occurring set of ' L, α, C ' relations depends on various factors: the colour of the light in question, the form of the object, whether or not the location of the object is known to the observer, and the adaptation time of the eye.

No attention has been paid to cases in which there are, for example, *two* stages with the same lowest number of events. (This may be the case for normal

radiography; see Teves [10], figure 7). It follows both from Mandels compound noise relation [11] (his equation (6)), and also from equation (15) if $p = 1$, that in this case a factor 2 appears in the square noise relations. This factor 2 appears on the same grounds in the development of minimum detectable power expressions for photoconductive and ideal thermal detectors.

L'œil est capable de distinguer deux plages voisines de luminance comparable, seulement si le rapport signal/bruit dépasse, dans des conditions bien définies, une certaine valeur minimum. Le bruit peut avoir des origines diverses. Les cas où les fluctuations statistiques du nombre des messages envoyés par la rétine vers l'intérieur constituent une limitation naturelle de la perception ont déjà été beaucoup étudiés.

Lorsqu'on regarde une scène à l'aide d'un système intermédiaire (p. ex. un amplificateur d'images), deux autres phénomènes au moins peuvent limiter encore la limite de perception. Le premier phénomène est une sorte de bruit d'amplificateur, qui se manifeste comme un fond de bruit sur l'écran sur lequel on regarde. Le second phénomène est l'apparition d'un petit nombre d'événements dans une des étapes intermédiaires du processus de vision composé dont il s'agit.

Ces deux sortes de bruits sont élucidés, et l'on calcule la sensibilité de l'œil en leur présence.

Das Auge kann zwischen zwei benachbarten Feldern vergleichbarer Leuchtdichte nur dann unterscheiden, wenn das Verhältnis vom signal zum Rauschen unter genau festgelegten Bedingungen einen gewissen Minimalwert übersteigt. Das Rauschen kann verschiedene Ursachen haben. Die Gruppe von Fällen, wo die statistischen Schwankungen in der Zahl der Informationen, die von der Netzhaut weitergeleitet werden, der Wahrnehmung eine natürliche Grenze setzt, ist oft untersucht worden.

Beim Sehen über ein Zwischenglied hinweg (z.B. über einen Bildverstärker) können wenigstens noch zwei andere Erscheinungen die Wahrnehmbarkeit beeinträchtigen. Die erste ist eine Art von Verstärkerrauschen, das sich selbst als Untergrundrauschen auf dem letzten Bildschirm bemerkbar macht. Die andere Erscheinung ist das Auftreten einer kleinen Zahl von Elementarvorgängen in einer der Zwischenstufen der zusammengeetzten Anordnung zur Bilderzeugung. Diese zwei Arten von Rauschen werden dargelegt und die dadurch bedingte Empfindlichkeitsleistung des Auges wird berechnet.

REFERENCES

- [1] BARNES, R. B., and CZERNY, M., 1932, *Z. Phys.*, **79**, 436.
- [2] HECHT, S., SHLAER, S., and PIRENNE, M. H., 1942, *J. gen. Physiol.*, **25**, 819.
- [3] SCHADE, O. H., 1948, *R.C.A. Rev.*, **9**, 5, 245, 490, 633.
- [4] BLACKWELL, H. R., 1946, *J. opt. Soc. Amer.*, **36**, 624.
- [5] ROSE, A., 1948, *J. opt. Soc. Amer.*, **38**, 196.
- [6] ROSE, A., 1948, *Advances in Electronics*, Vol. I (New York: Academic Press Inc.), p. 131.
- [7] JONES, R. C., 1959, *J. opt. Soc. Amer.*, **49**, 645.
- [8] ZWORKIN, V. K., and MORTON, G. A., 1954, *Television*, second edition (New York: John Wiley & Sons Inc.), p. 348.
- [9] SCHNEIDER, T., and SCHRANZ, P., 1958, *Z. angew. Math. Phys.* A, **9**, 251.
- [10] TEVES, M. C., and TOL, T., 1952, *Philips tech. Rev.*, **14**, 33.
- [11] MANDEL, L., 1959, *Brit. J. appl. Phys.*, **10**, 233.

The refractive index of materials from 0.2μ to 5μ †

by J. W. GATES, K. J. HABELL and A. JACKSON

Communication from the National Physical Laboratory, Teddington, England

(Received 7 September 1961)

A new technique is described for the measurement of refractive indices at selected wavelengths in the ultra-violet, visible and infra-red regions of the spectrum. The indices throughout this waveband may be obtained in one continuous run. The accuracy of measurement is better than ± 0.00003 in refractive index for good quality materials in favourable spectral regions, and is nowhere worse than ± 0.00010 in the range covered.

At the C.I.O. meeting in Brussels in 1958, K. J. Habell and K. W. Brittan described a technique of angle measurement using radial moiré-fringe gratings [1], which was also applied to the measurement of the dispersion of refractive

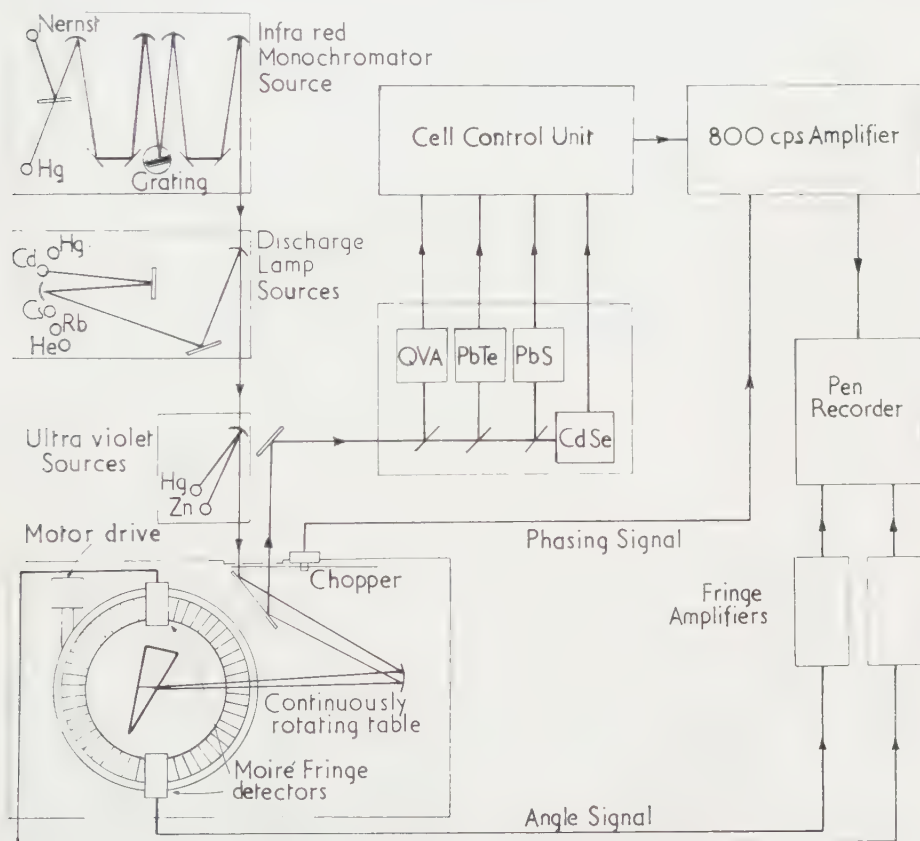


Figure 1. Recording refractometer.

† The work described in this paper was reported by J. W. Gates at the International Colloquium "Les Matériaux Optiques" on 5 July 1961 in Paris.

index of a glass prism in the visible part of the spectrum. The work-table carrying the angle gauge was made to rotate continuously at a steady rate, and its progress was registered continuously by observing and counting the passage of moiré fringes formed between a stationary index grating and a radial grating rotating with the work-table. As the faces defining the angle came successively into the same position, a beam of light was reflected into the detector and was recorded alongside the angle signal. The angle between two reflecting surfaces was then obtained as the interval between the two reflection signals in terms of the moiré fringe interval.

In the present arrangement, shown in figure 1, a development of the same technique is used [2]. The specimen is in the form of a prism of small refracting angle (30° or less) with a fully reflecting back surface, and is mounted on the rotating table, which rotates slowly at a steady rate. A beam of monochromatic light from the appropriate source, selected by manipulation of the auxiliary mirrors,

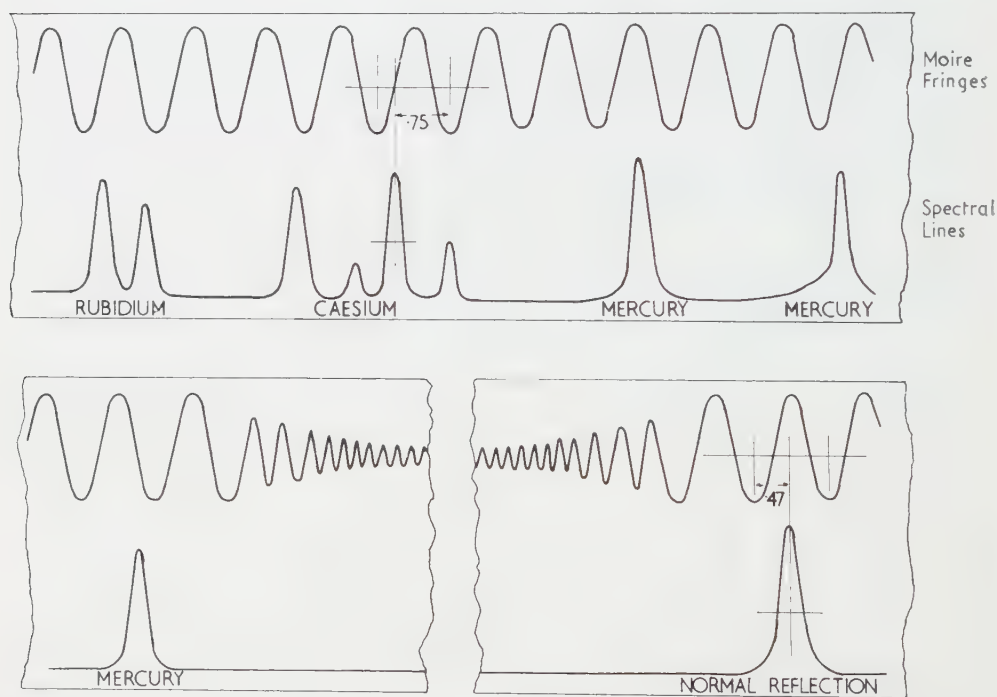


Figure 2. Spectral and angular records. (Only one of the two independent moiré fringe angular records is shown.)

illuminates the slit source at the focus of the collimating mirror, and then falls on the refracting face of the prism. After refraction, and reflection internally at the rear face of the prism, the beam emerges by refraction again at the front face and returns along its own path to the exit slit immediately below the entrance slit and thence to one of the detectors. (In the figure the entrance and exit slits are shown separated, for clarity.) The image of the entrance slit passes across the exit slit as the table and prism rotate, and the prism is then at the refracting angle for the wavelength of the light in use and is also at minimum deviation. The detector and amplifier produce a corresponding signal which is recorded

on the same chart as the moiré fringe angular signal (figure 2). The angular signal is obtained in the present arrangement from two moiré patterns formed between a radial grating of 10 800 lines mounted on the same spindle as the rotating table and two stationary index gratings at opposite ends of a diameter. The grating was made at the National Engineering Laboratory [3] and the angles obtained from the record can be interpolated accurately to better than 5 sec.

The line sources used at present are shown in table 1.

Table 1. Wavelengths of spectral lines in angstrom units.

Hg	Zn	Cd	He	Rb	Cs
2378	2139				
2399					
2753					
2894					
2925					
2967					
3341	3076				
4047					
4358		4678			
		4800			
		5086			
5461			5876		
		6438	6678		
			7065		
				7800	
				7948	
					8521
					8944
10140					
11287					
13950					
15295					
18131					
19701					
23253					

To extend the measurements beyond $2.3\ \mu$ into the infra-red, a Nernst filament is used as a source with a grating monochromator to isolate narrow wavebands. The monochromator is accurately set on successively higher orders of the mercury green line $5461\ \text{\AA}$, and the spectrum emitted when the continuous source is substituted consists of peaks corresponding to infra-red wavelengths which are usually separated by approximately $0.27\ \mu$ and extend to $5.46\ \mu$ or beyond.

The deviation angle for each wavelength is obtained from the interval between the interpolated fractional value of the moiré fringe interval for the appropriate record and the interpolated value for the normal reflection from the front face of the prism which is recorded in the same run. In principle the

refracting angle of the prism could similarly be obtained in the same run from the interval between the normal reflections from the front and back surfaces of the prism, but it is more convenient at present to measure the refracting angle separately.

The detectors employed for the wavebands shown are

2138 Å–5876 Å	QVA vacuum emission photocell.
4000 Å–8000 Å	Cadmium selenide photoconductive cell at room temperature.
8000 Å–3.2 μ	Lead sulphide photoconductive cell at the temperature of solid CO ₂ .
3 μ –5.5 μ	Lead telluride photoconductive cell at the temperature of liquid air.

In each case the radiation is chopped at 800 c/s and the signal is amplified by a tuned amplifier.

The materials so far submitted for measurement include optical glasses, which can be measured in the visible region to within ± 0.00003 , high grade silica, lithium and calcium fluorides, and infra-red materials of all kinds. Some selected figures for a typical infra-red material are given in table 2.

Table 2. Refractive indices of one form of arsenic trisulphide (temperature 20°C).

Wavelength (microns)	Refractive index	
0.78002 (Rb)	2.49771	± 0.00010
0.79476 „	2.49296	„
0.85211 (Cs)	2.47716	± 0.00008
0.89435 „	2.46776	„
1.01398 (Hg)	2.44797	± 0.00006
1.12866 „	2.43512	„
1.39506 „	2.41726	„
1.52952 „	2.41173	„
1.81307 „	2.40384	„
1.97009 „	2.40081	„
2.32542 „	2.39599	„
2.7304 (monochromator)	2.39243	„
3.0034 „	2.39068	„
3.2764 „	2.38912	„
3.5495 „	2.38783	„
3.8225 „	2.38664	„
4.0956 „	2.38555	„
4.3686 „	2.38450	„
4.6416 „	2.38348	„
4.9147 „	2.38248	„
5.1877 „	2.38147	„

The refinement of this technique is proceeding, and it is hoped to replace the radial grating in use by a better one, making higher accuracy possible.

ACKNOWLEDGMENT

The work described above has been carried out as part of the research programme of the National Physical Laboratory, and this paper is published by permission of the Director of the Laboratory.

On décrit une nouvelle technique pour la mesure des indices de réfraction pour des longueurs d'onde choisies dans l'ultra-violet, le visible et l'infra-rouge. Les indices sont obtenus dans toute la région spectrale à partir d'une mesure continue. La précision des mesures est supérieure à $\pm 0,00003$ pour l'indice de réfraction de matériaux de bonne qualité dans des régions spectrales favorables, et n'est jamais inférieure à $\pm 0,00010$ dans toute la région spectrale couverte par les mesures.

Die Brechwerte bei ausgesuchten Wellenlängen im ultravioletten, im sichtbaren und im infraroten Gebiet des Spektrums werden nach einem neuen Verfahren gemessen. Man kann dabei die Brechwerte über dieses Wellengebiet hinweg in ihrem kontinuierlichen Verlauf erhalten. Die Meßgenauigkeit ist besser als $\pm 0,00003$ im Brechwert, wenn das Material hinreichend gut ist und man in einem günstigen Spektralgebiet liegt; sie übersteigt nirgends in dem betrachteten Bereich den Betrag von $\pm 0,00010$.

REFERENCES

- [1] BRITTAN, K. W., and HABELL, K. J., 1960, *Optics in Metrology* (London: Pergamon Press), p. 141.
- [2] FLUDE, M. J. C., HABELL, K. J., and JACKSON, A., 1961, *J. sci. Instrum.*, **38**, 445.
- [3] *Mechanical Engineering Research* 1958 (London: H.M.S.O., 1959), p. 20.

The colour change of monochromatic light with retinal angle of incidence

by J. M. ENOCH

Department of Ophthalmology and Oscar Johnson Institute, Washington
University Medical School, St. Louis, Missouri

and W. S. STILES

National Physical Laboratory, Teddington, Middlesex

(Received 3 June 1961)

The few previous measurements of the small change of apparent colour of a monochromatic light stimulus when its angle of incidence on the foveal retina is varied (or SC II effect), have been confined to changes of apparent hue. A differential, three-colour mixture method, with alternating instead of juxtaposed presentation of the test and comparison stimuli, has now been applied to determine the complete colour change, hue and saturation. For the main subject, the results show hue shifts of the expected kind and a small but significant supersaturation of the apparent colour of an obliquely, compared with a normally incident stimulus, in the wavelength range 485 to 510 m μ . From earlier qualitative observations, such a supersaturation appears to occur for most subjects. The SC II colour changes are attributable to differences in the directional response of the receptors associated respectively with the three colour systems of the trichromatic scheme. From the relative spectral sensitivities of these systems and the complete SC II colour changes, the variation with wavelength of the directional sensitivity of each system has been computed for the data of the main subject. The possibility of explaining the derived wavelength variation in terms of self-screening by visual pigment present in the receptors in sufficiently high density, is examined. Self-screening appears not to be a factor for the blue-sensitive system, and although for the red- and green-sensitive systems it predicts minima in the directional sensitivity v. wavelength curve, resembling those observed, the quantitative agreement is poor and there are other objections. The wave-mode disposition of light in the receptors, now being studied, should yield a better explanation.

1. INTRODUCTION

The small change of observed colour when a monochromatic stimulus is incident at different angles on the same small retinal area at the fovea—or SC II effect†—was attributed [6], to differences in the directional sensitivity (change in magnitude of response with change in the angle of incidence) of the end-organs associated respectively with the three systems postulated in the trichromatic scheme. If the relative spectral sensitivities of these systems—the so-called fundamental sensitivities—are known, data on the SC II effect then lead to conclusions about the directional sensitivities of the respective end-organs. It was shown that for sets of fundamentals of an acceptable kind the data of the SC II effect could not be explained by the assumption of different

† Following Hansen [4], it is convenient to refer to the colour change as the Stiles-Crawford effect of the second kind or SC II effect, and to reserve SC effect for the more familiar change of brightness with angle of incidence.

directional sensitivities for the three sets of end-organs, if these directional sensitivities were taken to be independent of wavelength. The tentative suggestion was then made that the directional effect of a class of end-organs might be minimal for the stimulus wavelength at which the absorption by the photosensitive pigment contained in the end-organs was maximal. This would follow if the density of pigment in the cone were sufficiently high to attenuate strongly the incident light in its passage down the cone and if the directional intensity effect arose because obliquely incident light was prevented wholly or in part from reaching the distal end of the cone end-organ.

Brindley [1] established directly that the directional sensitivity of at least one of the three classes of end-organ must be wavelength dependent, by demonstrating and measuring the breakdown in colour-matches between stimuli of different spectral composition when the common angle of incidence of the two stimuli was changed from normal to oblique. It may be noted that breakdown of colour-match would occur if the directional sensitivities of the three classes of cone end-organ all varied with wavelength, but in the same manner, and if at each wavelength their values were the same. However, this latter possibility is excluded by the existence of the SC II effect as well as by the nature of the breakdown of different colour-matches observed by Brindley. From his results on directional sensitivity and, more particularly, on colour-adaptation, Brindley developed an interesting theory that the end-organs associated with the red-fundamental show strong self-screening (i.e. pronounced attenuation of the light in its passage down the end-organ by absorption in the photosensitive pigment). More recently Walraven and Bouman [12], basing themselves on the theoretical notions of Stiles and Brindley, have formulated a theory of the SC II effect, that involves more specific assumptions about the way the incident light is distributed in its passage through the cone: their paper includes some additional observations of the apparent hue change.

The only measurements hitherto made of the SC II effect have been of the changes in apparent hue, although qualitative changes of saturation, particularly an increased saturation of the obliquely incident ray for wavelengths near 500 m μ , have been reported [6, 12]. To investigate further the relation between the directional and spectral sensitivities of the cone end-organs, measurements of the complete colour-change—hue and saturation—have now been carried out using a differential three-colour mixture method, and the results are presented in this paper.

2. METHOD

The two stimuli to be matched by foveal vision consist in the main of monochromatic light of the same wavelength—the wavelength under test. But for one stimulus, the comparison stimulus, this main component enters the dilated eye pupil as a narrow pencil near its centre, while for the other—the test stimulus—the main component enters at a point displaced a given amount from the pupil centre. The position of the point of entry in the pupil determines the angle of incidence on the retina; the point of entry for the comparison stimulus is chosen so that, for the particular subject, the intensity response is maximal (for most subjects this occurs for a point of entry near the pupil centre); the corresponding retinal angle of incidence will be regarded, by convention, as ‘normal incidence’. In the absence of SC II effect, a complete colour-match between test and comparison stimuli can be made, when each consists solely of light of the test wavelength,

merely by adjusting the intensity of one of them—normally of the test stimulus. But usually when the test stimulus is adjusted to give the best brightness match there remains a slight difference of colour and this is eliminated and a complete match made by adding to the main components of the test and comparison stimuli small quantities of three fixed primaries (monochromatic stimuli in the red, $1/\lambda = 15\,500\text{ cm}^{-1}$; green, $1/\lambda = 19\,000\text{ cm}^{-1}$; blue, $1/\lambda = 22\,500\text{ cm}^{-1}$). To whichever of the two stimuli a small quantity of a primary is added, it is always sent into the eye pupil through the same point as the main component of the comparison beam, and is incident normally on the retina (see figure 1). Thus the main component of the test stimulus is the only radiation whose retinal angle of incidence is varied from the normal, and its consequent change of colour can be determined in terms of a straight forward trichromatic system appropriate to normally incident stimuli.

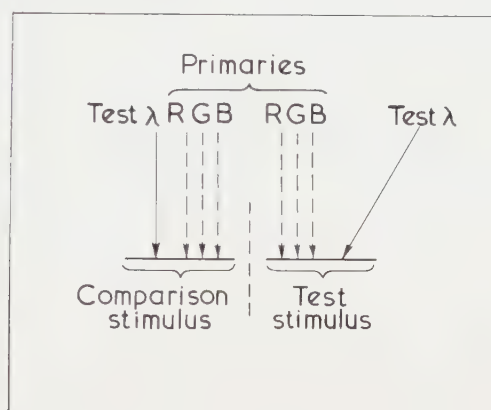


Figure 1. Incidence conditions for test and comparison stimuli.

The second feature of the method is the use of alternating presentation of the 1° diameter test and comparison stimuli on the same retinal area, at a slow rate of alternation of 0.75 sec total period, approximately. In this method imperfections of retinal image formation for oblique incidence were considered to be less disturbing than with the use of juxtaposed matching fields. Moreover—at least for the principal subject—the tendency for the colour difference to fade out by ‘local adaptation’ was reduced.

3. EXPERIMENTAL

The apparatus used was an adaptation of the NPL Trichromator which together with the appropriate calibration methods has been fully described [9]. The trichromator consists essentially of three double ‘monochromators’ forming three tiers mounted one above the other. The top and bottom monochromators are equipped with three slits instead of one slit in the central spectrum, so that they supply three-colour mixtures. The familiar principle used is recalled by the sketch (not to scale) of figure 2. The three vertically superimposed exit slits of the instrument deliver normally a mixture of three monochromatic primary stimuli (top tier), a monochromatic test colour (middle tier) and a second so-called desaturating mixture of the same three monochromatic primary stimuli (bottom tier). In the modified instrument, the upper half of the parallel beam incident on the final trichromator collimator

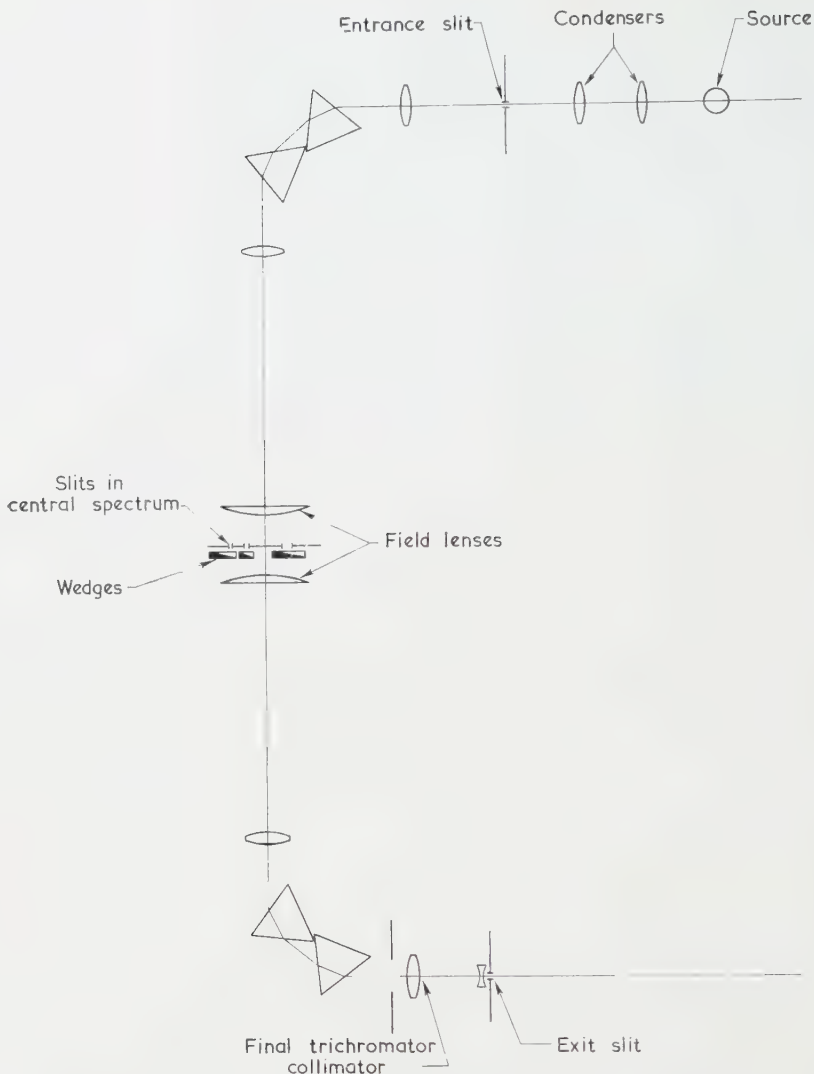


Figure 2. Diagram (not to scale) of the top or bottom tier of NPL Trichromator.

lens in the middle tier is reflected to the side by a front silvered mirror M_1 and re-directed by two similar prisms M_2 and M_3 to enter finally the side of a beam-splitter cube M_4 placed in the parallel beam of the top tier (see figure 3 (a) and (b)). After reflection in the diagonal surface of M_4 , the tapped-off portion of the test beam, and the primary mixture of the top tier—transmitted by the b-s cube M_4 —form a common mixed beam constituting the comparison stimulus. After passing through the final trichromator collimator lens and the exit slit (a clearance slit only, which removes stray light of the wrong colour dispersed outside the main slit image), the combined beam is collimated and reflected down by the mirror M_5 to the b-s cube M_6 , which reflects it to the Maxwellian lens L_1 to form a sharply focused slit image in the pupil plane of the subject's eye, O. The residual half of the middle tier beam also yields a focused slit image in the pupil plane, by transmission through the b-s cube M_6 . The desaturating primary

mixture beam, by reflection at the full mirrors M_7 and M_8 , and the plain glass plate M_9 (which is placed at 45° in the descending comparison stimulus beam), is incident on the diagonal surface of the b-s cube M_6 and is finally focused by L_1 to a slit image in the pupil plane. In the pupil plane, the slit images providing the main components of the test and comparison stimuli are approximately 0.5 mm square: the slit image for the mixture primaries is approximately 0.7 mm wide \times 0.4 mm high and for the desaturating primaries, 0.7 mm wide \times 0.2 mm high. All the slit images except that of the residual half of the middle tier beam (which constitutes the main component of the test stimulus) are centred on a common point in the pupil plane. The slit image of the main component of the test stimulus is shifted to various points in the pupil plane, by small displacements of the post-exit slit collimator L_2 in its own plane, the lens being mounted for this purpose in a frame with micrometer vertical and transverse adjustments. The

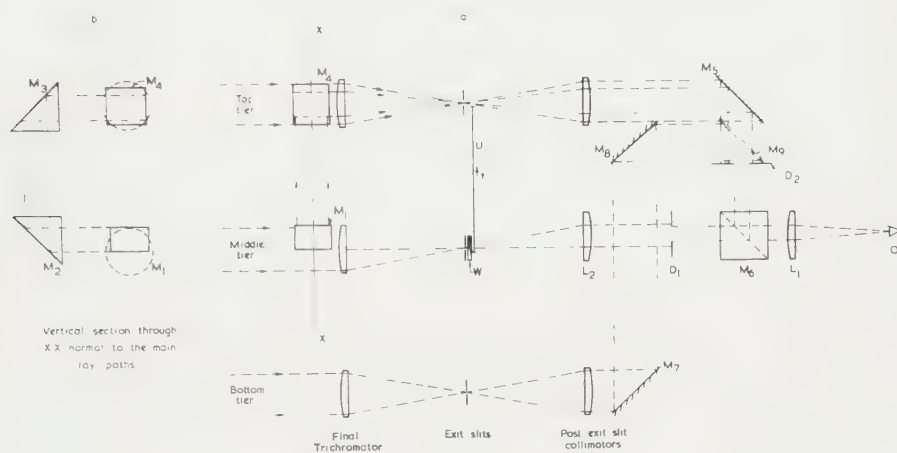


Figure 3. Diagrams showing adaptation of trichromator for directional colour-change measurements.

comparison and test stimulus fields actually imaged on the subject's foveal retina are delimited by two circular diaphragms D_1 and D_2 at the forward focus of the Maxwellian lens L_1 . The diaphragm D_1 is mounted in a frame enabling it to be displaced in its own plane (by the subject) so as to bring the circular 1° test and comparison stimuli to superposition. As the point of entry of the main component of the test stimulus is altered, the corresponding field patch moves out of position as a result of the aberrations of the optical system of the eye. The subject restores complete superposition of the fields by re-adjusting diaphragm D_1 . A double shutter U operated by a solenoid is arranged to open the top exit slit and close the centre exit slit simultaneously, or vice versa, and a synchronized shutter at the entrance slit of the bottom tier exposes and occults the desaturating mixture beam in phase with the shutter over the exit slit of the middle tier. Thus the subject sees, alternately, (a) a circular 1° test stimulus comprising the 'residual' beam of the test wavelength, whose intensity is controlled by the 'neutral' test wedge W , and a suitable desaturating mixture of the primaries, whose respective intensities are controlled by three wedges located in the central

spectrum of the bottom tier of the trichromator, and (b) a similar 1° comparison stimulus imaged on the same foveal area of the subject's retina, comprising the tapped-off beam of the test wavelength (of fixed intensity), and a suitable mixture of the primaries whose respective intensities are controlled by three wedges located in the centre spectrum of the top tier of the trichromator.

The point of entry for maximum response (normal incidence position) for a given subject is determined from preliminary observations. The comparison and test stimuli are then both sent into the eye pupil through this point, and with all the six primaries extinguished, the quality of the colour-match obtainable by adjusting wedge *W* to equate brightnesses is examined. The colour-match should be perfect (ideally the alternating presentation method is fully symmetric) and in the actual work, there was in fact no detectable colour difference. The point of entry of the main component of the test stimulus is then shifted to a new position, diaphragm D_1 is re-adjusted, and wedge *W* is set to give the optimum brightness match. After that, small quantities of the primaries are added to the test and comparison stimuli by the subject to correct the colour match, the number and choice of added primaries depending on the test colour and the nature of the colour shift.

The main subject (J.M.E. male, aged 31) used his left eye with a correcting lens of -4.0 Sph., while the second subject (J.M.B. male, aged 35 years) used his right eye (no correcting lens required). The specified displacement of the point of entry is the apparent displacement in the pupil plane as seen through the corneal refraction of the subject's eye, but not through the eye correction lens. A mydriatic (eucadryl or euphthalmine) was used to dilate the pupil for J.M.E.: J.M.B. had an exceptionally large natural pupil and no mydriatic was required.

Colour-matching with alternating presentation was found to demand of the subject some training and a high degree of concentration. It was essential to distinguish the two fields by including in one of them a small black marker spot near its edge.

4. COMPUTATION OF RESULTS

The first objective is to express the results with the minimum of assumptions about the way the SC II colour shift is produced. A typical match is represented in the usual colorimetric notation as follows:

$$E'_\lambda|_\theta(\lambda) + D_A(A) + D_B(B) + D_C(C) \mathbf{M} E_\lambda(\lambda) + M_A(A) + M_B(B) + M_C(C), \quad (1)$$

where $E'_\lambda|_\theta$ = energy intensity of the test wavelength λ in the test stimulus, incident on the retina at angle θ° (corresponding to a displacement of *s* millimetres of the point of entry from the normal incidence position).

E_λ = energy intensity of the test wavelength in the comparison stimulus.

D_A, D_B, D_C = energy intensities of the three primaries

A (15 000), B (19 000), C (22 500) in the test stimulus.

M_A, M_B, M_C = ditto in the comparison stimulus.

M means "matches by alternating presentation on the same retinal area".

(All stimuli other than $E'_\lambda|_\theta$ are incident normally.) Obviously,

$$D_A(A) + D_B(B) + D_C(C) \mathbf{M} D_A(A) + D_B(B) + D_C(C). \quad (2)$$

We shall assume the validity of the general additive law when the stimuli to a given retinal area are not all incident on the retina at the same angle. The available evidence on this point rests on comparison of the observed luminous efficiency for large eye pupils and the value computed by integration of the luminous efficiencies measured at individual 'points' in the pupil. The evidence is not conclusive: but for the small additions of primary stimuli being used here the law probably holds to a sufficient approximation. Assuming this, we may subtract (2) from (1) and divide out by E'_λ , to obtain:

$$1|_{\theta}(\lambda) \mathbf{M} \frac{E_\lambda}{E'_\lambda}(\lambda) + \frac{M_A - D_A}{E'_\lambda}(A) + \frac{M_B - D_B}{E'_\lambda}(B) + \frac{M_C - D_C}{E'_\lambda}(C). \quad (3)$$

If $A_\lambda, B_\lambda, C_\lambda$ are the subject's colour-matching functions when all the stimuli are incident normally, we have

$$1|_{\theta}(\lambda) \mathbf{M} A_\lambda(A) + B_\lambda(B) + C_\lambda(C). \quad (4)$$

Using this result, (3) becomes:

$$1|_{\theta}(\lambda) \mathbf{M} \left[\frac{E_\lambda}{E'_\lambda} \left(A + \frac{M_A - D_A}{E_\lambda} \right) \right] (A) + \left[\frac{E_\lambda}{E'_\lambda} \left(B_\lambda + \frac{M_B - D_B}{E_\lambda} \right) \right] (B) + \left[\frac{E_\lambda}{E'_\lambda} \left(C_\lambda + \frac{M_C - D_C}{E_\lambda} \right) \right] (C). \quad (5)$$

The coefficients in square brackets in (5) are the tristimulus values in the normal incidence system corresponding to the visual sensation produced by unit energy intensity of wavelength λ incident at angle θ , and are conveniently represented by $A'_\lambda, B'_\lambda, C'_\lambda$ respectively. For generality, the above equations allow for the introduction of small quantities of all six primaries (three mixture, three desaturation) but of course in practice as few as possible are used.

In deriving unit coordinates (chromaticities) it is convenient to adopt the W. D. Wright method of normalizing the colour-matching functions, which is particularly suitable when, as in this case, spectral primaries are being used. The normalized colour-matching functions are obtained by multiplying A by the constant ω_1 so that $\omega_1 A_2 = B_2$ at $1/\lambda = 17\,250 \text{ cm}^{-1}$ and C_λ by the constant ω_2 so that $\omega_2 C_\lambda = B_\lambda$ at $1/\lambda = 20\,500 \text{ cm}^{-1}$. Putting $U_\lambda = \omega_1 A_\lambda$, $V_\lambda = B_\lambda$, $W_\lambda = \omega_2 C_\lambda$ the tristimulus values of unit intensity of the test wavelength incident at angle θ are:

$$\begin{aligned} U'_\lambda &= \frac{E_\lambda}{E'_\lambda} \left[U_\lambda + \omega_1 \frac{M_A - D_A}{E_\lambda} \right], \\ V'_\lambda &= \frac{E_\lambda}{E'_\lambda} \left[V_\lambda + \frac{M_B - D_B}{E_\lambda} \right], \\ W'_\lambda &= \frac{E_\lambda}{E'_\lambda} \left[W_\lambda + \omega_2 \frac{M_C - D_C}{E_\lambda} \right]. \end{aligned} \quad (6)$$

The unit coordinates of the test wavelength incident normally or at angle θ are respectively

$$u_\lambda = \frac{U_\lambda}{\Sigma_\lambda}, \quad v_\lambda = \frac{V_\lambda}{\Sigma_\lambda}, \quad w_\lambda = \frac{W_\lambda}{\Sigma_\lambda}, \quad \Sigma_\lambda = U_\lambda + V_\lambda + W_\lambda$$

(normal incidence)

and

$$u' = \frac{U'_\lambda}{\Sigma'_\lambda}, \quad v' = \frac{V'_\lambda}{\Sigma'_\lambda}, \quad w' = \frac{W'_\lambda}{\Sigma'_\lambda}, \quad \Sigma'_\lambda = U'_\lambda + V'_\lambda + W'_\lambda$$

(incidence at angle θ)

(7)

and the SC II chromaticity shift is given by

$$\delta u_\lambda = u'_\lambda - u_\lambda, \quad \delta v_\lambda = v'_\lambda - v_\lambda, \quad \delta w_\lambda = w'_\lambda - w_\lambda. \quad (8)$$

If the measurements are made by the procedure described above, the ratio $E_\lambda/E'_\lambda = \eta_\lambda$ is the relative luminous efficiency for wavelength λ at angle of incidence θ ; η_λ measures the change of brightness of the monochromatic test stimulus with angle of incidence, when the small colour change remains uncorrected. On the assumption of Abney's law of additivity of luminance in hetero-chromatic brightness-matching—extended to the case when the stimuli being added may be incident on the retina at different angles—we should expect to find

$$\eta_\lambda = \frac{L_R(U'_\lambda/\omega_1) + L_G V'_\lambda + L_B(W'_\lambda/\omega_2)}{L_R(U_\lambda/\omega_1) + L_G V_\lambda + L_B(W_\lambda/\omega_2)}, \quad (9)$$

where L_R , L_G , L_B are the relative luminous efficiency factors for normal incidence of the primary stimuli at wave-numbers 15 500, 19 000, and 22 500 cm^{-1} , respectively.

The energy intensities of monochromatic stimuli are expressed in terms of ergs per sec entering the eye pupil per square degree of the stimulus field, light losses by interface reflection or absorption in the cornea and aqueous humour being ignored.

5. RESULTS

5.1. *J.M.E. Left eye*

The point of entry P_M for maximal visual response was located at 0.4 mm on the nasal side and 0.3 mm below the pupil centre. A series of measurements was made, for six selected wave-numbers—16 000, 17 000, 19 000, 20 000, 21 000 and 24 500 cm^{-1} —of the variation of brightness and colour as the point of entry of the main monochromatic component of the test stimulus was moved from P_M along a horizontal chord of the pupil, to the edge of the pupil on the temporal side. Figure 4 shows the observed change in η_λ . These curves represent the straightforward SC intensity effect and correspond to a value for the coefficient p in the empirical expression $\eta_\lambda(s) = 10^{-ps^2}$, in the neighbourhood of 0.04 (for the wavelength dependence of p , see below).

To compute the chromaticity shift (δu_λ , δv_λ , δw_λ) from equations (6), (7) and (8), the subject's normal incidence colour-matching functions U_λ , V_λ , W_λ are required. These were obtained in preliminary measurement but using the customary method of juxtaposed—not alternating—matching fields (total field diameter, 2°), and were very similar to the mean 2° colour-matching function determined with the same apparatus for a group of 10 subjects (Stiles 1955). The small colour shifts in question here are not sensitive to the exact value of the normal incidence colour-matching functions, and the use of the juxtaposed field method here is not material. The mean chromaticity shifts for the six wavelengths are plotted in figure 5 (a) and (b), (i) in a chromaticity chart, (ii) as a plot of δu_λ and δv_λ against s expressed in millimetres. (N.B. we have, approximately, θ (degrees) = $2.5s$ (mm).)

5.2. *Two-point spectral runs*

The dependence of the colour shift on the displacement s shows some complexities, but, on the whole, the shift increases with s , at least up to a value of

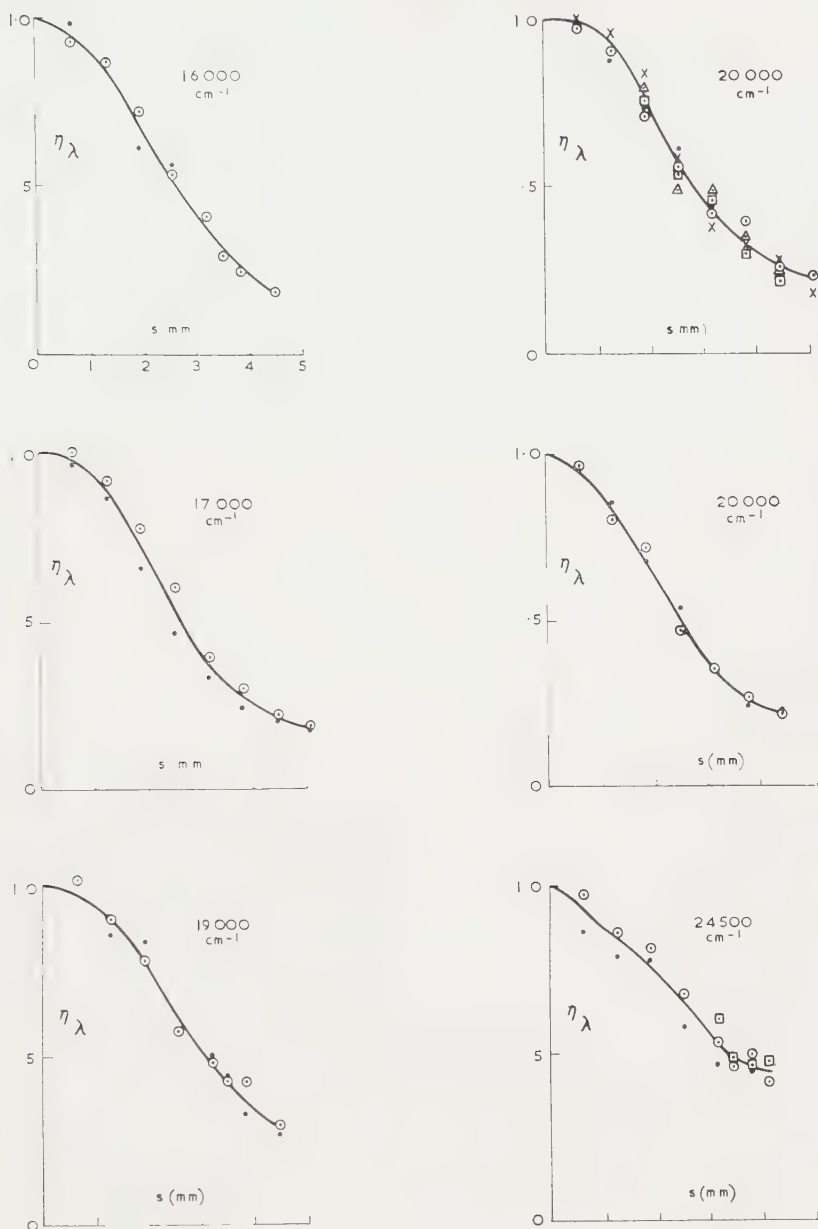


Figure 4. Change of luminous efficiency with displacement of point of entry in the pupil. (Subject J.M.E.)

about 3.5 mm. By confining the observations to two points of entry—normal and 3.5 mm temporal—the colour shift at about its maximal value was determined, in a single run, at some 17 wave-numbers through the spectrum. In figure 6(a), (b) and (c) are plotted the individual results for $\log \eta_\lambda$ and δu_λ and δv_λ obtained in four main runs of this kind. The spread in the values at any one wave-number is large, but the mean curves show a satisfactory regularity. In the chromaticity chart of figure 7(a) the spectrum locus defined by the circle

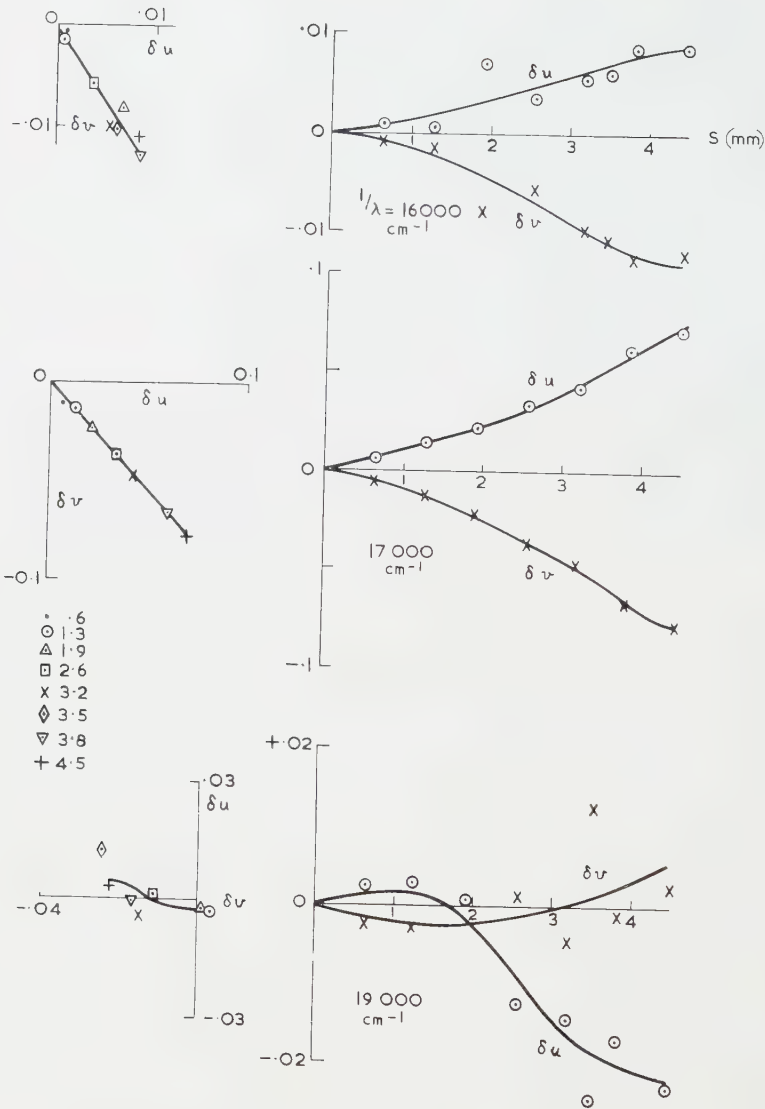


Figure 5 (a).

Right-hand graphs. Changes, δu and δv , of the chromaticity coordinates, plotted as ordinates, against displacement of the point of entry in millimetres, plotted as abscissa.

Left-hand graphs. Locus in the chromaticity diagram of the point corresponding to a monochromatic stimulus as the point of entry is displaced. The different point symbols correspond to different displacements. The position of the chromaticity point for normal incidence of the given wave-number is placed at the origin in each diagram.

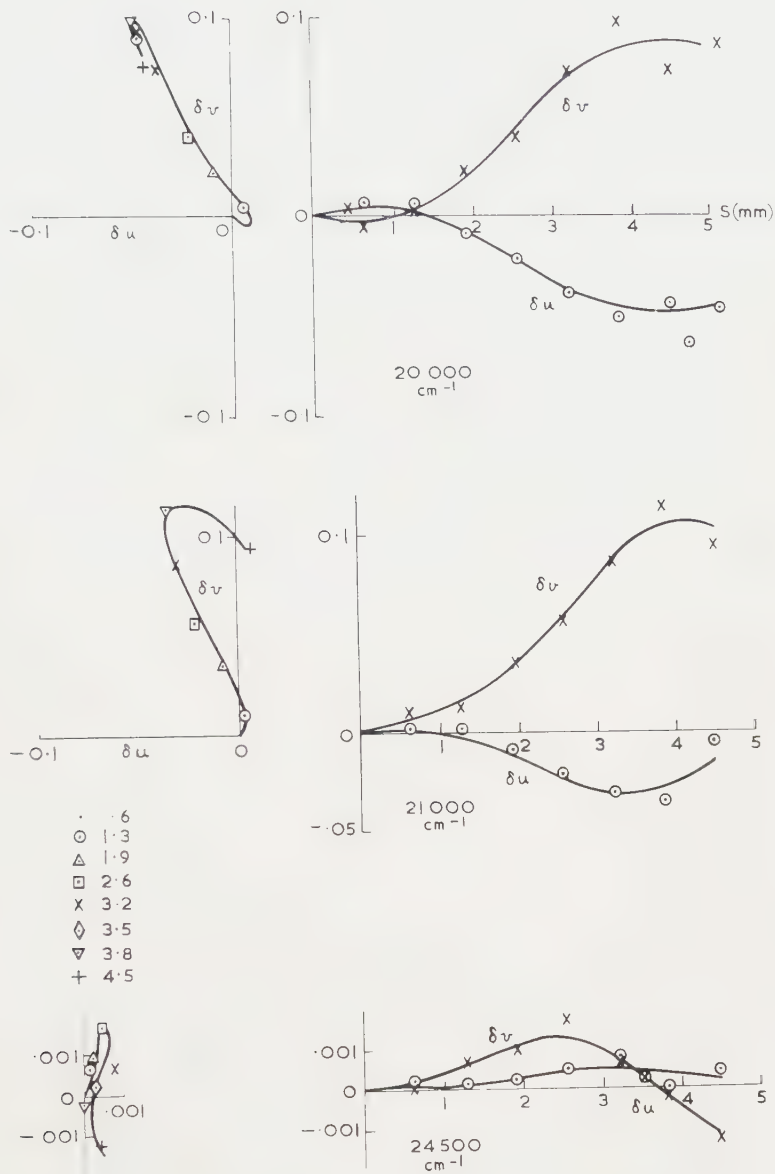


Figure 5 (b).

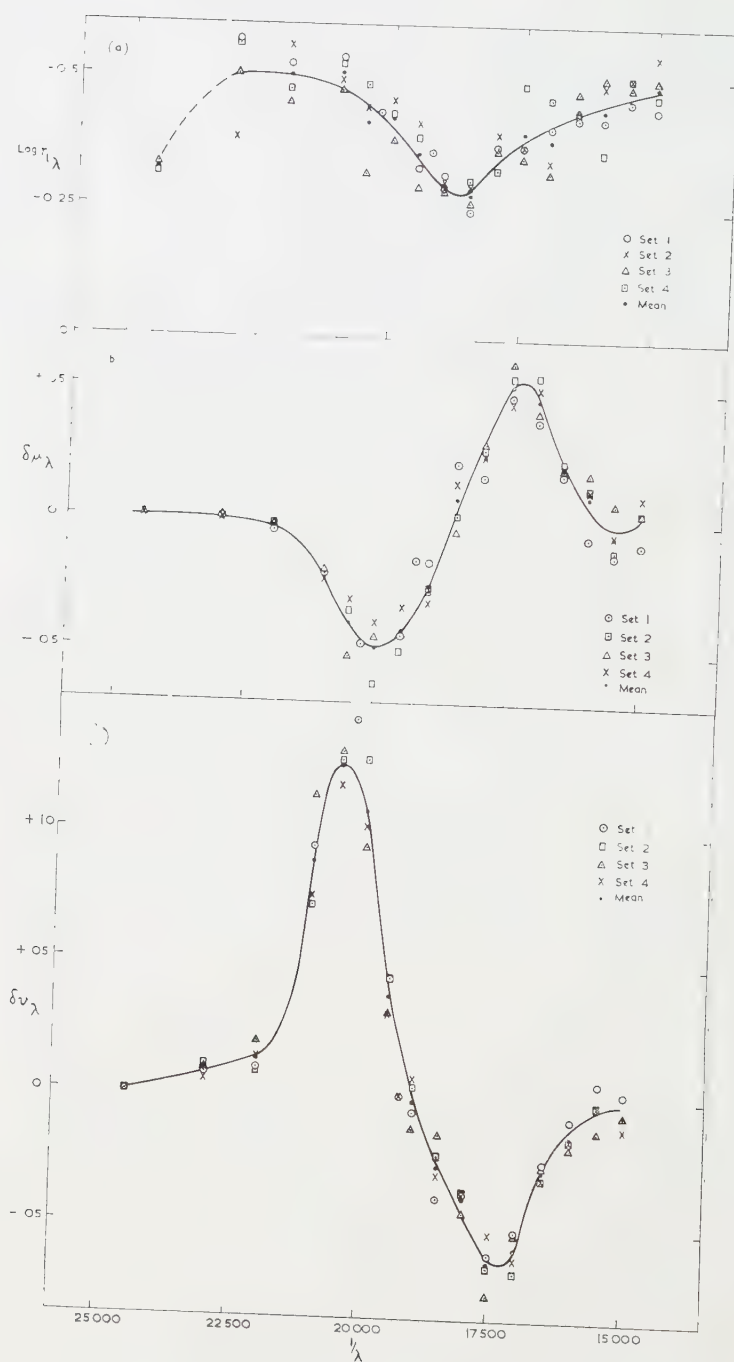


Figure 6. Variation with wave-number of (a) $\log \eta_\lambda$, (b) δu_λ , (c) δv_λ for $s = 3.8$ mm. Subject J.M.E.

points represents the mean 2° field results of 10 subjects taken from an earlier investigation [10]. The colour shifts (δu_λ , δv_λ) for J.M.E. at the 17 wave-numbers studied have been drawn in as vector lines originating in each case from the appropriate point of the spectrum locus. (An approximate determination of the spectrum locus for J.M.E. had been made for computing (δu_λ , δv_λ); it differs little from the mean curve, which was preferred for this present purpose because being based on observations at many more wave-numbers it fixes more precisely, the spacing of the wave-number points along the locus.) The terminal points of the colour shift-vectors determine the modified spectrum locus for oblique incidence ($s=3.5$ mm) which has been drawn in as

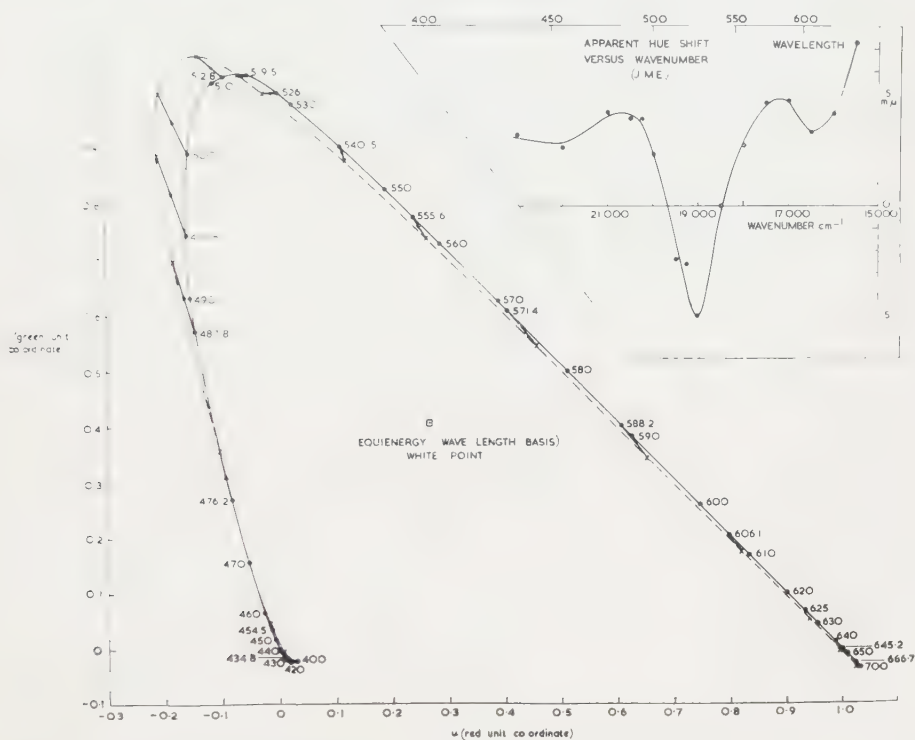


Figure 7. Chromaticity diagram showing SC II colour shift vectors. Inset: derived shift in apparent hue. Subject J.M.E.

a broken line curve. It is clear that for this subject the SC II colour shift consists of a hue change towards the red and probably a slight desaturation, for longer wavelengths ($\lambda > 530 \text{ m}\mu$)^o. There occurs a reversal of the direction of the hue shift and a change from desaturation to supersaturation in the region 530 to 505 $\text{m}\mu$ approximately, and a second reversal of the hue shift, which again is towards long wavelengths, accompanied by supersaturation, as the short-wave end of the spectrum is approached. By joining the extremity of the colour-shift vector to the equi-energy white point, and finding by interpolation, the wavelength corresponding to the intercept of this line with the full-line spectrum locus, the apparent hue shifts plotted in the inset diagram of figure 7 were obtained.

5.3. *J.M.B. Right eye*

For the second subject only a few observations were obtained. He was found to have a rather anomalous one-sided SC intensity effect and his SC II colour shift fails to show the supersaturation at shorter wavelengths which other observers report, at least qualitatively. The observations were confined to two point measurements, taking 1 mm nasal temporal entry as normal incidence and 3 mm temporal as oblique incidence. The wavelength variation of $\log \eta_\lambda$ and of $(\delta u_\lambda, \delta v_\lambda)$ and the derived change of apparent hue are shown in figure 8.

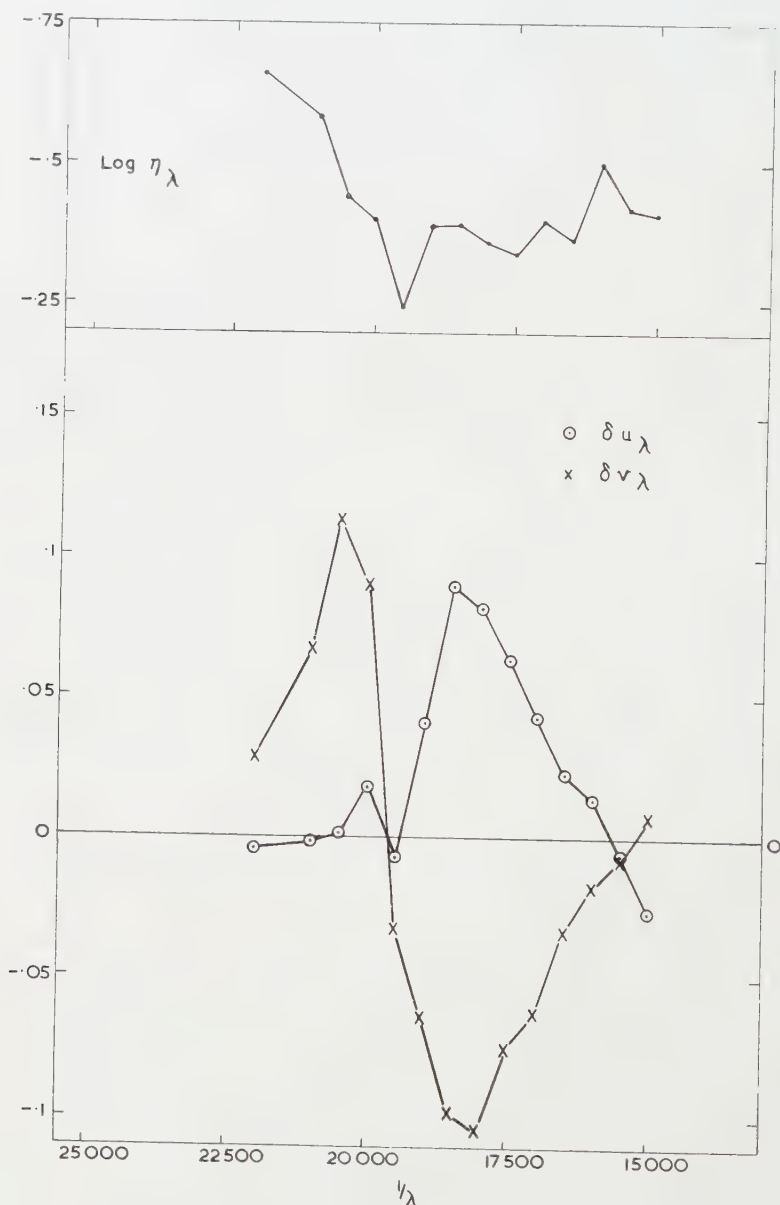


Figure 8. Variation with wave-number of (a) $\log \eta_\lambda$, (b) δu_λ and δv_λ for $s = 4$ mm. Single sets. Subject J.M.B.

6. DISCUSSION

The apparent hue shifts measured for six subjects (2 by Stiles [6], 2 by Walraven and Bouman [12] and 2 in present work) are compared in figure 9. The differences between different individuals are considerable although there is a qualitative similarity in all the curves. Adequate data on the complete colour shifts are available only for J.M.E.; the following discussion will deal with their interpretation in terms of fundamental spectral sensitivities.

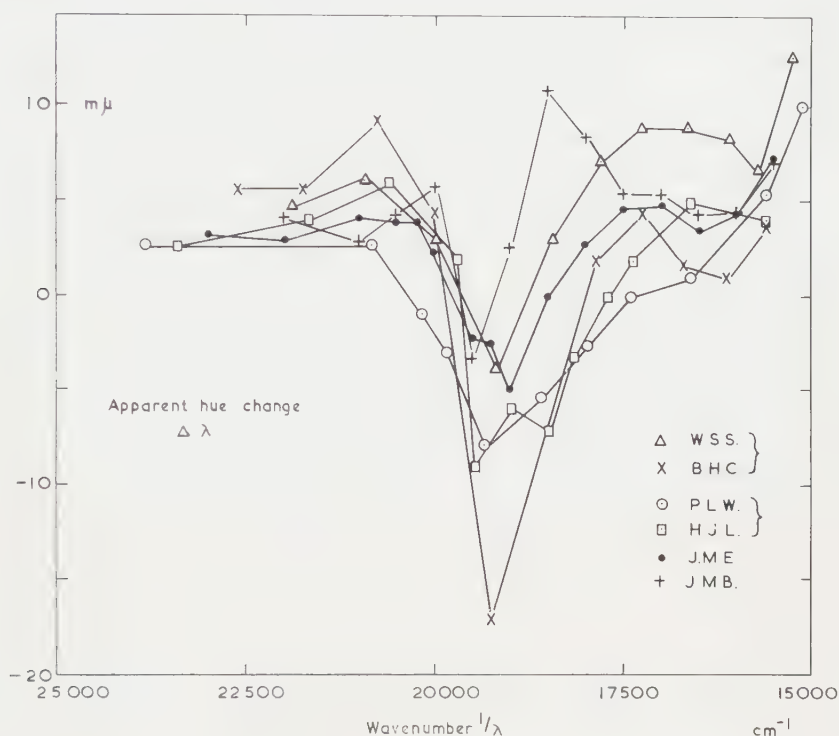


Figure 9. Shift of apparent hue $\Delta\lambda$ as a function of wave-number $1/\lambda$ for six subjects.

W.S.S. }
B.H.C. } [6]

P.L.W. }
H.J.L. } [12]

J.M.E. }
J.M.B. } Present work.

Given a perfect match between normally incident and obliquely incident stimuli on the same retinal area, we may conclude that beyond a certain stage of the visual process, the effects produced by the two stimuli are identical. In practice, the foveal retinal area used is not perfectly homogeneous, and, because of aberrations of the dioptric system, the obliquely incident stimulus tends to have a fuzzy edge. These factors make difficult a judgment on perfection of match; we shall assume that any deviations from perfect match arise from such secondary factors. Unfortunately we cannot be sure that the observed colour changes are entirely unaffected by these optical imperfections.

The simplest hypothesis on which to interpret the results is that there are just three types of receptor whose respective end-organs contain just one photo-sensitive pigment, different in the different receptor types. At colour-match,

the response of each type of receptor to the matched stimuli must be the same. If R_λ , G_λ , B_λ are the relative spectral sensitivities of the receptor types for normally incident light the matching conditions between two normally incident stimuli $\{F_\lambda d\lambda\}$ and $\{F'_\lambda d\lambda\}$ take the usual form

$$\int F_\lambda R_\lambda d\lambda = \int F'_\lambda R_\lambda d\lambda, \quad \int F_\lambda G_\lambda d\lambda = \int F'_\lambda G_\lambda d\lambda, \quad \int F_\lambda B_\lambda d\lambda = \int F'_\lambda B_\lambda d\lambda. \quad (10)$$

Although each of R_λ , G_λ , B_λ is undetermined to a constant factor independent of wavelength, it is essential for what follows to suppose that R_λ is fixed by convention once and for all in absolute as well as relative value through the spectrum, and similarly for G_λ and B_λ . When one of the stimuli, $\{F'_\lambda d\lambda\}$, is incident obliquely—at angle θ say—the matching conditions become

$$\int F_\lambda R_\lambda d\lambda = \int F'_\lambda R'_\lambda d\lambda, \quad \int F_\lambda G_\lambda d\lambda = \int F'_\lambda G'_\lambda d\lambda, \quad \int F_\lambda B_\lambda d\lambda = \int F'_\lambda B'_\lambda d\lambda, \quad (11)$$

where R'_λ , G'_λ , B'_λ are the spectral sensitivities of the receptor types, for obliquely incident light. Since the absolute values of R_λ , G_λ and B_λ have been fixed by a convention the sensitivities R'_λ , G'_λ , B'_λ are determined in both absolute and relative values through the spectrum. The matching conditions (11) imply that the effect of oblique incidence operates at a stage of the visual process where the effects of radiations of different wavelengths are still compounded by the simple linear law.

The spectral sensitivities for normally incident light— R_λ , G_λ , B_λ —must be homogeneous linear functions of the colour-matching functions for normally incident light, for which we may take the W.D.W. normalized system U_λ , V_λ , W_λ .

$$\left. \begin{aligned} R_\lambda &= t_{11}U_\lambda + t_{12}V_\lambda + t_{13}W_\lambda, \\ G_\lambda &= t_{21}U_\lambda + t_{22}V_\lambda + t_{23}W_\lambda, \\ B_\lambda &= t_{31}U_\lambda + t_{32}V_\lambda + t_{33}W_\lambda. \end{aligned} \right\} \quad (12)$$

From the definition of U'_λ , V'_λ , W'_λ it is clear by applying the additive law that the conditions for a match between $\{F'_\lambda d\lambda\}$ (incident at angle θ) and $\{F_\lambda d\lambda\}$ (incident normally) may also be written:

$$\int F'_\lambda U'_\lambda d\lambda = \int F_\lambda U_\lambda d\lambda, \quad \int F'_\lambda V'_\lambda d\lambda = \int F_\lambda V_\lambda d\lambda, \quad \int F'_\lambda W'_\lambda d\lambda = \int F_\lambda W_\lambda d\lambda. \quad (13)$$

It follows from (11), (12) and (13), that

$$\left. \begin{aligned} R'_\lambda &= t_{11}U'_\lambda + t_{12}V'_\lambda + t_{13}W'_\lambda, \\ G'_\lambda &= t_{21}U'_\lambda + t_{22}V'_\lambda + t_{23}W'_\lambda, \\ B'_\lambda &= t_{31}U'_\lambda + t_{32}V'_\lambda + t_{33}W'_\lambda. \end{aligned} \right\} \quad (14)$$

Thus the spectral sensitivities of the three receptor types for incidence at angle θ , R'_λ , G'_λ , B'_λ , are derivable from the experimentally determined U'_λ , V'_λ , W'_λ once the transformation $T = \{t_{ij}\}$ has been fixed. Of principal interest for each receptor type is the ratio of the sensitivities for oblique and normal incidence as a function of wavelength:

$$\rho_\lambda = \frac{R'_\lambda}{R_\lambda}, \quad \gamma_\lambda = \frac{G'_\lambda}{G_\lambda}, \quad \beta_\lambda = \frac{B'_\lambda}{B_\lambda}.$$

Given the spectral sensitivity of a receptor type—which is fixed by three coefficients forming a row in the matrix of T —the directional sensitivity of the receptor type ($1/\rho_\lambda$, $1/\gamma_\lambda$ or $1/\beta_\lambda$) can be derived.

It is convenient to split the variation of $\rho_\lambda(\gamma_\lambda \text{ or } \beta_\lambda)$ into two factors:

$$\log \rho_\lambda = \log \frac{R'_\lambda}{R_\lambda} = \log \frac{\sum'_\lambda}{\sum_\lambda} + \log \left(\frac{t_{11}u'_\lambda + t_{12}v'_\lambda + t_{13}w'_\lambda}{t_{11}u_\lambda + t_{12}v_\lambda + t_{13}w_\lambda} \right), \quad (15)$$

where

$$\sum'_\lambda = U'_\lambda + V'_\lambda + W'_\lambda,$$

$$\sum_\lambda = U_\lambda + V_\lambda + W_\lambda.$$

The first term is independent of the transformation coefficients t_{11} , t_{12} , t_{13} . Its mean value for the subject J.M.E. is plotted in figure 10 (circle points).

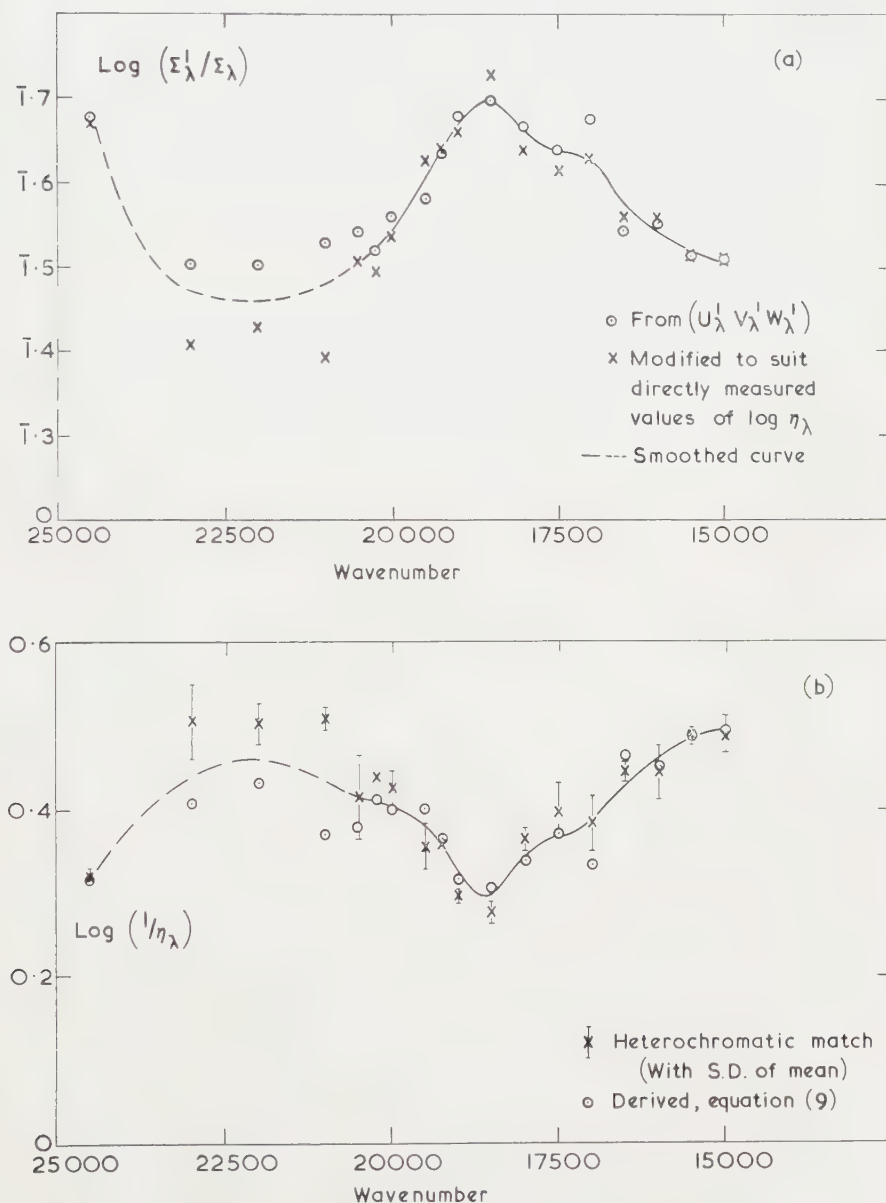


Figure 10. (a) Variation of $\log (\Sigma'_\lambda / \Sigma_\lambda)$ with $1/\lambda$ (J.M.E.).

(b) Variation of $\log (1/\eta_\lambda)$ with $1/\lambda$ (J.M.E.).

A graphical evaluation of the second term helps in visualizing the effect on $\log \rho_\lambda$ of selecting different possible spectral sensitivities for the R receptors. The line $t_{11}u + t_{12}v + t_{13}w = 0$ in the chromaticity chart determines what may be called the 'receptor alychne', all points of which represent the stimuli (non-real) eliciting zero response from the R receptors. The expression

$$\frac{t_{11}u' + t_{12}v' + t_{13}w'}{t_{11}u_\lambda + t_{12}v_\lambda + t_{13}w_\lambda}$$

is simply the ratio of the perpendicular distances from the receptor alychne of the points representing the origin and end-point of the SC II colour shift vector corresponding to the wavelength λ : d'/d in figure 11.

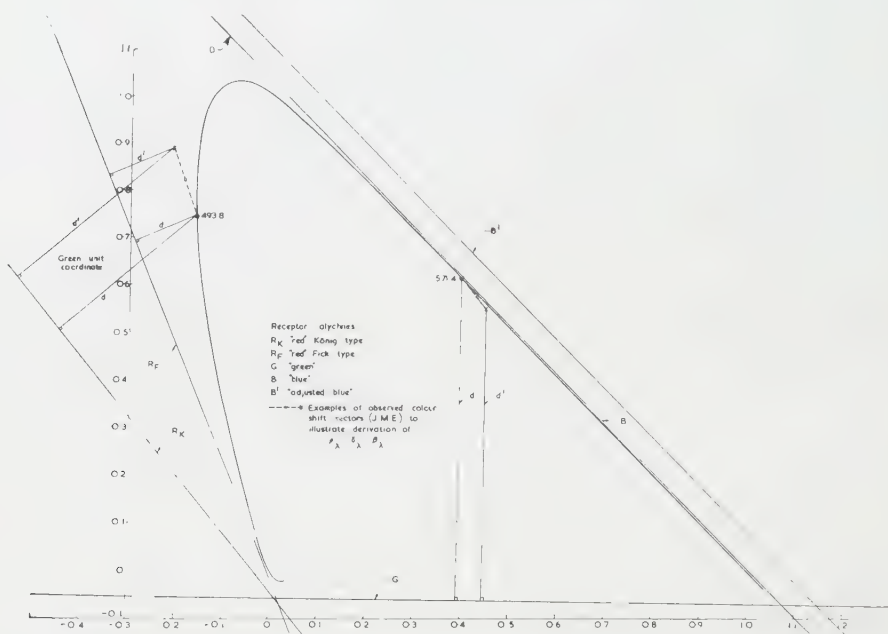


Figure 11. Receptor alychnes in the chromaticity diagram:

R_K, R_F, G, B, B' . Graphical Derivation of $\frac{t_{11}u'_\lambda + t_{12}v'_\lambda + t_{13}w'_\lambda}{t_{11}u_\lambda + t_{12}v_\lambda + t_{13}w_\lambda}$ for a given SC II colour shift: the ratio = d'/d .

Before using equation (14) to derive directional sensitivities (which may be defined as the reciprocals: $1/\rho_\lambda$, $1/\gamma_\lambda$, etc.) for different receptor spectral sensitivities, we will compare the directly measured η_λ values (means) with those computed from $U'_\lambda, V'_\lambda, W'_\lambda$ (means) using formula (9). In the latter, the values adopted for L_R, L_G and L_B are taken from Judd's modified C.I.E. V_λ -curve [5]; $L_R/L_G = 0.17$, $L_B/L_G = 0.052$ (the calculation is not sensitive to the precise values assumed). The comparison (figure 10 b) shows fair agreement except at wave-numbers 21 000, 22 000 and 23 000 cm^{-1} ($\lambda = 476$ to $435 \text{ m}\mu$), where the computed values are systematically low. While the discrepancy could represent a breakdown of Abney's additivity law in this application, it is also possible that the subject's equalization of brightness in making the full colour-match was at fault. In the colour-matches in the short-wave range, the small

energy intensity of green primary which must be added to the comparison field to counterbalance the greenness of the obliquely incident test stimulus, carries with it a luminosity which is not small compared with that of the main stimuli. This makes the simultaneous matching of brightness and colour more difficult: by concentrating on the colour (hue and saturation) match and accepting a residual brightness difference, the measurement is simplified and this may have occurred to some extent. If so, the discrepancy propagates to the quantity $\log \sum'_\lambda / \sum_\lambda$ required to compute the directional sensitivities of receptors, and makes their values uncertain for $1/\lambda > 20\,500\text{ cm}^{-1}$. If the directly measured η_λ values and the changes of chromaticity (figure 6 (a), (b) and (c)) (mean values) are accepted as correct, this would correspond approximately to adopting in formula (15) the values of $\log \sum'_\lambda / \sum_\lambda$ plotted as crosses in figure 10 (a). The discrepancy between the two determinations of $\log \eta_\lambda$ for $1/\lambda > 20\,500\text{ cm}^{-1}$ was not discovered until after the experimental part of the work was completed, and its cause could not be followed up. In the calculations that follow the values of $\log \sum'_\lambda / \sum_\lambda$ have been taken from the smoothed curve in figure 10 (a) which attempts to average the two determinations.

6.1. 'Blue' receptor type

It is commonly accepted that the 'blue' receptors have a spectral sensitivity not very different from the C.I.E. \tilde{s}_λ function, and that the sensitivity becomes vanishingly small at long wavelengths, say λ greater than $550\text{ m}\mu$. This implies that the receptor alychne—a straight line—runs very close to the spectrum locus in that region of the spectrum. The small but consistent desaturation of obliquely incident light of long wavelength shown by J.M.E. (figure 7 a), then leads to a difficulty. If the B-receptor alychne is very close to the spectrum locus, the desaturation although small corresponds to a large value for

$$\log \frac{t_{31}u'_\lambda + t_{32}v'_\lambda + t_{33}w'_\lambda}{t_{31}u_\lambda + t_{32}v_\lambda + t_{33}w_\lambda}$$

and the resultant β_λ could in fact have values greatly exceeding unity, i.e. the blue receptors would be much more sensitive to oblique than to normally incident light. To illustrate this point, the coefficients t_{31} , t_{32} and t_{33} have been chosen to yield a B-receptor spectral sensitivity curve very similar to the C.I.E. \tilde{s}_λ in the short wave region ($\lambda < 500\text{ m}\mu$) but dropping less abruptly at long waves, so as to make the receptor alychne still parallel to, but displaced slightly outwards from the long-wave section of the spectrum locus (alychne B in figure 11). The spectral sensitivity and corresponding directional sensitivity of the B-type receptors are plotted in figure 12. The unexpected drop in directional sensitivity for wavelengths greater than about $505\text{ m}\mu$ ($1/\lambda = 19\,800\text{ cm}^{-1}$) could only be reduced by shifting the receptor alychne still farther from the spectrum locus, with a consequent elevation of the long-wave section of the spectral sensitivity curve.

The relation is illustrated by taking different values for t_{31} , t_{32} , t_{33} to obtain the modified sensitivity curve B' (figure 12). Thus the small desaturation effect at long wavelengths shown by the J.M.E. data and, qualitatively, clearly evident to the subject—implies either an unexpected drop in the directional effect of the blue receptors at long wavelengths ($\lambda > 505\text{ m}\mu$) or a spectral sensitivity curve that is elevated in this spectral range even more than the B' curve shown here, or, finally, an artifact in the measurements that might be connected with the optical imperfection of the obliquely incident field already noted.

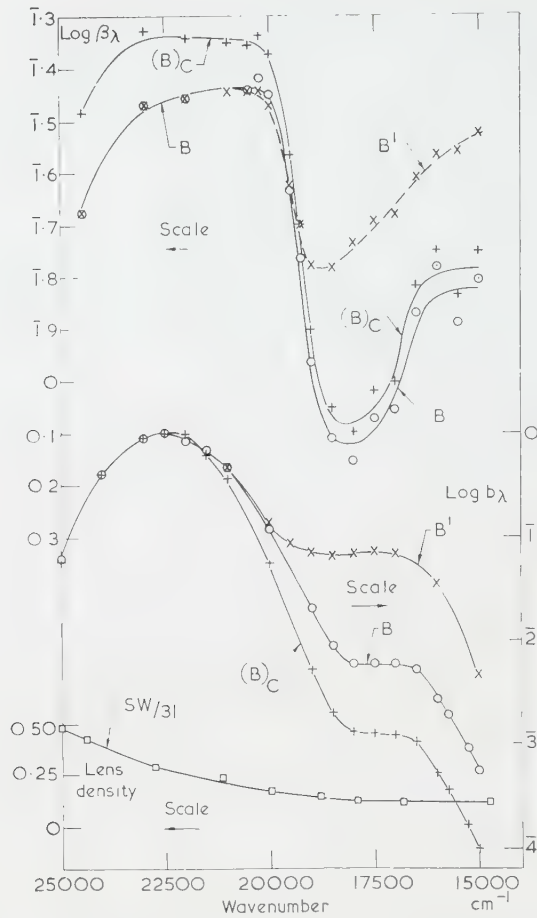


Figure 12. Log directional sensitivity, $-\log \beta_\lambda$, and log spectral sensitivity, $\log b_\lambda$, plotted against wave-number. The relative spectral sensitivity (energy basis) of the B system is taken to be

$$b_\lambda = \text{const.} (0.0013A_\lambda + 0.0207B_\lambda + 1C_\lambda)$$

and of the B' system, as

$$b_\lambda = \text{const.} (0.0156A_\lambda + 0.0679B_\lambda + 1C_\lambda).$$

Here A_λ , B_λ , C_λ are the 2° colour-matching functions obtained as a mean for ten subjects by Stiles and Burch [10] and listed in table 2 of their paper. The constant in each case is supposed adjusted by convention to make the maximum value of b_λ equal to unity. The graph $(B)_C$ gives the spectral sensitivity of system B converted to quantum basis and corrected for macular pigment and lens losses, using for the latter the lens density data of Said and Weale [11] for age 31 which are plotted as SW/31 in the lower part of the figure.

6.2. 'Green' receptor type

There is a convergence of evidence on the form of the spectral sensitivity of the green-sensitive receptor system and in figure 13, $\log g_\lambda$ is a representative curve of this type together with the derived directional sensitivity $-\log \gamma_\lambda$ (the G curve). The corresponding receptor alychne (line G) is shown in figure 11.

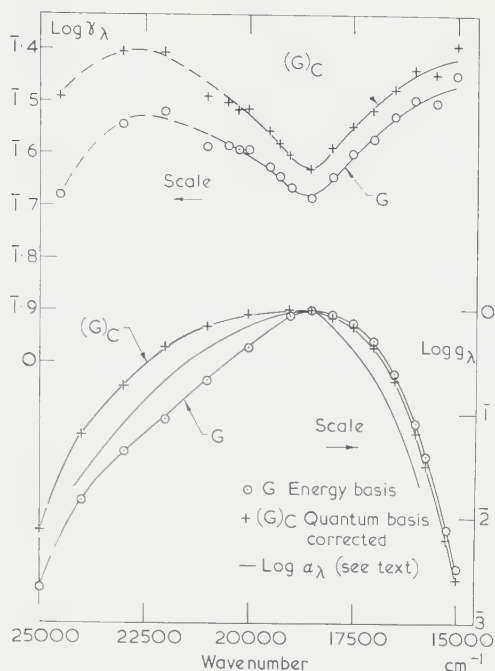


Figure 13. As for figure 12, but for green-sensitive system G with $g_\lambda = \text{const. } (0.0202A_\lambda + 1B_\lambda + 0.0736C_\lambda)$ (energy basis).

6.3. 'Red' receptor type

Of the two main kinds of spectral sensitivity for 'red' receptors that have emerged in visual colour theory, the first or König type is represented by the curve R_K of figure 14. It differs from the Fick type (curve R_F) in having no secondary maximum in the short-wave end of the spectrum. The corresponding directional sensitivities (based on the J.M.E. data) show very little difference for wavelengths greater than $520 \text{ m}\mu$ ($1/\lambda = 19200 \text{ cm}^{-1}$) but at shorter wavelengths a slight oscillation in the value present in the König type appears in an exaggerated form in the Fick curve.

As the SC II colour shifts are not determinable with high accuracy and there are considerable individual differences, it is of interest to raise here a general question. Suppose the three receptor systems all have different directional sensitivities that vary with wavelength but suppose that their relative values at the same wavelength remain in an approximately constant ratio. Could this assumption lead to about the same kind of intensity effect and colour shift as observed. The assumption may be written $\rho_\lambda = j_1 \gamma_\lambda$ and $\beta_\lambda = j_2 \gamma_\lambda$ where j_1 and j_2 are independent of wavelength. By the appropriate choice of j_1 and j_2 the apparent hue shifts in the yellow and blue can readily be reproduced and the wavelength variation of γ_λ can be taken to suit any observed values of η_λ . But with acceptable sets of three receptor types—(R_K , G , B) or (R_F , G , B) for example—the colour shifts predicted by this assumption show desaturation not supersaturation in the blue-green and a very small (probably unobservable) supersaturation instead of desaturation at long wavelength. This conclusion is illustrated by the solid line colour shifts in figure 15 which are derived for the

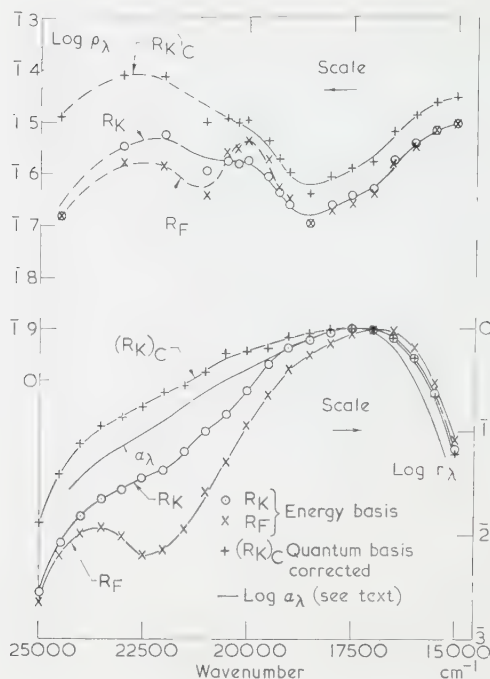


Figure 14. As for figure 12 but for the alternative König and Fick type red-sensitive systems with
 r_{λ} (energy basis) = const. $(0.358 A_{\lambda} + 1B_{\lambda} + 0.0543C_{\lambda})$
König type
= const. $(0.714 A_{\lambda} + 1B_{\lambda} + 0.0216C_{\lambda})$
Fick type.

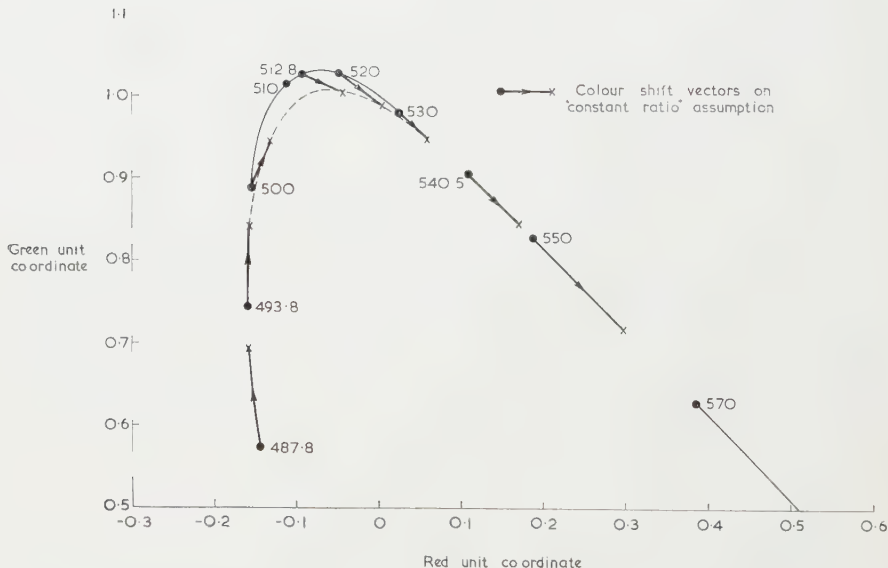


Figure 15. Hypothetical SC II colour-shift vectors in chromaticity diagram, derived by assuming the directional sensitivities of the three colour systems to remain in the same constant ratios at all wavelengths.

receptor types (R_F , G , B) with $j_1=1.148$ and $j_2=0.692$. Thus the observation of supersaturation in the blue-green is useful qualitative evidence that the simplifying assumption just mentioned is untenable.

A complicating factor in the interpretation of measurements of directional sensitivity is the possibility of different light losses in the optic media for normally and obliquely incident rays, which, in particular, pass through different thicknesses of the eye lens. The latter is selective in its light transmission and becomes increasingly yellow with age. Said and Weale [11] have recently made measurements of the transmission of the lens of the living eye and Weale and others have emphasized the need to allow for such light losses, particularly for light in the blue, when passing from the apparent values of directional sensitivity, as normally measured, to the true retinal directional effect. Said and Weale's values for light losses in the lens, they (Said and Weale) believe to be lower limits, and the values certainly appear to be rather lower (in the blue) than those deduced by comparisons of normal and aphakic eyes. If the light losses in the lens arose simply from a single yellow pigment distributed uniformly throughout the lens (or from uniform scattering), the lens correction to the apparent directional effect could be obtained from measured values of light loss and from the estimated difference of path length in the lens. Although the actual situation is almost certainly more complicated than this, it is of some interest to compute the correction on the simple assumption. We may note first that differential light losses in the eye media leave unchanged the SC II colour shifts (δu_λ , δv_λ) plotted in figures 5, 6 and 7, but they modify $\log \eta_\lambda$ and enter in the comparisons of spectral and directional sensitivities displayed in figures 12 to 14. In the latter figures the directional sensitivity curves marked $(B)_C$, $(G)_C$, $(R_K)_C$ are hypothetical lens-corrected curves which would have been obtained if the light losses in the lens had been zero. The curves were computed from (B) , (G) , and (R_K) by assuming an eye lens whose optical density (attributable to light losses in the lens) for rays passing through the lens centre (normal incidence), has the values measured by Said and Weale for subjects of age 31 (curve SW/31 in figure 12), and, for rays entering peripherally at $s=3.8$ mm, these same values reduced by a factor representing the ratio of the lengths of the light path in the lens—a factor of 0.56 approximately. While for several reasons the lens correction is a tentative one, the resulting change in shape of the directional sensitivity curves—which are raised, and bent up in the blue—is probably qualitatively correct and may be an underestimate of the change. In the modified spectral sensitivity curves $(B)_C$, $(G)_C$ and $(R_K)_C$, the estimated effect of lens pigmentation has been removed and at the same time corrections have been made to allow for macular pigmentation (for correction curve, see [8]) and to convert the sensitivities from relative reciprocal energies to relative reciprocal numbers of quanta (this is done by multiplying each energy sensitivity by the wave number $1/\lambda$). Thus, ignoring light losses in the optic media other than the lens, the curves aim to represent, on a quantum basis, the relative sensitivities at the receptor layer. This is the form needed for the following comparison.

The suggestion (see Introduction) that the directional effect is minimal where the spectral sensitivity is maximal is tolerably well borne out for the 'green' receptor type, at least as far as the positions of the respective maximum and minimum wavelengths are concerned. For the 'red' receptor type, the

minimal directional sensitivity occurs at about the same wavelength as for the 'green', instead of being displaced towards long waves as is the maximum of the spectral sensitivity curve: the dip in the directional sensitivity curve is however broader on the long-wave side. For the 'blue' receptor type, the directional sensitivity shows no minimum in the region where the spectral sensitivity is maximal.

According to Brindley's work on the breakdown of colour-matches when the angle of incidence of all the matching stimuli is changed [1], the directional sensitivity ($1/\rho_\lambda$) of the 'red' receptor type increases on either side of the wavelength of maximum spectral sensitivity (a result attributed to self-screening) but the corresponding change for the 'green' receptor type is absent, or at least much smaller. (Brindley's data on this point are confined to wavelengths greater than $550\text{ m}\mu$ where it is the 'green' and 'red' receptors that are principally involved.) But the directional sensitivities $(R)_C$ and $(G)_C$ (figures 13 and 14) both show the kind of variation with wavelength that Brindley attributed to the 'red' receptor only. The conflict probably corresponds to a significant difference in properties of the two subjects: G.S.B. (Brindley) and J.M.E. (present work). From the present data for J.M.E., the expected results of Brindley's experiments can be predicted by calculation, the validity of the additive law of colour-matching being assumed. Spectral mixture primaries at $1/\lambda = 15\,000\text{ cm}^{-1}$ ($\lambda = 667\text{ m}\mu$), $18\,000\text{ cm}^{-1}$ ($556\text{ m}\mu$), $22\,500\text{ cm}^{-1}$ ($444\text{ m}\mu$) are assumed in place of Brindley's filter primaries of equivalent wavelengths 680, 550, $454\text{ m}\mu$ respectively, but this difference should be immaterial. To restore a match on a test colour of fixed wavelength and intensity when all the matching stimuli are shifted from central to peripheral entry in the pupil, the intensities P_R, P_G, P_B of the primaries expressed in log units must be changed by amounts $\Delta \log P_R, \Delta \log P_G, \Delta \log P_B$ respectively. In the spectral region of Brindley's measurements the small contribution of the blue primary is unimportant. The results can therefore be compared by plotting $(\Delta \log P_R - \Delta \log P_G)$ (figure 16). This quantity would be constant if there were no SC II effect and its constant value would then equal the difference of the ordinary directional effect at the wavelengths of red and green mixture primaries: $\log (1/\eta)_G - \log (1/\eta)_R$. In figure 16 the greater steepness of the G.S.B. curve corresponds to a somewhat larger SC II colour change in this spectral region, but the uniformly higher values for J.M.E. indicate a greater change with wavelength (between the red and green primaries) of the intensity effect of the 'red' and 'green' receptors.

These differences bear strongly on the interpretation of the SC II effect in terms of the self-screening hypothesis. The hypothesis has been formulated in a more specific form by Walraven and Bouman [12] who assume a leakage of the obliquely incident light at a uniform rate along the outer segment. Their formula for the directional sensitivity of a receptor (say the 'red') due to self-screening is

$$\frac{1}{\rho_\lambda} = \frac{\alpha_\lambda c l + \xi l}{\alpha_\lambda c l} \frac{1 - \exp(-\alpha_\lambda c l)}{1 - \exp(-\alpha_\lambda c l - \xi l)}, \quad (16)$$

where α_λ = absorption coefficient of the photosensitive pigment in the outer segment;

c = concentration of the same (assumed uniform);

l = length of outer segment;

ξ = fractional loss of light to surrounding tissues per unit length of outer segment of the radiation passing down the outer segment. ξ is taken to be independent of wavelength, increasing with obliquity and equal to zero for normally incident light.

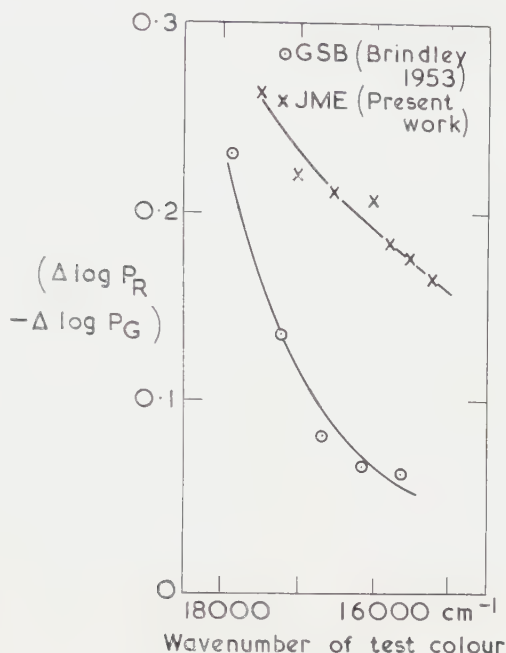


Figure 16. Brindley's data on colour-match break-down for oblique incidence of all the stimuli, compared with predicted effect for J.M.E.

In applying this formula, it is convenient to consider two wavelengths: λ_m where the pigment has maximum absorption coefficient α_m and total density $D_m = \alpha_m c l \log_{10} e$, and λ_0 , sufficiently remote from λ_m for the corresponding total density to be so low that with sufficient accuracy $1 - \exp(-\alpha_\lambda c l) = \alpha_\lambda c l$ and $\alpha_\lambda c l + \xi l = \xi l$. Then putting ρ_m and ρ_0 for the values of ρ_λ at λ_m and λ_0 respectively, and defining the 'leakage density' to be $A = \xi l \log_{10} e$, we have

$$\log\left(\frac{1}{\rho_m}\right) = \log\left(\frac{1 - 10^{-D_m}}{D_m}\right) - \log\left(\frac{1 - 10^{-(D_m + A)}}{D_m + A}\right), \quad (17)$$

$$\begin{aligned} \delta \log\left(\frac{1}{\rho}\right) &= \log\left(\frac{1}{\rho_0}\right) - \log\left(\frac{1}{\rho_m}\right) \\ &= -\log\left(\frac{1 - 10^{-A}}{A}\right) + \log\left(\frac{1 - 10^{-(D_m + A)}}{D_m + A}\right) - \log\left(\frac{1 - 10^{-D_m}}{D_m}\right). \end{aligned} \quad (18)$$

Taking any specified values for the quantities $\log(1/\rho_m)$ and $\delta \log(1/\rho)$ the above equations can be solved for D_m and A . A grid for obtaining approximate solutions quickly is shown in figure 17.

For the 'green' receptor type, $1/\lambda_m$ is taken as 18500 cm^{-1} and $1/\lambda_0$ (on the long-wave side) as 15000 cm^{-1} , for which the directional sensitivity curve (G)₀ of figure 13 gives $\log(1/\gamma_m) = 0.38$, $\delta \log(1/\gamma) = 0.21$, and then from figure 17,

$D_m = 1.0$, $A = 1.6$ approximately. At any wavelength λ the corresponding pigment density D_λ is derived from the spectral sensitivity curve $(G)_\lambda$ using the equation:

$$\log g_\lambda = \log [1 - 10^{-D_\lambda}] - \log [1 - 10^{-D_m}]$$

and the directional sensitivity, on the self-screening hypothesis, from equation (17) substituting D_λ for D_m and putting $A = 1.6$. The curve computed in this way is compared with the experimental values in figure 18, which includes a similar comparison for the red receptor type using the following values of the parameters:

$$(1/\lambda_m) = 17\,500\text{ cm}^{-1}, (1/\lambda_0) = 15\,000\text{ cm}^{-1}, \log(1/\rho_m) = 0.39, \delta \log(1/\rho) = 0.15, \\ D_m = 0.7_2, A = 1.45.$$

(The two sets of experimental points are based not on the smoothed values of $\log \sum'_\lambda / \sum_\lambda$ but on the alternative experimental values plotted in figure 10(a).)

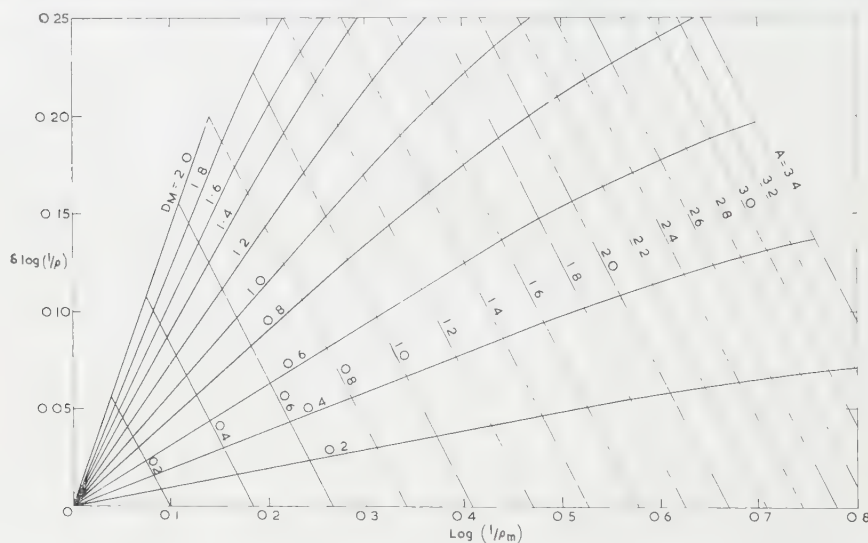


Figure 17. Diagram for deriving the maximum visual pigment density D_M and the leakage density A , from the minimum value $\log(1/\rho_m)$ and the total range $\delta \log(1/\rho)$ of the directional sensitivity of a visual receptor system, according to the self-screening hypothesis.

The agreement between the curves computed on the self-screening hypothesis and the experimental data is not very good but is perhaps not so unsatisfactory as to exclude the hypothesis as a first approximation. The corresponding pigment densities $D_m = 1.0$ (G) and 0.7_2 (R_K)—if correct, would mean that the spectral sensitivity curves $\log g_\lambda((G))_C$ and $\log r_\lambda((R))_C$ are appreciably less sharp than the corresponding curves of $\log \alpha_\lambda$ (where α_λ is the absorption coefficient of the green or red pigment). These latter curves have been included in figures 13 and 14. For the 'green' receptor the $\log \alpha_\lambda$ curve differs in shape from the typical rhodopsin type curve more than does the original $\log g_\lambda$ curve, and this is not a favourable sign. The high pigment densities derived on the hypothesis, result from the large variation of the directional sensitivity, defined by $\delta \log(1/\rho)$, or $\delta \log(1/\gamma)$ compared with the minimum value, $\log(1/\rho_m)$ or

$\log(1/\gamma_m)$, as observed for the subject J.M.E. This is reflected in the large percentage variation of $\log(1/\eta_\lambda)$ in passing from the wavelength of the minimum to the extreme red. Subjects in earlier work (WSS and GSB) gave results corresponding to a smaller variation of $\log(1/\eta_\lambda)$ on the long-wave side, and this would lead, for the same colour shifts, to smaller densities for the 'green' and 'red' pigments.

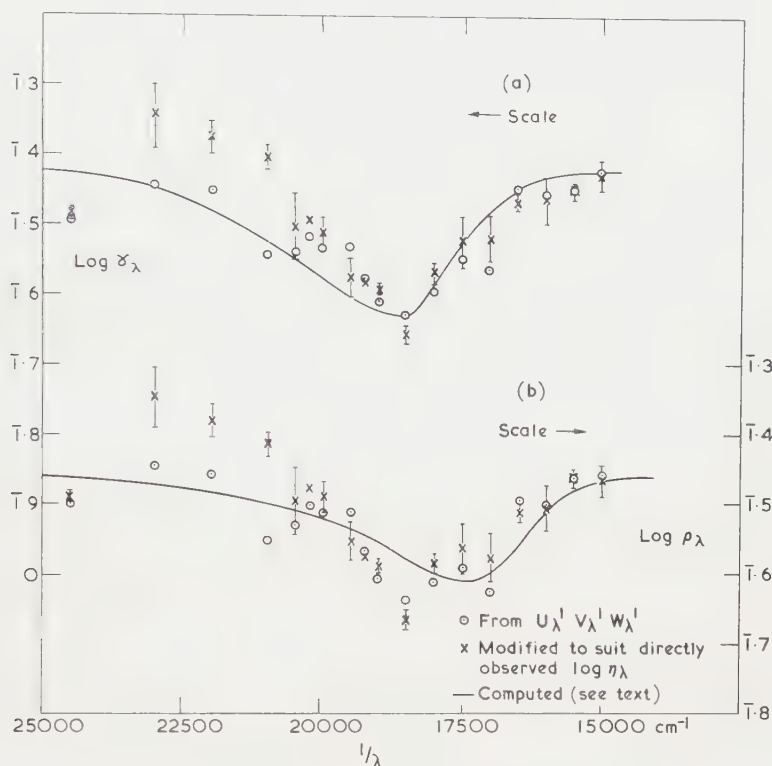


Figure 18. Wavelength dependence of the directional sensitivities of the green- and red-sensitive system from the observed SC II colour shifts (points), and as computed from the spectral sensitivity curves on the self-screening hypothesis with appropriate choice of maximum pigment density and leakage density.

Walraven and Bouman [12] introduced what, in effect, is an additional hypothesis, namely that there is a leakage of obliquely incident light compared with normally incident light—the reduction factor being put equal to $q(q < 1)$ —that occurs in the inner segment of the receptor. The inner segment does not contain photosensitive pigment, so that self-screening is not involved. This very reasonable hypothesis provides a new variable parameter with which to adjust theory to experiment and Walraven and Bouman discuss the sets of corresponding values of D_m , A and q (q assumed independent of wavelength) that might suit the experimental data then available (largely the hue and brightness changes for subject WSS). We will only note that assuming for q any value less than unity and independent of wavelength, the data of J.M.E. would yield still higher values for the pigment density D_m .

For the 'blue' receptor type, the present data provide no evidence that self-screening is playing any part. In the blue-green and blue ($1/\lambda > 20\,000\text{ cm}^{-1}$) the directional sensitivity shows no minimum corresponding to the maximum of the spectral sensitivity curve and the pigment density could be quite small ($D_m < 0.2$): unfortunately in this region of the spectrum the experimental $\log \beta_\lambda$ values and the correction for lens absorption are subject to considerable uncertainty. The greater directional sensitivity of the 'blue' ($\lambda < 520\text{ m}\mu$), compared with the 'green' and 'red' receptors, is consistent with the results of measurements made by the two-colour threshold method [7]. It could be attributed to a high leakage density A (outer segment) or a high loss in the inner segment (q small) but at present there is no means of distinguishing these alternatives.

The application of the self-screening hypothesis to the SC II data of J.M.E. has not proved very successful. The high pigment densities of 'green' and 'red' receptors and the large variations in these densities that would follow from observed individual differences, are difficult to accept. To enable conclusions to be drawn, the simplifying assumption has been made that the leakage of obliquely incident light is independent of wavelength, i.e. that, in the absence of self-screening, each receptor type would have the same directional sensitivity at all wavelengths. The leakage mechanism has not been specified but on the elementary ideas that rest on total internal reflection in the outer segment, a variation with wavelength in the relative refractive index of the outer segment with respect to the surrounding medium, would make the leakage wavelength dependent. It appears certain that the more realistic treatment of the disposition of light in receptors, that takes account of the comparable values of the receptor diameter and the wavelengths of the light must also make the 'leakage' wavelength dependent, but the magnitude and nature of the variation is not yet clear.

ACKNOWLEDGMENT

This study was supported in part by a research grant from the National Institute of Neurological Diseases and Blindness, National Institutes of Health, Bethesda, Maryland. The work formed part of the programme of general research of the National Physical Laboratory, and the paper is published by permission of the Director of the Laboratory.

ADDENDUM

Recently, in studies of wave-guide modal patterns in retinal receptors, one of us (J.M.E.) has noted certain facts which bear upon this problem. The spatial energy distribution in the receptor outer segments varies in some receptors as a function of wavelength and the angle of obliquity of the incident energy. These variations in physical distribution are (to some extent) related to each other. The wavelength distribution of energy reaching the termination of the receptor varies from that of the incident distribution, varies between receptors, and changes with angle of obliquity. Energy leaks from the receptor inner segments, ellipsoids, and outer segments. This leaked energy varies in its wavelength, magnitude and spatial physical distribution at different points along the receptor. Directional sensitivity (SC I) was evident in all receptors.

These findings are based on *in vitro* studies of human, primate and rat receptors. Considerable quantification of these findings must first be achieved before an attempt is made to associate these findings with data reported in this paper†.

Dans les quelques mesures antérieures, on s'est borné à considérer comme des changements de tonalité apparente, le léger changement de couleur apparente d'un test de lumière monochromatique arrivant sur la rétine fovéale sous des angles d'incidence variés (ou effet SC II). Une méthode différentielle de mélange trichromatique, avec présentation des tests alternée au lieu d'être simultanée, vient d'être appliquée à la détermination du changement complet de couleur, tonalité et saturation. Pour la moyenne des sujets, les résultats montrent des déplacements de la tonalité dans le sens prévu, ainsi qu'une augmentation légère mais significative de la saturation de la couleur apparente, pour un test arrivant obliquement, par rapport à celui arrivant normalement, et pour des longueurs d'onde allant de 485 à 510 m μ . D'après les observations qualitatives antérieures, cette augmentation de saturation paraît générale à presque tous les sujets. Les changements de couleur du SC II peuvent être attribués à des différences de réponse directionnelle des récepteurs associés respectivement aux 3 systèmes de couleur du schéma trichromatique. A partir des sensibilités spectrales relatives de ces systèmes, et des changements de couleur complets du SC II, la variation avec la longueur d'onde de la sensibilité directionnelle de chaque système a été calculée, en se servant des valeurs trouvées pour la moyenne des sujets. On examine la possibilité d'expliquer la variation de longueur d'onde qui en résulte par une filtration due à un pigment visuel présent dans les récepteurs en assez forte densité. Cette filtration ne paraît pas être possible pour le système sensible au bleu, et quoique, pour les systèmes sensibles au rouge et au vert, elle donne un minimum sur la courbe de sensibilité directionnelle en fonction de la longueur d'onde, minimum ressemblant à ceux observés, l'accord quantitatif n'est pas bon, et il y a d'autres objections. La considération de la lumière dans les récepteurs sous forme de guide-onde, actuellement à l'étude, aboutirait à une meilleure explication.

Über die geringe Verschiebung der Farberscheinung eines monochromatischen Lichtreizes, wenn sein Einfallswinkel auf die Netzhautgrube sich ändert, liegen nur wenig ältere Messungen vor; sie sind auf die Verschiebung der scheinbaren Farbtöne beschränkt. Hier ist nun eine Differenzialmethode mit einer Drei-Farben-Mischung benutzt worden, wobei die Prüf- und Vergleichsreize nacheinander anstatt nebeneinander dargeboten werden, um die vollständige Farbänderung nach Ton und Sättigung zu bestimmen. In der Hauptsache zeigen die Ergebnisse Farbtonverschiebungen der erwarteten Art und eine kleine aber deutliche Übersättigung der Farberscheinung eines schräg einfallenden Reizes gegenüber einem senkrecht einfallenden im Wellenlängenbereich von 485 bis 510 m μ . Nach älteren qualitativen Beobachtungen scheinen solche Übersättigungen in den meisten Fällen aufzutreten. Die SC II Farbverschiebungen lassen sich zu Unterschieden in der Richtungsempfindlichkeit der Rezeptoren der drei Farbensysteme des trichromatischen Auges zuordnen. Aus den relativen spektralen Empfindlichkeiten dieser drei Systeme und aus den vollständigen Farbänderungen im SC II läßt sich die Wellenlängenänderung der Richtungsempfindlichkeit jedes Systems berechnen. Es wird auch die Möglichkeit geprüft, die hergeleitete Wellenlängenänderung in Form einer Selbstabschirmung durch das Sehpigment, das in den Rezeptoren mit genügend hoher Dichte vorhanden ist. Die Selbstabschirmung scheint für das blauempfindliche System keine Rolle zu spielen und wenn sie auch für die rot- und grünempfindlichen Systeme Minima in der Kurve der Richtungsempfindlichkeit gegenüber der Wellenlänge voraussagt, die den beobachteten nahe kommen, so ist doch die quantitative Übereinstimmung schlecht und es gibt auch noch andere Bedenken. Die 'wave-mode' Verteilung des Lichtes in den Rezeptoren, die jetzt untersucht wird, könnte zu einer besseren Erklärung führen.

† These findings will be reported in articles which will shortly appear in *Science*, the *American Journal of Ophthalmology*, and the *Journal of the Optical Society of America*. One preliminary discussion has appeared: J. Enoch, 1960, *J. opt. Soc. Amer.*, **50**, 1025.

REFERENCES

- [1] BRINDLEY, G. S., 1953, *J. Physiol., Lond.*, **122**, 332.
- [2] BRINDLEY, G. S., 1955, *Proc. phys. Soc., Lond.*, B, **68**, 862.
- [3] ENOCH, J. M., 1960, *J. opt. Soc. Amer.*, **50**, 1025.
- [4] HANSEN, G., 1943, *Die Naturwiss.*, 35/36, p. 416.
- [5] JUDD, D. B., 1951, C.I.E. 12th Plenary Session (Stockholm).
- [6] STILES, W. S., 1937, *Proc. roy. Soc. B*, **123**, 90.
- [7] STILES, W. S., 1939, *Proc. roy. Soc. B*, **127**, 64.
- [8] STILES, W. S., 1953, *Coloquio sobre problemas opticos de la vision, Proc. I* (Madrid), p. 65.
- [9] STILES, W. S., 1955, *Phys. Soc. Year Book*, p. 44.
- [10] STILES, W. S., and BURCH, J. M., 1955, *Opt. Acta* **2**, 168.
- [11] SAID, F. S., and WEALE, R. A., 1959, *Gerontologia* **3**, 213.
- [12] WALRAVEN, P. L., and BOUMAN, M. A., 1960, *J. opt. Soc. Amer.*, **50**, 780.

International Commission for Optics

Nomenclature for Fourier Transforms of Spread Functions

THE International Commission for Optics (I.C.O.) has formed a Subcommittee for Image Assessment Problems. It consists of Professor A. Arnulf, Paris, Dr. H. H. Hopkins, London, Professor H. Kubota, Tokyo, Dr. K. Rosenhauer, Braunschweig, and Dr. R. Scott, Norwalk, Conn., U.S.A., with the writer as Chairman. Following a proposal of Dr. C. G. Higgins, Rochester, N.Y., U.S.A., this Committee has made recommendations on nomenclature for what is at present known under a variety of names, e.g. sine-wave response, frequency response, contrast transfer, etc. After extensive correspondence and examination of the matter, the Committee has, at sessions in Paris and London in July 1961, unanimously arrived at the recommendations below. Dr. Kubota could not be present and was represented by Drs. K. Kinoshita, K. Murata and K. Sayanagi; Dr. D. L. MacAdam, Rochester, N.Y., U.S.A., also took part in the discussions and decisions. In making recommendation No. 1, the Committee had in mind first that response ordinarily means that the output is of a different nature from the input, and should on this account be avoided, and secondly that the word contrast is not uniquely defined and is moreover a concept much used in photography in another sense. The recommendations are given here in English, together with the proposed equivalent terms in French and German.

Recommendations

(1) The functions indicated in the heading, the curve representing it and its value for a given spatial frequency shall be called the:

Optical transfer function/curve/factor;
Fonction/courbe/facteur de transfert optique;
Optische(r) Übertragungsfunktion/kurve/factor.

The function as denoted is the complex function. When the modulus is referred to, it shall be denoted by the terms:

Modulation transfer function/curve/factor;
Fonction/courbe/facteur de transfert de modulation;
Modulationsübertragungsfunktion/kurve/faktor.

The argument of this shall be referred to by the terms:

Phase transfer function/curve/value;
Fonction/courbe/valeur de transfert de phase;
Phasenübertragungsfunktion/kurve/wert.

It is to be understood that the prefix of transfer may be omitted when confusion cannot arise.

(2) The variables of these functions shall be termed:

Spatial Frequency;
Fréquence spatiale;
Ortsfrequenz.

(3) The unit of spatial frequency shall be described by either:

Cycles per mm or lines per mm.

(The latter when no confusion can occur with television lines, since 2 T.V. lines = 1 cycle). The corresponding terms are:

Cycles par mm;	Lignes par mm;
Perioden pro mm;	Linien pro mm.

ERIK INGELSTAM,
Institute of Optical Research,
Stockholm 70, Sweden.



INDEX OF AUTHORS (WITH TITLES)

	PAGE
Baumeister, Philip: The transmission and degree of polarization of quarter-wave stacks at non-normal incidence	105
Book Reviews:	
BORN, Max, and WOLF, Emil: Principles of Optics.	181
GÖRLICH, Paul (Herausgeber): Jenaer Jahrbuch	182
HAINE, M. E.: The electron microscope	279
KAMMERER, Wilhelm: Ziffern-Rechenautomaten.	183
Burch, J. M., and Palmer, D. A.: Interferometric methods for the photographic production of large gratings	73
Bryngdahl, Olof: Effect of retinal image motion on visual acuity	1
Caprioli, Luigi, Scheggi, Anna Maria, and Toraldo di Francia, Giuliano: Approximate synthesis of a prescribed diffraction pattern by means of different aperture distributions	175
Clarke, F. J. J.: Visual recovery following local adaptation of the peripheral retina (Troxler's Effect)	121
Clowes, M. B.: Some factors in brightness discrimination with constraint of retinal image movement	81
Crisp, R. S.: The reflectivity of glass and aluminium gratings at grazing incidence below 100 Å	137
Dyson, J.: Optical alignment devices based on a two-mirror system.	217
Enoch, J. M., and Stiles, W. S.: The colour change of monochromatic light with retinal angle of incidence	329
Gates, J. W., Habell, K. J., and Jackson, A.: The refractive index of materials from 0.2 μ to 5 μ	323
Habell, K. J., with Gates, J. W., and Jackson, A.: The refractive index of materials from 0.2 μ to 5 μ	323
Havlíček, F. I.: Definitionshelligkeit und Kontrastübertragung	213
Hisdal, B.: Colorimetric daylight illuminant with high ultra-violet content	199
Ishiguro, K., and Tako, T.: An estimation of Smith-Purcell effect as the light source in the infra-red region	25
Jackson, A., with Gates, J. W., and Habell, K. J.: The refractive index of materials from 0.2 μ to 5 μ	323
Kard, Paul G., and Knittl, Zdeněk: On some degenerate cases of thin film interference	185
Karp, Samuel N., and Keller, Joseph B.: Multiple diffraction by an aperture in a hard screen	61
Keller, Joseph B., with Karp, Samuel N.: Multiple diffraction by an aperture in a hard screen	61
Knittl, Zdeněk, with Kard, Paul G.: On some degenerate cases of thin film interference	185
Linfoot, E. H.: Focal tolerances and best focal setting for model photographic images with primary spherical aberration	233
McCree, K. J.: The saturation of spectral colours viewed in a small field	21
Marquet, Mme M., et Tsujiuchi, J.: Interpretation des aspects particuliers des images obtenues dans une expérience de déramage	267

	PAGE
Ments, M. v.: The sensitivity performance of the eye, in the presence of various limiting mechanisms of different origin	313
Palmer, D. A., with Burch, J. M.: Interferometric methods for the photographic production of large gratings	73
Palmer, D. A.: Measurement of the horizontal extent of Panum's Area by a method of constant stimuli	151
Parrent, George B., Jr., and Skinner, Thomas J.: Diffraction of partially coherent light by a plane aperture	93
Ramsay, J. V.: The optical performance of windows with axial temperature gradients	169
Ronchi, Laura, Russo, Vera, Toraldo di Francia, Giuliano, and Zaccagnini, Corrado: Scattering of evanescent waves by cylindrical structures	281
Rumsey, N. J.: A 'sky lens' for an auroral spectrograph	17
Russo, Vera, with Ronchi, Laura, Toraldo di Francia, Giuliano, and Zaccagnini, Corrado: Scattering of evanescent waves by cylindrical structures	281
Šantavý, Ivan: On the reversibility of light beams in conducting media	301
Scheggi, Anna Maria, with Caprioli, Luigi, and Toraldo di Francia, Giuliano: Approximate synthesis of a prescribed diffraction pattern by means of different aperture distributions	175
Simonsohn, Gerhard: Beugungsexperimente zur Vielstrahlinterferometrie	34
Simonsohn, Gerhard: Vielstrahlinterferenz als Hohlleiterproblem	49
Skinner, Thomas J., with Parrent, George B., Jr.: Diffraction of partially coherent light by a plane aperture	93
Stiles, W. S., with Enoch, J. M.: The colour change of monochromatic light with retinal angle of incidence	229
Tako, T., with Ishiguro, K.: An estimation of Smith-Purcell effect as the light source in the infra-red region	25
Toraldo di Francia, Giuliano, with Caprioli, Luigi, and Scheggi, Anna Maria: Approximate synthesis of a prescribed diffraction pattern by means of different aperture distributions	175
Toraldo di Francia, Giuliano, with Ronchi, Laura, Russo, Vera, and Zaccagnini, Corrado: Scattering of evanescent waves by cylindrical structures	281
Tsujiuchi, Jumpei: Restitution des images aberrantes par le filtrage des fréquences spatiales. III: Restitution de l'image prise avec un filtre à deux foyers	161
Tsujiuchi, J., et Marquet, Mme M.: Interpretation des aspects particuliers des images obtenues dans une expérience de détramage	267
Verheijen, F. J.: A simple after image method demonstrating the involuntary multi-directional eye movements during fixation	309
Wynne, C. G.: Thin-lens aberration theory	255
Zaccagnini, Corrado, with Ronchi, Laura, Russo, Vera, and Toraldo di Francia, Giuliano: Scattering of evanescent waves by cylindrical structures	281

*Printed by Taylor & Francis Ltd
Red Lion Court, Fleet Street, London, E.C.4*